Université Lille 1
UMR CNRS 8008 Laboratoire de Structure et Propriétés de l'Etat Solide

THÈSE

pour obenir le diplôme
d'Habilitation à Diriger les Recherches
Spécialité : Sciences Physiques
présentée et soutenue publiquement le 17 novembre 2009

par

Sébastien Merkel

Approche expérimentale de la plasticité sous haute pression

Devant la commission d'examen formée de :

Monsieur Patrick Cordier	Membre/ Directeur
Monsieur Philippe Gillet	Membre/ Président
Monsieur David Mainprice	Membre/ Rapporteur
Monsieur Paul McMillan	Membre/ Rapporteur
Monsieur Jean-Paul Montagner	Membre
Monsieur Bruno Reynard	Membre/ Rapporteur

Table des matières

Première partie

Introduction

Introduction

Les processus dynamiques qui opèrent à l'intérieur de la terre sont la cause de déformations à toutes les échelles, du micromètre à plusieurs centaines de kilomètres. L'étude de la plasticité des minéraux représente donc un enjeu majeur pour la connaissance de l'intérieur de la terre et de sa dynamique. Ces observations ont dirigé mes efforts de recherche, qui portent principalement sur l'étude des minéraux du manteau et noyau terrestre. En effet, ces enveloppes sont essentiellement constituées de roches solides et sont, pour le manteau en tous cas, le siège de vastes mouvements de convection. Je m'attache donc à étudier les mécanismes de plasticité des phases majeures qui constituent ces couches en utilisant, en particulier, les techniques d'expérimentation à très hautes pressions.

Le comportement plastique des matériaux dans les couches profondes de la terre est un phénomène complexe. A l'échelle microscopique, il faut établir et caractériser les mécanismes contrôlant la déformation. A l'échelle du polycristal, il faut évaluer les distributions de contraintes, de déformations, d'orientations de grains, et leurs effets sur les propriétés macroscopiques. Une fois ces propriétés établies, on peut enfin revenir à notre objet de départ, la terre, afin d'identifier le lien entre la dynamique, les champs de déformation, et l'anisotropie sismique.

Dans ce but, je participe activement au développement de nouvelles expériences de déformation sous haute pression et haute température. L'objectif est de pouvoir travailler directement sur les matériaux du manteau et noyau, en insistant sur une caractérisation in-situ par diffraction de rayons X. Ces travaux impliquent aussi un effort de modélisation numérique, principalement pour bien comprendre et caractériser le passage de l'échelle du grain à celle du polycristal.

Ces travaux ont donné lieu à de nombreux résultats concernant le comportement plastique des phases du manteau et noyau, le développement d'anisotropie sismique à la frontière noyau-manteau, et les problèmes d'analyses de contrainte dans des polycristaux déformés plastiquement. Ils seront décrits dans le premier chapitre. Dans le second chapitre de ce manuscrit, je décris les limites auxquelles j'ai pu être confronté et comment je compte les résoudre à l'avenir. Dans ce but, je développe maintenant une activité à la croisée de quatre axes principaux : expériences de déformation sur polycristaux sous haute pression et haute température, mesures de diffraction X tridimensionnelle pour l'étude individuelle de cristaux au sein de polycristaux, modélisation numérique du passage de l'échelle du grain au polycristal et, enfin, simulations d'anisotropie sismique. Le troisième chapitre, enfin, décrit mon implication dans l'encadrement et la gestion de la recherche.

A terme, j'espère être en mesure d'apporter une contribution importante à la compréhen-

sion du comportement plastique de polycristaux sous pression. Mes travaux restent toujours ancrés dans les sciences de la terre, avec d'importantes applications pour la compréhension des phénomènes dynamiques en profondeur. En revanche, l'application de ces développement ne se cantonne pas aux sciences de la terre et pourrait servir de point de départ pour explorer le comportement de phases dites "super-dures" ou encore de nouveaux alliages métalliques fabriqués sous pression, un domaine totalement vierge qui ne demande qu'à être exploré.

Deuxième partie

Description des travaux scientifiques

Chapitre 1

Travaux antérieurs

1.1 Plasticité des minéraux sous haute pression et anisotropie sismique

Les mesures d'anisotropie et tomographie sismique ainsi que leur couplage avec les modèles numériques de convection ont fait d'énormes progrès ces derniers temps, mais leur interprétation pour des profondeurs au delà de quelques centaines de kilomètres reste difficile du fait du manque de données minéralogiques correspondantes. En particulier, les propriétés physiques telles que l'élasticité, la plasticité et la rhéologie des matériaux composant les couches profondes de la terre sont encore mal contraintes. Modéliser les propriétés plastiques des enveloppes profondes de la terre comporte plusieurs étapes qui peuvent se décomposer sur trois échelles : l'échelle microscopique, l'échelle mésoscopique, et enfin l'échelle macroscopique.

Au niveau microscopique, il faut mesurer les propriétés plastiques de polycristaux représentatifs telles que l'évolution de la contrainte avec la déformation, des lois de relaxation, et des mécanismes de développement d'orientations préférentielles, ou encore l'influence des transitions de phase, in-situ, sous haute pression et haute température. Ces problèmes peuvent être étudiés par cinq techniques :

- expériences en presses multi-enclumes pour la caractérisation de lois de comportement et de développement d'orientations préférentielles in-situ aux pressions du manteau supérieur, haute température, en conditions contrôlées, et en particulier en découplant pression et déformation (Wang *et al.*, 2003),
- expériences en presses de types "Rotationnal Drickamer" pour des expériences aux conditions de la zone de transition (Yamazaki & Karato, 2001)
- investigations en microscopie électronique à transmission (MET) sur des échantillons trempés d'expériences sous haute pression et haute température pour l'identification directe des microstructures (Cordier, 2002)
- modélisations numériques de type ab-initio qui, une fois comparés aux expériences, permettent d'explorer les conditions inaccessibles expérimentalement (Cordier *et al.*, 2005),
- expériences en cellule diamant pour la caractérisation de lois de comportement et de développement d'orientations préférentielles in-situ jusqu'aux pressions de la frontière noyau-manteau et température ambiante (Merkel *et al.*, 2002b, page 57), et haute température

par application de chauffage externe (**?**, page 293) ou laser (Kunz *et al.*, 2007), ce qui est ma spécialité.

On trouvera une revue des travaux expérimentaux récents dans Raterron & Merkel (2009), page 315 de ce document.

Au niveau mésoscopique, les résultats obtenus dans l'expérience permettent de modéliser des phénomènes à l'échelle du grain tels que la dynamique des dislocations (Carrez *et al.*, 2005). Cette étape de modélisation numérique est indispensable pour comprendre le passage entre l'échelle microscopique, la maille cristalline, et l'échelle macroscopique, le polycristal, et implique aussi un saut d'échelle de complexité, en passant du défaut individuel au comportement collectif de défauts. De plus, elle permet d'aborder les problèmes de dépendance temporelle qui ne peuvent pas être résolus expérimentalement.

Au niveau macroscopique, une fois contraints les mécanismes de déformation aux conditions voulues, ceux ci peuvent être introduits dans des modèles plasticité polycristalline (Lebensohn & Tomé, 1993) pour des applications directes aux problèmes géophysiques. Ces simulations consistent à appliquer une déformation à un agrégat polycristallin par incréments. Au cours de la déformation plastique se développent des orientations préférentielles qui, combinées à une anisotropie élastique des matériaux présents, génèrent une anisotropie élastique de l'agrégat. Connaissant les propriétés des matériaux constituant l'agrégat et les orientations préférentielles développées, on peut remonter aux propriétés élastiques de l'agrégat comme les vitesses sismiques (Mainprice *et al.*, 2000). En incluant ces résultats dans des champs de pression, température et déformation obtenus à partir de simulations de convection on peut ainsi estimer l'anisotropie résultante (Merkel *et al.*, 2006a, 2007, pages 159, 163). Inversement, les mesures d'anisotropie sismique peuvent aussi servir à contraindre la géométrie des champs de déformation en profondeur, comme on le fait déjà pour la partie supérieur du manteau (Silver & Holt, 2002).

1.2 Technique expérimentale : la diffraction radiale

La diffraction radiale en cellule diamant est une technique expérimentale que j'utilise souvent. J'ai amplement participé à son développement et démontré son utilité pour les études de plasticité sous pression. Elle sera donc décrite et discutée en détail dans ce manuscrit. La particularité de cette technique est de réaliser une expérience de diffraction sur des polycristaux déformés en cellule diamant, avec un faisceau de rayons X incident orthogonal à l'axe des diamants, ce qui est contraire à la pratique usuelle.

C'est une technique particulièrement pertinente pour l'étude des propriétés plastiques de matériaux sous très haute pression. Dans cette géométrie, les rayons X incidents sont perpendiculaires à l'axe de compression et on étudie les distorsions des figures de diffraction ainsi que les variations d'intensités de diffraction avec l'orientation. Ces expériences, couplées à des modèles numériques de plasticité, permettent d'obtenir des informations importantes : mesure de la contrainte réelle appliquée à l'échantillon, identification et caractérisation des mécanismes contrôlant la déformation plastique, et quantification des hétérogénéités de contraintes locales. Ces résultats pouvant ensuite servir dans les modèles de calculs d'anisotropie du manteau et

noyau terrestres.

Cette technique, originellement développée pour l'étude de propriétés élastiques (Mao *et al.*, 1996, 1998; Singh *et al.*, 1998b), fut contestée car les modules élastiques obtenus diffèrent de ceux obtenus par d'autres techniques (Duffy *et al.*, 1999; Antonangeli *et al.*, 2006). En revanche, l'application de la diffraction radiale pour l'étude de propriétés plastiques de polycristaux s'est révélée particulièrement fructueuse (Wenk *et al.*, 2000; Merkel *et al.*, 2002b, 2006a; Wenk *et al.*, 2006; Merkel *et al.*, 2007).

Au cours des 10 dernières années, j'ai amplement contribué au développement et au rayonnement de cette méthode, en démontrant l'utilité des mesures de développement d'orientations préférentielles, en résolvant le problème de mesures de contraintes par diffraction, et en développant la technique expérimentale.

Les bases de la technique et la description de son application on été décrits dans l'article Merkel *et al.* (2002b), page 57, rédigé pendant ma thèse. Dans les années qui ont suivi, j'ai aussi amélioré le dispositif expérimental, avec une nouvelle technique de confinement pour l'échantillon (Merkel & Yagi, 2005, page 289) et des expériences à des températures de l'ordre de 1000°C (**?**, page 293).

1.2.1 Dispositif expérimental

Dans le cas des expériences en cellule diamant, la contrainte maximale est habituellement orientée selon l'axe de compression. Dans les études de plasticité et élasticité par diffraction, on cherche à étudier les variations des figures de diffraction en fonction de leur orientation par rapport à cet axe particulier. Cet objectif impose des expériences de diffraction dans une direction orthogonale à l'axe des diamants, ce qui est contraire à la pratique usuelle. En effet, la transparence du diamant a toujours encouragé les expériences utilisant des faisceaux incidents, réfléchis, ou diffractés au travers des diamants.

La géométrie radiale, développée par Kinsland & Bassett (1976, 1977), Funamori *et al.* (1994), et Mao *et al.* (1996), permet d'effectuer des mesures de diffraction de rayons X sur des échantillons dans des cellules à enclumes opposées avec le rayon incident passant au travers du joint. On étudie ainsi les variations des figures de diffraction en fonction de l'orientation des plans diffractant dans le champ de contrainte et de déformation (Figure 1.1). Ces expériences demandent des rayons X intenses, de haute énergie, et bien focalisés. Elles sont donc réalisées sur synchrotron.

Généralement, on fait l'hypothèse d'un champ de contraintes et de déformations axisymétrique autour de l'axe des enclumes. On cherche alors à déterminer l'angle ψ entre la normale au plan diffractant et la direction de compression. Dans le cas d'un montage en dispersion angulaire avec l'axe de symétrie perpendiculaire au faisceau incident, on calcule cet angle en utilisant la relation

$$\cos\psi = \cos\theta\cos\delta, \tag{1.1}$$

où δ est l'angle azimutal sur le détecteur et θ l'angle de diffraction.

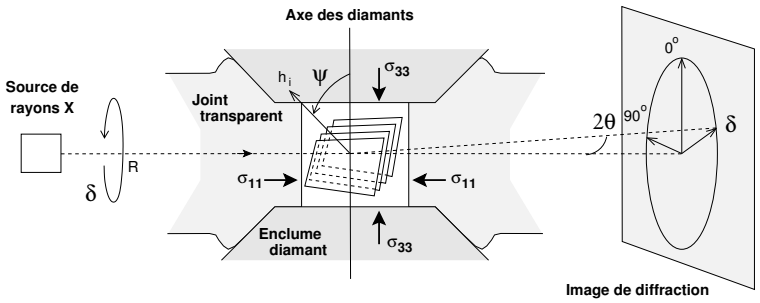

FIG. 1.1: Vue schématique d'une expérience de diffraction radiale utilisant un faisceau incident monochromatique. L'échantillon est confiné sous des contraintes non-hydrostatiques entre les deux enclumes de diamant. σ_{33} et σ_{11} sont respectivement la contrainte axiale imposée par les diamants et la contrainte radiale imposée par le joint. Un faisceau monochromatique passe au travers du joint, perpendiculairement à la direction de compression, et les données sont collectées sur un détecteur plan perpendiculaire au faisceau indicent. Les positions et intensités des lignes de diffraction sont analysées en fonction de l'angle azimutal δ, à partir duquel on peut calculer l'angle ψ entre la normale au plan diffractant et la direction de compression.

Il n'est pas absolument nécessaire de faire l'hypothèse de symétrie axiale. Les effets de contraintes non-axiales sur les mesures de distances inter-réticulaires peuvent être observés et interprétés (Merkel, 2006, page 235). De même, la symétrie de la déformation plastique appliquée peut être observée et vérifiée à l'aide des mesures d'orientations préférentielles et de l'algorithme E-WIMV disponible dans le logiciel MAUD (Miyagi *et al.*, 2006, page 115).

1.2.2 Contraintes techniques : les joints transparents

La diffraction radiale nécessite l'envoi du faisceau incident dans une direction perpendiculaire à l'axe de compression, soit au travers du joint de confinement. Plusieurs solutions ont été développées :

1. en retirant le joint et en plaçant uniquement l'échantillon entre les diamants (Kinsland & Bassett, 1976, 1977). L'énorme inconvénient de cette géométrie est de considérer dans une même mesure des portions d'échantillon se trouvant dans des conditions de contraintes très différentes. De plus, le domaine de pression accessible par cette technique est limité.
2. En perçant le joint selon deux orientations particulières (Funamori *et al.*, 1994), ce qui ne permet d'obtenir de mesures que pour ces deux orientations et n'est pas facilement applicable à la cellule diamant.
3. En utilisant un joint en mélange composite de bore amorphe et colle époxy, transparent aux rayons X (Mao *et al.*, 1996). Cette technique est efficace, permet d'obtenir des mesures sur tout l'espace d'orientations, mais l'utilisation de ce type de joint n'est pas aisée et est limitée en pression.
4. En utilisant un joint en béryllium durci (Hemley *et al.*, 1997). Cette méthode permet une mesure sur tout l'espace des orientations, supporte des pressions supérieures à 290 GPa, mais présente aussi des risques sanitaires pour le manipulateur. De plus, le signal dû au joint en béryllium est clairement visible et peut masquer celui de l'échantillon.

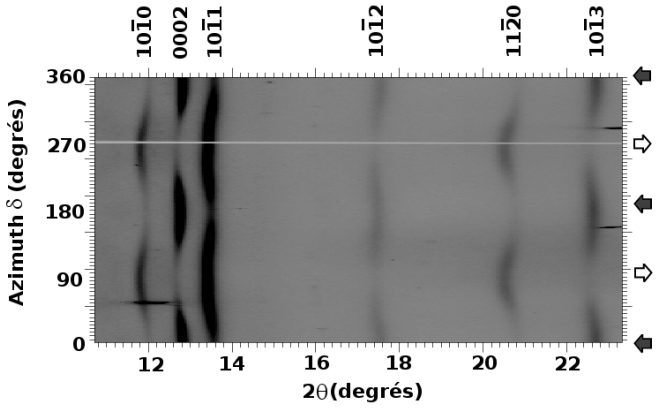

FIG. 1.2: Image de diffraction radiale déroulée pour un échantillon de cobalt hcp à 42,6 GPa dans un joint de kapton-bore-époxy (Merkel *et al.*, 2006b, page 255). Cette figure montre les figures de diffraction en fonction de l'angle 2θ et l'angle azimutal δ. Les variations sinusoïdales de positions de diffraction avec l'orientation sont liées à une déformation élastique. Les variations d'intensité de diffraction avec δ sont liées aux orientations préférentielles et la déformation plastique. Les flèches grises indiquent la direction de compression, les flèches blanches indiquent la direction de contrainte minimale.

5. En utilisant un cerclage en kapton autour d'un insert fait de bore amorphe et colle époxy (Merkel & Yagi, 2005, page 289). Cette technique est facile d'utilisation, permet d'obtenir des mesures sur tout l'espace d'orientations et donne un signal très propre (figure 1.2). En revanche, les pressions maximales atteintes avec cette technique sont de l'ordre de 60 GPa. De plus, le kapton perd ses propriétés mécaniques à des températures relativement peu élevées. Ces joints ne peuvent donc pas être utilisés dans des cellules avec chauffage externe. Enfin, cette technique n'est pas applicable aux échantillons liquides qui diffusent dans l'insert de bore-époxy.
6. En utilisant un cerclage en mica fluoré autour d'un insert fait de bore amorphe et colle époxy (**?**, page 293). Cette technique, en cours de développement, permet de travailler jusqu'à des pressions de 65 GPa et des températures de 1300 K. En revanche, le mica monocristallin laisse des tâches de diffraction d'intensité importante sur le détecteur plan.

A l'heure actuelle, les joints en béryllium restent donc l'unique solution pour des expériences sur des échantillons fluides ou des pressions supérieures à 60 GPa. Pour des expériences sur échantillons solides, à des pressions et températures inférieures à 60 GPa et 600 K, on devra choisir des joints en kapton-bore-époxy. Au delà de 600 K, les joints en mica fluoré, bore, et époxy sont la meilleure solution disponible. Ces deux dernières méthodes (joints en kapton-bore-époxy et joints en mica fluoré, bore, et époxy) sont les résultats de mes travaux et ont demandé plus d'effort qu'il n'y parait.

1.2.3 Analyse des images

La figure 1.2 montre un exemple de résultats obtenus en diffraction radiale. Elle doit être calibrée avec un standard pour la longueur d'onde, la distance échantillon-détecteur et l'orientation du détecteur. Après avoir été centrée, l'image est décomposée en secteurs azimutaux (en général

5°, 10° ou 15°). On étudie alors la variation des positions et intensités de pics de diffraction avec l'orientation.

1.3 Mesures de contraintes, orientations préférentielles, et applications géophysiques

1.3.1 Polycristaux et orientations préférentielles

L'orientation des cristaux qui constituent un polycristal n'est que rarement aléatoire, surtout en présence de déformation plastique, on parle alors d'orientations préférentielles ou de texture, ce qui a d'importantes implications sur les propriétés macroscopiques du matériau. Les orientations préférentielles sont généralement l'effet d'une déformation plastique et en particulier de l'action de mécanismes microscopiques comme le glissement de dislocations ou le maclage. Connaissant la texture d'un polycristal et les propriétés des cristaux qui le composent, il est possible de remonter aux caractéristiques globales du polycristal, telles les propriétés optiques, électriques ou élastiques (Kocks *et al.*, 1998).

Les orientations préférentielles sont représentées à l'aide de la fonction de distribution des orientations (Orientation Distribution Function, ou ODF). L'ODF sert à calculer les propriétés anisotropes des polycristaux. Pour chaque orientation, elle représente la probabilité de trouver un cristal ayant acquis cette orientation. Un agrégat sans orientation préférentielle aura une probabilité de un pour toutes les orientations. Pour un agrégat orienté, certaines orientations auront des probabilités supérieures à un et d'autres auront des probabilités inférieures à un.

En pratique, l'ODF peut être calculée à partir des variations d'intensité de diffraction avec l'orientation en utilisant des algorithmes tomographiques de type WIMV (Matthies & Vinel, 1982), dans le logiciel BEARTEX (Wenk *et al.*, 1998), ou encore dans le logiciel d'analyse Rietveld MAUD (Lutterotti *et al.*, 1999).

1.3.2 Application aux données de diffraction radiale

Les données de diffraction radiale sont parfaitement appropriées pour l'inversion d'ODF pour les polycristaux déformés en cellule diamant. Par exemple, la figure 1.3 présente les intensités de diffraction en fonction de l'angle ψ entre la normale au plan diffractant et la direction de compression pour un échantillon de $MgGeO_3$ dans la structure post-perovskite. Les données ont été mesurées in-situ à 130 GPa, en géométrie radiale, et en utilisant un joint en béryllium. On a ensuite utilisé l'algorithme WIMV pour extraire une ODF à partir de mesures pour les lignes de diffraction 020, 002, 022, 110, 112, et 130 en faisant l'hypothèse de symétrie de l'ODF autour de l'axe de compression. Le logiciel simule les intensités de diffraction pour une ODF donnée et utilise un processus itératif pour ajuster l'ODF aux données expérimentales. Dans ce cas, l'accord entre les données expérimentales et les données simulées est particulièrement bon.

On peut ensuite comparer les ODF obtenues expérimentalement aux résultats de plasticité polycristalline. En effet, le développement de texture dépend de la géométrie de déformation

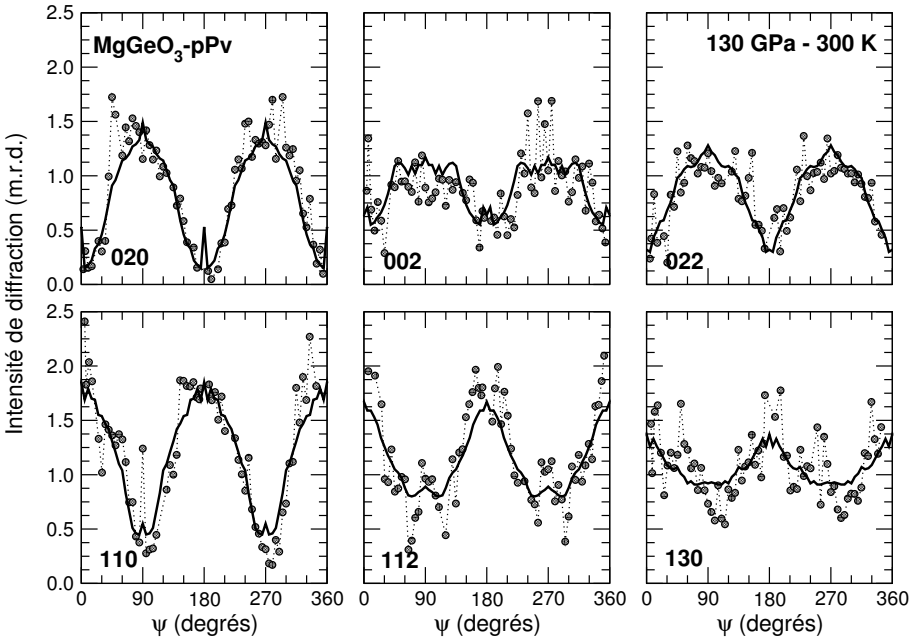

FIG. 1.3: Intensités de diffraction mesurées sur un échantillon de $MgGeO_3$ dans la structure post-perovskite après déformation en fonction de l'angle ψ (Merkel *et al.*, 2006a, page 159). Les cercles indiquent des intensités mesurées sur le détecteur, les lignes épaisses sont les intensités recalculées à partir de l'ODF, calculée à l'aide de l'algorithme WIMV. Les données présentées correspondent à une mesure in-situ à 130 GPa pour les lignes de diffraction 020, 002, 022, 110, 112, et 130 de $MgGeO_3$-pPv. L'échelle des données expérimentales à été ajustée sur celle des données recalculées, exprimées en m.r.d.

ainsi que des modes de déformation (systèmes de glissement, macles) activés dans le polycristal. Ainsi, une comparaison entre résultats expérimentaux et simulations permet d'identifier les modes activés et dominants au cours de l'expérience. En général, les simulations utilisent le code VPSC (Visco-Plastic Self-Consistent) développé par R. Lebensohn à Los Alamos (Lebensohn & Tomé, 1994). Dans ces simulations, on représente l'agrégat par un nombre discret d'orientations en y associant des fractions volumiques, choisies pour reproduire la texture initiale de l'agrégat. Chaque orientation est traitée comme une inclusion dans un milieu homogène, anisotrope, ayant les propriétés moyennes du polycristal. Avec la déformation, les orientations tournent pour accommoder la déformation plastique et génèrent donc une nouvelle texture. En appliquant différentes combinaisons de contraintes limites résolues (Critical Resolved Shear Stress, CRSS) pour les systèmes de glissement ou les macles, une simulation peut favoriser tel ou tel mécanisme. Ainsi, en déterminant les textures simulées se rapprochant le plus des textures mesurées expérimentalement, on peut déduire quels mécanismes ont été activés lors de l'expérience.

La figure 1.4, par exemple, montre les orientations déduites pour l'échantillon de $MgGeO_3$-pPv à 130 GPa et des résultats de calculs VPSC favorisant le glissement le long des plans (100), (010), (001) et une combinaison de (100) et (110). Il apparaît clairement que les simulations favorisant le glissement selon les plans (100), (110), ou une combinaison des deux sont les plus proches de celles mesurées expérimentalement. Dans ce cas, j'ai donc pu déduire que, dans les conditions de cette expérience, l'échantillon de $MgGeO_3$-pPv se déformait probablement par glissement le long de plans (100), (110), ou une combinaison des deux (Merkel *et al.*, 2006a,

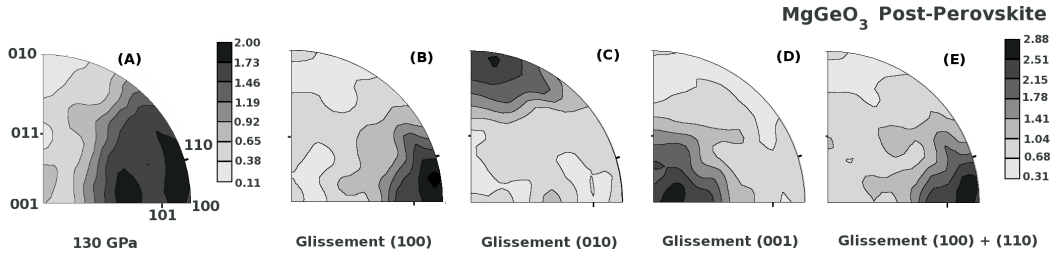

FIG. 1.4: Figures de pôle inverses illustrant les orientations préférentielles au sein du polycristal de $MgGeO_3$, déduites des mesures de la figure 1.3 (A), ou (B,C,D,E) simulées après une déformation de 20% en compression avec des modèles favorisant le glissement le long des plans (100), (010), (001) et une combinaison de (100) et (110). Projection "aire égale", contours linéaires exprimés en m.r.d.

page 159).

Cette technique a été appliquée avec succès sur de nombreux matériaux (voir Wenk *et al.* (2006), page 127, pour une revue exhaustive). Voici une liste des matériaux que j'ai pu étudier

- MgO et la magnésiowüstite : Merkel *et al.* (2002b), page 57, et Tommaseo *et al.* (2006), page 101,
- la perovskite $(Mg,Fe)SiO_3$: Merkel *et al.* (2003), page 77,
- le fer ϵ : Merkel *et al.* (2004), page 87,
- la perovskite calcique : Miyagi *et al.* (2006), page 115, et Miyagi *et al.* (2009), page 151,
- le cobalt : Merkel *et al.* (2006b), page 255,
- les post-perovskites $MgGeO_3$ (Merkel *et al.*, 2006a, page 159), $(Mg,Fe)SiO_3$ (Merkel *et al.*, 2007, page 163), et $CaIrO_3$ (Niwa *et al.*, 2007, page 143).

1.3.3 Mesures de contraintes

Les déformations élastiques supportées par l'échantillon apparaissent comme des variations sinusoïdales de distances inter-réticulaires en fonction de l'angle ψ. Les distances inter-réticulaires les plus faibles correspondent aux plans orientés perpendiculairement à l'axe de compression, les distances inter-réticulaires les plus importantes correspondent aux plans parallèles à l'axe de compression. L'interprétation de ces mesures est difficile et a donné lieu à de nombreux débats dans la littérature (Singh & Montagner, 1999; Weidner *et al.*, 2004; Antonangeli *et al.*, 2006; Merkel *et al.*, 2009; Karato, 2009). Je reviendrai sur ces aspect techniques dans la section 1.4, page 22.

Ces mesures sont importantes. En effet, elles permettent de quantifier la dureté et les lois de comportement mécanique des matériaux étudiés. En particulier, on peut s'intéresser aux mesures de viscosité des matériaux du manteau, ce qui est d'un intérêt primordial pour la compréhension des processus dynamiques contrôlant la convection mantellique.

Pour ces mesures, la cellule diamant présente quelques faiblesses. En effet, on ne peut pas contrôler le taux de déformation appliqué à l'échantillon et pression et déformations ne peuvent

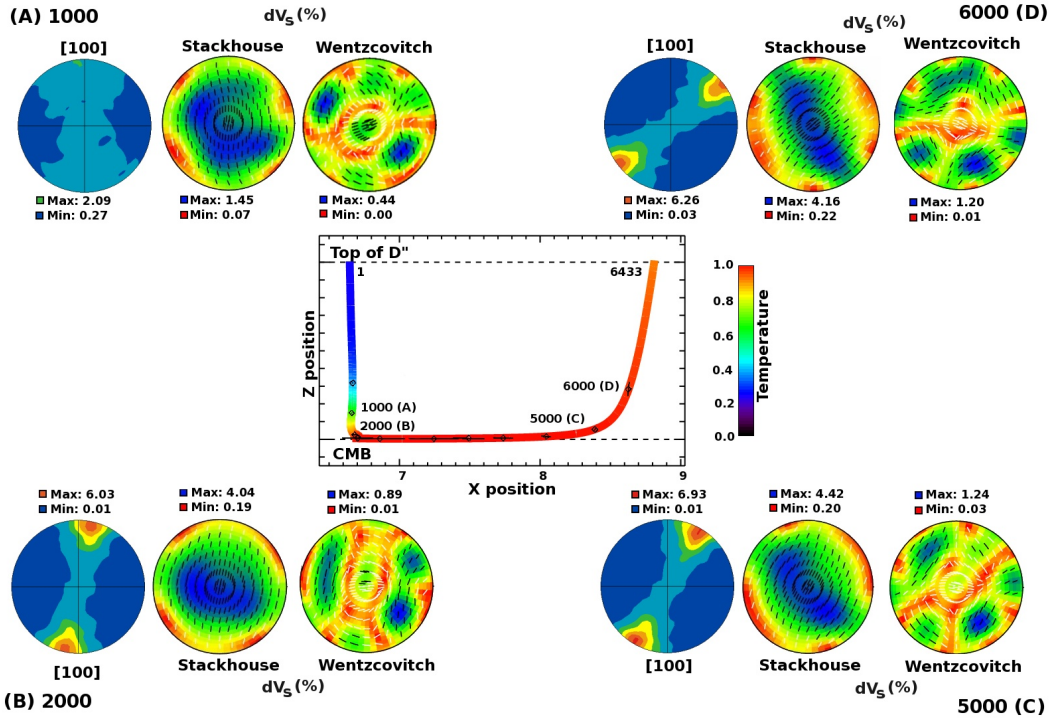

FIG. 1.5: Modélisation de température, déformation, texture, and biréfringence des ondes S dues à la post-perovskite dans D"(Merkel *et al.*, 2007, 163). Les températures sont normalisées pour avoir $T = 0$ à la surface de la terre et $T = 1$ à la frontière noyau-manteau. La figure centrale montre l'évolution de la déformation et de la température le long d'un traceur pris dans un mouvement de convection du manteau. Les figures (A), (B), (C), et (D) présentent des modèles d'orientations des axes [100] de la post-perovskite et de la biréfringence des ondes S calculés aux pas 1000, 2000, 5000, et 6000 indiqués sur la figure centrale. Les amplitudes de biréfringence des ondes S ont été calculées à partir des constantes élastiques de Wentzcovitch *et al.* (2006) et Stackhouse *et al.* (2005). Échelles linéaires, projections aires-égales. Les contours pour les orientations des axes [100] sont exprimés en m.r.d., ceux des biréfringence des ondes S en pourcentages. Les traits noirs et blancs indiquent les directions de polarisation rapides.

être découplées. En revanche, les presses de types D-DIA sont idéales pour ce type de mesure, en permettant de choisir le taux de déformation, la pression, et la température indépendemment.

Parmi mes contributions, on citera les travaux sur

- MgO : Merkel *et al.* (2002b), page 57,
- la perovskite $(Mg,Fe)SiO_3$: Merkel *et al.* (2003), page 77,
- la perovskite calcique : Miyagi *et al.* (2009), page 151,
- les serpentines : Hilairet *et al.* (2007), page 167.

1.3.4 Applications géophysiques

En dehors de la performance expérimentale et de l'obtention de données importantes sur les propriétés de matériaux, les mesures de diffraction radiale peuvent être appliquées à la compréhension et l'interprétation de données géophysiques telles que l'anisotropie sismique et les

mouvements de convection.

En 2006-2007, par exemple, je me suis intéressé aux propriétés de la phase post-perovskite. Cette phase, découverte vers 130 GPa d'une transformation de Mg-Pv vers une phase plus dense de structure $CaIrO_3$ a sans doute représenté la découverte la plus marquante de ces dernières années (Murakami *et al.*, 2004; Oganov & Ono, 2004). L'existence de cette phase éclaire d'un jour nouveau les caractéristiques très particulières (hétérogénéité, anisotropie sismique) de la frontière noyau-manteau, la couche D" (Hirose *et al.*, 2007). Les pressions associées à cette transformation étant très élevées, beaucoup d'études se tournent vers des composés isostructuraux stables à plus basses pressions comme $MgGeO_3$ (pour lequel la phase post-perovskite apparaît dès 60 GPa, Hirose *et al.* (2005)), voire $CaIrO_3$ qui présente cette structure à pression ambiante.

Après avoir effectué des expériences sur la phase $MgGeO_3$ (Merkel *et al.*, 2006a, page 159), j'ai réussi la première expérience de déformation de Mg-pPv en cellule diamants (Merkel *et al.*, 2007, page 163). Dans ces expériences, nous avons montré que les orientations préférentielles obtenues expérimentalement correspondaient à un plan de glissement dominant de type (100) ou (110). Nous avons ensuite testé l'influence d'un plan de glissement dominant de type (100) ou (110) dans la post-perovskite sur l'anisotropie de la couche D". Nous avons ainsi montré que les anisotropies calculées pour de la post-perovskite déformée en cisaillement par les mouvements de convection dans le manteau et dans D" ne correspondaient pas aux observations sismologiques (Figure 1.5). Ces résultats soulèvent de nombreuses questions, concernant la validité des mesures de plasticité en cellule diamant, la géométrie du champ de déformation dans D", ou encore l'origine de l'anisotropie sismique mesurée dans D", qui sont le sujet de recherches très actives.

Parmi mes travaux, les résultats ayant donné lieu à des interprétations géophysiques les plus avancées sont

- les mesures de développement d'orientations préférentielles dans les post-perovskites $MgGeO_3$ (Merkel *et al.*, 2006a, page 159) et $(Mg,Fe)SiO_3$ (Merkel *et al.*, 2007, page 163), et leurs implications pour le problème de l'anisotropie de D",
- les mesures de lois de comportement de la serpentine (Hilairet *et al.*, 2007, page 167), et l'influence de ce matériau sur la répartition géographique des séismes.

1.4 Le problème des constantes élastiques

1.4.1 Introduction

La diffraction radiale fut originellement développée pour l'étude de propriétés élastiques (Mao *et al.*, 1996, 1998; Singh *et al.*, 1998b) et fut contestée car les modules élastiques obtenus différaient de ceux obtenus par d'autres techniques (Duffy *et al.*, 1999; Singh & Montagner, 1999; Weidner *et al.*, 2004; Antonangeli *et al.*, 2006). J'ai été impliqué très tôt dans ce problème, en comparant les modules élastiques déduits par spectroscopie Raman et diffraction radiale pour le fer ϵ (Merkel *et al.*, 2000; Matthies *et al.*, 2001a; Merkel *et al.*, 2005, pages 173, 177, et 199) et en effectuant des mesures sur la pyrite (Merkel *et al.*, 2002a, page 189) et MgO (Merkel *et al.*, 2002b, page 57).

Fin 2002, nous avons lancé, avec Guillaume Fiquet et Daniele Antonangeli, un programme d'étude sur le cobalt, matériau de structure hcp, aux propriétés proches de celles du fer ϵ, et pour lequel nous disposons de monocristaux. L'objectif de ces travaux était de mesurer les modules élastiques de ce matériau, sous pression, en associant les différentes techniques disponibles et, éventuellement, de résoudre les problèmes associés.

Comme préssenti, les contraintes et modules élastiques déduits par diffraction radiale étaient irréalistes (Merkel *et al.*, 2006b; Antonangeli *et al.*, 2006, pages 255 et 249). Ce résultat impliquait que toutes les mesures de contraintes par diffraction étaient erronées, ce qui posait de nombreux problèmes pour l'interprétation de toute expérience de déformation sous haute pression. J'ai donc passé plusieurs années à résoudre ce problème en parvenant, après une rencontre décisive avec C. Tomé de Los Alamos, à la solution en 2009 (Merkel *et al.*, 2009, page 263). Ces travaux sont décrits ci-dessous.

1.4.2 Observations expérimentales

Les déformations élastiques supportées par un échantillon étudié en diffraction radiale apparaissent comme des variations sinusoïdales de distances inter-réticulaires en fonction de l'angle ψ. Les distances inter-réticulaires les plus faibles correspondent aux plans orientés perpendiculairement à l'axe de compression, les distances inter-réticulaires les plus importantes correspondent aux plans parallèles à l'axe de compression.

De nombreuses expériences (Mao *et al.*, 1996; Singh *et al.*, 1998b; Duffy *et al.*, 1999; Merkel *et al.*, 2002b; Kavner & Duffy, 2003; Speziale *et al.*, 2006; Kavner, 2007; Weinberger *et al.*, 2008) ont montré que les distances inter-réticulaires mesurées en diffraction radiale dépendent pratiquement linéairement de la quantité $(1-3\cos^2\psi)$. De plus, les valeurs de distances inter-réticulaires mesurées à $\psi = 54.7°$, soit $1-3\cos^2\psi = 0$, correspondent à celles attendues lors de mesures en conditions hydrostatiques. On introduit donc le paramètre Q tel que

$$\begin{aligned} \epsilon(hkl,\psi) &= \frac{d_m(hkl,\psi) - d_P(hkl)}{d_P(hkl)} \\ &= Q(hkl)\left(1-3\cos^2\psi\right), \end{aligned} \tag{1.2}$$

où $d_m(hkl,\psi)$ est la distance inter-réticulaire mesurée pour la ligne d'indice hkl à l'angle ψ, $d_P(hkl)$ est la distance inter-réticulaire de la ligne hkl sous la pression hydrostatique P, et $Q(hkl)$ est le paramètre de déformation de réseau.

La valeur de $Q(hkl)$ indique l'amplitude des déformations élastiques subies par la ligne de diffraction d'indice hkl. Elle est liée à la contrainte différentielle t appliquée à l'échantillon, aux coefficients élastiques du matériau C_{ijkl} et à la déformation plastique subie par l'échantillon.

La figure 1.6, par exemple, montre les distances inter-réticulaires extraites de la figure 1.2. Les déformations mesurées $\epsilon = (d_m - d_P)/d_P$ sont pratiquement linéaires avec $(1-3\cos^2\psi)$. En première approximation, la représentation des données par l'équation 1.2 est donc pertinente.

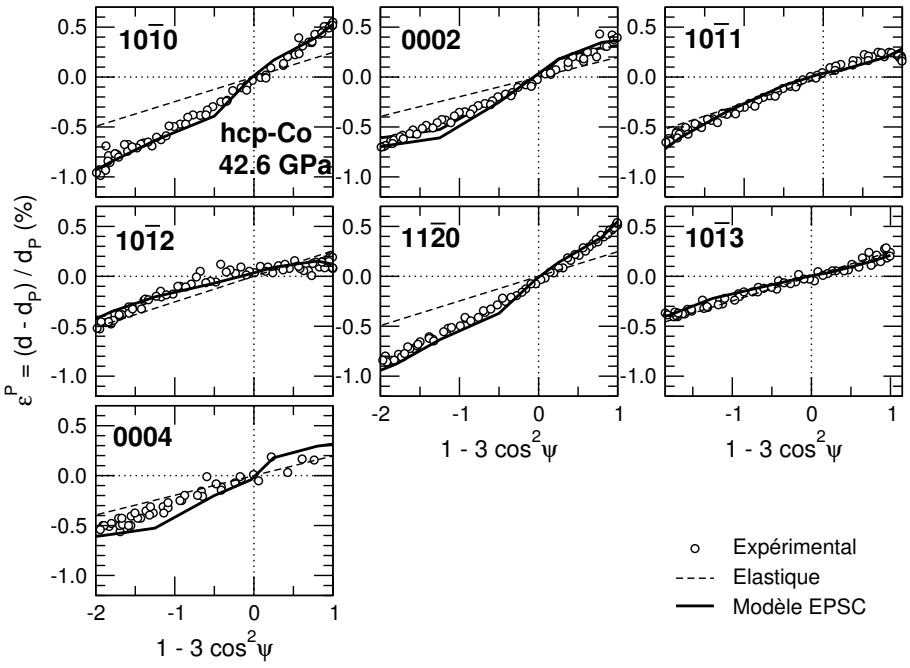

FIG. 1.6: Distances inter-réticulaires mesurées dans un échantillon de cobalt hcp à 42,6 GPa (Merkel *et al.*, 2006b, page 255). Les cercles sont les données expérimentales. Les lignes brisées sont déduites de la théorie élastique négligeant les effets d'orientations préférentielles (Singh *et al.*, 1998a), en utilisant une contrainte différentielle de 4 GPa et des coefficients élastiques connus (Antonangeli *et al.*, 2004). Les lignes continues sont les résultats de modèles élasto plastiques récents (Merkel *et al.*, 2009, page 263).

1.4.3 Le modèle élastique

La géométrie de la cellule diamant définit un champ de contrainte axial, avec l'axe de contrainte maximale aligné avec la direction de compression. Le tenseur des contraintes peut donc se décomposer en

$$\sigma = \begin{bmatrix} P & 0 & 0 \\ 0 & P & 0 \\ 0 & 0 & P \end{bmatrix} + \begin{bmatrix} -\frac{t}{3} & 0 & 0 \\ 0 & -\frac{t}{3} & 0 \\ 0 & 0 & 2\frac{t}{3} \end{bmatrix}, \tag{1.3}$$

où P est la pression hydrostatique et t la contrainte différentielle.

Pour un polycristal, un pic de diffraction est la somme des contributions de tous les cristaux orientés en condition de diffraction, c.a.d., ceux pour qui la normale au plan (hkl) est parallèle au vecteur de diffraction. Les distances inter-réticulaires correspondantes dépendent du champ de contrainte local autour de chacun de ces cristaux et de leurs propriétés élastiques ; la distance mesurée par diffraction est la moyenne arithmétique des valeurs de distances inter-réticulaires de ces grains.

Des théories ont été développées pour lier les coefficients élastiques des cristaux, C_{ijkl}, la contrainte appliquée t, et les distances mesurées. Ces modèles reposent sur la théorie de l'élasticité et font l'hypothèse d'une continuité au sein du polycristal, soit de contrainte, soit de déformation.

De plus si l'on suppose que le polycristal ne présente pas d'orientations préférentielles, on trouve que les distances inter-réticulaires suivent l'équation 1.2 ainsi qu'une relation entre les paramètres Q, la contrainte différentielle, et les coefficients élastiques (Singh *et al.*, 1998a). On peut aussi démontrer que

$$t \approx 6G < Q(hkl) >, \tag{1.4}$$

où G est le module de cisaillement de l'agrégat.

Des théories incluant les effets d'orientations préférentielles existent aussi (Matthies *et al.*, 2001b). Dans ce cas, les distances mesurées ne sont pas linéaires en $(1 - 3\cos^2\psi)$, mais on peut toujours établir une relation entre les coefficients élastiques, la contrainte appliquée, et les distance mesurées. En revanche, les effets d'orientations préférentielles sont particulièrement faibles et peuvent être difficiles à discerner expérimentalement (Matthies *et al.*, 2001a; Merkel & Yagi, 2006, pages 177 et 221).

1.4.4 Limitations du modèle élastique

Très rapidement, ces théories ont été utilisées pour déduire des coefficients élastiques sous haute pression, en particulier pour un matériau comme la phase ϵ du fer. Cette phase est considérée comme le composant principal de la graine du noyau terrestre. De plus, les métaux hexagonaux sont des matériaux modèles permettant de tester les techniques expérimentales et numériques les plus avancées. Rapidement, il est apparu que le modèle élastique couplé à la diffraction radiale donnait des résultats incohérents (Singh *et al.*, 1998b; Mao *et al.*, 1998; Merkel *et al.*, 2005; Mao *et al.*, 2008).

Ce résultat fut confirmé par nos travaux sur le cobalt qui ont démontré que les coefficients élastiques obtenus par diffraction radiale sont en désaccord avec ceux obtenus par une multitude de techniques (Steinle-Neumann *et al.*, 1999; Antonangeli *et al.*, 2004; Goncharov *et al.*, 2004; Antonangeli *et al.*, 2005, 2006; Merkel *et al.*, 2006b; Crowhurst *et al.*, 2006).

Les limitations de la théorie élastique peuvent apparaître sous plusieurs formes. Si l'on cherche à étudier les propriétés élastiques, les coefficients obtenus sont faux, et de plusieurs ordres de grandeur. Dans les métaux hexagonaux, cette erreur apparaît sous la forme caractéristique de cloche pour la variation de vitesse de propagation des ondes de compression en fonction de l'angle avec l'axe c (Antonangeli *et al.*, 2006, page 249, figures 1 et 2). Cette théorie est aussi beaucoup utilisée pour les mesures de contraintes par diffraction. Dans ce cas, les limites du modèle élastique apparaissent par des mesures de contraintes très dépendantes du plan considéré (Weidner *et al.*, 2004; Merkel *et al.*, 2006b, page 255).

La figure 1.6, par exemple, montre les prévisions du modèle élastique pour un échantillon de cobalt à une pression de 42,6 GPa et une contrainte différentielle de 4 GPa. Ces prévisions sont en accord avec les mesures sur $10\bar{1}1$ ou $10\bar{1}3$ mais sous-estiment largement les variations de distances inter-réticulaires pour $10\bar{1}0$ ou 0002. Les contraintes déduites du modèle élastique dépendront donc de la ligne de diffraction considérée.

1.4.5 Prise en compte de la plasticité

Les limitations du modèle élastique peuvent être résolues par l'utilisation de modèles de type élasto-plastique, ce qui a été démontré par des travaux sur MgO (Weidner *et al.*, 2004; Li *et al.*, 2004), le quartz (Burnley & Zhang, 2008), et le cobalt (Merkel *et al.*, 2009, page 263).

Comme les modèles VPSC, un modèle élasto-plastique (Elasto-Plastic Self Consistent, EPSC) représente l'agrégat par un nombre discret d'orientations en y associant des fractions volumiques, choisies pour reproduire la texture initiale de l'agrégat. Le modèle EPSC traite chaque orientation comme une inclusion ellipsoïdale élasto-plastique plongée dans un milieu effectif, anisotrope, caractéristique de l'agrégat. Les conditions aux limites (contrainte, déformation) sont supportées en moyenne dans le polycristal par les déformations plastiques et élastiques au sein de chacun des grains. De tels modèles peuvent ainsi prendre en compte le fait que certains grains sont dans des orientations plus favorables à la déformation plastique. Ces grains ont tendance à se déformer en premier, en diminuant la contrainte locale, et en transférant la contrainte moyenne sur les grains dans les orientations plus "dures" qui gardent un comportement élastique plus longtemps.

Ces modèles utilisent des valeurs connues de coefficients élastiques, un champs de déformation moyen appliqué à l'échantillon, et les contraintes limites résolues (CRSS) associées à chacun des mécanismes de déformation. Les déformations simulées à l'échelle microscopique sont comparées aux observations expérimentales en identifiant, dans le modèle, les orientations contribuant à un signal de diffraction et en calculant la distance inter-réticulaire moyenne correspondante.

Dans le cas du cobalt, j'ai ainsi été capable d'interpréter complètement les mesures effectuées précédemment (Merkel *et al.*, 2009, page 263). Par exemple, la figure 1.7 présente la distribution de contrainte obtenue pour un échantillon de cobalt après une déformation axiale ϵ_{33} moyenne de 17%, tout en conservant $\epsilon_{11} = \epsilon_{22} = 0$, soit une pression de 46,2 GPa. Ces calculs ont été effectués pour deux modèles de plasticité, l'un favorisant les glissements basal, prismatique et pyramidal $<c+a>$, l'autre favorisant les glissements basal et prismatique ainsi que des macles $\{2\overline{1}\overline{1}2\}$.

Les contraintes latérales $(\sigma_{22} - \sigma_{11})$ ont une distribution centrée sur 0 GPa, mais certains grains sont soumis à des contraintes latérales de l'ordre de 2 GPa, soit l'ordre de grandeur de la contrainte différentielle moyenne. Les contraintes différentielles $t = \sigma_{33} - (\sigma_{11} + \sigma_{22})$ ont une distribution bi-modale dont la moyenne correspond à la contrainte différentielle moyenne dans le polycristal. Deux familles de grains (ou orientations) peuvent être identifiées : les orientations "molles" et les orientations "dures". Les orientations "molles" sont favorables à la déformation plastique et ont une contrainte différentielle relativement faible. Les orientations "dures" sont peu favorables à la déformation plastique et ont une contrainte différentielle relativement élevée.

La déformation plastique induit donc une forte hétérogénéité des contraintes locales au sein de l'échantillon. Les modèles élastiques négligent complètement ce phénomène et reposent toujours sur des hypothèses de contrainte ou déformation moyenne. Comme le montre la figure 1.7, ces concepts ne sont plus pertinents pour des polycristaux ayant subi une déformation plastique, ce qui explique les résultats étonnants obtenus précédemment.

Les résultats des modèles EPSC sont importants. En effet, ils permettent d'obtenir une mesure

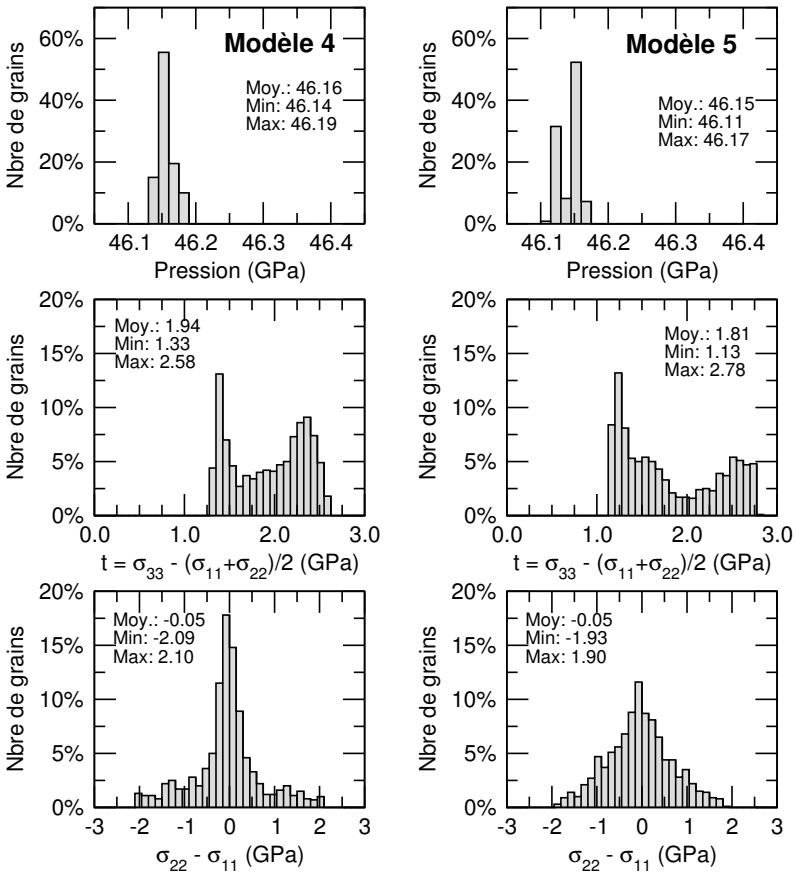

FIG. 1.7: Histogrammes des distributions de contrainte dans les grains composant un échantillon de cobalt déformé à 46,2 GPa (Merkel *et al.*, 2009, page 263). Ces résultats ont été obtenus à l'aide de modèles élasto-plastiques incluant le glissement basal, prismatique, ainsi que le système de glissement pyramidal <*c*+*a*> (Modèle 4) ou des macles $\{2\bar{1}\bar{1}2\}$ (Modèle 5).

de la contrainte réelle appliquée à l'échantillon, ce qui est un paramètre critique dans toutes les expériences de déformation. De plus, la comparaison de mesures de distances inter-réticulaires en diffraction radiale et de modèles EPSC permet une identification des mécanismes contrôlant la déformation plastique plus fine que celle obtenue par analyses d'orientations préférentielles. Dans le cas du cobalt par exemple, nous avons non seulement identifié les mécanismes de déformation, mais aussi la valeur de leurs contraintes limites résolues, en GPa, ainsi que leurs coefficients de durcissement (Merkel *et al.*, 2009, page 263).

Chapitre 2

Évolution thématique

2.1 Limites des travaux réalisés

Les travaux que j'ai réalisés ces dernières années ont permis de belles avancées dans la compréhension du comportement plastique de matériaux sous haute pression et de l'anisotropie sismique en profondeur. En revanche, certains de ces projets atteignent leurs limites. Voici celles que j'ai pu identifier :

i) absence de température dans les expériences de déformation en cellule diamant,
ii) absence d'identification directe et in-situ de mécanismes de déformation,
iii) incertitudes dans les paramètres utilisés dans la modélisation d'anisotropie.

Jusqu'en 2007, toutes les expériences de déformation en cellule diamant ont été effectuées à température ambiante. C'est un défaut majeur de la technique. En effet, les mécanismes de plasticité sont très sensibles à la température. Contrairement aux études de diagramme de phase, pour lesquelles le paramètre thermodynamique primordial est la pression, la température joue un rôle prépondérant sur l'activation de mécanismes plastiques. Pour résoudre ce problème, j'ai donc engagé le développement d'expériences de déformation à haute température (section 2.2, page 29). La technique est en place et devrait porter ses fruits dans les années à venir.

Dans toutes les expériences de déformation sous pression (cellule diamant, presses D-DIA, RDA...), l'identification des mécanismes activés est indirecte : mesure de texture, modélisation élasto-plastique... Ceci pose problème. En effet, les mécanismes de déformation, et en particulier les plans et directions de glissement, doivent être configurés et testés manuellement et les solutions ne sont pas uniques. De plus, dans les expériences mesurant les orientations préférentielles, certaines textures peuvent être formées lors de la synthèse du matériau et l'effet des mécanismes plastiques difficiles à discerner.

Pour les matériaux stables à pression ambiante, on utilise la microscopie électronique en transmission. On peut alors observer directement les mécanismes microscopiques (macles, dislocations...). En revanche, pour les matériaux qui ne peuvent être ramenés à pression ambiante, nous ne disposons pas de solution. Depuis 2008, j'ai donc engagé un programme de diffraction X 3D et d'analyses de profils de pics pour y remédier. Ces travaux sont en cours et brièvement décrits en section 2.3, page 30.

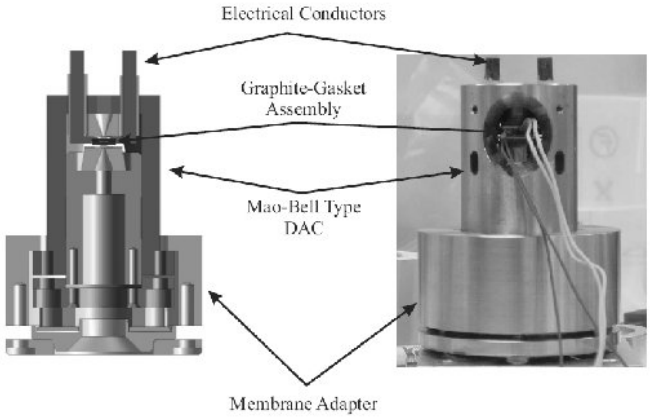

FIG. 2.1: Image de la nouvelle cellule diamant pour diffraction radiale à haute température. Cette cellule, construite en inconel, permet de déformer des échantillons in-situ sur une gamme de pression et température 0-65 GPa et 300-1300 K. Le chauffage est effectué grâce à un four en graphite disposé autour de l'échantillon, la pression est contrôlée à distance en jouant sur une membrane, et l'oxydation des diamants et de la cellule ralentie en maintenant l'ensemble sous un flux de mélange Ar-H.

Enfin, l'application de mes mesures aux problématiques d'anisotropie sismique requiert systématiquement l'utilisation de modèles de plasticité polycristalline de type VPSC. Les paramètres principaux de ces modèles sont le champs de déformation et les mécanismes de plasticité à activer. Dans les expériences, les champ de déformation sont simples et le système de déformation le plus actif domine l'évolution de la texture. Les systèmes de glissement secondaires sont difficiles à identifier. Dans un contexte géophysique en revanche, les champs de déformation deviennent complexes ; les mécanismes de déformation secondaire peuvent influencer la texture, et donc l'anisotropie sismique simulée. Je présenterai mes idées pour résoudre ce problème dans la section 2.5, page 32.

2.2 Diffraction radiale à haute pression et haute température

Depuis 2006, j'ai engagé une collaboration avec Peter Liermann au synchrotron APS (USA), maintenant au synchrotron DESY à Hambourg, ainsi que Hans-Rudolf Wenk et Lowell Miyagi à Berkeley, pour surmonter l'une des plus grandes limitations des expériences de déformation en cellule diamant : l'impossibilité de combiner pression, déformation, et haute température. Nous avons donc dessiné un nouveau type de cellule diamant et de méthode de chauffage de l'échantillon permettant de réaliser des expériences sur des gammes de pression 0-65 GPa et température 300-1300 K. Le développement de ces expériences a pris du temps et nécessité plusieurs séances de test sur synchrotron. Finalement, en février 2008, novembre 2008, et août 2009, nous avons pu réaliser les premières expériences couronnées de succès, sur les phases α, γ, et ϵ du fer et sur MgO. Les résultats de ces expériences sont toujours en cours d'analyse et l'article décrivant le protocole expérimental est sous presse (**?**, page 293).

La figure 2.2 montre les résultats préliminaires obtenus sur les phases α, γ, et ϵ du fer. Elle

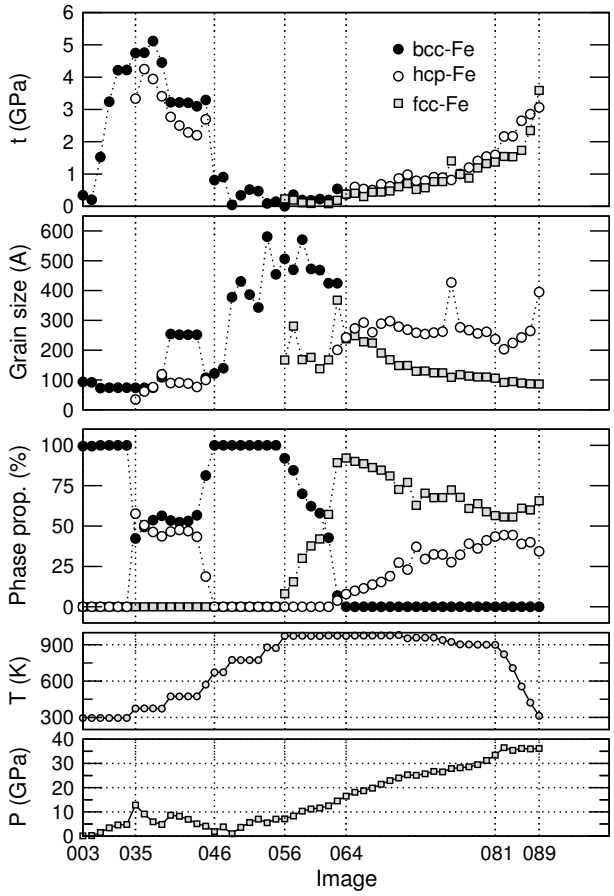

FIG. 2.2: Résultats des expériences de diffraction radiale à haute température sur le fer : contrainte différentielle t, en GPa, taille de grain moyenne, en Å, proportions des phase α, γ, et ϵ, température, en K, et pression, en GPa, en fonction du numéro de l'image.

démontre notre capacité à mesurer des contraintes, tailles de grains, et proportions entre phases dans des échantillons déformés plastiquement à plus de 900 K entre 0 et 35 GPa. Nous disposons aussi de mesures d'orientations préférentielles qui restent à interpréter.

Ces travaux ouvrent la voie à l'étude des mécanismes de déformation plastique de polycristaux sur une gamme 300-1300 K et 0-65 GPa. L'étude de propriétés de minéraux du manteau comme la perovskite $(Mg,Fe)SiO_3$ et la perovskite calcique est à portée de main et nous fournira, j'en suis sûr, multitudes de résultats importants.

2.3 Diffraction X-3D et densités de dislocations

Les techniques de diffraction radiale sont utiles pour l'étude de comportement de polycristaux mais elles souffrent de plusieurs inconvénients comme

i) une faible déformation appliquée à des pressions supérieures à 50 GPa, et donc des textures faibles, difficiles à interpréter, et susceptibles d'être affectées par les étapes de synthèse d'échantillons,
ii) l'impossibilité de caractériser directement les mécanismes de déformation.

En 2008, j'ai donc engagé un programme important pour la caractérisation directe de dislocations dans les minéraux, in-situ et sous haute pression, en collaboration avec P. Cordier

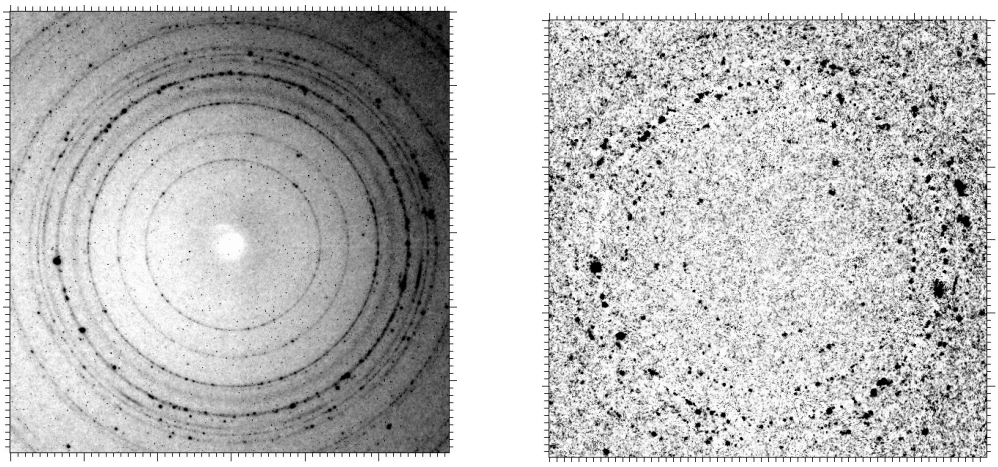

FIG. 2.3: Image de diffraction obtenue lors d'expériences de diffraction X - 3D sur un échantillon de post-perovskite $MgGeO_3$ à environ 80 GPa. L'image de droite est brute. L'image de gauche a été obtenue en retirant le bruit de fonds et le signal du à la partie poudre de l'échantillon et ne laisse apparaître que les taches de diffraction des plus gros grains.

du laboratoire et T. Ungár de l'université Eötvös à Budapest. Ce projet est financé par une ANR Jeunes Chercheurs (DiUP, Dislocations Under Pressure). Ces études sont basées sur les techniques de diffraction X-3D dans lesquelles on cherche à caractériser des propriétés de monocristaux au sein d'échantillons polycristallins (Margulies *et al.*, 2001). Ici, nous cherchons à y observer des dislocations. En effet, les dislocations induisent une distorsion de structure résultant en un élargissement des pics de Bragg. Cet effet peut être déconvolué sur les images de diffractions obtenues sur monocristaux (Ungár & Borbély, 1996). En utilisant cette technique, on peut mesurer les caractéristiques des dislocations présentes dans le matériau ainsi que leurs densités, ce qui a déjà été réalisé sur la perovskite, par exemple (Cordier *et al.*, 2004). Dans ce projet, nous combinons les études de diffraction X -3D à l'ESRF et les techniques d'extraction de densités de dislocations de T. Ungár pour étudier les dislocations dans les minéraux du manteau directement, in-situ, sous pression, sans synthèse de monocristaux, ni trempe d'échantillon vers les conditions ambiantes de pression.

J'ai donc engagé une étudiante en thèse, C. Nisr, pour y travailler. Nous avons réalisé deux campagnes d'expériences à l'ESRF et deux voyages à Budapest dans le laboratoire de T. Ungár pour nous former aux techniques d'extraction de densités de dislocations par diffraction. Après un an de travaux, nous sommes en mesure de retrouver des figures de diffraction de monocristaux dans le signal expérimental en utilisant les algorithmes de l'ESRF et débutons l'analyse de densités de dislocations. Ce projet combine trois difficultés : expérimentation sous haute pression, diffraction X - 3D, et extraction de densités de dislocations. Ces techniques n'ont jamais été combinées par le passé. A terme, je pense être en mesure de décrire avec précision les dislocations présentes dans certains minéraux du manteau, ce qui sera très utile à la compréhension et modélisation des mouvements de convection et du développement d'anisotropie sismique dans le manteau. Ces techniques pourront aussi être appliquées à d'autres domaines, et en particulier en sciences des matériaux pour l'étude des propriétés de phases ultra-dures.

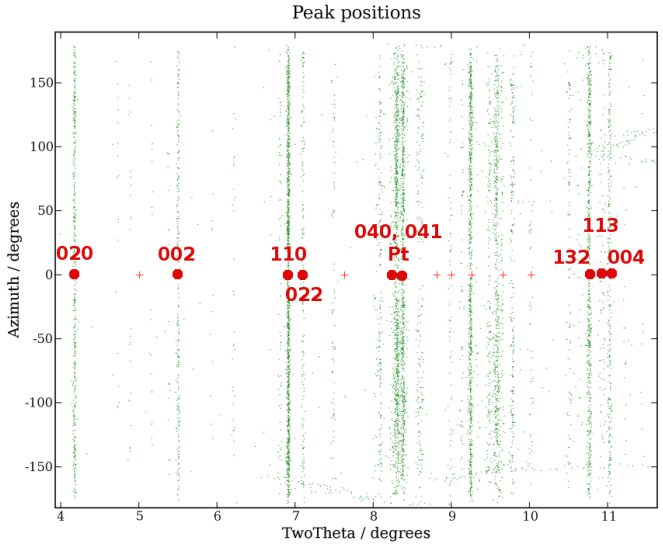

FIG. 2.4: Positions de 12000 taches de diffraction de grains de $MgGeO_3$ extraites de 90 images filtrées. Ces taches sont utilisées pour la recherche et l'indexation de signal de type monocristal pour quelques grains de l'échantillon.

2.4 Installation d'une presse de déformation D-DIA à l'ESRF

L'installation d'une nouvelle presse multi-enclumes équipée d'un système de déformation D-DIA sur la ligne ID06 de l'ESRF ouvre de nouvelles perspectives. Cet instrument nous permettra de mesurer des lois de comportement et des développements de textures dans des polycristaux, in-situ, dans les conditions du manteau supérieur.

Avec P. Raterron, du laboratoire, nous avons donc lancé un projet d'étude des propriétés plastiques de l'olivine sous haute pression et haute température. Ce projet combinera mon expérience en analyses de données de contraintes et d'orientations préférentielles, de modélisations élasto- et visco-plastiques, et celle de P. Raterron pour l'utilisation de la D-DIA. Ce projet est dans l'attente de l'installation de la presse (Janvier 2010) et du recrutement d'un étudiant en thèse et d'un post-doc, prévus pour fin 2009.

2.5 Comportement de polycristaux et modélisation d'anisotropie

Pour comprendre le comportement de polycristaux, dans les expériences de déformation ou dans un contexte géophysique, il faut faire appel aux modèles de plasticité polycristalline comme les modèles EPSC ou VPSC.

Du point de vue expérimental, ils interviennent pour

- la simulation et l'interprétation des textures mesurées (section 1.3.2, page 18)
- la simulation et l'interprétation des variations de distances inter-réticulaires mesurées (section 1.4.5, page 26).

Pour une application géophysique en revanche, on s'intéresse surtout aux simulations d'orienta-

tions préférentielles qui permettent ensuite de simuler des mesures d'anisotropie.

Hors, il apparaît que les textures expérimentales, mesurées en compression, ne permettent pas toujours d'obtenir toutes les informations voulues. En particulier, dans les structures à basse symétrie, le système le plus actif domine complètement l'évolution de la texture et il est très difficile d'obtenir des informations sur les systèmes les moins actifs. A l'inverse, dans un contexte géophysique, la géométrie de déformation peut être complexe et l'arrangement des systèmes moins actifs devient important.

En revanche, dans mes travaux sur la modélisation élasto-plastique du comportement mécanique du cobalt, j'ai pu observer que les simulations de variations de distances inter-réticulaires sont très sensibles à tous les systèmes activés. En effet, les contraintes appliquées sur des systèmes très actifs sont relaxées très vite. A l'inverse, les systèmes peu actifs supportent des contraintes plus importantes. Les mesures de variations de distances inter-réticulaires, qui sont liées aux contraintes supportées dans le polycristal, y sont donc très sensibles.

Une combinaison entre ces deux types de simulation permet donc de compléter les lacunes des interprétations basées sur la texture uniquement. Les jeux paramètres obtenus sont donc mieux contraints et peuvent donc être injectés dans des modèles géophysiques.

Dans ce cadre, nous avons, Paul Raterron, Olivier Castelnau, et moi-même, engagé un programme ANR sur les propriétés plastiques de l'olivine. Ce programme comprendra des expériences de déformation sur échantillons polycristallins d'olivine sur la nouvelle presse de l'ESRF et une comparaison des résultats obtenus avec les modélisations de polycristaux. A terme, nous espérons pouvoir injecter ces paramètres dans des modèles de convection.

2.6 Opportunités de développement

Mon activité de recherche porte donc sur la compréhension du comportement plastique de polycristaux sous pression. Dans ce cadre, les paramètres clés résident dans l'identification des mécanismes contrôlant la déformation plastique et le changement d'échelle entre le grain et le polycristal.

Mes travaux s'articulent actuellement autour de quatre axes principaux

- expériences de déformation sur polycristaux, en cellules diamant ou presses D-DIA,
- mesure de diffraction X tridimensionnelle pour l'étude individuelle de cristaux au sein de polycristaux,
- modélisation numérique du passage de l'échelle du grain au polycristal,
- simulations d'anisotropie sismique.

Chacun de ces axes offre des opportunités importantes et pourrait constituer une activité à part entière. On peut aussi envisager de nouveaux sujets combinant ces différents axes.

De plus mon activité peut aussi être étendue au dehors des sciences de la Terre. Par exemple, l'étude du comportement mécanique de phases dites "super-dures" ou encore de nouveaux alliages métalliques fabriqués sous pression est un domaine totalement vierge qui ne demande qu'à être exploré...

Chapitre 3

Encadrement et gestion de la recherche

3.1 Collaborations

J'ai beaucoup voyagé au cours de mon service national, ma thèse, et mes post-docs. J'ai donc réussi à me constituer un important réseau de collaborateurs nationaux et internationaux. Voici un liste exhaustive des gens, en dehors de mon laboratoire, avec qui j'ai pu travailler récemment

- en Europe
  - Guillaume Fiquet, James Badro, Daniele Antonangelli, IMPMC, Institut de Physique du Globe, Paris VI
  - Isabelle Daniel, Bruno Reynard, ENS Lyon
  - Denis Andrault, Nathalie Bolfan, LMV, Clermont-Ferrand
  - Andreas Zerr, Olivier Castelnau, LPMTM, Université Paris Nord
  - Philippe Cardin, Renaud Deguen, LGIT Grenoble
  - Hans-Peter Liermann, DESY, HASYLAB, Hambourg, Allemagne
  - Sergio Speziale, GeoForschungsZentrum, Potsdam, Allemagne
  - Tamas Ungàr, université Eötvös, Budapest, Hongrie
- aux Etats-Unis
  - Hans-Rudolf Wenk, Lowell Miyagi, UC Berkeley
  - Allen McNamara, Arizona State University
  - Ho-kwang Mao, Russell J. Hemley, Geophysical Laboratory, Carnegie Institution of Washington
  - Tom Duffy, Princeton University
  - Carlos Tomé, Sven Vogel, Los Alamos National Labs
  - Yanbin Wang, Nadège Hilairet, Argonne National Labs
- au Japon
  - Takehiko Yagi, Université de Tokyo

- Norimasa Nishiyama, Geodynamics Research Center, université Ehime

ainsi que nombreuses personnes en charges de lignes de lumière sur les synchrotrons dont

- BL13A sur le synchrotron Photon Factory au Japon,
- BL10XU sur le synchrotron Spring8 au Japon,
- tout le secteur HPCAT sur APS, près de Chicago, aux Etats-Unis,
- tout le secteur GSECARS sur APS, près de Chicago, aux Etats-Unis,
- 12.2.2 sur ALS, à Berkeley, aux Etats-Unis,
- ID11, ID9, et ID27 à l'ESRF.

3.2 Encadrement d'étudiants

Ces dernières années, j'ai aussi eu l'occasion d'interagir, d'encadrer, ou de co-encadrer des étudiants. Ces expériences m'ont beaucoup appris et ont, pour certaines déjà donné lieu à des publications. Parmi ces personnes, je pourrais citer

- Ken Niwa, avec qui j'ai interagi pendant sa thèse à l'université de Tokyo sous la direction de T. Yagi. Notre interaction a donné lieu à une publication dans *Physics and Chemistry of Minerals*, Niwa *et al.* (2007), page 143. Ken est maintenant assistant à l'université de Nagoya.
- Tristan Ferroir, qui est venu de l'ENS Lyon pour effectuer son stage de maîtrise à l'université de Tokyo, ce qui a donné lieu à une publication dans *American Mineralogist*, Ferroir *et al.* (2006), page 309. Tristan a ensuite continué sur une thèse à l'ENS avec Philippe Gillet et Alexandre Simionovici, qu'il a soutenue en 2009.
- Nadège Hilairet, que j'ai aidée sur ses expériences de déformation en presse D-DIA, ce qui a donné lieu à une publication dans *Science*, Hilairet *et al.* (2007), page 167. Nadège est maintenant post-doctorante aux Argone National Labs.
- Lowell Miyagi, dont j'ai encadré, non officiellement et sous la supervision de Rudy Wenk à l'université de Californie à Berkeley, les deux premières années de thèse. Nous avons écrit de nombreux articles ensemble, dont deux dans *Science* (Merkel *et al.*, 2006a, 2007; Wenk *et al.*, 2006; Miyagi *et al.*, 2006, 2009). Lowell soutiendra sa thèse fin 2009 et enchaînera sur un post-doctorat à l'université de Yale.
- Carole Nisr, dont j'ai encadré le stage de master 2 à l'université Lille 1 et qui est maintenant en thèse avec moi et Patrick Cordier.
- Marion Gruson, de l'école Centrale de Nantes, dont j'encadre actuellement le stage de master 2.

3.3 Ressources

Au cours de ma carrière, j'ai très vite appris à travailler indépendemment, obtenir des financements, et du temps d'expérience sur les synchrotrons. Ceci ce concrétise par 3 à 4 sessions d'expérience sur synchrotron par an, dont la majeur partie obtenue en mon nom.

Parmi les différents financements et bourses que j'ai pu obtenir, citons

- un financement de deux ans pour mon post-doctorat au Japon de la Japanese Society for the Promotion of Science (salaire, déménagement et environ 10k€ de dépenses par an),
- une bourse de trois ans de la fondation Miller à Berkeley pour mon séjour à UC Berkeley (salaire, déménagement et environ 15k€ de dépenses par an),
- une BQR de l'Université Lille 1 pour mon installation en 2006 : 50k€,
- un contrat annuel du programme national SEDIT de l'INSU en 2007 : 23 k€,
- une ANR Jeunes Chercheurs "Dislocations Under Pressure", programme de 4 ans débuté en 2008, 200k€,
- participation au projet ANR blanc "Mantle Rheology" de Paul Raterron (LSPES, Lille 1), programme de 4 ans débuté en 2009, 368 k€
- participation au projet ANR blanc "SUBDEF : Deformation and transformations of hydrous minerals in subduction zones" de Bruno Reynard (Laboratoire des Sciences de la Terre, ENS Lyon), programme de 4 ans débuté en 2009, environ 300 k€.

J'ai donc largement démontré ma capacité à travailler de manière indépendante financièrement, pour moi et les gens qui m'entourent.

Depuis mon arrivée à Lille, je me suis aussi attaché à la mise en place d'un laboratoire hautes-pressions. Je dispose maintenant de 5 cellules diamant et du matériel nécessaire à la préparation d'échantillons (microscopie, mesure de fluorescence de rubis, spectroscopie Raman) qui me permettent, à moi et mes étudiants, de travailler indépendemment.

Bibliographie

D. Antonangeli, M. Krisch, G. Fiquet, J. Badro, D. L. Farber, A. Bossak, & S. Merkel. Aggregate and single crystalline elasticity of hcp cobalt at high pressure. *Phys. Rev. B*, **72** :134303, 2005.

D. Antonangeli, M. Krisch, G. Fiquet, D. L. Farber, C. M. Aracne, J. Badro, F. Occelli, & H. Requardt. Elasticity of cobalt at high pressure studied by inelastic x-ray scattering. *Phys. Rev. Lett.*, **93** :215505, 2004.

D. Antonangeli, S. Merkel, & D. L. Farber. Elastic anisotropy in hcp metals at high pressure and the sound wave anisotropy of the earth's inner core. *Geophys. Res. Lett.*, **33** : L24303, 2006.

P. C. Burnley & D. Zhang. Interpreting in situ x-ray diffraction data from high pressure deformation experiments using elastic–plastic self-consistent models : an example using quartz. *J. Phys. : Condens. Matter*, **20** :285201, 2008.

P. Carrez, P. Cordier, B. Devincre, & L. P. Kubin. Dislocation reactions and junctions in MgO. *Mater. Sci. Eng., A*, **400** :325–328, 2005.

P. Cordier. Dislocations and slip systems of mantle minerals In : *Pastic deformation of minerals and rocks*. S. Karato & H.R. Wenk, Eds, volume **51** des *Reviews in Mineralogy and Geochemistry*, pages 137–179. Mineralogical Society of America, 2002.

P. Cordier, F. Barbe, J. Durinck, A. Tommasi, & A. M. Walker. Plastic deformation of minerals at high pressure : Multiscale numerical modelling In : *Mineral Behaviour at Extreme Conditions*. R. Miletich, Ed, volume **7** des *EMU Notes in Mineralogy*, chapitre 16, pages 389–416. European Mineralogical Union, 2005.

P. Cordier, T. Ungár, L. Zsoldos, & G. Tichy. Dislocation creep in $MgSiO_3$ perovskite at conditions of the earth's uppermost lower mantle. *Nature*, **428** :837–840, 2004.

J. C. Crowhurst, D. Antonangeli, J. M. Brown, A. F. Goncharov, D. L. Farber, & C. M. Aracne. Determination of the high pressure elasticity of cobalt from measured interfacial acoustic wave velocities. *Appl. Phys. Lett.*, **89** :111920, 2006.

T. S. Duffy, G. Shen, D. L. Heinz, J. Shu, Y. Ma, H. K. Mao, R. J. Hemley, & A. K. Singh. Lattice strains in gold and rhenium under non-hydrostatic compression to 37 GPa. *Phys. Rev. B*, **60** :15063–15073, 1999.

T. Ferroir, T. Yagi, T. Onozawa, S. Merkel, N. Miyajima, N. Nishiyama, T. Irifune, & T. Kikegawa. Equation of state and phase transition in $KAlSi_3O_8$ hollandite at high pressure. *Am. Mineral.*, **91** :327–332, 2006.

N. Funamori, T. Yagi, & T. Uchida. Deviatoric stress measurement under uniaxial compression by a powder x-ray diffraction method. *J. Appl. Phys.*, **75** :4327–4331, 1994.

A. F. Goncharov, J. Crowhurst, & J. M. Zaug. Elastic and vibrational properties of cobalt to 120 GPa. *Phys. Rev. Lett.*, **92** :115502, 2004.

R. J. Hemley, H. K. Mao, G. Shen, J. Badro, Ph. Gillet, M. Hanfland, & D. Häusermann. X-ray imaging of stress and strain of diamond, iron, and tungsten at megabar pressures. *Science*, **276** :1242–1245, 1997.

N. Hilairet, B. Reynard, Y. Wang, I. Daniel, S. Merkel, N. Nishiyama, & S. Petitgirard. High-pressure creep of serpentine, interseismic deformation, and initiation of subduction. *Science*, **318** :1910–1913, 2007.

K. Hirose, J. Brodholt, T. Lay, & D. Yuen, Eds. *Post-perovskite : The Last Mantle Phase Transition*. American Geophysical Union, Washington, DC, 2007.

K. Hirose, K. Kawamura, Y. Ohishi, S. Tateno, & N. Sata. Stability and equation of state of $MgGeO_3$ post-perovskite phase. *Am. Mineral.*, **90** :262–265, 2005.

S. Karato. Theory of lattice strain in a material undergoing plastic deformation : Basic formulation and applications to a cubic crystal. *Phys. Rev. B*, **79** :214106, 2009.

A. Kavner. Garnet yield strength at high pressures and implications for upper mantle and transition zone rheology. *J. Geophys. Res.*, **112** :B12207, 2007.

A. Kavner & T. S. Duffy. Elasticity and rheology of platinum under high pressure and nonhydrostatic stress. *Phys. Rev. B*, **68** :144101, 2003.

G. L. Kinsland & W. A. Bassett. Modification of the diamond anvil cell for the measuring strain and the strength of materials at pressures up to 300 kilobar. *Rev. Sci. Instrum.*, **47** : 130–132, 1976.

G. L. Kinsland & W. A. Bassett. Strength of MgO and NaCl polycrystals to confining pressures of 250 kbar at 25 C. *J. Appl. Phys.*, **48** :978–984, 1977.

U. F Kocks, C. Tomé, & H. R. Wenk. *Texture and Anisotropy : Preferred Orientations and their Effects on Material Properties*. Cambridge Univ. Press, Cambridge, 1998.

M. Kunz, W. A. Caldwell, L. Miyagi, & H.-R. Wenk. In situ laser heating and radial synchrotron x-ray diffraction in a diamond anvil cell. *Rev. Sci. Instrum.*, **78** :063907, 2007.

R. A. Lebensohn & C. N. Tomé. A selfconsistent anisotropic approach for the simulation of plastic deformation and texture development of polycrystals : application to zirconium alloys. *Acta Metall. Mater.*, **41** :2611–2624, 1993.

R. A. Lebensohn & C. N. Tomé. A self-consistent visco-plastic model : calculation of rolling textures of anisotropic materials. *Mater. Sci. Eng. A*, **175** :71–82, 1994.

L. Li, D. J. Weidner, J. Chen, M. T. Vaughan, M. Davis, & W. B. Durham. X-ray strain analysis at high pressure : Effect of plastic deformation in MgO. *J. Appl. Phys.*, **95** : 8357–8365, 2004.

L. Lutterotti, S. Matthies, & H. R. Wenk. Maud : a friendly java program for materials analysis using diffraction. *IUCr : Newsletter of the CPD*, **21** :14 – 15, 1999.

D. Mainprice, G. Barruol, & W. Ben Ismaïl. The seismic anisotropy of the earth's mantle : from single crystal to polycrystal In : *Earth's Deep Interior. Mineral Physics and Tomography. From the Atomic to the Global Scale.* S. Karato, A. M. Forte, R. C. Liebermann, G. Master, & L. Stixrude, Eds, pages 237–264. Am. Geophys. Union, Washington, DC, 2000.

H. K. Mao, J. Shu, Y. Fei, J. Hu, & R. J. Hemley. The wüstite enigma. *Phys. Earth Planet. Inter.*, **96** :135–145, 1996.

H. K. Mao, J. Shu, G. Shen, R. J. Hemley, B. Li, & A. K. Singh. Elasticity and rheology of iron above 220 GPa and the nature of the earth's inner core. *Nature*, **396** :741–743, 1998. Correction, Nature 399, 280, 1999.

W. L. Mao, V. V. Struzhkin, A. Q. R. Baron, S. Tsutsui, C. E. Tommaseo, H.-R. Wenk, M. Y. Hu, P. Chow, W. Sturhahn, J. Shu, R. J. Hemley, D. L. Heinz, & H.-K. Mao. Experimental determination of the elasticity of iron at high pressure. *J. Geophys. Res.*, **113** :B09213, 2008.

L. Margulies, G. Winther, & H. F. Poulsen. In situ measurement of grain rotation during deformation of polycrystals. *Science*, **291** :2392–2394, 2001.

S. Matthies, S. Merkel, H. R. Wenk, R. J. Hemley, & H. K. Mao. Effects of texture on the high pressure elasticity of iron from x-ray diffraction. *Earth Planet. Sci. Lett.*, **194** : 201–212, 2001a.

S. Matthies, H. G. Priesmeyer, & M. R. Daymond. On the diffractive determination of single-crystal elastic constants using polycrystalline samples. *J. Appl. Cryst.*, **34** :585–601, 2001b.

S. Matthies & G. W. Vinel. On the reproduction of the orientation distribution function of texturized samples from reduced pole figures using the conception of a conditional ghost correction. *Phys. Status Solidi B*, **112** :K111–K114, 1982.

S. Merkel. X-ray diffraction evaluation of stress in high pressure deformation experiments. *J. Phys. : Condens. Matter*, **18** :S949–S962, 2006.

S. Merkel, A. F. Goncharov, H. K. Mao, Ph. Gillet, & R. J. Hemley. Raman spectroscopy of iron to 152 gigapascals : implications for earth's inner core. *Science*, **288** : 1626–1629, 2000.

S. Merkel, A. P. Jephcoat, J. Shu, H. K. Mao, Ph. Gillet, & R. J. Hemley. Equation of state, elasticity and shear strength of pyrite under high pressure. *Phys. Chem. Miner.*, **29** : 1–9, 2002a.

S. Merkel, A. Kubo, L. Miyagi, S. Speziale, T. S. Duffy, H.-K. Mao, & H.-R. Wenk. Plastic deformation of $MgGeO_3$ post-perovskite at lower mantle pressures. *Science*, **311** : 644–646, 2006a.

S. Merkel, A. K. McNamara, A. Kubo, S. Speziale, L. Miyagi, Y. Meng, T. S. Duffy, & H.-R. Wenk. Deformation of (Mg,Fe)SiO_3 post-perovskite and D" anisotropy. *Science*, **316** :1729 – 1732, 2007.

S. Merkel, N. Miyajima, D. Antonangeli, G. Fiquet, & T. Yagi. Lattice preferred orientation and stress in polycrystalline hcp-Co plastically deformed under high pressure. *J. Appl. Phys.*, **100** :023510, 2006b.

S. Merkel, J. Shu, P. Gillet, H.K. Mao, & R.J. Hemley. X-ray diffraction study of the single crystal elastic moduli of ϵ-Fe up to 30 GPa. *J. Geophys. Res.*, **110** :B05201, 2005.

S. Merkel, C. Tomé, & H.-R. Wenk. A modeling analysis of the influence of plasticity on high pressure deformation of hcp-co. *Phys. Rev. B*, **79** :064110, 2009.

S. Merkel, H. R. Wenk, J. Badro, G. Montagnac, P. Gillet, H. K. Mao, & R. J. Hemley. Deformation of (Mg,Fe)SiO_3 perovskite aggregates up to 32 GPa. *Earth Planet. Sci. Lett.*, **209** :351–360, 2003.

S. Merkel, H. R. Wenk, P. Gillet, H. K. Mao, & R. J. Hemley. Deformation of polycrystalline iron up to 30 GPa and 1000 K. *Phys. Earth Planet. Inter.*, **145** :239–251, 2004.

S. Merkel, H. R. Wenk, J. Shu, G. Shen, P. Gillet, H. K. Mao, & R. J. Hemley. Deformation of polycrystalline MgO at pressures of the lower mantle. *J. Geophys. Res.*, **107** : 2271, 2002b.

S. Merkel & T. Yagi. X-ray transparent gasket for diamond anvil cell high pressure experiments. *Rev. Sci. Instrum.*, **76** :046109, 2005.

S. Merkel & T. Yagi. Effect of lattice preferred orientation on lattice strains in polycrystalline materials deformed under high pressure : Application to hcp-co. *J. Phys. Chem. Solids*, **67** : 2119–2131, 2006.

L. Miyagi, S. Merkel, T. Yagi, N. Sata, Y. Ohishi, & H. R. Wenk. Quantitative Rietveld texture analysis of $CaSiO_3$ perovskite deformed in a diamond anvil cell. *J. Phys. : Condens. Matter*, **18** :S995–S1005, 2006.

L. Miyagi, S. Merkel, T. Yagi, N. Sata, Y. Ohishi, & H.-R. Wenk. Diamond anvil cell deformation of $CaSiO_3$ perovskite up to 49 GPa. *Phys. Earth Planet. Inter.*, **174** :159–164, 2009.

M. Murakami, K. Hirose, K. Kawamura, N. Sata, & Y. Ohishi. Post-perovskite phase transition in MgSiO3. *Science*, **304**(5672) :855–858, 2004.

K. Niwa, T. Yagi, K. Ohgushi, S. Merkel, N. Miyajima, & T. Kikegawa. Lattice preferred orientation in $CaIrO_3$ perovskite and post-perovskite formed by plastic deformation under pressure. *Phys. Chem. Miner.*, **34** :679–686, 2007.

A. R. Oganov & S. Ono. Theoretical and experimental evidence for a post-perovskite phase of $MgSiO_3$ in earth's d" layer. *Nature*, **430** :445–448, 2004.

P. Raterron & S. Merkel. In situ rheological measurements at extreme pressure and temperature using synchrotron x-ray diffraction and radiography. *J. Synchrotron Radiat.*, **16** : 748–756, 2009.

P. G. Silver & W. E. Holt. The mantle flow field beneath western north america. *Science*, **295** :1054–1057, 2002.

A. K. Singh, C. Balasingh, H. K. Mao, R. J. Hemley, & J. Shu. Analysis of lattice strains measured under non-hydrostatic pressure. *J. Appl. Phys.*, **83** :7567–7575, 1998a.

A. K. Singh, H. K. Mao, J. Shu, & R. J. Hemley. Estimation of single crystal elastic moduli from polycrystalline x-ray diffraction at high pressure : Applications to FeO and iron. *Phys. Rev. Lett.*, **80** :2157–2160, 1998b.

S. C. Singh & J. P. Montagner. Anisotropy of iron in the earth's inner core. *Nature*, **400** : 629–629, 1999.

S. Speziale, S. R. Shieh, & T. S. Duffy. High-pressure elasticity of calcium oxide : A comparison between brillouin spectroscopy and radial x-ray diffraction. *J. Geophys. Res.*, **111** :B02203, 2006.

S. Stackhouse, J.P. Brodholt, J. Wookey, J.M. Kendall, & G.D. Price. The effect of temperature on the seismic anisotropy of the perovskite and post-perovskite polymorphs of $MgSiO_3$. *Earth Planet. Sci. Lett.*, **230**(1-2) :1–10, 2005.

G. Steinle-Neumann, L. Stixrude, & R. E. Cohen. First-principles elastic constants for the hcp transition metals Fe, Co, and Re at high pressure. *Phys. Rev. B*, **60** :791–799, 1999.

C. E. Tommaseo, J. Devine, S. Merkel, S. Speziale, & H.-R. Wenk. Texture development and elastic stresses in magnesiowüstite at high pressure. *Phys. Chem. Miner.*, **33** :84–97, 2006.

T. Ungár & A. Borbély. The effect of dislocation contrast on x-ray line broadening : A new approach to line profile analysis. *Appl. Phys. Lett.*, **69** :3173–3175, 1996.

Y. Wang, W. B. Duhram, I. C. Getting, & D. J. Weidner. The deformation-DIA : A new apparatus for high temperature triaxial deformation to pressures up to 15 GPa. *Rev. Sci. Instrum.*, **74** :3002–3011, 2003.

D. J. Weidner, L. Li, M. Davis, & J. Chen. Effect of plasticity on elastic modulus measurements. *Geophys. Res. Lett.*, **31** :L06621, 2004.

M. B. Weinberger, S. H. Tolbert, & A. Kavner. Osmium metal studied under high pressure and nonhydrostatic stress. *Phys. Rev. Lett.*, **100** :045506, 2008.

H. R. Wenk, I. Lonardelli, S. Merkel, L. Miyagi, J. Pehl, S. Speziale, & C. E. Tommaseo. Deformation textures produced in diamond anvil experiments, analysed in radial diffraction geometry. *J. Phys. : Condens. Matter*, **18** :S933–S947, 2006.

H. R. Wenk, S. Matthies, J. Donovan, & D. Chateigner. Beartex : a windows-based program system for quantitative texture analysis. *J. Appl. Cryst.*, **31** :262–269, 1998.

H. R. Wenk, S. Matthies, R. J. Hemley, H. K. Mao, & J. Shu. The plastic deformation of iron at pressures of the Earth's inner core. *Nature*, **405** :1044–1047, 2000.

R.M. Wentzcovitch, T. Tsuchiya, & J. Tsuchiya. $MgSiO_3$ postperovskite at D" conditions. *Proc. Nat. Acad. Sc.*, **103** :543–546, 2006.

D. Yamazaki & S.-I. Karato. High-pressure rotational deformation apparatus to 15 gpa. *Rev. Sci. Instrum.*, **72** :4207–4211, 2001.

Troisième partie

Informations personnelles

Curriculum Vitae

Personnel

Né le 11 septembre 1974 à Ambilly (Haute-Savoie)
Nationalité française

Situation actuelle

Chargé de recherches 2ème classe au CNRS, depuis le 1er Janvier 2006
Laboratoire de Structures et Propriétés de l'Etat Solide
Université Lille 1
59655 Villeneuve d'Ascq Cedex

Parcours professionel

2006-

Chargé de recherches au CNRS

2004-2006

Miller Research Fellow, Department of Earth and Planetary Science,
University of California, Berkeley, Etats-Unis.

2002-2004

Post-doctorant (bourse JSPS), Institute for Solid State Physics,
Université de Tokyo, Japon.

1999-2002

Thèse de doctorat à l'École Normale Supérieure de Lyon.
Directeurs de thèse : Philippe Gillet (ENS Lyon) et Russell J. Hemley (Geophysical Laboratory, Washington DC, États-Unis).

1997-1999

Service national en coopération au Geophysical Laboratory,
Carnegie Institution of Washington, Washington DC, États-Unis

Parcours académique

1999-2002

Thèse de doctorat à l'École Normale Supérieure de Lyon. Directeurs de thèse : Philippe Gillet (ENS Lyon) et Russell J. Hemley (Geophysical Laboratory, Washington DC, États-Unis).

1994-1997

Élève normalien, magistère des sciences de la matière à l'École Normale Supérieure de Lyon

1996-1997

DEA de physique statistique et phénomènes non linéaires à l'ENS Lyon

1994-1996

License et maîtrise de physique à l'ENS Lyon

1992-1994

Mathématiques spéciales et supérieures au Lycée du Parc, Lyon

Distinctions

2002

Mineral and Rock Physics Outstanding Student Award, American Geophysical Union

Responsabilités collectives

- Membre du conseil de laboratoire du LSPES, Université Lille 1
- Membre du vivier pour comités de sélection, section 28, Université Lille 1
- 2007-2008 : Membre de la commission de spécialistes, section 28, Université Lille 1
- Commission de recrutement de maîtres de conférences à l'université Lyon 1 en sciences de la terre en 2009
- Évaluations d'articles scientifiques : environ 25 évaluations, pour Science, Nature, Journal of Geophysical Research, Earth and Planetary Science Letters, Geophysical Research Letters, Journal of Applied Physics, Physics of the Earth of Planetary Interiors, International Journal of Plasticity, Comptes Rendus de l'Académie des Sciences, Journal of Synchrotron Radiation, Journal of Physics and Chemistry of Solids, Journal of Physics B : Condensed Matter, Physics and Chemistry of Minerals, Tectonophysics...
- évaluation de projets pour l'ANR et la NSF
- Organisation de congrès : une session au congrès d'automne de l'American Geophysical Union, San Francisco, États-Unis, décembre 2007
- Webmaster du LSPES

Enseignements

- 40h de travaux dirigés de biophysique en 1ère année de médecine à l'Institut Catholique de Lille. Années 2006-2007, 2007-2008, 2008-2009, et probablement 2009-2010.
- Moniteur pendant la thèse, années 2000-2001 et 2001-2002 :
    - encadrement d'un projet commun ENS-Lyon/INSA de site internet pour l'aide à l'enseignement des professeurs de lycée en sciences de la terre. Projet "Voyage au centre de la terre", CD disponible auprès de Gérard Vidal, ENS Lyon.
    - participation au module "Introduction à la géophysique" en maîtrise de physique, ENS Lyon,
    - TD pour le cours "Flux de chaleur", "Ondes et champs", et informatique en licence et maîtrise de sciences de la terre, ENS Lyon,
- 1999 : Participation au stage de terrain de la première année du magistère des Sciences de la terre, ENS Lyon, et réalisation du site internet d'accompagnement.
- 1999-2002 : Nombreuses participations à la conception du site Planet-Terre (http ://planet-terre.ens-lyon.fr/) : soutient à l'enseignement des sciences de la terre pour les enseignants du secondaire.

Encadrement

Encadrement doctoral

- Co-encadrement de thèse de Carole Nisr, Université Lille 1, thèse débutée en 2008
- Co-encadrement, non officiel, de la thèse de Lowell Miyagi, Department of Earth and Planetary Science, University of California, Berkeley, États-Unis, en 2004-2005. Directeur de thèse : Hans-Rudolf Wenk. Soutenance prévue : été 2009.

Master

- Co-encadrement du stage de master 1 de Tristan Ferroir, Ecole Normal Supérieure de Lyon, à l'Université de Tokyo, Japon, 2003.
- Encadrement du stage de master 2 de Carole Nisr, Université Lille 1, à l' Université Lille 1, année 2007-2008.
- Encadrement du stage de master 2 de Marion Gruson, École Centrale de Nantes, à l' Université Lille 1, 2009.

Financements

- Responsable, avec Ph. Carrez du LSPES, du projet ANR Jeunes Chercheurs "Dislocations Under Pressure", programme de 4 ans débuté en 2008, 200k€
- Participation au projet ANR blanc "Mantle Rheology" de Paul Raterron (LSPES, Lille 1), programme de 4 ans débuté en 2009, 368 k€
- Participation au projet ANR blanc "SUBDEF : Deformation and transformations of hydrous minerals in subduction zones" de Bruno Reynard (Laboratoire des Sciences de la Terre, ENS Lyon), programme de 4 ans débuté en 2009, environ 300 k€
- S. Merkel et Ph. Carrez "Plasticité des phases post-perovskites", contrat annuel (2007) du programme national SEDIT de l'INSU : 23 k€.
- BQR de l'Université Lille 1 en 2006 : 50k€.

Production scientifique

Publications internationales de rang A non liées à la thèse : 21, dont 8 en 1er auteur

1. P. Raterron, S. Merkel, In situ rheological measurements at extreme P and T using synchrotron x-ray diffraction and radiography, Journal of Synchrotron Radiation, sous presse.
2. H.P. Liermann, S. Merkel, L. Miyagi, H. Wenk, G. Shen, H. Cynn, W. J. Evans, New Experimental Method for In Situ Determination of Material Textures at Simultaneous High-Pressure and –Temperature by Means of Radial Diffraction in the Diamond Anvil Cell, Rev. Sci. Instrum., sous presse
3. S. Merkel, C. Tomé, H. R. Wenk, Modeling analysis of the influence of plasticity on high pressure deformation of hcp-Co, Phys. Rev. B, 79, 064110 (2009)
4. L. Miyagi, S. Merkel, T. Yagi, N. Sata, Y. Ohishi and H.-R. Wenk, Diamond anvil cell deformation of CaSiO3 perovskite up to 49 GPa, Physics of the Earth and Planetary Interiors , 174, pp. 159-164 (2009)
5. S. Merkel, A. K. Mcnamara, A. Kubo, S. Speziale, L. Miyagi, Y. Meng, T. S. Duffy, and H.-R. Wenk, Deformation of (Mg,Fe)SiO3 Post-Perovskite and D" Anisotropy, Science, 316, pp. 1729-1732 (2007)
6. N. Hilairet, B. Reynard, Y. Wang, I. Daniel, S. Merkel, N. Nishiyama, S. Petitgirard, High-pressure creep of serpentine, interseismic deformation, and initiation of subduction, Science, 318, pp. 1910-1913 (2007)
7. K. Niwa, T. Yagi, K. Ohgushi, S. Merkel, N. Miyajima and T. Kikegawa, Lattice preferred orientation in CaIrO3 perovskite and post-perovskite formed by plastic deformation under pressure, Phys. Chem. Min., 34, pp. 679-686 (2007)
8. S. Merkel, A. Kubo, L. Miyagi, S. Speziale, T. S. Duffy, H.-K. Mao and H.-R. Wenk , Plastic Deformation of MgGeO3 Post-Perovskite at Lower Mantle Pressures , Science, 311, pp. 644-646 (2006)
9. S. Merkel, X-ray diffraction evaluation of stress in high pressure deformation experiments, J. Phys. : Condens. Matter, 18, S949-S962 (2006)
10. S. Merkel, N. Miyajima, D. Antonangeli, G. Fiquet and T. Yagi, Lattice preferred orientation and stress in polycrystalline hcp-Co plastically deformed under high pressure, Journal of Applied Physics, 100, 023510 (2006)
11. S. Merkel and T. Yagi, Effect of lattice preferred orientation on lattice strains in polycrystalline materials deformed under high pressure : Application to hcp-Co, J. Phys. Chem. Solids, 67, pp. 2119-2131 (2006)
12. D. Antonangeli, S. Merkel and D. L. Farber, Elastic anisotropy in hcp metals at high pressure and the sound wave anisotropy of the Earth's inner core, Geophys. Res. Lett., 33, L24303 (2006)
13. T. Ferroir, T. Yagi, T. Onozawa, S. Merkel, N. Miyajima, N. Nishiyama, T. Irifune, T. Kikegawa, Equation of state and phase transition in KAlSi3O8 hollandite at high pressure, American Mineralogist, 91, 327-332 (2006)

14. L. Miyagi, S. Merkel, T. Yagi, N. Sata, Y. Ohishi and H.-R. Wenk , Quantitative Rietveld texture analysis of CaSiO3 perovskite deformed in a diamond anvil cell, J. Phys. : Condens. Matter , 18, S995-S1005 (2006)
15. H-R Wenk, I Lonardelli, S Merkel, L Miyagi, J Pehl, S Speziale and C E Tommaseo , Deformation textures produced in diamond anvil experiments, analysed in radial diffraction geometry, J. Phys. : Condens. Matter, 18, S933-S947 (2006)
16. C.E. Tommaseo, J. Devine, S. Merkel, S. Speziale and H.-R. Wenk, Texture development and elastic stresses in magnesiowüstite at high pressure, Physics and Chemistry of Minerals , 33, pp. 84-97 (2006)
17. S. Merkel and T. Yagi, X-ray transparent gasket for diamond anvil cell high pressure experiments, Review of Scientific Instruments, 76, 046109 (2005)
18. D. Antonangeli, M. Krisch, G. Fiquet, J. Badro, D. L. Farber, A. Bossak, and S. Merkel, Aggregate and single crystalline elasticity of hcp cobalt at high pressure, Physical Review B, 72, 134303 (2005)
19. S. Merkel, The mantle deformed, Nature, 428, pp. 812-813 (2004)
20. Y. Sueda, T. Irifune, N. Nishiyama, R.P. Rapp, T. Ferroir, T. Onozawa, T. Yagi, S. Merkel, N. Miyajima and K. Funakoshi, A new high-pressure form of KAlSi3O8 under lower mantle conditions, Geophysysical Research Letters, 31, L23612 (2004)
21. J. Chéry, S. Merkel and S. Bouissou, A physical basis for time clustering of large earthquakes, Bull. Seismol. Soc. Am., 91, p. 1685-1693 (2001)

Publications internationales de rang A sur les travaux de thèse : 8, dont 7 en 1er auteur

1. S. Merkel, J. Shu, P. Gillet, H.K. Mao and R.J. Hemley, X-ray diffraction study of the single crystal elastic moduli of e-Fe up to 30 GPa, Journal of Geophysical Research, 110, B05201 (2005)
2. S. Merkel, H.R. Wenk, P. Gillet, H.K. Mao and R.J. Hemley, Deformation of polycrystalline iron up to 30 GPa and 1000 K, Physics of the Earth and Planetary Interiors, 145, pp 239-251 (2004)
3. S. Merkel, H.R. Wenk, J. Badro, G. Montagnac, P. Gillet, H.K. Mao, R.J. Hemley, Deformation of (Mg0.9,Fe0.1)SiO3 perovskite aggregates up to 32 GPa, Earth and Planetary Science Letters, 209, pp. 351-360 (2003)
4. S. Merkel, H.R. Wenk, J. Shu, G. Shen, P. Gillet, H.K. Mao, and R.J. Hemley, Deformation of polycrystalline MgO at pressures of the lower mantle, Journal of Geophysical Research, 107, 2271 (2002)
5. S. Merkel, A.P. Jephcoat, J. Shu, H.K. Mao, P. Gillet and R.J. Hemley, Equation of state, elasticity and shear strength of pyrite under high pressure, Physics and Chemistry of Minerals, 29, pp. 1-9 (2002)
6. S. Matthies, S. Merkel, H.R. Wenk, R.J. Hemley and H.K. Mao, Effects of texture on the determination of elasticity of polycrystalline e-iron from diffraction measurements, Earth and Planetary Science Letters, 194, pp. 201-212 (2001)

7. S. Merkel, A.F. Goncharov, H.K. Mao, P. Gillet and R.J. Hemley, Raman spectroscopy of Iron to 152 Gigapascals : Implications for Earth's Inner Core, Science, 288, pp. 1626-1629 (2000)
8. S. Merkel, R.J. Hemley and H.K. Mao, Finite-element modeling of diamond deformation at multimegabar pressures, Applied Physics Letter, 74, pp. 656-658 (1999)

Autres publications : 4

1. S. Merkel, Diffraction radiale en cellule diamant : contraintes et applications, Les verrous technologiques dans l'expérimentation haute pression, Réseau des hautes pressions du CNRS, pp. 101-117 (2008)
2. P. Cordier, H. Couvy, S. Merkel and D. Weidner, Plastic deformation of minerals at high pressure : Experimental techniques, EMU Notes in Mineralogy, 7, Chapter 14 (2005)
3. S. Merkel, Élasticité et orientations préférentielles dans la Terre profonde : approche expérimentale, Thèse de doctorat, École Normale Supérieure de Lyon, 255 p. (2002)
4. S. Merkel, R.J. Hemley, H.K. Mao and D.M. Teter, Finite-element modeling and ab initio calculations of megabar stresses in the diamond anvil cell, Science and technology of high pressure, proceedings of the conference AIRAPT-XVII, edited by M.H. Maghnani W.J. Nellis and M.F. Nicol, pp. 68-73, University Press (India) Limited (2000)

Séminaires : 8

1. Laboratoire de Géophysique Interne et Tectonophysique, Grenoble, Octobre 2009
2. Geodynamic Research Center, Université Ehime, Mastuyama, Japon, Janvier 2009
3. Laboratoire Magmas et Volcans, Université Blaise Pascal de Clermont-Ferrand, Janvier 2008
4. Laboratoire de Structures et Propriétés de l'Etat Solide, Université des Sciences et Technologies de Lille, Février 2007
5. Laboratoire de Géologie de l'Ecole normale supérieure, Paris, Novembre 2006
6. Berkeley Seismological Laboratory, University of California, Berkeley, USA, Novembre 2004
7. Laboratoire de Structures et Propriétés de l'Etat Solide, Université des Sciences et Technologies de Lille, Decembre 2003
8. Laboratoire des Sciences de la Terre, Ecole Normale Supérieure de Lyon, France, 2002

Enseignements en écoles thématiques : 3

1. International School of Crystallography, 4-14 juin 2009, Erice, Sicile
2. Expériences de déformation, Structure et dynamique du manteau profond, 12-17 octobre 2008, École de Physique des Houches
3. Progress in in-situ measurement at high P and T, Textures and Microstructures in the Earth Sciences DFH-UFA Summer School, Freiberg, Allemagne, 2005

Communications invitées : 11

1. S. Merkel, Plastic properties of deep Earth minerals, Symposium of Japanese-French Frontiers of Science, Shonan Village Center, Kanagawa, Japon, 24-26 janvier 2009.

2. S. Merkel, Modèles numériques pour l'évaluation de contraintes résiduelles au sein d'échantillons déformés : application au Co hexagonal, Forum 2008 du réseau de technologie des Hautes Pressions, Batz sur Mer, France, 6-10 octobre 2008
3. S. Merkel, Modeling analysis of the influence of plasticity on x-ray diffraction measurements in high pressure deformation apparatus, Rheology Grand Challenge Workshop on Plastic Deformation of Minerals and the Dynamics of Earth's Deep Interior, MIT, Cambridge, MA, USA, 1-3 August 2008
4. S. Merkel, High pressure deformation mechanisms from in situ texture measurements, International Conference on the Texture of Materials (ICOTOM), Pittsburgh, PA, USA, 2008
5. S. Merkel, H.R. Wenk, C. Tomé, Evaluation of stress in high pressure radial diffraction experiments : application to Co, Study of Matter at Extreme Conditions, Miami, FL, USA, 2007
6. S. Merkel, Plasticity in the diamond anvil cell : implications for deep Earth geophysics, Gordon Research Conference on Research at High Pressure, Biddeford, ME, USA, 2006
7. S. Merkel, Radial diffraction in the DAC : pratical and theoretical considerations, COMPRESS workshop on rheology and elasticity studies at ultrahigh pressures and temperatures, Advanced Photon Source, Argonne National Laboratory, USA, 2005
8. S. Merkel, T. Yagi, N. Miyajima, H.R. Wenk, H.K. Mao, and R.J. Hemley, Deformation of polycrystalline Ca-perovskite up to 50 GPa, American Geophysical Union fall meeting, San Francisco, CA, USA, 2004
9. S. Merkel, High pressure study of stress, elasticity, and lattice preferred orientations using the diamond anvil cell and x-ray diffraction, IUCr/COMPRES High Pressure Workshop, Non-ambient Crystallography : The Science of Change, Berkeley, CA, USA, 2003
10. S. Merkel, P. Gillet, H.R. Wenk, H.K. Mao, R.J. Hemley , The diamond anvil cell as a utrahigh pressure deformation apparatus : application to epsilon-iron, EGS-AGU-EGU joint assembly, Nice, France, 2003
11. S. Merkel, H.K. Mao, R.J. Hemley , Finite-element modeling of stress and strain in the diamond anvil cell, International Conferences on High Pressure Science and Technology (Airapt), Honolulu, HI, USA 1999

Communications orales non invitées : 18

1. S. Merkel, C.N. Tomé, H.R. Wenk, P. Cordier, Elasto-plastic interpretation of lattice strains measured in non hydrostatic x-ray diffraction data, Study of matter at extreme conditions, Miami - Western Caribbean. March 28 - April 2, 2009
2. S. Merkel, C.N. Tomé, B. Clausen, H.R. Wenk, A modeling analysis of internal elastic strains in polycrystalline cobalt deformed under high pressure, American Geophysical Union fall meeting, San Francisco, CA, USA, 2008
3. S. Merkel, Elasto-plastic modeling of stress and strain in samples plastically deformed in the diamond anvil cell, International workshop on high pressure science and technology, Shloss Ringberg, Germany, 2008

4. S. Merkel, A.K. McNamara, A. Kubo, S. Speziale, L. Miyagi, Y. Meng, T.S. Duffy, and H.R. Wenk, Diamond anvil cell study of the plastic deformation of post-perovskite phases : implication for D" anisotropy, High Pressure Mineral Physics Seminar, Matsushima, Japan, 2007
5. S. Merkel, Plasticité des minéraux du manteau : expériences de déformation au mégabar, Plasticité, Poitiers, France, 2007
6. S. Merkel L. Miyagi A. Kubo S. Speziale T.S. Duffy H.R. Wenk, Étude expérimental et in-situ des propriétés plastiques de la post-perovskite, Réunion des Sciences de la Terre, Dijon, France, 2006
7. S. Merkel, Joints transparents pour la diffraction radiale en cellule diamant, Forum de technologie des hautes pressions, Monthieux, France, 2006
8. S. Merkel, L. Miyagi, A. Kubo, S. Speziale, T.S. Duffy, H.R. Wenk, High pressure deformation of post-perovskite phases, International Symposium on Experimental Mineralogy, Petrology and Geochemistry (EMPG), Bristol, UK, 2006
9. S. Merkel, T. Yagi, and H.R. Wenk Radial x-ray diffraction study of hcp-cobalt under uniaxial deformation : lattice preferred orientation, stress, and elasticity, Study of Matter at Extreme Conditions, Miami, FL, USA, 2005
10. S. Merkel, A. Kubo, S. Speziale, L. Miyagi, H.R. Wenk, T. Duffy, and H.K. Mao, Plastic deformation of MgGeO3 post-perovskite at megabar pressures, American Geophysical Union fall meeting, San Francisco, CA, 2005
11. S. Merkel, N. Miyajima, T. Yagi, Deformation of polycrystalline Ca-perovskite up to 50 GPa, Japan Earth and Planetary Science Joint Meeting, Makuhari, Chiba, Japan, 2004
12. S. Merkel, T. Yagi, High pressure deformation of polycrystalline cobalt with the diamond anvil cell, High Pressure Conference of Japan, Yokohama, Japan, 2003
13. S. Merkel, P. Gillet, H.R. Wenk, H.K. Mao, R.J. Hemley , Deformation of lower mantle minerals under ultrahigh pressure, EGS-AGU-EGU joint assembly, Nice, France, 2003
14. S. Merkel, H. R. Wenk, J. Badro, G. Montagnac, P. Gillet, H. K. Mao, and R. J. Hemley , In situ high-pressure deformation studies of deep earth materials by radial X-ray diffraction, Study of Matter at Extreme Conditions, Miami, Fl, USA, 2003
15. S. Merkel , Deformation of lower mantle minerals at high pressure, International Union of Geodesy and Geophysics (IUGG), Sapporo, Japan, 2003
16. P. Gillet, S. Merkel, H.R. Wenk, G. Shen, J. Shu, R.J. Hemley, H.K. Mao , The diamond anvil cell as a deformation apparatus for investigating the rheology of the deep Earth, American Geophysical Union fall meeting, San Francisco, CA, USA, 2001
17. A. F. Goncharov, Merkel, S , Hemley, R J, Mao, HK, Gillet, P , Raman Spectroscopy of e-Iron to Earth Core Pressures, American Geophysical Union spring meeting, Washington, DC, USA, 2000
18. S. Merkel, Shu, J, Wenk, H.R., Mao, H.K., Gillet, P., Hemley, R.J. , Diamond anvil cell study of the elasticity and texture of FeS2 pyrite, European Geophysical Society General Assembly, Nice, France, 2000

Communications par affiches : 9

1. H. P. Liermann, S. Merkel, L. Miyagi, H.R. Wenk, G. Shen, H. Cynn, W.J. Ewans, In Situ Determination of BCC-, FCC- and HPC-Iron Textures at Simultaneous High- Pressure and –Temperature by Means of the Resistive Heated Radial Diffraction Diamond Anvil Cell (RH-RD-DAC) : Implications for the iron core, American Geophysical Union fall meeting, San Francisco, CA, USA, 2008
2. S. Merkel, C.N. Tomé, H.-R. Wenk, Evaluation of stress in high pressure radial diffraction : application to hcp metals, American Geophysical Union fall meeting, San Francisco, CA, USA, 2007
3. S. Merkel, D. Antonangelli, G. Fiquet, T. Yagi, Ultrahigh pressure deformation of polycrystaline hcp-cobalt, American Geophysical Union fall meeting, San Francisco, CA, USA, 2003
4. S. Merkel, H.R. Wenk, P. Gillet, R.J. Hemley, and H.K. Mao , Deformation of silicate perovskite aggregates up to 30 GPa, American Geophysical Union fall meeting, San Francisco, CA, USA, 2002
5. S. Merkel, H.R. Wenk, G. Shen, J. Shu, P. Gillet, R.J. Hemley, H.K. Mao , Diamond anvil cell investigation of lattice strains and preferred orientation in iron at high pressure and temperature, American Geophysical Union fall meeting, San Francisco, CA, USA, 2001
6. S. Merkel S., Hemley, R.J., Mao, H.K., Goncharov, A.F, Wenk, H.R., and Gillet P. , Elasticity and preferred orientation in e-Fe under high pressure, European Union of Geosciences General Assembly, Strasbourg, France, 2001
7. S. Merkel, Somayazulu, M, Shu, J, Ma, YZ, Hemley, RJ, Gillet, P, Mao, HK , Elasticity and rheology of iron at high-pressure from radial x-ray diffraction, American Geophysical Union spring meeting, Washington, DC, USA, 2000
8. S. Merkel, H.R. Wenk, J. Shu, H.K. Mao, R.J. Hemley, P. Gillet , High Pressure properties of FeS2 pyrite, American Geophysical Union fall meeting, San Francisco, CA, USA, 1999
9. S. Merkel, RJ. Hemley, H.K. Mao, Theoretical study of diamond deformation to multimegabar pressures, American Geophysical Union fall meeting, San Francisco, CA, USA, 1998

Quatrième partie

Articles : La diffraction radiale

JOURNAL OF GEOPHYSICAL RESEARCH, VOL. 107, NO. B11, 2271, doi:10.1029/2001JB000920, 2002

Deformation of polycrystalline MgO at pressures of the lower mantle

Sébastien Merkel,[1,2] Hans Rudolf Wenk,[3] Jinfu Shu,[2] Guoyin Shen,[4] Philippe Gillet,[1] Ho-kwang Mao,[2] and Russell J. Hemley[2]

Received 13 August 2001; revised 8 March 2002; accepted 13 July 2002; published 5 November 2002.

[1] Room temperature investigations on the shear strength, elastic moduli, elastic anisotropy, and deformation mechanisms of MgO (periclase) are performed in situ up to pressures of 47 GPa using radial X-ray diffraction and the diamond anvil cell. The calculated elastic moduli are in agreement with previous Brillouin spectroscopy studies. The uniaxial stress component in the polycrystalline MgO sample is found to increase rapidly to 8.5(±1) GPa at a pressure of 10(±1) GPa in all experiments. Under axial compression, a strong cube texture develops which was recorded in situ. It is probable that the preferred orientation of MgO is due to deformation by slip. A comparison between the experimental textures and results from polycrystal plasticity suggest that the $\{110\}\langle 1\bar{1}0\rangle$ is the only significantly active slip system under very high confining pressure at room temperature. These data demonstrate the feasibility of analyzing elastic moduli, shear strength, and deformation mechanisms under pressures relevant for the Earth's lower mantle. Implications for the anisotropy and rheology of the lower mantle are discussed. *INDEX TERMS:* 3909 Mineral Physics: Elasticity and anelasticity; 3924 Mineral Physics: High-pressure behavior; 5112 Physical Properties of Rocks: Microstructure; 5194 Physical Properties of Rocks: Instruments and techniques; *KEYWORDS:* MgO, high pressure, texture, anisotropy, deformation, elastic constants

Citation: Merkel, S., H. R. Wenk, J. Shu, G. Shen, P. Gillet, H. K. Mao, and R. J. Hemley, Deformation of polycrystalline MgO at pressures of the lower mantle, *J. Geophys. Res.*, *107*(B11), 2271, doi:10.1029/2001JB000920, 2002.

1. Introduction

[2] Considerable progress has been made in establishing deformation mechanisms for minerals and rocks from the Earth's crust and upper mantle. Much of our knowledge about deformation of minerals such as halite, calcite, quartz, feldspars, and olivine relies on laboratory experiments on single crystals and rocks. It has been established that under a wide range of conditions minerals deform by dislocation glide and climb; in a polycrystalline rock, this leads to preferred orientation, which, in turn, leads to an anisotropic behavior, for example, for propagation of seismic waves. With the knowledge of deformation mechanisms we can understand and even model the development of anisotropy in the crust and the upper mantle [*Chastel et al.*, 1993]. However, much less is known about the deeper Earth, because pressures are beyond conditions reached by ordinary deformation devices such as the Griggs, Heard, or Paterson apparatus [see *Tullis and Tullis*, 1986].

[3] While the pressure and temperature conditions are more extreme, the phases which are present in the lower mantle tend to have simpler crystal structures than minerals in the crust, as established by high-pressure experiments and theory (for a review, see *Fiquet* [2001]). Major phases in the lower mantle include $CaSiO_3$ perovskite, $(Mg,Fe)SiO_3$ silicate perovskite, (Mg,Fe)O magnesiowüstite, and possibly SiO_2 stishovite. Very little is known about the deformation mechanisms of these phases at the conditions relevant to the Earth's mantle. This can be approached experimentally by studying analog materials that have the same structure but are stable at much lower pressure. For example, $CaTiO_3$ perovskite has been used as an analog for $MgSiO_3$ [*Karato and Li*, 1992; *Li et al.*, 1996], halite has been considered as an analog for magnesiowüstite and TiO_2 rutile for stishovite. Unfortunately the concept of analogs does not work very well for deformation mechanisms that depend on the local electronic structure around the dislocation core [e.g., *Poirier and Price*, 1999]. For example, slip systems of magnesite are entirely different than those of isostructural calcite. Halite has different slip systems than isostructural periclase or galena. In order obtain reliable results on deformation mechanisms that are active in the deep Earth, it is necessary to investigate the phases at prevailing pressure and temperature.

[4] Diamond anvil cells allow experimental investigations over the whole pressure and temperature range of the lower mantle. They consist of different pressure steps and the degree of nonhydrostaticity of the stress conditions in the sample can be controlled by changing parameters such as

[1]Laboratoire des sciences de la Terre, École normale supérieure de Lyon, Lyon, France.
[2]Geophysical Laboratory, Carnegie Institution of Washington, Washington, District of Columbia, USA.
[3]Department of Earth and Planetary Science, University of California, Berkeley, California, USA.
[4]Consortium for Advanced Radiation Sources, University of Chicago and Advanced Photon Source, Argonne National Laboratory, Argonne, Illinois, USA.

0148-0227/02/2001JB000920$09.00

the diamonds geometry or the pressure medium. Polycrystalline samples subjected to nonhydrostatic conditions in these experiments can develop preferred orientation. During such experiments the powder is first compacted and then plastically deformed by loading which has a directional stress component. While this is a detriment in the study of phase relations and equilibrium structures, it can become an advantage for investigating deformation at extreme pressure. This nonhydrostatic stress has been used to perform deformation experiments on lower mantle materials such as MgO [*Meade and Jeanloz*, 1988] or $(Mg,Fe)SiO_3$ perovskite [*Meade et al.*, 1995] but the texture analysis was performed on samples quenched to ambient pressure and temperature that were removed from the diamond anvil cell. In recent years, new experimental techniques, based on radial diffraction experiment, have been developed in order to study the influence of nonhydrostatic stress on the lattice strains of the sample, for example to deduce shear strength and single crystal elastic moduli [*Singh*, 1993; *Mao et al.*, 1996; *Singh et al.*, 1998b; *Mao et al.*, 1998; *Duffy et al.*, 1999a, 1999b; *Cynn and Yoo*, 2000; *Merkel et al.*, 2002]. In pilot experiments on iron at 54 and 220 GPa development of strong textures was observed and, based on the pattern, slip systems in hexagonal closed packed iron (ϵ-Fe) could be identified [*Wenk et al.*, 2000].

[5] In this study, the experimental technique has been further refined in order to study the shear strength, elastic moduli, and deformation mechanisms in greater detail. Our experiments were performed on a composite sample with iron powder embedded in MgO powder. In this report, we discuss the shear strength, single crystal elastic moduli, elastic anisotropy, and texture development in MgO from ambient pressure to 47 GPa at room temperature. We also describe the experimental technique and data reduction in some details. In a subsequent paper, we will discuss the texture development, including the bcc-hcp phase transition, and elastic properties of iron with increasing pressure.

[6] MgO is a simple oxide with the NaCl structure stable to high temperatures and megabar pressures [*Duffy et al.*, 1995; *Dewaele et al.*, 2000]. The P-V-T equation of state has been subject of numerous experimental and theoretical studies (see *Speziale et al.* [2001] for a review) and is well constrained over the pressure range (and part of the temperature range) of the lower mantle. Elastic moduli have been measured experimentally under ambient pressure up to 1800 K [*Isaak et al.*, 1989; *Sinogeikin et al.*, 2000], under ambient temperature up to 50 GPa [*Yoneda*, 1990; *Shen et al.*, 1998; *Reichmann et al.*, 1998; *Sinogeikin and Bass*, 2000; *Zha et al.*, 2000], and both pressure and temperatures of 8 GPa and 1600 K [*Chen et al.*, 1998]. Theoretical calculations of the moduli have been performed to lower mantle conditions [*Mehl et al.*, 1986; *Isaak et al.*, 1990; *Karki et al.*, 1997, 1999; *Stixrude*, 2000]. The shear strength of polycrystalline MgO has been studied at low pressures and high temperatures [*Paterson and Weaver*, 1970], ambient temperature and high pressures [*Bridgman*, 1937; *Kinsland and Bassett*, 1977; *Meade and Jeanloz*, 1988; *Duffy et al.*, 1995; *Uchida et al.*, 1996], and moderate pressures and high temperatures [*Weidner et al.*, 1994]. Deformation mechanisms have been examined under low pressure conditions [*Weaver and Paterson*, 1969; *Paterson and Weaver*, 1970], on quenched sample from high-pressure and ambient temperature diamond anvil cell experiments [*Meade and Jeanloz*, 1988], but no analysis was performed in situ under pressures relevant for the Earth's mantle. Recently some simple shear deformation experiments were performed on magnesiowüstite and texture patterns were used to identify deformation mechanisms [*Stretton et al.*, 2001]. We will compare those results with data for pure MgO in the discussion section. The motivation of this research is to develop methods for quantitative high-pressure deformation experiments at conditions corresponding to the lower mantle and inner core and investigate the ductile deformation, elastic behavior and shear strength of important deep mantle and core phases. We are starting with MgO but this experimental technique can be applied to a whole range of materials. In the first section of this paper we describe the high-pressure experimental techniques and the fundamentals of the data analysis we perform. We then present X-ray measurements and results for the uniaxial stress, single crystal elastic moduli and preferred orientation in the sample. Finally, we discuss the implications of these results for the shear strength of polycrystalline MgO, its deformation mechanisms under high pressure and ambient temperature, single-crystal elastic anisotropy, and implications for the anisotropy of the Earth's mantle.

2. Experimental Details

2.1. Experimental Technique

[7] High pressures and deformation of the sample were produced using a diamond anvil cell. Diamonds with a 300-μm tip diameter were chosen and a 65-μm hole drilled in the gasket to form a sample chamber. To allow diffraction in a direction orthogonal to the compression axis (Figure 1), the confining gasket was made of a mixture of amorphous boron and epoxy. The gasket thickness under the diamond tip was 80 μm at the beginning of the experiment. The samples were ground to a grain size of less than 1 μm to ensure a sufficient number of crystallites for reliable statistics in the analysis. The samples were pressed into platelets between two large diamonds (1000 μm tip diameter). In order to fill the sample chamber, a layer of MgO was deposited at the bottom of the gasket hole. Then, we added a small platelet of iron. Finally, another platelet of MgO was added above the Fe platelet and pressed with the diamond anvils. The geometry of the samples was slightly different between experiment 1 and 2. In experiment 2, the Fe platelet was well centered in the MgO powder during the whole experiment. In experiment 1, it moved while the cell was being closed and was not completely surrounded by the MgO powder.

[8] Diffraction experiments were conducted using angle-dispersive synchrotron X-ray diffraction techniques at the ID-13 beam line of the GSECARS sector at the Advanced Photon Source. The incident monochromatic X-ray beam of wavelength 0.4246 Å was focused to 10 μm $\times$ 6 μm. The size of the incident X-ray beam was measured using a sharp edge. Incoming and diffracted beam passed through the amorphous gasket that absorbed little of the X-ray beam; the diffraction patterns were collected using an imaging plate orthogonal to the incoming beam. The diamond anvil cell was oriented with the diamond axis perpendicular to the incoming X-ray beam (Figure 1).

[9] In order to locate the sample, we performed X-ray scans while moving the diamond cell in directions orthog-

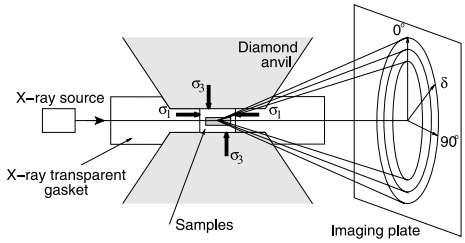

Figure 1. Schematic of the experiment. The polycrystalline sample is confined under nonhydrostatic stress conditions between the two diamond anvils. σ_3 is the axial stress imposed by the diamonds and σ_1 the radial stress imposed by the gasket. A monochromatic X-ray beam is sent through the gasket with the direction of the incoming beam orthogonal to the diamond axis and the data collected on an imaging plate orthogonal to the incoming beam. The position of the diffraction lines and intensity of diffraction are analyzed as a function of the azimuthal angle δ.

onal to the X-ray scans. The exact position of the sample was obtained by recording changes in the X-ray absorption. The result of these scans was then used to estimate the macroscopic size of the sample (thickness and width).

[10] Two sets of experiments were performed. Pressures in the first experiment ranged from 2 to 36 GPa. For experiment 2, patterns were recorded between 2 and 47 GPa on compression and 42 to 18 GPa on decompression. Each pattern took 7 to 10 min to record. Five diffraction peaks of MgO (111, 200, 220, 311, and 222) were used in the analysis. Equivalent hydrostatic pressures were measured according to the hydrostatic equation of state of MgO [*Speziale et al.*, 2001] after correcting the data for effects of nonhydrostatic stress [*Singh et al.*, 1998a]. In all cases, the pressures inferred from Fe do not differ from those deduced from MgO by more than 2 GPa.

2.2. Data Reduction

[11] The image plate diffraction data are analyzed with FIT2D [*Hammersley*, 1998]. Figure 2a shows an example of a measured diffraction spectrum. The variation of the diffraction intensity along the diffraction rings yields information about the orientations of the lattice planes and thus plastic strains, while the variation of the position of the diffraction peak along the rings is related to elastic properties of the sample. The imaging plate azimuthal angle δ is chosen to be zero when the diamond axis is in the plane defined by the diffracted and incoming beams (Figure 1). The raw image was corrected for distortion using a CeO_2 standard.

[12] In order to study the variations in the position of the diffraction peaks and their intensity with the azimuthal angle δ, the diffraction patterns are cut into small arcs of 2° to 4° and integrated with FIT2D. For each pattern, this produces between 55 and 110 segments with the diffraction intensity as a function of the diffraction angle 2θ for δ between −110° and 110°. Figure 2b presents some representative spectra from experiment 1 at 9.0 and 20.3 GPa, for δ = −90°, −44°, 0°, 44°, and 88° obtained with integrations

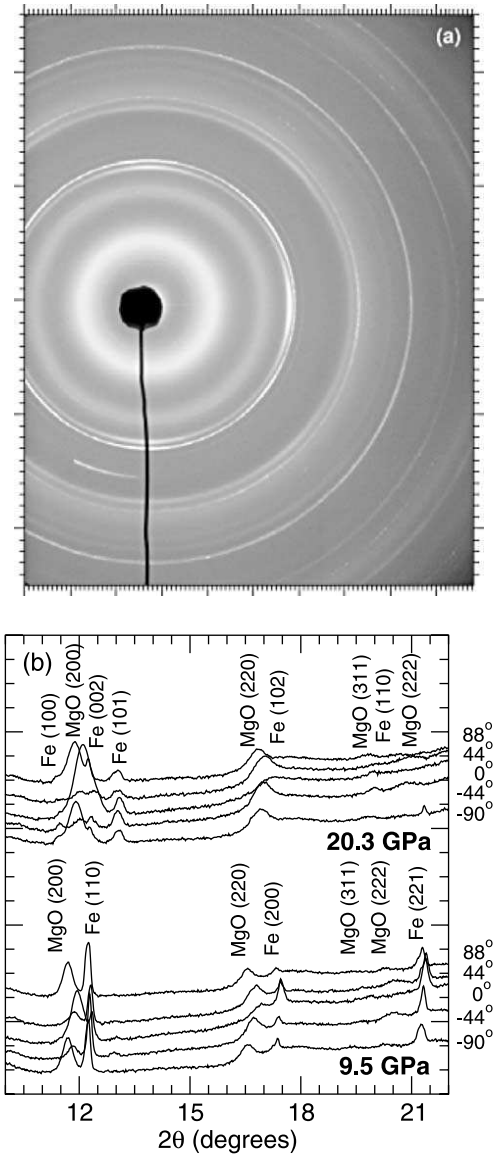

Figure 2. (a) Diffraction pattern at 9.5 GPa (experiment 1). (b) Representative spectra extracted from diffraction patterns from experiment 1 at 9.5 and 20.3 GPa for δ = −90°, −44°, 0°, 44°, and 88° obtained with integrations over 2° intervals. Diffraction peaks for MgO, α-Fe (P = 9.5 GPa) and ϵ-Fe (P = 20.3 GPa) are labeled on the figure.

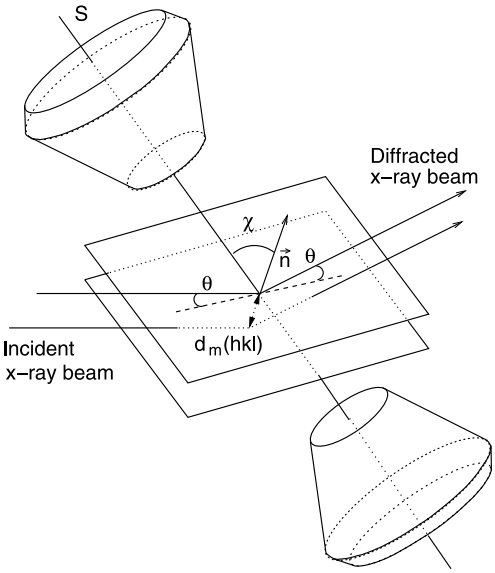

Figure 3. Geometry of the diffraction for a given χ angle between the diffracting plane normal $\vec{n}$ and the maximum stress axis S, we measure a d-spacing $d_m(hkl)$ function of the Miller indices h, k, and l, but also the angle χ because of the nonhydrostatic compression. When $\chi = 0°$, the diffracting plane is orthogonal with the maximum stress axis S, thus $d_m(hkl)$ is minimum. When $\chi = 90°$, the diffracting plane is aligned with the maximum stress axis S, thus $d_m(hkl)$ is maximum.

over 2° intervals. Diffraction peaks for MgO and Fe are labeled on the figure.

[13] The patterns are then fitted individually assuming Gaussian peak profiles and a linear local background. The pole distance χ, which corresponds to the angle between the diffracting plane normal and the load axis (Figure 3), is calculated from

$$\cos \chi = \cos \theta \cos \delta, \tag{1}$$

where θ is the diffraction angle.

2.3. Uniaxial Stress and Elasticity Analysis

[14] Because of the symmetry of the experiment (Figure 1), the stress conditions in the sample can be described as

$$\sigma = \begin{bmatrix} \sigma_1 & 0 & 0 \\ 0 & \sigma_1 & 0 \\ 0 & 0 & \sigma_3 \end{bmatrix} = \begin{bmatrix} \sigma_P & 0 & 0 \\ 0 & \sigma_P & 0 \\ 0 & 0 & \sigma_P \end{bmatrix} + \begin{bmatrix} -\frac{t}{3} & 0 & 0 \\ 0 & -\frac{t}{3} & 0 \\ 0 & 0 & 2\frac{t}{3} \end{bmatrix}, \tag{2}$$

where σ_1 and σ_3 are the radial and axial stress components, respectively; σ_P is the normal mean stress or equivalent hydrostatic pressure, and $t = (\sigma_3 - \sigma_1)$ is the uniaxial stress component (a measure of the deviatoric stress). Because of the nonhydrostatic stress, the observed d-spacings depend on the angle χ between the diffracting plane normal and the load axis (Figure 3).

[15] Variation of the d-spacings with χ, stress conditions in the sample and their relation to the uniaxial stress component, shear strength, and the elastic moduli of MgO were analyzed using the theory described by *Singh* [1993] and *Singh et al.* [1998a]. It relates the macroscopic strain and microscopic single crystal elastic moduli assuming a randomly textured sample under the Reuss-Voigt-Hill average [*Matthies et al.*, 2001] and has been successfully applied to other cubic symmetry materials under high pressure such as pyrite [*Merkel et al.*, 2002], gold and molybdenum [*Duffy et al.*, 1999b] and tantalum [*Cynn and Yoo*, 2000]. Other determinations of the single-crystal elastic moduli from diffraction experiments on polycrystals include copper, steel or aluminum at ambient pressure by X-ray diffraction [*Ganäupel-Herold et al.*, 1998], Ni-Cr-Fe alloy, hexagonal Ti, cubic zirconia, tetragonal zirconia under ambient pressure by neutron diffraction [*Howard and Kisi*, 1999], and ϵ-Fe up to 220 GPa by radial X-ray diffraction [*Mao et al.*, 1998]. The details of this analysis have been described elsewhere [*Singh*, 1993; *Singh et al.*, 1998a]. We present here a short summary of the main features.

[16] The d-spacings for a given set of lattice planes measured by X-ray diffraction is a function of the angle χ between the principal stress axis of the diamond cell and the diffracting plane normal (see Figure 3) and can be expressed as:

$$d_m(hkl) = d_P(hkl)[1 + (1 - 3\cos^2 \chi)Q(hkl)], \tag{3}$$

where $d_m(hkl)$ is the measured d-spacing and $d_P(hkl)$ the d-spacing under the hydrostatic pressure σ_P. $Q(hkl)$ is given by

$$Q(hkl) = \frac{t}{3}\left[\frac{\alpha}{2\,G_R(hkl)} + \frac{1-\alpha}{2\,G_V}\right]. \tag{4}$$

$G_R(hkl)$ and $G_V(hkl)$ are the shear moduli of the aggregate under the Reuss (iso-stress) and Voigt (iso-strain) approximations, respectively, and are not orientation dependent. The factor α, which lies between 0 and 1, determines the relative weight of isostress (Reuss) and isostrain (Voigt) conditions. It specifies the degree of stress and strain continuity across grains in the sample.

[17] For a cubic system, we have

$$(2\,G_V)^{-1} = \frac{5}{2}\frac{(S_{11} - S_{12})S_{44}}{[3(S_{11} - S_{12}) + S_{44}]} \tag{5}$$

and

$$(2\,G_R)^{-1} = S_{11} - S_{12} - 3\,S\,\Gamma(hkl), \tag{6}$$

where

$$S = S_{11} - S_{12} - S_{44}/2 \tag{7}$$

and

$$\Gamma(hkl) = \frac{h^2k^2 + k^2l^2 + l^2h^2}{(h^2 + k^2 + l^2)^2}. \tag{8}$$

The S_{ij} are the single crystal elastic compliances; S is a measure of elastic anisotropy.

[18] According to equation (3), $d_m(hkl)$ should vary linearly with $(1 - 3\cos^2\chi)$. The intercept ($\chi = 54.7°$) yields $d_P(hkl)$, the d-spacing due to the hydrostatic component of the stress, and the slope the product $d_P(hkl)Q(hkl)$.

[19] Equations (4)–(6) imply a linear relationship between $Q(hkl)$ and $3\Gamma(hkl)$ with intercept m_0 and slope m_1 given by

$$m_0 = \frac{t}{3}\left[\alpha(S_{11} - S_{12}) + (1 - \alpha)\frac{5}{2}\frac{(S_{11} - S_{12})S_{44}}{[3(S_{11} - S_{12}) + S_{44}]}\right] \quad (9)$$

$$m_1 = -\frac{\alpha t}{3}[S_{11} - S_{12} - S_{44}/2]. \quad (10)$$

[20] The bulk modulus K is defined by

$$K_T = -V\left(\frac{\partial p}{\partial V}\right)_T = \frac{1}{3[S_{11} + 2\,S_{12}]}. \quad (11)$$

The uniaxial stress component in the sample t is estimated with the relation

$$t = 6G\langle Q(hkl)\rangle, \quad (12)$$

where G is the shear modulus of the aggregate.

[21] Deducing m_0 and m_1 from the experimental data, using the bulk modulus calculated from an equation of state, and estimating the uniaxial stress t, we have enough information to deduce the three elastic compliances S_{11}, S_{12}, and S_{44} of a cubic material that can be inverted to the three independent elastic stiffnesses C_{11}, C_{12}, and C_{44}.

[22] The bulk modulus and its variation with pressure is calculated using a third-order finite strain equation

$$K_T = (1 + 2f)^{5/2}[k_0 + k_1 f], \quad (13)$$

where

$$k_0 = K_{0T}$$
$$k_1 = 3K_{0T}K'_{0T} - 5K_{0T}, \quad (14)$$

The Eulerian strain f is given by

$$f = \frac{1}{2}\left[\left(\frac{\rho}{\rho_0}\right)^{2/3} - 1\right]. \quad (15)$$

For the shear modulus, it is necessary to use a fourth-order finite-strain equation [*Davies and Dziewonski*, 1975; *Duffy and Ahrens*, 1992]

$$G_T = (1 + 2f)^{5/2}[g_0 + g_1 f + g_2 f^2], \quad (16)$$

where

$$g_0 = G_{0T}$$
$$g_1 = 3K_{0T}G'_{0T} - 5G_{0T}$$
$$g_2 = \frac{9}{2}\left[K^2_{0T}\left(G''_{0T} + (K'_{0T} - 4)\frac{G'_{0T}}{K_{0T}}\right) + \frac{35G_{0T}}{9}\right]. \quad (17)$$

[23] For MgO, we calibrate our analysis with the bulk and shear moduli obtained from Brillouin spectroscopy up to 50 GPa [*Zha et al.*, 2000] and first principles calculation at 300 K [*Karki et al.*, 1999]. Differences between isothermal and adiabatic parameters are defined by

$$\frac{K_S}{K_T} = 1 + \alpha\gamma T, \quad (18)$$

where the subsequent T and S refer to isothermal and adiabatic. For MgO, we use $\alpha_0 = 1.5 * 10^{-5}\mathrm{K}^{-1}$ and $\gamma_0 = 1.52$ [*Speziale et al.*, 2001]; thus, differences between adiabatic and isothermal parameters are on the order of 1.5% and are neglected in this study. Numerical values fitted to results from Brillouin spectroscopy and 300 K first-principles calculations are given in Table 1. The parameters used are in agreement with numerous high pressure and high temperature equation of state measurements (for a review, see *Speziale et al.* [2001]).

Table 1. Finite Strain Parameters Used to Scale This Analysis[a]

	Brillouin	First Principles
K_0, GPa	162.5	162
K_0'	3.99	4.15
G, GPa	130.4	128
G_0', GPa	2.89	2.90
G_0'', GPa^{-1}	−0.084	−0.042

[a] Fitted to results from Brillouin spectroscopy [*Zha et al.*, 2000] between 0 and 50 GPa and first principles calculations [*Karki et al.*, 1999] at 300 K and between 0 and 100 GPa.

2.4. Preferred Orientation Analysis

[24] Because of the application of nonhydrostatic stress, the polycrystalline MgO, after compaction, undergoes ductile deformation and strong lattice preferred orientation is produced. The texture in the sample can be represented by the orientation distribution function (ODF) which is a probability function for finding an orientation and it is normalized such that the integral over the whole orientation space is unity. An aggregate with a random orientation distribution has a probability of one for all orientations, or one multiple of a random distribution (m.r.d.). If preferred orientation is present, some orientations have probabilities higher than one and others lower than one [*Kocks et al.*, 1998].

[25] For each orientation g, the ODF $f(g)$ describes the probability density of finding crystallites that have the orientation g within dg. We have

$$f(g) > 0; \quad \int_G f(g)d\overline{g} = 1 \text{ where } d\overline{g} = \frac{1}{8\pi^2}dg. \quad (19)$$

The degree of anisotropy in the sample is expressed by the texture sharpness F_2 defined as

$$F_2 = \int_G [f(g)]^2 d\overline{g}. \quad (20)$$

For a material with random texture, the texture sharpness F_2 is equal to 1, for a textured material $F_2 > 1$.

[26] The analysis of the diffraction intensities to deduce the ODF is similar to that of *Heidelbach et al.* [1999] and *Wenk et al.* [2000]. Because of the axial symmetry of the stress conditions in the experiment (Figure 1 and equation (2)), it is sufficient to study the variation of the diffraction intensities with angle χ between the diffracting plane

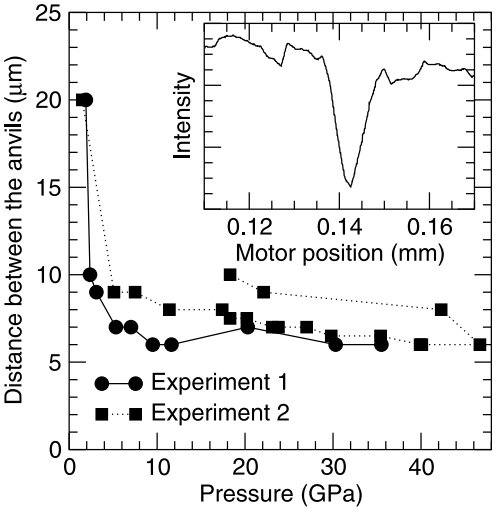

Figure 4. Distance between the diamond anvils as a function of pressure. Upon compression this is a good estimation of the sample thickness. However, upon decompression these quantities differ as the sample is not put into extension. In the inset we show an example of transmitted X-ray intensity measured while moving the diamond anvil cell perpendicular to the incoming beam that is used to deduce the sample thickness for experiment 1 at 7 GPa.

normal and the diamond axis in order to deduce the full ODF of the sample. The angle χ is related to the azimuth angle δ on the imaging plate by equation (1). Thus there is a blind region and orientations with $|\chi| < \theta$ cannot be probed in the experiment. The incomplete pole figures obtained from the measurements are nevertheless sufficient for calculating the three-dimensional ODF.

3. Results

3.1. Macroscopic and Microscopic Deformation

[27] Figure 4 shows the distance between the diamond anvils we deduce from the X-ray scans as a function of pressure for the two experiments. Upon compression, this is a good estimation of the macroscopic sample thickness. However, upon decompression, these quantities differ as the sample is not put into extension. The process can be divided into three sections. First, we observe a compaction of the sample powder due to the fact that the sample chamber was not fully filled with sample at the start of the experiment. The thickness varies greatly without any large pressure increase. Later the sample deforms regularly and the macroscopic strain of the sample reaches the order of 200%. This region is where we expect to see the texture developing. Above 15 GPa, the resolution of the X-ray scans does not allow us to observe any change in the thickness.

[28] Figure 5 presents the variation of *d*-spacing of the (200) line of MgO with $(1 - 3\cos^2\chi)$ for experiment 2 and selected pressures, where χ is the pole figure distance. Assuming a Reuss-Voigt-Hill micromechanical model and a sample with randomly oriented grains, a linear relationship is expected (section 2.3). Deviations between the linear fits and the data are due to intrinsic experimental errors and effects of texture on the lattice strains. These deviations cannot be resolved on these figures.

[29] Assuming a random texture and using the Reuss-Voigt-Hill approximation, the *d*-spacings at χ =57.4° correspond to the crystal unit cell under equivalent hydrostatic pressure (section 2.3). These were used to calibrate the pressure in the experiment with a previously measured hydrostatic equation of state [*Speziale et al.*, 2001].

3.2. Uniaxial Stress

[30] Using the least squares fits of the data from Figure 5, the shear modulus obtained from Brillouin spectroscopy or first-principle calculations (Table 1), we can evaluate the uniaxial stress component $t = \sigma_3 - \sigma_1$ in the sample (section 2.3). Figure 6 shows the evolution of t for experiments 1 and 2. In experiment 1, we see a sharp increase of t from 0 to 7 GPa between ambient pressure and 10 GPa. Above 10 GPa, the uniaxial stress component in the MgO sample remains approximately constant at 8 GPa. In experiment 2 (Figure 6b), t is better resolved and its behavior more complicated. With the phase transition of the companion Fe sample from the α-phase to the ϵ phase around 12 GPa, we observe a decrease of the uniaxial stress component within the MgO sample. This can be explained by the decrease in unit cell volume associated to the phase transition of iron which created a release of the stresses in the whole sample chamber. The companion Fe sample was

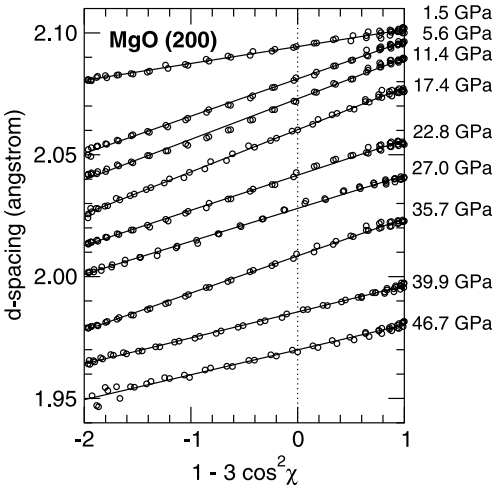

Figure 5. Variation of the *d*-spacing of the MgO (200) plane with $(1 - 3\cos^2\chi)$ where χ is the pole distance for selected pressures of experiment 2. The dotted line indicates the angle χ = 57.4° where, under a Reuss-Voigt-Hill and no texture approximation, the measured *d*-spacing corresponds to the unit cell under equivalent hydrostatic pressure. Solid lines are linear least squares fits through the data.

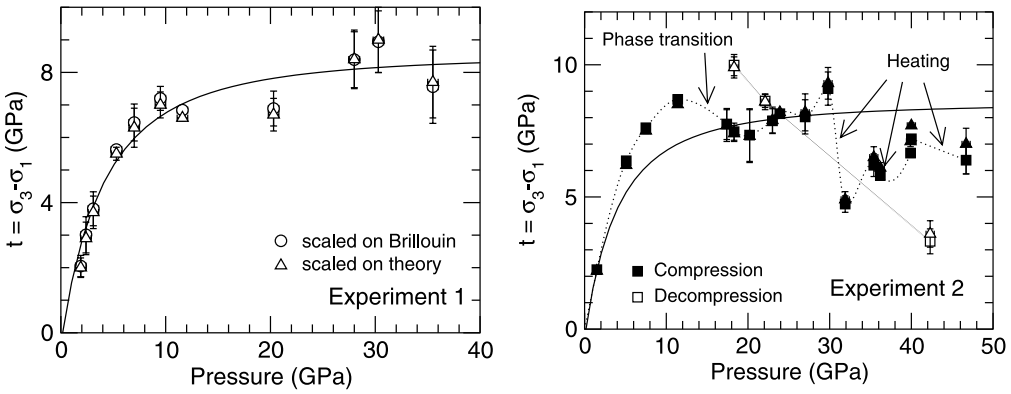

Figure 6. Uniaxial stress component in the MgO sample. (a) Uniaxial stress component in MgO upon compression for experiment 1 calculated using shear moduli from Brillouin spectroscopy (open squares) or first principles calculations (open triangles) (see Table 1). Solid line is a fit to the data. (b) Uniaxial stress component in MgO upon compression (solid symbols) and decompression (open symbols) for experiment 2 calculated using shear moduli from Brillouin spectroscopy (squares) or 300 K first principles calculations (triangles). Solid line is the fit from experiment 1, and dotted line a guide to the eye based on results scaled on Brillouin data. Operations performed on the Fe in contact with the MgO (phase transition, laser heating) are labeled.

heated using a YAG laser three times along the pressure increase, at 30, 35, and 40 GPa. We estimate that the temperature in Fe reached approximately 1200 K. However, this temperature is too low to allow precise measurement using the spectral radiometry techniques [*Heinz and Jeanloz*, 1987]. After heating, the MgO diffraction peaks remained very intense. Even though the iron might have reacted with the surrounding MgO powder, the amount of MgO present in the cell was still very important and we do not think it affected the data presented here. In all cases, the heating of the Fe sample released the stresses in the sample chamber, decreasing the uniaxial stress component in MgO.

3.3. Calculation of Elastic Moduli

[31] Assuming a random texture and a Reuss-Voigt-Hill micromechanical model, the single crystal elastic moduli can also be calculated from the fits in Figure 5 (section 2.3). The stress conditions in the sample, equivalent hydrostatic pressure and uniaxial stress, have to be precisely calibrated. Figure 7 presents the elastic moduli we obtained from experiment 1 using pressures deduced from the hydrostatic EOS of MgO [*Speziale et al.*, 2001] and uniaxial stress values from Figure 6 for $\alpha = 1$ (Reuss bound) and $\alpha = 0.5$ (Hill average) along with results from Brillouin spectroscopy [*Zha et al.*, 2000] and 300 K first principles calculations [*Karki et al.*, 1999].

[32] At low pressures, results from first principles calculations and Brillouin spectroscopy are not distinguishable and the Reuss average provides a better agreement for our results. It appears that the use of linear elasticity theory (section 2.3) still holds even though the uniaxial stress t is very large compared to the pressure. At higher pressures, results from the Reuss and Hill averages are very similar. This is due to the drop of elastic anisotropy of MgO (see section 4.4). m_1 in the lattice strains equations (equation (9)) is close to zero. Therefore we have a direct relation between $(C_{11} - C_{12})$ and C_{44} and the calculated elastic moduli do not depend on α. However, results from Brillouin spectroscopy and 300 K first-principles calculations diverge and our measurements are in better agreement with the elastic moduli from Brillouin spectroscopy.

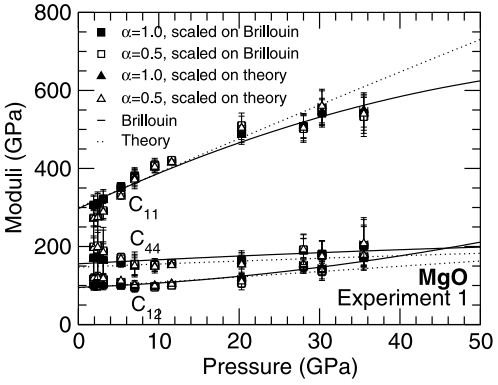

Figure 7. Elastic moduli of MgO calculated for experiment 1 assuming no texture in the sample We used both the Reuss bound (α =1, solid symbols) and Hill-average (α = 0.5, open symbols), and scaled the calculations on results from Brillouin spectroscopy from (squares) or 300 K first-principles calculations (triangles) (see Table 1). Solid and dotted lines show elastic moduli from Brillouin spectroscopy.

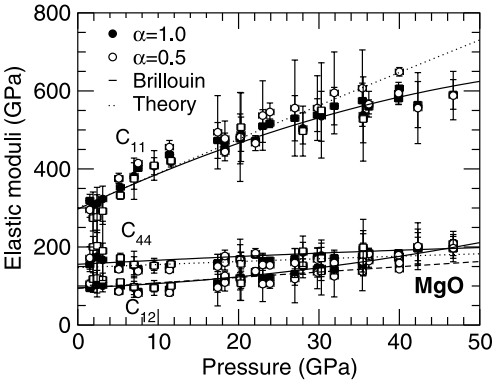

Figure 8. Elastic moduli of MgO calculated assuming no texture in the sample and using the Reuss bound (closed symbols) or Hill-average (open symbols) for experiment 1 and 2 and scaled on Brillouin spectroscopy (Table 1). Circles and squares are results from experiment 1 and 2, respectively. Solid and dotted lines are fits to results from Brillouin spectroscopy.

[33] Figure 8 and Table 2 present the elastic moduli of MgO from experiment 1 and 2 calculated under the Reuss or Hill approximation with uniaxial stress values scaled on Brillouin spectroscopy along with the results from Brillouin spectroscopy and 300 K first-principles calculations. The good agreement between the results of the two experimental methods proves the utility of the lattice strain analysis for determining elastic moduli using X-ray diffraction for materials with cubic symmetry. The very large degree of preferred orientations in the sample does not appear to have a great influence on the calculations. A critical step in the analysis is to constrain the exact stress conditions (pressure and uniaxial stress) in the sample.

3.4. Preferred Orientation

[34] Figure 9 presents the intensities of diffraction for MgO (200) and MgO (220) as a function of the angle χ between the diffraction plane normal and the diamonds axis for all increasing pressures in the first experiment. At 1.90 GPa we do not see any preferred orientation. The variation of the intensity of diffraction with χ is the same for both peaks (200) and (220). We deduce that this intensity variation is created by our experimental setup and this is used as a background correction for all other analyses. Above 1.90 GPa, we observe the progressive development of a sharp texture in the sample. The (200) peak exhibits a maximum of intensity of diffraction at $\chi = 0°$ and $\chi = 90°$, meaning that the $\langle 100 \rangle$ axis of the sides of the crystallites align parallel or orthogonal to the compression axis. The same relationship is observed in experiment 2.

[35] The intensity variations such as that shown in Figure 9 are used to calculate the ODF of the sample using the Beartex package [*Wenk et al.*, 1998]. Figure 10 shows a comparison between the observed intensities and those recalculated from the ODF for experiment 2 at 47 GPa. The good agreement between these curves gives us confidence in the quality of the fitted ODF.

3.5. Texture Evolution With Pressure

[36] Figure 11 shows the evolution of the texture index in the sample with pressure. In experiment 1, we reach a saturation of the texture index at 2.7 around 20 GPa, while in experiment 2 saturation occurs at 1.3 around 12 GPa.

[37] An efficient way to represent the complete orientation distribution of an axially symmetric texture is the inverse pole figure. An inverse pole figure represents the unique symmetry axis, in our case the compression direction, relative to crystal coordinates. An inverse pole figure displays the symmetry of the crystal, and for cubic MgO a triangle extending from 100 to 110 and 111 is sufficient for a complete representation.

[38] Figure 12 shows inverse pole figures for experiment 1 at 1.9, 5.3, 11.6, and 35.4 GPa. We observe the continuous development of a single fiber component 100 texture with pressure above 1.9 GPa. At highest pressure, the maximum pole density is 9.12 multiples of random distribution (m.r.d.). Results from experiment 2 are similar, although the magnitude of the preferred orientation is different, with a maximum pole density at highest pressures of 3.07 m.r.d.

4. Discussion

4.1. Pressure Dependence of the Yield Strength

[39] Before heating, the uniaxial stress component in MgO increases with the loading pressure and it saturates

Table 2. Uniaxial Stress and Single Crystal Elastic Moduli of MgO as a Function of Pressure for Experiments 1 and 2[a]

Experiment	P	$\sigma(P)$	t	$\sigma(t)$	C_{11}	$\sigma(C_{11})$	C_{12}	$\sigma(C_{12})$	C_{44}	$\sigma(C_{44})$
1	1.9	0.5	2.0	0.3	307	34	101	17	172	55
1	2.4	0.5	3.0	0.6	311	42	103	21	175	68
1	3.1	0.5	3.8	0.5	323	33	101	16	167	43
1	5.3	0.5	5.6	0.2	353	8	99	4	159	7
1	7.0	0.5	6.5	0.6	382	34	95	17	152	23
1	9.5	0.5	7.2	0.3	407	22	96	11	153	13
1	11.6	0.5	6.8	0.1	419	9	101	5	157	5
1	20.3	0.5	6.9	0.5	489	44	116	22	165	21
1	30.3	0.5	8.9	0.9	535	64	146	32	178	32
1	35.5	0.5	7.4	1.1	538	71	175	35	194	48
2	1.5	0.5	2.2	0.1	319	16	94	8	155	18
2	5.1	0.5	6.4	0.1	375	7	86	4	143	4
2	7.5	0.5	7.6	0.1	402	1	86	1	144	1
2	11.4	0.5	8.7	0.1	436	8	92	4	150	4
2	17.4	0.5	7.7	0.6	473	46	107	23	159	22
2	18.3	0.5	7.4	0.3	468	24	114	12	165	13
2	20.2	0.5	7.3	1.0	477	64	122	32	170	36
2	23.0	0.5	7.8	0.5	510	42	119	21	165	19
2	23.9	0.5	8.1	0.1	517	11	121	5	166	5
2	27.0	0.5	7.9	0.6	530	58	131	29	170	26
2	29.8	0.5	9.0	0.6	538	42	144	21	176	21
2	31.9	0.5	4.6	0.3	561	48	142	24	172	20
2	35.4	0.5	6.1	0.4	575	45	153	23	176	20
2	36.2	0.5	5.7	0.2	559	18	168	9	185	10
2	39.9	0.5	6.5	0.2	580	15	177	7	185	8
2	40.0	0.5	7.0	0.1	607	5	164	2	176	2
2	46.7	0.5	6.2	0.5	591	38	208	19	195	24
2	42.3	0.5	3.2	0.5	565	59	195	30	197	40
2	22.1	0.5	8.6	0.2	473	12	134	6	180	8
2	18.3	0.5	9.9	0.4	451	15	123	7	173	10

[a] Values were calculated using the Reuss bound and scaled on Brillouin spectroscopy (Table 1). Pressures, uniaxial stresses, moduli, and standard deviations are given in GPa.

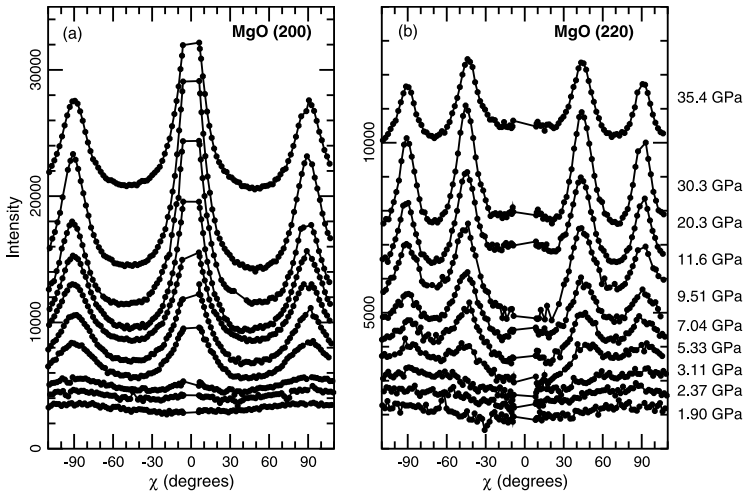

Figure 9. Intensity of diffraction as a function of the pole distance χ for MgO (200) (a) and MgO (220) (b) for all increasing pressures in experiment 1.

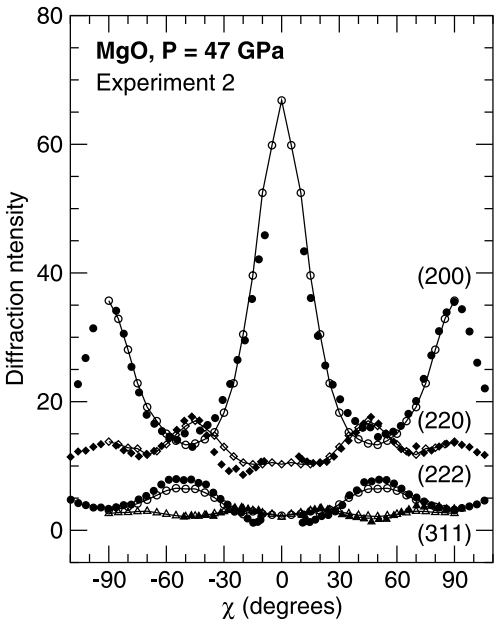

Figure 10. Observed intensities of diffraction and those recalculated from the orientation distribution function (ODF) as a function of the pole distance χ for the peaks (200), (220), (311), and (222), and experiment 2 at $P = 47$ GPa. Closed and open symbols are experimental and recalculated data, respectively. Peaks are labeled on the image.

around 10 GPa (Figure 6). Other studies of the uniaxial stress component in MgO under pressure include, opposed anvils and Paterson deformation apparatus experiments to 5 GPa [*Bridgman*, 1937; *Weaver and Paterson*, 1969; *Paterson and Weaver*, 1970], multianvil experiments to 8 GPa [*Weidner et al.*, 1994], Drickamer-type press experiments to 20 GPa [*Uchida et al.*, 1996] and diamond anvil cell experiments to 25 GPa [*Kinsland and Bassett*, 1977], between 10 and 40 GPa [*Meade and Jeanloz*, 1988], and to 225 GPa [*Duffy et al.*, 1995]. In all experiments, an increase in the uniaxial stress in the MgO sample with

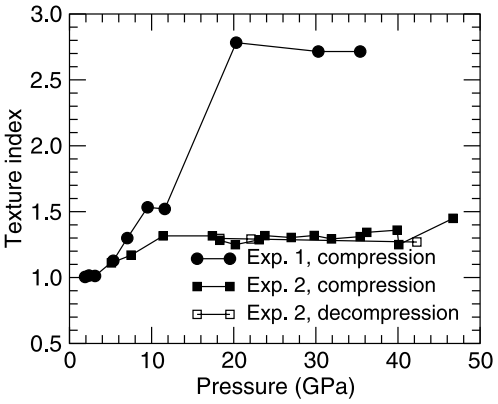

Figure 11. Evolution of texture index of MgO with pressure for experiment 1 upon compression and experiment 2 upon compression and decompression. In experiment 1, we reach a saturation at 2.7 around $P = 20$ GPa, while we reach saturation at 1.3 around $P = 12$ GPa in experiment 2.

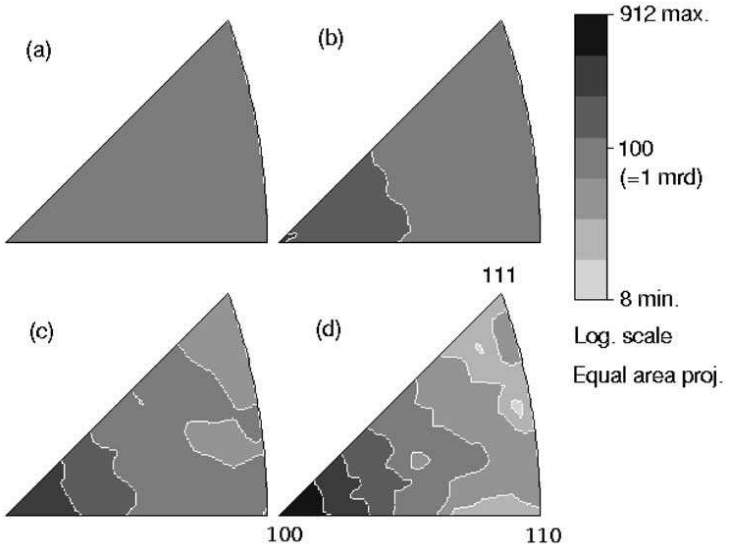

Figure 12. Experimental inverse pole figures illustrating the development of preferred orientation in MgO at 1.9 (a), 5.3 (b), 11.6 (c), and 35.4 (d) GPa for experiment 1. The maximum pole density is 1.0, 2.45, 4.59, and 9.12 multiples of random distribution (m.r.d.) for 1.9, 5.3, 11.6, and 35.4 GPa, respectively.

pressure was observed, although the magnitude of the increase differed (e.g., Figure 13).

[40] The maximum uniaxial stress supported by a material is determined by its yield strength; that is $t \leq \sigma_y$, where σ_y is the material yield strength. The uniaxial stress t varies with sample environment and equality holds only if the sample deforms plastically. The yield strength of a polycrystalline material depends on the possible slip systems and their critical resolved shear stress (CRSS), but also on the texture in the sample. Moreover, an increase in the density of dislocations in the sample will result in hardening, that is an increase of the yield stress [*Poirier*, 1985]. It is worth noting that most of the experiments from Figure 13 differ from mechanical tests at constant strain rate which provide a measure of the yield stress at a given pressure, temperature, and imposed strain rate. In these experiments, strain, strain rate and pressure cannot be decoupled, and therefore, we use a more general definition of the yield stress.

[41] As seen on Figure 13, several experiments, including this one, observe a similar behavior of the uniaxial stress in polycrystalline MgO at low pressure. It increases linearly with pressure with $dt/dP \approx 0.5-0.85$ up to a maximum pressure, function of the experiment, after which it saturates. Results from *Meade and Jeanloz* [1988] and *Duffy et al.* [1995] show a much smoother increase of the uniaxial stress with pressure. Table 3 summarizes the maximum values of uniaxial stress obtained in different experiments on polycrystalline MgO and the pressures at which they were obtained. In these experiments, we obtain a value of t

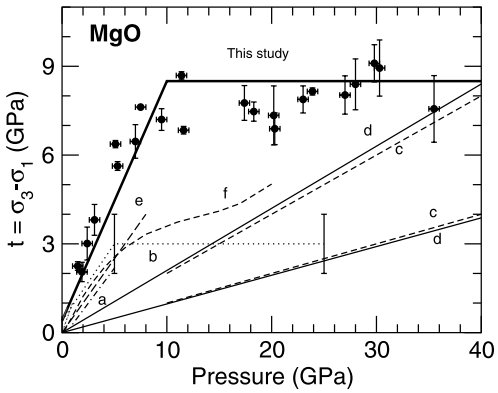

Figure 13. Uniaxial stress component in MgO measured in this study (thick solid line) compared with previous measurements from *Bridgman* [1937] (dot-dashed line, a), *Kinsland and Bassett* [1977] (dotted line, b), *Meade and Jeanloz* [1988] (dashed line c), *Duffy et al.* [1995] (solid line, d), *Weidner et al.* [1994] (long-dashed line, e), and *Uchida et al.* [1996] (dashed line, f). Measurements from *Paterson and Weaver* [1970] fall between just above those of *Bridgman* [1937].

Table 3. Maximum Uniaxial Stress Component and Pressure at Which It Was Obtained in Polycrystalline MgO From Different Experiments[a]

	P	$t = \sigma_3 - \sigma_1$
Paterson and Weaver [1970]	0.5	0.85
Bridgman [1937]	5	2.5
Kinsland and Bassett [1977]	5(±1)	3 ± 1
Weidner et al. [1994]	8	4.5(±1)
Uchida et al. [1996]	20	5
Meade and Jeanloz [1988]	40	8
Meade and Jeanloz [1988]	40	4
Duffy et al. [1995]	100	20
Duffy et al. [1995]	220	>22
This experiment	10(±1)	8.5(±1)

[a] Stress component $t = \sigma_3 - \sigma_1$ and pressure are in GPa.

of 8.5(±1) GPa at 10(±1) GPa that is about twice larger that other observations.

[42] Several observations can explain the apparent disagreement between these data. First of all, the yield strength is an upper bound for the uniaxial stress, and it is reached only if the material deforms plastically. For the case of opposed anvil geometry such as the diamond anvil cell, this limit is not always reached between the anvil tips, as shown by finite element modeling [*Merkel et al.*, 2000]. The second effect that has to be taken in consideration is that the yield stress actually depends on the stress history of the polycrystalline sample, and is increased by an augmentation of the dislocation density. In our experiments, the uniaxial stress increases drastically up to a pressure of about 10(±1) GPa, after which the increase is much smoother. It can be noticed that this coincides with a change of slope in the curve of the macroscopic deformation of the sample with pressure (Figure 4), changes in the evolution of the texture sharpness with pressure (Figure 11), and the phase transition in the companion Fe sample. Therefore, we infer that there must have been stress hardening in our sample, because of an increase in dislocation density, up to a pressure of about 10(±1) GPa, after which it either stopped or slowed down drastically.

[43] No general conclusion about the evolution of a polycrystalline yield stress of MgO with pressure can be drawn from these experiments. However, for our sample, we observed an uniaxial stress component of about 8.5(±1) GPa at 10(±1) GPa, that implies $\sigma_y \geq 8.5$ GPa at pressures greater than 10 GPa, but this value of σ_y probably includes effects of stress hardening.

4.2. Texture Evolution

[44] The observed texture pattern is comparatively simple with a maximum at [100] in the inverse pole figure; the result can be described as a single fiber component 100 (Figure 12). In experiment 1, the texture increases systematically with pressure and reaches a saturation at 20 GPa with a very high maximal value in the inverse pole figure of over 9 m.r.d. and a corresponding texture index of 2.8. In experiment 2, the texture increases with pressure and reaches saturation at about 12 GPa with a maximum in the inverse pole figure of 3.07 m.r.d. and a texture index of 1.3. During unloading the texture is preserved. Differences between the two experiments are attributed to two factors. The grain size distribution may differ between the two samples, although the average grain size was always less than 1 μm according to visual observations. A small grain size may cause grain boundary sliding and randomization. But the different disposition of the MgO and companion Fe samples might also have this effect. In experiment 1, the MgO and Fe sample were contiguous, unlike experiment 2 where the MgO sample completely surrounded the Fe. This might explain why in experiment 2, the evolution of texture in MgO stopped with the phase transition of the iron from bcc to hcp at 12 GPa.

[45] The (100) texture is similar to that observed in previous compression experiments on MgO [*Meade and Jeanloz*, 1988] but different from other phases with NaCl structure (e.g., halite [*Kern and Braun*, 1973; *Franssen and Spiers*, 1990], LiF [*Kruger and Bowman*, 1996], PbS [*Siemes and Hennig-Michaeli*, 1985]), which generally display two components, a (110) fiber connected with a (100) fiber.

[46] The 100 (cube) texture has been observed after recrystallization, both in extension [*Skrotzki and Welch*, 1983] and compression but our room temperature samples are likely to experience minimal diffusion and show no indication of grain growth. A cube texture could also be expected to develop during compaction if the original fragments were platy parallel to the {100} cleavage. However, there is no evidence that the original grains were platy rather than equiaxed, and the main texture development occurred after compaction. Accordingly, it is reasonable to argue that preferred orientation is due to deformation by slip. In this case the interpretation of deformation mechanisms is aided by comparing the experimental textures with simulated textures based on polycrystal plasticity theory.

4.3. Polycrystal Plasticity

[47] The classic theory of *Taylor* [1938] has been extensively applied to the prediction of plastic deformation of single-phase cubic metallic polycrystals (for reviews, see, e.g., *Kocks et al.* [1998]). This approach assumes homogeneous strain (compatibility) and requires all crystals to deform at the same rate. However, this behavior is not always observed, particularly in low-symmetry minerals where some orientations deform more easily than others to maintain stress equilibrium. In real materials both compatibility and equilibrium need to be maintained, resulting in heterogeneous deformation at the local intracrystalline scale which is still difficult to model numerically and has so far only been attempted for cubic metals with finite element methods [*Mika and Dawson*, 1999]. In recent years, several less sophisticated approaches to model heterogeneous deformation of anisotropic polycrystals have been developed. One is the viscoplastic self-consistent (VPSC) method that is based on regarding each grain as an inclusion embedded in an homogeneous equivalent medium, having the average properties of the polycrystal [*Molinari et al.*, 1987; *Tomé and Canova*, 1998]. This method has been used to predict texture development in various minerals (for a review, see *Wenk* [1999]).

[48] Most relevant for this investigation are simulations of texture development for halite [*Chin*, 1973; *Chin and Mammel*, 1973; *Siemes*, 1974; *Wenk et al.*, 1989] (R. A. Lebensohn et al., Heterogeneous deformation and texture development in halite: Modeling with finite element and

Table 4. Slip Systems, Critical Resolved Shear Stress Ratios (CRSS), and Hardening Parameters Used in the Simulations

Slip System	CRSS ratio	Hardening Parameter
$\{110\}\langle 1\bar{1}0\rangle$	1	2
$\{111\}\langle 1\bar{1}0\rangle$	10	2
$\{100\}\langle 011\rangle$	10	2

self-consistent approaches, submitted to *Tectonophysics*, 2002, hereinafter referred to as Lebensohn et al., submitted manuscript, 2002.). Simulations for halite are rather extraordinary because Taylor and VPSC predicted a very different deformation behavior, particularly for deformation in axial extension. The reason for this difference is that halite, though a mineral with cubic crystal structure, has several slip modes with different relative threshold stresses that vary with temperature and strain rate. In the case of halite at low temperature the $\{110\}\langle 1\bar{1}0\rangle$ slip mode is soft and the $\{100\}\langle 011\rangle$ and $\{111\}\langle 1\bar{1}0\rangle$ slip modes are much harder [*Carter and Heard*, 1970; *Strotzki and Haasen*, 1981]. However, activation of only the soft system does not satisfy the von Mises criterion [*von Mises*, 1928] for an arbitrary deformation. Any combination of soft $\{110\}$ slip systems is unable to accommodate shears of the elementary cube and therefore a combination of hard $\{100\}$ and $\{111\}$ systems become activated. *Chin and Mammel* [1973] discussed the influence of slip systems on texture development in a qualitative way and suggest that $\{110\}$ slip compression axes rotate toward (100), whereas with $\{100\}$ slip they rotate toward (110).

[49] There is little information on deformation mechanisms for MgO. The few studies that exist indicate that slip systems similar to those in halite deformed at low temperature are active, but the plastic anisotropy is even more extreme with $\{110\}\langle 1\bar{1}0\rangle$ being by far the easiest system [*Weaver and Paterson*, 1969; *Paterson and Weaver*, 1970; *Skrotzki and Haasen*, 1984; *Meade and Jeanloz*, 1988; *Foitzik et al.*, 1989]. Based on these results, we assumed a high plastic anisotropy with hard slip modes [i.e., the $\{100\}$ and $\{111\}$ modes being 10 times harder than the $\{110\}$ soft mode] (Table 4).

[50] In order to simulate texture evolution in these deformation experiments on MgO we have used both the Taylor and the self-consistent approaches as implemented in the polycrystal plasticity method of *Lebensohn and Tomé* [1994]. An initial assembly of 2000 randomly oriented grains were deformed in axial compression with 2.5% strain increments to a total von Mises strain of 100%. A linear hardening law was used with a hardening coefficient (stress/strain slope) of 2. The rate-sensitivity of the material was taken as m = 0.05 (stress exponent n = 20) as determined by *Paterson and Weaver* [1970]. Previous studies showed that Taylor and self-consistent simulations give very different results [*Wenk et al.*, 1989] (Lebensohn et al., submited manuscript, 2002). In Taylor simulations the hard $\{100\}$ system is the most active in order to enable compatibility, whereas in self-consistent simulations all deformation occurs on the soft $\{110\}$ system. The resulting textures are different. As in previous simulations Taylor simulations (not shown) show in inverse pole figures a maximum at (110) with a broad shoulder toward (100). Self-consistent simulations (Figure 15) show a single maximum at (100) that can be directly compared with the experimental inverse pole figures in Figure 12.

[51] Some statistical considerations need to be clarified for comparing the experimental and simulated textures to get an independent estimation of strain. We obtained a continuous orientation distribution from discrete orientations in the simulations by entering individual orientations into $5^\circ \times 5^\circ \times 5^\circ$ cells of the ODF. These cells were then smoothed with a Gauss filter. From the smoothed ODF, inverse pole figures were calculated, which are represented as contoured diagrams. The texture strength (expressed as the texture index F_2 and as maximum pole densities) depends on the smoothing, as well as on the number of orientations [*Matthies and Wagner*, 1996]. In Figure 14 we show the evolution of F_2 with deformation for different conditions. While there is some uncertainty, 2000 grains and a 7.5° Gauss filter reasonably represent the experimental conditions. A texture index between 1.5 and 2 corresponds to a 50–75% von Mises strain.

[52] While the Taylor texture (not shown) is very different from that observed in experiment, the self-consistent texture with a single fiber component at (100) is very similar to that observed in the experiments (Figure 15). In the simulations the maximum increases from 1.8 at 25% strain to 3.0 at 50%, 5.7 at 75% and 10.7 at 100%. $\{110\}\langle 1\bar{1}0\rangle$ is the only active slip system. If the CRSS ratio is reduced from 10 to below 5, harder slip systems become active, and below 2 the self-consistent texture pattern resembles that observed with the Taylor approach. Obviously, deformation that only activates the $\{110\}$ system results in high local incompatibilities, which have to be accommodated by other mechanisms such as grain boundary sliding. Unfortunately we have no information on the microstructures that develop at high pressure in these experiments and therefore this issue cannot be resolved.

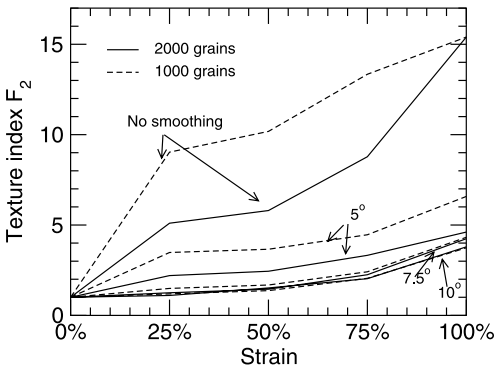

Figure 14. Texture index calculated in the self-consistent simulations as a function a strain for different statistical parameters. Dashed and solid lines are calculations for 1000 and 2000 grains, respectively. For both hypotheses, the ODF was calculated without smoothing or with a 5°, 7.5°, and 10° Gauss filter. Results with 2000 grains and a 7.5° Gauss filter were used for comparison with experimental results.

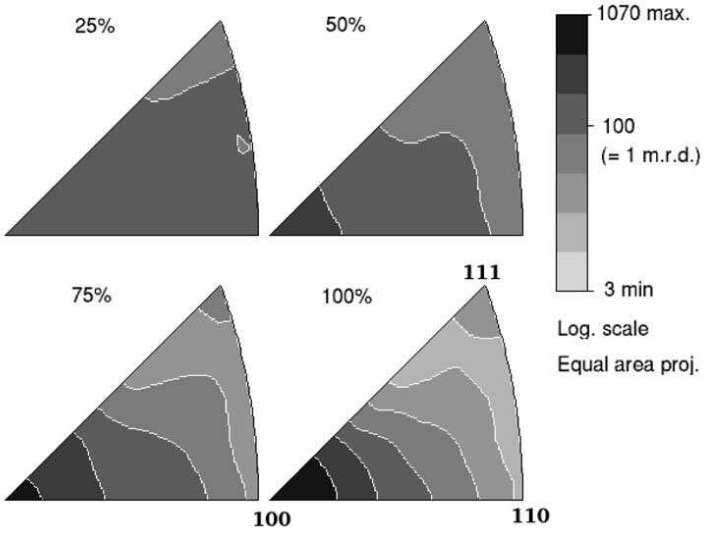

Figure 15. Inverse pole figures illustrating simulated texture development in MgO for 20°C conditions after 25, 50, 75, and 100% strain in axial compression calculated with the viscoplastic self-consistent model.

[53] We have attempted many conditions and slip systems with both models but, except for self-consistent solutions with $\{110\}\langle 1\bar{1}0\rangle$ models, we could not reproduce the observed texture. We conclude that the {110} slip system is the only significantly active slip system in MgO at high pressure and ambient temperature.

4.4. Elastic Anisotropy

[54] Understanding the evolution of elastic anisotropy of deep Earth's minerals with increasing pressure and temperature is of fundamental importance for the understanding of the seismic anisotropy of the Earth's interior [*Mainprice et al.*, 2000]. For cubic materials, it is convenient to express the single crystal anisotropy in terms of the Zener ratio which is the ratio of the shear moduli in the (100) and (110) planes in the [100] direction,

$$Z = \frac{2C_{44}}{C_{11} - C_{12}} = \frac{2(S_{11} - S_{12})}{S_{44}} \tag{21}$$

For elastically isotropic materials, we have $Z = 1$. Under the Reuss approximation, Z can be directly measured from radial diffraction experiments, without the use of any assumed bulk property [*Singh et al.*, 1998a; *Duffy et al.*, 1999b; *Merkel et al.*, 2002].

[55] In our experiments, and under the Reuss approximation, Z decreases from its ambient pressure value of 1.546 and saturates at about 0.9 (±0.2) at highest pressures, in agreement with measurements from Brillouin spectroscopy [*Zha et al.*, 2000; *Sinogeikin and Bass*, 2000]. Calculations under the Hill-average provides similar results, increasing the scatter in the data and the anisotropy (Figure 16). Theoretical calculations [*Mehl et al.*, 1986; *Karki et al.*, 1999] predict a continuous decrease in Z with increasing pressures. Observation on the *hkl*-dependence of the lattice strains in conventional diffraction experiments

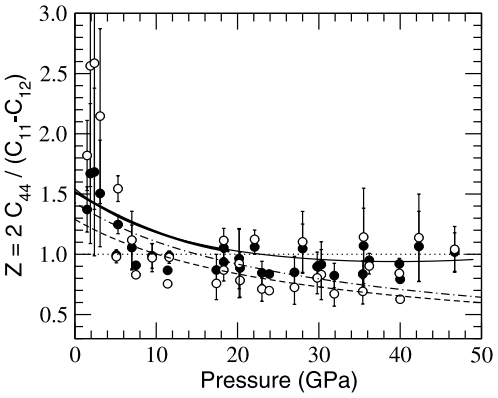

Figure 16. Elastic anisotropy in MgO expressed with the Zener ratio Z. Results from these experiments calculated under the Reuss bound (solid circles) and Hill average (open circles), Brillouin spectroscopy to 19 GPa from *Sinogeikin and Bass* [2000] (thick solid line) and to 55 GPa from *Zha et al.* [2000] (thin solid line), and first principles calculations from *Mehl et al.* [1986] (dotted line) and *Karki et al.* [1999] (dot-dashed line) are indicated.

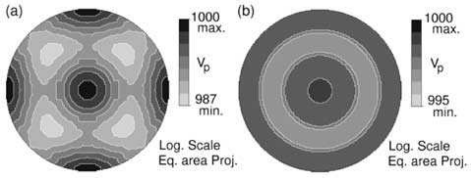

Figure 17. P wave velocity surfaces at 47 GPa. (a) Single crystal velocity surface (b) Velocity surface for the experimental texture measured in this experiment.

such as *Duffy et al.* [1995] and *Speziale et al.* [2001] or radial diffraction experiment [*Uchida et al.*, 1996] require an anisotropy less than 1 at high pressure, with a change in the sign of the anisotropy between 3 and 10 GPa. This is not inconsistent with the results presented here, that show an anisotropy roughly lower than 1 at high pressure, with a change of sign around 8 GPa.

[56] Figure 17 shows the P wave velocity surfaces at 47 GPa for an MgO single crystal and for the polycrystal with the experimental texture from Figure 12 calculated with the single crystal elastic moduli at this pressure. In the case of the aggregate, the velocity surface displays the symmetry of the sample and is axially symmetric. There are two trends: with increasing pressure the texture increases; however, at the highest pressures the single crystal-elastic anisotropy decreases, resulting in a reduced aggregate anisotropy.

4.5. Implications for the Lower Mantle

[57] Magnesiowüstite is generally believed to be the second most abundant mineral in the Earth's lower mantle. Therefore, understanding the elasticity and rheology of the pure MgO end-member can yield important information about this region of the planet. For cubic materials, single crystal elastic anisotropy and seismic anisotropy can be conveniently related through the anisotropy factor A, defined as

$$A = \frac{2C_{44} + C_{12}}{C_{11}} - 1 \tag{22}$$

For an isotropic material, A equals zero. The anisotropies of the P, S1, and S2 waves are then given by [e.g., *Karki et al.*, 1997]

$$A_P = \frac{2A}{3},\ A_{S1} = -\frac{A}{2} \text{ and } A_{S2} = -\frac{3A}{8} \tag{23}$$

These experiments (consistent with Brillouin measurements [*Zha et al.*, 2000]) indicate a decrease in A from its value of 0.36 at ambient conditions to $-0.05(\pm 0.10)$ at 45 GPa, giving an almost elastically isotropic material at deep mantle pressures. However, zero pressure measurements of the temperature dependence of the elastic moduli of MgO predict an increase of A to 0.77 at 1800 K [*Isaak et al.*, 1989]. Therefore, there is a competing effect of pressure and temperature on the single crystal elastic anisotropy of MgO that could lead to significant anisotropy under lower mantle conditions.

[58] In order to estimate the elastic moduli of MgO at high pressure and temperature, we carry a second-order polynomial extrapolation. We used the pressure and temperatures derivatives from this analysis and *Isaak et al.*'s [1989], respectively. Cross pressure and temperature derivatives have been measured at 8 GPa and between 300 and 1500 K [*Chen et al.*, 1998] but they were not fitted with the same pressure derivatives and are not consistent with this analysis, thus they are not used here. The data fitted ranges between 0 and 47 GPa at 300 K and 300 to 1800 K at ambient pressure. Therefore we feel confident with an extrapolation between 660 km (24 GPa, 1900–2300 K) to about 1660 km depth (70 GPa, 2300–2700 K). This is shown in Figure 18 for the warm and cold geotherms used by *Gillet et al.* [2000]. The anisotropy factor A varies from $0.115(\pm 0.010)$ at 670 km to $0.180(\pm 0.005)$ at 1660 km with a minimum of $0.050(\pm 0.010)$ at 1050 km. Moreover, *Chen et al.* [1998] showed that neglecting temperature derivative of the pressure derivatives underestimates the elastic anisotropy of MgO. Thus, a fairly high single crystal elastic anisotropy of MgO under lower mantle conditions is expected.

[59] The influence of iron substitution on the single-crystal elastic anisotropy of (Mg, Fe)O magnesiowüstite under lower mantle conditions remains to be examined directly by experiments. High P-T element partitioning experiments indicate that the amount of Fe present in (Mg, Fe)O in the lower mantle could range from around 10 to 45 mol % FeO [e.g., *Mao et al.*, 1997; *Andrault*, 2001, and references therein]. Ambient conditions measurements of elastic moduli show that A is essentially constant from pure periclase end-member to compositions with ~25% FeO, but then decreases sharply with the FeO end-member being nearly isotropic [*Jacobsen et al.*, 2002]. Thus there are three competing effects of pressure, temperature and composition for the anisotropy of magnesiowüstite. The anisotropy tends to decrease with increasing iron content and increasing pressure, while it increases with temperature. Such conclusions may have to be modified if (Mg, Fe)O undergoes phase transformations at high pressure and temperature [*Mao et al.*, 1996; *Dubrowinsky et*

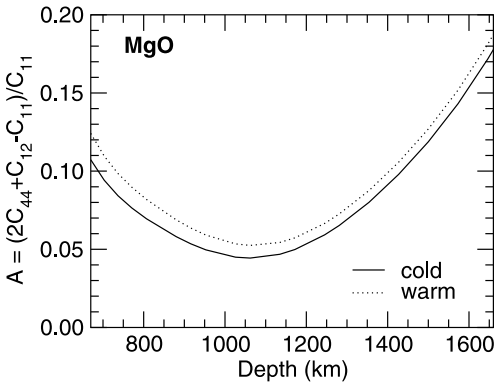

Figure 18. Elastic anisotropy of MgO under the conditions of the upper part of the lower mantle for a cold (T = 1900 K at 670 km, solid line) and a warm (T = 2300 K at 670 km, dotted line) average lower mantle geotherm.

al., 2000]. This study focused on the high-pressure properties of pure MgO to establish trends for the simple endmember. Additional work, using the techniques presented here, is required to determine the deformation mechanisms and elastic anisotropy of magnesiowüstite under lower mantle conditions.

[60] As for the anisotropy of an aggregate, our deformation experiments on MgO show the development of a very large degree of preferred orientation with increasing pressure. Although we did not measure strain rates, it was observed that 10 to 20 min were needed to stabilize the stress conditions after each increase of load. Therefore, we estimate that the time range of the experiments was about 10^3 s and that our strain rates are on the order of 10^{-3} s^{-1}. Extrapolating our observations to deep Earth conditions (in terms of strain rates and temperature), we infer that a noticable anisotropy could develop in polycrystalline MgO under lower mantle conditions.

[61] The possibility that different slip systems operate at high temperature at these pressures needs to be considered. In NaCl other slip systems do become active as the homologous temperature is approached. In alkali halides there is a high plastic anisotropy at room temperature which decreases with increasing temperature [*Strotzki and Haasen*, 1981; *Strotzki et al.*, 1981]. This may also apply to MgO, though probably not as drastically, so that {110} slip still dominates. At the high temperatures and slow strain rates in the lower mantle, diffusive processes during recovery would alleviate heterogeneity and incompatibility due to activation of a single slip system. Ambient pressure experiments have demonstrated that the CRSS for the {110} and {100} slip systems decrease drastically between ambient temperature and 1500 K, but the plastic anisotropy (i.e., the difference between the CRSS) remains [*Foitzik et al.*, 1989]. Multianvil experiments on MgO at 8 GPa between 300 and 1200° showed a significant temperature dependence of the yield strength with an abrupt change at 500° [*Weidner et al.*, 1994]. This was explained by a change of deformation mechanism from dislocation glide to power law creep with increasing temperature and decreasing deviatory stress. Deformation mechanisms may also be influenced by chemical composition. Simple shear experiments at 0.3 GPa and above 1000 K on magnesiowüstite by *Stretton et al.* [2001] produced texture patterns similar to those observed in fcc metals [e.g., *Hughes et al.*, 2000] suggesting that in this material, and at high temperature, many slip systems are active, including $\{111\}\langle 1\bar{1}0\rangle$. Unfortunately simple shear texture patterns of cubic materials are rather insensitive to slip system activity. Therefore, further high P-T investigations of the rheology of MgO and magnesiowüstite of realistic mantle composition, as well as polyphase mixtures, are needed to establish deformation mechanisms and their relevance for the dynamic processes in the deep mantle.

5. Conclusions

[62] We have presented experimental methods to investigate the evolution of single crystal elastic moduli and anisotropy, polycrystal yield strength and deformation mechanisms at pressures relevant to the Earth's deep interior. Measurements are obtained in situ using diamond cell synchrotron X-ray diffraction techniques. In this study, we applied this technique to MgO polycrystals to 47 GPa at room temperature. The results demonstrate the development of a strong texture with increasing pressure in this material. The elastic distortion of the lattice suggests that nonhydrostatic stresses reaches 8.5(±1) GPa and causes deformation of 50–100%. A quantitative comparison of experimental textures and results from polycrystal plasticity simulations suggests that $\{110\}\langle 1\bar{1}0\rangle$ is the only significantly active slip system at the conditions of these experiments.

[63] Although we may include effects of stress hardening because of an increased dislocation density, analysis of the low temperature yield strength suggests an increase from the ambient pressure value of 0.4 GPa to a minimum of 8.5(±1) GPa at 10(±1) GPa and higher pressures. The single crystal elastic anisotropy tends to decrease with pressure, with the material becoming almost elastically isotropic at pressures of about 50 GPa. However, a competing effect of pressure and temperature results in single crystal elastic anisotropy of MgO at lower mantle conditions. The anisotropy factor A decreases from 0.115(±0.010) at 670 km depth to 0.050(±0.010) at 1050 km depth and then increases again to 0.180(±0.005) at 1660 km depth.

[64] With this study we show the feasibility of the experimental study of deformation mechanisms, single crystal and polycrystal elastic moduli and anisotropy, as well as polycrystal strength at deep mantle pressures. This approach can now be extended to study the behavior at both high pressure and temperature. The same technique can also be used to study other mantle component, including the influence of iron substitution in (Mg, Fe)O magnesiowüstite and (Mg, Fe)SiO_3 perovskite, as well as deformation of composites of the two minerals. Such experiments will provide information about deformation mechanisms and mechanical properties of minerals in the deep Earth that are a prerequisite for realistic geodynamic models.

[65] **Acknowledgments.** The authors are grateful to Emmanuel Soignar for assistance during the experiment, Patrick Cordier for comments on the manuscript, and Tom Duffy and David Mainprice for useful reviews. This work was supported by NSF, DOE, the Center for High Pressure Research, the W.M. Keck Foundation, and the CNRS-INSU program "Intérieur de la Terre." H. R. W. acknowledges support from NSF (EAR 99-02866), IGPP-LANL, the UC Education Abroad Program. and the A. von Humboldt Foundation. He appreciates the hospitality while visiting ENS-Lyon during a sabbatical leave.

References

Andrault, D., Evaluation of (Mg, Fe) partitioning between silicate perovskite and magnesiowüstite up to 120 GPa and 2300 K, *J. Geophys. Res.*, *106*, 2079–2087, 2001.

Bridgman, P. W., Shearing phenomena at high pressures, particularly in inorganic compounds, *Proc. Am. Acad. Sci.*, *71*, 387–460, 1937.

Carter, N. L., and H. C. Heard, Temperature and rate dependent deformation of halite, *Am. J. Sci.*, *269*, 193–249, 1970.

Chastel, Y. B., P. R. Dawson, H. R. Wenk, and K. Bennett, Anisotropic convection with implications for the upper mantle, *J. Geophys. Res.*, *98*, 17,757–17,771, 1993.

Chen, G., R. C. Liebermann, and D. J. Weidner, Elasticity of single crystal MgO to 8 gigapascals and 1600 kelvins, *Science*, *280*, 1913–1916, 1998.

Chin, G. Y., A theoretical examination of the plastic deformation of ionic crystals, I, Maximum work analysis for slip on $\{110\}\langle 110\rangle$ and $\{100\}\langle 110\rangle$ systems, *Metall. Trans.*, *4*, 329–333, 1973.

Chin, G. Y., and W. L. Mammel, A theoretical examination of the plastic deformation of ionic crystals, II, Analysis of uniaxial deformation and axisymmetric flow for slip on $\{110\}\langle 110\rangle$ and $\{100\}\langle 110\rangle$ systems, *Metall. Trans.*, *4*, 335–340, 1973.

Cynn, H. C., and C. S. Yoo, Elasticity of tantalum to 105 GPa using a stress and angle-resolved X-ray diffraction, in *Science and Technology of High Pressure*, edited by M. Manghnani, W. Nellis, and M. F. Nicol, pp. 432–435, Univ. Press (India), Hyderabad, 2000.

Davies, G. F., and A. M. Dziewonski, Homogeneity and constitution of the Earth's lower mantle and outer core, *Phys. Earth Planet. Inter.*, *10*, 336–343, 1975.

Dewaele, A., G. Fiquet, D. Andrault, and D. Häusermann, P-V-T equation of state of periclase from synchrotron radiation measurements, *J. Geophys. Res.*, *105*, 2869–2877, 2000.

Dubrowinsky, L. S., N. A. Dubrovinskaia, S. K. Saxena, H. Annersten, E. Hålenius, H. Harryson, F. Tutti, S. Rekhi, and T. LeBihan, Stability of ferropericlase in the lower mantle, *Science*, *289*, 430–432, 2000.

Duffy, T. S., and T. J. Ahrens, Sound velocities at high pressure and temperature and their geophysical implications, *J. Geophys. Res.*, *97*, 4503–4520, 1992.

Duffy, T. S., R. J. Hemley, and H. K. Mao, Equation of state and shear strength at multimegabar pressures: Magnesium oxide to 227 GPa, *Phys. Rev. Lett.*, *74*, 1371–1374, 1995.

Duffy, T. S., G. Shen, D. L. Heinz, J. Shu, Y. Ma, H. K. Mao, R. J. Hemley, and A. K. Singh, Lattice strains in gold and rhenium under non-hydrostatic compression to 37 GPa, *Phys. Rev. B*, *60*, 1–10, 1999a.

Duffy, T. S., G. Shen, J. Shu, H. K. Mao, R. J. Hemley, and A. K. Singh, Elasticity, shear strength and equation of state of molybdenum and gold from X-ray diffraction under nonhydrostatic compression to 24 GPa, *J. Appl. Phys.*, *86*, 1–8, 1999b.

Fiquet, G., Mineral phases of the earth's mantle, *Z. Krystallogr.*, *216*, 248–271, 2001.

Foitzik, A., W. Skrotzki, and P. Haasen, Correlation between microstructure, dislocation dissociation and plastic anisotropy in ionic crystals, *Mater. Sci. Eng., A113*, 399–407, 1989.

Franssen, R. C. M. W., and C. J. Spiers, Deformation of polycrystalline salt in compression and in shear at 250–350°C, in *Deformation Mechanisms. Rheology and Tectonics*, *Geol. Soc. London, Spec. Publ.*, vol. 45, edited by R. J. Knipe and E. H. Rutter, pp. 201–213, Geol. Soc., London, 1990.

Gillet, Ph., I. Daniel, F. Guyot, J. Matas, and J. C. Chervin, A thermodynamical model for $MgSiO_3$-perovskite derived from pressure, temperature and volume dependence of Raman mode frequencies, *Phys. Earth Planet. Inter.*, *117*, 361–384, 2000.

Gnäupel-Herold, T., P. C. Brand, and H. J. Prask, The calculation of single crystal elastic constants for cubic crystal symmetry from powder diffraction data, *J. Appl. Crystallogr.*, *31*, 929–935, 1998.

Hammersley, A. P., Fit2d: V9.129 reference manual v3.1, *Internal Rep. ESRF98HA01*, ESRF, Grendole, France, 1998.

Heidelbach, F., C. Riekel, and H. R. Wenk, Quantitative texture analysis of small domains with synchrotron radiation X-rays, *J. Appl. Crystallogr.*, *32*, 841–849, 1999.

Heinz, D. L., and R. Jeanloz, Temperature measurement in the laser heated diamond anvil cell, in *High Pressure Researches in Mineral Physics*, edited by M. H. Manghnanin and Y. Syono, pp. 113–127, AGU, Washington, D. C., 1987.

Howard, C. J., and E. H. Kisi, Measurement of single-crystal elastic constants by neutron diffraction from polycrystals, *J. Appl. Crystallogr.*, *32*, 624–633, 1999.

Hughes, D. A., R. A. Lebensohn, H. R. Wenk, and A. Kumar, Stacking fault energy and microstructure effects on torsion texture evolution, *Proc. R. Soc. London, Ser. A*, *456*, 921–953, 2000.

Isaak, D. G., O. L. Anderson, and T. Goto, Measured elastic moduli of single crystal MgO up to 1800 K, *Phys. Chem. Miner.*, *16*, 704–713, 1989.

Isaak, D. G., R. E. Cohen, and M. E. Mehl, Calculated elastic constants and thermal properties of MgO at high pressures and temperatures, *J. Geophys. Res.*, *95*, 7055–7067, 1990.

Jacobsen, S. D., H. J. Reichmann, H. A. Spetzler, S. J. Mackwell, J. R. Smyth, R. J. Angel, and C. A. McCammon, Structure and elasticity of single-crystal (Mg, Fe)O and a new method of generating shear waves for gigahertz ultrasonic interferometry, *J. Geophys. Res.*, *107*, 2037, doi:10.1029/2001JB000490, 2002.

Karato, S., and P. Li, Diffusion creep in perovskite: Implications for the rheology of the lower mantle, *Science*, *255*, 1238–1240, 1992.

Karki, B. B., L. Stixrude, S. J. Clark, M. C. Warren, G. J. Ackland, and J. Crain, Structure and elasticity of MgO at high pressure, *Am. Mineral.*, *82*, 51–60, 1997.

Karki, B. B., R. M. Wentzcovitch, S. de Gironcoli, and S. Baroni, First-principles determination of elastic anisotropy and wave velocities of MgO at lower mantle conditions, *Science*, *286*, 1705–1707, 1999.

Kern, H., and G. Braun, Deformation und gefügeregelung von steinsalz im temperaturbereich 20–200 C, *Contrib. Mineral. Petrol.*, *40*, 169–181, 1973.

Kinsland, G. L., and W. A. Bassett, Strength of MgO and NaCl polycrystals to confining pressures of 250 kbar at 25 C, *J. Appl. Phys.*, *48*, 978–984, 1977.

Kocks, F. U., C. Tomé, and H. R. Wenk, *Texture and Anisotropy: Preferred Orientations and Their Effects on Material Properties*, Cambridge Univ. Press, New York, 1998.

Kruger, K. L., and K. J. Bowman, A comparison of texture development in plane strain and axisymmetrically compressed lithium fluoride, in *Proceedings of the Eleventh International Conference on Textures of Materials* (*ICOTOM 11*), edited by Z. Liang, L. Zuo, and Y. Chu, pp. 998–1003, Int. Acad. Publ., Beijing, 1996.

Lebensohn, R. A., and C. N. Tomé, A self-consistent visco-plastic model: Calculation of rolling textures of anisotropic materials, *Mater. Sci. Eng., A*, *175*, 71–82, 1994.

Li, P., S. Karato, and Z. Wang, High-temperature creep in fine-grained polycrystalline $CaTiO_3$, an analogue material of (Mg, Fe)SiO_3 perovskite, *Phys. Earth Planet. Inter.*, *95*, 19–36, 1996.

Mainprice, D., G. Barruol, and W. Ben Ismail, The seismic anisotropy of the earth's mantle: From single crystal to polycrystal, in *Earth's Deep Interior*: *Mineral Physics and Tomography From the Atomic to the Global Scale*, edited by S. Karato et al., pp. 237–264, AGU, Washington, D. C., 2000.

Mao, H. K., J. Shu, Y. Fei, J. Hu, and R. J. Hemley, The wüstite enigma, *Phys. Earth Planet. Inter.*, *96*, 135–145, 1996.

Mao, H. K., G. Shen, and R. J. Hemley, Multivariable dependence of Fe-Mg partitioning in the lower mantle, *Science*, *278*, 2098–2100, 1997.

Mao, H. K., J. Shu, G. Shen, R. J. Hemley, B. Li, and A. K. Singh, Elasticity and rheology of iron above 220 GPa and the nature of the earth's inner core, *Nature*, *396*, 741–743, (Correction, *Nature*, *399*, 280, 1999), 1998.

Matthies, S., and F. Wagner, On a 1/n law in texture related single orientation analysis, *Phys. Status Solidi*, *196*, 1996.

Matthies, S., S. Merkel, H. R. Wenk, R. J. Hemley, and H. K. Mao, Effects of texture on the high pressure elasticity of iron from X-ray diffraction, *Earth Planet. Sci. Lett.*, *194*, 201–212, 2001.

Meade, C., and R. Jeanloz, Yield strength of MgO to 40 GPa, *J. Geophys. Res.*, *93*, 3261–3269, 1988.

Meade, C., P. G. Silver, and S. Kanshima, Laboratory and seismological observations of lower mantle isotropy, *Geophys. Res. Lett.*, *22*, 1293–1296, 1995.

Mehl, M. J., R. J. Hemley, and L. L. Boyer, Potential-induced breathing model for the elastic moduli and high-pressure behavior of the cubic alkaline-earth oxides, *Phys. Rev. B*, *33*, 8685–8696, 1986.

Merkel, S., R. J. Hemley, H. K. Mao, and D. M. Teter, Finite element modeling and ab-initio calculations of megabar stresses in the diamond anvil cell, in *Science and Technology of High Pressure Research*, edited by M. Manghnani, W. J. Nellis, and M. F. Nicol, pp. 68–73, Univ. Press (India), Hyderabad, 2000.

Merkel, S., A. P. Jephcoat, J. Shu, H. K. Mao, Ph. Gillet, and R. J. Hemley, Equation of state, elasticity and shear strength of pyrite under high pressure, *Phys. Chem. Miner.*, *29*, 1–9, 2002.

Mika, D. P., and P. R. Dawson, Polycrystal plasticity modeling of intracrystalline boundary textures, *Acta Mater.*, *47*, 1355–1369, 1999.

Molinari, A., G. R. Canova, and S. Ahzi, A self-consistent approach of the large deformation polycrystal viscoplasticity, *Acta Metall.*, *35*, 2983–2994, 1987.

Paterson, M. S., and C. W. Weaver, Deformation of polycrystalline MgO under pressure, *J. Am. Ceram. Soc.*, *53*, 463–471, 1970.

Poirier, J. P., *Creep of Crystals*, Cambridge Univ. Press, New York, 1985.

Poirier, J. P., and G. D. Price, Primary slip system of ϵ-iron and anisotropy of the Earth's inner core, *Phys. Earth Planet. Inter.*, *110*, 147–156, 1999.

Reichmann, H. J., R. J. Angel, H. Spetzler, and W. A. Bassett, Utrasonic interferometry and X-ray measurements on MgO in a new diamond anvil cell, *Am. Mineral.*, *83*, 1357–1360, 1998.

Shen, A. H., H. J. Reichmann, G. Shen, R. J. Angel, W. A. Bassett, and H. Spetzler, GHz ultrasonic interferometry in a diamond anvil cell: P-wave velocities in periclase to 4.4 GPa and 207°C, in *Properties of Earth and Planetary Materials at High Pressure and Temperature*, edited by M. Manghnani and T. Yagi, pp. 71–77, AGU, Washington, D. C., 1998.

Siemes, H., Anwendung der taylor theorie auf die regelung von kubischen mineralen, *Contrib. Mineral. Petrol.*, *43*, 149–157, 1974.

Siemes, H., and V. Hennig-Michaeli, Ore minerals, in *Preferred Orientations in Deformed Metals and Rocks: An Introduction to Modern Texture Analysis*, edited by H. R. Wenk, pp. 335–360, Academic, San Diego, Calif., 1985.

Singh, A. K., The lattice strains in a specimen (cubic system) compressed nonhydrostatically in an opposed anvil device, *J. Appl. Phys.*, *73*, 4278–4286, 1993.

Singh, A. K., C. Balasingh, H. K. Mao, R. J. Hemley, and J. Shu, Analysis of lattice strains measured under non-hydrostatic pressure, *J. Appl. Phys.*, *83*, 7567–7575, 1998a.

Singh, A. K., H. K. Mao, J. Shu, and R. J. Hemley, Estimation of single crystal elastic moduli from polycrystalline X-ray diffraction at high pressure: Applications to FeO and iron, *Phys. Rev. Lett.*, *80*, 2157–2160, 1998b.

Sinogeikin, S. V., and J. D. Bass, Single crystal elasticity of pyrope and MgO to 20 GPa by brillouin spectroscopy scattering in the diamond cell, *Phys. Earth Planet. Inter.*, *120*, 43–62, 2000.

Sinogeikin, S. V., J. M. Jackson, B. O'Neil, J. W. Palko, and J. D. Bass, Compact high pressure cell for brillouin scattering measurements, *Rev. Sci. Instrum.*, *71*, 201–206, 2000.

Skrotzki, W., and P. Haasen, Hardening mechanisms of ionic crystals on {110} and {100} slip planes, *J. Phys. (Paris)*, *42*, 119–148, 1981.

Skrotzki, W., and P. Haasen, Plastic hardening of polycrystalline halides, in *Materials Research: Deformation of Ceramic Materials II*, edited by R. Tressler and R. Bradt, vol. 18, pp. 429–444, Plenum, New York, 1984.

Skrotzki, W., and P. Welch, Development of texture and microstructure in extruded ionic polycrystalline aggregates, *Tectonophysics*, *99*, 47–61, 1983.

Skrotzki, W., G. Frommeyer, and P. Haasen, Plasticity of polycrystalline ionic solids, *Phys. Status Solidi*, *A66*, 219, 1981.

Speziale, S., C. S. Zha, T. S. Duffy, R. J. Hemley, and H. K. Mao, Quasi-hydrostatic compression of magnesium oxide to 52 GPa: Implications for the pressure-volume-temperature equation of state, *J. Geophys. Res.*, *106*, 515–528, 2001.

Stixrude, L., Elasticity of mantle phases at high pressure and temperature, in *Earth's Deep Interior*: *Mineral Physics and Tomography From the Atomic to the Global Scale*, edited by S. Karato et al., pp. 201–213, AGU, Washington, D. C., 2000.

Stretton, I., F. Heidelbach, S. Mackwell, and F. Langenhorst, Dislocation creep of magnesiowüstite ($Mg_{.8}Fe_{0.2O}$), *Earth Planet. Sci. Lett.*, *94*, 229–240, 2001.

Taylor, G. I., Plastic strain in metals, *J. Inst. Met.*, *62*, 307–324, 1938.

Tomé, C. N., and G. R. Canova, in *Texture and Anisotropy*: *Preferred Orientations in Polycrystals and Their Effect on Materials Properties*, edited by U. F. Kocks, C. N. Tomé, and H. R. Wenk, chap. 11, pp. 561–595, Cambridge Univ. Press, New York, 1998.

Tullis, T. E., and J. Tullis, Experimental rock deformation techniques, in *Mineral and Rock Deformations: Laboratories Studies*, edited by B. E. Hobbs and H. C. Heard, pp. 297–324, AGU, Washington, D. C., 1986.

Uchida, T., N. Funamori, T. Ohtani, and T. Yagi, Differential stress of MgO and Mg_2SiO_4 under uniaxial stress field: Variation with pressure, temperature, and phase transition, in *High Pressure Science and Technology*, edited by W. A. Trzeciatowski, pp. 183–185, World Sci., River Edge, N. J., 1996.

von Mises, R., Mechanik der plastischen Formänderung von Kristallen, *Z. Angew. Math. Mech.*, *8*, 161–185, 1928.

Weaver, C. W., and M. S. Paterson, Deformation of cube-oriented MgO crystals under pressure, *J. Am. Ceram. Soc.*, *52*, 293–302, 1969.

Weidner, D. J., Y. Wang, and M. T. Vaughan, Yield strength at high pressure and temperature, *Geophys. Res. Lett.*, *21*, 753–756, 1994.

Wenk, H. R., A voyage through the deformed earth with the self-consistent model, *Model. Simul. Mater. Sci. Eng.*, *7*, 699–722, 1999.

Wenk, H. R., G. R. Canova, A. Molinari, and H. Mecking, Texture development in halite: Comparison of Taylor model and self-consistent theory, *Acta Metall.*, *37*, 2017–2029, 1989.

Wenk, H. R., S. Matthies, J. Donovan, and D. Chateigner, Beartex: A windows-based program system for quantitative texture analysis, *J. Appl. Crystallogr.*, *31*, 262–269, 1998.

Wenk, H. R., S. Matthies, R. J. Hemley, H. K. Mao, and J. Shu, The plastic deformation of iron at pressures of the Earth's inner core, *Nature*, *405*, 1044–1047, 2000.

Yoneda, A., Pressure derivatives of elastic constants of single crystal MgO and $MgAl_2O_4$, *J. Phys. Earth*, *38*, 19–55, 1990.

Zha, C. S., H. K. Mao, and R. J. Hemley, Elasticity of MgO and a primary pressure scale to 55 GPa, *Proc. Natl. Acad. Sci. U.S.A.*, *97*, 13,494–13,499, 2000.

P. Gillet and S. Merkel, Laboratoire des sciences de la Terre, École normale supérieure de Lyon, 46 allée d'Italie, 69364 Lyon, Cedex 07, France. (sebastien.merkel@ens-lyon.fr)

R. J. Hemley, H. K. Mao, and J. Shu, Geophysical Laboratory, Carnegie Institution of Washington, 5251 Broad Branch Rd., NW, Washington, D. C. 20015, USA.

G. Shen, Consortium for Advanced Radiation Sources, University of Chicago and Advanced Photon Source, Argonne National Laboratory, 9700 South Cass Avenue, Argonne, IL 60439, USA.

H. R. Wenk, Department of Earth and Planetary Science, University of California, Berkeley, CA 94720, USA.

Cinquième partie

Articles : Mesures de contraintes et orientations préférentielles

ELSEVIER

Earth and Planetary Science Letters 209 (2003) 351–360

EPSL

www.elsevier.com/locate/epsl

Deformation of $(Mg_{0.9},Fe_{0.1})SiO_3$ Perovskite aggregates up to 32 GPa

Sébastien Merkel [a,b,*], Hans Rudolf Wenk [c], James Badro [d], Gilles Montagnac [b], Philippe Gillet [b], Ho-kwang Mao [a], Russell J. Hemley [a]

[a] *Geophysical Laboratory, Carnegie Institution of Washington, Washington, DC, USA*
[b] *Laboratoire des Sciences de la Terre, UMR 5570 CNRS, École normale supérieure de Lyon, Lyon, France*
[c] *Department of Earth and Planetary Science, University of California, Berkeley, CA, USA*
[d] *Laboratoire de Minéralogie-Cristallographie, Université Paris VI, Paris, France*

Received 18 September 2002; received in revised form 3 February 2003; accepted 11 February 2003

Abstract

Room temperature investigations on the shear stress and deformation mechanisms of $(Mg_{0.9}Fe_{0.1})SiO_3$ perovskite are performed in situ up to 32 GPa using radial X-ray diffraction and the diamond anvil cell as a deformation apparatus. The uniaxial stress supported by the perovskite aggregate is found to increase continuously with pressure up to 10.9(±1.9) GPa at 32(±1) GPa. Our measurements show no development of significant lattice preferred orientations in the sample, which indicates that deformation by dislocation glide is not the dominant deformation mechanism under these conditions. Assuming that the underlying cause for seismic anisotropy in the deep Earth is elastic anisotropy combined with lattice preferred orientation, our results indicate that silicate perovskite deformed under the conditions of this experiment would not be the source of seismic anisotropy.

Keywords: high pressure; deformation; perovskite; shear strength; texture; anisotropy

1. Introduction

Silicate perovskite is the most abundant mineral in the Earth's lower mantle and, although it has been subjected to numerous experimental and theoretical investigations, its rheological properties remain poorly understood. Information on the shear strength and deformation mechanisms of $(Mg,Fe)SiO_3$ is crucial for constraining mantle convection and the development of seismic anisotropy in the deep Earth (e.g. [1]). However, $(Mg,Fe)SiO_3$ perovskite is known to be extremely difficult to study with conventional laboratory deformation experiments: for the most part, only analogs with the perovskite structure have been investigated under the assumption that such materials have similar mechanical properties. From such analog studies, creep laws and deformation mechanisms of silicate perovskite were implied (see [2–10] and references therein). Despite consid-

* Corresponding author. Present address: Institute for Solid State Physics, University of Tokyo, Kashiwa, Chiba 277-8581, Japan. Tel.: +41-4-7136-3231; Fax: +41-4-7136-3230.
E-mail address: smerkel@issp.u-tokyo.ac.jp (S. Merkel).

0012-821X/03/$ – see front matter © 2003 Elsevier Science B.V. All rights reserved.
doi:10.1016/S0012-821X(03)00098-0

erable efforts, these experiments have demonstrated that the analog approach is problematic [4]. Silicate perovskite is very unstable at ambient pressure and it is very difficult to obtain high quality and large dimension samples. Therefore, very few studies have investigated the rheological properties of silicate perovskite directly. Among them are micro-indentation hardness measurements under ambient conditions [11], shear stress estimations up to 60 GPa using an approximate relation between pressure gradient and uniaxial stress component in the diamond anvil cell [12], shear stress measurements up to 20 GPa and 1073 K in large volume press [13], electron microscopy analysis of samples quenched from multianvil experiments [14], and lattice preferred orientation (LPO) analysis of samples quenched from high pressure diamond anvil cell experiments [15]. However, the understanding of the rheology of silicate perovskite is still in its infancy. Most studies on lower mantle deformation are still based on analogies with $CaTiO_3$ perovskite ([1,7,9] for instance) in spite of the considerable uncertainties indicated above.

In recent years, a new diamond anvil cell X-ray diffraction technique has been developed to study the strength and elasticity of materials under high pressure [16–24]. This technique later emerged as a powerful tool to obtain direct observations of the deformation mechanisms and the development of LPO of deep Earth materials in situ at relevant pressure, as demonstrated with pilot experiments on ε-Fe and MgO [25,26]. We applied this method to study the development of textures in $(Mg,Fe)SiO_3$ perovskite with pressure under uniaxial stress and deduce information about its strength and deformation mechanisms at room temperature.

2. Experiment

In this study, we perform a deformation experiment with a diamond anvil cell, analyzing the stress state and polycrystalline texture using X-ray diffraction in a direction orthogonal to the compression axis (Fig. 1). In order to obtain reliable statistics in the analysis, we used an angular-dispersive diffraction technique [26]. The background from the confining beryllium gasket was reduced by drilling an opening along the incoming X-ray path which was filled with a mixture of amorphous boron and epoxy to maintain the gasket's mechanical stability. The perovskite sample with a Fe/(Fe+Mg) ratio of 0.01 was synthesized from $(Mg,Fe)SiO_3$ orthopyroxene on the multianvil apparatus of the Center for High Pressure Research. The grain size was reduced to the order of a couple of μm by crushing the chips extracted from the multianvil runs between tungsten carbide cubes. The sample was then loaded and repeatedly pressed until fully compacted in a 100 μm hole along with ruby chips and a layer of polycrystalline platinum. To ensure homogeneous stress conditions in all sections of the sample, diamond anvils with 500 μm tip diameters were used. The measurements were performed on the ID-30 beamline of the European Synchrotron Radiation Facility in Grenoble, using a monochromatic beam of wavelength 0.3738 Å and the in-house fast-scan detector. Each pattern took 1–5 min to record. Details on the experimental technique and data reduction are given elsewhere [26].

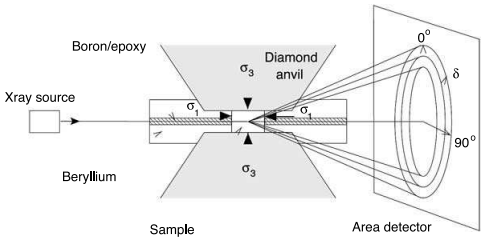

Fig. 1. Schematic of the experiment. The perovskite aggregate is confined under non-hydrostatic stress conditions between two diamond anvils. A monochromatic X-ray beam is sent through the gasket with a direction orthogonal to the diamond axis and the data collected on an area detector orthogonal to the incoming beam. The positions and intensities of the diffraction lines are analyzed as a function of the azimuthal angle δ.

Pressures were estimated using the ruby scale, the equation of state of platinum [27] and that of perovskite itself [28]. We collected data upon compression between 0 and 32 GPa, and decompression between 32 and 1 GPa. However, above 20 GPa in compression the large peak widths and

low diffraction intensities of perovskite made the analysis impossible. This can be attributed to an increase in stress inhomogeneities between grains with compression. These problems disappeared upon decompression as we relaxed the sample. Therefore the results presented here will range between 0 and 19 GPa upon compression and 32 and 1 GPa upon decompression. The distance between the diamond anvils, estimated by recording changes in X-ray absorption while moving the diamond cell in a direction perpendicular to the incoming beam, shows a continuous decrease from 32 to 7 μm during compression to 32 GPa and a continuous increase from 7 to 10 μm during decompression (Fig. 2). Upon compression, this is a good estimation of the sample thickness. Because the deformation is continuous over the whole pressure range, we estimate that it cannot be attributed to compaction and that our sample was submitted to 65% plastic deformation. In order to reduce the background from the sample environment, a diffraction image was collected after removing the sample from the incident beam at each pressure and dividing the diffraction pattern from the sample by this image. The processed diffraction images were then divided into small arcs of 10° intervals to determine the influence of the azimuthal angle δ on the pattern. Figs. 3 and 4 show a representative diffraction pattern at 19 GPa and the spectra we extracted for δ between 0 and 360° with 10° intervals, respectively. In Fig. 4, the variations of the peak posi-

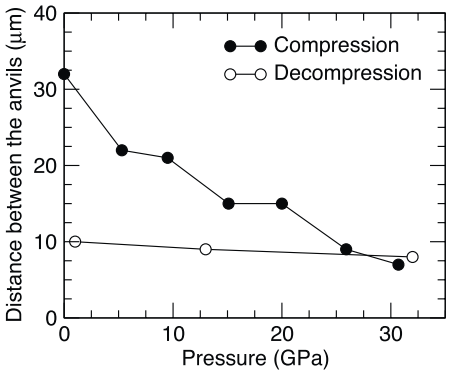

Fig. 2. Distance between the diamond anvils as a function of pressure. Upon compression, this is a good estimation of the sample thickness. From this figure, we estimate that the plastic deformation imposed on the sample is of the order of 65%.

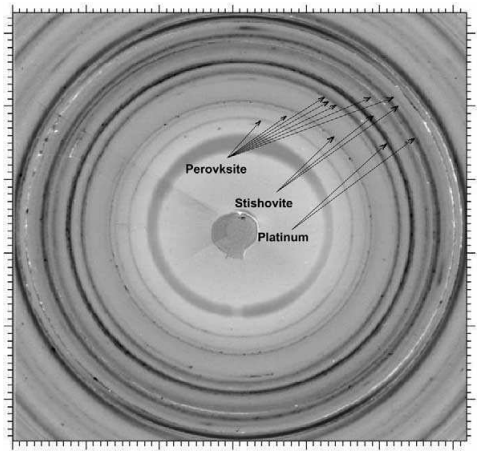

Fig. 3. Representative diffraction pattern at 19 GPa after removing the signal from the background. Selected diffraction lines for perovskite, stishovite (left over from synthesis) and platinum (pressure calibrant) are indicated.

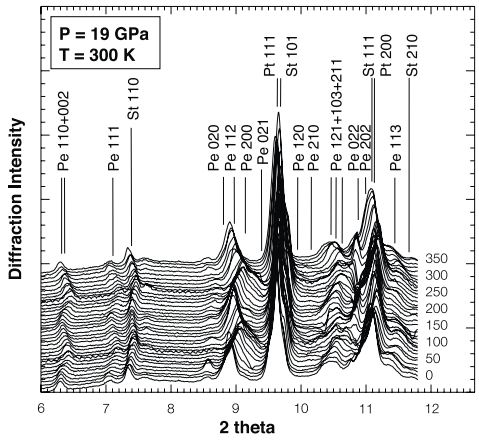

Fig. 4. Spectra extracted from the diffraction pattern at 19 GPa (Fig. 3) for δ between 0 and 360° with 10° intervals. Diffraction lines for perovskite (Pe), platinum (Pt) and stishovite (St) are labeled in the figure.

tion with δ are related to elastic deformation due to non-hydrostatic stress while the variation of the diffraction intensities can be attributed to LPO. For the following analysis, data for the (002) and (110), (111), (020), (112), (200), and (113) peaks of silicate perovskite were fitted using pseudo-Voigt peak profiles.

3. Results

Samples in these diamond anvil cell experiments are subjected to a non-hydrostatic stress, where the principal stress in the loading direction, σ_3, is greater than the radial stress, σ_1, imposed by the gasket. The angle χ between the diffracting plane normal and the maximum stress axis can be calculated from the azimuth angle on the detector, δ, with the relation:

$$\cos\chi = \cos\theta\cos\delta \quad (1)$$

where θ is the diffraction angle. Assuming a Reuss–Voigt–Hill micromechanical model and neglecting the effect of preferred orientations, the measured d-spacings vary with χ as:

$$d_m(hkl) = d_P(hkl)[1 + (1-3\cos^2\chi)Q(hkl)] \quad (2)$$

where $d_m(hkl)$ is the measured d-spacing, $d_P(hkl)$ the d-spacing under the equivalent hydrostatic pressure P, and $Q(hkl)$ is a function of the Miller indices, lattice parameters, and elastic moduli [18]. The variations of the d-spacings of the (112) planes of perovskite with χ upon compression and decompression are shown in Fig. 5 along with results from least-squares fits of Eq. 2. The good agreement between the measured and theoretically predicted χ dependence of the d-spacing assesses the quality of the experimental data. The results of these least-squares fits can then be used to estimate the uniaxial stress component supported by the sample with the relation:

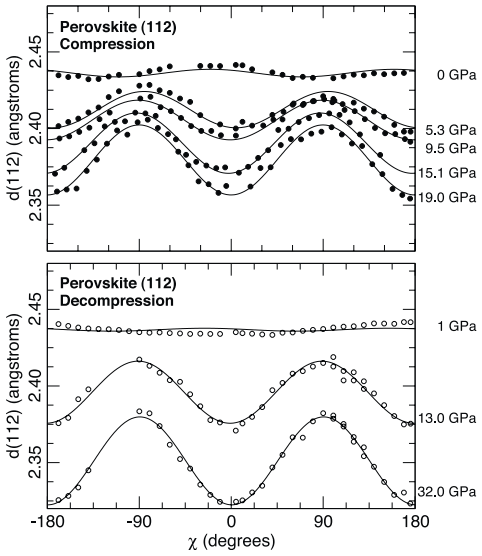

Fig. 5. Variation of the d-spacing of the (112) plane of perovskite as a function of χ upon compression and decompression. Symbols and solid line are experimental data and least-squares fits of a Reuss–Voigt–Hill micromechanical model to the data.

Table 1
Pressure, distance between the anvils, and uniaxial stress component $t = \sigma_3 - \sigma_1$ in perovskite calculated from the measured $\langle Q \rangle$ and the shear modulus G deduced from first-principles calculations [29]

P (GPa)	h (μm)	$\langle Q \rangle$ ($\times 10^3$)	G (GPa)	t (GPa)
0.0 ± 0.1	32	−0.4 ± 0.2	178.6 ± 0.2	−0.4 ± 0.2
5.3 ± 0.3	22	3.1 ± 0.4	186.9 ± 0.5	3.4 ± 0.4
9.5 ± 0.5	21	3.7 ± 0.5	193.4 ± 0.8	4.3 ± 0.6
15.1 ± 0.3	15	5.0 ± 0.6	201.9 ± 0.5	6.0 ± 0.7
19.0 ± 0.5	15	5.3 ± 1.3	207.8 ± 0.7	6.6 ± 1.6
32.0 ± 1.0	8	8.0 ± 1.3	226.8 ± 1.4	10.9 ± 1.9
13.0 ± 0.3	9	4.7 ± 0.9	198.7 ± 0.5	5.6 ± 1.1
1.0 ± 0.5	10	−0.1 ± 0.1	180.2 ± 0.8	−0.1 ± 0.1

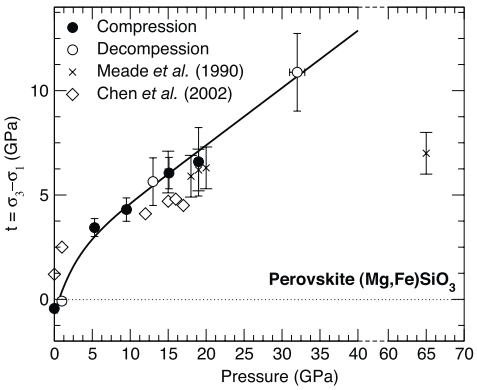

Fig. 6. Uniaxial stress component $t=\sigma_3-\sigma_1$ in perovskite vs. pressure. Closed and open circles are data upon compression and decompression, respectively, crosses are the results of [12] measured using the pressure gradient method, open diamonds are results of multianvil experiments [13], and solid line is a fit to the data of this experiment.

$$t = \sigma_3-\sigma_1 \approx 6G\langle Q(hkl)\rangle \quad (3)$$

where G is the shear modulus of the aggregate [18]. Since no experimental measurement of the shear modulus of perovskite in the present pressure range was available, results from first-principles calculations were used [29]. The results we obtained are presented in Table 1 and Fig. 6. Above 2 GPa the uniaxial stress in our sample increases linearly with pressure up to 10.9(±1.9) GPa at 32 GPa. The values of uniaxial stress in the sample deduced upon compression and decompression cannot be distinguished.

In order to study the development of LPO with compression, we use the relative intensity variations of diffraction peaks to calculate the orientation distribution function (ODF) of the sample, which contains all information about the crystallite orientations and can be used for deformation mechanism analysis. Fig. 7 presents the measured diffraction intensities for the (110)+(002), (020), (112) (200) and (113) diffraction lines of perovskite at the end of the decompression along with those recalculated from the ODF. There is considerable dispersion in the experimental data and no clear systematic variation of intensities with χ can be observed, except for the weak reflection (200). The texture in the sample is axially symmetric around the compression axis, consistent with deformation performed in axial compression. It is therefore most efficiently displayed in the form of

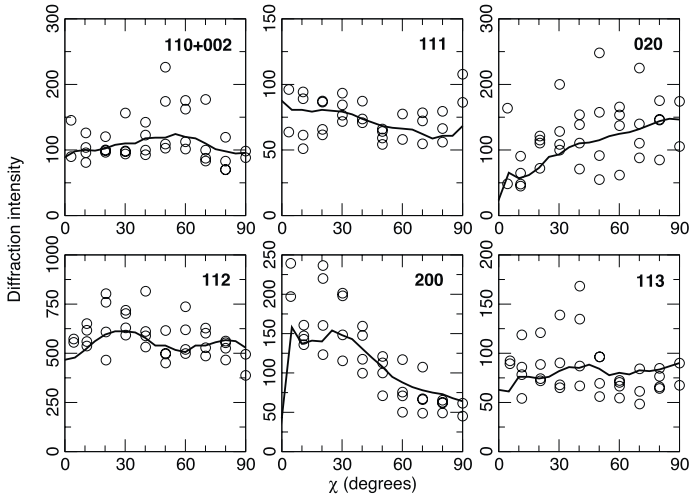

Fig. 7. Diffraction intensities vs. χ for perovskite at the end of the decompression. Open circles are experimental data and solid lines are recalculated from the ODF.

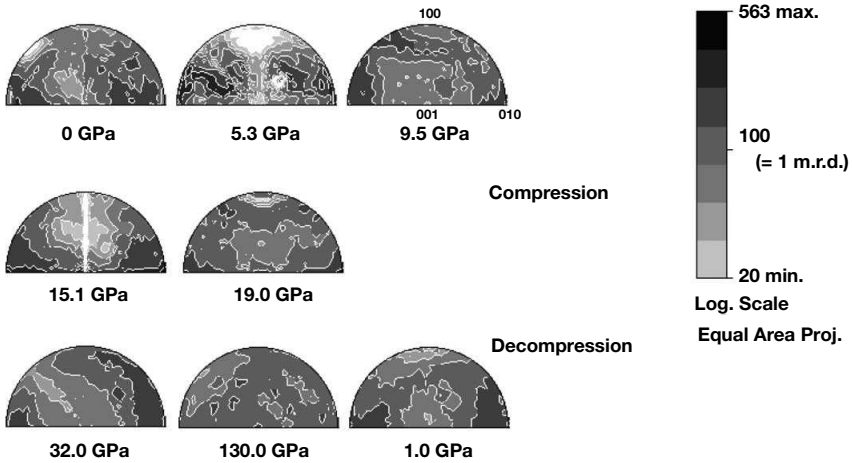

Fig. 8. Experimental inverse pole figures for perovskite upon compression and decompression.

inverse pole figures (Fig. 8), which show the orientation distribution of the experimental compression axis relative to the crystallographic coordinate system of the orthorhombic perovskite structure. The inverse pole figures show no significant changes with compression or decompression, which implies that the sample did not develop any significant LPO in this experiment. This is also apparent in Fig. 4, which shows very little intensity variation with angle, for instance for reflections (110)+(002), (111) and (113).

4. Discussion

According to the von Mises yielding criterion, the measured uniaxial stress (Fig. 6) provides a lower bound on the yield strength of perovskite as $t = \sigma_3 - \sigma_1 \leq \sigma_y$, where σ_y is the yield strength. The uniaxial stress varies with sample environment and equality holds only if the sample deforms plastically. It should also be noted that the experiments presented here are different from mechanical tests at a given pressure, temperature, and imposed strain-rate. In these experiments, strain, strain rate and pressure cannot be decoupled and therefore we rely on a more general definition of the yield strength that may include effects of hardening. Above 2 GPa, we find $t = 1.8(3) + 0.28(2)P$ where t and P are in GPa. Therefore:

$$\sigma_y \geq 1.8(3) + 0.28(2)P \quad (4)$$

for perovskite up to 30 GPa, where σ_y and P are in GPa. Comparison with other measurements of uniaxial stress in perovskite is shown in Fig. 6. Between 15 and 25 GPa, our results agree with those of [12] and [13]. However, the saturation observed above 25 GPa in [12] is not seen in our experiments. As mentioned above, the uniaxial stress is only a lower bound on the yield strength and its actual value depends on sample environment. Our results are thus not incompatible with the previous work since t might have saturated in their experiments for a variety of reasons. One should also point out, however, that these authors used a technique based on measuring the pressure gradient across the diamond anvil and estimating t by $t \approx h(\mathrm{d}P/\mathrm{d}r)$ where h is the sample thickness and r the radial distance from the center of the diamond. The sample thickness is poorly estimated at high pressure; moreover, the above relation holds only if the sample continues to flow plastically on each loading. Arrest of plastic flow often occurs in the vicinity of the maximum pressures of these experiments, as does

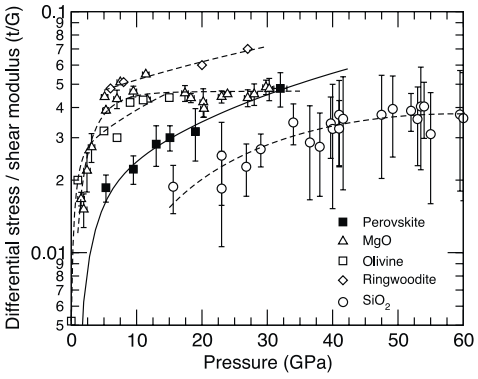

Fig. 9. Ratio of uniaxial stress component to shear modulus t/G as a function of pressure. Solid squares are measurements on perovskite from this study, open triangles, squares, diamonds, and circles are results for MgO [26], olivine [32], ringwoodite [22], and SiO_2 [24], respectively.

the increase of uniaxial stress below the diamond tips [30]. We conclude that the saturation previously observed is not intrinsic to perovskite and that its yield strength can be well over 10 GPa at a pressure of 30 GPa at room temperature, making it one of the hardest silicates of the Earth's interior. This conclusion is consistent with that of [13] based on measurements up to 20 GPa and 1073 K, where perovskite was shown to display very little relaxation and became much stronger than other silicates, such as ringwoodite, upon heating.

The dimensionless parameter τ/G, where τ is the shear strength and G the shear modulus, is a useful quantity for comparing strength between different materials [31]. Moreover, the quantity t/G is measured directly in the radial diffraction experiments (e.g. Eq. 3) and no bulk parameter needs to be assumed. Fig. 9 shows the results we obtain for perovskite along with measurements on olivine [32], ringwoodite [22], MgO [26], and SiO_2 [24]. The t/G ratio for perovskite at ambient temperature lies between those of SiO_2 and the other silicates. Notably, the trend for $(Mg,Fe)SiO_3$ is quite similar to that observed for SiO_2 (stishovite and $CaCl_2$-type), which also has Si in octahedral coordination.

However, the representation of uniaxial stress as a function of pressure has been problematic: results from different experiments can be inconsistent and the evolution of t or t/G with pressure tends to be highly non-linear. Fig. 10 presents the evolution of the normalized uniaxial stress t/G with macroscopic strain $\gamma=(h_0-h)/h_0$ where h is the distance between the anvils (e.g. Table 1). In this representation the evolution of uniaxial stress can be easily decomposed into two domains where t evolves linearly with γ (i.e. increasing strain and decreasing strain). In our experiments, pressure, strain, and uniaxial stress cannot be decoupled. Therefore a comparison with results from mechanical tests at constant pressure, temperature and strain rate is not trivial. However, because strain is strongly related to plastic deformation, we feel that this representation should provide valuable information when data from other experiments become available.

The absence of LPO in perovskite in our experiments is consistent with previous observations on $(Mg,Fe)SiO_3$ perovskite [15]. In those experiments, perovskite had been deformed under uniaxial compression in the diamond anvil cell and quenched to ambient conditions. No texture could be observed. In our experiments, we followed the development of texture under uniaxial compression in situ up to 30 GPa, with 10 GPa uniaxial stress at the highest pressures, after 65% plastic

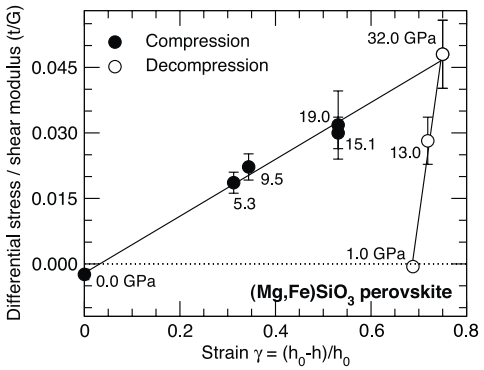

Fig. 10. Normalized uniaxial stress component t/G in perovskite vs. strain. Closed and open circles are data upon compression and decompression, respectively. Solid lines are linear fits to the data from 0 to 32 GPa and from 32 to 0 GPa.

deformation, and a homologous temperature $T/T_m \approx 0.1$, and found no clear sign of LPO. Although further experiments are required to identify the specific deformation mechanism, the absence of significant LPO indicates that plastic deformation by dislocation is not dominant. This is in agreement with deduction from high temperature relaxation at high pressure where the evolution of stress and strain in perovskite was shown to be incompatible with both dislocation glide and power-law creep [13]. This has also been documented for fine-grained $CaTiO_3$, from which it was inferred that silicate perovskite undergoes superplastic deformation [7]. Deformation mechanisms depend strongly on stress, temperature and grain size. Thus, the influence of all these factors needs to be further investigated in order to infer the behavior of silicate perovskite in the lower mantle. To this end, the in situ experiments described here should be extended to higher temperature and grain sizes varied.

The major cause for seismic anisotropy in the deep Earth is elastic anisotropy combined with LPO. Therefore, a perovskite aggregate deformed in conditions similar to those of this study would not generate any seismic anisotropy. While the effect of higher temperature, controlled strain rate and grain size should be investigated to fully understand the rheology of silicate perovskite in the deep mantle, our in situ experiments have demonstrated the feasibility of direct investigations on the strength and deformation mechanisms of silicate perovskite under high pressure. The lack of significant LPO in perovskite is in contrast with similar experiments on another lower mantle mineral, magnesiowuestite, where strong LPO was observed at low temperature and high pressure [26].

Seismological observations about the anisotropy in the deep mantle have only recently been well documented. There have been numerous reports of anisotropy in its lowermost boundary layer, D″ (e.g. [33,34]), and near the 660 km discontinuity [35,36] the few studies that concentrated on the mid-to-lower mantle region found little evidence for anisotropy [15,35]. These studies, however, were limited in global coverage and recent numerical calculations assuming composite mantle rheology have shown that the deformation of subducting slabs in the lower mantle occurs mostly by dislocation creep and could therefore exhibit significant anisotropy [1,37]. Reliably detecting anisotropy in these regions requires careful seismological experiments. Moreover, interpreting data from geological settings which exhibit 3D variations in heterogeneity and anisotropy is difficult as the nature of wave propagation in such complex settings is not well understood [34]. Recent experiments have documented the development of significant LPO in magnesiowuestite, both under low pressure and high temperature [38,39] and high pressure and low temperature [26]. In contrast, our experiments have shown that it is extremely difficult to generate significant LPO in silicate perovskite. Although the critical parameters of the effect such as temperature and grain size should be investigated for a direct comparison with the lower mantle, this implies that perovskite is less likely to be the source of seismic anisotropy than these other silicates.

Acknowledgements

The authors are grateful to Yingwei Fei for providing the sample and Mohamed Mezouar for assistance during the experiment. We also thank P. Cordier, D. Price, and the anonymous reviewers whose comments significantly improved the manuscript. *[SK]*

References

[1] A.K. McNamara, P.E. van Keken, S. Karato, Development of anisotropic structure in the Earth's lower mantle by solid state convection, Nature 416 (2002) 310–314.
[2] J.P. Poirier, J. Peyronneau, J.Y. Gesland, G. Berbec, Viscosity and conductivity of the lower mantle: an experimental study on a $MgSiO_3$ perovskite analogue, $KZnF_3$, Phys. Earth Planet. Inter. 32 (1983) 273–287.
[3] S. Beauchesne, J.P. Poirier, Creep of barium titanate perovskite: a contribution to a systematic approach to the viscosity of the lower mantle, Phys. Earth Planet. Inter. 55 (1989) 187–199.
[4] S. Beauchesne, J.P. Poirier, In search of a systematics for the viscosity of perovskites: creep of potassium tantalate and niobate, Phys. Earth Planet. Inter. 61 (1990) 182–198.

[5] S. Karato, P. Li, Diffusion creep in perovskite: implications for the rheology of the lower mantle, Science 255 (1992) 1238–1240.
[6] Z. Wang, S. Karato, F. Fujino, High temperature creep of single crystal strontium titanate ($SrTiO_3$): a contribution to creep systematics in perovskites, Phys. Earth Planet. Inter. 79 (1993) 299–312.
[7] S. Karato, S. Zhang, H.R. Wenk, Superplasticity in Earth's lower mantle: evidence from seismic anisotropy and rock physics, Science 270 (1995) 458–461.
[8] P. Besson, J.P. Poirier, G.D. Price, Dislocations in $CaTiO_3$ perovskite deformed at high temperature: a transmission electron microscopy study, Phys. Chem. Min. 23 (1996) 337–344.
[9] P. Li, S. Karato, Z. Wang, High-temperature creep in fine-grained polycrystalline $CaTiO_3$, an analogue material of (Mg, Fe)SiO_3 perovskite, Phys. Earth Planet. Inter. 95 (1996) 19–36.
[10] Z.C. Wang, C. Dupas-Bruzek, S. Karato, High temperature creep of an orthorhombic perovskite - $YAlO_3$, Phys. Earth Planet. Inter. 110 (1999) 51–69.
[11] S. Karato, F. Fujino, E. Ito, Plasticity of $MgSiO_3$ perovskite: the results of microhardness tests on single crystals, Geophys. Res. Lett. 17 (1990) 13–16.
[12] C. Meade, R. Jeanloz, The strength of mantle silicates at high pressure and room temperature: implications for the viscosity of the mantle, Nature 348 (1990) 533–535.
[13] J. Chen, D.J. Weidner, M.T. Vaughan, The strength of $Mg_{0.9}Fe_{0.1}SiO_3$ perovskite at high pressure and temperature, Nature 419 (2002) 824–826.
[14] Y. Wang, F. Guyot, R.C. Liebermann, Electron microscopy of (Mg,Fe)SiO_3 perovskite: evidence for structural phase transition and implications for the lower mantle, J. Geophys. Res. 97 (1992) 12327–12347.
[15] C. Meade, P.G. Silver, S. Kanshima, Laboratory and seismological observations of lower mantle isotropy, Geophys. Res. Lett. 22 (1995) 1293–1296.
[16] R.J. Hemley, H.K. Mao, G. Shen, J. Badro, P. Gillet, M. Hanfland, D. Häusermann, X-ray imaging of stress and strain of diamond, iron, and tungsten at megabar pressures, Science 276 (1997) 1242–1245.
[17] A.K. Singh, H.K. Mao, J. Shu, R.J. Hemley, Estimation of single crystal elastic moduli from polycrystalline X-ray diffraction at high pressure: Applications to FeO and iron, Phys. Rev. Lett. 80 (1998) 2157–2160.
[18] A.K. Singh, C. Balasingh, H.K. Mao, R.J. Hemley, J. Shu, Analysis of lattice strains measured under non-hydrostatic pressure, J. Appl. Phys. 83 (1998) 7567–7575.
[19] H.K. Mao, J. Shu, G. Shen, R.J. Hemley, B. Li, A.K. Singh, Elasticity and rheology of iron above 220 GPa and the nature of the Earth's inner core, Nature 396 (1998) 741–743; correction, Nature 399 (1999) 280.
[20] T.S. Duffy, G. Shen, J. Shu, H.K. Mao, R.J. Hemley, A.K. Singh, Elasticity, shear strength and equation of state of molybdenum and gold from X-ray diffraction under nonhydrostatic compression to 24 GPa, J. Appl. Phys. 86 (1999) 1–8.
[21] T.S. Duffy, G. Shen, D.L. Heinz, J. Shu, Y. Ma, H.K. Mao, R.J. Hemley, A.K. Singh, Lattice strains in gold and rhenium under non-hydrostatic compression to 37 GPa, Phys. Rev. B 60 (1999) 1–10.
[22] A. Kavner, T.S. Duffy, Strength and elasticity of ringwoodite at upper mantle pressures, Geophys. Res. Lett. 28 (2001) 2691–2694.
[23] S. Merkel, A.P. Jephcoat, J. Shu, H.K. Mao, P. Gillet, R.J. Hemley, Equation of state, elasticity and shear strength of pyrite under high pressure, Phys. Chem. Min. 29 (2002) 1–9.
[24] S. Shieh, T.S. Duffy, B. Li, Strength and elasticity of SiO_2 across the stishovite-$CaCl_2$-type structural phase boundary, Phys. Rev. Lett. 89 (2002) 255507.
[25] H.R. Wenk, S. Matthies, R.J. Hemley, H.K. Mao, J. Shu, The plastic deformation of iron at pressures of the Earth's inner core, Nature 405 (2000) 1044–1047.
[26] S. Merkel, H.R. Wenk, J. Shu, G. Shen, P. Gillet, H.K. Mao, R.J. Hemley, Deformation of polycrystalline MgO at pressures of the lower mantle, J. Geophys. Res. 107 (2002) 2271.
[27] N.C. Holmes, J.A. Moriarty, G.R. Gathers, W.J. Nellis, The equation of state of platinum to 660 GPa (6.6 Mbar), J. Appl. Phys. 66 (1989) 2962–2967.
[28] G. Fiquet, D. Andrault, A. Dewaele, T. Charpin, M. Kunz, D. Häusemann, P-v-t equation of state of $MgSiO_3$ perovskite, Phys. Earth Planet. Inter. 105 (1998) 21–31.
[29] R.M. Wentzcovitch, B.B. Karki, S. Karato, C.R.S.D. Silvera, High pressure elastic anisotropy of $MgSiO_3$ and geophysical implications, Earth Planet. Sci. Lett. 164 (1998) 371–378.
[30] S. Merkel, R.J. Hemley, H.K. Mao, D.M. Teter, Finite element modeling and ab-initio calculations of megabar stresses in the diamond anvil cell, in: M. Manghnani, W.J. Nellis, M.F. Nicol (Eds.), Science and Technology of High Pressure Research, University Press (India) Limited, 2000, pp. 68–73.
[31] S. Karato, Plasticity-crystal structure systematics in dense oxides and its implications for the creep strength of the Earth's deep interior: a preliminary result, Phys. Earth Planet. Inter. 55 (1989) 234–240.
[32] T. Uchida, N. Funamori, T. Ohtani, T. Yagi, Differential stress of MgO and Mg_2SiO_4 under uniaxial stress field: Variation with pressure, temperature, and phase transition, in: W.A. Trzeciatowski (Ed.), High Pressure Science and Technology, World Scientific Publishing, Singapore, 1996, pp. 183–185.
[33] T. Lay, Q. Williams, E.J. Garnero, The core-mantle boundary layer and deep Earth dynamics, Nature 392 (1998) 461–468.
[34] J.M. Kendall, Seismic anisotropy in the boundary layers of the mantle, in: S. Karato, A.M. Forte, R.C. Liebermann, G. Master, L. Stixrude (Eds.), Earth's Deep Interior. Mineral Physics and Tomography. From the Atomic to the Global Scale, Am. Geophys. Union, Washington, DC, 2000, pp. 133–159.
[35] J.P. Montagner, Where can seismic anisotropy be detected

in the Earth's mantle? in the boundary layers..., Pure Appl. Geophys. 151 (1998) 223–256.
[36] J. Wookey, J.M. Kendall, G. Barruol, Mid-mantle deformation inferred from seismic anisotropy, Nature 415 (2002) 777–780.
[37] A.K. McNamara, S.I. Karato, P.E. van Keken, Localization of dislocation creep in the lower mantle: implications for the origin of seismic anisotropy, Earth Planet. Sci. Lett. 191 (2001) 85–99.
[38] I. Stretton, F. Heidelbach, S. Mackwell, F. Langenhorst, Dislocation creep of magnesiowüstite ($Mg_{.8}Fe_{0.2}O$), Earth Planet. Sci. Lett. 194 (2001) 229–240.
[39] D. Yamazaki, S. Karato, Fabric development in (Mg, Fe)O during large strain, shear deformation: implications for seismic anisotropy in Earth's lower mantle, Phys. Earth Planet. Inter. 131 (2002) 251–267.

Available online at www.sciencedirect.com
SCIENCE DIRECT®
Physics of the Earth and Planetary Interiors 145 (2004) 239–251
PHYSICS OF THE EARTH AND PLANETARY INTERIORS
www.elsevier.com/locate/pepi

Deformation of polycrystalline iron up to 30 GPa and 1000 K

Sébastien Merkel [a,b,*], Hans-Rudolf Wenk [c], Philippe Gillet [b], Ho-kwang Mao [a], Russell J. Hemley [a]

[a] *Geophysical Laboratory, Carnegie Institution of Washington, Washington, DC 20015-1305, USA*
[b] *Laboratoire des Sciences de la Terre, École Normale Supérieure de Lyon, 69364 Lyon Cedex 07, France*
[c] *Department of Earth and Planetary Science, University of California, Berkeley, CA 94720-4767, USA*

Received 3 November 2003; received in revised form 16 March 2004; accepted 14 April 2004

Abstract

Angle-dispersive radial X-ray diffraction measurements were conducted on α- and ϵ-Fe under nonhydrostatic stress conditions up to 30 GPa and 1000 K in laser heated diamond anvil cells. α-Fe (bcc) is found to develop preferred orientation compatible with observations under ambient conditions. The preferred orientation of the α-phase is inherited by the ϵ-phase (hcp) in accordance with the Burgers orientation relationship. A comparison between the observed texture in ϵ-Fe with results from polycrystal plasticity modeling suggests that the predominant deformation mechanisms are basal slip $(0\,0\,0\,1)\langle\bar{1}\,2\,\bar{1}\,0\rangle$ and prismatic slip $\{1\,0\,\bar{1}\,0\}\langle\bar{1}\,2\,\bar{1}\,0\rangle$, presumably associated with minor mechanical twinning. We do not observe any evidence of slip on the $\{1\,1\,\bar{2}\,2\}\langle1\,1\,\bar{2}\,3\rangle$ system that was proposed based on analogies with Cr–Ni stainless steel. Finally, we do not observe any change in preferred orientation upon heating in situ at 28 GPa and 1000 K.

Keywords: High pressure; Deformation; Iron; Slip system; Texture; Anisotropy; Earth core

1. Introduction

Ever since it was first discovered (Poupinet et al., 1983; Morelli et al., 1986), the origin and variability of the seismic anisotropy of the earth's inner core has been a matter of debate (e.g. Ishii and Dziewoński, 2003). Early on, it was proposed that the anisotropy might be caused by preferred alignment of crystals of iron that would have been acquired during the solidification of the inner core (Bergman, 1997) or as a result of plastic deformation (Wenk et al., 1988; Yoshida et al., 1996; Karato, 1999; Wenk et al., 2000a; Buffet and Wenk, 2001). However, support for these hypotheses and modelings have been limited by the lack of information on the deformation mechanisms of iron under extreme conditions. Although the crystal structure of iron at these depths is still being discussed, it is accepted that the ϵ-phase has a wide stability field and serves as a starting point for modeling the bulk of the inner core (Hemley and Mao, 2001). Therefore, obtaining reliable information on the rheology of ϵ-Fe is of great interest for our understanding of deep earth seismic anisotropy.

In recent years, a new diamond anvil cell X-ray diffraction technique has been developed that allows the strength and elasticity of materials to be studied under high pressure (e.g. Hemley et al., 1997; Singh

* Corresponding author. Present address: Institute for Solid State Physics, University of Tokyo, Kashiwanoha 5-1-5, Kashiwa, Chiba 277-8581, Japan. Tel.: +81 471363231; fax: +81 471363230.
E-mail address: smerkel@issp.u-tokyo.ac.jp (S. Merkel).

0031-9201/$ – see front matter © 2004 Elsevier B.V. All rights reserved.
doi:10.1016/j.pepi.2004.04.001

et al., 1998; Mao et al., 1998). This technique has emerged as a powerful tool for the in situ investigation of the development of lattice preferred orientations in deep earth materials aggregates in situ at relevant pressures, as demonstrated by pilot experiments on ϵ-Fe, MgO and (Mg,Fe)SiO_3 perovskite (Wenk et al., 2000b; Merkel et al., 2002, 2003). These preferred orientation patterns can then be used to obtain valuable information about active deformation mechanisms. In this paper, we apply this technique to study the development of lattice preferred orientation in α-Fe, during the transition from the α- to the ϵ-phase, and ϵ-Fe under uniaxial compression at high pressure, as well as high temperature.

The transition from the α (bcc)- to the ϵ (hcp)-phase of iron has been investigated by numerous experimental techniques, such as X-ray diffraction (Mao et al., 1967; Jephcoat et al., 1986; Bassett and Huang, 1987), Mössbauer spectroscopy (Pipkorn et al., 1964; Williamson et al., 1972; Taylor et al., 1991), electrical resistivity (Von Bargen and Boehler, 1990; Boehler et al., 1990), X-ray absorption (Wang and Ingalls, 1998) and X-ray emission spectroscopy (Rueff et al., 1999), as well as simulations (Hasegawa and Pettifor, 1983; Lee and Ray, 1989; Stixrude et al., 1994; Ekman et al., 1998). At room temperature, the transition begins around 13 GPa and spreads over a domain extending up to a pressure of 21 GPa, depending on the specific experimental conditions, in particular on the level of deviatoric stress in the sample (Taylor et al., 1991; Von Bargen and Boehler, 1990; Boehler et al., 1990). Under quasi-hydrostatic conditions, the transition is very sharp. The α–ϵ transition may be martensitic (Giles et al., 1971), i.e. produced by internal shears, particularly at low temperature where diffusion is limited. The martensitic mechanisms are fairly well understood (Mao et al., 1967; Bassett and Huang, 1987; Wang and Ingalls, 1998). This transition is not only structural, but also magnetic. The low pressure α-phase is ferromagnetic but the high pressure ϵ-phase does not show magnetic ordering (Williamson et al., 1972; Rueff et al., 1999). First-principles calculations have emphasized the importance of this magnetic transition for calculating and understanding the high pressure phase diagram of iron (Stixrude et al., 1994; Ekman et al., 1998).

The deformation mechanisms of the α-phase (steel) have already been studied extensively (Rollett and Wright, 1998). However, little is known about the high pressure ϵ-phase; this phase cannot be quenched to ambient conditions in sufficient quantities for plasticity study and its pressure stability field is above the range attainable by conventional deformation apparatus. Information about slip systems relies on indirect comparison with other hcp metals based on *c*/*a* ratios (Wenk et al., 1988), first-principles calculations based on stacking fault energies (Poirier and Price, 1999), comparison of the lattice preferred orientation (LPO) observed in iron under compression in the diamond anvil cell and that obtained by polycrystal plasticity modeling (Wenk et al., 2000b), and microstructures observed in a Ni–Cr stainless steel analog (Poirier and Langenhorst, 2002). Despite these efforts, our understanding of the plasticity of iron at high pressure remains poor.

2. Experimental methods

In this study, we perform an uniaxial deformation experiment on a polycrystalline iron sample using the diamond anvil cell. The stress state in the sample and polycrystalline texture are analyzed using synchrotron X-ray diffraction in a direction orthogonal to the compression axis (Fig. 1). In this experiment,

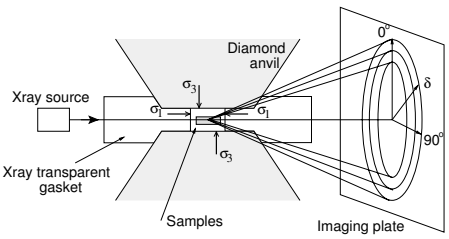

Fig. 1. Schematic of the experiment. The polycrystalline sample is confined under non-hydrostatic stress conditions between the two diamond anvils. σ_3 is the axial stress imposed by the diamonds and σ_1 the radial stress imposed by the gasket. A monochromatic X-ray beam is sent through the gasket with the direction of the incoming beam orthogonal to the diamond axis and the data collected on a imaging plate orthogonal to the incoming beam. The position of the diffraction lines and intensity of diffraction are analysed as a function of the azimuthal angle δ from which we calculate the angle χ between the normal to the diffracting plane and the compression direction (Merkel et al., 2002).

we used diamonds with a 300 μm diameter tip and a confining gasket made of a mixture of amorphous boron and epoxy, with a 65 μm diameter hole drilled in the center to form the sample chamber. The iron sample was a pure commercial product of grain size lower than 1 μm in order to ensure a large number of crystallites and orientations in the analysis. For the pressure medium, we used pure magnesium oxide grinded in mortar with acetone to a grain size lower than 1 μm. Before the loading, the sample powders were pressed into platelets between two large diamonds (1000 μm tip diameter). A layer of MgO was deposited at the bottom of the gasket hole, above which we added a small platelet of pure polycrystalline iron. Finally, another platelet of MgO was added above the Fe platelet and pressed using the diamond anvils. In order to ensure uniform laser heating of the Fe sample, the sample size was limited to less than 20 μm in diameter. Initial thinkness is estimated to be around 20 μm and simple geometrical calculations based on sample and grain sizes indicate that the number of grains in the Fe sample was in the order of 5000–10000. Neither Fe or MgO were submitted to any large macroscopic deformation prior to the experiment. Therefore, we infer that the starting texture was random. This was also confirmed by the low pressure X-ray diffraction patterns that showed a very small degree of lattice preferred orientations.

Diffraction experiments were conducted at the ID-13 beam line of the GSECARS sector at the Advanced Photon Source with an incident monochromatic X-ray beam focused to 10 μm × 6 μm and diffraction patterns were recorded with 2000 × 2700 pixels image plates. The raw X-ray diffraction images were corrected for non-orthogonality by comparing to a CrO_2 standard pattern taken prior to the experiment. Wavelength was fixed to 0.4246 Å and the sample to image plate distance calibrated using the CrO_2 standard was 290.7 mm. More experimental details along with analysis of the stress state, polycrystalline texture, and deformation mechanisms of the MgO surrounding the Fe sample have been given elsewhere (Merkel et al., 2002).

MgO and Fe were compressed at 300 K up to 30 GPa. At this pressure we performed several sets of laser-heating of the sample. During the last heating at this pressure (about 28 GPa, up to 1300 K), part of the ϵ-Fe sample converted into the γ-phase (e.g. Fig. 2).

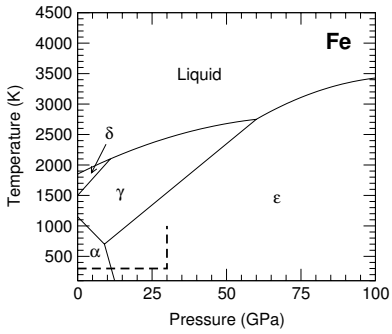

Fig. 2. Phase diagram of iron (thin solid lines, after Shen et al., 1998) and pressure/temperature domain covered in this experiment (thick dashed line). α- and δ-phase are bcc, γ-phase is fcc and ϵ-phase is hcp.

This phase is quenchable to ambient temperature and has diffraction peaks which partially overlap those of ϵ-Fe. Because of this, we did not take the analysis further and the data presented here will only range up to 30 GPa and during the first laser heating run, before the conversion to γ-Fe.

For each measurement, the diffraction image was integrated over small arcs of 2–4° interval. The patterns were then fitted individually assuming Gaussian peak profiles and a linear local background in order to determine the variation of the diffraction intensity with the azimuthal angle δ. The angle χ between the diffraction plane normal and the maximum stress axis was calculated from the azimuthal angle δ using the relation

$$\cos\chi = \cos\theta\cos\delta, \quad (1)$$

where θ is the diffraction angle. Assuming an axial symmetry about the compression direction, the orientation distribution functions (ODFs) of the sample were calculated using the variation of diffraction intensity with χ and the WIMV algorithm, as implemented in the BEARTEX package (Wenk et al., 1998). The ODF is a probability function for finding an orientation and it is normalized over the whole orientation space to unity. An aggregate with a random distribution function has a probability of one for all orientations, or one multiple of a random distribution (m.r.d.). If preferred orientation is present, some orientations

have probabilities higher than one and others lower than one but orientation probabilities can never be less than zero. The degree of anisotropy in the sample is expressed by the texture index F_2 defined as

$$F_2 = \int_G [f(g)]^2 \, \mathrm{d}\bar{g} \quad (2)$$

where f is the ODF. For a material with random texture, the texture index F_2 is equal to 1, for a textured material $F_2 > 1$.

The pressures and temperatures corresponding to the data presented in this paper are summarized in Table 1. Pressures were estimated using the hydrostatic equation of state of the pressure medium, MgO (Speziale et al., 2001), and iron itself (Jephcoat et al., 1986; Zhang and Guyot, 1999), after correcting the data for the effect of non-hydrostatic stress (e.g. Merkel et al., 2002). The temperatures upon heating were too low to be measured by spectral radiometry (Heinz and Jeanloz, 1987) but because of the shining appearance of the sample, the pressure drop associated with heating, and the transition from ϵ-Fe to γ-Fe upon further heating, they were estimated to be around 1000 K. Fig. 2 presents the phase diagram of iron (Shen et al., 1998) along with the pressure/temperature domain covered in this experiment.

3. Results

3.1. Preferred orientation in α-iron

Fig. 3 presents the variations in the diffraction intensity for some lattice planes with orientation relative to the compression direction (angle χ) for α-iron, at 8.9 GPa and compares the measured values with those recalculated from the ODF fitted to the sample. The agreement is good for (1 1 0) and (2 2 0). The texture is weak for (2 1 1) and thus this profile is not very informative. (2 0 0) is a weak diffraction peak that partially overlaps with the third order peak from the amorphous boron and this results in a large dispersion of experimental data seen in Fig. 3. The texture index, a bulk measure for texture strength, increases between 2.8 and 6.6 GPa and reaches a plateau at a value of about 1.1 (Table 1). We note that the texture index for α-Fe is significantly lower than that for MgO in the same sample and at the same pressure (Merkel et al., 2002). It was therefore substantially easier to generate LPO in MgO than in iron in those conditions.

Fig. 4 shows the inverse pole figures we obtain for α-iron in compression at 2.8, 6.6, 8.9 and 12.4 GPa. We observe the progressive development of two fiber components, (1 1 1) and (1 0 0). Before the transition to the ϵ-phase, α-iron is in an orientation such that the probability of having (1 1 1) and (1 0 0) planes

Table 1
Pressure, temperature, phase, texture index, and maximum pole densities

Number	P—MgO (GPa)	P—Fe (GPa)	T (K)	Phase	Texture index	Maximum pole density (m.r.d.)
1	1.5 ± 0.5	2.8 ± 0.5	300	α	1.009	1.35
2	5.1 ± 0.5	6.6 ± 0.5	300	α	1.119	2.84
3	7.5 ± 0.5	8.9 ± 0.5	300	α	1.117	2.40
4	11.4 ± 0.5	12.4 ± 0.5	300	α	1.112	1.97
5	17.4 ± 0.5	17.7 ± 0.5	300	ϵ	1.300	2.79
6	18.3 ± 0.5	18.5 ± 0.5	300	ϵ	1.416	3.20
7	20.2 ± 0.5	20.3 ± 0.5	300	ϵ	1.229	2.48
8	23.0 ± 0.5	22.7 ± 0.5	300	ϵ	1.317	2.67
9	23.9 ± 0.5	24.1 ± 0.5	300	ϵ	1.375	2.57
10	27.0 ± 0.5	27.2 ± 0.5	300	ϵ	1.241	2.67
11	29.8 ± 0.5	30.3 ± 0.5	300	ϵ	1.239	2.75
11b[a]		28.8 ± 0.5	300	ϵ	1.212	2.57
11c			1000	ϵ	1.373	3.51

Pressures were calibrated using the equation of state of the pressure medium, MgO (Speziale et al., 2001), or iron itself (Jephcoat et al., 1986; Zhang and Guyot, 1999). Texture index and maximum pole densities were calculated from the ODF fitted to the sample. The maximum pole density is expressed in multiples of a random distribution (m.r.d.).

[a] After heating up to about 1000 K.

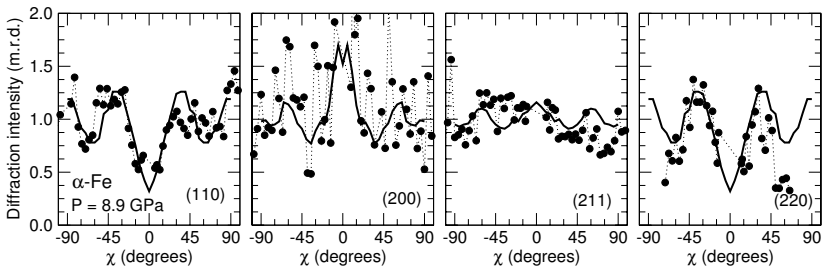

Fig. 3. Diffraction intensity vs. χ for α-Fe at 8.9 GPa. Black dots are experimental data and solid lines are recalculated from the ODF. Experimental intensities have been scaled to match those deduced from the ODF, expressed in multiples of a random distribution (m.r.d.). Axial symmetry was assumed for the calculation of the ODF.

orthogonal to the compression axis is high, and that the probability of having the (1 1 0) planes orthogonal to the compression axis is low.

3.2. Preferred orientation in ϵ-iron

Fig. 5a and b show the variation in intensity of diffraction with orientations for the (1 0 0), (0 0 2), (1 0 1), and (1 1 0) diffraction peaks of ϵ-iron measured at 17.7 and 30.3 GPa, respectively, along with those recalculated from the ODF. The ODF was calculated using the variation of the diffraction intensities of the (1 0 0), (0 0 2), (1 0 1), (1 1 0), (1 0 3), (1 1 2), and (2 0 1) diffraction peaks, except for the spectrum at about 1000 K and 28 GPa for which only the (1 0 0), (0 0 2), (1 0 1), (1 1 2) and (2 0 1) peaks were used. At 18 GPa, after the transition to the ϵ-phase, the *c*-axes of the iron crystals tend to be aligned in a direction orthogonal to the compression axis with large diffraction intensities for (0 0 2) at $\chi = \pm 90^\circ$. Upon further compression, the *c*-axes rotate and become parallel to the compression axis at the highest pressures with a maximum diffraction intensity for (0 0 2) at $\chi = 0^\circ$. Diffraction intensities for *a*-axes (1 1 0) are initially highest parallel to the compression direction and this maximum attenuates as the *c*-axis maximum develops but a weaker concentration remains.

Fig. 6 shows the representations of the textures we obtain in terms of inverse pole figures of the compression direction for ϵ-iron between 18 and 30 GPa, after heating to about 1000 K at 30 GPa, and in situ at 28 GPa and 1000 K. At 18 GPa, we observe a maximum around (1 1 $\bar{2}$ 0) which implies that the crystallites are preferentially oriented with their *a*-axes parallel to the compression axis.[1] We then observe a smooth transition towards a single fiber (0 0 0 1) texture, with the basal planes of the polycrystal orthogonal to the compression axis. The (0 0 0 1) texture is similar to that observed in the diamond anvil cell at 54 and 220 GPa (Wenk et al., 2000b). The presence of the MgO pressure medium surrounding the sample does not appear to affect the high pressure texture.

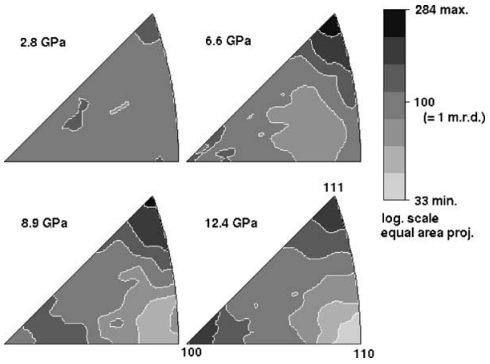

Fig. 4. Inverse pole figures for α-Fe at 2.8, 6.6, 8.9, and 12.4 GPa. Equal area projection, contours in multiples of a random distribution.

The texture we measure after heating to 1000 K at 30 GPa, or in situ at 28 GPa and 1000 K, does not differ significantly from those observed before heating (Fig. 6). Therefore, our experiment does not show any

[1] Note that in an earlier paper (Wenk et al., 2000b), inverse pole figures were mislabeled, i.e. 1 0 $\bar{1}$ 0 and 1 1 $\bar{2}$ 0 were switched.

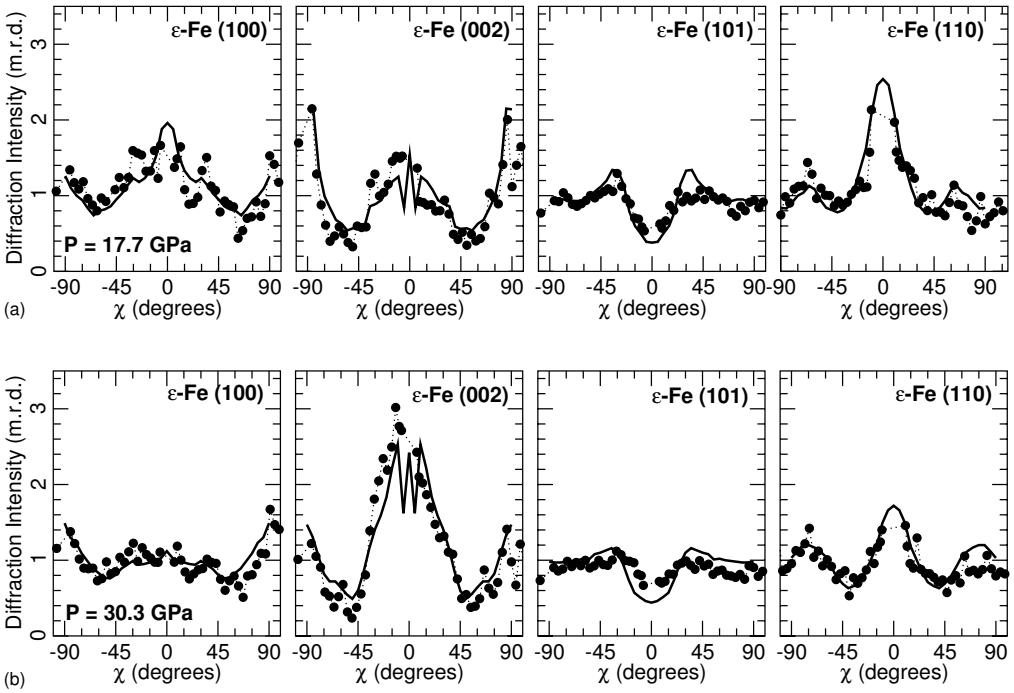

Fig. 5. Diffraction intensity vs. χ for the (1 0 0), (0 0 2), (1 0 1) and (1 1 0) planes of ϵ-Fe at 17.7 GPa (a) and 30.3 GPa (b). Black dots are experimental data and solid lines are recalculated from the ODF. Experimental intensities have been scaled to match those deduced from the ODF, expressed in m.r.d. (multiples of a random distribution).

measurable sign of recrystallization or rearrangements upon heating under the conditions of this study. Because of the existence of a phase transition to fcc (e.g. Fig. 2), we were not able investigate this property upon further heating.

4. Discussion

4.1. Lattice preferred orientation in α-iron

The textures we obtain for the α-phase (bcc) of iron (2.8–12.4 GPa) conform to compression textures observed by metallurgists (Rollett and Wright, 1998; Barrett and Massalski, 1980). In inverse pole figures, we identify two fiber components, a major component at (1 1 1) and a secondary component at (1 0 0). The main active slip system in bcc metals is $\{1\,1\,0\}\langle 1\,1\,1\rangle$. This is analogous to fcc metals but with slip plane and slip direction reversed. Such a reversal produces compression textures for bcc metals that are similar to tension textures in fcc metals. The fact that we observe the standard bcc compression texture in our experiments is important since it validates the use of the diamond anvil cell as a deformation apparatus and synchrotron X-ray diffraction as an in situ texture probe (Wenk et al., 2000b; Merkel et al., 2002, 2003).

4.2. Phase transition

Between 12.4 and 17.7 GPa the phase transformation occurs and produces a texture with a main component at $(1\,1\,\bar{2}\,0)$ in ϵ-iron of similar strength as the

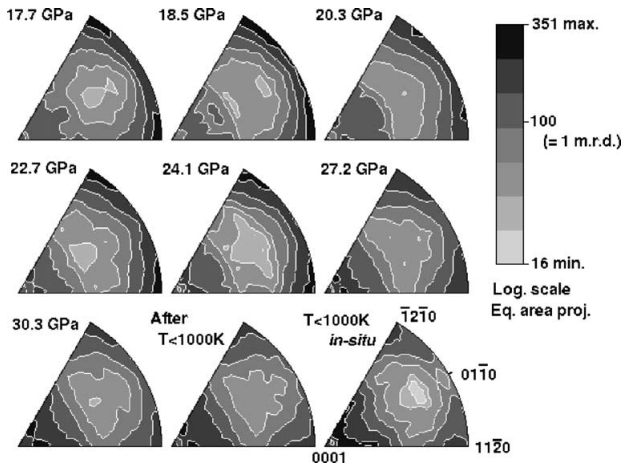

Fig. 6. Inverse pole figures for ϵ-Fe in compression between 17.7 and 30.3 GPa, at 28 GPa after heating to about 1000 K and in situ at about 1000 K and 28 GPa. Equal area projection, contours in multiples of a random distribution.

(1 1 1) component in α-iron; some texture has been inherited during the phase transformation. For the reverse transformation (hcp to bcc), Burgers established an orientation relationship $(0\,0\,0\,1)_{hex}$–$(1\,1\,0)_{bcc}$ and $[1\,1\,\bar{2}\,0]_{hex}$–$[\bar{1}\,1\,\bar{1}]_{bcc}$, based on the most obvious structural relationships (Burgers, 1934, Fig. 7) and they have been confirmed in single crystal heating experiments of titanium (e.g. Jourdan et al., 1991). However, the situation is more complicated for polycrystals where variant selection occurs and a martensitic mechanism is not established (Gey and Humbert, 2002; Zhu et al., 2000; Wenk et al., 2004). In our experiments, comparing the bcc and hcp inverse pole figures close to the transition (Fig. 4 and 6) we find that the Burgers relation largely applies with a high value for (1 1 1) and $(1\,1\,\bar{2}\,0)$ components and low values for (1 1 0) and (0 0 0 1) in inverse pole figures of the compression direction.

The α–ϵ transition in iron with pressure has been established as martensitic on the basis of X-ray diffraction (Mao et al., 1967; Bassett and Huang, 1987; Giles et al., 1971), X-ray absorption (Wang and Ingalls, 1998) and molecular dynamics calculations (Lee and Ray, 1989) and detailed models about atomic displacements have been proposed that all lead to the Burger's relationship and thus conform with the data of our experiments (Wang and Ingalls, 1998). In reality, the situation is complicated by the existence of internal stresses between grains that develop during the phase transformation. They also influence the orientation relations and variant selection and can not be deduced from simple crystallographic considerations. Within the scope of our experiment, these effects could not be investigated.

4.3. Lattice preferred orientation in ϵ-iron

4.3.1. Main features

There is an extensive literature on the deformation of hexagonal metals and the most relevant systems are summarized in Table 2. For fairly isotropic materials with low *c/a* ratios, such as zirconium and titanium, it is generally found that prismatic slip dominates with subordinate mechanical twinning (Tenckhoff, 1988; Pochettino et al., 1992). For materials such as zinc and beryllium that are more anisotropic elastically and with a high *c/a* ratio, basal slip dominates (Greenspan, 1965). However, there have been reports of prismatic and basal slip, tensile and compressive mechanical twinning, and pyramidal slip for all hexagonal metals (e.g. Akhtar, 1973; Tenckhoff, 1988; Pochettino et al., 1992). The critical resolved shear stresses

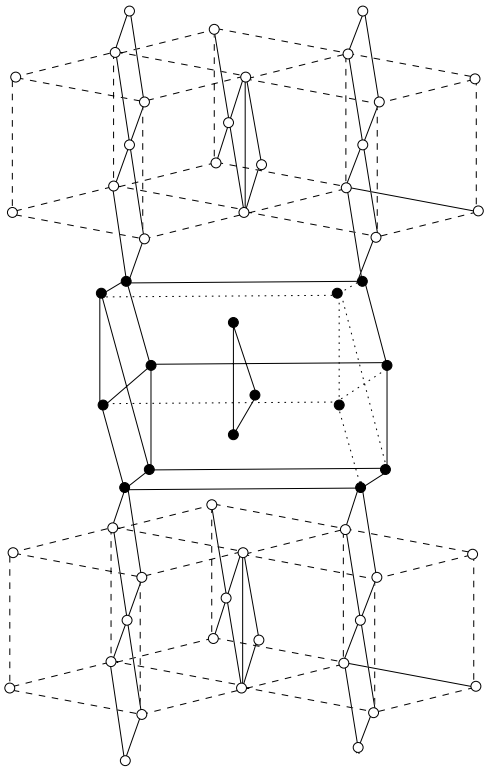

Fig. 7. Three-dimensional representation of the crystallographic relations between the hcp and bcc phases according to Burgers relationship.

(CRSS) have been shown to depend on temperature and deformation geometry. Hcp iron has a low *c/a* ratio but a different electronic structure, as emphasized by the unique nature of its phase diagram (Fig. 2), therefore comparisons based on *c/a* ratios are not relevant and it has been argued, based on ab initio calculations, that basal slip may be important (Poirier and Price, 1999). Recent TEM observations on Ni–Cr stainless steel also reported dislocations consistent with basal and pyramidal $\{2\,\bar{1}\,\bar{1}\,2\}\langle 2\,\bar{1}\,\bar{1}\,3\rangle$ slip (Poirier and Langenhorst, 2002) and it was suggested that these systems may be active in ϵ-iron at high pressure. But all of these deductions are not based on direct observation of the ϵ-phase and need to be clarified experimentally.

The lattice preferred orientations that develop upon compression are a good probe of active deformation systems. They can be compared with polycrystal plasticity simulations to asses the activities of different slip systems. Such comparisons have been made for zirconium (e.g. Tomé et al., 1991; Lebensohn et al., 1994, 1996) using viscosplastic self-consistent models (e.g. Lebensohn and Tomé, 1993). In the case of axial compression with activity of both prismatic slip and twinning, a texture develops with two fiber components, the major and second component displaying a maximum near $(0\,0\,0\,1)$ and $(1\,1\,\bar{2}\,0)$, respectively (Tomé and Canova, 1998). It is worth noting that the $(0\,0\,0\,1)$ maximum can be attributed to tensile twinning since prismatic slip does not contribute to the reorientation of basal planes. In the present analysis, we used similar plasticity models to look into texture variations in more detail, and in particular by adding basal and pyramidal slip as well as results for five different combinations of CRSS (Table 2). Results are summarized

Table 2
Table of critical resolved shear stresses (CRSS) for the deformation systems assumed in texture simulations for models A–E (Figs. 8 and 9)

Model		A	B	C	D	E
Basal	$(0\,0\,0\,1)\langle\bar{1}\,2\,\bar{1}\,0\rangle$	0.5	1	2	1^{m}	1
Prismatic	$\{1\,0\,\bar{1}\,0\}\langle\bar{1}\,2\,\bar{1}\,0\rangle$	1	1	1	1^{m}	–
Pyramidal	$\{1\,0\,\bar{1}\,1\}\langle\bar{1}\,2\,\bar{1}\,0\rangle$	2^{i}	2^{i}	2^{i}	1^{m}	–
Pyramidal	$\{1\,0\,\bar{1}\,1\}\langle\bar{1}\,\bar{1}\,2\,3\rangle$	3^{i}	3^{i}	3^{i}	1	–
Pyramidal	$\{2\,\bar{1}\,\bar{1}\,2\}\langle 2\,\bar{1}\,\bar{1}\,\bar{3}\rangle$	–	–	–	1^{m}	1
Tensile twinning	$\{1\,0\,\bar{1}\,2\}\langle\bar{1}\,0\,1\,1\rangle$	1.25^{m}	1.25^{m}	1.25	1^{m}	–
Compressive twinning	$\{2\,\bar{1}\,\bar{1}\,2\}\langle 2\,\bar{1}\,\bar{1}\,\bar{3}\rangle$	2.5^{i}	2.5^{m}	2.5^{m}	1^{m}	–

The symbol '–' indicates slip systems that were not included in the simulations, while superscripts m and i indicate systems that were only moderately active or inactive, respectively.

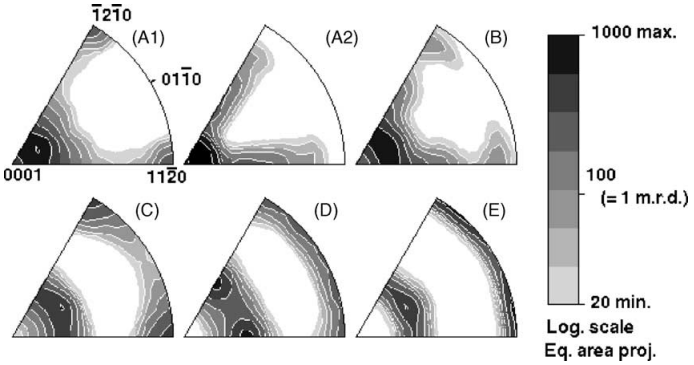

Fig. 8. Inverse pole figures illustrating texture evolution in compression based on viscoplastic self-consistent simulations for the CRSS combinations given in Table 2. Strains are 50%, except for (A2), where it is 100%. Equal area projection, contours in multiples of a random distribution.

in inverse pole figures for 50% strain in Fig. 8. For easier comparison with previous studies, the CRSS for twinning of Tomé and Canova (1998) was used. For all cases, we used a stress exponent of $n = 19$.

4.3.2. Results for model A

The best agreement with the measured high pressure textures is obtained when basal slip is highly favored. At low strain (50%), we expect the development of a double maximum with the two (0 0 0 1) and (1 1 $\bar{2}$ 0) fiber components (Fig. 8-A1). As strain increases (100%, Fig. 8-A2) the (1 1 $\bar{2}$ 0) component disappears and the (0 0 0 1) component becomes more pronounced. The calculated slip system activities indicate that most of the deformation occurs by basal slip accompanied by moderate prismatic slip and, at higher strains, minor compressional twinning (Fig. 9a). In a simplified way, the (1 1 $\bar{2}$ 0) component develops by prismatic (1 0 $\bar{1}$ 0) slip and the (0 0 0 1) component by basal slip.

4.3.3. Results for model B

When assigning the same CRSS to basal and prismatic slip, slip activity on basal and prismatic systems

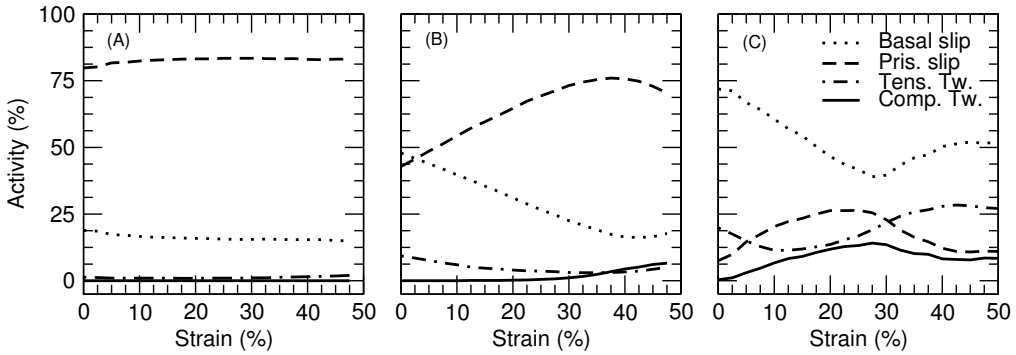

Fig. 9. Evolution of slip system activities for models A–C for basal slip (dotted lines), prismatic slip (dashed line), tensile twinning (dot-dashed line) and compressive twinning (solid line). These correspond to the models which produce the textures that conform best with experiments.

is similar and moderate twinning occurs. The maximum near $(1\,1\,\bar{2}\,0)$ is spread out and slightly shifted (Fig. 8-B). This also compares reasonably well with the experimental inverse pole figures obtained at the highest pressure. As mentioned above, prismatic slip does not contribute to rotations of the basal planes.

4.3.4. Results for model C

In agreement with previous calculations (Tomé and Canova, 1998), a double fiber texture develops if prismatic slip is dominantly active (Fig. 8-C). However, the maximum near $(0\,0\,0\,1)$ is distinctly moved by 20° from $(0\,0\,0\,1)$; this is not observed experimentally. In this case, pyramidal slip and tensile twinning are inactive, but compressive twinning becomes activated at larger strain to maintain compatibility.

4.3.5. Results for model D

If all systems have equal shear stresses, the main activity occurs on pyramidal $\langle a+c\rangle$ slip, moderate twinning occurs, yet the texture is not dramatically different from model C (Fig. 8-D). The main difference is the broad girdle distribution for compression axes in prism directions with no preference for $(1\,1\,\bar{2}\,0)$ or $(1\,0\,\bar{1}\,0)$. This texture pattern does not agree with the experiments. Moreover, pyramidal $\langle a+c\rangle$ slip is very rarely observed in hexagonal metals. These simulations are shown here to illustrate the influence of these slip systems on texture.

4.3.6. Results for model E

Finally we show textures obtained when basal and pyramidal $\{2\,\bar{1}\,\bar{1}\,2\}\langle 2\,\bar{1}\,\bar{1}\,\bar{3}\rangle$ slip are active, as previously suggested (Poirier and Langenhorst, 2002). The pattern is very different from the experimental results (Fig. 8-E). A modification of the weighting of these slip systems would not introduce any major changes in the resulting textures. This indicates that the combination of those two slip systems is not active in ε-iron at the conditions reported here. One should also note that the implied pyramidal slip system corresponds to the well-established mechanical twinning system.

4.3.7. Conclusions from polycrystalline plasticity simulations

The comparison between experimental textures and simulations establish the activity of basal and prismatic slip at the conditions of our experiments, probably modified by minor mechanical twinning. The maximum near $(0\,0\,0\,1)$ can only be produced by basal slip, and the maximum near $(1\,1\,\bar{2}\,0)$ is due to prismatic slip. Pyramidal slip would produce very different texture patterns from those that are observed experimentally.

Although the precision of the experimental measurements has been greatly improved, a comparison of the new observation with the older results (Wenk et al., 2000b) is appropriate. In the earlier experiments, performed at higher pressure (54 and 220 GPa), the $(1\,1\,\bar{2}\,0)$ component is largely absent while the $(0\,0\,0\,1)$ component appears much stronger and better defined. This behavior can be reproduced with a high strain simulation allowing easy basal slip (Fig. 8-A2). Thus, the strains in the higher pressure experiment were larger (producing maxima of 6.7 and 7.3 m.r.d., respectively, compared to 3.5 m.r.d. in our experiment) and basal slip is more favorable than prismatic slip.

4.3.8. Effect of temperature

We measured the texture in polycrystalline Fe at 28 GPa after heating to about 1000 K for 10 min and in situ at about 28 GPa and 1000 K ($T/T_m \approx 0.4$) and could not observe any significant change in the texture pattern. The heating did indeed create a decrease in stress in the sample, both in terms of pressure and uniaxial stress, but this did not generate any rearrangement of the preferred orientations of the crystallites and the sample kept all of its texture characteristics. This does not preclude recrystallization since it is observed that often recrystallization does not induce profound texture changes in hcp metals (Wagner et al., 2002; Puig-Molina et al., 2003).

The heating experiment is a first attempt for radial diffraction studies under simultaneous high temperature and high pressure in order to bring these diamond anvil experiments closer to conditions of the deep earth. In order to fully understand the rheology of materials, the influence of temperature, pressure, deformation and recrystallization on texture need to be evaluated and this can be difficult if no microstructural data are available. In the future, these techniques could eventually be extended to extract this information from the diffraction patterns by a precise analysis of the shape and position of

diffraction peaks using techniques such as Rietveld refinement.

5. Conclusions

We measured the evolution of preferred orientation in polycrystalline α- and ϵ-Fe under compression in the diamond anvil cell up to 30 GPa, after heating to about 1000 K, and in situ at about 28 GPa and 1000 K. These measurements present the first quantitative analysis of the development of texture and deformation mechanisms under combined high pressure and high temperature for phases that are unstable under ambient conditions. The preferred orientations we obtain in the α-phase are compatible with those observed in bcc iron at ambient conditions (Barrett and Massalski, 1980), thus confirming the validity of the approach we developed for using the diamond anvil cell as a deformation apparatus (Wenk et al., 2000b; Merkel et al., 2002, 2003). Our observations are also consistent with a martensitic nature of the α–ϵ phase transition in iron since the preferred orientation of the α-phase is inherited by the ϵ-phase in accordance with the Burgers orientation relationship.

After the phase transition (at 18 GPa) ϵ-Fe displays a $(1\,1\,\bar{2}\,0)$ texture, with the *c*-axis in a direction orthogonal to the compression direction. As previously reported, ϵ-Fe under uniaxial compression at high pressure develops a strong $(0\,0\,0\,1)$ single fiber texture with the *c*-axis of the polycrystal aligned with the compression direction. A comparison between the experimental textures and results from polycrystal plasticity modeling allows us to deduce the two active deformation mechanisms in this transition: basal slip $(0\,0\,0\,1)\langle\bar{1}\,2\,\bar{1}\,0\rangle$ and prismatic slip $\{1\,0\,\bar{1}\,0\}\langle\bar{1}\,2\,\bar{1}\,0\rangle$, presumably associated with minor mechanical twinning. No evidence for slip on the $\{1\,1\,\bar{2}\,2\}\langle1\,1\,\bar{2}\,3\rangle$ system, proposed on the basis of analogies with Cr–Ni stainless steel (Poirier and Langenhorst, 2002), was observed. Finally, we did not observe any evidence for change in texture upon heating in situ at about 28 GPa and 1000 K. Although the sample experienced a decrease in stress, the preferred orientation remained. With current techniques, an even broader range of pressure and temperature conditions can be covered, making the radial diffraction technique even better suited for studying the deformation in the deep earth.

Acknowledgements

We thank G. Shen and E. Soignar for assistance during the experiment and S. Gramsch for his comments on the manuscript. Reviews by D. Price and F. Langenhorst have significantly improved the manuscript. This work was supported by the NSF and the DOE/NNSA through the Carnegie/DOE Alliance Center (CDAC).

References

Akhtar, A., 1973. Basal slip in zirconium. Acta Metall. 21, 1–11.
Barrett, C., Massalski, T.B., 1980. Structure of Metals. Pergamon Press, Oxford, UK.
Bassett, W.A., Huang, E., 1987. Mechanism of the body-centered cubic-hexagonal close-packed phase transition in iron. Science 238, 780–783.
Bergman, M.I., 1997. Measurements of elastic anisotropy due to solidification texturing and the implication for the Earth's inner core. Nature 389, 60–63.
Boehler, R., Von Bargen, N., Chopelas, A., 1990. Melting, thermal expansion, and phase transitions of high at high pressure. J. Geophys. Res. 95, 21731–21736.
Buffet, B.A., Wenk, H.R., 2001. Texturing of the Earth's inner core by Maxwell stresses. Nature 413, 60–63.
Burgers, M.G., 1934. On the process of transition of the cubic-body-centered modification into hexagonal-close-packed modification of zirconium. Physica 1, 561–586.
Ekman, M., Sadigh, B., Einarsdotter, K., Blaha, P., 1998. Ab initio study of the martensitic bcc–hcp transformation in iron. Phys. Rev. B 58, 5296–5304.
Gey, N., Humbert, M., 2002. Characterization of the variant selection occurring during the α–β–α phase transformations of a cold-rolled titanium sheet. Acta Mater. 50, 277–287.
Giles, P.M., Longenbach, M.H., Marder, A.R., 1971. High-pressure α–ϵ martensitic transformation in iron. J. Appl. Phys. 42, 4290–4295.
Greenspan, J., 1965. Ductibility problems. In: Hausner, H. (Ed.), Beryllium, Its Metallurgy and Properties. University of California Press, Berkeley, pp. 240–246.
Hasegawa, H., Pettifor, G.D., 1983. Microscopic theory of the temperature–pressure phase diagram of iron. Phys. Rev. Lett. 50, 130–133.
Heinz, D.L., Jeanloz, R., 1987. Temperature measurement in the laser heated diamond anvil cell. In: Manghnani, M.H., Syono, Y. (Eds.), High Pressure Research in Mineral Physics. American Geophys. Union, pp. 113–127.
Hemley, R.J., Mao, H.K., 2001. In situ studies of iron under pressure: new windows on the Earth's core. Int. Geol. Rev. 43, 1–30.
Hemley, R.J., Mao, H.K., Shen, G., Badro, J., Gillet, P., Hanfland, M., Häusermann, D., 1997. X-ray imaging of stress and strain of diamond, iron, and tungsten at megabar pressures. Science 276, 1242–1245.

Ishii, M., Dziewoński, A.M., 2003. The innermost inner core of the earth: Evidence for a change in anisotropic behavior at the radius of about 300 km. Proc. Natl. Acad. Sci. 99, 14026–14030.

Jephcoat, A.P., Mao, H.K., Bell, P.M., 1986. Static compression of iron to 78 GPa with rare gas solids as pressure-transmitting media. J. Geophys. Res. 91 (B5), 4677–4684.

Jourdan, C., Gastaldi, J., Amd, G., Grange, P.M., 1991. In situ statistical study of the nucleation, the variant selection and the orientation memory effect during the α–β titanium martensitic transformation. J. Mater. Sci. 26, 4355–4360.

Karato, S., 1999. Seismic anisotropy of the Earth's inner core resulting from flow induced Maxwell stresses. Nature 402, 871–873.

Lebensohn, R.A., Gonzalez, M.I., Pochettino, A.A., Tomé, C., 1996. Measurement and prediction of texture development during a rolling sequence of zircaloy-4 tubes. J. Nucl. Mater. 229, 57–64.

Lebensohn, R.A., Sanchez, P.V., Pochettino, A.A., 1994. Modelling texture development of zirconium alloys at high temperature. Scripta Metall. Mater. 30, 481–486.

Lebensohn, R.A., Tomé, C., 1993. A selfconsistent anisotropic approach for the simulation of plastic deformation and texture development of polycrystals: application to zirconium alloys. Acta Metall. Mater. 41, 2611–2624.

Lee, K.Y., Ray, J.R., 1989. Mechanism of pressure-induced martensitic phase transformations: A molecular-dynamics study. Phys. Rev. B 39, 565–574.

Mao, H.K., Bassett, W.A., Takahashi, T., 1967. Effect of pressure on crystal structure and lattice parameters of iron up to 300 kbars. J. Appl. Phys. 38, 272–276.

Mao, H.K., Shu, J., Shen, G., Hemley, R.J., Li, B., Singh, A.K., 1998. Elasticity and rheology of iron above 220 GPa and the nature of the earth's inner core. Nature 396, 741–743, correction, Nature 399, 280, 1999.

Merkel, S., Wenk, H.R., Badro, J., Montagnac, G., Gillet, P., Mao, H.K., Hemley, R.J., 2003. Deformation of (Mg,Fe)SiO_3 perovskite aggregates up to 32 GPa. Earth Planet. Sci. Lett. 209, 351–360.

Merkel, S., Wenk, H.R., Shu, J., Shen, G., Gillet, P., Mao, H.K., Hemley, R.J., 2002. Deformation of polycrystalline MgO at pressures of the lower mantle. J. Geophys. Res. 107, 2271, doi: 10.129/2001JB000920.

Morelli, A., Dziewoński, A.M., Woodhouse, J.H., 1986. Anisotropy of the inner core inferred from PKIKP travel times. Geophys. Res. Lett. 13, 1545–1548.

Pipkorn, D.N., Edge, C.K., Debrunner, P., De Pasquali, G., Drickamer, H.G., Frauenfelder, H., 1964. Mössbauer effect in iron under very high pressure. Phys. Rev. 135, A1604–A1612.

Pochettino, A.A., Gannio, N., Edwards, C.V., Penelle, R., 1992. Texture and pyramidal slip in Ti, Zr and the their alloys. Scripta Metall. Mater. 27, 1859–1863.

Poirier, J.P., Langenhorst, F., 2002. TEM study of an analogue of the Earth's inner core ϵ-Fe. Phys. Earth Panet. Int. 129, 347–358.

Poirier, J.P., Price, G.D., 1999. Primary slip system of ϵ-iron and anisotropy of the Earth's inner core. Phys. Earth Panet. Int. 110, 147–156.

Poupinet, G., Pillet, R., Souriau, A., 1983. Possible heterogeneity of the Earth's inner core deduced from PKIKP travel times. Nature 305, 204–206.

Puig-Molina, A., Wenk, H.R., Berberich, F., Graafsma, H., 2003. Method for in situ investigation of recrystallization of copper and titanium by high-energy synchrotron X-ray diffraction. Zeitschr. Metallkunde 94, 1199–1205.

Rollett, A.D., Wright, S.I., 1998. Typical textures in metals. In: Kocks, U.F., Tomé, C.N., Wenk, H.R. (Eds.), Texture and Anisotropy. Preferred orientations in Polycrystals and their Effect on Materials Properties. Cambridge University Press, Cambridge, Ch. 5, pp. 179–239.

Rueff, J.P., Krisch, M., Cai, Y.Q., Kaprolat, A., Hanfland, M., Lorenzen, M., Masciovecchio, C., Verbeni, R., Sette, F., 1999. Magnetic and structural α–ϵ phase transition in Fe monitored by X-ray emission spectroscopy. Phys. Rev. B 60, 14510–14512.

Shen, G., Mao, H.K., Hemley, R.J., Duffy, T.S., Rivers, M.L., 1998. Melting and crystal structure of iron at high pressures and temperatures. Geophys. Res. Lett. 25, 373–376.

Singh, A.K., Balasingh, C., Mao, H.K., Hemley, R.J., Shu, J., 1998. Analysis of lattice strains measured under non-hydrostatic pressure. J. Appl. Phys. 83, 7567–7575.

Speziale, S., Zha, C.S., Duffy, T.S., Hemley, R.J., Mao, H.K., 2001. Quasi-hydrostatic compression of magnesium oxyde to 52 GPa: implications for the pressure–volume–temperature equation of state. J. Geophys. Res. 106, 515–528.

Stixrude, L., Cohen, R.E., Singh, D.J., 1994. Iron at high pressure: Linearized-augmented-plane-wave computations in the generalized-gradient approximation. Phys. Rev. B 50, 6442–6445.

Taylor, R.D., Pasternak, M.P., Jeanloz, R., 1991. Hysteresis in the high pressure transformation of bcc- to hcp-iron. J. Appl. Phys. 69, 6126–6128.

Tenckhoff, E. (Ed.), 1988. Deformation Mechanisms, Texture and Anisotropy in Zirconium and Zircaloy. ASTM, Philadelphia, PA.

Tomé, C.N., Canova, G.R., 1998. Self consistent modeling of heterogeneous plasticity. In: Kocks, U.F., Tomé, C.N., Wenk, H.R. (Eds.), Texture and Anisotropy. Preferred orientations in Polycrystals and their Effect on Materials Properties. Cambridge University Press, Cambridge, Chapter 11, pp. 466–511.

Tomé, C.N., Lebensohn, R.A., Kocks, U.F., 1991. A model for texture development dominated by deformation twinning: application to zirconium alloy. Acta Metall. Mater. 39, 2667–2680.

Von Bargen, N., Boehler, R., 1990. Effect of non-hydrostaticity on the α–ϵ phase transition of iron. High Pressure Res. 6, 133–140.

Wagner, F., Bozzolo, N., Landuyt, D.V., Grosdidier, T., 2002. Evolution of recrystallisation texture and microstructure in low alloyed titanium sheets. Acta Mater. 50, 1245–1259.

Wang, F.M., Ingalls, R., 1998. Iron bcc–hcp transition: Local structure from X-ray-absorption fine structure. Phys. Rev. B 57, 5647–5654.

Wenk, H., Lonardelli, I., Williams, D., 2004. Texture changes in the hcp–bcc–hcp transformation of zirconium studied in situ by neutron diffraction. Acta Mater. 52, 1899–1907.

Wenk, H.R., Bamgardner, J.R., Lebensohn, R.A., Tomé, C.N., 2000a. A convection model to explain the anisotropy of the inner core. J. Geophys. Res. 105, 5663–5677.

Wenk, H.R., Matthies, S., Hemley, R.J., Mao, H.K., Shu, J., 2000b. The plastic deformation of iron at pressures of the Earth's inner core. Nature 405, 1044–1047.

Wenk, H.R., Matthies, S., Donovan, J., Chateigner, D., 1998. Beartex: a windows-based program system for quantitative texture analysis. J. Appl. Cryst. 31, 262–269.

Wenk, H.R., Takeshita, T., Jeanloz, R., Johnson, G.C., 1988. Development of texture and elastic anisotropy during deformation of hcp metals. Geophys. Res. Lett. 15 (1), 76.

Williamson, D.L., Bukshpan, S., Ingalls, R., 1972. Search for magnetic ordering in hcp iron. Phys. Rev. B 6, 4194–4206.

Yoshida, S., Sumita, I., Kumazawa, M., 1996. Growth model of the inner core coupled with outer core dynamics and the resultant elastic anisotropy. J. Geophys. Res. 101, 28085–28103.

Zhang, J., Guyot, F., 1999. Thermal equation of state of iron and $Fe_{0.91}Si_{0.09}$. Phys. Chem. Miner. 26, 206–211.

Zhu, Z.S., Gu, J.L., Liu, R.Y., Chen, N.P., Yan, M.G., 2000. Variant selection and its effect on phase transformation textures in cold rolled titanium sheet. Mater. Sci. Eng. A 280, 199–203.

Phys Chem Minerals (2006) 33: 84–97
DOI 10.1007/s00269-005-0054-x

ORIGINAL PAPER

Caterina E. Tommaseo · Jim Devine
Sébastien Merkel · Sergio Speziale · Hans-Rudolf Wenk

Texture development and elastic stresses in magnesiowűstite at high pressure

Received: 27 June 2005 / Accepted: 25 November 2005 / Published online: 17 January 2006

Abstract Cubic magnesiowűstite has been deformed in a diamond anvil cell at room temperature. We present results for $(Mg_{0.4}Fe_{0.6})O$, $(Mg_{0.25}Fe_{0.75})O$, and $(Mg_{0.1}Fe_{0.9})O$ up to 37, 16, and 18 GPa, respectively. The diffraction images, obtained with the radial diffraction technique, are analyzed using both single peak intensities and a Rietveld method. For all samples, we observe a [100] fiber texture but the texture strength decreases with increasing iron content. This texture pattern is consistent with {110}⟨1-10⟩ slip. The images were also analyzed for stress, elastic strains, and elastic anisotropy. In general, the stress measured in magnesiowűstite samples is lower than previously measured on MgO. The elastic anisotropy deduced from the X-ray measurements shows a broad agreement with models based on measurements with other techniques.

Keywords (Mg,Fe)O · Texture · DAC · Synchrotron X-rays · Deformation mechanisms · Magnesiowűstite · Elasticity

Introduction

Magnesiowűstite [(Mg,Fe)O] is a major component of the lower mantle and its deformation behavior is important for understanding the rheology of the deep earth. The amount of Fe present in (Mg,Fe)O in the lower mantle has been estimated to be 10–45 mol% FeO, based on high *P*–*T* element partitioning experiments (e.g. Mao et al. 1997; Andrault 2001 and references therein). Both wűstite, which has a nonstoichiometric formula $Fe_{1-x}O$ (e.g. McCammon 1993), and periclase (MgO) have a NaCl (B1) structure at ambient conditions. Intermediate and iron-rich compositions of magnesiowűstite show a phase transition to a rhombohedral phase at high pressure (Yagi et al. 1985; Richet et al. 1989; Kondo et al. 2004; Lin et al. 2003). There is also a pressure-induced electronic spin transitions of iron in (Mg,Fe)O at high pressure (Sherman 1988, 1991; Sherman and Jansen 1995; Cohen et al. 1997; Badro et al. 2003; Lin et al. 2005; Speziale et al. 2005), and a possible dissociation of intermediate compositions into magnesium-rich and iron-rich components (Dubrovinsky et al. 2000, 2001, 2005). Magnesiowűstite is of central importance for geodynamics due to two unique properties. Firstly, its creep strength is likely to be considerably smaller than that of $(Mg,Fe)SiO_3$ perovskite (Yamazaki and Karato 2001) and recent simulations suggest that perovskite will control the strength of the lower mantle while (Mg,Fe)O may accommodate most of the strain (Madi et al. 2005). Secondly, despite its cubic crystal structure, (Mg,Fe)O is likely to have large elastic anisotropy: according to first principles calculations, elastic anisotropy in (Mg,Fe)O is similar to that of orthorhombic $(Mg,Fe)SiO_3$ perovskite at lower mantle conditions (Karki et al. 1997; Wentzcovitch et al. 1998). Consequently, magnesiowűstite may contribute significantly to the development of seismic anisotropy (e.g. Karato 1998a, b).

Several studies have focused on texture development in periclase and magnesiowűstite. Merkel et al. (2002) deformed MgO at room temperature and high pressure. Yamazaki and Karato (2002), Stretton et al. (2001), and Heidelbach et al. (2003) deformed magnesiowűstite at moderate pressure and high temperature in torsion as well as axial compression. The results indicate that at low temperature {110}⟨1–10⟩ is the only significantly active slip system, whereas at higher temperature {100} and {111} slips become equally active. In this report we investigate texture development in magnesiowűstite with compositions $(Mg_{0.4}Fe_{0.6})O$, $(Mg_{0.25}Fe_{0.75})O$, and

C. E. Tommaseo (✉) · S. Merkel · S. Speziale · H.-R. Wenk
Department of Earth and Planetary Science,
University of California, 307 McCone Hall,
Berkeley, CA , 94720 USA
E-mail: tommaseo@eps.berkeley.edu
Tel.: +1-510-6427431
Fax: +1-510-6439980

J. Devine
University of Chicago, Geophysical Science,
Chicago, IL, 60637 USA

$(Mg_{0.1}Fe_{0.9})O$ in axial compression at high pressure and room temperature, measured in situ by synchrotron X-ray diffraction and a diamond anvil cell (DAC), with the goal to study the influence of iron content on texture development and elastic properties.

Experimental details

The starting materials were synthetic polycrystalline $(Mg_{0.4}Fe_{0.6})O$, $(Mg_{0.25}Fe_{0.75})O$, and $(Mg_{0.1}Fe_{0.9})O$ that belong to the collection of magnesiowűstites synthesized and investigated by Bonczar and Graham (1982). They were prepared by reacting finely ground and well-mixed powders of oxides and iron in the appropriate proportions. To induce reaction, the palletized mixtures were sintered at 1,000°C for several hours in iron crucibles within an evacuated silica tube. Samples were then ground and the conversion to the B1 phase checked by X-ray diffraction. The chemical composition of the samples was determined using electron microprobe and wet chemical analyses. Before the present experiments, each sample was further ground in an corund mortar and loaded as a powder in the DAC. The grain size of the starting material, estimated in a stereomicroscope (Stemi SV11) with a zoom range 11:1 with a built in scale, was in the submicron range.

We performed X-ray diffraction experiments at the 16-IDB beamline of HPCAT at APS (Advanced Photon Source, Argonne National Laboratory) and at beamline 12.2.2. at ALS (Advanced Light Source, Lawrence Berkeley National Laboratory). For the experiments at HPCAT a monochromatic X-ray beam ($\lambda = 0.42275$ Å), approximately 15–17 μm in diameter, was focused on the sample either through a beryllium gasket for $(Mg_{0.25}Fe_{0.75})O$ or amorphous boron and epoxy gasket for $(Mg_{0.4}Fe_{0.6})O$. Exposure time was 30 s for $(Mg_{0.25}Fe_{0.75})O$ and 1 s for $(Mg_{0.4}Fe_{0.6})O$. $(Mg_{0.1}Fe_{0.9})O$ samples were studied at beamline 12.2.2 at ALS using monochromatic X-ray beam ($\lambda = 0.4133$ Å for the first run and $\lambda = 0.49593$ Å for the second run). In this case, the 70 μm diameter beam was focused on the sample through a composite gasket made of an amorphous boron/epoxy disk confined within a kapton supporting ring (Merkel and Yagi 2005) with an exposure time of 240 s per image. Simple geometrical calculations indicate that for a beam of 15 and 70 μm diameter, the irradiated volume is on the order of 2.5×10^4 and 10^5 μm^3, respectively. Therefore, each diffraction image includes a contribution from thousands of grains and is appropriate for texture refinement.

In all experiments X-ray diffraction was measured in radial geometry with the DAC compression axis perpendicular to the incident beam. Diffraction images were recorded with a MAR345 image-plate system (3,450×3,450 pixels). On those images, the intensity variations along Debye rings are indicative of preferred orientation while variations in diffraction angles are related to stress and elasticity (Fig. 1a, b). For the measurements performed at the APS the detector to sample distance, calibrated using a Si standard, was 36.12 cm, thus optimizing the range of diffraction rings recorded for the opening cone of a standard symmetric piston-cylinder DAC to $2\Theta_{max} = 18°$. In the experiments performed at beamline 12.2.2 at ALS, the sample to detector distance, calibrated using a LaB_6 standard, was 29.69 cm, thus optimizing the range of diffractions recorded for the opening cone of a large-opening Mao-Bell type DAC to $2\Theta_{max} = 26°$. In all cases, hydrostatic pressures were estimated from the lattice parameter of a gold standard using the equation of state of gold (Anderson et al. 1989; Duffy et al. 1999). The uncertainty of the estimated pressures is ±3 GPa in average due to uncertainties in the equations of state of gold and nonhydrostatic stress conditions.

Data analysis

Rietveld analysis with MAUD

The X-ray diffraction images were analyzed with the Rietveld method using the software MAUD (Lutterotti et al. 1999; Lonardelli et al. 2005). This software refines instrumental, structural, microstructural parameters and texture from continuous diffraction spectra. Spectra were obtained by integrating the images over 5° azimuthal angular slices resulting in 72 spectra per image. In some of the experiments a few spectra had to be removed due to a saturation of the image because of a few large grains. Figure 2a, b shows representative spectra at different angles relative to the compression direction for $(Mg_{0.4}Fe_{0.6})O$ and $(Mg_{0.1}Fe_{0.9})O$ at 13 GPa.

For $(Mg_{0.4}Fe_{0.6})O$ and $(Mg_{0.25}Fe_{0.75})O$ we applied the Rietveld refinement method to all the azimuthal diffraction profiles with *d*-spacings ranging from 1.4 to 2.78 Å which included 111, 200, and 220 (Fig. 2a). Diffraction profiles of $(Mg_{0.1}Fe_{0.9})O$ were refined over a *d*-spacing range from 0.92 to 2.78 Å (which includes six diffraction lines, 400, 222, 311, 220, 200, 111) (Fig. 2b). Instrument parameters (detector distance, beam center, peak profile, and detector tilt) were refined on the calibrant patterns. For each image, we then refined four background parameters per orientation, crystallographic parameters, stress, and texture with a composite sample of (Mg,Fe)O and gold. Stress was assumed to be triaxial with $2\sigma_{11} = 2\sigma_{22} = -\sigma_{33}$ (axial symmetry) and refined using a simple isotropic model based on Young's modulus and Poisson ratio.

In absence of experimental or theoretical data regarding the single-crystal elasticity of magnesiowűstite at high pressure we estimated the aggregate bulk and shear moduli of our sample using third order Eulerian strain equations (Davies 1974) based on the ambient pressure bulk and shear moduli of Jacobsen et al. (2002) and the pressure derivatives of Bonczar and Graham (1982). Once a satisfying fit between the calculated and measured *d*-spacings was achieved, we applied the tex-

86

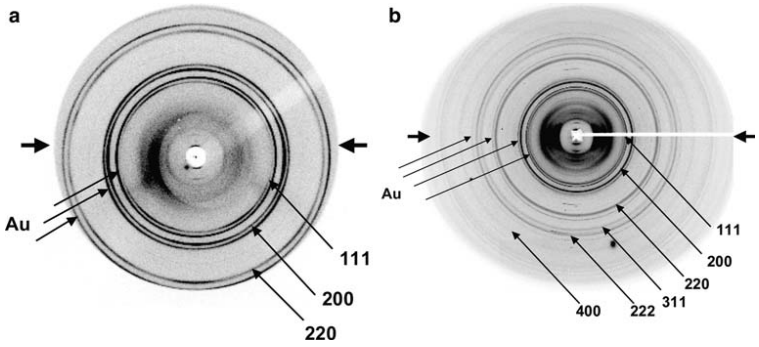

Fig. 1 Representative diffraction patterns of magnesiowüstite, $(Mg_{0.4}Fe_{0.6})O$ (**a**) and $(Mg_{0.1}Fe_{0.9})O$ (**b**), both recorded at 13 GPa

ture model EWIMV that relies on the discrete tomographic method WIMV (Matthies and Vinel 1982) to deduce the orientation distribution function (ODF) of the sample. The main difference between EWIMV and WIMV is that in EWIMV the ODF cell path for each data point is computed explicitly for the true measurement angles, no longer requiring a regular grid coverage and interpolation. In this process, we chose a resolution of 10° and a projection tube radius of 20°. First, no sample symmetry was imposed. Under this approximation, we were able to obtain qualitatively reasonable pole figures from a single image (e.g. Ischia et al. 2005) indicating overall axial symmetry with some deviations that can be attributed to the minimal pole figure coverage. Figure 3a presents the 100 pole figure obtained in such refinement for $(Mg_{0.4}Fe_{0.6})O$ at 13 GPa. In a second cycle of refinements, cylindrical symmetry was imposed and Fig. 3b presents the symmetrical 100 pole figure obtained for the same conditions as Fig. 3a. After confirming axial symmetry we assumed it for all results presented in this paper.

At the end of the Rietveld refinement in MAUD the ODFs were exported and further smoothed in BEARTEX (Wenk et al. 1998) with a 11° Gauss filter to reduce stochastic effects. From this smoothed ODF we calculated inverse pole figures that represent the probability of finding crystal directions parallel to the compression direction. Densities are expressed in multiples of a random distribution (m.r.d.). For axially symmetric texture, inverse pole figures provide a complete texture description. The texture is also represented by some numerical parameters such as minimum and maximum of the ODF and the texture index $F2$ (Bunge 1982). The texture index is the integral over squared ODF values and thus it is a measure for the texture strength. Since all textures display a main concentration near 001 we also calculated how much grains with the compression direction parallel to 001 contribute to the overall texture. This was done by calculating the orientation volume of a sphere centered at Euler angles $\alpha = 0°$, $\beta = 0°$, $\gamma = 0°$ (Matthies convention) with a radius of 20° (program COMP in BEARTEX).

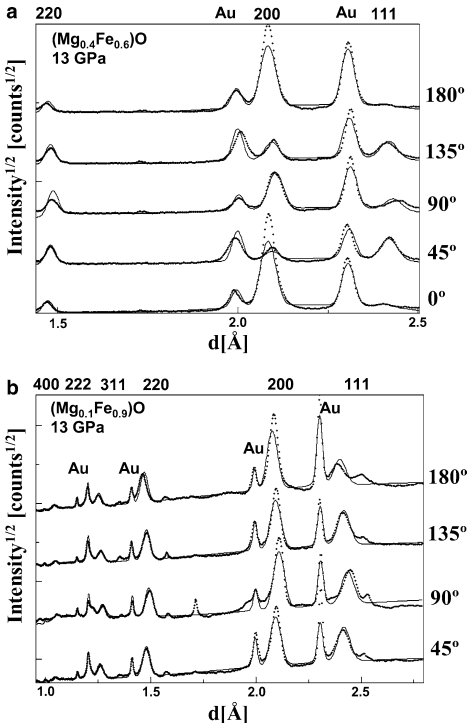

Fig. 2 Selected diffraction profiles for $(Mg_{0.4}Fe_{0.6})O$ (**a**) and $(Mg_{0.1}Fe_{0.9})O$ (**b**) at 13 GPa. *Dotted lines* are experimental data, *solid lines* are results from full profile refinement with the Rietveld technique. The profiles at 0° and 180° are in the compression direction and the profiles at 90° are in the extension direction. The 0° spectrum in **b** is not shown as it corresponds to the position of the beam-stop. Note the variations in peak positions and peak intensities with orientation, which are related to deviatoric stress and texture. A broadening of the peaks is observed. Diffraction lines of the sample are labeled in the figure. The diffraction peaks of the Au pressure standard are also indicated

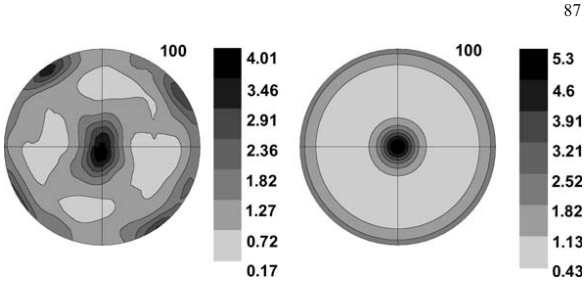

Fig. 3 (100) pole figures of $(Mg_{0.4}Fe_{0.6})O$ smoothed with 11° Gauss filter without imposing symmetry (**a**) and with imposed cylindrical symmetry (**b**) at 13 GPa. Equal area projection. Four-fold symmetry in **a** is an artifact resulting from the pole figure coverage

Texture analysis with the single peak method

One of the major difficulties encountered in the refinement of the X-ray diffraction data of magnesiowűstite is the presence of a large elastic strain anisotropy for different crystallographic directions. This reflects a strong directional dispersion of the Young's modulus *E(hkl)*. Based on data at ambient conditions (Jackson and Khanna 1990; Sinogeikin and Bass 2000; Jacobsen et al. 2002), the variation of Young's modulus between [100] and [111] ranges between 6 and 20% in the range of compositions investigated in this study. Because of this, texture analysis with the Rietveld method that uses an isotropic stress model was limited and we also applied a different approach based on single peak fit to extract texture and stress information.

In this second approach, we analyzed the variations in the position of the diffraction peaks and their intensity with the azimuthal angle δ by integrating intensities in 5° slices with the software FIT2D (Hammersley 1998). For each image, this produces 72 segments for δ between 0° and 360°. The patterns were then fitted individually assuming Gaussian peak profiles and a linear local background. The pole distance χ, which corresponds to the angle between the diffracting plane normal and the load axis, was calculated from

$$\cos\chi = \cos\theta\cos\delta, \tag{1}$$

where θ is the diffraction angle [see Fig. 3 in Merkel et al. (2002)].

Using this alternative approach each peak was fitted individually, and the diffraction intensities for each peak at all orientations could be satisfactorily reproduced. The extracted variations of diffraction intensity with orientation for (200), (220), and (111) were then used to calculate the ODF of the sample, assuming axial symmetry, with the WIMV algorithm of the BEARTEX package. Figure 4a–d presents a comparison for reflection (200) between the experimental intensities (circles and dots), those recalculated from the ODF fitted in the Rietveld package MAUD (dashed lines), and those recalculated from the ODF fitted in BEARTEX (solid lines). Overall, only small differences are observed.

Lattice strain analysis

The X-ray diffraction data were then analyzed to determine strain and stress using the procedure outlined in Singh et al. (1998) and briefly summarized here. Following the convention used in elasticity theory of single crystals (e.g. Nye 1960), the stress state at the center of the specimen is given by

$$\sigma_{ij} = \begin{pmatrix} \sigma_1 & 0 & 0 \\ 0 & \sigma_1 & 0 \\ 0 & 0 & \sigma_3 \end{pmatrix} = \begin{pmatrix} \sigma_P & 0 & 0 \\ 0 & \sigma_P & 0 \\ 0 & 0 & \sigma_P \end{pmatrix} + \begin{pmatrix} -t/3 & 0 & 0 \\ 0 & -t/3 & 0 \\ 0 & 0 & 2t/3 \end{pmatrix}, \tag{2}$$

where $(\sigma_3 - \sigma_1) \equiv t$. t is a measure of the deviatoric stress and is defined as uniaxial stress component (USC) following the nomenclature of Singh and Kennedy (1974) and Singh and Balasingh (1977). σ_P is the equivalent hydrostatic pressure.

The *d*-spacings for a given set of lattice planes measured by X-ray diffraction vary as a function of the angle χ between the compression direction and the diffracting plane normal according to the relation:

$$d_m(hkl) = d_P(hkl)[1 + (1 - 3\cos^2\chi)Q(hkl)], \tag{3}$$

where $d_m(hkl)$ is the measured *d*-spacing and $d_P(hkl)$ the *d*-spacing under the equivalent hydrostatic pressure σ_P and

$$Q(hkl) = \frac{t}{3}\left[\frac{\alpha}{2G_R(hkl)} + \frac{1-\alpha}{2G_V}\right], \tag{4}$$

where $G_R(hkl)$ and G_V are bounds to the shear modulus of the aggregate under the Reuss (iso-stress) and Voigt (iso-strain) approximations, respectively (Singh et al. 1998). The factor α which lies between 0 and 1 determines the relative weight of isostress (Reuss) and isostrain (Voigt) conditions. It specifies the degree of stress and strain continuity across grains in the sample.

For a cubic material, we have

$$(2G_V)^{-1} = \frac{5}{2}\frac{(S_{11} - S_{22})S_{44}}{[3(S_{11} - S_{12}) + S_{44}]} \tag{5}$$

88

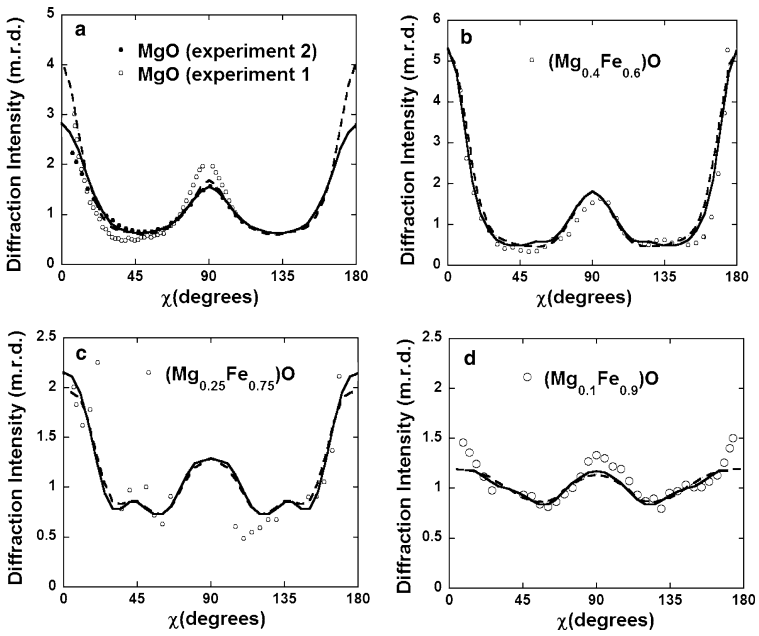

Fig. 4 Variation of the diffraction intensities with χ for **a** pure MgO, **b** $(Mg_{0.4}Fe_{0.6})O$, **c** $(Mg_{0.25}Fe_{0.75})O$, and **d** $(Mg_{0.1}Fe_{0.9})O$ at about 13 GPa. *Open* (1. experiment) and *full circles* (2. experiment) are experimental data and *solid and dashed lines* are recalculated from the ODF fitted to the experimental intensities with WIMV as implemented in BEARTEX (*solid lines*) and ODF fitted with MAUD using the EWIMV algorithm (*dashed lines*), respectively

and

$$[2G_R(hkl)]^{-1} = S_{11} - S_{12} - 3S\Gamma(hkl), \quad (6)$$

where $S = (S_{11} - S_{12} - S_{44})/2$ is a measure of elastic anisotropy, and where the S_{ij} are the single crystal elastic compliances. The orientation factor $\Gamma(hkl) = \left(\frac{h^2k^2+k^2l^2+l^2h^2}{(h^2+k^2+l^2)^2}\right)$ ranges from 0 for the 200 line to a maximum of 1/3 for 111.

The axial stress, which represents a proxy for the material's strength (e.g. Singh et al. 1998; Kavner 2003) can be estimated from experimental results using the relation:

$$t = \sigma_3 - \sigma_1 \approx 6G < Q(hkl) >, \quad (7)$$

where G is Hill's average of the Voigt and Reuss bounds to the shear modulus of the aggregate, and $\langle Q(hkl)\rangle$ is the average of the $\langle Q(hkl)\rangle$ deduced from the experimental data for the different diffraction lines (Singh et al. 1998).

The variations of the experimental d-spacings of the (111), (200), and (220) planes with χ upon compression and decompression were least-square fitted to Eq. 3 (Fig. 5a–c) in order to deduce $d_P(hkl)$ and $Q(hkl)$. In each case we allowed the maximum stress direction to be slightly shifted from $\delta = 0°$ by introducing an offset in Eq. 3 as it could be observed in the experimental data that the d-spacings minima and maxima were not always perfectly aligned at 0° and 90°. This offset (on the order of 5–10°) could only be observed for lattice strains measurements and is not observed in the sample texture (i.e. diffraction intensities). $Q(hkl)$ values were then plotted as a function of Γ and fitted to Eq. 4, which is linear in Γ for the cubic case (Fig. 6). $\langle Q(hkl)\rangle$, which represents an estimation of the strength of the sample normalized to the shear modulus ($\langle Q(hkl)\rangle = t/6G$, from Eq. 7) was calculated from the linear regression. Finally, the fitted slope (m_1) and the ordinate axis value (m_0) was used to calculate elastic anisotropy (A) (Fig. 6).

$$A = \left(\frac{2C_{44}}{C_{11} - C_{12}}\right) = \frac{3m_0}{3m_0 + m_1} \quad (8)$$

where the C_{ij} are the single crystal elastic moduli of the material.

Results

Rietveld analysis with MAUD

Lattice parameters of $(Mg_{0.40}Fe_{0.60})O$, $(Mg_{0.25}Fe_{0.75})O$, and $(Mg_{0.10}Fe_{0.90})O$ were refined for each pressure and composition (Table 1). We have fixed the uncertainty on the refined unit cell parameters to an average value of ± 0.005 Å, consistent with the precision of peak position determination in our X-ray diffraction experiments [$\sigma(d_{hkl}) \sim 10^{-4}$ at beamline 12.2.2 of the Advanced Light Source]. The estimated standard deviations on the unit cell parameter calculated in the Rietveld refinement appear largely underestimated because of the many

89

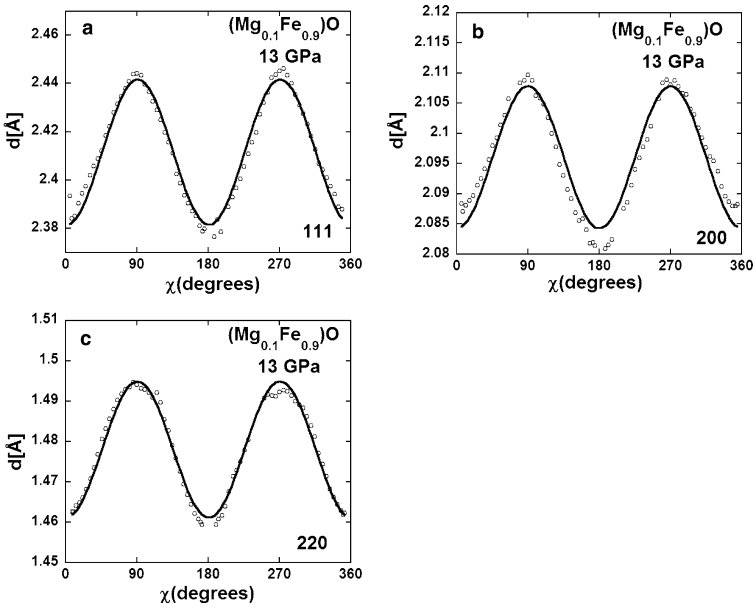

Fig. 5 $d_m(111)$ (**a**), $d_m(200)$ (**b**), and $d_m(220)$ (**c**) versus χ for $(Mg_{0.1}Fe_{0.9})O$ at 13 GPa. *Circles* are experimental data and *solid lines* are fits of lattice strain equations

assumptions involved in this whole spectrum fit procedure. The pressure dependence (V/V_0) that we determined for $(Mg_{0.40}Fe_{0.60})O$, $(Mg_{0.25}Fe_{0.75})O$, and $(Mg_{0.10}Fe_{0.90})O$ is in agreement, within estimated uncertainties, with the existing 300 K isothermal equation of state for similar compositions (Jacobsen et al. 2002; Mao et al. 2002) (Fig. 7a–c).

The principal components of the deviatoric stress tensor (σ_{11}, σ_{22}, σ_{33}) were evaluated using a simple triaxial stress model as part of MAUD refinement procedure, based on estimated bulk and shear moduli (see "Data analysis"). To account for the typical geometry of stress in the DAC, σ_{33} was refined with $\sigma_{22}=\sigma_{11}$ and $\sigma_{11}+\sigma_{22}+\sigma_{33}=0$. The maximum principal component

Table 1 Unit cell parameters of $(Mg_{0.4}Fe_{0.6})O$, $(Mg_{0.25}Fe_{0.75})O$, $(Mg_{0.1}Fe_{0.9})O$ (run 1) $(Mg_{0.4}Fe_{0.6})O$ (run 2). Principal stresses components obtained from the MAUD refinements

	a_{MW} [Å] (± 0.005)	V/V_0	σ_{33} (GPa)	Gold a (Å)	P (GPa)
Sample $(Mg_{0.4}Fe_{0.6})O$					
4060_2_004	4.243	0.980	−0.5	4.048	4
4060_2_005	4.215	0.961	−1.5	4.018	9
4060_2_006	4.197	0.948	−1.7	4.002	11
4060_2_009	4.175	0.934	−1.3	3.974	16
4060_2_011	4.144	0.913	−2.5	3.948	22
4060_2_013	4.116	0.895	−2.9	3.925	27
4060_2_015	4.099	0.883	−2.6	3.912	30
4060_2_016	4.086	0.875	−2.6	3.901	33
4060_2_018	4.075	0.868	−3.0	3.884	37
Sample $(Mg_{0.25}Fe_{0.75})O$					
2575_003	4.265	0.988	−0.1	4.067	2
2575_017	4.243	0.973	−0.7	4.048	4
2575_019	4.230	0.964	−1	4.038	6
2575_027	4.188	0.935	−1.3	4.011	10
2575_028	4.162	0.918	−1.4	3.978	16
Sample $(Mg_{0.1}Fe_{0.9})O$					
1090_005	4.258	0.974	−1	4.047	4
1090_006	4.197	0.933	−1.4	3.994	13
1090_007	4.167	0.913	−1.8	3.968	18
Sample $(Mg_{0.1}Fe_{0.9})O$					
1090_2_006	4.262	0.977	−1.1		4
1090_2_008	4.191	0.929	−1.6		12

90

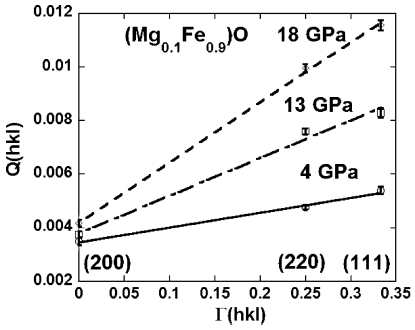

Fig. 6 Q(hkl) versus Γ(hkl) for $(Mg_{0.1}Fe_{0.9})O$ at 4, 13, and 18 GPa

of the deviatoric stress tensor (σ_{33}) obtained from the refinements tends to increase and later saturate with increasing pressure and range from 0 to 3 GPa (Tables 1).

Our texture analysis with the Rietveld approach shows that $(Mg_{0.4}Fe_{0.6})O$, $(Mg_{0.25}Fe_{0.75})O$, and $(Mg_{0.1}Fe_{0.9})O$ deformed in compression in the DAC mainly have a [100] texture as displayed in inverse pole figures (Fig. 8). Table 2 presents the minima and maxima of all ODFs calculated in this study. The texture strength $F2$ ranges between 1.7 and 2.3 for $(Mg_{0.4}Fe_{0.6})O$, 1.1 and 1.3 for $(Mg_{0.25}Fe_{0.75})O$, and 1.0 and 1.02 for $(Mg_{0.1}Fe_{0.9})O$. The texture index of MgO determined by Merkel et al. (2002) in a comparable pressure range (0–35 GPa) ranges between 1 and 2.7 in two different experiments.

The volume fraction of the main texture component at [100] (as defined in "Experimental details") for all the samples and all pressures is reported in Table 2 and plotted as a function of pressure in Fig. 9. Its pressure and compositional dependencies are in good agreement with those observed for both $F2$ index and ODF maximum values. The combination of these results shows that the texture strength of magnesiowűstites (a) increases and later saturates with increasing pressure, and (b) weakens with increasing Fe content. One of the experiments (experiment 2) performed on MgO by Merkel et al. (2002) shows a weaker pressure dependence of texture strength. One possible reason of this behavior could be found in the sample arrangement used in this second experiment (MgO was loaded as thermal insulator and pressure transmitting medium around Fe).

Texture analysis performed independently by individual fit of peaks confirms that the main texture of magnesiowűstites is at [100]. Figure 4a–d presents the intensities of diffraction peak 200 of MgO, $(Mg_{0.4}Fe_{0.6})O$, $(Mg_{0.25}Fe_{0.75})O$, and $(Mg_{0.1}Fe_{0.9})O$ as a function of the angle χ at comparable pressures. The overall variation of amplitude of the diffraction intensities with χ decreases with increasing iron content, such that $(Mg_{0.1}Fe_{0.9})O$ shows a nearly random distribution. The inverse pole figures obtained with the whole spectrum fit approach (Rietveld method) (Fig. 8a.1, b.1)

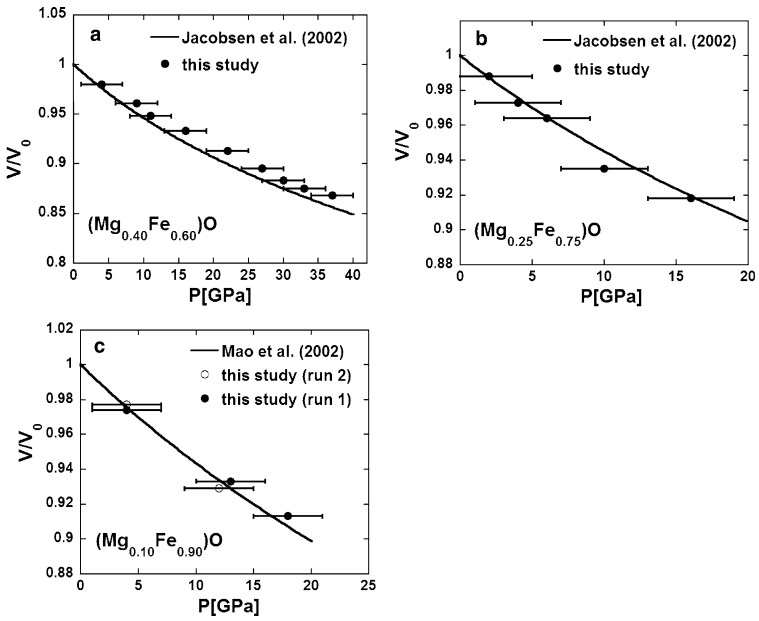

Fig. 7 V/V_0 versus pressure for $(Mg_{0.4}Fe_{0.6})O$ (**a**), $(Mg_{0.25}Fe_{0.75})O$ (**b**) and $(Mg_{0.1}Fe_{0.9})O$ (**c**)

Table 2 Texture index *F*2, minima and maxima of the ODF, and principal pole figures 100 with imposing cylindrical symmetry. $(Mg_{0.4}Fe_{0.6})O$, $(Mg_{0.25}Fe_{0.75})O$, $(Mg_{0.1}Fe_{0.9})O$ (run 1), and $(Mg_{0.1}Fe_{0.9})O$ (run 2)

	ODF[a] (m.r.d.)		ODF[b] (m.r.d.)		*F*2	Vol% component
	Min	Max	Min	Max		
Sample $(Mg_{0.4}Fe_{0.6})O$						
4060_2_004	0.35	4.25				7.76
4060_2_005	0.41	4.32	0.39	3.96	1.44	11.18
4060_2_006	0.32	3.08	0.79	1.23	1.47	11.65
4060_2_009	0.37	5.23	0.30	6.03	1.96	15.30
4060_2_011	0.04	7.82	0.41	5.21	1.91	14.93
4060_2_013	0.26	5.82	0.38	5.05	1.89	15.05
4060_2_015	0.23	5.73	0.43	5.44	1.89	14.36
4060_2_016	0.31	5.27	0.35	6.16	2.00	15.92
4060_2_018	0.20	6.89	0.44	5.87	2.07	16.40
Sample $(Mg_{0.25}Fe_{0.75})O$						
2575_003	0.53	2.06	0.47	1.73	1.04	5.19
2575_017	0.36	1.99	0.43	2.25	1.16	8.18
2575_019	0.33	2.30	0.38	2.24	1.15	8.32
2575_027	0.36	2.15	0.40	2.17	1.18	7.70
2575_028	0.62	1.79	0.33	1.60	1.13	5.99
Sample $(Mg_{0.1}Fe_{0.9})O$						
1090_005	0.83	1.13	0.90	1.13	1.00	1.42
1090_006	0.82	1.14	0.79	1.23	1.01	2.12
1090_007	0.83	1.13	0.63	1.17	1.02	2.91
Sample $(Mg_{0.1}Fe_{0.9})O$						
1090_2_006	0.75	1.14	0.92	1.09	1.00	0.82
1090_2_008	0.48	1.35	0.59	1.21	1.02	3.27

[a]Minima and maxima of the ODF recalculated with WIMV as implemented in BEARTEX from the single peak fits
[b]Minima and maxima of the ODF recalculated from MAUD using the EWIMV algorithms. The ODF were smoothed using a Gaussian filter of width of 1-1°. The radius of the texture components were set to 20°

confirm the results obtained in the inverse pole figures recalculated from the individual peak fits are shown in Fig. 8a.2, b.2.

Elastic anisotropy and stress

The axial stress component in the sample can be calculated from the variations of the *d*-spacings with orientation in the diffraction pattern. In the present analysis, we calculated the average axial stress component $\langle t \rangle$, defined as $6G\langle Q(hkl)\rangle$, where G is the average shear modulus of the aggregate under the Hill approximation. In order to assess effects of plastic deformation, we also evaluated individual stress components using Eq. 4 and the Reuss approximation for (200), (111), and (222) when data for (111) was not available.

The value of $\langle Q(hkl)\rangle$ increases with pressure from 0.03 to 0.06 in $(Mg_{0.40}Fe_{0.60})O$, 0.02–0.05 in $(Mg_{0.25}Fe_{0.75})O$, 0.03–0.06 in $(Mg_{0.10}Fe_{090})O$ (run 1), and 0.03–0.05 in $(Mg_{0.10}Fe_{0.90})O$ (run 2). In general, we find that stress ($6G\langle Q(hkl)\rangle$) increases and later saturates with increasing pressure. It is higher for the MgO samples measured by Merkel et al. (2002) than for the present magnesiowűstite samples (Fig. 10a; Table 3). For MgO, stresses measured on (222) tend to be larger than stresses on (200). For other compositions, stresses measured on (200) tend to be larger than those measured on (111).

The elastic anisotropy factor A for $(Mg_{0.40}Fe_{0.60})O$, $(Mg_{0.25}Fe_{0.75})O$, and $(Mg_{0.10}Fe_{0.90})O$ decreases with increasing pressure and increasing iron content (Fig. 10b; Table 3). A is the ratio of the shear moduli in the (100) and (110) planes in the [100] direction. If $A = 1$ the material is elastically isotropic. We find a change of sign of the anisotropy factor of magnesiowűstite at a pressure that depends on composition, leading to an interchange in the direction of fastest and slowest compression and shear wave propagation. For instance, at low pressure, compression waves travel faster along $\langle 111\rangle$, at high pressure $\langle 100\rangle$ is the fastest direction. The pressure of reversal obtained from the radial diffraction data is in reasonable agreement with simple models based on third order Eulerian strain equations (Davies 1974) using the ambient pressure elastic moduli of Jacobsen et al. (2002) and the pressure derivatives of Bonczar and Graham (1982) (Fig. 10b).

Discussion

Lattice preferred orientation

For all examined compositions, our experiments document the development of a main texture component at [100] with increasing pressure. The [100] texture is due to $\{110\}\langle 1\text{–}10\rangle$ slip as explored previously (Wenk et al. 1989; Merkel et al. 2002). If $\{110\}\langle 1\text{–}10\rangle$, $\{111\}\langle 1\text{–}10\rangle$, and $\{100\}\langle 011\rangle$ slip systems were all active simultaneously, the maximum in the inverse pole figure would be a girdle between [110] and [100]. Textures we obtain in $(Mg_{0.1}Fe_{0.9})O$ are particularly weak and sometimes show other maxima than [100]. However, the intensity of those secondary maxima is weak and depends on the fitting method.

In order to study the influence of iron on (Mg,Fe)O we compared our results with those of pure MgO as a reference under similar experimental conditions (Merkel

92

Table 3 Values of effective stresses deduced from the X-ray data on (111) and (200), mean stress value ($\langle t\rangle = 6G\langle Q(hkl)\rangle$), and elastic anisotropy for all compositions studied here along with the MgO results of Merkel et al. (2002). For MgO, minima and maxima of the ODF were deduced from experimental ODF calculated with WIMV and smoothed using a Gaussian filter of width of 11°, as implemented in BEARTEX

P (GPa)	t(222)	t(200)	$< t >$	$A[2C_{44}/(C_{11}\text{-}C_{12})]$	ODF		$F2$
					Min	Max	
MgO (experiment 1)							
1.9	1.5	1.7	1.7	1.674	0.91	1.10	1.00
2.4	2.0	3.0	2.7	1.681	0.89	1.19	1.01
3.1	3.0	2.7	3.1	1.508	0.87	1.26	1.01
5.3	5.6	5.1	5.5	1.252	0.70	2.20	1.11
7.0	5.9	5.5	6.0	1.058	0.63	2.96	1.24
9.5	7.1	6.1	6.8	0.984	0.52	3.78	1.41
11.6	7.0	6.0	6.6	0.987	0.52	3.81	1.41
20.3	8.1	6.4	7.1	0.885	0.22	6.84	2.17
30.3	10.3	9.6	9.5	0.912	0.27	6.46	2.25
35.5	9.4	9.5	8.6	1.071	0.27	6.46	2.25
MgO (experiment 2)							
1.5	2.0	2.0	2.1	1.371			
5.1	4.8	3.8	4.3	0.991	0.71	2.00	1.09
7.5	8.6	6.0	7.5	0.910	0.61	2.15	1.14
11.0	9.8	7.0	8.5	0.869	0.53	2.76	1.26
17.4	9.5	6.8	8.0	0.870	0.52	2.78	1.26
18.3	8.7	6.9	7.7	0.931	0.48	2.57	1.24
20.2	9.0	7.2	7.8	0.960	0.40	2.34	1.21
23.0	10.5	7.3	8.6	0.844	0.53	2.58	1.24
23.9	9.1	7.6	8.3	0.836	0.46	2.80	1.27
27.0	9.6	7.9	8.4	0.852	0.40	2.74	1.26
29.8	10.6	9.5	9.7	0.895	0.47	2.81	1.27

P (GPa)	t(111)	t(200)	$\langle t\rangle$	$A[2C_{44}/(C_{11}-C_{12})]$
$(Mg_{0.4}Fe_{0.6})O$				
4	2.1	1.9	2.1	0.923
9	1.9	1.9	2.0	0.810
11	2.3	2.3	2.3	0.739
16	1.8	1.9	1.9	0.637
22	3.2	3.7	3.3	0.572
27	3.7	4.7	3.9	0.530
30	2.8	4.3	3.3	0.578
33	4.5	5.6	4.7	0.412
37	4.2	6.0	4.7	0.406
$(Mg_{0.25}Fe_{0.75})O$				
4	0.9	1.1	1.0	1.152
6	1.2	1.5	1.4	0.953
10	2.4	2.7	2.5	0.676
16	2.2	3.2	2.6	0.588
$(Mg_{0.1}Fe_{0.9})O$ (run 1)				
4	1.6	1.4	1.5	0.651
13	1.9	2.1	2.0	0.449
18	2.2	2.8	2.5	0.360
$(Mg_{0.1}Fe_{0.9})O$ (run 2)				
4	1.9	1.7	1.8	0.658
12	1.3	1.9	1.5	0.410

et al. 2002). Indeed, we find that pure MgO has the same main texture component at [100] as our magnesiowűstite samples (Fig. 8). The texture strength tends to decrease with increasing iron content (Table 2; Figs. 8, 9). With increasing iron content, bonding becomes less ionic and the strength decreases. This could result in lower

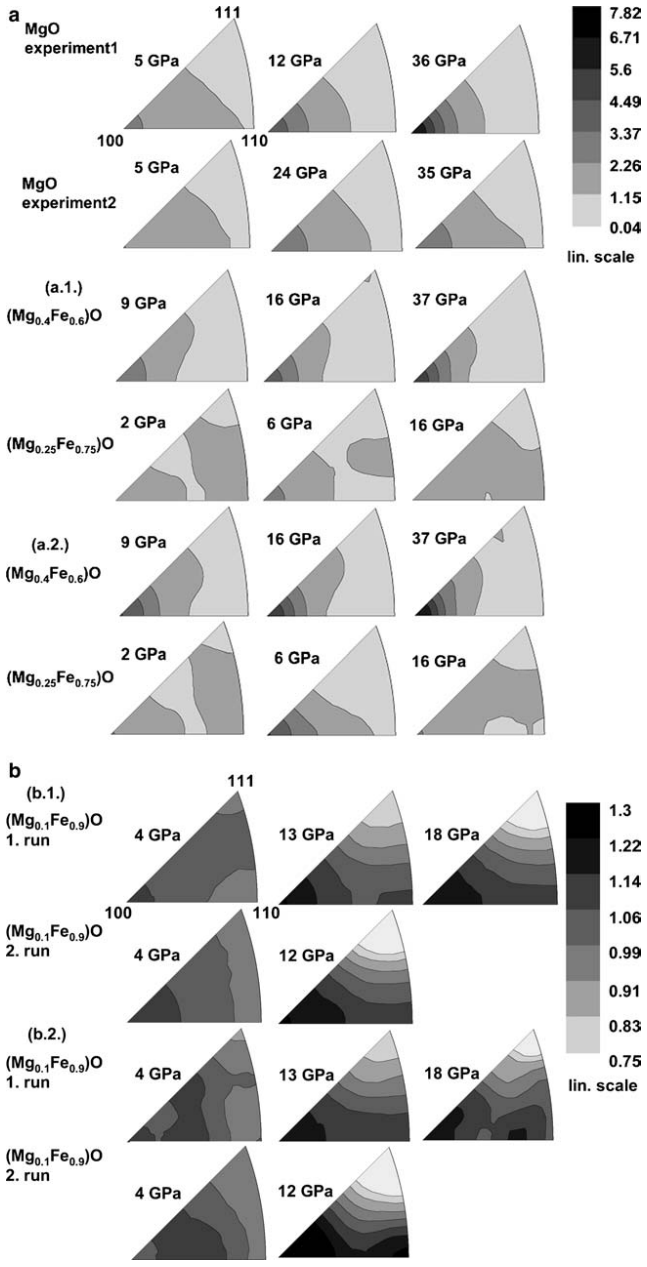

Fig. 8 Inverse pole figures for different compositions in the MgO–FeO series: **a.1** MgO (experiment 1 and 2), $(Mg_{0.4}Fe_{0.6})O$, $(Mg_{0.25}Fe_{0.75})O$ recalculated from MAUD using EWIMV algorithms. **a.2** The same as **a.1** recalculated with WIMV as implemented in BEARTEX from the single peak fits. **b.1** Inverse pole figures for $(Mg_{0.1}Fe_{0.9})O$ (runs 1 and 2) from MAUD using the EWIMV algorithms. **b.2** The same as **b.1** recalculated with WIMV as implemented in BEARTEX from the single peak fits. Because of the weaker texture, the $(Mg_{0.1}Fe_{0.9})O$ composition is presented with a different gray scale. Equal projection area

94

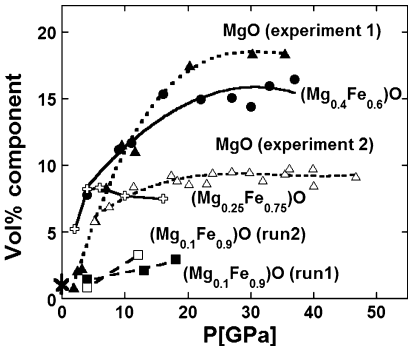

Fig. 9 100 texture component (vol%) versus pressure for different compositions in the MgO–FeO solid solution series. The radius of the spherical texture component was chosen at 20°. Data for $(Mg_{0.1}Fe_{0.9})O$ (*open and closed squares*), $(Mg_{0.25}Fe_{0.75})O$ (*crosses*), $(Mg_{0.4}Fe_{0.6})O$ (*circles*), and MgO (*open and closed triangles*) are shown in the figure. *Lines* are guide to the eye through the experimental data and the *star symbol* indicates the value that would be obtained for a random texture

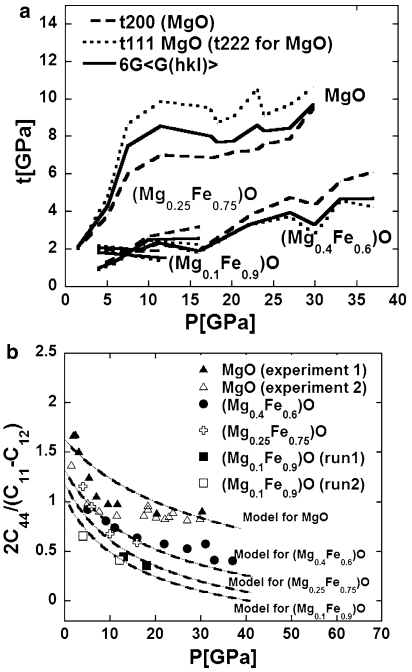

Fig. 10 **a** Mean stress ($6G\langle Q(hkl)\rangle$), and effective stresses deduced from measurements on (111) and (200) versus pressure for all samples as a function of pressure. For the measurements on MgO, effective stresses were calculated on (222) and (200) as no data for (111) was available. For clarity, measurements of MgO (experiment 1) and $(Mg_{0.1}Fe_{0.9})O$ (run 1) were not included in the figure but they do not differ significantly. **b** Elastic anisotropy in magnesiowüstite expressed with the Zener ratio $A = 2C_{44}/(C_{11} - C_{12})$ as a function of pressure. Results deduced from the X-ray data under the Reuss limit are compared with models based on data from literature (Jackson and Khanna 1990; Sinogeikin and Bass 2000; Jacobsen et al. 2002, 2004) (*dashed lines*)

stacking fault energy for the slip system {110}⟨1–10 (Miranda and Scandolo 2005). Another explanation could be that in iron-rich, more compressible, magnesiowüstites a larger portion of strain is accommodated elastically. The observed broadening of the diffraction lines in all three magnesiowüstite compositions with increasing pressure, may also be an expression of such heterogeneous elastic strain, probably because of higher dislocations densities.

$(Mg_{0.80}Fe_{0.20})O$ up to 300 MPa and 1,400 K by Stretton et al. (2001) show [100] and [110] texture in analyses using the EBSD technique. The samples at higher temperature (1,400 *K*) and larger grain size and those at lower temperature (1,200 *K*) and smaller grain size, show a stronger texture at [110], which broadens towards [100] with a minimum at [111]. The texture is only slightly stronger for the sample deformed at lower temperature (1,200 K). This suggests that temperature plays a relevant role on deformation mechanisms of magnesiowüstite, similar to isostructural halite (Carter and Heard 1970).

Heidelbach et al. (2003) studied texture evolution as a function of strain, observing a change from a dislocation creep texture at low strains to a recrystallization texture at high strains. With increasing strain the texture components in the following order become more evident: {111}⟨110⟩, {100}⟨110⟩ and finally at the highest strains the texture component {112}⟨110⟩. The overall observed texture strengths in this study are relatively low compared to the high strains. This is explained with the subgrain rotation recrystallization, weakening strong maxima due to rotation of the crystals.

Another aspect that has to be considered in order to understand the deformation behavior of magnesiowüstites is the complex defect structure associated with very high Fe contents. The less ionic bonding strength in (Mg,Fe)O and the probably existing vacancies in the (Mg,Fe)O crystal structure (Jacobsen et al. 2002) might increase the density of dislocations (Luecke and Kohlstedt 1988; Pulliam 1963; Heidelbach et al. 2003).

Finally, we cannot neglect that grain size, grain shape, grain distribution, configuration of the existing phases, deformation history, etc. in the sample can play a role in the deformation process.

Orientation of stress in the DAC

For each pressure, we could observe a slight offset in the maximum stress direction in the measured *d*-spacings. This indicates that the maximum stress applied to the sample is not always aligned with the anvil directions but

can be shifted by a few degrees. This is probably related to details of the experimental setup such as diamond alignment and sample loading. This has been also observed on other samples in DAC radial diffraction experiments (Merkel et al. 2005; S. Merkel and T. Yagi, submitted for publication). Interestingly, this offset is not observed in the measured diffraction intensities, indicating that the texture and plastic deformation of the sample is indeed axisymmetric. It should be noted that this can be problematic for whole profile Rietveld refinements in MAUD as this stress geometry cannot be readily refined.

Effect of plasticity on the deduced anisotropy

In order to better quantify the combined effects of pressure increase and Fe–Mg substitution on the elastic anisotropy in magnesiowűstites we have compared our experimental values of the anisotropy factor (A), with model anisotropies calculated from low-pressure single-crystal elasticity data (Jackson and Khanna 1990; Sinogeikin and Bass 2000; Jacobsen et al. 2002, 2004) extrapolated using Eulerian finite strain equations (Davies 1974). The model agrees reasonably well with our experimental results (Fig. 10b). These results indicate that the lattice strain theory (Singh et al. 1998) can be applied to obtain a first estimate of the anisotropies of cubic materials.

In recent years, models based on a combination of polycrystal plasticity and lattice strain theories predicted that for materials such as MgO, stresses deduced from lattice strain measurements on (111) should become over 50% greater than deduced from (200), once plastic deformation is activated (Weidner et al. 2004). This model appears to agree with the results on MgO of Merkel et al. (2002). However, it contradicts our measurements for iron-rich magnesiowűstites for which the stress measured on (200) is larger than that measured on (111) (Fig. 10a). Our experiments do indicate an (hkl)-dependence of stress but much lower than predicted by Weidner et al. (2004). It should be noted that elasto-plastic models such as those used by Weidner et al. (2004) and Li et al. (2004) depend on a number of parameters, such as the combination of active slip system and the elastic anisotropy of the material. Our results indicate that the combination of parameters used in those models was optimized to match the data measured for MgO. In particular, elastic anisotropy in magnesiowűstite changes greatly with increasing iron content and therefore the models of Weidner et al. (2004) and Li et al. (2004) may not apply directly. The evolution of elastic anisotropy with pressure and composition deduced from this study is in fairly good agreement with other techniques (Fig. 10b). This indicates that the radial diffraction data can be used to extract trends of variation of anisotropies with composition. However, as pointed out by Weidner et al. (2004) and Li et al. (2004), the absolute values obtained should be treated with caution.

Conclusion

Axial deformation experiments on $(Mg_{0.4}Fe_{0.6})O$, $(Mg_{0.25}Fe_{0.75})O$, and $(Mg_{0.1}Fe_{0.9})$ with the DAC show the development of a [100] texture. The comparison between the lattice preferred orientation in our (Mg,Fe)O samples with those observed in pure MgO, both at room temperature, suggests that the $\{1\text{–}10\}\langle 110\rangle$ is the main active slip system at these conditions. However, the weakening of texture with increasing iron content is significant.

Stress measured in our magnesiowűstite samples is significantly lower than previously measured in MgO (Merkel et al. 2002). Contrary to models based on polycrystal plasticity and lattice strain theories and applied to MgO (Weidner et al. 2004), we find that for iron-rich compositions, the effective stress measured on (111) is lower than that measured on (200). Elasto-plastic models such as the ones used in Weidner et al. (2004) and Li et al. (2004) depend on a number of parameters, such as the combination of active slip system and the elastic anisotropy of the material, and our results underline that they can only be used to interpret and analyze the experiments they were designed for.

Finally, the elastic anisotropy deduced from the X-ray diffraction data decreases with increasing pressure and iron content, in a agreement with model bases on low-pressure single-crystal elasticity data (Jackson and Khanna 1990; Sinogeikin and Bass 2000; Jacobsen et al. 2002, 2004) extrapolated using Eulerian finite strain equations (Davies 1974). This indicates that the radial diffraction data could be used to extract trends of variation of anisotropies with composition.

Acknowledgement C.E.T. thanks the DFG (TO257/3–1) for financial support. This work was supported by NSF and CDAC. We are appreciative for access to the facilities at APS and ALS. We acknowledge help by M. Kunz and L. Miyagi with the experiment and Ivan Lonardelli, Gloria Ischia, Ingwar Huensche, and Jenny Pehl with MAUD data analysis and fruitful discussions. Comments on the manuscript by reviewers were very helpful. We also thank R. Jeanloz for providing some of the samples used in the experiments.

References

Anderson OL, Isaak DG, Yamamoto S (1989) Anharmonicity and the equation of state for gold. J Appl Phys 65:1534–1543

Andrault D (2001) Evaluation of (Mg,Fe) partitioning between silicate perovskite and magnesiowűstite up to 120 GPa and 2300 K. J Geophys Res 106:2079–2087

Badro J, Fiquet G, Guyot F, Rueff JP, Struzhkin VV, Vankó G, Monaco G (2003) Iron partitioning in Earths mantle: toward a deep lower mantle discontinuity. Science 300:789–791

Bonczar LJ, Graham EK (1982) The pressure and temperature dependence of the elastic properties of polycrystal magnesiowűstite. J Geophys Res 87:1061–1078

Bunge HJ (1982) Texture analysis in materials science. Butterworths, London, 593 pp

Carter NL, Heard HC (1970) Temperature and rate-dependent deformation of halite. Am J Sci 269:193–249

Cohen RE, Mazin II, Isaak DG (1997) Magnetic collapse in transition metal oxides at high pressure: implications for the Earth. Science 275:654–657

Davies GF (1974) Effective elastic moduli under hydrostatic stress I. Quasi harmonic theory. J Phys Chem Solids 35:1513–1520

Dubrovinsky LS, Dubrovinskaia NA, Saxena SK, Annersten H, Halenius E, Harryson H, Tutti F, Rekhi S, Le Bihan T (2000) Stability of ferropericlase in the lower mantle. Science 289: 430–432

Dubrovinsky LS, Dubrovinskaia N, Annersten H, Halenius E, Harrison H (2001) Stability of $(Mg_{0.5}Fe_{0.5})O$ and $(Mg_{0.8}Fe_{0.2})O$ magnesiowűstites in the lower mantle. Eur J Mineral 13:857–861

Dubrovinsky LS, Dubrovinskaia N, Kantor I, McCammon C, Crichton W, Urusov V (2005) Decomposition of ferropericlase $(Mg_{0.80}Fe_{0.20})O$ at high pressures and temperatures. J Alloys Comp 390:41–45

Duffy TS, Shen G, Heinz DL, Shun J, Me Y, Mao HK (1999) Lattice strains in gold and rhenium under non-hydrostatic compression to 37 GPa. Phys Rev B 60:15063–15073

Hammersley AP (1998) FIT2D reference manual (European Synchrotron Radiation Facility, Grenoble, France), version 4.0

Heidelbach F, Stretton I, Langenhorst F, Mackwell S (2003) Fabric evolution during high shear–strain deformation of magnesiowűstite. J Geophys Res B 108:2154

Ischia G, Wenk HR, Lutterotti L, Berberich (2005) Quantitative Rietveld texture analysis of zirconium from single synchrotron diffraction images. J Appl Crystallogr 38:377–380

Jackson I, Khanna SK (1990) Elasticity, shear-mode softening and high-pressure polymorphism of wuestite $(Fe_{1-x}O)$. J Geophys Res 95:21671–21685

Jacobsen SD, Reichmann HJ, Spetzler HA, Mackwell SJ, Smyth JR, Angel RJ, McCammon C (2002) Structure and elasticity of single-crystal (Mg,Fe)O and a new method of generating shear waves for gigahertz ultrasonic interferometry. J Geophys Res 107(B2):1–14

Jacobsen SD, Spetzler HA, Reichmann HJ, Smyth JR (2004) Shear waves in the diamond-anvil cell reveal pressure-induced instability in (Mg,Fe)O. Proc Natl Acad Sci USA 101: 5867–5871

Karato SI (1998a) Seismic anisotropy in the deep mantle and the geometry of mantle convection. Pure Appl Geophys 151: 565–587

Karato SI (1998b) Some remarks on the origin of seismic anisotropy in D″ layer. Earth Planets Space 50:1019–1028

Karki B, Stixrude L, Clark S, Warren M, Ackland G, Crain J (1997) Elastic properties of orthorhombic $MgSiO_3$ perovskite at lower mantle pressures. Am Mineral 82:635–638

Kavner A (2003) Elasticity and strength of hydrous ringwoodite at high pressure. Earth Planet Sci Lett 214:645–654

Kondo T, Ohtani E, Hirao E, Yagi T, Kikegawa T (2004) Phase transitions of (Mg,Fe)O at megabar pressures. Phys Earth Planet Interiors 143–144:201–213

Li L, Weidner DJ, Raterron P, Chen J, Vaughan MT (2004) Stress measurements of deforming olivine at high pressure. Phys Earth Planet Interiors 143–144: 357–367

Lin JF, Heinz DL, Mao HK, Hemley RJ, Devine JM, Li J, Shen G (2003) Stability of magnesiowűstite in earth's lower mantle. Proc Natl Acad Sci 8:4405–4408

Lin JF, Struzhkin VV, Jacobsen SD, Hu MY, Chow P, Kung J, Liu H, Mao HK, Hemley RJ (2005) Spin transition of iron in magnesiowüstite in the Earths lower mantle. Nature 436: 377–380

Lonardelli I, Wenk H-R, Lutterotti L, Goodwin M (2005) Texture analysis from synchrotron diffraction images with the Rietveld method: dinosaur tendon and salmon scale. J Synchroton Radiat 12:354–360

Luecke W, Kohlstedt DJ (1988) Kinetics of the internal oxidation of (Mg,Fe)O solid solutions. J Am Ceram Soc 71:189–196

Lutterotti L, Matthies S, Wenk HR (1999) MAUD: a friendly Java program for materials analysis using diffraction. Int U Crystallogr Comm Powder Diffraction Newsletter 21:14–15

Madi K, Forest S, Cordier P, Boussuge M (2005) Numerical study of creep in two-phase aggregates with a large rheology contrast: implications for the lower mantle. Earth Planet Sci Lett 237:223–238

Mao HK, Shu J, Fei Y, Hu J, Hemley RJ (1997) Multivariable dependence of Fe–Mg partitioning in the lower mantle. Science 278:2098–2100

Mao W, Shu J, Hu J, Hemley R, Mao HK (2002) Displacive transition in magnesiowűstite. J Phys Condens Matter 14:11349–11354

Matthies S, Vinel GW (1982) On the reproduction of the orientation distribution function of textured samples from reduced pole figures using the concept of conditional ghost correction. Phys Status Solidi 112:K111–K114

McCammon CA (1993) Effect of pressure on the composition of the lower mantle end member Fe_xO. Science 259:66–68

Merkel S, Yagi T (2005) X-ray transparent gasket for diamond anvil cell high pressure experiments. Rev Sci Instrum 76:046109

Merkel S, Wenk HR, Shu J, Shen G, Gillet P, Mao HK, Hemley RJ (2002) Deformation of polycrystalline MgO at pressures of the lower mantle. J Geophys Res 107:2271

Merkel S, Shu J, Gillet P, Mao HK, Hemley RJ (2005) X-ray diffraction study of the single crystal elastic moduli of e-Fe up to 30 GPa. J Geophys Res 110:B05201

Miranda CR, Scandolo S (2005) Computational materials science meets geophysics: dislocations and slip planes of MgO. Comput Phys Commun 169:24

Nye JF (1960) Physical properties of crystals. Clarendon, Oxford, 322 pp

Pulliam GR (1963) Decorated dislocations in magnesia crystals. J Am Ceram Soc 46:202–206

Richet P, Mao HK, Bell PM (1989) Bulk moduli of magnesiowűstites from static compression measurements. J Geophys Res 94:3037–3045

Sherman DM (1988) In: Ghose S, Coey JMD, Salje E (eds) Structural and magnetic phase transitions in minerals. Springer, Berlin Heidelberg New York, pp 113–118

Sherman DM (1991) The high-pressure electronic structure of magnesiowüstite (Mg,Fe)O: applications to the physics and chemistry of the lower mantle. J Geophys Res 96:14299–14312

Sherman DM, Jansen HJF (1995) First-principles predictions of the high-pressure phase transition and electronic structure of FeO: implications for the chemistry of the lower mantle and core. Geophys Res Lett 22:1001–1004

Singh AK, Balasingh C (1977) Uniaxial stress component in diamond anvil high-pressure X-ray cameras. J Appl Phys 48:5338

Singh AK, Kennedy GC (1974) Uniaxial stress component in tungsten carbide anvil high-pressure X-ray cameras. J Appl Phys 45:4686

Singh AK, Balasingh C, Mao HK, Hemley RJ, Shu J (1998) Analysis of lattice strains measured under non-hydrostatic pressure. J Appl Phys 83:7567–7575

Sinogeikin SV, Bass JD (2000) Single-crystal elasticity of pyrope and MgO to 20 GPa by Brillouin scattering in the diamond cell. Phys Earth Planet Interiors 120:43–62

Speziale S, Milner A, Lee VE, Clark SM, Pasternak MP, Jeanloz R (2005) Iron spin transition in Earth's mantle. Proc Natl Acad Sci (in press)

Stretton I, Heidelbach F, Mackwell SJ, Langenhorst F (2001) Dislocation creep of magnesiowűstite $(Mg_{0.8}Fe_{0.2}O)$. Earth Planet Sci Lett 194:229–240

Weidner DJ, Li L, Davis M, Chen J (2004) Effect of plasticity on elastic modulus measurements. Geophys Res Lett 31:1–4

Wenk HR, Canova GR, Molinari A, Mecking HH (1989) Texture development in halite: comparison of Taylor model and self-consistent theory. Acta Metall 37:2017–2029

Wenk HR, Matthies S, Donovan J, Chateigner D (1998) BEARTEX, a Windows-based program system for quantitative texture analysis. J Appl Crystallogr 31:262–269

Wentzcovitch RM, Karki BB, Karato S, Silvera CRSD (1998) High pressure elastic anisotropy of $MgSiO_3$ and geophysical implications. Earth Planet Sci Lett 164:371–378

97

Yagi T, Suzuki T, Akimoto S (1985) Static compression of wüstite ($Fe_{0.98}O$) to 128 GPa. J Geophys Res 90:8784–8788

Yamazaki D, Karato SI (2001) Some mineral physics constraints on the rheology and geothermal structure of Earth's lower mantle. Am Mineral 86:385–391

Yamazaki D, Karato SI (2002) Fabric development in (Mg,Fe)O during large strain, shear deformation: implications for seismic anisotropy in Earth's lower mantle. Physics Earth Planet Interiors 131:251–267

INSTITUTE OF PHYSICS PUBLISHING JOURNAL OF PHYSICS: CONDENSED MATTER
J. Phys.: Condens. Matter **18** (2006) S995–S1005 doi:10.1088/0953-8984/18/25/S07

Quantitative Rietveld texture analysis of $CaSiO_3$ perovskite deformed in a diamond anvil cell

Lowell Miyagi[1], Sébastien Merkel[1], Takehiko Yagi[2], Nagayoshi Sata[3], Yasuo Ohishi[4] and Hans-Rudolf Wenk[1]

[1] Department of Earth and Planetary Science, University of California, Berkeley, CA 94720, USA
[2] Institute for Solid State Physics, University of Tokyo, Kashiwanoha 5-1-5, Kashiwa, Chiba 277-8581, Japan
[3] Institute for Research on Earth Evolution, Japan Agency for Marine-Earth Science and Technology, Natsushima-cho, Yokosuka, Kanagawa 237-0061, Japan
[4] Japan Synchrotron Radiation Research Institute, Mikazuki-cho, Sayo-gun, Hyogo 679-5198, Japan

Received 30 November 2005, in final form 25 April 2006
Published 8 June 2006
Online at stacks.iop.org/JPhysCM/18/S995

Abstract
The Rietveld method is used to extract quantitative texture information from a single synchrotron diffraction image of a $CaSiO_3$ perovskite sample deformed in axial compression in a diamond anvil cell. The image used for analysis was taken in radial geometry at 49 GPa and room temperature. We obtain a preferred orientation of {100} lattice planes oriented perpendicular to the compression direction and this is compatible with $\{110\}\langle 1\bar{1}0\rangle$ slip.

1. Introduction

Although $CaSiO_3$ perovskite is thought to be the major calcium silicate component of the lower mantle, its properties are still poorly understood. Even the structure that $CaSiO_3$ assumes at high pressures is not well defined. Experimentally, $CaSiO_3$ perovskite is generally reported to assume a cubic structure [1, 2]. Shim *et al* [3] reported a lower symmetry structure based on high resolution synchrotron data, and proposed several possible tetragonal structures. Theoretical calculations have predicted small symmetry lowering distortions of the cubic structure which yield tetragonal or even orthorhombic symmetries [4, 5]. Caracas *et al* [6] predict a multitude of structural instabilities with minor distortions of the cubic lattice that would be barely discernable in x-ray data. These symmetry lowering distortions are accomplished by rotation or distortion of the $Si–O_6$ octahedra.

The deformation mechanisms of $CaSiO_3$ perovskite are also poorly understood, and this is largely due to the fact that it is unquenchable to ambient conditions. This is a problem commonly encountered in the study of mineral phases that compose the deep earth. One way that mechanical properties at high pressures have been studied is through the use of diamond anvil cells (DACs) in radial diffraction geometry [7, 8]. Radial diffraction yields information on lattice strains as well as lattice preferred orientation (texture).

0953-8984/06/250995+11$30.00

In synchrotron diffraction images, preferred orientation manifests itself as systematic intensity variations along Debye rings. If the lattice planes in a sample are predominantly oriented in a particular direction, more intense diffraction will be observed in the corresponding position on the Debye ring. It has been shown that the full orientation distribution (OD) can often be determined from a single two-dimensional synchrotron diffraction image utilizing the Rietveld method [9]. Here we perform quantitative texture analysis on radial diffraction measurements taken *in situ* on $CaSiO_3$ perovskite deformed in a DAC at high pressure. The emphasis is on the procedure of the refinement.

2. Experimental technique

Starting material of $CaSiO_3$ wollastonite, ground to a fine powder and mixed with amorphous boron to serve as laser absorber, was loaded into an 80 μm hole in an amorphous boron–epoxy gasket supported by a kapton confining ring [10]. The starting thickness of the amorphous boron–epoxy insert was 40 μm with an outer diameter of 400 μm. The sample was compressed with 350 μm diameter culet flat diamonds in a laser heated diamond anvil cell with large openings to allow radial diffraction. The starting material was initially compressed to a pressure of about 20 GPa. At this pressure, the phase transformation to the perovskite phase was induced by heating with a focused yttrium–aluminium–garnet laser on one side. The pressure was then increased in steps up to 49 GPa. Angle-dispersive x-ray diffraction spectra were collected in radial geometry with a 2000 $\times$ 2000 pixels Rigaku imaging plate at beamline BL10XU of SPring-8 using a monochromatic incident x-ray beam (wavelength 0.412 Å) of 20 μm in diameter. The exposure time was of the order of 15 min. The sample to detector distance (447.6 mm) and detector tilt were calibrated with a CeO_2 standard taken prior to the experiment. In order to accommodate a shift in the position of the imaging plates between each exposure, the direct beam was exposed briefly at the beginning of each exposure and used for beam centre calibration at each pressure. The image used in the present study is shown in figure 1.

3. Data processing

The MAUD (material analysis using diffraction) software package [11] was used to perform texture analysis via the Rietveld method. Prior to analysis, the images were first processed in FIT2D [12]. The beam centre was found using the 2D Gaussian fit function. Distortions due to tilt, as well as sample to detector distance, were calibrated with the CeO_2 standard. The cake function was used to select the start and end azimuth and 2θ range. A macro was then used to prepare a series of chi files of integrated slices. For this analysis the full 360° coverage was integrated over 5° increments of the azimuth angle into 72 slices and saved in 2θ versus intensity text files. The text files were converted into an esg format file and imported into the data files window in MAUD as spectra for refinement. Images in tiff format can also be processed directly in MAUD using the image manager function. In this case it is necessary to designate the beam centre, azimuth range, increment of integration, and outer limit for integration. Once integration is complete an esg file (input file for MAUD) is produced. Rietveld refinement proceeded as follows.

(1) First esg files for the CeO_2 standard were imported. Instrument geometry, measurement type, source, and detector type were selected under instrument options. Wavelength and detector distance were also entered. Spectra from the CeO_2 standard were used to calibrate Caglioti and Gaussian peak profile parameters. Background parameters and crystallite size

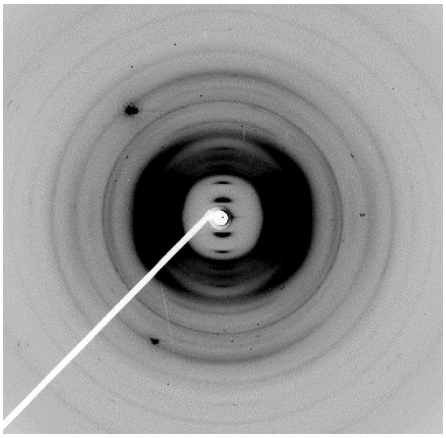

Figure 1. Diffraction pattern of $CaSiO_3$ at 49 GPa. The small spot in the centre of the beam stop is the mark from briefly exposing the direct beam. The gasket assembly diffracts at low 2θ angles producing the dark region in the middle of the image. Note also the presence of the beam stop arm and diamond spots.

were refined along with the Caglioti and Gaussian values. Once calibration was finished, Caglioti and Gaussian peak profile parameters were fixed and CeO_2 spectra were removed.

(2) The diffraction pattern of $CaSiO_3$ perovskite (figure 1) was processed and imported. Spectra containing diamond spots or the beam stop arm were removed from the refinement, and a 2θ range was designated.

(3) A structure model for $CaSiO_3$ perovskite was selected from a mineral database. In this case a cif (crystallographic information file) with space group $Pm\bar{3}m$ was used [13]. Models can also be built manually in MAUD by designating the space group, chemical composition, atomic positions, temperature factors, and oxidation states.

(4) Backgrounds were fitted to a seventh-order polynomial in a plotting program and these values were used in MAUD to define global background parameters. Global backgrounds were fixed and third-order polynomial backgrounds were added to each of the spectra to account for variations with azimuth. Individual backgrounds were refined along with incident intensity and lattice parameters to adjust the peak height and position.

(5) A strain model was then selected for the sample. Moment pole stress [14] with the Reuss model was used. For cubic symmetry only C_{11}, C_{12}, and C_{44} are needed to define the full elastic tensor. All other C_{ij} values were fixed accordingly ($C_{11} = C_{22} = C_{33}$, $C_{12} = C_{13} = C_{23}$, and $C_{44} = C_{55} = C_{66}$). According to the geometry of stress in diamond anvil cell radial diffraction experiments, macrostresses were fixed with $\sigma_{ij} = 0$ for $i \neq j$, $\sigma_{11} = \sigma_{22}$, and $\sigma_{33} = -2\sigma_{11}$, where σ_{33} is the largest principal stress. With the conventions implemented in MAUD, σ_{33} is negative for compression. With these constraints imposed, σ_{11} was freed and the parameters were refined. In the initial refinement of the stress model, the pressure was estimated and C_{ij}s were calculated for the pressure based on the theoretical values of Karki and Crain [4]. Once the lattice parameters converged, the pressure was calculated using the third-order Birch–Murnaghan equation of

state and values of K_{T0} and K'_{T0} from Shim *et al* [15, 16]. The elastic constants were then recalculated at this pressure and entered into the strain model.

(6) To fit peak heights and shapes, isotropic crystallite size and microstrains were refined with all the previous parameters. To determine the crystallite size, Popa line broadening [17] with an isotropic size-strain model was used.

(7) Isotropic thermal vibrations were then freed for each of the atoms to improve the balance of the relative intensities of peaks with respect to each other. This parameter is the isotropic B-factor, which is given by $B = 8\pi^2\langle u\rangle^2$, where $\langle u\rangle^2$ is the mean-squared amplitude of vibration [18]. Care should be taken to ensure that none of the B-factors become negative.

(8) Once a reasonably good fit ($R = 2.22$ and $R_w = 2.87$) was attained, a texture model was selected for calculation of the orientation distribution function (ODF). The R-factor in MAUD is equivalent to the 'R-structure factor' or R_F and R_w is analogous to the 'R-weighted pattern' or R_{wp} [19]. The difference between the R_w of MAUD and R_{wp} is that R_w is taken over all the patterns used in the texture analysis rather than over just the one pattern that would be used for a standard Rietveld analysis.

(9) Quality of a fit is conveniently shown in a map plot, analogous to a 'cake' in Fit 2D. The experimental data set is shown in figure 2(a). A map plot of the fit prior to texture refinement is shown in figure 2(b). The tomography based E-WIMV algorithm which is similar to WIMV [20] was used for the texture refinement. An ODF grid size of 10° and tube projection radius of 20° were used. Initially no symmetry was imposed and the texture was refined with the other parameters. An R-value of 1.97% and an R_w of 2.45% were obtained. A map plot of the refinement without symmetry imposed is shown in figure 2(c), and selected profiles are shown in figures 3(a) and (b).

(10) Pole figures of (100), (110), and (111) poles were calculated from the ODF (figure 4(a)). Pole densities are expressed in multiples of a random distribution (mrd). The textures are approximately axially symmetric about the compression axis (centre).

(11) Once it was verified that the textures were approximately symmetric, the ODF was reset and cylindrical symmetry was imposed. A map plot is shown in figure 2(d). With a symmetric texture R and R_w increased slightly to 2.09% and 2.65% respectively. This is due to the fact that textures in a DAC are not perfectly axially symmetric. The change in the quality of fit can be seen particularly well in the (210) peak (figures 2(c), (d)). Along this peak, intensity variations fit well in the instance where no symmetry was imposed. However, once cylindrical symmetry is imposed intensity variations along this peak are not as well correlated between the calculated and experimental data. One can also see that intensity maxima along other peaks are more symmetric than in the initial refinement. These differences are very slight, reconfirming that the assumption of cylindrical symmetry is justified. Other aspects of the fit have remained the same. Pole figures with symmetry imposed (figure 4(b)) are similar to those previously plotted but have a slightly lower maximum. This is a result of the averaging of the ODF to meet symmetry requirements. From the ODF with symmetry imposed an inverse pole figure of the compression direction was calculated.

4. Results

Crystallographic and microstructural parameters from the refinement and values for elastic constants are shown in table 1. Errors are indicated in parentheses. It should be noted that in general errors calculated by Rietveld refinement tend to be underestimated [21]. Estimated

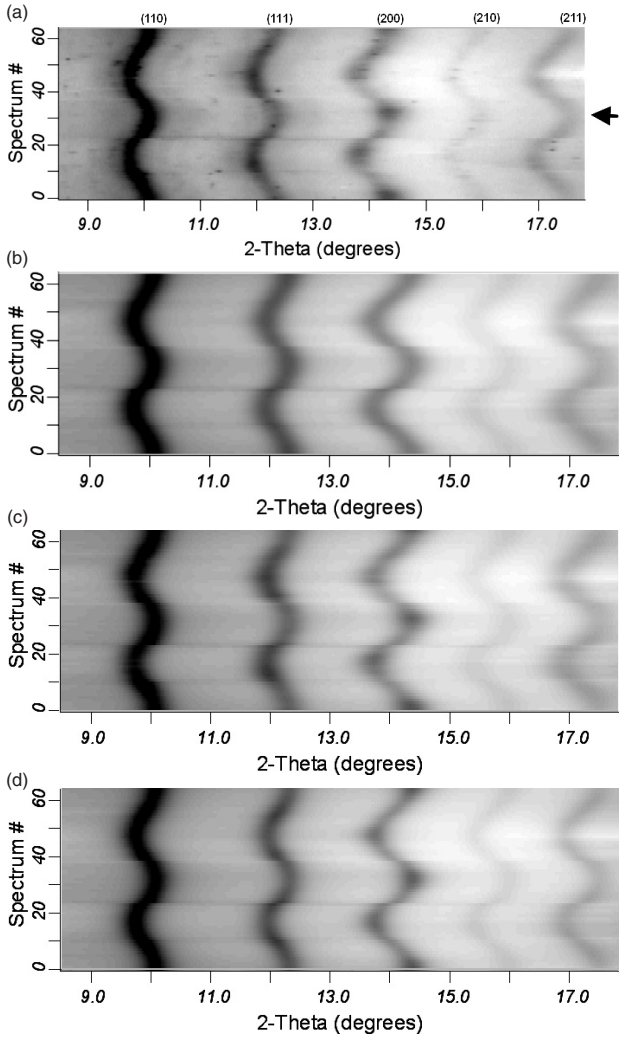

Figure 2. (a) Map plot of the experimental data with the compression direction indicated by an arrow. Peaks are labelled for reference. (b) Fit to the data prior to refinement of texture. Backgrounds are well correlated as are sinusoidal variations due to non-hydrostatic stresses. Intensity variations (texture) are still not matched. ((c) and (d)) Map plots showing the quality of fits after texture refinement for (c) no symmetry imposed, (d) cylindrical symmetry imposed. In (c), texture with no symmetry shows a good fit of the intensity variations. With symmetry imposed in (d), the quality of the fit is slightly lower. In the (111) peak (second peak from the left) the intensity maxima do not correlate as well as in (c).

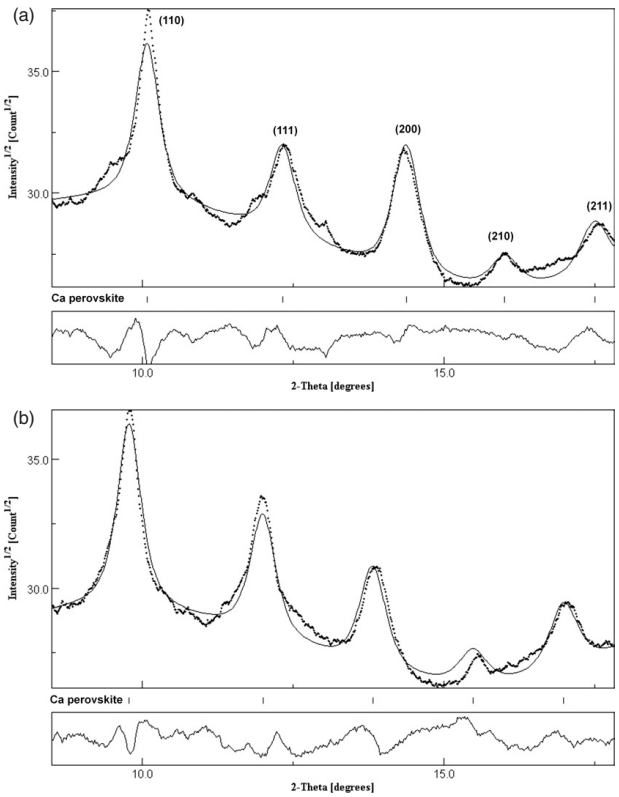

Figure 3. Diffraction profiles along (a) compression direction and (b) extension direction. For the profiles shown in (a) and (b), slight mismatches in the 2θ variation can be seen in these two orientations. Texture is visible as an intensity variation between corresponding peaks at these two different azimuths. Difference plots are shown below (a) and (b).

standard deviations are only a measure of the precision and do not account for additional errors introduced during the experiment or calibration.

Texture results for an ODF which is axially symmetric are conveniently represented by the inverse pole figure of the compression direction. The inverse pole figure is shown in figure 5. In this case only the cubic sector is needed to represent the texture. It shows a ⟨100⟩ maximum with a shoulder towards ⟨110⟩ and a depleted region around ⟨111⟩. The textures are moderate, with a maximum of 1.5 times random distribution.

5. Considerations on Rietveld refinement

Diffraction patterns of samples in DAC often contain large diamond spots. Since these are the result of single crystal diffraction, in many cases it is possible to rotate the DAC a few

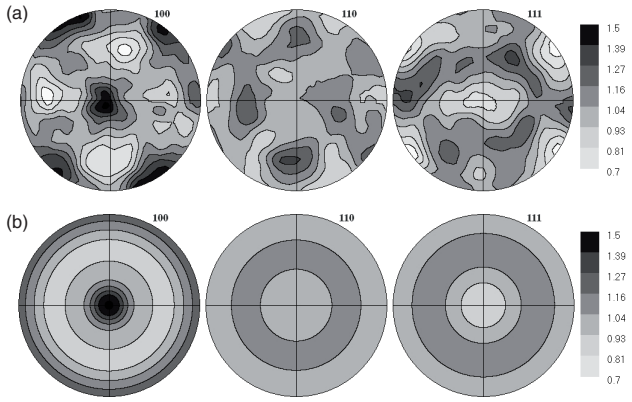

Figure 4. Pole figures plotted for (a) no symmetry imposed and (b) cylindrical symmetry imposed. The centre of the figures corresponds to the compression direction. Pole figures are equal area projections with linear contours (in mrd). In the case of (a) it can be seen that the textures are approximately axially symmetric. The pole figures in (b) are averaged to meet the requirements of the imposed symmetry. This results in the slightly lower maximum observed in (b). Both sets show a distinct maximum of ⟨100⟩ in the compression direction.

Table 1. Refinement parameters from MAUD. Errors are shown in parentheses. Incident intensity and microstrain are unitless. Values of the elastic constants are for a pressure of 49 GPa.

Refinement parameters from MAUD	
Parameter	Value (error)
Incident intensity	1.589 (0.007)
Lattice parameter a (Å)	3.3959 (0.0001)
Crystallite size (Å)	43.00 (0.1)
Microstrain	0.0048 (0.0001)
σ_{33} (Gpa)	−12.56(0.03)
Ca isotropic B-factor (Å^2)	2.017 (0.04)
Si isotropic B-factor (Å^2)	12.62 (0.05)
O isotropic B-factor (Å^2)	7.50 (0.03)
C_{11} (GPa)	712.4 (fixed)
C_{12} (GPa)	291.9 (fixed)
C_{44} (GPa)	310.5 (fixed)

degrees, avoiding diffraction conditions and thereby removing the spots. However, it is not always possible or convenient to take these precautions. Absorption from the beam stop arm can also hamper refinement. To remedy this, of all 72 spectra, seven spectra, one containing the beam stop arm and six containing large diamond spots, were discarded from the refinement.

Radial diffraction geometry introduces the additional complication that the x-ray beam not only passes through the sample but also through the gasket and the diamonds. An advantage of the boron and kapton gasket assembly is that diffraction from the gasket is almost entirely due to the kapton and only occurs at low angles [10]. Likewise, absorption effects from the

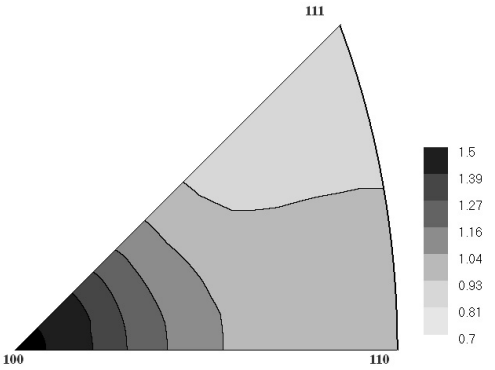

Figure 5. Equal area projection of the inverse pole figure for the compression direction. The scale is in multiples of random distribution (mrd).

diamonds are most problematic at low angles (figure 1). In order to avoid this region, the refinement was restricted to the 2θ range 8.5°–18.1°.

Because of probable stress gradients and weak diffraction from $CaSiO_3$, peaks are of low intensity and quite diffuse. One complication resulting from this is that backgrounds are difficult to fit. This was remedied by plotting one spectrum with a representative background in an independent plotting program, manually selecting points along the background, and fitting them with a seventh-order polynomial. This was then used to assign values for global background parameters in MAUD. In this case, this method proved considerably faster than fitting backgrounds directly in MAUD. Poorly resolved peaks can also make proper assignment of a crystal structure difficult as it may be impossible to observe subtle peak splits. This is particularly a problem in this analysis since several non-cubic structures, resulting from minute distortions of the cubic structure, have been proposed for $CaSiO_3$ [4–6].

Refinement with the cubic $Pm\bar{3}m$ structure did not properly account for the relative intensities of the peaks. In order to address this issue, we investigated the effects of several non-cubic structures on the refinement. The structures used were $P4/mmm$, $I4/mcm$, $Pnma$, and $Pbnm$. For all cases it became clear by visual inspection that the cubic structure provided the best match to the data. Consequently the $Pm\bar{3}m$ structure was retained and used for refinement. To obtain a better fit, isotropic thermal parameters were refined.

Complications in calculating the texture may occur if the stress model does not accurately predict the variation of d-spacing with azimuth that results from lattice strains. If the model is not correct the variation with azimuth may be overestimated for some peaks and underestimated for others. If the peak positions are not matched, the intensities will be fitted based on where the calculated peak intersects the data and this may not be the maximum intensity. If this is the case, intensity variations along a given Debye ring will not be accurately modelled and errors in the texture extraction may result. Although the stress model used in this refinement provides a reasonably good fit for these variations in lattice spacing, there are some slight mismatches in peak positions and intensities between the calculated model and the experimental data. For example, in figures 3(a) and (b), the (210) peak is well correlated in figure 3(a) but is shifted to the left in figure 3(b), resulting in an artificially high intensity maximum for that orientation. It

is likely that this is due to a few degrees of deviation in the maximum compression axis from the diamond axis [22].

One way to resolve this issue is to refine the elastic constants. We chose to refine the shear related elastic constants C_{12} and C_{44}, as variations in d-spacing should be more sensitive to these than to C_{11} [23, 24]. These constants were refined in two separate refinements, the first resulting in a 20% decrease for C_{12} and the second a 12% decrease in C_{44}. No significant difference in the quality of fit between these two refinements could be observed. As is often the case for cubic minerals, the texture is not very sensitive to these minor mismatches in the stress model and the texture results from these two refinements were practically identical to the initial texture calculation.

6. Discussion

The lattice parameter obtained from the refinement correlates well with values from previous experimental work as well as theoretical values for corresponding conditions [3–5, 15, 16, 25]. It is likely, however, that there are additional errors associated with this parameter. For example, the sample may have moved slightly during the experiment as a result of removing the DAC to increase the pressure. As a consequence the actual error for this parameter is probably much higher than the given value.

The crystallite size is unreasonably small. This could be partially due to imperfect calibration of the Caglioti function from the standard. Since the crystallite size is determined from the peak shapes, if aberrations in peak broadening are not properly corrected, the crystallite size obtained will have larger errors. In addition the peaks are not well resolved from the background and appear broader. This may result in obtaining an artificially low crystallite size that correlates with peak broadening. It is important to note that crystallite size is not synonymous with grain size, but refers to the size of the coherently scattering domains within the grains.

For a well defined crystal structure, isotropic B-factors should be positive and less than 1 $Å^2$; however, they are significantly higher. This most likely indicates that the structure model is not entirely correct. If $CaSiO_3$ perovskite in the sample is not truly cubic but pseudo-cubic, deviations from the cubic structure would cause the calculated thermal parameters to be large for those atoms which are misplaced in the model. The especially large thermal vibrations associated with Si and O atoms could support some sort of rotation or distortion of the Si–O_6 octahedra. It is also possible that a variety of these structures could exist in the sample.

We obtain a value of -12.6 GPa for σ_{33}. In the convention used in MAUD the negative value indicates a compressive stress. This corresponds to an axial stress component t of 18.9 at 49 GPa. This is considerably higher than the value found by Shieh *et al* [25], who found that the axial stress component increased from 3 GPa at a pressure of 19 GPa to 11 GPa at 61 GPa for $CaSiO_3$ perovskite. Our value is also larger than deviatoric stresses previously obtained in DAC experiments [8]. The actual stress depends on many factors, including the gasket material.

Based on geometrical considerations as well as TEM observations on a variety of perovskites ($KNbO_3$, $KTaO_3$, $BaTiO_3$, $CaTiO_3$, and $MnGeO_3$), Poirier *et al* [26] proposed that crystals with the cubic perovskite structure deform on the $\{110\}\langle 1\bar{1}0\rangle$ slip system at room temperature and on both the $\{110\}\langle 1\bar{1}0\rangle$ and $\{100\}\langle 001\rangle$ systems at high temperatures. These slip systems have also been observed in $SrTiO_3$ perovskite [27] and in $CaTiO_3$ [28]. No texture information is available on these materials except for a simple shear experiment on $CaTiO_3$ [29]. The proposed slip systems for cubic perovskite are similar to those of the cubic mineral halite [30, 31] and periclase [8]. In this case texture information is available and can be compared with our new results for $CaSiO_3$ perovskite.

In halite and periclase at low temperature, deformation in compression produces a ⟨100⟩ maximum parallel to the compression direction. Self-consistent polycrystal plasticity modelling of the compression of halite with hardening and dominant {110}⟨1$\bar{1}$0⟩ slip produces inverse pole figures that are strikingly similar to the inverse pole figure obtained for $CaSiO_3$ perovskite [32]. This family is particularly interesting because the two slip systems (110) ⟨1$\bar{1}$0⟩ and (1$\bar{1}$0) ⟨110⟩ are equally favoured and their resulting plastic rotations cancel. Texture in this case develops as a result of flattening of grains and shape-dependent rotation [33]. Based on these considerations, we conclude that the $CaSiO_3$ texture is compatible with {110}⟨1$\bar{1}$0⟩ slip as has been identified for cubic perovskite at low temperatures [26–28].

7. Conclusions

Quantitative texture analysis by the Rietveld method as implemented in MAUD is used to gain insight into the deformation mechanisms of $CaSiO_3$ perovskite at high pressures and room temperature. Using a single synchrotron image taken in radial geometry at 49 GPa we obtain a compression texture with {100} lattice planes oriented perpendicular to the compression. This indicates that (110) ⟨1$\bar{1}$0⟩ slip is the dominant slip system. The refinement suggests that deviatoric compressive stresses in the DAC were 18.9 GPa at 49 GPa. The crystallographic and microstructural parameters are consistent with a distortion of the cubic structure. This paper illustrates a relatively quick and convenient method to obtain quantitative texture and structure information from materials deformed at high pressure conditions.

Acknowledgments

The synchrotron radiation experiments were performed at the BL10XU in SPring-8 with the approval of the Japan Synchrotron Radiation Research Institute (JASRI) (Proposal No. 2003B0243-ND2b-np). The authors would like to thank I Lonardelli, S Speziale, and M Kunz for their valuable discussions, H Liu and COMPRES for an exciting workshop at APS, and two anonymous reviewers whose comments improved the manuscript. L Miyagi greatly appreciates support given by CDAC.

References

[1] Mao H-K, Chen L C, Hemley R J, Jephcoat A P, Wu Y and Bassett W A 1989 *J. Geophys. Res.* **94** 17889–94
[2] Wang Y, Weidner D J and Guyot F 1996 *J. Geophys. Res.* **101** 661–72
[3] Shim S H, Jeanloz R and Duffy T S 2002 *Geophys. Res. Lett.* **29** 2166 doi:10.1029/2002GL016148
[4] Karki B B and Crain J 1998 *Geophys. Res. Lett.* **25** 2741–4
[5] Akber-Knutson S, Bukowinski M S T and Matas J 2002 *Geophys. Res. Lett.* **29** 1034 doi:10.1029/2001GL013523
[6] Caracas R, Wentzcovitch R, Price G D and Brodholt J 2005 *Geophys. Res. Lett.* **32** L06306 doi:10.1029/2004GL022144
[7] Wenk H-R, Matthies S, Hemley R J, Mao H-K and Shu J 2000 *Nature* **405** 1044–7
[8] Merkel S, Wenk H-R, Shu J, Shen G, Gillet P, Mao H-K and Hemley R J 2002 *J. Geophys. Res.* **107** B11 2271 doi:10.1029/2001JB000920
[9] Ischia G, Wenk H-R, Lutterotti L and Berberich F 2005 *J. Appl. Crystallogr.* **38** 377–80
[10] Merkel S and Yagi T 2005 *Rev. Sci. Instrum.* **76** 046109
[11] Lutterotti L, Matthies S and Wenk H-R 1999 *Int. U. Crystallogr. Comm. Powder Diffraction Newsletter* **21** 14–5
[12] Hammersley A P 1998 *Internal Report* ESRF-98-HA01
[13] Finger L W and Hazen R M 1991 *Acta Crystallogr.* B **47** 561–80
[14] Matthies S, Priesmeyer H G and Daymond M R 2001 *J. Appl. Crystallogr.* **34** 585–601 doi:10.1107/S0021889801010482
[15] Shim S-H, Duffy T S and Shen G 2000 *Phys. Earth Planet. Inter.* **120** 327–38

[16] Shim S-H, Duffy T S and Shen G 2000 *J. Geophys. Res.* **105** 25955–68
[17] Popa N C and Balzar D 2001 *J. Appl. Crystallogr.* **34** 187–95 doi:10.1107/S0021889801002060
[18] Stout G H and Jensen L H 1989 *X-ray Structure Determination* (New York: Wiley–Interscience) p 189
[19] Young R A 1993 *The Rietveld Method* ed R A Young (New York: Oxford University Press) chapter 1, p 1
[20] Matthies S and Vinel G W 1982 *Phys. Status Solidi* b **112** K111–4
[21] Prince E 1993 *The Rietveld Method* ed R A Young (New York: Oxford University Press) chapter 3, p 43
[22] Merkel S 2006 *J. Phys.: Condens. Matter* **18** S949–62
[23] Singh A K 1993 *J. Appl. Phys.* **73** 4278–86
[24] Singh A K, Balasingh C, Mao H-K, Hemley R J and Shu J 1998 *J. Appl. Phys.* **83** 7567–75
[25] Shieh S R, Duffy T S and Shen G 2004 *Phys. Earth Planet. Inter.* **143/144** 93–105 doi:10.1016/j.pepi.2003.10.006
[26] Poirier J P, Beauchesne S and Guyot F 1989 *Perovskites, A.G.U. Monograph* vol 45, ed A Navrotsky and D Weidner (Washington, DC: Amer. Geophys. U.) pp 119–23
[27] Wang Z, Karato S-I and Fujino K 1993 *Phys. Earth Planet. Inter.* **79** 299–312
[28] Besson P, Poirier J P and Price G D 1996 *Phys. Chem. Minerals* **23** 337–44
[29] Karato S, Zhang S, Zimmerman M E, Daines M J and Kohlstedt D L 1998 *Pure Appl. Geophys.* **151** 589–603
[30] Skrotzki W and Haasen P 1981 *J. Physique Coll.* **42** C3 119
[31] Carter N L and Heard H C 1970 *Am. J. Sci.* **269** 193
[32] Wenk H-R, Canova G, Molinari A and Mecking H 1988 *Acta Metall.* **37** 2017–29
[33] Wenk H-R 2000 *Texture and Anisotropy. Preferred Orientations in Polycrystals and Their Effect on Materials Properties* 2nd paperback edn, ed U F Kocks, C N Tomé and H-R Wenk (Cambridge: Cambridge University Press) chapter 14, p 560

INSTITUTE OF PHYSICS PUBLISHING JOURNAL OF PHYSICS: CONDENSED MATTER
J. Phys.: Condens. Matter **18** (2006) S933–S947 doi:10.1088/0953-8984/18/25/S02

Deformation textures produced in diamond anvil experiments, analysed in radial diffraction geometry

H-R Wenk, I Lonardelli, S Merkel, L Miyagi, J Pehl, S Speziale and C E Tommaseo

Department of Earth and Planetary Science, University of California, Berkeley, CA 94720, USA

Received 17 November 2005, in final form 14 March 2006
Published 8 June 2006
Online at stacks.iop.org/JPhysCM/18/S933

Abstract
Diamond anvil cells may not only impose pressure upon a sample but also a compressive stress that produces elastic and plastic deformation of polycrystalline samples. The plastic deformation may result in texture development if the material deforms by slip or mechanical twinning, or if grains have a non-equiaxed shape. In radial diffraction geometry, texture is revealed by variation of intensity along Debye rings relative to the compression direction. Diffraction images (obtained by CCD or image plate) can be used to extract quantitative texture information. Currently the most elegant and powerful method is a modified Rietveld technique as implemented in the software package MAUD. From texture data one can evaluate the homogeneity of strain in a diamond anvil cell, the strain magnitude and deformation mechanisms, the latter by comparing observed texture patterns with results from polycrystal plasticity simulations. Some examples such as olivine, magnesiowuestite, $MgSiO_3$ perovskite and ε-iron are discussed.

1. Introduction

The deep earth is not accessible to direct observation and most information about its structure and composition relies on interpretation of geophysical data, mainly seismic evidence. Much information on potential phase relations has been gained from experiments at high pressure and high temperature. Of those, shock compression and diamond anvil cells have been essential [1]. In many sectors of the earth there is evidence for dynamic processes that produce heterogeneity and anisotropy. Thus mechanical properties of minerals, influencing the plastic and elastic behaviour as well as the rheology, have become of great interest to the geophysics community. Currently it is not possible to perform quantitative deformation experiments in large volume apparatus to constrain flow laws beyond pressure conditions of the transition zone [2, 3] and models based on first principles still poorly constrain the deformation behaviour [4–6], leaving much uncertainty about deformation mechanisms at ultrahigh pressure. Of considerable interest has been observation of seismic anisotropy in the earth that can be interpreted as evidence for

deformation, producing preferred orientation. In order to understand seismic anisotropy one needs to know the elastic tensor of crystals and microscopic mechanisms that align them during deformation. Both can be addressed with diamond anvil cells (DAC), but using a radial, rather than the conventional axial, diffraction geometry.

In addition to confining pressure, an axial compressive stress is imposed by the diamonds, as has been established by finite element modelling [7], and in a radial diffraction geometry Debye rings reveal variations in d-spacings and intensity of lattice planes that are in different orientations relative to the compression direction. The radial diffraction geometry in DAC experiments was introduced by Kinsland and Bassett [8] and used by Hemley *et al* [9] to investigate stresses and elastic properties up to megabar pressures [10]. Intensity variations along Debye rings are indicative of preferred orientation (texture) that is evidence for crystal rotations due to plastic deformation. In this paper we will review some aspects of the radial diffraction technique to obtain texture information at high pressure and illustrate it with examples. It has been observed that many materials, brittle at ambient conditions, become ductile at pressure above 5 GPa, even at room temperature (olivine, periclase, perovskite and spinel are examples). We will focus on *in situ* texture measurements and discuss how texture patterns can be interpreted to indicate intracrystalline deformation mechanisms as well as overall strain.

Right up front it should be made clear that the DAC deformation experiments are by no means ideal to investigate the rheology of earth materials, which depends on many factors such as stress, strain rate, pressure, temperature, grain size and composition [11, 12], including water content as in the case of quartz [13] and olivine [14–16]. Diffraction volumes in DAC experiments are small, strain as well as stress may be heterogeneous, it is not possible to separate pressure from stress, stresses are generally very large, and at most facilities it is not possible to conduct radial diffraction experiments *in situ* at high temperature. Despite these deficiencies, radial DAC remains the only method to conduct deformation experiments at pressures corresponding to the lower mantle, the D″ zone and the solid inner core and to investigate texture development of phases such as $MgSiO_3$ perovskite and postperovskite, $CaSiO_3$ perovskite and rhombohedral FeO, as well as ε-iron, that are unstable at ambient conditions and can either not be quenched or suffer substantial obliteration of microstructural details when decompressed to ambient conditions.

2. Experiments and data analysis

2.1. DAC experiments

DAC experiments use the x-ray and optical transparency of diamonds to conduct spectroscopic as well as diffraction experiments at high pressure. Depending on the application, polychromatic or monochromatic x-rays are used. For the experiments reported here we use monochromatic x-rays and diffraction patterns are recorded with a 2D detector positioned perpendicular to the incident beam. CCD detectors have the advantage of fast readout, while image plates have higher resolution and a larger dynamic range, but are slower.

In conventional geometry the beam enters along the diamond axis and the diffraction pattern contains information about lattice planes that are oriented close to parallel to the incident x-ray, thus—in axial geometry—the DAC axis. If only phase relations are of interest this is the preferred geometry because of the high transparency of diamond along the ray path. Often efforts are made to obtain hydrostatic pressure by immersing the sample in a gas or liquid. Without such precautions diamond pistons not only produce confining pressure but also a compressive stress, and the material deforms elastically as well as plastically (figure 1).

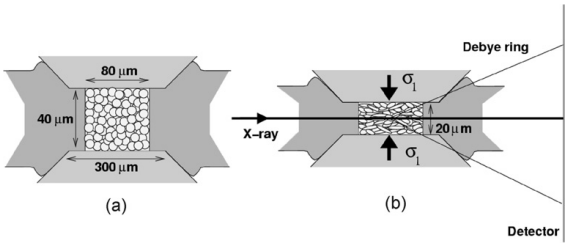

Figure 1. Schematic of a radial DAC cell that is used a deformation apparatus. (a) Initial dimensions, (b) deformed dimensions and diffraction geometry.

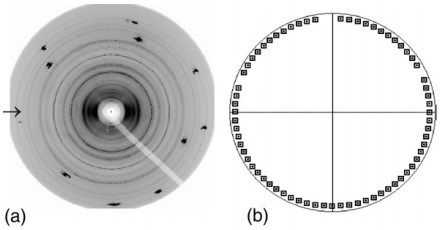

Figure 2. (a) Diffraction image of $MgSiO_3$ perovskite transformed from enstatite, collected *in situ* at 43 GPa with an image plate detector at APS-HPCAT. Strong intensity spots are due to diffractions from diamond. The compression direction is indicated with an arrow. (b) Pole figure coverage for a Debye ring.

In radial diffraction geometry, the beam passes through the DAC perpendicular to the axis (figure 1(b)) and in this case Debye rings in diffraction patterns record a whole range of orientations, with lattice planes from parallel to nearly perpendicular to the DAC axis. The diffraction pattern illustrates elastic deformation effects expressed in elliptical distortions of Debye rings and intensity variations that signify texture, as for $MgSiO_3$ perovskite at 42 GPa in figure 2(a) (the compression direction is indicated with an arrow). Both the elliptical distortion and the intensity variations are best seen if we 'cake' the diffraction pattern by 'unrolling' it, e.g. in Fit2D (figure 3). *Elastic deformation* appears as sinusoidal variations in d-spacings that are smaller (and correspondingly diffraction angles θ are larger) perpendicular to the compression direction (arrow). The changes in d-spacings depend upon the applied compressive stress and elastic properties. In the case of MgO, where elastic properties are well known, deviatoric stresses ranging from 5 to 9 GPa (above 10 GPa confining pressure) have been observed [17]. This value depends on material and gasket type. *Plastic deformation* is expressed in intensity variations that signify preferred orientation, attained e.g. through dislocation glide.

In contrast to the axial geometry, in radial geometry x-rays not only pass through diamond and sample but also through a gasket that maintains the pressure (figure 1(b)). The diffraction pattern shown in figure 2(a) not only contains diffraction from the sample but from the gasket and diamonds as well. Diamond diffractions are visible as high intensity spots. In figure 2(a), diffraction from the confining Kapton gasket produces diffuse rings at low scattering angles.

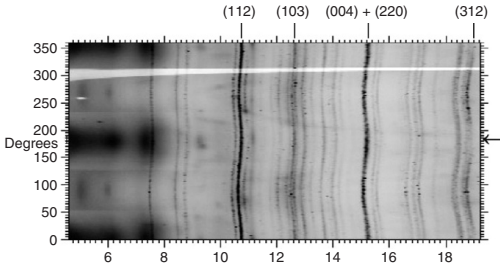

Figure 3. Unrolled diffraction image (figure 2(a)) in Fit2D, plotting azimuthal angle along the Debye ring as a function of Bragg angle θ. The sinusoidal variations in diffraction lines are due to elastic deformation; intensity differences along lines indicate preferred orientation caused by plastic deformation. Compression direction is indicated by the arrow.

Furthermore, the incident x-ray passes through the peripheral and central portions of the sample, and, if there are gradients in pressure, stress and temperature, the diffraction signal provides an average that needs to be deconvoluted. To facilitate the interpretation of diffraction images, experiments need to be designed to minimize gradients and signals from the gasket material.

Gaskets are mainly chosen for strength, combined with x-ray transparency. A favourite material has been Be, that can be used beyond 200 GPa [9]. A disadvantage is that Be scatters strongly and its diffraction lines may overlap with the much weaker lines from the sample, making the analysis difficult. Tilting the DAC 20°–30° can reduce or eliminate this interference. For moderate pressures (<50 GPa) gaskets produced by mixing a powder of amorphous boron with epoxy can be used [17, 18]. This is particularly efficient if the size of the boron gasket is minimized by enclosing a small disk in a ring of x-ray transparent Kapton [19]. No doubt more flexible designs will be developed in the future. As will be shown later, the present gasket geometry limits the strain to about 20%. Preferred orientation generally develops quickly and stabilizes, changing little upon further compression.

2.2. Image analysis

The image in figure 3 illustrates some complications often encountered in the radial diffraction data analysis. There are many diffraction lines; some of these are partially or completely overlapped. Also, background intensities vary as a function of azimuthal angle, mainly due to differences in absorption. An efficient and quantitative approach to analyse such images is the Rietveld method, that applies a physical model to express spectral intensities and refines instrumental parameters (e.g. image position, resolution, background), sample characteristics (absorption, microstructure), crystallographic properties (e.g. lattice parameters and atomic coordinates) and stress (using an appropriate model), as well as texture, our primary interest. We apply the Rietveld method in the MAUD software, that is unique in implementing advanced direct methods of quantitative texture analysis [20, 21].

Images must be calibrated with a standard for wavelength and sample–detector distance. After being centred, the image is decomposed into spectra by integrating over azimuthal sectors (usually 5°, 10° or 15°). As an example, two of these spectra with experimental data and the Rietveld fit are shown in figure 4(a). Indicated below the spectra are the positions of

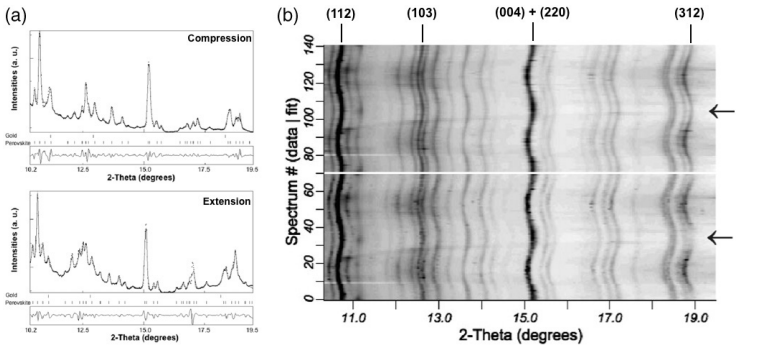

Figure 4. Rietveld method applied to diffraction image of perovskite (figure 2(a)). (a) Two experimental and fitted spectra parallel (top) and perpendicular to compression direction (bottom). (b) Map plot of stacked normalized spectra, experimental at bottom and calculated at top. Compression direction indicated by arrow.

diffraction lines and the deviations between experiment and fit. The two spectra correspond to different slices and represent different orientations relative to the compression direction. In the spectrum on top the lattice planes are perpendicular to the compression direction and in the bottom spectrum they are parallel. An overall assessment of the quality of the Rietveld fit is displayed in a 'map plot' (figure 4(b)) that compares a stack of experimental spectra (bottom) with recalculated spectra (top), expressed as grey shades. Note that not only peak intensities, but also background variations, are well reproduced.

The pole figure coverage of a Debye ring from a diffraction image with 5° integration is shown in figure 2(b). The pole figure is in the same orientation as the image (figure 2(a)) and the coverage is a ring near the periphery. Clearly this coverage is very sparse, extending roughly from parallel to perpendicular to the compression direction and, if axial symmetry (around the compression axis) is assumed, contains all information required to reconstruct a quantitative model of the orientation distribution (OD).

Often it is useful to establish if axial symmetry is indeed satisfied in an experiment and that sample rotations in the Rietveld program have been done correctly. It has been shown that a single 2D image (figure 2(a)) with a sparse coverage (figure 2(b)) can be sufficient to derive an approximate 3D OD [22]. From the OD, pole figures can be generated. In the case of the image in figure 2(a), and without imposing any sample symmetry, we obtain a (100) pole figure for perovskite with (100) lattice planes parallel to the compression direction and a (001) pole figure with (001) lattice planes perpendicular to the compression direction (figure 5(a)). Note that the sample has been rotated with respect to figure 2, to bring the compression direction into the centre. The rotated coverage is shown in figure 5(b) (compare with figure 2(b)). We verify that the pole figure symmetry is roughly axially symmetric about the diamond axis, as would be expected from the DAC geometry, and thus, in a next step of the analysis, axial symmetry can be imposed on the measured data (figure 5(c)) and the OD calculation can be refined. A compact method to represent axially symmetric textures is with inverse pole figures of the compression direction relative to crystal coordinates, as shown in figure 5(d). The (001) pole figure displays a maximum in the compression direction (figures 5(a) and (c)). This is expressed in the inverse pole figure with a maximum near (001) (figure 5(d)). In the following section we will illustrate

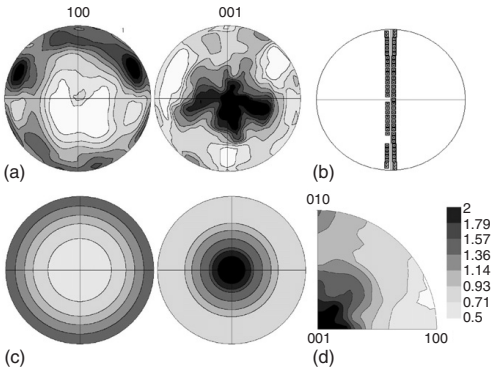

Figure 5. Texture representations of OD data obtained from the image shown in figure 2(a) for orthorhombic $MgSiO_3$ perovskite at 43 GPa. (a) (100) and (001) pole figures without imposing sample symmetry; (b) pole figure coverage; (c) (100) and (001) pole figures imposing axial sample symmetry. The compression direction is in the centre. (d) Inverse pole figure of the compression direction. Equal area projection with linear contours.

some examples of radial diffraction DAC experiments where quantitative texture information was obtained and could be interpreted.

3. Examples

The radial DAC experiments that are discussed in this report were conducted at ALS beamline 12.2.2 (wuestite, magnesiowuestite and perovskite) and APS GSECARS beamline 13-ID (olivine, perovskite, periclase and iron), APS HPCAT beamline 16-ID-B (perovskite) and BNL beamline X17-C (iron).

3.1. Olivine

The preferred orientation of olivine Mg_2SiO_4 has been of longstanding interest because of its importance for interpreting the strong seismic anisotropy in the upper mantle [23]. Numerous experimental studies documented changes in orientation patterns with temperature, strain rate, pressure and most recently water content [24, 14–16]. Olivine can be deformed in conventional deformation apparatus and DAC is not required. We use it here to test the radial DAC method to see if similar results are obtained as with other methods for corresponding conditions. Olivine powder (grain size 1–5 μm) was compressed in the DAC to 27 GPa, at which point the phase transformation to perovskite was induced by laser heating [25]. Between 10 and 15 GPa a distinct texture pattern evolved (figure 6(a)) that strengthened slightly when pressure was increased to 27 GPa (figure 6(b)). The inverse pole figures display a broad minimum at (001) and concentrations along the (100)–(110)–(010) girdle, with maximal pole densities of 1.5 multiples of a random distribution (mrd). This pattern is consistent with deformation mechanisms where [001] is the principal slip direction such as (100)[001] and {hk0}[001] pencil glide as determined for low temperature deformation of olivine [26]. Indeed, polycrystal plasticity simulations for this mechanism produce an inverse pole figure that is very similar to

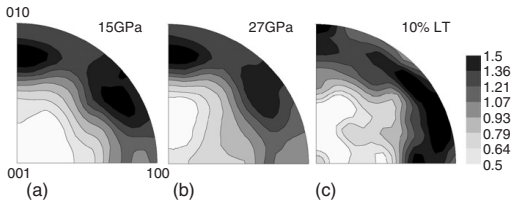

Figure 6. Inverse pole figures for olivine obtained from images measured *in situ* at (a) 15 GPa and (b) 27 GPa (APS-GSECARS). (c) Polycrystal plasticity simulation for {*hk*0}[001] pencil glide 10% strain (table 1) [25]. Equal area projection with linear contours.

Table 1. Slip systems assumed in polycrystal plasticity simulations of olivine. Critical shear stress coefficients (CRSS) and average activity at 10% strain are given (for texture pattern see figure 6(c)).

Slip system	CRSS	Activity (%)
(100)[001]	1	33
(010)[001]	1	20
(100)[010]	5	3
{110}[001]	1	44

the experimental ones (figure 6(c)). Assumed critical shear stresses on slip systems and slip system activities are summarized in table 1. The best agreement in texture strength is obtained for a shortening of 10%, which provides an estimate for the overall strain in this experiment and may be typical for many DAC experiments. This texture pattern and deformation mechanism do not apply to mantle conditions but may be significant for metamorphic rocks, and the high pressure experiments provide ductility to obtain significant plastic strains at high strain rates.

3.2. Periclase, magnesiowuestite and wuestite

Some of the early radial DAC texture experiments were done with periclase (MgO) [17]. It was observed that periclase started to deform plastically at 5 GPa confining pressure, with development of a {001} texture that became very strong upon further straining to 35 GPa, with a maximum of 9.1 mrd. This texture type indicates that only $\{110\}\langle 1\bar{1}0\rangle$ slip was significantly active. First principles calculations confirm this slip system for high pressure and low temperature [5]. At lower pressure and high temperature large volume experiments produce textures consistent with activity of {110}, {111} as well as {100} slip [27–29]. The change of slip system activity with temperature for MgO is analogous to isostructural halite where {110} slip dominates at low temperature, and {110}, {111} and {100} slip systems are equally active at higher temperature [30].

The original experiments were done with a mixture of periclase and iron [17]. More recent experiments with single phase oxides, but ranging in composition from periclase (MgO) to wuestite (FeO), confirm these results [31] but also indicate a change in texture strength with composition. Figure 7 compares inverse pole figures for 15–20 GPa confining pressure. For Mg 40% Fe 60% a strong {001} texture develops, similar to pure MgO (figure 7(a); the maximum is 7 mrd). For the same pressure but for Mg 25% Fe 75% the texture is much attenuated (figure 7(b), 2.3 mrd), and for Mg 10% Fe 90% even weaker (figure 7(c), 1.2 mrd). With increasing iron content, magnesiowuestite becomes more compressible [32, 33] and it is

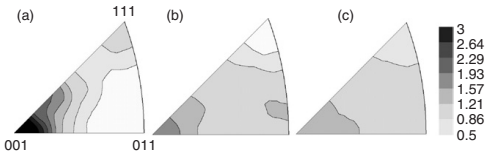

Figure 7. Inverse pole figures for magnesiowuestite. (a) $Fe_{0.60}Mg_{0.40}O$, 16 GPa (APS-HPCAT); (b) $Fe_{0.75}Mg_{0.25}O$, 16 GPa (ALS-12.2.2); (c) $Fe_{0.90}Mg_{0.10}O$, 18 GPa (ALS-12.2.2) [31]. Equal area projection, linear contours.

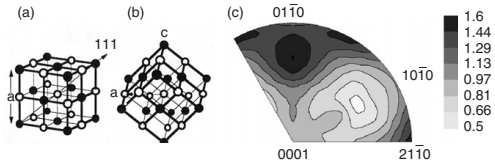

Figure 8. Transformation of cubic B1 wuestite (a) to rhombohedral wuestite (b) by a distortion of the lattice [18]. (c) Inverse pole figure of rhombohedral wuestite at 25 GPa (ALS-12.2.2). Equal area projection, linear contours.

plausible that for high Mg content, plastic deformation dominates, whereas for high Fe content elastic deformation may contribute significantly to the accommodation of the moderate strain.

Iron-rich magnesiowuestite undergoes a phase transformation from cubic to rhombohedral at high pressure (20 GPa) [18, 34–36]. The transformation corresponds to a displacive distortion of the B1 structure (figure 8(a)) along one body diagonal (figure 8(b)). Interestingly, when cubic FeO transforms to rhombohedral FeO under stress, it displays immediately a strong texture with a maximum at $\{01\bar{1}2\}$ (figure 8(c)). The $\{01\bar{1}2\}$ planes of the rhombohedral phase (hexagonal setting) correspond to {001} lattice planes in the cubic structure. It is conceivable that this texture develops by transformation twinning with variant selection due to stress.

3.3. $MgSiO_3$ perovskite

Textures of perovskites are not only relevant for geophysics, since they constitute the major phase in the lower mantle [37], they are also of interest to materials science as important ferroelectrics [38]. Perovskite occurs in cubic, tetragonal and orthorhombic structures [39]. Orthorhombic $MgSiO_3$ perovskite (space group $Pbnm$) is stable above 23–25 GPa and the preferred orientation that develops during mantle convection could be expressed in seismic anisotropy. Thus deformation mechanisms of this mineral are of great importance and currently only with radial DAC experiments can we investigate the evolution of preferred orientation *in situ* at lower mantle pressure.

In recent DAC experiments perovskite has been produced from olivine (Mg_2SiO_4), ringwoodite (Mg_2SiO_4) and enstatite ($MgSiO_3$) as starting materials [25, 40]. If enstatite is used, the product is pure perovskite; with olivine and ringwoodite it is a mixture of perovskite and periclase (MgO). Figure 9 displays some portions of unrolled images, highlighting the strong diffraction lines 004 + 220, with the main intensity contribution from 004. In all experiments significant preferred orientation was produced, visible in the intensity variations.

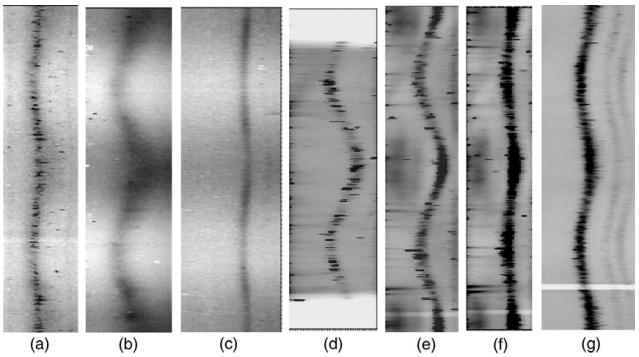

Figure 9. 004 + 220 diffraction lines of $MgSiO_3$ perovskite measured *in situ* for different experimental conditions. (a) Perovskite transformed from olivine at 25 GPa, (b) after increasing pressure to 43 GPa (APS-GSECARS). (c) Perovskite transformed from ringwoodite at 43 GPa (APS-GSECARS). (d) Perovskite transformed from enstatite at 50 GPa, (e) increase in texture strength after maintaining stress for 24 h, (f) change in pattern and microstructure after laser heating at 1400 °C for 30 min (APS-GSECARS). (g) Perovskite transformed from enstatite at 44 GPa (APS-HPCAT).

But even a qualitative glance reveals considerable differences, depending on starting material and conditions.

When perovskite transforms from olivine at 25 GPa first a spotty pattern develops due to a fairly large grain size produced during the phase transformation induced by laser heating at 1200 °C (figure 9(a)). Upon increasing pressure to 43 GPa, stresses become more pronounced and effective grain size is reduced by plastic deformation, resulting in a smooth intensity distribution with a regular pattern (figure 9(b)). When perovskite is formed from ringwoodite at 43 GPa a different but well defined texture is present with a maximum intensity of the 004 diffraction line between compression and extension direction (figure 9(c)). An interesting experiment is with enstatite as starting material. Unfortunately in this case a small (10 μm) beam had to be used and grain size was rather coarse after transformation at 1350 °C and 40 GPa, resulting in a spotty pattern and poor grain statistics. Increasing pressure to 50 GPa, texture is first moderate (figure 9(d)) but increases when the DAC is maintained at that pressure for 24 h (figure 9(e)), with a main maximum parallel to the compression direction and a subsidiary maximum perpendicular to it. This is analogous to a creep experiment where deformation occurs at constant stress. Upon heating at 1400 °C for thirty minutes stresses are reduced (less curvature) and the grain structure changes, documenting on-going recrystallization (figure 9(f)). Maxima parallel and perpendicular to the compression direction are of equal strength. A second experiment with enstatite as starting material, but a boron-epoxy gasket, produced a similar texture pattern at 44 GPa (figure 9(g)).

Figure 9 only displays the intensity distribution of two overlapped diffraction lines, illustrating qualitative differences. Some images could be quantitatively analysed with the Rietveld method, as illustrated in section 2, to obtain orientation distributions and inverse pole figures (figure 10). When perovskite transforms from olivine, there is shortly after the transformation a maximum in the inverse pole figure near (100) (figure 10(a)). With increasing pressure and deformation a second concentration develops near (011) (figure 10(b)).

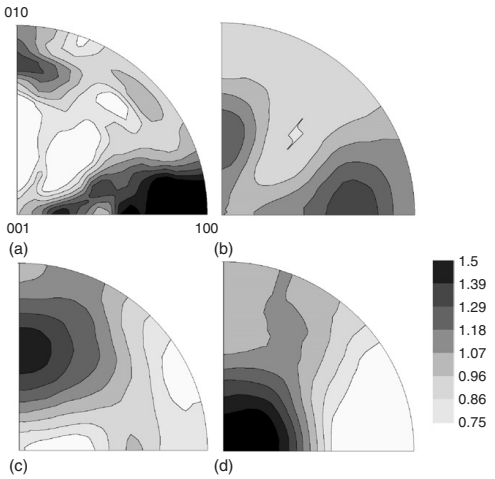

Figure 10. Inverse pole figures for orthorhombic $MgSiO_3$ perovskite. (a) Transformed from olivine at 25 GPa (APS-GSECARS) (compare figure 9(a)), (b) increasing pressure to 43 GPa (APS-GSECARS) (compare figure 9(b)), (c) transformed from ringwoodite at 43 GPa (APS-GSECARS) (compare figure 9(c)), (d) transformed from enstatite at 44 GPa (APS-HPCAT) (compare figure 9(g)). Equal area projection, linear contours.

Table 2. Slip systems assumed in polycrystal plasticity simulations of orthorhombic perovskite. Critical shear stress coefficients (CRSS) and average activity (in %) at 20% strain (see figure 11 for corresponding texture types).

Slip system	CRSS	Activity	CRSS	Activity	CRSS	Activity	CRSS	Activity
	A		B		C		D	
(100)[010]	1	40	5	18	5	0	5	8
(001)[100]	5	0	5	18	1	44	5	8
(001)[100]	5	41	1	47	1	44	5	0
(001)⟨110⟩	20	18	20	19	20	11	1	84

We tentatively attribute the (100) maximum to (110) twinning [41]. When perovskite forms from the intermediate phase ringwoodite, the main maximum is near (011) (figure 10(c)). Perovskite transforming from enstatite displays a maximum near (001), with a minimum at (100) (figure 10(d)). We think that the (011) and (001) texture types were produced by slip.

In order to estimate deformation mechanisms, we compare the experimental texture with polycrystal plasticity simulations, assuming slip systems that have been proposed: (010)[100], (001)[100], (100)[010] and (001)⟨110⟩ [42–44]. A single crystal diffraction study did not find evidence for ⟨110⟩ slip [45]. We report results for four models of slip systems with widely different critical shear stress coefficients (table 2). Surprisingly texture patterns are not dramatically different (figure 11). For dominant (100)[010] slip (model A, figure 11(a)), there is still significant (001)[100] slip to maintain compatibility, and a broad girdle between (001) and (100) is quite different from observed textures. The best match for the texture of perovskite

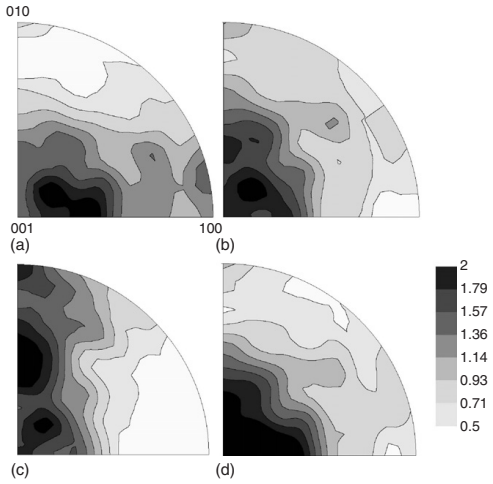

Figure 11. Polycrystal plasticity simulations for orthorhombic perovskite. For slip systems, critical resolved shear stress coefficients and activities see table 2. (a) Model A, (b) model B, (c) model C and (d) model D. Equal area projection, linear contours.

transformed from ringwoodite (figure 10(c)) is obtained if (010)[100] and (001)[100] slip are equally active (model C, figure 11(c)). The texture of perovskite transformed from enstatite (figure 10(d)) can be explained if (001)[100] is the dominant slip system (model B, figure 11(b)) or if the slip system is (001)⟨110⟩ (model D, figure 11(d)). At this point interpretations are tentative and more experiments are needed. Issues not considered in the simulations are complications introduced by multiple phases and mechanical twinning that may influence texture patterns [41]. From a comparison of texture strength in experiments and simulations we imply an overall strain of about 20%.

One conclusion of experiments and simulations is quite definite: all observed textures are strongly "orthorhombic", requiring slip systems also to be orthorhombic and not pseudo-cubic. In inverse pole figures pole densities at (100), (010) and (001) are very different. This indicates that cubic perovskites are poor analogues to infer the deformation behaviour in the lower mantle [46]. This is consistent with elastic properties and structural features that become more orthorhombic with increasing pressure and temperature [47, 48].

The $MgSiO_3$ perovskite emerges as a very complex and interesting system with large texture variations depending on experimental conditions. In addition to the range of results described above, some radial DAC experiments produced insignificant textures [40] and experiments on pseudo-cubic $CaSiO_3$ produced a texture compatible with {110} slip [49].

3.4. Iron

Pure iron is the first material where radial diffraction DAC measurements were used to extract quantitative texture information [50]. In this case, and in contrast to all other DAC experiments discussed in this paper, white x-rays were used and diffraction effects were recorded with an energy-dispersive point detector. Iron is of considerable importance in geophysics because it

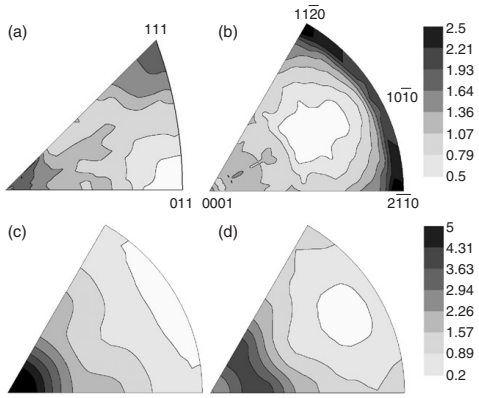

Figure 12. Radial DAC deformation of iron. (a) Bcc iron in a mixture with MgO deformed to a pressure of 12.4 GPa, (b) immediately after phase transformation to hcp at 17.7 GPa [53]. (c) Texture of hcp iron at 220 GPa [50]. (d) Polycrystal plasticity simulation favouring basal slip. Equal area projection, linear contours.

constitutes the solid inner core, where seismic anisotropy was documented that may be caused by texturing [51]. At ambient temperature iron transforms from a bcc structure to hcp at 15 GPa. Experiments at 220 GPa, close to pressures in the centre of the earth, reveal a strong (0001) texture (figure 12(c)), that can only be explained with significant basal slip (figure 12(d)). This slip system has been predicted for hcp iron, based on theory [52].

The investigation of iron was continued with monochromatic x-rays and CCD detectors, at lower pressures [53]. In a mixture of iron and MgO, bcc iron develops a texture with {111} lattice planes perpendicular to the compression direction (figure 12(a)). This is typical of bcc metals and attributed to dominant $\{110\}\langle\bar{1}11\rangle$ slip [54]. Above 15 GPa the transition to hcp occurs and the transformation texture has a main concentration at $\{11\bar{2}0\}$ (figure 12(b)), which is qualitatively consistent with the Burgers' relationship [55] that predicts close-packed bcc directions {111} to become aligned with close-packed hcp directions $\{11\bar{2}0\}$, though this is accompanied by variant selection, most likely influenced by stress. Upon further increase in pressure and stress, the hcp $\{11\bar{2}0\}$ transformation texture changes to a (0001) deformation texture (figure 12(c)).

4. Discussion

Recent radial diffraction geometry DAC experiments have illustrated that oxides and silicates become ductile at pressures above 5 GPa even at room temperature, activating slip systems and producing deformation textures. Quantitative texture analysis requires determination of the orientation distribution, which is now feasible from radial DAC diffraction images. This is much more informative than a merely qualitative assessment of relative intensity differences that are difficult to interpret, especially if polychromatic radiation is used. Only quantitative texture patterns can be interpreted with some degree of confidence.

In cases where textures can be compared with conventional deformation experiments at similar conditions, and with polycrystal plasticity simulations based on known slip systems, the patterns are consistent as illustrated for olivine and periclase. With polycrystal plasticity

we can further estimate an overall strain of about 10–20% for DAC deformation experiments conducted so far. Image analysis without imposing sample symmetry establishes that strain is approximately axially symmetric, confirming results from finite element simulations [7], except for experiments with obvious deficiencies and highly ductile materials such as fcc metals [56].

If active deformation mechanisms are not known they can be implied from texture patterns by comparisons with polycrystal plasticity simulations, as we have shown here for magnesiowuestite and perovskite. In some cases these room temperature slip systems agree with slip systems predicted based on theory, as in the case of post-perovskite ([57] versus 6) and ringwoodite ([58] versus 4). In MgO different slip systems are active at high temperature [17, 27–29]. In the future it may be possible to extrapolate slip system activity to different pressure and temperature conditions and the combined information contributes to a better understanding of deformation in the deep earth.

Naturally the DAC deformation technology needs to be refined in the future. Foremost it is necessary to be able to control pressure changes and associated stress increase *in situ*, which could not be done in the current experiments, though such methods are used in axial geometry DAC experiments [59]. It would be highly desirable to investigate slip systems at higher temperature. Also here methods exist for *in situ* heating by resistance furnaces [60–62] as well as laser heating [63] but require non-trivial modifications for radial diffraction that are currently not available at high pressure beamlines. With *in situ* control of pressure and temperature it will become possible to investigate texture changes during initial deformation and particularly address issues of texture memory during phase transformations that may indicate martensitic mechanisms, which have been proposed for the olivine–ringwoodite transition but could not be verified in these experiments [64, 65].

With microbeam techniques it may become possible to investigate microstructure and orientation grain by grain [66]. A further limitation of the current radial DAC technology is the relatively limited strain in compressive geometry. Low strain is preferable for identification of intracrystalline slip systems from textures since polycrystal plasticity theories break down at large strains, with significant strain hardening [67], activation of subordinate systems and grain boundary sliding to provide compatibility as well as dynamic recrystallization [68]. Rotational DAC cells that produce torsion deformation have been developed and provide exciting opportunities for large strain experiments [69, 70]. Many of these experimental improvements of DAC technology are currently under development and should become available for users in the near future.

There is a wide range of applications of DAC deformation experiments to new materials to not only explore deformation mechanisms at ultrahigh pressure but also to better understand processes such as texture changes and variant selection during phase transformations, or changes that occur during static and dynamic recrystallization. Obviously DAC experiments only provide limited information to infer rheological conditions in the deep earth. Whereas they may never yield reliable stress–strain curves, we have illustrated that they provide information on texture development that is a fairly robust indicator of intracrystalline mechanisms, responsible for grain rotations to achieve anisotropic polycrystal properties. This information can be used to interpret observed seismic anisotropy patterns in the deep earth [71].

Acknowledgments

The authors are grateful for access to high pressure beamlines at the Advanced Light Source (LBNL 12.2.2), the Advanced Photon Source (ANL) GSECARS and HPCAT where experiments were performed, and help from beamline scientists. We are indebted to Haozhe

Liu and COMPRES for a stimulating workshop at APS that generated a lot of interest in DAC deformation experiments. HRW is appreciative of Dave Mao for seducing him into this fascinating field of research. The work has been supported by CDAC, NSF and IGPP-LANL. S Merkel and S Speziale acknowledge support from the Miller Institute of Basic Research at Berkeley and C E Tommaseo from the Deutsche Forschungsgemeinschaft.

References

[1] Manghnani M H and Syono Y (ed) 1987 *High-Pressure Research in Mineral Physics. Geophysical Monograph* vol 39 (Washington, DC: Amer. Geophys. Union)
[2] Wang Y, Durham W B, Getting I C and Weidner D J 2003 *Rev. Sci. Instrum.* **74** 3002–11
[3] Yamazaki D and Karato S I 2001 *Rev. Sci. Instrum.* **72** 4207–11
[4] Carrez P, Cordier P, Mainprice D and Tommasi A 2006 *Eur. J. Mineral.* at press
[5] Miranda C R and Scandolo S 2005 *Comput. Phys. Commun.* **169** 24–7
[6] Oganov A R, Martonák R, Laio A, Raiteri P and Parrinello M 2005 *Nature* **438** 1142–4
[7] Merkel S, Hemley R, Mao H-K and Teter D M 2000 Science and technology of high pressure *Proc. AIRAPT* vol 17, ed M H Manghnani, W J Nellis and M F Nicol, pp 68–73
[8] Kinsland G L and Bassett W A 1976 *Rev. Sci. Instrum.* **47** 130–2
[9] Hemley R J, Mao H-K, Shen G, Badro J, Gillet P, Hanfland M and Häusermann D 1997 *Science* **276** 1242–5
[10] Singh A K, Mao H-K, Shu J and Hemley R J 1998 *Phys. Rev. Lett.* **80** 2157–60
[11] Frost H J and Ashby M F 1982 *Deformation Mechanism Maps* (Toronto: Pergamon) p 166
[12] Yamazaki D and Karato S 2001 *Am. Mineral.* **86** 385–91
[13] Griggs D T 1967 *Geophys. J. R. Astron. Soc.* **14** 19–31
[14] Jung H and Karato S-I 2001 *Science* **293** 1460–2
[15] Karato S I, Paterson M S and Fitzgerald J D 1986 *J. Geophys. Res.* **91** 8151–76
[16] Katayama I, Jung H and Karato S I 2004 *Geology* **32** 1045–8
[17] Merkel S, Wenk H-R, Shu J, Shen G, Gillet P, Mao H-K and Hemley R J 2002 *J. Geophys. Res.* **107 2271** (doi:10.1029/2001JB000920)
[18] Mao H K, Shu J, Fei Y and Hemley R J 1996 *Phys. Earth Planet. Inter.* **96** 135–45
[19] Merkel S and Yagi T 2005 *Rev. Sci. Instrum.* **76** 046109 (doi:10.1063/1.1884195)
[20] Lonardelli I, Wenk H-R, Goodwin M and Lutterotti L 2005 *J. Synchrotron Res.* **12** 354–60
[21] Lutterotti L, Matthies S and Wenk H-R 1999 *Int. U. Crystallogr. Comm. Powder Diffraction Newslett.* **21** 14–5
[22] Ischia G, Wenk H-R, Lutterotti L and Berberich F 2005 *J. Appl. Crystallogr.* **38** 377–80
[23] Montagner J P and Tanimoto T 1990 *J. Geophys. Res.* **95** 4797–819
[24] Carter N L and Ave'Lallemant H G 1970 *Geol. Soc. Am. Bull.* **81** 2181–208
[25] Wenk H-R, Lonardelli I, Pehl J, Devine J, Prakapenka V, Shen G and Mao H-K 2004 *Earth Planet. Sci. Lett.* **226** 507–19
[26] Raleigh C B 1968 *J. Geophys. Res.* **73** 5391–406
[27] Heidelbach F, Stretton I, Langenhorst F and Mackwell S 2003 *J. Geophys. Res.* **108** 2154 (doi:10.1029/2001JB001632)
[28] Stretton I, Heidelbach F, Mackwell S and Langenhorst F 2001 *Earth Planet. Sci. Lett.* **194** 229–40
[29] Yamazaki D and Karato S I 2002 *Phys. Earth Planet. Inter.* **131** 251–67
[30] Carter N L and Heard H C 1970 *Am. J. Sci.* **269** 193–249
[31] Tommaseo C E, Merkel S, Speziale S, Devine J and Wenk H-R 2006 *Phys. Chem. Mineral.* **33** 84–97
[32] Bonczar L J and Graham E K 1982 *J. Geophys. Res.* **87** 1061–78
[33] Jacobsen S D, Reichmann H-J, Spetzler H A, Mackwell S J, Smyth J R, Angel R J and McCammon C A 2002 *J. Geophys. Res.* **107** 2037 (doi:10.1029/2001JB000490)
[34] Jacobsen S D, Lin J-F, Angel R J, Shen G, Prakapenka V B, Dera P, Mao H-K and Hemley R J 2005 *J. Sychrotron Radiat.* **12** 577–83
[35] Mao W, Shu J, Hemley R J and Mao H-K 2002 *J. Phys. Condens. Matter* **14** 11349–54
[36] Shu J, Mao H-K, Hu J, Fey Y and Hemley R J 1998 *Neues Jahrb. Mineral. Abh.* **172** 309–23
[37] Ito E M and Takahashi E 1989 *J. Geophys. Res.* **94** 10637–46
[38] Lines M E and Glass A M 1977 *Principles and Applications of Ferroelectrics and Related Materials* (Oxford: Clarendon)
[39] Galasso S 1969 *Structure, Properties and Preparation of Perovskite Type Compounds* (New York: Pergamon) p 207

[40] Merkel S, Wenk H-R, Badro J, Montagnac J, Gillet P, Mao H-K and Hemley R J 2003 *Earth Planet. Sci. Lett.* **209** 351–60
[41] Wang Y, Guyot F, Yeganeh-Haeri A and Liebermann R C 1990 *Science* **248** 468–71
[42] Besson P, Poirier J P and Price G D 1996 *Phys. Chem. Minerals* **23** 337–44
[43] Poirier J P, Beauchesne S and Guyot F 1991 *Perovskites, A.G.U. Monograph* vol 45, ed A Navrotsky and D Weidner (Washington, DC: Amer. Geophys. Union) pp 119–23
[44] Wright K, Price G D and Poirier J P 1992 *Phys. Earth Planet. Inter.* **74** 9–22
[45] Cordier P, Ungár T, Zsoldos L and Tichy G 2004 *Nature* **428** 837–40
[46] Karato S-I, Zhang S and Wenk H-R 1995 *Science* **270** 458–61
[47] Oganov A R, Brodholt J P and Price G D 2001 *Nature* **411** 934–7
[48] Wentzcovitch R M, Karki B B, Cococcioni M and de Gironcoli S 2004 *Phys. Rev. Lett.* **92** 018501 (doi:10.1103)
[49] Miyagi L, Merkel S, Yagi T, Sata N, Ohishi Y and Wenk H-R 2006 *J. Phys. Condens. Matter* **18** S995–1005
[50] Wenk H-R, Matthies S, Hemley R J, Mao H-K and Shu J 2000 *Nature* **405** 1044–7
[51] Song X 1997 *Rev. Geophys.* **35** 297–313
[52] Poirier J P and Price G D 1999 *Phys. Earth Planet. Inter.* **110** 147–56
[53] Merkel S, Wenk H-R, Gillet P, Mao H-K and Hemley R J 2004 *Phys. Earth Planet. Inter.* **145** 239–51
[54] Rollett A D and Wright S I 2000 *Texture and Anisotropy. Preferred Orientations in Polycrystals and Their Effect on Materials Properties* 2nd Paperback edn, ed U F Kocks, C N Tomé and H-R Wenk (Cambridge: Cambridge University Press) chapter 5, pp 178–238
[55] Burgers W G 1934 *Physica* **1** 561–86
[56] Speziale S, Lonardelli I, Miyagi L, Pehl J, Tommaseo C E and Wenk H-R 2006 *J. Phys. Condens. Matter* **18** S1007–20
[57] Merkel M, Kubo A, Miyagi L, Speziale S, Duffy T S, Mao H-K and Wenk H-R 2006 *Science* **311** 644–6
[58] Wenk H-R, Ischia G, Nishiyama N, Wang Y and Uchida T 2005 *Phys. Earth Planet. Inter.* **152** 191–9
[59] Liu J, Li X D and Li Y C 2002 *J. Phys. Condens. Matter* **14** 10505–9
[60] Dubrovinskaia N and Dubrovinsky L S 2003 *Rev. Sci. Instrum.* **74** 3433–7
[61] Dubrovinsky L S, Saxena S K and Lazor P 1997 *Geophys. Res. Lett.* **24** 1835–8
[62] Dubrovinsky L S, Dubrovinskaia N, Annesten H, Hålenius H and Harryson H 2001 *Eur. J. Mineral.* **13** 857–61
[63] Ming L C and Bassett W A 1974 *Rev. Sci. Instrum.* **45** 1115–8
[64] Burnley P C and Green H W 1989 *Nature* **338** 753–6
[65] Poirier J P 1981 *Phys. Earth Planet. Inter.* **26** 179–87
[66] Larson B C, Yang W, Ice G E, Budal J D and Tischler J Z 2002 *Nature* **415** 887–90
[67] Kocks U F and Mecking H 2003 *Prog. Mater. Sci.* **48** 171–273
[68] Gottstein G 2002 *Proc. ICOTOM 13; Mater. Sci. Forum* **408–412** 1–24
[69] Novikov N V, Polotnyak S B, Shvedov L K and Levitas V I 1999 *J. Superhard Mater.* **21** 36–48
[70] Levitas V I 2004 *Phys. Rev.* B **70** 184118
[71] Wenk H-R, Speziale S, McNamara A K and Garnero E J 2006 *Earth Planet. Sci. Lett.* **245** 302–14

Phys Chem Minerals (2007) 34:679–686
DOI 10.1007/s00269-007-0182-6

ORIGINAL PAPER

Lattice preferred orientation in $CaIrO_3$ perovskite and post-perovskite formed by plastic deformation under pressure

Ken Niwa · Takehiko Yagi · Kenya Ohgushi · Sébastien Merkel · Nobuyoshi Miyajima · Takumi Kikegawa

Received: 7 November 2006 / Accepted: 30 July 2007 / Published online: 31 August 2007

Abstract Lattice preferred orientations (LPO) developed in perovskite and post-perovskite structured $CaIrO_3$ were studied using the radial X-ray diffraction technique combined with a diamond anvil cell. Starting materials of each phase were deformed from 0.1 MPa to 6 GPa at room temperature. Only weak LPO was formed in the perovskite phase, whereas strong LPO was formed in the post-perovskite phase with an alignment of the (010) plane perpendicular to the compression axis. The present result suggests that the (010) is a dominant slip plane in the post-perovskite phase and it is in good agreement with the crystallographic prediction, dislocation observations via transmission electron microscopy, and a recent result of simple shear deformation experiment at 1 GPa–1,173 K. However, the present result contrasts markedly from the results on $MgGeO_3$ and $(Mg,Fe)SiO_3$, which suggested that the (100) or (110) is a dominant slip plane with respect to the post-perovskite structure. Therefore it is difficult to discuss the behavior of the post-perovskite phase in the Earth's deep interior based on existing data of $MgGeO_3$, $(Mg,Fe)SiO_3$ and $CaIrO_3$. The possible sources of the differences between $MgGeO_3$, $(Mg,Fe)SiO_3$ and $CaIrO_3$ are discussed.

Keywords Post-perovskite · $CaIrO_3$ · High-pressure · Lattice preferred orientation

K. Niwa (✉) · T. Yagi · K. Ohgushi
Institute for Solid State Physics, University of Tokyo, Kashiwa 277-8581, Japan
e-mail: niwa@issp.u-tokyo.ac.jp

S. Merkel
Laboratoire de Structure et Propriétés de l'Etat Solide UMR CNRS 8008, Université des Sciences et Technologies de Lille, Bâtiment C6, 59655 Villeneuve d'Ascq, France

N. Miyajima
Bayerisches Geoinstitut, Universität Bayreuth, 95440 Bayreuth, Germany

T. Kikegawa
Photon Factory, KEK, Tsukuba, Ibaraki 305-0801, Japan

Introduction

Since the discovery of a "post-perovskite" phase in $MgSiO_3$ (Murakami et al. 2004; Oganov and Ono 2004), numerous studies have been conducted to explain the characteristic properties of the D″ layer assuming the existence of this phase at the bottom of the lower mantle. Based on theoretical calculations, strong elastic anisotropy is expected to exist in the post-perovskite phase of $MgSiO_3$ (Iitaka et al. 2004; Tsuchiya et al. 2004). Therefore if lattice preferred orientation (LPO) is formed in this phase in the D″ layer, many features of seismic observations, which were difficult to understand so far (e.g., Ritsema et al. 1998; Lay et al. 1998), can then be explained.

The post-perovskite phase is regarded as having a layered structure formed by the stacking of two different layers in a [010] direction and it has been suggested that the (010) plane would be the most favorable slip plane (Murakami et al. 2004; Iitaka et al. 2004; Carrez et al. 2007). Recently, Merkel et al. (2006, 2007) made radial X-ray diffraction experiments using diamond anvil cell on $MgGeO_3$ and $(Mg,Fe)SiO_3$ with the post-perovskite structure and observed very similar LPOs in both materials. Unlike the above crystallographic expectation for the slip plane in the post-perovskite structure, Merkel et al. (2006, 2007) found that [100] or [110] became parallel to the compression axis and concluded that either the (100) plane,

the (110) plane, or both are the most dominant slip planes in this structure. These studies were made at above 100 GPa and it is not clear if the results represent the deformation fabric because usually little deformation of the sample occurs in this pressure range. Moreover, since the slip system of crystal might be a complicated property governed not only by the crystal structure but also by various factors such as pressure, temperature and the nature of bonding, it is necessary to study various materials under wide P-T conditions for the discussion of the Earth's deep interior.

$CaIrO_3$ is known as a prototype for the post-perovskite structure. There are two different phases in $CaIrO_3$; one is a perovskite phase, which is stable at low pressure and high temperature while the other is a post-perovskite phase, which is stable at high pressure and low temperature (Hirose and Fujita 2005). All silicates or germanates with the post-perovskite structure formed under high pressure amorphize on release of pressure but the post-perovskite phase of $CaIrO_3$ can be recovered at ambient conditions. This is quite useful for the study of its plastic properties because we can use transmission electron microscopy (TEM) to directly examine the dislocations in the sample. Miyajima et al. (2006) have studied the dislocations of the post-perovskite phase of $CaIrO_3$ recovered from high pressure and temperature synthesis experiments and concluded that the (010) plane would be the most favorable slip plane for deformation. Yamazaki et al. (2006) made simple shear deformation experiment on post-perovskite type $CaIrO_3$ at around 1 GPa and 1,173 K using a modified Griggs-type apparatus and reported that [100] (010), which means that the (010) and [100] is a slip plane and slip direction, respectively, is a dominant slip system. The results of Miyajima et al. (2006) and Yamazaki et al. (2006) on $CaIrO_3$ are in good agreement with the crystallographic prediction for the slip plane in the post-perovskite structure. On the other hand, the studies on $MgGeO_3$ and $(Mg,Fe)SiO_3$ show marked difference from above crystallographic prediction.

In the present study, we have carried out radial X-ray diffraction (Merkel et al. 2002) experiments on both perovskite and post-perovskite phases of $CaIrO_3$ which were deformed by the uniaxial compression in a diamond anvil cell. LPOs of the both phases formed by the plastic deformation and lattice strain under the uniaxial stress field were measured. These results will provide useful information for the discussion of anisotropy in the D″ layer.

Experiment

Starting materials were synthesized from a mixture of CaO and IrO_2 to obtain stoichiometric $CaIrO_3$ with perovskite and post-perovskite phase using a cubic-anvil type high-pressure apparatus. Because, when this material is synthesized at atmospheric pressure, it is difficult to obtain a single phase but by synthesizing it under appropriate high-pressure conditions we can easily make each phase as a single phase. Synthesis conditions were at around 2 GPa–1,550 K and at around 4 GPa–1,450 K, for perovskite and post-perovskite, respectively, based on our pressure and temperature calibrations. This temperature for perovskite phase was about 200 K lower than its stability field ($T > 1{,}740$ K at 2 GPa) reported by Hirose and Fujita (2005). Our synthesis experiments were made without using thermocouple and the temperature was estimated from the input power. Slight difference of the heater design might have affected the efficiency and temperature distribution in the sample chamber. Temperatures measured during laser heating have large uncertainty as well. Combination of all these effects may have lead to the discrepancy of the temperature conditions but we have successfully made a single phase of each phase with the orthorhombic cell parameters $a = 5.348(1)$ Å, $b = 5.592(1)$ Å, $c = 7.618(1)$ Å, and $V = 229.7(1)$ Å^3 for perovskite (space group: *Pbnm*) and $a = 3.147(1)$ Å, $b = 9.863(2)$ Å, $c = 7.299(1)$ Å, and $V = 226.5(2)$ Å^3 for post-perovskite (space group: *Cmcm*). Each of the recovered samples was ground and then placed in a hole of an "X-ray transparent gasket", which is made of a combination of amorphous boron and Kapton sheet (Merkel and Yagi 2005). X-ray experiments were carried out at BL13A of the Photon Factory, KEK, Tsukuba. Compression experiments were made up to about 6 GPa at room temperature. The hole, initially 200 μm in diameter and 200 μm in height, was filled with a sample together with a few grains of ruby chips, which worked as a pressure marker. The assembly was then compressed using diamond anvils with a culet diameter of 600 μm and powder X-ray diffraction experiments were performed with increasing pressure. In the radial diffraction experiments, a very thin X-ray beam of about 30 μm in diameter with an energy of about 30 keV ($\lambda = 0.4265$ Å) was irradiated to the sample perpendicular to the compression axis of the diamond anvil. Thickness and diameter of the sample under pressure was measured from the X-ray transmission image of the sample (Merkel et al. 2002). For the post-perovskite sample, axial diffraction measurements were also made, in which the X-ray beam was irradiated along the compression axis. Diffracted X-rays were recorded using an imaging plate and a typical exposure time was 10 min. Pressures were measured using ruby fluorescence technique (Mao et al. 1986). Since the powdered sample was directly compressed without using pressure medium, relatively large pressure gradient was formed from the center to the margin of the sample chamber. The pressure gradient in the sample chamber was

Phys Chem Minerals (2007) 34:679–686 681

estimated from a few ruby chips distributed in the sample chamber. At the margin, the pressure was about 20% lower compared to the center of the sample.

In the radial diffraction experiments, the observed diffraction patterns were cut into every 10° of azimuthal angle (δ), which is an angle defined by the incoming and diffracted X-ray, on the imaging plate and integrated using Fit2D software (Hammersley 1997). The $\delta = 0°$ and 90° correspond to the direction of compression axis and perpendicular to it, respectively. The background was subtracted from the diffraction profile and then individual peaks were fitted by the Ps-Voigt function to determine the peak intensity and the 2θ value. The χ, which is the angle between the diffraction plane normal and the compression axis, is calculated from

$$\cos\chi = \cos\theta\cos\delta$$

where (θ) and (δ) are the diffraction angle and azimuthal angle, respectively (Merkel et al. 2002).

To evaluate the development of LPO with increasing pressure, the intensity ratio of the horizontal direction ($I_{hor} = I_{\delta=0°}$) to the vertical direction ($I_{ver} = I_{\delta=90°}$) was calculated. To reduce the effect of spotty pattern of the data, the I_{hor} and I_{ver} were obtained by integrating the diffraction pattern of ±20° of each δ value.

Results

Typical 2-D diffraction patterns of the post-perovskite phase are shown in Fig. 1 and examples of the integrated 1-D profiles are shown in Figs. 2 and 3. Figure 2 was obtained from the 6.5(1) GPa pattern of the radial diffraction in Fig. 1a at $\delta = 0°$ and 90° while Fig. 3 was obtained by integrating the whole circle of axial diffraction patterns at each pressure. In powder diffraction using high energy X-ray, crystal planes nearly parallel to the incident X-ray beam give strong peaks. Therefore the diffraction profiles obtained in the axial diffraction geometry are very similar to those in the radial diffraction geometry at $\delta = 90°$, as is clear from Figs. 2 and 3. Because of the low background of the X-ray transparent gasket used in the present study and large scattering factors of the sample, high quality X-ray diffraction patterns were obtained. Variation of the diffraction intensity of selected indices as a function of the χ angle is shown in Fig. 4. The starting sample originally had a needle-like morphology (Miyajima et al. 2006) but it was ground into powder and no preferred orientation was observed when loaded in the sample chamber. By applying load, the sample chamber was squeeze, the crystals were crushed further into fine grains, and porosity became almost zero at 1 GPa. By increasing the pressure, the sample chamber deformed so that it was compressed along the compression axis while enlarged in radial directions and an LPO was formed gradually. As shown in Fig. 4c, a weak LPO was formed in the perovskite phase with the diffraction intensity of the (020) line being slightly stronger at $\chi = 90°$. On the other hand, much stronger LPO was formed in the post-perovskite phase. Two diffraction lines, (020) and (040), showed high intensities at $\chi = 0°$ while two other lines, (002) and (110), showed high intensities at $\chi = 90°$. This LPO was formed gradually with increasing pressure by the deformation of

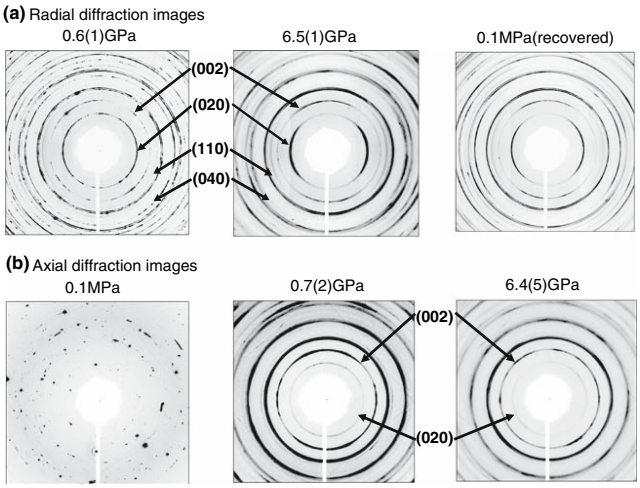

Fig. 1 2-D diffraction images of $CaIrO_3$ with post-perovskite (ppv) phase. Radial diffraction images of $CaIrO_3$ with ppv phase at 0.6(1) GPa, 6.5(1) GPa and 0.1 MPa (recovered), respectively. The horizontal of the diffraction image corresponds to the compression axis. **b** Axial diffraction images of $CaIrO_3$ with ppv phase at 0.1 MPa, 0.7(2) GPa and 6.4(5) GPa, respectively. All patterns were taken at room temperature

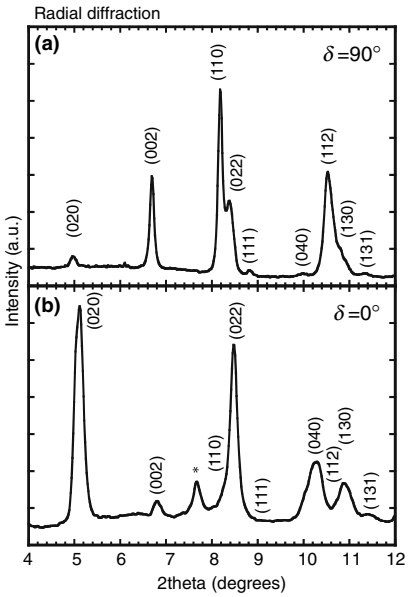

Fig. 2 Integrated 1-D diffraction profiles of the post-perovskite phase observed by radial diffraction at 6.5(1) GPa. **a** azimuthal angle of $\delta = 0°$ and **b** $\delta = 90°$. Diffraction peaks were labeled with miller indices of the post-perovskite phase. The *asterisk* indicates the diffraction from boron-epoxy gasket

the sample. Figure 5 shows the intensity ratio I_{hor}/I_{ver} for (020) as a function of sample thickness and it is clear from this figure that the LPO was developed gradually by the decrease of the sample thickness. In the present study, all deformation experiments were made at room temperature and the pressure was increased from 0.1 MPa to about 6 GPa. The sample was then recovered to ambient condition. The strong preferred orientation of the crystal formed during compression remained unchanged even after recovering the sample to 0.1 MPa.

In the radial diffraction experiments, the X-ray beam was always positioned so that the beam passes through the center of the sample. In axial diffraction experiments, however, the measurements were repeated by shifting the beam from the center to the margin of the sample. No meaningful change of the diffraction pattern was observed depending on the beam position. Moreover, at the margin of the sample chamber, where one dimensional flow of the sample towards the side of the gasket hole occurs, no anisotropic feature of the Debye ring was observed relative to the flow direction. In other words, no clear LPO was observed within the plane perpendicular to the compression axis.

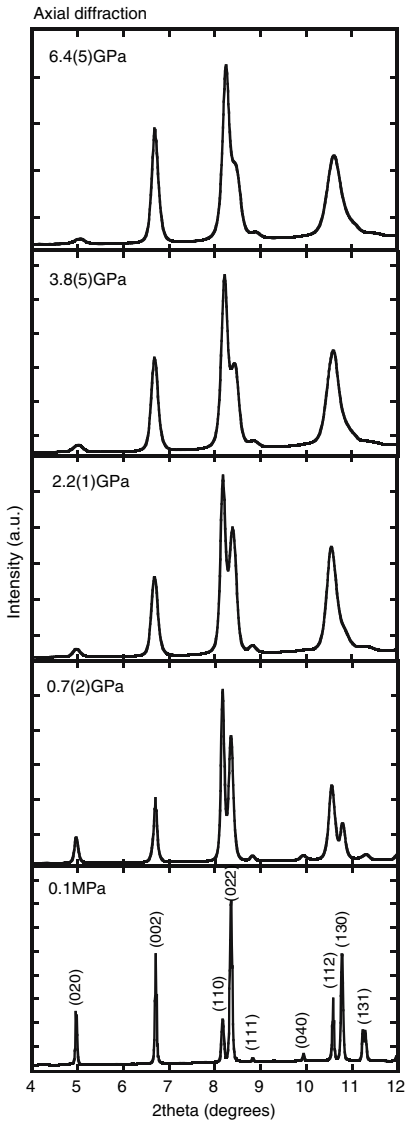

Fig. 3 Integrated 1-D diffraction profiles of post-perovskite phase observed by axial diffraction with increasing pressure. Peaks were labeled with miller indices of the post-perovskite phase

The d-values of two independent peaks (020) and (002) of the post-perovskite phase, measured in axial geometry, are plotted in Fig. 6 as a function of pressure, which was measured by ruby fluorescence technique. The change of

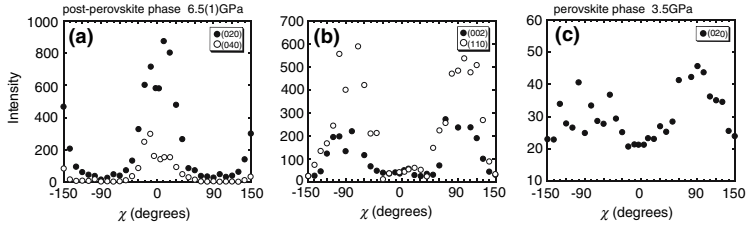

Fig. 4 Diffraction intensities of selected indices observed by radial diffraction for the post-perovskite [at 6.5(1) GPa] and perovskite [at 3.5 GPa] phases as a function of χ angle. **a** *Solid* and *open circles* represent the 020 and 040 diffractions, respectively, for post-perovskite phase. **b** *Solid* and *open circles* represent the 002 and 110 diffractions, respectively, for post-perovskite phase. **c** Intensity of the 020 diffraction for perovskite phase. In all figures, $\chi = 0°$ corresponds to the compression axis

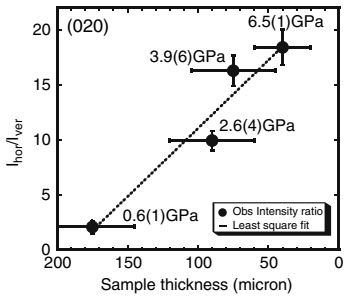

Fig. 5 Intensity ratio (I_{hor}/I_{ver}) of the 020 diffraction of post-perovskite phase as a function of sample thickness. Intensity of I_{hor} and I_{ver} were calculated from the range of $-20 < \delta < 20$ and $70 < \delta < 110$, respectively, and the sample thickness was measured at each pressure from the X-ray radiography of the sample under pressures. *Dashed line* is a guide for eye. It is clear that the LPO developed gradually with the plastic deformation of the sample

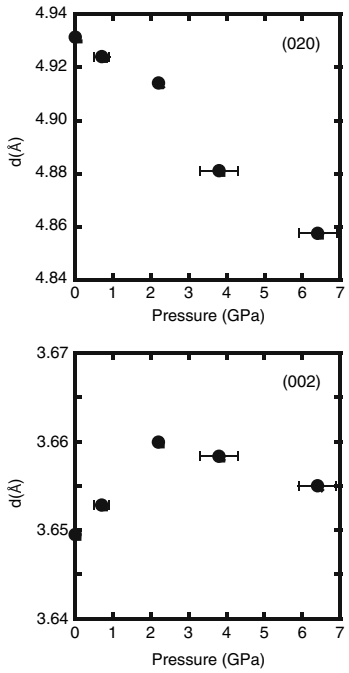

Fig. 6 Pressure dependence of the d-values of 020 and 002 diffractions of post-perovskite phase observed by axial diffraction. Errors in pressure are from the change of pressure values before and after the X-ray experiments and those in the d-values by fitting the spectrum are less than the size of the symbol

the *b* and *c* axes of the orthorhombic unit cell can be directly calculated from these two peaks. It is clear from Fig. 6 that the *b*-axis decreases monotonously with increasing pressure while the *c*-axis increases first up to about 2 GPa and then decreases with increasing pressure.

Discussion

The main purpose of the present study was to clarify the LPO of $CaIrO_3$ formed by plastic deformation under uniaxial stress field. In the present experiments, a very large plastic deformation of the sample chamber occurred during compression. The height of the sample chamber decreased to about 25% of the original value while the diameter of the sample chamber increased to about 150%. In spite of such large deformation, only a weak LPO was formed in the perovskite sample, as shown in Fig. 4c.

On the other hand, much stronger LPO was observed in the post-perovskite sample under the same uniaxial compression. As shown in Fig. 4a and b, the intensities of (020) and (040) are very strong at $\chi = 0°$ while they are almost zero at $\chi = 90°$. For (002) and (110) lines, on the other hand, the intensities are very strong at $\chi = 90°$ while they

are almost zero at $\chi = 0°$. It should be noted that this strong LPO was developed gradually with decreasing the sample thickness, as shown in Fig. 5. The starting sample was a compressed powder and has some porosity but the porosity decreased rapidly at the initial stage of the compression and became almost zero at 1 GPa. Therefore it is clear that the observed LPO was formed by the plastic deformation, not by the reorientation of the crystals during primary compaction. The big difference between the results in the perovskite and post-perovskite phases indicates that LPO formed in the post-perovskite phase reflects a characteristic feature of the post-perovskite structure.

The LPO found in the post-perovskite phase strongly suggests that (010) was the dominant slip plane during plastic deformation. When the (010) plane works as dominant slip plane, it becomes parallel to the flow plane and the *b*-axis is aligned to the compression axis while the *a*-axis and the *c*-axis are aligned perpendicular to it. This explains why the diffraction intensity of (020) and (040) becomes strong at $\delta = 0°$ while that of (002) becomes strong at $\delta = 90°$. Although (200) diffraction is weak and overlapped with other lines, (110) appeared strongly around $\delta = 90°$ because the *b*-axis is more than three times longer than the *a*-axis and the direction normal to (110) plane is close parallel to the *a*-axis.

When the post-perovskite phase was found in $MgSiO_3$, it was expected that the (010) plane would be the easiest slip plane because the post-perovskite phase is basically a sheet structure of BO_6 octahedra stacked along the *b*-axis. The octahedra are connected by edge and corner sharings along the [100] and [001] directions, respectively, and the post-perovskite phase is formed by stacking these layers alternatively with a layer of A cations (Murakami et al. 2004; Iitaka et al. 2004). Results of ab-initio calculations for dislocation cores, based on the Peierls–Nabarro model, also supported that the (010) would be the easiest slip plane in $MgSiO_3$ post-perovskite phase at 120 GPa (Carrez et al. 2007). In the TEM observation of $CaIrO_3$ with the post-perovskite phase, Miyajima et al. (2006) found dislocations with a Burgers vector b = [100] and <*u*0*w*> and concluded that the potential slip system during plastic deformation could be [100] (010). Yamazaki et al. (2006) made a simple shear deformation experiments on $CaIrO_3$ at 1 GPa and 1,173 K and observed that the *a*- and *b*-axes were aligned in the shear direction and perpendicular to it, respectively. Based on this observation, they concluded that dominant slip system of $CaIrO_3$ during plastic deformation is [100] (010) and it is in good agreement with the dislocations observed by Miyajima et al. (2006). Therefore our present result for slip plane is in agreement with these two experimental studies (Miyajima et al. 2006; Yamazaki et al. 2006) and the results of ab-initio calculation (Carrez et al. 2007). Although a strong LPO was formed with an alignment of the (010) plane perpendicular to the compression axis, we could not find clear direction in the (010) plane for which the deformation glide occurs easily. This is probably because in the present experiment the deformation was not a simple shear even at the margin of the sample chamber.

The anomalous expansion of *d* (002) shown in Fig. 6 is interesting and can be understood from the anisotropy of the crystal structure and uniaxial compression of the present experiment. In this structure, IrO_6 octahedra are connected by corner sharing and are extended in the direction of the *c*-axis, forming zigzag chains in the *b*–*c* plane. Therefore, if the crystals are aligned so that the *b*-axis is compressed uniaxially, it is likely that this zigzag chain will be straightened and expanded along the *c*-axis. Recently, Martin et al. (2007) made compression experiments of $CaIrO_3$ with post-perovskite structure from 0.3 to 29 GPa and, contrary to our result, reported smooth compression of all axes. It is reasonable because they used NaCl as a pressure transmitting medium and heated the sample by laser after each increment of the pressure. In such condition, uniaxial stress is annealed and no strong preferred orientation of the crystal is formed.

Merkel et al. (2006, 2007) reported a completely different behavior of the post-perovskite phase using $MgGeO_3$ and $(Mg,Fe)SiO_3$. They observed that both (020) and (002) diffraction intensities became strong in the direction perpendicular to the compression axis and concluded that the planes close to (100) were aligned perpendicular to the compression axis. Based on this result, and in agreement with the first principles calculation by Oganov et al. (2005), they concluded that planes near (100) or (110) were dominant slip planes in the post-perovskite phase. It is known that the slip system of olivine changes systematically with pressure, temperature, and strain rate (e.g., Zhang and Karato 1995). On the other hand, in the crystals with a distinct layered structure such as graphite, hexagonal BN and mica, the major slip system is the same, even though the chemical composition is different. Therefore we expected that the behavior of $MgGeO_3$, $(Mg,Fe)SiO_3$ and $CaIrO_3$ would be very similar. They are in fact found to be quite different and there are several possibilities to explain this difference.

It is known that even when the structure is the same, if the relative size of the component ions is quite different, the deformation mechanism can change as well (e.g., Poirier and Price 1999). The axial ratios of various oxides with a post-perovskite phase reported so far are summarized in Table 1. It is clear that the axial ratio of the orthorhombic unit cell varies considerably depending on the composition. The *b*/*c* ratio of $CaIrO_3$ is larger compared to other compounds which suggests that the *b*-axis of $CaIrO_3$ is elongated. This conclusion is reversed, however,

Table 1 Unit cell parameters and axial ratios of various oxides with post-perovskite structure

Composition	*a* (Å)	*b* (Å)	*c* (Å)	*b*/*a*	*c*/*a*	*b*/*c*	Condition	Reference
$MgSiO_3$	2.456 (1)	8.042 (1)	6.093 (1)	3.27	2.48	1.31	120 GPa–300 K	Murakami et al. (2004)
$MgGeO_3$	2.613 (1)	8.473 (3)	6.443 (3)	3.24	2.46	1.31	78 GPa–300 K	Hirose et al. (2005)
$MnGeO_3$	2.703 (1)	8.921 (3)	6.668 (1)	3.30	2.46	1.33	72 GPa–1700 K	Tateno et al. (2006)
$CaIrO_3$	3.147 (1)	9.863 (2)	7.299 (1)	3.13	2.31	1.35	1 atm–300 K	This study

if the *b*/*a* is compared, and it is difficult to conclude that the (010) plane of $CaIrO_3$ deforms easily because the *b*-axis is relatively elongated compared to $MgGeO_3$. It is known that the *b*-axis of the post-perovskite phase is more compressible than other axes (Murakami et al. 2004) and theoretical calculations predict that elastic anisotropy changes with compression (Tsuchiya et al. 2004). The present experiments on $CaIrO_3$ were made at a low pressure from 0.1 MPa to 6 GPa while those on $MgGeO_3$ were made in a pressure range from 104 GPa to 130 GPa (Merkel at al. 2006). Oganov et al. (2005) made a theoretical argument to predict the slip plane in post-perovskite structure. If we could compare the γC for (010) and (110) planes of $CaIrO_3$, where γ and C are stacking fault energy and relevant shear elastic constant, respectively, it would be quite useful to test their theory. At this moment, however, the calculation is difficult because of the lack of data for the elastic constants.

Another possibility to explain the difference between our results and those of Merkel et al. (2006, 2007) is that the LPO in $MgGeO_3$ and $(Mg,Fe)SiO_3$ which they reported may not be related to the plastic deformation of the sample. They reported that a strong LPO was formed before the "deformation experiment". Instead, it was formed when the starting material [orthopyroxene-type $MgGeO_3$ and $(Mg,Fe)SiO_3$] was transformed into post-perovskite phase by heating it above 100 GPa. The LPO formed by this process remains unchanged during the subsequent compression to higher pressures. This is conceivable because the thickness of the sample in diamond anvil is very thin at 100 GPa and deformation during the subsequent pressure increase is expected to be very small.

When the powdered sample is directly compressed at room temperature by an opposed anvil apparatus, the sample deforms under strong uniaxial stress field and the LPO is formed. But when the sample is transformed to a high-pressure phase by heating, the differential stress drops considerably (Uchida et al. 1996). Therefore, the LPO observed in $MgGeO_3$ and $(Mg,Fe)SiO_3$ could be related to the LPO of the starting material and to the transition mechanism from the starting material to the post-perovskite phase. Alternatively, it could be related to the lower differential stress or thermal annealing, as Santillan et al. (2006) have reported. They compressed Mn_2O_3 using diamond anvil and have reported that the post-perovskite type phase formed by their experiment had LPO. When it was formed at room temperature, the dominant plane perpendicular to the compression axis was (010) plane but it has changed into (100) and (110) planes after thermal annealing.

Recent theoretical studies for post-perovskite phase of $MgSiO_3$ suggested that seismic anisotropy observed in the D″ layer can be well explained by the slip plane of (110), rather than (010), because it explains by a much smaller degree of preferred orientation (Oganov et al. 2005) and the experimental results of $MgGeO_3$ (Merkel et al. 2006) and $(Mg,Fe)SiO_3$ post-perovskite (Merkel et al. 2007) are in agreement with this theoretical prediction. On the other hand, present study together with the work by Yamazaki et al. (2006) show quite different LPO and indicates that it is dangerous to discuss the Earth's interior based on the above assumption. Because, very recent theoretical calculation (Carrez et al. 2007) suggests that (010) is the easiest slip plane, contrary to the results of Oganov et al. (2005). Moreover, experimentally obtained LPOs in $MgGeO_3$ and $(Mg,Fe)SiO_3$ were formed from the beginning of formation of the post-perovskite phases and these samples have experienced no large deformation. Therefore, in order to make reliable arguments about the D″ layer of the Earth, it is necessary to develop a new experimental methods or devices (e.g., Ma et al. 2006) for "large" deformation experiments of silicate materials expected to exist in the Earth. Alternatively, more systematic studies on the model material are required to clarify the slip system in post-perovskite structure by changing various parameters such as pressure, temperature, chemical composition and strain rate.

Acknowledgments This paper was improved by the constructive comments of two reviewers, J. Ando and anonymous reviewer, and we deeply appreciate their efforts. This work has been performed under the approval of the Photon Factory Program Advisory Committee (Proposal No. 06G047).

References

Carrez P, Ferre D, Cordier P (2007) Implications for plastic flow in the deep mantle from modeling dislocations in $MgSiO_3$ minerals. Nature 446:68–70

Hammersley AP (1997) Fit2D: an introduction and overview. ESRF97HA02T, ESRF Grenoble, France

Hirose K, Fujita Y (2005) Clapeyron slope of the post-perovskite phase transition in $CaIrO_3$. Geophys Res Lett 32:L13313. doi:10.1029/2005GL023219

Hirose K, Kawamura K, Ohishi Y, Tateno S, Sata N (2005) Stability and equation of state of $MgGeO_3$ post-perovskite phase. Am Mineral 90:262–265

Iitaka T, Hirose K, Kawamura K, Murakami M (2004) The elasticity of the $MgSiO_3$ post-perovskite phase in the Earth's lowermost mantle. Nature 430:442–445

Lay T, Williams Q, Gamero EJ (1998) The core-mantle boundary layer and deep earth dynamics. Nature 392:461–468

Ma Y, Selvi E, Levitas VI, Hashemi J (2006) Effect of shear strain on the α-ε phase transition of iron: a new approach in the rotational diamond anvil cell. J Phys Condens Matter 18:S1075–S1082

Mao HK, Xu J, Bell PM (1986) Calibration of ruby pressure gauge to 800 kbar under quasi-hydrostatic conditions. J Geophys Res 91:4673–4676

Martin CD, Chapman KW, Chupas PJ, Prakapenka V, Lee PL, Shastri SD, Parise JB (2007) Compression, thermal expansion, structure, and instability of $CaIrO_3$, the structure model of $MgSiO_3$ post-perovskite. Am Mineral 92:1048–1053

Merkel S, Yagi T (2005) X-ray transparent gasket for diamond anvil cell high pressure experiments. Rev Sci Instrum 76:046109

Merkel S, Wenk HR, Shu J, Shen G, Gillet P, Mao HK, Hemley RJ (2002) Deformation of polycrystalline MgO at high pressures of the lower mantle. J Geophys Res 107:2271. doi:10.1029/2001JB000920

Merkel S, Kubo A, Miyagi L, Speziale S, Duffy TS, Mao HK, Wenk HR (2006) Plastic deformation of $MgGeO_3$ post-perovskite at lower mantle pressures. Science 311:644–646

Merkel S, McNamara AK, Kubo A, Speziale S, Miyagi L, Meng Y, Duffy TS, Wenk HR (2007) Deformation of $(Mg,Fe)SiO_3$ post-perovskite and D″ anisotropy. Science 316:1729–1732

Miyajima N, Ohgushi K, Ichihara M, Yagi T, Frost DJ (2006) Crystal morphology and dislocation microstructure of $CaIrO_3$: a TEM study of an anologue of the $MgSiO_3$ post-perovskite phase. Geophys Res Lett 33:L12302. doi:10.1029/2005GL025001

Murakami M, Hirose K, Kawamura K, Sata N, Ohishi Y (2004) Post-perovskite phase transition in $MgSiO_3$. Science 304:855–858

Oganov AR, Ono S (2004) Theoretical and experimental evidence for a post-perovskite phase of $MgSiO_3$ in Earth's D″ layer. Nature 430:445–448

Oganov AR, Martonak R, Laio A, Raiteri P, Parrinello M (2005) Anisotropy of Earth's D″ layer and stacking faults in the $MgSiO_3$ post-perovskite phase. Nature 438:1142–1144

Poirier JP, Price GD (1999) Primary slip system of ε-iron and anisotropy of the Earth's inner core. Phys Earth Planet Inter 110:147–156

Ritsema J, Lay T, Garnero EJ (1998) Seismic anisotropy in the lowermost mantle beneath the Pacific. Geophys Res Lett 25:1229–1232

Santillan J, Shim SH, Shen G, Prakapenka VB (2006) High-pressure phase transition in Mn_2O_3: application for the crystal structure and preferred orientation of the $CaIrO_3$ type. Geophys Res Lett 33:L15307. doi:10.1029/2006GL026423

Tsuchiya T, Tsuchiya J, Umemoto K, Wentzcovitch RM (2004) Elasticity of post-perovskite $MgSiO_3$. Geophys Res Lett 31:L14603. doi:10.1029/2004GL020278

Tateno S, Hirose K, Sata N, Ohishi Y (2006) High-pressure behavior of $MnGeO_3$ and $CdGeO_3$ perovskites and the post-perovskite phase transition. Phys Chem Miner 32:721–725

Uchida T, Funamori N, Ohtani T, Yagi T (1996) Differential stress of MgO and Mg_2SiO_4 under luniaxial stress field. In: High pressure science and technology, World Scientific, London, pp 183–185

Yamazaki D, Yoshino T, Ohfuji H, Ando J, Yoneda A (2006) Origin of seismic anisotropy in the D" layer inferred from shear deformation experiments on post-perovskite phase. Earth Planet Sci Lett 252:372–378

Zhang S, Karato S (1995) Lattice preferred orientation of olivine deformed in simple shear. Nature 375:774–777

Physics of the Earth and Planetary Interiors 174 (2009) 159–164

Contents lists available at ScienceDirect

Physics of the Earth and Planetary Interiors

journal homepage: www.elsevier.com/locate/pepi

Diamond anvil cell deformation of $CaSiO_3$ perovskite up to 49 GPa

Lowell Miyagi[a], Sébastien Merkel[b,*], Takehiko Yagi[c], Nagayoshi Sata[d], Yasuo Ohishi[e], Hans-Rudolf Wenk[a]

[a] Department of Earth and Planetary Science, University of California, Berkeley, CA 94720, United States
[b] Laboratoire de Structure et Propriétés de l'Etat Solide, CNRS, Université des Sciences et Technologies de Lille, 59655 Villeneuve d'Ascq, France
[c] Institute for Solid State Physics, University of Tokyo, Kashiwanoha 5-1-5, Kashiwa, Chiba 277-8581, Japan
[d] Institute for Research on Earth Evolution, Japan Agency for Marine-Earth Science and Technology, Natsushima-cho, Yokosuka, Kanagawa 237-0061, Japan
[e] Japan Synchrotron Radiation Research Institute, Mikazuki-cho, Sayo-gun, Hyogo 679-5198, Japan

ARTICLE INFO

Article history:
Received 27 September 2007
Received in revised form 7 April 2008
Accepted 30 May 2008

Keywords:
Plastic deformation
High pressure
$CaSiO_3$ perovskite
Slip
Strength
Plasticity

ABSTRACT

Radial X-ray diffraction measurements are performed on $CaSiO_3$ perovskite between 25.5 and 49.3 GPa at 300 K. The Rietveld method is used to extract quantitative texture and stress information. We find some mismatches in lattice strains evaluated in the Rietveld method with variations of *d*-spacings for 2 0 0 and 2 1 0 over-estimated while those for 1 1 1 are under-estimated and attribute it to the effect of plastic deformation. The differential stress supported by $CaSiO_3$ perovskite in this study is approximately twice as large as previous measurements and the ratio of differential stress to shear modulus t/G varies between 5.4% and 7.2% between 25 and 49 GPa. The sample displays preferred orientation of the $\{1\,0\,0\}$ planes perpendicular to the compression direction, compatible with slip on $\{1\,1\,0\}\langle 1\,\bar{1}\,0\rangle$.

1. Introduction

$CaSiO_3$ perovskite is believed to be the major calcium rich phase of the transition zone and lower mantle (Fiquet, 2001; Ricard et al., 2005). Based on laboratory experiments, thermodynamical models, and considerations on the chemical composition of the mantle it is thought to be the third most abundant mineral in the lower mantle, accounting for about 7 wt% of the average composition and up to 20 wt% in subducted slabs (Fiquet, 2001; Ricard et al., 2005; Perrillat et al., 2006). Despite its importance, little is know about this material and its mechanical properties, in large because $CaSiO_3$ is not quenchable to ambient conditions. Previous studies on both the stable structure of $CaSiO_3$ perovskite and its elastic properties have yielded varied results. Early experimental studies reported a cubic unit cell (Liu and Ringwood, 1975; Mao et al., 1989; Tamai and Yagi, 1989). However, first principles calculations predict that lower symmetry, tetragonal or even orthorhombic, structures should be stable (Stixrude et al., 1996; Akber-Knutson et al., 2002; Caracas et al., 2005; Adams and Oganov, 2006; Li et al., 2006b). The calculated structural distortions and energy differences between these structures are small and it is therefore difficult to discern the stable structure (Caracas et al., 2005). Recently, using high-resolution synchrotron X-rays, Shim et al. (2002) reported a lower symmetry structure, leading them to propose a tetragonal unit cell. This result was later confirmed by further experimental work (Ono et al., 2004; Kurashina et al., 2004). According to the latest results, the stable structure of $CaSiO_3$ perovskite under ambient temperature is tetragonal with a phase transition to a cubic structure above 490–580 K in the 27–72 GPa pressure range (Komabayashi et al., 2007). Studies of the elastic constants of $CaSiO_3$ are limited to theoretical work (Karki and Crain, 1998; Li et al., 2006a) and to date no direct measurements of the elastic constants have been published.

The mechanical properties of high-pressure minerals can be studied using radial X-ray diffraction in the diamond anvil cell (DAC) (Merkel et al., 2002). In those experiments, a polycrystalline sample is confined under non-hydrostatic stress in a DAC. The elastic deformation of the crystals is expressed in changes in *d*-spacings measured on the diffraction images which can be used to estimate the differential stress supported by the sample and provide a lower bound to the yield strength. Plastic deformation by dislocation glide and mechanical twinning produces rotations of crystals and lattice preferred orientation (LPO) which causes intensity variations along the Debye rings. This can be used to infer slip systems and to understand the development of aggregate anisotropy. Radial diffraction studies on the strength of $CaSiO_3$ between 19 and 65 GPa have been performed before (Shieh et al., 2004) but no texture analysis

* Corresponding author. Tel.: +33 3 20 43 46 86; fax: +33 3 20 43 65 91.
E-mail address: sebastien.merkel@univ-lille1.fr (S. Merkel).

0031-9201/$ – see front matter © 2008 Elsevier B.V. All rights reserved.
doi:10.1016/j.pepi.2008.05.018

was made. In a previous paper (Miyagi et al., 2006), we presented texture and stress analysis using the Rietveld method with data measured on a single image at 49.3 GPa. Here, we report the full analysis of this experiment with results on the differential stress and development of LPO in $CaSiO_3$ deformed in a DAC from 25.5 to 49.3 GPa.

2. Experiment

Starting material of $CaSiO_3$ wollastonite, ground to a fine powder and mixed with amorphous boron to serve as laser absorber, was loaded into an 80 μm hole in an amorphous boron-epoxy gasket supported by a kapton confining ring (Merkel and Yagi, 2005). Starting thickness of the amorphous boron-epoxy insert was 40 μm with an outer diameter of 400 μm. The sample was compressed with 350 μm diameter culet flat diamonds in a laser heated diamond anvil cell with large openings to allow radial diffraction. The starting material was initially compressed to a pressure of about 20 GPa. At this pressure, the phase transformation to the perovskite phase was induced by single-sided heating with a focused yttrium-aluminum-garnet laser.

Pressure was then increased in six steps up to 49.3 GPa at 300 K. Angle-dispersive X-ray diffraction spectra were collected in radial geometry with a 2000 × 2000 pixels Rigaku R-AXIS IV imaging plate equipped with online reader at beamline BL10XU of SPring-8 using a monochromatic incident X-ray beam (wavelength 0.412 Å) of 20 μm in diameter. The incident X-ray beam was perpendicular to the compression direction and exposure time was about 15 min. Sample to detector distance (447.6 mm) and detector tilt were calibrated with a CeO_2 standard taken prior to the experiment. During the reading process in this detector, the imaging plate is rotated within the detector. This results in a shift of the position of the beam center between exposures. In order to accommodate this shift, the direct beam was exposed briefly at the beginning of each exposure and used for beam center calibration.

3. Results

A total of seven diffraction images were taken at 20, 25.5, 29.5, 32.1, 34.8, 43.7, and 49.3 GPa. Of these seven patterns two were unusable due to poor diffraction quality (20 and 34.8 GPa) and were discarded. Representative diffraction spectra are shown in Fig. 1. They show considerable variations in peak position with azimuth angle δ and systematic intensity variations with δ. Variations of peak positions with orientation are related to stress while the variations of diffraction intensity are indicative of LPO in the sample.

Diffraction images were quantitatively analyzed for texture and lattice strains using the Rietveld method as implemented in the software package MAUD (Lutterotti et al., 1999). Details of the analysis are given in Miyagi et al. (2006) and consequently only relevant features will be discussed here.

Data was fit using a cubic $Pm\bar{3}m$ structure (Finger and Hazen, 1991). Although there may be some minor peak splitting, data quality was too poor to resolve any deviation from the cubic structure, and the data could not be fitted with a tetragonal or orthorhombic structure. The hydrostatic lattice parameter a obtained from the refinement was converted to pressures using a third-order Birch-Murnaghan equation of state for $CaSiO_3$ perovskite and values for K_0 and K_0' from Shim et al. (2000).

The variations of peak positions with azimuth were fit using the single crystal elastic constants of Karki and Crain (1998) and the Moment Pole Stress model (Matthies, 1996; Matthies et al., 2001) assuming a 50% Reuss condition. In this analysis, we assumed that

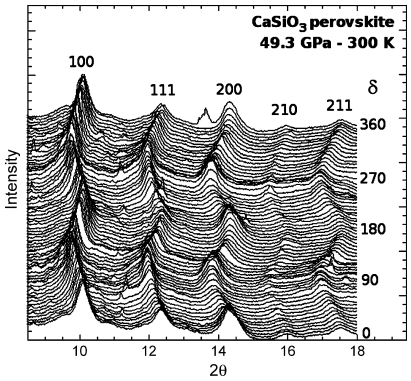

Fig. 1. Diffraction spectra extracted from the diffraction pattern at 49.3 GPa for azimuth angles δ between 0° and 360° with 5° intervals. Diffraction lines from the $CaSiO_3$ perovskite sample are indicated on the figures. Variations of diffraction intensities and peak positions with orientation are related to LPO and stress in the sample, respectively. Unlabelled peak at $2\theta \approx 13.5°$ and $\delta = 360°$ is a diamond spot.

the deviatoric component of the stress applied to the sample was

$$\sigma = \begin{bmatrix} \sigma_{11} & 0 & 0 \\ 0 & \sigma_{22} & 0 \\ 0 & 0 & \sigma_{33} \end{bmatrix} \quad (1)$$

with $\sigma_{11} = \sigma_{22}$, and $\sigma_{33} = -2\sigma_{11}$. The differential stress component t was then calculated using

$$t = \sigma_{33} - \sigma_{11}. \quad (2)$$

For comparison with other experiments, we also calculated the angle ψ between the maximum stress direction and the normal to the diffracting plane (e.g. Singh et al., 1998) using

$$\cos\psi = \cos\theta\cos\delta, \quad (3)$$

where θ is the diffraction angle and δ is the azimuth on the image plate.

After the first calculation of the stress model, we noticed systematic mismatches in peak positions for the calculated model and the data, such that the azimuthal variation of some peaks were over-estimated while others were under-estimated. For instance, Fig. 2 presents a comparison between the d-spacings obtained using single peak fitting techniques and those recalculated in the Rietveld refinement at 49.3 GPa. The d-spacings for the 2 0 0 lines are over-estimated for planes parallel to the compression direction ($\psi \approx 90°$) while those for 1 1 1 are under-estimated at this same orientation. Therefore, we performed new calculations including a refinement of either C_{12} or C_{44}. Both types of refinements equally improved the fit and the results will be presented for the three cases: refinement of t with no refinement of elastic moduli, refinement of t and C_{12}, and refinement of t and C_{44}. In all cases, refinements of t with no elastic moduli provided values between those obtained with C_{12} or C_{44} refined. Therefore, the two stress values obtained C_{12} or C_{44} refined were used to bound the uncertainty in our analysis. We find that the differential stress supported by the sample increases continuously with pressure from a value of 12.1 (±0.8) GPa at 25.5 GPa to 19.0 (±1.5) GPa at 49.3 GPa. Table 1 and Fig. 3 summarize these results.

LPO were fit using the E-WIMW algorithm available in MAUD. Initially, no symmetry was imposed and the texture was refined with the other parameters. Textures were found to be approximately axially symmetric about the compression direction (Miyagi

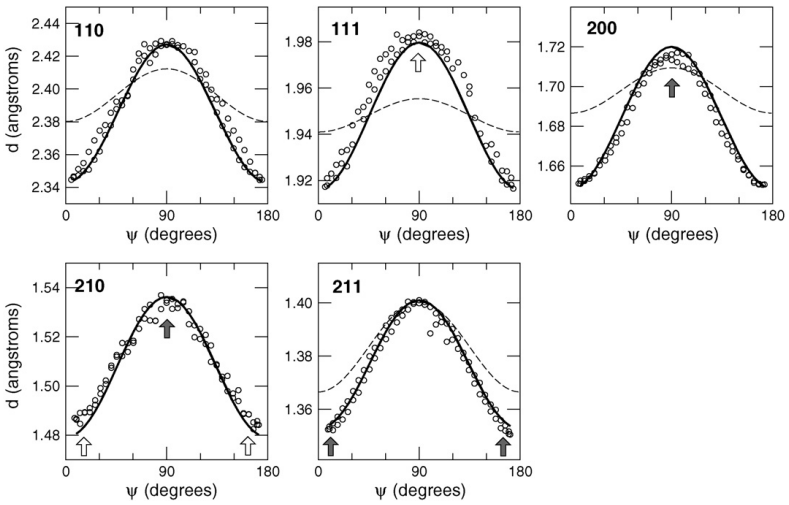

Fig. 2. *d*-Spacings vs. angle between the diffracting plane normal and the maximum stress axis ψ at 49.3 GPa. Open circles were extracted from the diffraction spectra using single peak fitting. Thick solid lines is recalculated from the Rietveld refinement with C_{12} or C_{44} refined. Thin dashed lines are fit to the results at 52 GPa from Shieh et al. (2004). Differences between refinements with no C_{ij} refined, C_{12} refined, or C_{44} refined can not be seen at this scale. White and dark arrows indicate orientations where the peak positions are under- and over-estimated, respectively.

Table 1
Pressure, corresponding elastic moduli C_{11}, C_{12}, and C_{44} (Karki and Crain, 1998), ODF minima and maxima, and differential stresses t fitted to the data

P	C_{11}	C_{12}	C_{44}	Min	Max	t	C_{12} refined		C_{44} refined		$\langle t \rangle$
							t	C_{12}	t	C_{44}	
25.5	554	234	274	0.77	1.38	12.3	11.3	275	12.9	314	12.1 ± 0.8
29.5	583	245	280	0.70	1.43	12.9	10.7	325	14.2	362	12.4 ± 1.7
32.1	601	251	285	0.77	1.53	14.7	14.8	249	14.7	283	14.7 ± 0.1
43.7	681	280	303	0.78	1.65	17.7	18.9	230	16.8	272	16.8 ± 1.0
49.3	712	292	311	0.71	1.61	18.8	20.6	221	17.5	264	17.5 ± 1.5

Table also includes results for differential stresses and elastic moduli for refinements including C_{12} or C_{44}. $\langle t \rangle$ is the final estimate of differential stress based on the results obtained for various hypothesis. Pressures, elastic moduli, and stresses are expressed in GPa, ODF minima and maxima in m.r.d. Note that the refined elastic moduli C_{12} or C_{44} are effective moduli which reproduce the X-ray data and do not directly correspond to single crystal elastic moduli.

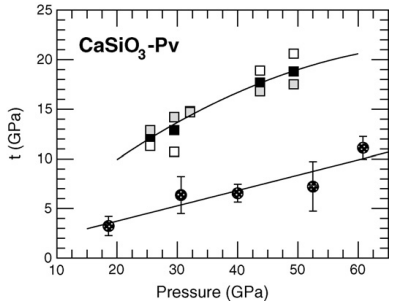

Fig. 3. Differential stress measured in $CaSiO_3$ perovskite. Squares are data from this study calculated using the elastic moduli of Karki and Crain (1998), with no refinement of elastic moduli (black squares), refining C_{12} (white squares), and refining C_{44} (grey squares). Circles are the results from Shieh et al. (2004). Solid lines are guide to eyes through the data.

et al., 2006). The orientation distribution functions (ODF) were therefore reset and fit with cylindrical symmetry about the compression direction imposed. Textures are moderate with the ODF maxima increasing from 1.38 m.r.d. at 25.5 GPa to 1.61 m.r.d. at 49.3 GPa (Table 1). Texture is conveniently represented by an inverse pole figure of the compression direction which shows the relation between crystallographic directions and the compression direction. The inverse pole figures for all pressures are shown in Fig. 4. In all cases, we find a ⟨1 0 0⟩ maximum with a shoulder towards ⟨1 1 0⟩ and a depleted region around ⟨1 1 1⟩.

4. Discussion

4.1. Structure

Data was fit using a cubic $Pm\bar{3}m$ structure although first-principles calculations and recent experiments suggest a lower symmetry (Stixrude et al., 1996; Akber-Knutson et al., 2002; Caracas et al., 2005; Adams and Oganov, 2006; Li et al., 2006b; Shim et al., 2002; Ono et al., 2004; Kurashina et al., 2004; Komabayashi et al., 2007). We did investigate the effect of various non-cubic structures on the refinement, $P4/mmm$, $I4/mcm$, $Pnma$, and $Pbnm$. For

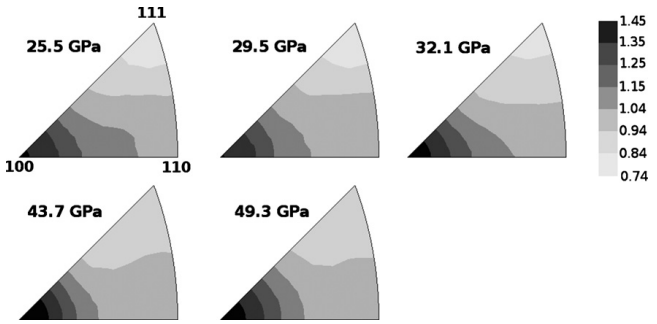

Fig. 4. Inverse pole figure of the compression direction illustrating the LPO in cubic $CaSiO_3$ perovskite compressed in a diamond anvil cell for all pressures measured in this study. Equal area is used and linear contours are expressed in multiples of random distribution.

all cases, it was clear that the cubic structure provided the best match to the data. Consequently, the $Pm\bar{3}m$ structure was retained and used for the refinements. As mentioned before, distortions between the tetragonal and cubic structure are small and it undergoes a phase transition to a cubic structure at higher temperature (Komabayashi et al., 2007). Moreover, the symmetry of the elastic moduli calculated using first-principles methods is consistent with cubic symmetry (Li et al., 2006a). Therefore, it is relevant to use a cubic reference frame to understand and model the plastic behavior of this phase in the mantle.

4.2. Stress

We find some mismatches in peak positions between the calculated model and the data, such that the azimuthal variation of some peaks are over-estimated while others were under-estimated (Fig. 2). Better results are obtained by including a fit of the shear related constants C_{12} and C_{44}, with both refinements equally improving the fit. Still, it can be seen that the amplitude of the variations of d-spacings is not fully accounted for (e.g. 1 1 1, 2 0 0, 2 1 0).

There are several reasons to account for these mismatches. First, we assumed a cubic symmetry and this could have an effect on the stress model. Second, errors in the calculations of elastic moduli we used (Karki and Crain, 1998) could also affect the stress model. However, the variations we observe in the refinement on the elastic moduli (up to 20% for C_{12} and up to 12% for C_{44}) are larger than what is usually expected for first-principles calculations on silicates. Third, it has been shown that errors in the calculation of stress models can occur if there is a small component of shear within the sample or if the axis of maximum compression deviates from the diamond axis (Merkel, 2006). It is most likely that those mismatches are due to yield strength anisotropy. It has been shown that stresses deduced using X-ray diffraction on materials that deform plastically can be drastically different when using different lattice planes (Weidner et al., 2004; Li et al., 2004; Merkel et al., 2006). In particular, Weidner et al. (2004) and Li et al. (2004) demonstrated that, for MgO, stresses deduced from 2 0 0 would be significantly smaller than those deduced from 1 1 1. This is in agreement with our measurements on $CaSiO_3$ perovskite where we over-estimate the amplitude of the variations of d-spacings for 2 0 0 and 2 1 0 while those for 1 1 1 are under-estimated.

Plastic deformation induces errors in X-ray stress measurements that can be difficult to account for. In this study, we decided to use the average stress obtained from the refinements using fixed elastic moduli, with C_{12} refined, and with C_{44} refined. The difference between the values we obtained are on the order of 10% and were used to estimate an error on our measurements (Table 1). In any case, mismatches in the stress model may also induce errors in texture calculation and thus is important to remedy prior to extraction of texture information (Miyagi et al., 2006). It should be noted that the values of C_{12} and C_{44} refined with the X-ray data are empirical and represent effective elastic moduli that can fit our data. They are not directly related to single crystal elastic moduli (Li et al., 2004; Merkel et al., 2006; Antonangeli et al., 2006).

4.3. Strength

By the von Mises yield criterion, the measured differential stress supported by a sample provides a lower bounds estimate for the yield strength. For the case of axial compression this is $t = \sigma_3 - \sigma_1 \leq \sigma_y$, where σ_y is the yield strength. If plastic deformation is achieved then the yield strength is equal to the maximum differential stress. Yield strength in a polycrystal depends on the available slip systems, their critical resolved shear stress (CRSS), and as well as the texture of the sample. Hardening or an increase in the yield strength can also result if the dislocation density of the sample increases (Kocks and Mecking, 2003). It is important to note that strain, strain rate, and pressure cannot be decoupled in our experiment and we must use a general definition of yield strength.

The values of differential stress supported by our sample are about twice as large as those of Shieh et al. (2004) (Fig. 3) and this observation is independent of the assumption used to deduce stress from the X-ray data, as our data shows significantly more variations of d-spacings with orientation (Fig. 2). In DAC experiments, the plastic yield limit is not always reached between the tips of the diamonds (Merkel et al., 2000). Therefore, lower values of differential stress may be obtained. Hardening due to an increase in dislocation density may also result in a higher yield strength and may affect the value of t. In our experiment, the sample was mixed with boron, while Shieh et al. (2004) added platinum to the sample. Platinum may have acted as a softer phase and accommodated some of the strain. It may also coat grains and promote deformation mechanisms such as grain boundary sliding that would prevent $CaSiO_3$ from reaching its yield point. Choice of gasket material may also affect the value of t, as a harder gasket material may support more stress, preventing the sample from reaching the yield point.

In order to compare the strengths of a range of materials, the dimensionless quantity t/G is often used, where t is the differential stress and G is the shear modulus (e.g. Ruoff, 1973; Chua and Ruoff, 1975). In general, this ratio tends to be in the 3–7% range for silicates and less than 3% for metals. Our value for $CaSiO_3$ perovskite is 5.4%

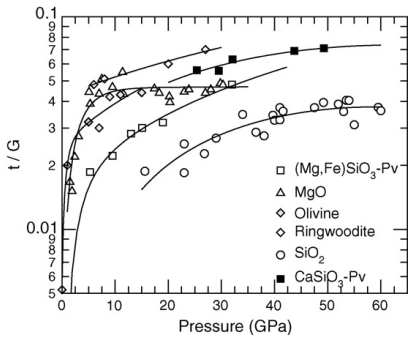

Fig. 5. Ratio of differential stress to shear modulus t/G as a function of pressure obtained in radial diffraction experiments in the DAC. Solid squares are measurements on $CaSiO_3$ perovskite from this study, open squares results for (Mg,Fe)SiO_3 perovskite (Merkel et al., 2003), open triangles results for MgO (Merkel et al., 2002), grey diamonds results for olivine (Uchida et al., 1996), open diamonds results for ringwoodite (Kavner and Duffy, 2001), and open circles results for SiO_2(Shieh et al., 2002). Lines are guides to the eyes through the experimental data.

at 25.5 GPa and becomes as high as 7.2% at 49.3 GPa, in the range of values obtained for other silicates and oxides (Fig. 5).

4.4. Texture

Texture strength increases with pressure and shows no indication of saturation with increasing stress. No change in texture type with pressure increase is observed. In order to interpret our experimental textures, we use the viscoplastic self-consistent polycrystal plasticity model (Lebensohn and Tomé, 1993) to simulate texture evolution in cubic perovskite polycrystal deformed by slip under axial compression. The experimental texture pattern of $CaSiO_3$ perovskite in axial compression is similar to textures obtained for MgO (Merkel et al., 2002), a cubic minerals with low temperature slip systems of $\{1\,1\,0\}\langle 1\,\bar{1}\,0\rangle$. This is the same slip system that has been proposed for cubic perovskites at low temperature (Poirier et al., 1989) and observed at high temperature in $CaTiO_3$(Besson et al., 1996) and $SrTiO_3$(Wang et al., 1993). Consequently, we chose to investigate deformation on these slip systems, as well as other slip systems common in cubic minerals. These include $\{1\,1\,1\}\langle 1\,\bar{1}\,0\rangle$ (the dominant slip system in minerals with fcc structure), $\{1\,1\,0\}\langle 1\,\bar{1}\,1\rangle$ (common in bcc structures), $\{1\,1\,0\}\langle 1\,\bar{1}\,0\rangle$ (MgO), $\{1\,0\,0\}\langle 0\,1\,1\rangle$ (galena), and $\{1\,0\,0\}\langle 0\,0\,1\rangle$ (pyrite). We find that only simulations that favor slip on $\{1\,1\,0\}\langle 1\,\bar{1}\,0\rangle$ produce textures that are very similar to the experimental results. We conclude that $\{1\,1\,0\}\langle 1\,\bar{1}\,0\rangle$ is most likely the dominant slip plane in pseudo-cubic $CaSiO_3$ perovskite.

This is in agreement with previous observations that the texture pattern for $CaSiO_3$ is compatible with dominant slip on $\{1\,1\,0\}\langle 1\,\bar{1}\,0\rangle$ (Miyagi et al., 2006; Fig. 5). It is interesting to note that, for this system, each slip plane and direction has an equivalent and opposite slip plane and direction e.g. $(1\,1\,0)[1\,\bar{1}\,0]$ and $(1\,\bar{1}\,0)[1\,1\,0]$. These equivalent systems have the same Schmid factor and their spins cancel each other. As a result texture does not develop due to shears on this slip system. Slip on this system does, however, induce an orientation dependent change in grain shape which leads to shape dependent reorientation. As texture develops due to grain shape changes, textures are weak at low strains but, at higher strains, grains become more elongated and stronger textures can develop (Wenk, 2000). Indeed, this is consistent with the moderate texture strengths observed here (up to 1.7 m.r.d.) since our deformation geometry only allows an approximate 20% strain (Wenk et al., 2006).

5. Conclusions

We performed radial X-ray diffraction on $CaSiO_3$ perovskite under non-hydrostatic loading between 25.5 and 49.3 GPa and analysed the data using the Rietveld method, as implemented in the software MAUD (Lutterotti et al., 1999). We investigated the effect of various non-cubic structures on the refinement and found that, for all cases, the cubic structure $Pm\bar{3}m$ provided the best match to the data. It should be noted, however, that our sample was highly stressed and that the data quality could have been too poor to resolve the small distortions between the proposed cubic and tetragonal structures (Shim et al., 2002; Komabayashi et al., 2007).

We find some mismatches between lattice strains evaluated in MAUD and the experimental data, with variations of d-spacings for 2 0 0 and 2 1 0 over-estimated while those for 1 1 1 are underestimated. Better results are obtained by including a fit of the shear related constants C_{12} or C_{44}. This is attributed to the effect of plastic deformation on lattice strains, as previously noticed in MgO (Weidner et al., 2004; Li et al., 2004) and cobalt (Merkel et al., 2006).

The differential stress supported by $CaSiO_3$ perovskite in this study is approximately twice as large as previous measurements (Shieh et al., 2004). The ratio of differential stress to shear modulus t/G varies between 5.4% and 7.2% between 25 and 49 GPa. This highlights the importance of insuring that samples reach the plastic yield point when deducing the yield strength of a material. It also indicates that the addition of a second phase, amorphous boron in this work and platinum in that of Shieh et al. (2004), may have a significant effect on measurements of strength.

Our results indicate that, at high pressure and room temperature, significant texture can be induced in $CaSiO_3$ perovskite. We obtained texture patterns with a $\langle 1\,0\,0\rangle$ maximum, a shoulder towards $\langle 1\,1\,0\rangle$, and a depleted region around $\langle 1\,1\,1\rangle$. Comparison with visco-plastic self-consistent modeling indicates that this texture is most likely due to dominant slip on $\{1\,1\,0\}\langle 1\,\bar{1}\,0\rangle$.

Acknowledgements

The authors wish to thank N. Funamori for providing the starting material. The synchrotron radiation experiments were performed at the BL10XU in SPring-8 with the approval of the Japan Synchrotron Radiation Research Institute (JASRI) (Proposal No. 2003B0243-ND2b-np). L.M. acknowledges support from the Carnegie DOE Alliance Center (CDAC). S.M. acknowledges support from the Japanese Society for the Promotion of Science and The Miller Institute for Basic Research in Science at UC Berkeley.

References

Adams, D.J., Oganov, A.R., 2006. Ab initio molecular dynamics study of $CaSiO_3$ perovskite at P–T conditions of earth's lower mantle. Phys. Rev. B 73, 184106.
Akber-Knutson, S., Bukowinski, M.S.T., Matas, J., 2002. On the structure and compressibility of $CaSiO_3$ perovskite. Geophys. Res. Lett. 29, 1034.
Antonangeli, D., Merkel, S., Farber, D.L., 2006. Elastic anisotropy in hcp metals at high pressure and the sound wave anisotropy of the earth's inner core. Geophys. Res. Lett. 33, L24303.
Besson, P., Poirier, J.P., Price, G.D., 1996. Dislocations in $CaTiO_3$ perovskite deformed at high temperature: a transmission electron microscopy study. Phys. Chem. Miner. 23, 337–344.
Caracas, R., Wentzcovitch, R., Price, G.D., Brodholt, J., 2005. $CaSiO_3$ perovskite at lower mantle pressures. Geophys. Res. Lett. 32, 06306.
Chua, J.O., Ruoff, A.L., 1975. Pressure dependence of the yield stress of potassium at low homologous temperature. J. Appl. Phys. 46, 4659–4663.
Finger, L.W., Hazen, R.M., 1991. Crystal chemistry of six-coordinated silicon: a key to understanding the earth's deep interior. Acta Crystallogr. B47, 561–580.

Fiquet, G., 2001. Mineral phases of the Earth's mantle. Z. Kristallogr. 216, 248–271.
Karki, B.B., Crain, J., 1998. First-principles determination of elastic properties of $CaSiO_3$ perovskite at lower mantle pressures. Geophys. Res. Lett. 25, 2741–2744.
Kavner, A., Duffy, T.S., 2001. Strength and elasticity of ringwoodite at upper mantle pressures. Geophys. Res. Lett. 28, 2691–2694.
Kocks, U.F., Mecking, H., 2003. Physics and phenomenology of strain hardening: the fcc case. Prog. Mater. Sci. 48, 171–273.
Komabayashi, T., Hirose, K., Sata, N., Ohishi, Y., Dubrovinsky, L.S., 2007. Phase transition in $CaSiO_3$ perovskite. Earth Planet. Sci. Lett. 260, 564–569.
Kurashina, T., Hirose, K., Ono, S., Sata, N., Ohishi, Y., 2004. Phase transition in al-bearing $CaSiO_3$ perovskite: implications for seismic discontinuities in the lower mantle. Phys. Earth Planet. Inter. 145, 67–74.
Lebensohn, R.A., Tomé, C.N., 1993. A selfconsistent anisotropic approach for the simulation of plastic deformation and texture development of polycrystals: application to zirconium alloys. Acta Metall. Mater. 41, 2611–2624.
Li, L., Weidner, D.J., Brodholt, J., Alfé, D., Price, G.D., Caracas, R., Wentzcovitch, R., 2006a. Elasticity of $CaSiO_3$ perovskite at high pressure and high temperature. Phys. Earth Planet. Inter. 155, 249–259.
Li, L., Weidner, D.J., Brodholt, J., Alfè, D., Price, G.D., Caracas, R., Wentzcovitch, R., 2006b. Phase stability of $CaSiO_3$ perovskite at high pressure and temperature: Insights from ab initio molecular dynamics. Phys. Earth Planet. Inter. 155, 260–268.
Li, L., Weidner, D.J., Chen, J., Vaughan, M.T., Davis, M., Durham, W.B., 2004. X-ray strain analysis at high pressure: Effect of plastic deformation in MgO. J. Appl. Phys. 95, 8357–8365.
Liu, L.-G., Ringwood, A.E., 1975. Synthesis of a perovskite-type polymorph of $CaSiO_3$. Earth Planet. Sci. Lett. 28, 209–211.
Lutterotti, L., Matthies, S., Wenk, H.R., 1999. Maud: a friendly java program for materials analysis using diffraction. Int. U. Crystallogr. Comm. Powder Diffr. Newslett. 21, 14–15.
Mao, H.K., Shen, L.C., Hemley, R.J., Jephcoat, A.P., Wu, Y., 1989. Stability and equation of state of $CaSiO_3$ perovskite to 134 GPa. J. Geophys. Res. 94, 17889–17894.
Matthies, S., 1996. Moment pole figures in residual stress analysis. Textures Microstruct. 25, 229–236.
Matthies, S., Priesmeyer, H.G., Daymond, M.R., 2001. On the diffractive determination of single-crystal elastic constants using polycrystalline samples. J. Appl. Cryst. 34, 585–601.
Merkel, S., 2006. X-ray diffraction evaluation of stress in high pressure deformation experiments. J. Phys.: Condens. Matter 18, S949–S962.
Merkel, S., Hemley, R.J., Mao, H.K., Teter, D.M., 2000. Finite element modeling and ab-initio calculations of megabar stresses in the diamond anvil cell. In: Manghnani, M., Nellis, W.J., Nicol, M.F. (Eds.), Science and Technology of High Pressure Research. University Press (India) Limited, pp. 68–73.
Merkel, S., Miyajima, N., Antonangeli, D., Fiquet, G., Yagi, T., 2006. Lattice preferred orientation and stress in polycrystalline hcp-Co plastically deformed under high pressure. J. Appl. Phys. 100, 023510.
Merkel, S., Wenk, H.R., Badro, J., Montagnac, G., Gillet, P., Mao, H.K., Hemley, R.J., 2003. Deformation of (Mg,Fe)SiO_3 perovskite aggregates up to 32 GPa. Earth Planet. Sci. Lett. 209, 351–360.
Merkel, S., Wenk, H.R., Shu, J., Shen, G., Gillet, P., Mao, H.K., Hemley, R.J., 2002. Deformation of polycrystalline MgO at pressures of the lower mantle. J. Geophys. Res. 107, 2271.
Merkel, S., Yagi, T., 2005. X-ray transparent gasket for diamond anvil cell high pressure experiments. Rev. Sci. Instrum. 76, 046109.
Miyagi, L., Merkel, S., Yagi, T., Sata, N., Ohishi, Y., Wenk, H.R., 2006. Quantitative Rietveld texture analysis of $CaSiO_3$ perovskite deformed in a diamond anvil cell. J. Phys.: Condens. Matter 18, S995–S1005.
Ono, S., Ohishi, Y., Mibe, K., 2004. Phase transition of Ca-perovskite and stability of Al-bearing Mg-perovskite in the lower mantle. Am. Miner. 89, 1480–1485.
Perrillat, J.-P., Ricolleau, A., Daniel, I., Fiquet, G., Mezouar, M., Guignot, N., Cardon, H., 2006. Phase transformations of subducted basaltic crust in the upmost lower mantle. Phys. Earth Planet. Inter. 157, 139–149.
Poirier, J.P., Beauchesne, S., Guyot, F., 1989. Deformation mechanisms of crystals with perovskite structure. In: Navrotsky, A., Weidner, D. (Eds.), Perovskite: A Structure of Great Interest to Geophysics and Materials Science. AGU, Washington, DC, pp. 119–123.
Ricard, Y., Mattern, E., Matas, J., 2005. Synthetic tomographic images of slabs from mineral physics. In: van der Hilst, R.D., Bass, J., Matas, J., Trampert, J., (Eds.), Earth's Deep Mantle: Structure, Composition, and Evolution, vol. 160 of AGU Geophys. Monograph Series. AGU, pp. 283–300.
Ruoff, A.L., 1973. Penultimate static pressure containment considerations and possible application to metallic hydrogen preparation. Adv. Cryog. Eng. 18, 435–440.
Shieh, S., Duffy, T.S., Li, B., 2002. Strength and elasticity of SiO_2 across the stishovite-$CaCl_2$-type structural phase boundary. Phys. Rev. Lett. 89, 255507.
Shieh, S.R., Duffy, T.S., Shen, G., 2004. Elasticity and strength of calcium silicate perovskite at lower mantle pressures. Phys. Earth Planet. Inter. 143–144, 93–105.
Shim, S.H., Duffy, T.S., Shen, G., 2000. The stability and *P–V–T* equation of state of $CaSiO_3$ perovskite in the Earth's lower mantle. J. Geophys. Res. 105, 25955–25968.
Shim, S.H., Jeanloz, R., Duffy, T.S., 2002. Tetragonal structure of $CaSiO_3$ perovskite above 20 GPa. J. Geophys. Res. 29, doi:10.1029/2002GL016148.
Singh, A.K., Balasingh, C., Mao, H.K., Hemley, R.J., Shu, J., 1998. Analysis of lattice strains measured under non-hydrostatic pressure. J. Appl. Phys. 83, 7567–7575.
Stixrude, L., Cohen, R.E., Yu, R., Krakauer, H., 1996. Prediction of phase transition in $CaSiO_3$ perovskite and implications for lower mantle structure. Am. Miner. 81, 1293–1296.
Tamai, H., Yagi, T., 1989. High-pressure and high-temperature phase relations in $CaSiO_3$ and $CaMgSi_2O_6$ and elasticity of perovskite-type $CaSiO_3$. Phys. Earth Planet. Inter. 54, 370–377.
Uchida, T., Funamori, N., Ohtani, T., Yagi, T., 1996. Differential stress of MgO and Mg_2SiO_4 under uniaxial stress field: variation with pressure, temperature, and phase transition. In: Trzeciatowski, W.A. (Ed.), High Pressure Science and Technology. World Scientific Publishing, Singapore, pp. 183–185.
Wang, Z., Karato, S., Fujino, F., 1993. High temperature creep of single crystal strontium titanate ($SrTiO_3$): a contribution to creep systematics in perovskites. Phys. Earth Planet. Inter. 79, 299–312.
Weidner, D.J., Li, L., Davis, M., Chen, J., 2004. Effect of plasticity on elastic modulus measurements. Geophys. Res. Lett. 31, 06621.
Wenk, H.R., 2000. Plasticity modeling in minerals and rocks. In: Kocks, U.F., Tomé, C.N., Wenk, H.R. (Eds.), Texture and Anisotropy: Preferred Orientations in Polycrystals and Their Effect on Materials Properties, second ed. Cambridge University Press, Cambridge, pp. 560–596, Chapter4.
Wenk, H.R., Lonardelli, I., Merkel, S., Miyagi, L., Pehl, J., Speziale, S., Tommaseo, C.E., 2006. Deformation textures produced in diamond anvil experiments, analysed in radial diffraction geometry. J. Phys.: Condens. Matter 18, S933–S947.

Sixième partie

Articles : État de l'art et applications géophysiques

REPORTS

alkene precursors. Moreover, if a precursor with more than one C=C bond were used, two or more stereogenic centers could be introduced in one step with absolute stereocontrol. Because (*E*)- and (*Z*)-olefins are converted to products of opposite configuration, the relative stereochemistry can be controlled by proper choice of the geometry of the individual C=C bonds.

In this way, to take one example, the stereocenters in the terpenoid side chain of tocopherols could be introduced stereoselectively (Fig. 3), providing an attractive route to these biologically and economically important fat-soluble antioxidants, which are the main components of vitamin E. Despite considerable effort in various laboratories, no commercially viable stereoselective total synthesis of (*RRR*)-tocopherols has been developed so far (*25*).

To demonstrate the potential of our catalysts for transformations of this type, we studied the hydrogenation of γ-tocotrienyl acetate **16** (Fig. 4). In this reaction, which involves hydrogenation of three C=C bonds, two new stereogenic centers are created and, therefore, four stereoisomers can be formed. Because the two prochiral double bonds are both (*E*)-configured, the sense of asymmetric induction at the two reaction sites is expected to be the same, leading either to the (*RR*)- or (*SS*)-configuration depending on the absolute configuration of the catalyst. The influence of the stereogenic center present in the substrate is very weak, as shown by hydrogenation with an achiral iridium catalyst [ligand **2** (R^1 = H, R^2 = Ph); face selectivity, 59:41 and 52:48 at the C(3′) and C(7′) double bond, respectively]. Determination of the isomeric composition of the hydrogenation product is difficult, but a suitable method has been described that involves GC analysis after conversion of the acetate **17** to the corresponding methyl ether (*26*, *27*).

We screened various iridium catalysts derived from ligands of types **2** to **6** (Fig. 1) in the hydrogenation of tocotrienol derivatives (*28*). Whereas oxazoline-based ligands showed disappointingly low stereoselectivities, imidazolines **4** and pyridine-phosphinites **6** gave encouraging results. The most efficient ligand in the imidazoline series was derivative (*R*)-**15**, producing a 90:5:4:1 mixture of (*RRR*)-, (*RRS*)-, (*RSR*)-, and (*RSS*)-tocopheryl acetates (*21*, *22*). However, the best stereoselectivity was achieved with the iridium catalyst derived from pyridine-phosphinite ligand **11**, which gave almost exclusively the natural (*RRR*)-isomer of γ-tocopheryl acetate **17** (*29*), thus providing a highly effective stereoselective route to this important class of bioactive antioxidants. Previously developed strategies for the stereoselective synthesis of vitamin E compounds (*25*) use a stepwise approach for the introduction of the stereogenic centers in the side chain. Here, the natural *RR* configuration is established in a single step.

References and Notes

1. J. M. Brown, in *Comprehensive Asymmetric Catalysis*, E. N. Jacobsen, A. Pfaltz, H. Yamamoto, Eds. (Springer, Berlin, 1999), vol. I, chap. 5.1, pp. 121–182.
2. R. Noyori, *Angew. Chem. Int. Ed. Engl.* **41**, 2008 (2002).
3. W. S. Knowles, *Angew. Chem. Int. Ed. Engl.* **41**, 1998 (2002).
4. H. U. Blaser, E. Schmidt, Eds., *Asymmetric Catalysis on Industrial Scale* (Wiley-VCH, Weinheim, Germany, 2004).
5. A. Lightfoot, P. Schnider, A. Pfaltz, *Angew. Chem. Int. Ed. Engl.* **37**, 2897 (1998).
6. A. Pfaltz *et al.*, *Adv. Synth. Catal.* **345**, 33 (2003).
7. S. P. Smidt, F. Menges, A. Pfaltz, *Org. Lett.* **6**, 2023 (2004).
8. W. J. Drury III *et al.*, *Angew. Chem. Int. Ed. Engl.* **43**, 70 (2004).
9. S. P. Smidt, N. Zimmermann, M. Studer, A. Pfaltz, *Chem. Eur. J.* **10**, 4685 (2004).
10. F. Menges, M. Neuburger, A. Pfaltz, *Org. Lett.* **4**, 4713 (2002).
11. F. Menges, thesis, University of Basel (2004).
12. For related work of other research groups, see (*13*–*18*); for a review of catalytic homogeneous asymmetric hydrogenations of largely unfunctionalized alkenes, see (*19*).
13. R. D. Broene, S. L. Buchwald, *J. Am. Chem. Soc.* **115**, 12569 (1993).
14. V. P. Conticello *et al.*, *J. Am. Chem. Soc.* **114**, 2761 (1992).
15. T. Bunlaksananusorn, K. Polborn, P. Knochel, *Angew. Chem. Int. Ed. Engl.* **42**, 3941 (2003).
16. Y. Fan, X. Cui, K. Burgess, M. B. Hall, *J. Am. Chem. Soc.* **126**, 16688 (2004).
17. K. Källström, C. Hedberg, P. Brandt, A. Bayer, P. G. Andersson, *J. Am. Chem. Soc.* **126**, 14308 (2004).
18. D. Liu, W. Tang, X. Zhang, *Org. Lett.* **6**, 513 (2004).
19. X. Cui, K. Burgess, *Chem. Rev.* **105**, 3272 (2005).
20. S. Kaiser, thesis, University of Basel (2005).
21. See supporting material on *Science* Online.
22. Catalysts were prepared as previously decribed; hydrogenations were carried out under standard conditions (*5*, *6*).
23. R. L. Danheiser, J. S. Novick, *J. Org. Chem.* **56**, 1176 (1991).
24. C. Wedler, W. Kunath, H. Schick, *J. Org. Chem.* **60**, 758 (1995).
25. T. Netscher, *Chimia (Aarau)* **50**, 563 (1996).
26. N. Cohen *et al.*, *Helv. Chim. Acta* **64**, 1158 (1981).
27. W. Walther, T. Netscher, *Chirality* **8**, 397 (1996).
28. B. Wüstenberg, thesis, University of Basel (2003).
29. In the hydrogenation of the enantiomeric substrate (*S*)-**16**, >98% of (*SRR*)-**17** was obtained with this ligand; this finding confirms that the stereoselectivity is controlled by the catalyst and that the influence of the stereogenic center in the substrate is negligible.
30. The absolute configuration of the products has not yet been determined. The ee values are based on HPLC (product **8**) and GC analysis (**10**) using chiral columns (*21*).

31. Supported by the Swiss National Science Foundation, the Commission for Technology and Innovation (Switzerland), and DSM Nutritional Products.

Supporting Online Material

www.sciencemag.org/cgi/content/full/1121977/DC1
Materials and Methods
Figs. S1 to S3
Table S1
References

28 October 2005; accepted 29 November 2005
Published online 8 December 2005;
10.1126/science.1121977
Include this information when citing this paper.

Plastic Deformation of $MgGeO_3$ Post-Perovskite at Lower Mantle Pressures

Sébastien Merkel,[1]* Atsushi Kubo,[2] Lowell Miyagi,[1] Sergio Speziale,[1] Thomas S. Duffy,[2] Ho-kwang Mao,[3] Hans-Rudolf Wenk[1]

Polycrystalline $MgGeO_3$ post-perovskite was plastically deformed in the diamond anvil cell between 104 and 130 gigapascals confining pressure and ambient temperature. In contrast with phenomenological considerations suggesting (010) as a slip plane, lattice planes near (100) became aligned perpendicular to the compression direction, suggesting that slip on (100) or (110) dominated plastic deformation. With the assumption that silicate post-perovskite behaves similarly at lower mantle conditions, a numerical model of seismic anisotropy in the D″ region implies a maximum contribution of post-perovskite to shear wave splitting of 3.7% with an oblique polarization.

The D″ region, the layer above the core-mantle boundary (CMB), exhibits a seismic discontinuity, substantial seismic anisotropy, and considerable lateral heterogeneity, and it plays a key role in our understanding of the deep Earth (*1*–*4*). Seismic anisotropy in D″ could reflect lattice preferred orientation (LPO) of minerals (*5*) or alignment of structural elements, including layers of melt (*6*, *7*). LPO patterns depend on deformation mechanisms, and interpretation of D″ anisotropy has been ambiguous because of the absence of any experimental constraints on such properties. Here, we report results of an experimental study of deformation of $MgGeO_3$ post-perovskite (pPv) at high pressures.

Post-perovskite is the stable phase of $MgSiO_3$ at D″ pressures and is likely to be one of the main constituents of D″ (*8*–*14*). First-

[1]Department of Earth and Planetary Science, University of California, Berkeley, CA 94720, USA. [2]Department of Geosciences, Princeton University, Princeton, NJ 08544, USA. [3]Geophysical Laboratory, Carnegie Institution of Washington, Washington, DC 20015, USA.

*To whom correspondence should be addressed. E-mail: smerkel@berkeley.edu

principles calculations indicate that it has a strong elastic anisotropy (*9*, *15*–*17*), and experimental results show that the *b* axis is more compressible than the *a* and *c* axes (*8*). On the basis of structural considerations, pPv has been suggested to form platy crystallites parallel to (010) (fig. S1) or needle-like crystallites in the direction of [100], and (010) has been suggested as the dominant slip plane (*8*, *9*, *15*). In contrast, first-principles calculations indicate that C_{66} is larger than C_{44} and C_{55}, which is incompatible with the concept of a layered structure parallel to (010) (*16*). More recent calculations have also identified a family of polytypes intermediate between Pv and pPv and suggest (110) as a dominant slip plane (*18*).

We deformed a sample of polycrystalline $MgGeO_3$-pPv plastically in the diamond anvil cell between 104 and 130 GPa, heating to 1600 K in different cycles, and observed the evolution of LPO in the sample in situ using radial x-ray diffraction (*19*). Germanates have long been regarded as suitable low-pressure analogs for silicates, based on crystal chemistry systematics and the similarity of slip systems (*20*–*22*). $MgGeO_3$ exhibits nearly the same transition sequence as $MgSiO_3$ with increasing pressure, including a transition to a pPv phase at about 63 GPa (*23*). $MgGeO_3$-pPv also displays a strong elastic anisotropy (*23*). The transition pressure to the pPv phase in $MgGeO_3$ is almost half that of $MgSiO_3$ (120 GPa), and the diffraction intensity of $MgGeO_3$ is greater than $MgSiO_3$. Therefore, $MgGeO_3$ is a good candidate for experimental investigation of plasticity of pPv phases under deep mantle pressures.

We performed an angle dispersive radial x-ray diffraction experiment (fig. S2) at the High-Pressure Collaborative Access Team (HPCAT) sector of the Advanced Photon Source (beamline 16-ID-B). Starting material was a powder of pure $MgGeO_3$ orthopyroxene mixed with 10 weight percent Pt powder that served as pressure calibrant and laser absorber. It was compressed to a pressure of 104 GPa and then converted into the pPv phase by laser heating in different locations at a temperature of 1600 K for about 10 min. Pressure was then increased to 124 GPa over 5 hours. At this stage, the sample was left for 15 hours to allow relaxation of stresses and strains. Later, the sample was further heated for about 20 min at 1600 K and left for 18 hours to allow relaxation. At the end of this cycle, pressure in the sample was on the order of 130 GPa (table S1). At every step, we collected radial diffraction patterns to evaluate the pressure, stress, and LPO in the sample (*24*).

The diffraction images show substantial variations of diffraction peak positions and intensities with orientation relative to the compression direction (Fig. 1) that can be used to estimate stress and deduce LPO. We analyzed the x-ray diffraction images with two different methods (*24*): One relies on individual peak fitting (*19*), and the other relies on a full image analysis with the Rietveld method (*25*). The differential stress in the $MgGeO_3$-pPv sample ranged from 3.6 to 8.9 GPa and evolved continuously with increasing pressure (table S1). The texture we obtained is represented as inverse pole figures of the compression direction in Fig. 2. We observed a texture with a maximum between (100) and (110) at 104 GPa that did not change with time, further heating, or further compression. At 104 and 130 GPa, the ODF maximums were 1.89 and 1.96 multiples of a random distribution, respectively (table S1). A distinct minimum was at (010). Results from individual peak fitting (Fig. 2B) and the Rietveld method (Fig. 2C) were similar.

To interpret the observed textures, we simulated the development of LPO in pPv polycrystals deformed by slip in compression using a viscoplastic self-consistent (VPSC) polycrystal plasticity model (*26*). The LPO evolution depends on the imposed deformation history and the active slip systems. At this point, little is known about deformation mechanisms in pPv. Therefore, we decided to investigate several combinations of slip systems and critical resolved shear stresses for (100), (010), (001), and (110) (table S2). In agreement with predictions of first-principles calculations suggesting (110) as slip plane in pPv (*18*), the best match with experiments was obtained for simulations with dominant slip on (100), (110), or a combination of the two (Fig. 2, D and G), indicating that those are the most likely slip planes at the conditions of the experiment. Slip on (010) and (001) did not produce a maximum near (100), and slip on (010) produced a maximum rather than the observed minimum at (010) (Fig. 2, E and F). A comparison between the strength of the experimental and calculated textures indicates that the macroscopic compressive strain was 0.2 in the experiment.

There are limitations in using analogs to extract meaningful rheological properties at temperature, stress, and strain rate conditions that are far removed from those in the earth. However, assuming that (100) and (110) slip also applies to $MgSiO_3$-pPv under deep mantle

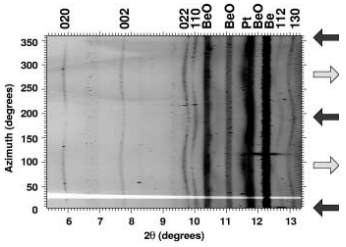

Fig. 1. Unrolled diffraction image of $MgGeO_3$ measured in radial geometry, in situ, at 130 GPa. The directions of maximum and minimum stress are indicated by the black and gray arrows, respectively. LPO and deviatoric stress are deduced from the variations of diffraction intensity and peak position with orientation. Diffraction peaks from the $MgGeO_3$ sample, Pt pressure calibrant, and Be and BeO from the gasket material are labeled on the figure. Because of the geometry of the experiment, Be and BeO peaks always appear as double lines.

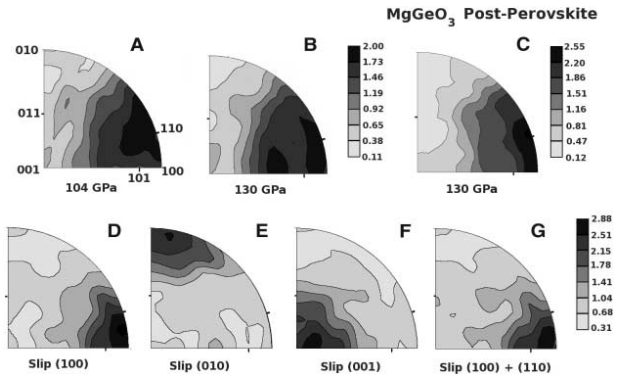

Fig. 2. Inverse pole figure showing the preferred orientation pattern in $MgGeO_3$ pPv in compression measured (**A**) at 104 GPa just after converting the material to the pPv phase; (**B**) at 130 GPa, 41 hours later, after cycles of laser heating and pressure increase, calculated using the individual peak fitting method; (**C**) at 130 GPa, calculated using the Rietveld method; and (**D** to **G**) simulated after 20% compressive strain with models that favor slip along (100), (010), (001), and both (100) and (110), respectively. Equal-area projection is used, and linear contours are expressed in multiples of random distribution.

REPORTS

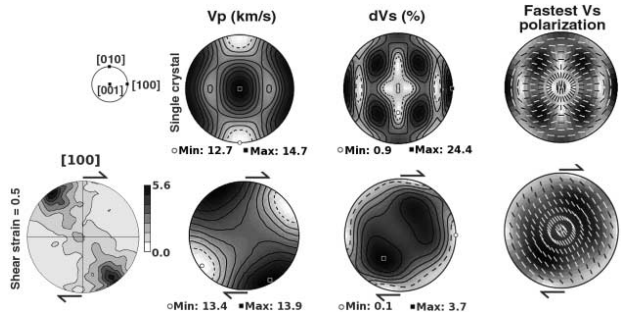

Fig. 3. Modeled three-dimensional compressional velocities (V_P), shear wave splitting (dV_S), and fastest shear wave polarization at 135 GPa and 4000 K for $MgSiO_3$ pPv single crystal (top row) and for a polycrystal aggregate (bottom row) after simple shear plastic deformation up to a strain of 0.5, along with the corresponding [100] pole figure. Linear scale, equal-area projection. Contours for [100], V_P, and dV_S pole figures are expressed in multiples of a random distribution, kilometers per second, and percentage, respectively. Black and white lines (for low and high anisotropy, respectively) in right panel indicate the direction of polarization of the fast shear wave.

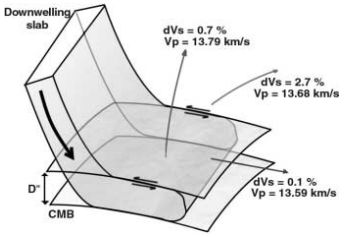

Fig. 4. Contribution of silicate-pPv to anisotropy in a region deformed in simple shear parallel to the CMB.

conditions, we obtained an estimate of expected anisotropies in the D″ layer using again VPSC polycrystal plasticity models to calculate the three-dimensional orientation distribution and then average the single-crystal elastic tensors as a function of crystallographic orientation. From the aggregate elastic tensor, we then calculated seismic velocities in different directions. As a typical deformation path for shear zones, we used simple shear to an equivalent strain of 0.5, corresponding to a shear $\gamma = 0.86$, and slip system combinations that favor slip on (100) and (110). For such a model, the [100] axes tend to align in an oblique maximum rotated from the shear plane normal against the direction of shear (Fig. 3).

The single-crystal anisotropy calculated at 135 GPa and 4000 K (*17*) for *P* waves is 15% (Fig. 3), and shear wave splitting (dV_S) reaches 24%, but the pattern is complex. The polycrystal average for simple shear deformation displays a weak directional anisotropy of only 3.4% for *P* waves and a maximum of 3.7% for shear wave splitting. The relatively low anisotropy is related to the complex single-crystal elastic tensor where maxima and minima are superposed during averaging. For *S* waves, the largest amount of splitting occurs at an inclination of about 45° from both the plane and direction of shear.

Seismological observations have reported large delays for shear waves that graze horizontally through the D″ region with shear wave splitting delays of up to 10 s, corresponding to a polarization anisotropy of up to 3% in D″. These observations have also shown that the anisotropy style—$V_{SH} > V_{SV}$, $V_{SH} < V_{SV}$ (where V_{SH} and V_{SV} are the velocities of the horizontally and vertically polarized shear waves, respectively), or tilted transverse anisotropy—varies regionally (*2*, *4*, *27*–*29*). For a region in which deformation occurs in simple shear parallel to the CMB, we found that the contribution of pPv to shear wave splitting should range from 0.1 to 3.1% for waves traveling in the plane of shear (Fig. 4). In agreement with recent seismic observations of tilted transverse anisotropy in D″ (*28*, *29*), we also found that for silicate pPv the polarization anisotropy is usually inclined by about 45° compared with the plane of shear.

These results underline the importance of high-pressure experimentation in assessing plasticity and seismic anisotropy in the deep Earth. In the future, this work will have to be complemented with experiments on silicate pPv itself, higher temperatures, and lower strain rates.

References and Notes

1. M. Wysession *et al.*, in *The Core-Mantle Boundary Region*, M. Gurnis, M. Wysession, E. Knittle, B. Buffet, Eds. (American Geophysical Union, Washington, DC, 1998), pp. 273–297.
2. T. Lay, Q. Williams, E. J. Garnero, *Nature* **392**, 461 (1998).
3. I. Sidorin, M. Gurnis, D. V. Helmberger, *Science* **286**, 1326 (1999).
4. M. Panning, B. Romanowicz, *Science* **303**, 351 (2004).
5. A. K. McNamara, P. E. van Keken, S. I. Karato, *Nature* **416**, 310 (2002).
6. Q. Williams, E. J. Garnero, *Science* **273**, 1528 (1996).
7. J. M. Kendall, in *The Core-Mantle Boundary Region*, M. Gurnis, M. E. Wysession, E. Knittle, B. A. Buffet, Eds. (American Geophysical Union, Washington, DC, 1998), pp. 97–118.
8. M. Murakami, K. Hirose, K. Kawamura, N. Sata, Y. Ohishi, *Science* **304**, 855 (2004).
9. A. R. Oganov, S. Ono, *Nature* **430**, 445 (2004).
10. W. L. Mao *et al.*, *Proc. Nat. Acad. Sci. U.S.A.* **101**, 15867 (2004).
11. S. Shim, T. S. Duffy, R. Jeanloz, G. Shen, *Geophys. Res. Lett.* **31**, L10603 (2004).
12. R. Caracas, R. E. Cohen, *Geophys. Res. Lett.* **32**, L16310 (2005).
13. J. W. Hernlund, C. Thomas, P. J. Tackley, *Nature* **434**, 882 (2005).
14. M. Murakami, K. Hirose, N. Sata, Y. Ohishi, *Geophys. Res. Lett.* **32**, L03304 (2005).
15. T. Iitaka, K. Hirose, K. Kawamura, M. Murakami, *Nature* **430**, 442 (2004).
16. T. Tsuchiya, J. Tsuchiya, K. Umemoto, R. M. Wentzcovitch, *Geophys. Res. Lett.* **31**, L14603 (2004).
17. S. Stackhouse, J. P. Brodholt, J. Wookey, J.-M. Kendall, G. D. Price, *Earth Planet. Sci. Lett.* **230**, 1 (2005).
18. A. R. Oganov, R. Martonák, A. Laio, P. Raiteri, M. Parrinello, *Nature* **438**, 1142 (2005).
19. S. Merkel *et al.*, *J. Geophys. Res.* **107**, 2271 (2002).
20. N. L. Ross, A. Navrotsky, *Am. Mineral.* **73**, 1355 (1988).
21. C. Dupas-Bruzek, T. N. Tingle, H. W. Green II, N. Doukhan, J.-C. Doukhan, *Phys. Chem. Mineral.* **25**, 501 (1998).
22. J. D. Lawlis, Y. H. Zhao, S. I. Karato, *Phys. Chem. Mineral.* **28**, 557 (2001).
23. K. Hirose, K. Kawamura, Y. Ohishi, S. Tateno, N. Sata, *Am. Mineral.* **90**, 262 (2005).
24. Materials and methods are available as supporting material on *Science* Online.
25. H. R. Wenk *et al.*, *Earth Planet. Sci. Lett.* **226**, 507 (2004).
26. H. R. Wenk, in *Texture and Anisotropy*, U. F. Kocks, C. N. Tomé, H. R. Wenk, Eds. (Cambridge University Press, Cambridge, UK, 1998), pp. 560–595.
27. M. Moore, E. J. Garnero, T. Lay, Q. Williams, *J. Geophys. Res.* **109**, B02319 (2004).
28. E. J. Garnero, V. Maupin, T. Lay, M. J. Fouch, *Science* **306**, 259 (2004).
29. J. Wookey, J. M. Kendall, G. Rümpker, *Geophys. J. Int.* **161**, 829 (2005).
30. We thank H. Liu, Y. Meng, and the HPCAT staff for support in the experiment, R. Cava for assistance in sample synthesis, G. Rose for building our diamond anvil cell, D. Mainprice for his petrophysics software package, and the two anonymous reviewers for their comments. This work was supported by NSF and Carnegie/Department of Energy Alliance Center. Use of the Advanced Photon Source was supported by the Department of Energy, Office of Science, Office of Basic Energy Sciences, under contract no. W-31-109-ENG-38. Use of the HPCAT facility was supported by the Department of Energy–Basic Energy Sciences, Department of Energy–National Nuclear Security Administration, NSF, Department of Defense–Tank-Automotive and Armaments Command, and the W. M. Keck Foundation. S.M. and S.S. also acknowledge support from the Miller Institute for Basic Research in Science.

Supporting Online Material

www.sciencemag.org/cgi/content/full/311/5761/644/DC1
Materials and Methods
Figs. S1 to S4
Tables S1 and S2
References

25 October 2005; accepted 30 December 2005
10.1126/science.1121808

17. G. Paglia, E. S. Bozin, S. J. L. Billinge, *Chem. Mater.* **18**, 3242 (2006).
18. W. H. Casey, *Chem. Rev.* **106**, 1 (2006).
19. I. Joumard *et al.*, *Phys. Rev. B* **74**, 205411 (2006).
20. G. W. Brady *et al.*, *Biochemistry* **7**, 2185 (1968).
21. R. A. Eggleton, R. W. Fitzpatrick, *Clays Clay Miner.* **36**, 111 (1988).
22. Q. A. Pankhurst, R. J. Pollard, *Clays Clay Miner.* **40**, 268 (1992).
23. Y. Pan *et al.*, *Micron* **37**, 403 (2006).
24. Y. Pan, Ph.D. thesis, University of Leeds, Leeds, UK (2007).
25. Y. Guyodo *et al.*, *Physics of the Earth and Planetary Interiors* **154**, 222 (2006).
26. E. Murad, U. Schwertmann, *Am. Mineral.* **65**, 1044 (1980).
27. J. van Slageren *et al.*, *Phys. Rev. B* **73**, 014422 (2006).
28. P. Juhas, D. M. Cherba, P. M. Duxbury, W. F. Punch, S. J. L. Billinge, *Nature* **440**, 655 (2006).
29. V. Petkov *et al.*, *Phys. Rev. B* **65**, 092105 (2002).
30. B. Gilbert, F. Huang, H. Z. Zhang, G. A. Waychunas, J. F. Banfield, *Science* **305**, 651 (2004).
31. This work is dedicated in memoriam to Charles E. McClennen, Professor of Geology, Colgate University. Support provided by the Center for Environmental Molecular Science (CEMS); NSF Awards CHE0221934, DMR-045244, and EAR-0510501; the U.S. Department of Education through the Graduate Assistance in Areas of National Need Program Sponsor identification P200A060248; and the U.S. Department of Energy, Basic Energy Sciences grant no. DE-FG02-03ER-47085. Data collection was performed at X-Ray Operation and Research beamline 11-ID-B at the Advance Photon Source, Argonne National Laboratory, and use is supported by the U.S. Department of Energy, Office of Science, Office of Basic Energy Sciences, under contract no. DE-AC02-06CH11357. We thank D. Dyar for her efforts in the collection of Mössbauer data on these samples.

Supporting Online Material
www.sciencemag.org/cgi/content/full/1142525/DC1
SOM Text
Fig. S1
Tables S1 and S2
Crystallographic Information Files
References

14 March 2007; accepted 9 May 2007
Published online 24 May 2007;
10.1126/science.1142525
Include this information when citing this paper.

Deformation of $(Mg,Fe)SiO_3$ Post-Perovskite and D″ Anisotropy

Sébastien Merkel,[1,2]* Allen K. McNamara,[3] Atsushi Kubo,[4]† Sergio Speziale,[1]‡ Lowell Miyagi,[1] Yue Meng,[5] Thomas S. Duffy,[4] Hans-Rudolf Wenk[1]

Polycrystalline $(Mg_{0.9},Fe_{0.1})SiO_3$ post-perovskite was plastically deformed in the diamond anvil cell between 145 and 157 gigapascals. The lattice-preferred orientations obtained in the sample suggest that slip on planes near (100) and (110) dominate plastic deformation under these conditions. Assuming similar behavior at lower mantle conditions, we simulated plastic strains and the contribution of post-perovskite to anisotropy in the D″ region at the Earth core-mantle boundary using numerical convection and viscoplastic polycrystal plasticity models. We find a significant depth dependence of the anisotropy that only develops near and beyond the turning point of a downwelling slab. Our calculated anisotropies are strongly dependent on the choice of elastic moduli and remain hard to reconcile with seismic observations.

Seismological observations of the lowermost mantle (the D″ region) have revealed a region of great complexity distinct from the overlying deep mantle (*1*, *2*). Unlike the bulk of the lower mantle, the core-mantle boundary (CMB) includes large-scale regions with apparent seismic anisotropy (*3*). It has been suggested that this anisotropy could reflect lattice-preferred orientation (LPO) of minerals (*4*) or alignment of structural elements, including layers of melt (*5*, *6*). A number of lines of evidence now suggest that the transition from a perovskite (Pv) to a post-perovskite (pPv) phase in $(Mg,Fe)SiO_3$ (*7*, *8*) could explain important properties of D″ (*9*–*13*). However, the influence of this phase transition on our understanding of D″ anisotropy remains ambiguous. In this paper, we present multiscale modeling of deformation-induced anisotropy from $(Mg,Fe)SiO_3$-pPv in D″. This work is a combination of high-pressure deformation experiments on $(Mg,Fe)SiO_3$-pPv and numerical modeling of convection using polycrystal plasticity to predict strain and anisotropy in D″.

We deformed a sample of polycrystalline $(Mg_{0.9},Fe_{0.1})SiO_3$-pPv plastically in the diamond anvil cell in compression between 145 and 157 GPa and observed the evolution of LPO in situ using angle dispersive radial x-ray diffraction (fig. S1) at the High-Pressure Collaborative Access Team (HPCAT) of the Advanced Photon Source (beamline 16-ID-B). Starting material was a powder of natural orthopyroxene (*14*) mixed with 10 weight percent Pt powder that served as a laser absorber. The sample was initially compressed to high pressure, at which we could not observe coherent diffraction from within the sample, and then converted into the pPv phase by laser heating at different sample positions at a temperature of 1700 K for 20 min and 2000 K for ~15 min. After the phase transformation, pressure and differential stress in the sample were 145 and 7.2 GPa, respectively. They were then increased in two steps to 157 and 8.5 GPa over the course of 30 hours. At every step, we collected radial diffraction patterns to evaluate the pressure, stress, and LPO in the sample (*14*) (table S1).

The diffraction images show substantial variations of diffraction peak positions and intensities with orientation relative to the compression direction that can be used to estimate stress and deduce LPO (*14*) (Fig. 1). For instance, we observed that the diffraction intensity in the compression direction is minimal for 004 and 022, whereas it is maximal for 113 and 132. The texture we obtain (*14*) is represented in Fig. 2. In contrast with low-temperature and lower-pressure observations on the Mn_2O_3 (*15*) and $CaIrO_3$ (*16*) pPv analogs, we observed LPO compatible with previous observations on a $MgGeO_3$-pPv analog deformed under similar conditions (*17*) with a clear minimum at (010) and (001). Those LPO are formed immediately upon synthesizing and heating $(Mg,Fe)SiO_3$-pPv at high pressure. Minima observed at (010) and (001) preclude slip on (001) and (010) planes, and a comparison of observed textures and results from viscoplastic self-consistent (VPSC) polycrystal plasticity simulations (*18*) indicate that the deformation is likely dominated by slip on planes such as (100) or (110), in agreement with results of first-principles modeling of stacking fault energetics and shear elastic constants SiO_3 (*19*) but in disagreement with first-principles modeling of dislocation cores based on the Peierls model that suggest [001](010) as the easiest slip system (*20*).

There are limitations in our experiment: time scale, grain size, strain, temperature, and deviatoric stresses are quite different from those in D″. Moreover, LPOs are formed immediately upon synthesizing and heating the pPv phase and do not evolve greatly upon further compression. However, assuming that (100) and (110) slip also applies to $(Mg,Fe)SiO_3$-pPv under deep mantle conditions, we simulated the development of LPO in $(Mg,Fe)SiO_3$-pPv in D″ combining geodynamic information about macroscopic deformation and the microscopic deformation mechanisms found in the experiment (table S2). Deformation in D″ can be quite complex because it is coupled to larger-scale mantle-wide convective processes. Therefore, we performed our modeling using the entire mantle domain. We used the numerical convection code Citcom (*21*) with the addition of Lagrangian tracers to obtain a proper estimation of the deformational characteristics of

[1]Department of Earth and Planetary Science, University of California, Berkeley, CA 94720, USA. [2]Laboratoire de Structure et Propriétés de l'Etat Solide, UMR CNRS 8008, Université des Sciences et Technologies de Lille, 59655 Villeneuve d'Ascq, France. [3]School of Earth and Space Exploration, Arizona State University, Box 871404, Tempe, AZ 85287–1404, USA. [4]Department of Geosciences, Princeton University, Princeton, NJ 08544, USA. [5]High-Pressure Collaborative Access Team, Carnegie Institution of Washington, Argonne, IL 60439, USA.

*To whom correspondence should be addressed. E-mail: sebastien.merkel@univ-lille1.fr
†Present address: Consortium for Advanced Radiation Sources, University of Chicago, Argonne, IL 60439, USA.
‡Present address: GeoForschungsZentrum Potsdam, Division 4.1, Telegrafenberg, 9-14482 Potsdam, Germany.

REPORTS

mantle strain expected in D″ and tracked deformation in tracers along several streamlines by computing the left-stretch tensor at each step (*14*, *22*, *23*). The two-dimensional (2D) convection calculation employed a Rayleigh number of 10^7, stress-free boundaries, a temperature-dependent rheology, and a viscosity jump of a factor of 50 across the 660-km phase transition (*14*). The formation of a rigid lid was inhibited by imposing a maximum allowable viscosity for the uppermost portion of the model, allowing strong slabs to form. As is typical for geodynamical modeling, we employed the Boussinesq approximation to minimize the number of free parameters. This approximation excludes the effects of compressibility, viscous dissipation, adiabatic heating/cooling, and buoyancy effects due to phase transitions, including the Pv-pPv phase transition. We would expect that our predicted strain values would be slightly modified with the inclusion of these smaller-order physical processes; however, given the uncertainties in the model parameters, we predict that the difference would be minor, particularly for this study.

We began tracking deformation in slab regions at about 290 km above the CMB, corresponding to an approximate depth at which the Pv-to-pPv phase transition is expected to occur. The general trend of strain appears to be similar for most tracers and is characterized by horizontal stretching as slab material impinges upon the CMB (Fig. S4). After investigating several streamlines and observing similar trends, we concentrated on one particular streamline for use in polycrystal plasticity models (*18*). Accumulated strains along a streamline are very large and, assuming that all this strain is accommodated by dislocation glide, polycrystal plasticity simulations would predict very sharp textures, close to a single crystal. This is clearly not realistic. At high temperatures, strain may be partially accommodated by climb, boundary diffusion, and dynamic recrystallization that may significantly weaken texture development. Furthermore, secondary phases may be present. Thus, after several tests (*14*), we found that a reasonable assumption is that 10% of the plastic strain recorded by the tracer is accommodated by dislocation glide in pPv and the rest by mechanisms that do not produce preferred orientation. Using the VPSC model, we simulated the LPO evolution of an aggregate of 2000 grains at each time step of the convection model. Most of the strain (Fig. 3 and fig. S5) occurs as the aggregate reaches the CMB and flows parallel to it. This configuration is very similar to a combination of pure and simple shear parallel along the freeslip surface of the CMB. As the tracer descends into D″, we observe very little development of LPO (Fig. 3A). Texture develops rapidly between steps 1000 (Fig. 3A) and 2000 (Fig. 3B) as the tracer turns at the CMB. The texture strengthens and evolves only moderately as the particle moves along the CMB (up to step 5000) (Fig. 3C) and is later modified during upwelling (Fig. 3D).

We obtained an estimate of expected anisotropies in the D″ by averaging the single-crystal elastic tensors as a function of crystallographic orientation. From the aggregate elastic tensor, we then calculated seismic velocities in different directions. First-principles calculations provide single-crystal elastic moduli for $MgSiO_3$-pPv at high pressure and high temperature (*24*, *25*) (table S3).

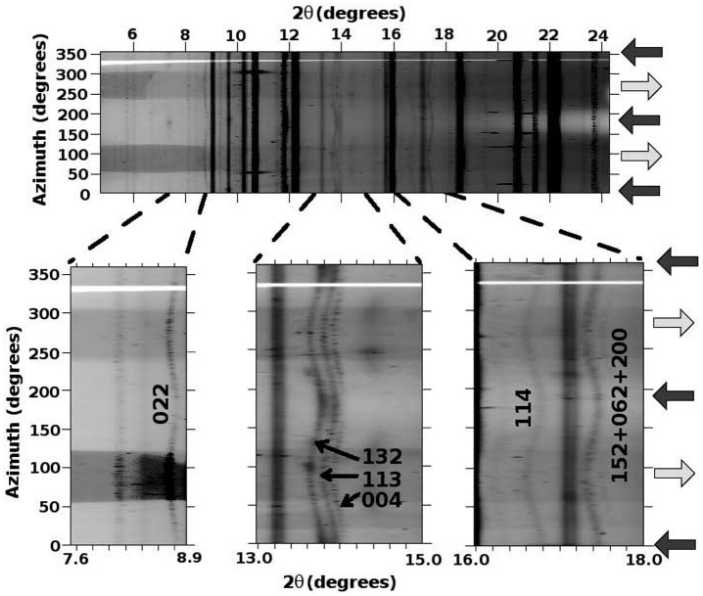

Fig. 1. Unrolled diffraction image of $(Mg,Fe)SiO_3$-pPv measured in radial diffraction, in situ, at 145 GPa. The directions of maximum and minimum stress are indicated by the black and gray arrows on the right, respectively. LPO and differential stress are deduced from the variations of diffraction intensity and peak position with orientation. Miller indices of the diffraction lines from the $(Mg,Fe)SiO_3$-pPv sample actually used in the analysis are labeled on the figure. Diffraction lines with no evidence of stress (straight lines) are from the gasket.

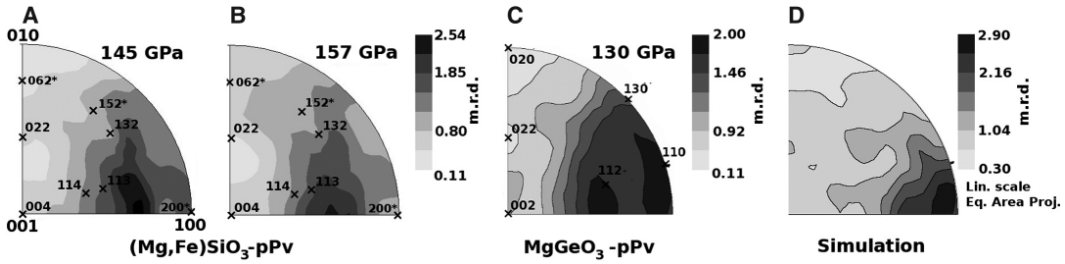

Fig. 2. Inverse pole figure showing the preferred orientation pattern in $(Mg,Fe)SiO_3$-pPv in compression measured (**A**) at 145 GPa just after converting the material to the pPv phase, (**B**) at 157 GPa, (**C**) in $MgGeO_3$ pPv at 130 GPa (*17*), and (**D**) simulated after 20% compressive strain with models that favor slip on (100) and (110). Equal-area projection is used, and linear contours express pole densities in multiples of a random distribution. Reflections used for inverting the orientation distribution function are indicated in the experimental inverse pole figures. The 152, 062, and 200 peaks of $(Mg,Fe)SiO_3$-pPv overlap and are not well resolved.

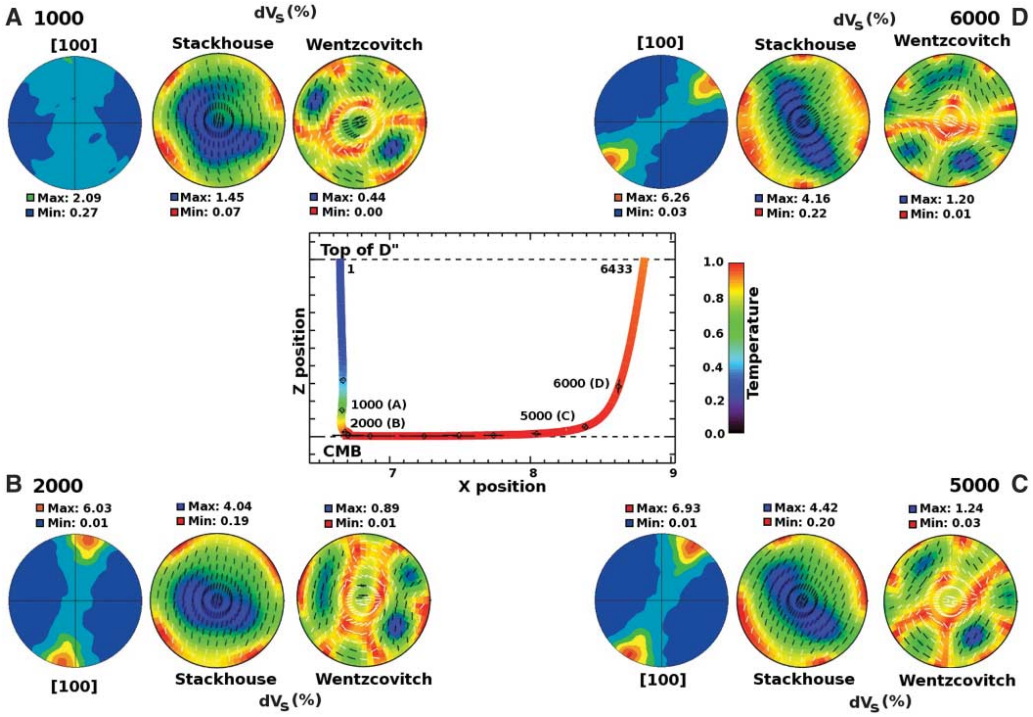

Fig. 3. Modeled temperature, strain, texture, and shear wave splitting from silicate post-perovskite in D″. The central figure illustrates the evolution of temperature and strain along a streamline. Temperatures are normalized so that $T = 0$ at Earth's surface and $T = 1$ at the CMB, strains are indicated by the black lines representing the evolution of maximum and minimum stretch of the Lagrangian particle for every 500 time steps, and numbers are time-step numbers. Panels (**A**) to (**D**) present the modeled 3D [100] orientations, shear wave splitting dV_S, and fastest shear wave polarizations at time steps 1000, 2000, 5000, and 6000, respectively. Shear wave splitting was calculated using the elastic moduli of Stackhouse *et al.* (*24*) and Wentzcovitch *et al.* (*25*). Linear scale, equal area projection. Contours for the [100] and dV_S pole figures are expressed in multiples of a random distribution and percentage, respectively. Black and white lines (for low and high anisotropies, respectively) indicate the direction of polarization of the fast shear wave.

The results of the two calculations differ significantly, and we decided to include both in our analysis (figs. S8 to S10). As the tracer plunges into the D″ layer, we observe very little anisotropy. It develops rapidly between steps 1000 and 2000 (Fig. 3, A and B), as the tracer reaches the CMB. At step 5000 (Fig. 3C), before entering the upwelling, shear wave splitting reaches 4.42% and 1.24% with the elastic moduli of Stackhouse *et al.* (*24*) and Wentzcovitch *et al.* (*25*), respectively.

Most seismic observations of shear wave polarization anisotropy in D″ involve delays of vertically polarized *S* wave components (*SV*) relative to horizontally polarized *S* wave components (*SH*) for paths that graze horizontally through the D″ region (*26*). However, other studies show tilted transverse anisotropy (*27*, *28*) or local variations of fast polarization directions (*29*–*31*). Our predictions of shear wave polarization anisotropies depend strongly on the choice of elastic moduli. Using both models, we found a significant depth dependence of the anisotropy that only develops near and beyond the turning point of a downwelling slab (Fig. 3 and figs. S8 to S10). In a slablike environment, we also found that the anisotropy for waves propagating parallel to the CMB should produce loosely symmetric patterns. Using the elastic moduli of Stackhouse *et al.* (*24*), we predict a maximum anisotropy of 4% perpendicular to the direction of flow, with the direction of fast polarization ranging from 60° to 90° ($V_{SH} < V_{SV}$). Using the elastic moduli of Wentzcovitch *et al.* (*25*), we obtain lower values of anisotropy with dV_S ranging between 0.5 and 0.6%, with a fast polarization near 0° ($V_{SH} > V_{SV}$) for waves traveling perpendicular to the direction of flow. Waves traveling parallel to the direction of flow would show varying anisotropies with very little anisotropy near the downwelling and up to 1.2% before upwelling, again with a fast polarization near 0° ($V_{SH} > V_{SV}$).

Predictions using the elastic moduli of Stackhouse *et al.* (*24*) systematically imply $V_{SH} < V_{SV}$ and are inconsistent with most seismic measurements that find either $V_{SH} > V_{SV}$ or locally varying fast polarization directions. Using the elastic moduli of Wentzcovitch *et al.* (*25*), we obtain complex patterns of anisotropies with lower amplitude than observed seismically. Although many characteristics of D″ are consistent with the properties of post-perovskite, other phases or structural mechanisms (e.g., layering) may be necessary to explain the seismic anisotropy of the region. Our study shows how ultrahigh pressure experiments on silicate post-perovskites combined with microscale (plasticity) and macroscale (mantle flow) modeling provide the means to test our understanding of deformation behavior at the base of Earth's mantle.

References and Notes

1. T. Lay, Q. Williams, E. J. Garnero, *Nature* **392**, 461 (1998).
2. R. D. van der Hilst *et al.*, *Science* **315**, 1813 (2007).
3. M. Panning, B. Romanowicz, *Science* **303**, 351 (2004).
4. A. K. McNamara, P. E. van Keken, S. I. Karato, *Nature* **416**, 310 (2002).
5. Q. Williams, E. J. Garnero, *Science* **273**, 1528 (1996).
6. J. M. Kendall, in *The Core-Mantle Boundary Region*, M. Gurnis, M. E. Wysession, E. Knittle, B. A. Buffet, Eds.

(American Geophysical Union, Washington, DC, 1998), pp. 97–118.
7. M. Murakami, K. Hirose, K. Kawamura, N. Sata, Y. Ohishi, *Science* **304**, 855 (2004).
8. A. R. Oganov, S. Ono, *Nature* **430**, 445 (2004).
9. D. Helmberger, T. Lay, S. Ni, M. Gurnis, *Proc. Nat. Acad. Sci. U.S.A.* **102**, 17257 (2005).
10. J. Wookey, S. Stackhouse, J. Kendall, J. Brodholt, G. D. Price, *Nature* **438**, 1004 (2005).
11. K. Hirose, *Rev. Geophys.* **44**, RG3001 (2006).
12. W. L. Mao *et al.*, *Science* **312**, 564 (2006).
13. T. Lay, J. Hernlund, E. J. Garnero, M. S. Thorne, *Science* **314**, 1272 (2006).
14. Materials and methods are available as supporting material on *Science* Online.
15. J. Santillán, S. Shim, G. Shen, V. Prakapenka, *Geophys. Res. Lett.* **33**, L15307 (2006).
16. D. Yamazaki, T. Yoshino, H. Ohfuji, J. Ando, A. Yoneda, *Earth Planet. Sci. Lett.* **252**, 372 (2006).
17. S. Merkel *et al.*, *Science* **311**, 644 (2006).
18. R. A. Lebensohn, C. N. Tomé, *Acta Metal. Mater.* **41**, 2611 (1993).
19. A. R. Oganov, R. Martonák, A. Laio, P. Raiteri, M. Parrinello, *Nature* **438**, 1142 (2005).
20. P. Carrez, D. Ferré, P. Cordier, *Nature* **446**, 68 (2007).
21. L. Moresi, M. Gurnis, *Earth Planet. Sci. Lett.* **138**, 15 (1996).
22. A. K. McNamara, P. E. van Keken, S.-I. Karato, *J. Geophys. Res.* **108**, 2230 (2003).
23. A. K. McNamara, S. Zhong, *Earth Planet. Sci. Lett.* **222**, 485 (2004).
24. S. Stackhouse, J. P. Brodholt, J. Wookey, J.-M. Kendall, G. D. Price, *Earth Planet. Sci. Lett.* **230**, 1 (2005).
25. R. Wentzcovitch, T. Tsuchiya, J. Tsuchiya, *Proc. Nat. Acad. Sci. U.S.A.* **103**, 543 (2006).
26. M. Moore, E. J. Garnero, T. Lay, Q. Williams, *J. Geophys. Res.* **109**, B02319 (2004).
27. E. J. Garnero, V. Maupin, T. Lay, M. J. Fouch, *Science* **306**, 259 (2004).
28. J. Wookey, J. M. Kendall, G. Rümpker, *Geophys. J. Int.* **161**, 829 (2005).
29. S. A. Russell, T. Lay, E. J. Garnero, *Nature* **396**, 255 (1998).
30. S. A. Russell, T. Lay, E. J. Garnero, *J. Geophys. Res.* **104**, 13,183 (1999).
31. J. M. Rokosky, T. Lay, E. J. Garnero, *Earth Planet. Sci. Lett.* **248**, 411 (2006).

32. We thank D. Mainprice for his petrophysics software package, P. Liermann for assistance during the experiment, and the two anonymous reviewers for their comments. This work was supported by NSF grants EAR-0510383 and EAR-0456356 (T.S.D., H.R.W., and A.K.M.) and the Carnegie/Department of Energy Alliance Center (T.S.D. and H.R.W.). Experiments were performed at HPCAT (Sector 16), Advanced Photon Source (APS), Argonne National Laboratory. Use of the HPCAT facility was supported by Department of Energy (DOE) Basic Energy Sciences (BES), DOE National Nuclear Security Administration, NSF, Department of Defense (DOD) Tank-Automotive and Armaments Command, and the W. M. Keck Foundation. Use of the APS was supported by DOE-BES under contract W-31-109-ENG-38. S.M. and S.S. also acknowledge support from the Miller Institute for Basic Research in Science.

Supporting Online Material
www.sciencemag.org/cgi/content/full/316/5832/1729/DC1
Materials and Methods
Figs. S1 to S10
Tables S1 to S3
References

31 January 2007; accepted 13 April 2007
10.1126/science.1140609

Weak Northern and Strong Tropical Land Carbon Uptake from Vertical Profiles of Atmospheric CO_2

Britton B. Stephens,[1]* Kevin R. Gurney,[2] Pieter P. Tans,[3] Colm Sweeney,[3] Wouter Peters,[3] Lori Bruhwiler,[3] Philippe Ciais,[4] Michel Ramonet,[4] Philippe Bousquet,[4] Takakiyo Nakazawa,[5] Shuji Aoki,[5] Toshinobu Machida,[6] Gen Inoue,[7] Nikolay Vinnichenko,[8]† Jon Lloyd,[9] Armin Jordan,[10] Martin Heimann,[10] Olga Shibistova,[11] Ray L. Langenfelds,[12] L. Paul Steele,[12] Roger J. Francey,[12] A. Scott Denning[13]

Measurements of midday vertical atmospheric CO_2 distributions reveal annual-mean vertical CO_2 gradients that are inconsistent with atmospheric models that estimate a large transfer of terrestrial carbon from tropical to northern latitudes. The three models that most closely reproduce the observed annual-mean vertical CO_2 gradients estimate weaker northern uptake of −1.5 petagrams of carbon per year (Pg C year^{-1}) and weaker tropical emission of +0.1 Pg C year^{-1} compared with previous consensus estimates of −2.4 and +1.8 Pg C year^{-1}, respectively. This suggests that northern terrestrial uptake of industrial CO_2 emissions plays a smaller role than previously thought and that, after subtracting land-use emissions, tropical ecosystems may currently be strong sinks for CO_2.

Our ability to diagnose the fate of anthropogenic carbon emissions depends critically on interpreting spatial and temporal gradients of atmospheric CO_2 concentrations (*1*). Studies using global atmospheric transport models to infer surface fluxes from boundary-layer CO_2 concentration observations have generally estimated the northern mid-latitudes to be a sink of approximately 2 to 3.5 Pg C year^{-1} (*2*–*5*). Analyses of surface ocean partial pressure of CO_2 (*2*), atmospheric carbon isotope (*6*), and atmospheric oxygen (*7*) measurements have further indicated that most of this northern sink must reside on land. Tropical fluxes are not well constrained by the atmospheric observing network, but global mass-balance requirements have led to estimates of strong (1 to 2 Pg C year^{-1}) tropical carbon sources (*4*, *5*). Attribution of the Northern Hemisphere terrestrial carbon sink (*8*–*13*) and reconciliation of estimates of land-use carbon emissions and intact forest carbon uptake in the tropics (*14*–*19*) have motivated considerable research, but these fluxes remain quantitatively uncertain. The full range of results in a recent inverse model comparison study (*5*), and in independent studies (*3*, *20*, *21*), spans budgets with northern terrestrial uptake of 0.5 to 4 Pg C year^{-1}, and tropical terrestrial emissions of −1 to +4 Pg C year^{-1}. Here, we analyzed observations of the vertical distribution of CO_2 in the atmosphere that provide new constraints on the latitudinal distribution of carbon fluxes.

Previous inverse studies have used boundary-layer data almost exclusively. Flask samples from profiling aircraft have been collected and measured at a number of locations for up to several decades (*22*–*24*), but efforts to compile these observations from multiple institutions and to compare them with predictions of global models have been limited. Figure 1 shows average vertical profiles of atmospheric CO_2 derived from flask samples collected from aircraft during midday at 12 global locations (fig. S1), with records extending over periods from 4 to 27 years (table S1 and fig. S2) (*25*). These seasonal and annual-mean profiles reflect the combined influences of surface fluxes and atmospheric mixing. During the summer in the Northern Hemisphere, midday atmospheric CO_2 concentrations are generally lower near the surface than in the free troposphere, reflecting the greater impact of terrestrial photosynthesis over industrial emissions at this time. Sampling locations over or immediately downwind of continents show larger gradients than those over or downwind of ocean basins in response to stronger land-based fluxes, and higher-latitude locations show greater CO_2 drawdown at high altitude. Conversely, during the winter, respiration and fossil-fuel sources lead to elevated low-altitude atmospheric CO_2 concentrations at northern locations. The gradients are comparable in magnitude in both seasons, but the positive

[1]National Center for Atmospheric Research, Boulder, CO 80305, USA. [2]Department of Earth and Atmospheric Sciences, Purdue University, West Lafayette, IN 47907, USA. [3]National Oceanic and Atmospheric Administration, Boulder, CO 80305, USA. [4]Le Laboratoire des Sciences du Climat et l'Environnement, 91191 Gif sur Yvette, France. [5]Center for Atmospheric and Oceanic Studies, Tohoku University, Sendai 980-8578, Japan. [6]National Institute for Environmental Studies, Onogawa, Tsukuba 305-8506, Japan. [7]Graduate School of Environmental Studies, Nagoya University, Nagoya City 464-8601, Japan. [8]Central Aerological Observatory, Dolgoprudny, 141700, Russia. [9]School of Geography, University of Leeds, West Yorkshire, LS2 9JT, UK. [10]Max Planck Institute for Biogeochemistry, 07701 Jena, Germany. [11]Sukachev Institute of Forest, Krasnoyarsk, 660036, Russia. [12]Commonwealth Scientific and Industrial Research Organisation (CSIRO) Marine and Atmospheric Research, Aspendale, Victoria 3195, Australia. [13]Department of Atmospheric Science, Colorado State University, Fort Collins, CO 80523, USA.

*To whom correspondence should be addressed. E-mail: stephens@ucar.edu
†Deceased.

REPORTS

extreme as some portions of the Martian mantle [e.g., (*26*)]. Although the Itsaq-DM seems to have been obliterated, or at least not sampled at present, the source mantle of the Narryer Complex crust persists to the present. These observations require an explanation for the differing behavior of the two depleted mantle components, the Narryer-DM able to retain its identity, despite ongoing mantle dynamics for >4.5 Gy, as compared with the transient Itsaq-DM. If all or much of the mantle was initially as highly fractionated as Itsaq-DM, then why was this mantle only partially, but apparently homogeneously, remixed such that all modern terrestrial rocks yield precisely the same ^{142}Nd, distinct from chondrites? The difference supports models of "hidden reservoirs" where part of the complementary, low Sm/Nd domain is locked in a region of Earth, where it is both never sampled at the surface [e.g., (*27*–*29*)] and isolated from remixing. More speculative suggestions are that part of the low Sm/Nd component may have been lost from Earth during accretion, with the missing material accounting for the present-day high ^{142}Nd, or that Earth accreted with a nonchondritic Sm/Nd ratio. In contrast, the Itsaq-DM mantle source persisted for at least a billion years after its formation, as recorded by compositions of 3.6-Gy-old Greenland samples, but was able to communicate with other less fractionated mantle reservoirs and eventually lost its distinct signature through remixing.

An enduring tenet of geology is that Earth started from a well-mixed homogeneous body and evolved progressively over geologic time to a more differentiated chemical state through observable processes such as plate tectonics and continental crust formation. The ^{142}Nd data presented here, however, provide strong evidence that terrestrial planets such as Earth were affected by non-uniformitarian processes early in their histories, resulting in locally extreme chemical differentiation. Furthermore, some of the chemical effects of these events appear to persist in silicate domains to the present day. Thus, an emerging challenge for understanding the Earth system is determining the relative roles of early planetary processes versus progressive differentiation in shaping Earth's chemical architecture.

References and Notes

1. L. Nyquist, H. Wiesmann, B. Bansal, *Geochim. Cosmochim. Acta* **59**, 2817 (1995).
2. M. Boyet, R. W. Carlson, *Science* **309**, 576 (2005).
3. C. N. Foley *et al.*, *Geochim. Cosmochim. Acta* **69**, 4557 (2005).
4. K. Rankenburg, A. D. Brandon, C. R. Neal, *Science* **312**, 1369 (2006).
5. C. L. Harper, S. B. Jacobsen, *Nature* **360**, 728 (1992).
6. M. Boyet *et al.*, *Earth Planet. Sci. Lett.* **214**, 427 (2003).
7. G. Caro, B. Bourdon, J.-L. Birck, S. Moorbath, *Nature* **423**, 428 (2003).
8. M. Sharma, C. Chen, *Precamb. Res.* **135**, 315 (2004).
9. G. Caro, B. Bourdon, J.-L. Birck, S. Moorbath, *Geochim. Cosmochim. Acta* **70**, 164 (2006).
10. M. Boyet, R. Carlson, *Earth Planet. Sci. Lett.* **250**, 254 (2006).
11. A. Polat, A. W. Hofmann, *Precamb. Res.* **126**, 197 (2003).
12. R. Frei, M. Rosing, T. Waight, D. G. Ulfbeck, *Geochim. Cosmochim. Acta* **66**, 467 (2002).
13. R. Andreasen, M. Sharma, *Science* **314**, 806 (2006).
14. R. W. Carlson, M. Boyet, M. Horan, *Science* **316**, 1175 (2007).
15. Materials and methods are available as supporting material on *Science* Online.
16. A. Nutman, V. McGregor, C. Friend, V. Bennett, P. Kinny, *Precamb. Res.* **78**, 1 (1996).
17. H. Smithies, D. Champion, K. Cassidy, *Precamb. Res.* **127**, 89 (2003).
18. A. Nutman, V. Bennett, C. Friend, K. Horie, H. Hidaka, *Contrib. Mineral. Petrol.* **154**, 385 (2007).
19. A. Nutman, V. Bennett, P. Kinny, R. Price, *Tectonics* **12**, 97 (1993).
20. C. Friend, A. Nutman, *J. Geol. Soc. Lond* **162**, 147 (2005).
21. $\varepsilon^{143}Nd(t) = [(^{143}Nd/^{144}Nd(t)_{sample}/^{143}Nd/^{144}Nd(t)_{CHUR})-1] \times 10^4$, where t refers to the crystallization age of the sample and CHUR is the chondritic reservoir composition used to represent bulk silicate Earth with present-day $^{143}Nd/^{144}Nd = 0.512638$ and $^{147}Sm/^{144}Nd = 0.1966$.
22. S. B. Jacobsen, *Annu. Rev. Earth Planet. Sci.* **33**, 531 (2005).
23. W. B. Tonks, H. J. Melosh, *J. Geophys. Res.* **98**, 5319 (1993).
24. Y. Abe, *Phys. Earth and Planet. Int.* **100**, 27 (1997).
25. M. Boyet, R. Carlson, *Earth Planet. Sci. Lett.* **262**, 505 (2007).
26. L. Borg, D. Draper, *Meteoritics Planet. Sci.* **34**, 439 (2003).
27. C. Chase, P. J. Patchett, *Earth Planet. Sci. Lett.* **91**, 66 (1988).
28. J. Blichert-Toft, F. Albaréde, *Earth Planet. Sci. Lett.* **148**, 243 (1997).
29. I. Tolstikhin, A. W. Hofmann, *Phys. Earth Planet. Int.* **148**, 109 (2005).
30. Y. Amelin *et al.*, *Science* **297**, 1678 (2002).
31. Y. Amelin, A. Ghosh, E. Rotenberg, *Geochim. Cosmochim. Acta* **69**, 505 (2005).

32. Greenland investigations by V.C.B. and A.P.N. were supported by Australian Research Council Discovery grant DP0342794. The manuscript was improved by the extensive comments of two anonymous reviewers and R. Carlson. V.C.B. thanks M. Norman and G. Caro for helpful discussions at various stages of this project.

Supporting Online Material

www.sciencemag.org/cgi/content/full/318/5858/1907/DC1
Materials and Methods
Figs. S1 to S3
Tables S1 to S3
References

31 May 2007; accepted 30 October 2007
10.1126/science.1145928

High-Pressure Creep of Serpentine, Interseismic Deformation, and Initiation of Subduction

Nadege Hilairet,[1]* Bruno Reynard,[1] Yanbin Wang,[2] Isabelle Daniel,[1] Sebastien Merkel,[3] Norimasa Nishiyama,[2]† Sylvain Petitgirard[1]

The supposed low viscosity of serpentine may strongly influence subduction-zone dynamics at all time scales, but until now its role could not be quantified because measurements relevant to intermediate-depth settings were lacking. Deformation experiments on the serpentine antigorite at high pressures and temperatures (1 to 4 gigapascals, 200° to 500°C) showed that the viscosity of serpentine is much lower than that of the major mantle-forming minerals. Regardless of the temperature, low-viscosity serpentinized mantle at the slab surface can localize deformation, impede stress buildup, and limit the downdip propagation of large earthquakes at subduction zones. Antigorite enables viscous relaxation with characteristic times comparable to those of long-term postseismic deformations after large earthquakes and slow earthquakes. Antigorite viscosity is sufficiently low to make serpentinized faults in the oceanic lithosphere a site for subduction initiation.

Subduction zones, in which slabs of oceanic lithosphere sink into the mantle, are active zones where frequent large earthquakes cause considerable human and material damage. Such events are triggered by stress buildup or strain localization, the understanding of which relies on identifying the materials involved and their rheology. On top of slabs of many subduction zones, a layer with low seismic velocity and high Poisson ratio (>0.29) is interpreted as extensively serpentinized mantle material (*1*, *2*), and may accommodate most of the deformation at the slab/mantle wedge interface. Serpentinites form by peridotite hydration either during hydrothermal alteration of the oceanic lithosphere before subduction or by percolation of the fluids released by mineral dehydration within the downgoing slab through the overlying mantle wedge (*3*). The high-pressure variety of serpentine, antigorite, can remain stable down to ~180 km depth in cold subduction zones (*4*). Serpentinites are highly deformed as compared to other exhumed materials in paleosubduction zones (*5*), which points to their crucial mechanical role. The expected low strength or viscosity of serpentinite

[1]Laboratoire des Sciences de la Terre, CNRS, Ecole Normale Supérieure de Lyon, Université Claude Bernard Lyon 1, 46 Allée d'Italie, 69364 Lyon Cedex 07, France. [2]Center for Advanced Radiation Sources, University of Chicago, 5640 South Ellis Avenue, Chicago, IL 60637, USA. [3]Laboratoire de Structure et Propriétés de l'Etat Solide, UMR CNRS 8008, Université des Sciences et Technologies de Lille, 59655 Villeneuve d'Ascq, France.

*To whom correspondence should be addressed. E-mail: nadege.hilairet@ens-lyon.fr
†Present address: Geodynamics Research Center, Ehime University, Japan.

has strong seismic implications because it may govern stress buildup and downdip relaxation over the slab surface, which are critical parameters for earthquake triggering and for the downdip extent of major ruptures (*6*). So far, only viscous relaxation of the anhydrous mantle has been considered a potential trigger of major earthquakes, such as the Tonankai 1944, Nankaido 1946 (*7*), and Alaska 1964 events (*8*). Serpentinites also have global geodynamic importance on the time scale of mantle convection because a serpentinite layer may decouple the mantle wedge from the downgoing slab (*9*). Its presence therefore is a defining condition of the plate tectonic regime on Earth.

The limitations of apparatus have restricted previous high-temperature deformation experiments on serpentinites to pressures below 0.7 GPa (*5*, *9*–*11*). Below the antigorite dehydration temperature (600°C), such low confining pressures favor brittle behavior, with deformation being governed by frictional forces, whereas different deformation mechanisms are to be expected at higher pressures (*11*), as suggested by numerous defects allowing for intracrystalline creep commonly observed in antigorite (*12*). In the absence of high-pressure data, quantifying the role of serpentinite at long and short time scales in subduction zones has remained beyond reach. We performed in situ measurements (*13*) of antigorite flow stress using the recently developed deformation-DIA (D-DIA) apparatus coupled with synchrotron x-ray analysis (*14*) under conditions of low constant strain rates (~10^{-4} to 10^{-6} s^{-1}) and pressure and temperature (*P*-*T*) of 1 and 4 GPa and 200° to 500°C, respectively; that is, over most of the antigorite stability field (*4*, *15*). We obtained a stress-strain curve for 14 sets of experimental conditions (tables S1 and S2). Strain values $\varepsilon(t)$ were measured on synchrotron x-ray radiographs, and differential stress σ was measured from elastic lattice strains on angle-dispersive x-ray diffraction patterns (*13*, *16*). The stress value taken or extrapolated at 15% axial strain was used arbitrarily as a measure of the ultimate flow stress (table S3). Because sample observation shows features consistent with intracrystalline deformation (*13*), flow stress values were fitted to power-law equations (Table 1), in which the stress exponent depends on the dominant deformation mechanism (dislocation creep, diffusion, etc.), and to an exponential law appropriate for low-temperature creep processes [the Peierls mechanism (*13*)]. The best fit to the present data, at 1 and 4 GPa, was obtained with a single power-law equation that yielded an activation volume of 3.2 ± 0.7 cm^3 mol^{-1}, activation energy of 8.9 ± 5.4 kJ mol^{-1}, and a stress exponent of 3.8 ± 0.8 (Table 1), consistent with deformation by dislocation creep. The decrease of the stress exponent with increasing pressure when fitting data at each pressure independently (*13*) is consistent with the activation of intracrystalline deformation mechanisms at the expense of frictional grain boundary sliding at low confining pressure.

The ductile deformation of antigorite observed above 1 GPa complements observations from previous triaxial experiments, showing brittle behavior of serpentinite below 0.7 GPa and a transition toward a distributed semi-brittle deformation up to 1 GPa (*5*, *11*). If controlled by antigorite, the transition from brittle to ductile creep at the slab interface with either the crust or the mantle wedge should depend mainly on depth, while the thermal structure of the subduction zone exerts only minor effects. In the case of high porosity (microcracks) with reduced effective confining pressure, the transition depth may depend indirectly on temperature through the amount of water released by mineral dehydration.

In order to depict further the potential role of antigorite rheology on wedge dynamics, we calculated a strength profile at a constant strain rate along a slab surface (Fig. 1), assuming a *P*-*T* profile in a moderately hot subduction zone and considering two extreme cases. In the first model, we assumed a 300-m-thick serpentinite layer formed by hydration above the subducting slab and sheared by 10 cm $year^{-1}$, corresponding to a strain rate of 10^{-10} s^{-1}. Such conditions correspond to those of a subduction zone characterized by strong mechanical coupling or fast postseismic deformation due to sparse serpentinization. In the second case, a 10-km-thick serpentinite layer sheared by 1 mm $year^{-1}$ deforms at a strain rate of 10^{-14} s^{-1}. Such conditions hold for a subduction zone with a layer of extensively serpentinized mantle decoupled from a slowly downgoing slab. These two end-member models indicate that, regardless of strain rate and subduction-zone setting, antigorite is the only mineral among the major phases in the subducting lithosphere and mantle wedge that is capable of yielding by creep at geophysically relevant strain rates and temperatures below 600°C (Fig. 1).

Table 1. Preferred fits to power law $\dot{\varepsilon} = A\sigma^n \exp[-(E_a + PV^*)/(RT)]$ and exponential law $\dot{\varepsilon}_p = A_p \exp[(-E_p/RT)(1 - \frac{\sigma}{\tau})^2]$. Standard errors (1σ) are in parentheses at the right of each parameter. *A* and A_p are material constants, E_a and E_p are activation energies, V^* is activation volume, *n* is a stress exponent, and τ is Peierls stress.

				Power law					
Data used	10^{-1} ln (*A*)		E_a (kJ)		V^* (cm^3)		*n*		R^2
1 and 4 GPa	−8.6	(1.6)	8.9	(5.4)	3.2	(0.7)	3.8	(0.8)	0.89
1 GPa	−12.6	(2.5)	17.6	(6.5)			5.8	(1.3)	0.90
4 GPa	−7.9	(2.8)	16.6	(10.5)			3.4	(1.4)	0.81
				Exponential law					
Data used	τ (GPa)		E_p (kJ)		10^4 A_p				R^2
1 GPa	1.97	(0.36)	59.9	(18.4)	9.8	(2.5)			0.83

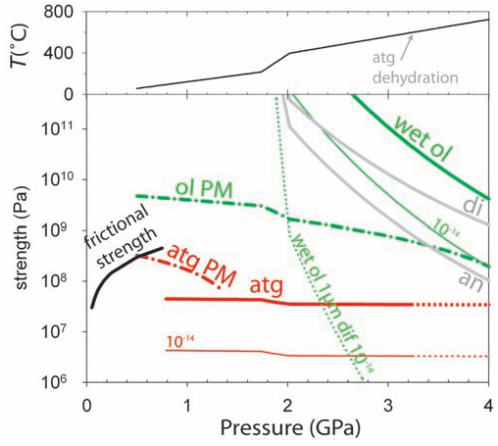

Fig. 1. Strength of antigorite (atg) and other major silicates along a slab surface. Strengths are calculated from deformation laws at a strain rate of 10^{-10} s^{-1} (thick curves) and 10^{-14} s^{-1} (thin curves) along a slab surface *P*-*T* profile [profile number i50 from (*28*)] (upper graph). The low-temperature dislocation glide Peierls mechanism (PM) (*29*), is the most realistic deformation mechanism for olivine (ol) at these pressure, temperature, and strain-rate conditions. Because the Peierls mechanism cannot be extrapolated to low strain rates, strength can be calculated from the creep law only at 10^{-14} s^{-1}. At 10^{-10} s^{-1}, the transition from frictional behavior according to Byerlee's law (thick black line), and antigorite deforming plastically by the Peierls mechanism, occurs between 0.7 and 1 GPa. Antigorite strength remains at least one order of magnitude lower than that of other major mantle and crust minerals regardless of the deformation mechanism and the strain rate, except for very fine-grained (1 μm) olivine deforming by diffusion creep (dif, dotted curve), the strength of which becomes inferior to that of antigorite before its dehydration at strain rates below ~10^{-12} s^{-1}. Millimeter-sized olivine deforming by diffusion creep yields much higher strength and plots off the graph. The Peierls mechanism is from (*29*) and the wet olivine dislocation creep and diffusion creep from (*30*). di, wet diopside; an, anorthite, dislocation creep laws (*31*).

REPORTS

The exception is fine-grained olivine, which may become weaker than antigorite above 2.5 GPa (Fig. 1). Shear instabilities may, therefore, be reconsidered as a possible mechanism for intermediate-depth seismicity, which may either be related to antigorite dehydration producing very fine-grained olivine or occur within fine-grained partly serpentinized peridotites (*17*).

These deformation experiments provide an upper bound for serpentinite viscosity, because naturally occurring localizations would induce high strain rates and lower the effective viscosity. The values we calculated for effective serpentinite viscosity, ~4.10^{19} Pa•s for a strain rate of 10^{-13} s^{-1} (*13*), are of the same orders of magnitude as those used in current numerical models (*18*). Serpentine viscosity as determined by us does not vary much with temperature, which precludes substantial shear heating in a low constant strain-rate system. Our flow law predicts that strain rate, hence viscosity as well, depends nonlinearly on stress. This would enhance positive feedbacks between strain and stress variations, as compared to models using linear stress dependence such as Newtonian rheology (*18*).

Seismologists define three zones downdip along the slab: seismic, transitional (locked during interseismic time), and aseismic. The factors controlling the downdip limit of the seismogenic and locked transitional zones will also govern the downdip propagation of megathrust ruptures, such as the event of 26 December 2004 in Java (*19*). Because serpentinite has a low viscosity, with little pressure and temperature dependence above 1 GPa, the depth at which nonseismogenic creep is possible is governed exclusively by the extent of the serpentinite layer in the subduction zone. This is consistent with observations in Japan, where shallow depths (a maximum of 30 km) of seismogenic zones are associated with Poisson ratios higher than 0.29 (*20*), a strong indication of serpentinization, whereas deeper (50 to 70 km) downdip limits coincide with no indices of serpentinization (*21*). In Sumatra, where no evidence of serpentinization is found, the downdip limit occurs even deeper in the mantle (*22*).

Because of its low viscosity, serpentine can relax stress at rates comparable to those of postseismic and slow seismic deformations. Using a modified Maxwell body with a nonlinear viscous behavior, subject to a permanent deformation ε_0 producing an initial stress $\sigma_0 = \varepsilon_0 E$, where E is the Young modulus (in pascals), the characteristic relaxation time τ_c required to relax half of the initial stress σ_0 is

$$\tau_c = \frac{2^{n-1}-1}{AE(n-1)\sigma_0^{n-1}} \exp\left(\frac{E_a + PV^*}{RT}\right) \quad (1)$$

(*23*), where E_a and V^* are the activation energy and volume, respectively; A and n are material parameters; R is the gas constant; P is the effective confining pressure; and T is the temperature. At temperatures of 200° to 500°C relevant to a slab surface, the relaxation times for antigorite are at least 10 orders of magnitude shorter than those for olivine (Fig. 2). For subduction-zone flow stress estimates up to ~100 MPa (*18*), antigorite relaxation times compare well with characteristic times of co- or postseismic surface deformations such as those measured by geodetic measurements for slow slip events, episodic tremor and slip, silent earthquakes, afterslips, and viscous relaxation (Fig. 2). Viscous relaxation of serpentinite therefore accounts for slow-slip events and for slow earthquakes occurring over periods of a few days to 1 year and which follow a scaling law different from that for regular earthquakes (*24*). These results also suggest that the importance of viscoelastic relaxation processes for triggering large earthquakes in subduction zones over interseismic periods of several years (*25*, *26*) should be reassessed, taking into account the low viscosity of serpentinites measured here. Thus, the triggering of future earthquakes, such as the Tokai event expected in Japan, may depend on serpentinite viscous relaxation (*7*).

Together with a strong stress dependence, the low viscosity of antigorite at *P-T* conditions where other minerals have viscosities orders of magnitude higher confirms that serpentinite is an ideal candidate for strain localization within subduction zones. Moreover, antigorite-bearing serpentinites formed deeply in oceanic transform faults and passive margins may constitute decisive weak zones in the oceanic lithosphere, because their viscosity is lower than the critical value of 10^{20} Pa•s required to initiate subduction (*27*). The present data quantitatively relate viscous deformation of serpentinites to interseismic deformation and slow earthquakes. They should help improve numerical modeling of seismicity and convection in subduction zones.

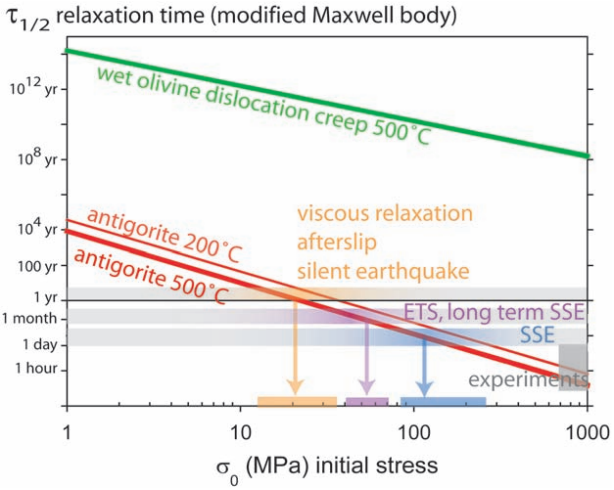

Fig. 2. Maxwell relaxation time for antigorite rheology and post- and slow seismic deformation time scales. $\tau_{1/2}$ is the time calculated (Eq. 1) to relax half of an initial stress σ_0 imposed at $t = 0$ (for instance, by the displacement field of an earthquake occurring close to a serpentinite body), using the antigorite power-law equation at 2 GPa (table S4) and $E = 89$ GPa (*20*). Stress above 20 MPa will be half-relaxed in less than 1 year by antigorite at 500°C (~40 MPa at 200°C), whereas stress relaxation is not possible in wet olivine deforming by dislocation creep (*30*) at these temperatures. Olivine diffusion creep (*30*), not reported here, leads to a constant characteristic relaxation time of ~ 10^7 years. Relaxation of high natural stress by antigorite flow is compatible with the time scales of postseismic deformation after large earthquakes (*7*, *8*, *25*, *26*) and slowslip events or silent earthquakes (*24*). ETS, episodic tremor and slip; SSE, slow slip events.

References and Notes

1. G. A. Abers, *Phys. Earth Planet. Int.* **149**, 7 (2005).
2. H. Kawakatsu, S. Watada, *Science* **316**, 1468 (2007).
3. W. S. Fyfe, A. R. McBirney, *Am. J. Sci.* **275A**, 285 (1975).
4. P. Ulmer, V. Trommsdorf, *Science* **268**, 858 (1995).
5. C. B. Raleigh, M. S. Paterson, *J. Geophys. Res.* **70**, 3965 (1965).
6. S. M. Peacock, R. D. Hyndman, *Geophys. Res. Lett.* **26**, 2517 (1999).
7. P. A. Rydelek, I. S. Sacks, *Earth Planet. Sci. Lett.* **206**, 289 (2003).
8. C. Zweck, J. T. Freymueller, S. C. Cohen, *Phys. Earth Planet. Int.* **132**, 5 (2002).
9. S. A. F. Murrell, I. A. H. Ismail, *Tectonophysics* **31**, 207 (1976).
10. E. H. Rutter, K. H. Brodie, *J. Geophys. Res.* **93**, 4907 (1988).
11. J. Escartin, G. Hirth, B. W. Evans, *J. Geophys. Res.* **102**, 2897 (1997).
12. A.-L. Auzende *et al.*, *Eur. J. Mineral.* **14**, 905 (2002).
13. Materials and methods are available as supporting material on *Science* Online.
14. Y. Wang, W. B. Durham, I. C. Getting, D. J. Weidner, *Rev. Sci. Instrum.* **74**, 3003 (2003).
15. N. Hilairet, I. Daniel, B. Reynard, *Geophys. Res. Lett.* **33**, L02302 (2006).
16. T. Uchida, N. Funamori, T. Yagi, *J. Appl. Phys.* **80**, 739 (1996).

17. J. M. Warren, G. Hirth, *Earth Planet. Sci. Lett.* **248**, 438 (2006).
18. T. V. Gerya, B. Stoeckhert, A. Perchuk, *Tectonics* **21**, 1056 (2002).
19. C. Subarya *et al.*, *Nature* **440**, 46 (2006).
20. N. I. Christensen, *Int. Geol. Rev.* **46**, 795 (2004).
21. T. Seno, *Earth Planet. Sci. Lett.* **231**, 249 (2005).
22. M. Simoes, J. P. Avouac, R. Cattin, P. Henry, *J. Geophys. Res. Solid Earth* **109**, B10402 (2004).
23. D. L. Turcotte, G. Schubert, *Geodynamics* (Cambridge Univ. Press, ed. 2, 2002).
24. S. Ide, G. C. Beroza, D. R. Shelly, T. Uchide, *Nature* **447**, 76 (2007).
25. A. M. Freed, R. Burgmann, *Nature* **430**, 548 (2004).
26. H. Ueda, M. Ohtake, H. Sato, *J. Geophys. Res. Solid Earth* **108**, 2151 (2003).
27. K. Regenauer-Lieb, D. A. Yuen, J. Branlund, *Science* **294**, 578 (2001).
28. J. A. Conder, *Phys. Earth Planet. Int.* **149**, 155 (2005).
29. P. Raterron, Y. Wu, D. J. Weidner, J. Chen, *Phys. Earth Planet. Int.* **145**, 149 (2004).
30. S. Karato, D. C. Rubie, H. Yan, *J. Geophys. Res. Solid Earth* **98**, 9761 (1993).
31. A. Dimanov, G. Dresen, *J. Geophys. Res. Solid Earth* **110**, B07203 (2005).
32. We thank B. Van de Moortèle for the electron microscopy and J. Blichert-Toft, F. Albarède, J. Bass, and the two anonymous reviewers for their suggestions. This work was supported by the Institut National des Sciences de l'Univers (SEDIT program). The experiment was carried out at GeoSoilEnviroCARS (Sector 13) at the Advanced Photon Source (APS), Argonne National Laboratory. Use of the APS was supported by the U.S. Department of Energy (DOE), Office of Science, Office of Basic Energy Sciences, under contract no. DE-AC02-06CH11357. GeoSoilEnviroCARS is supported by NSF–Earth Sciences (grant EAR-0217473), DOE-Geosciences (grant DE-FG02-94ER14466), and the State of Illinois.

Supporting Online Material

www.sciencemag.org/cgi/content/full/318/5858/1910/DC1
Materials and Methods
Figs. S1 to S8
Tables S1 to S3
References

30 July 2007; accepted 7 November 2007
10.1126/science.1148494

A Comprehensive Phylogeny of Beetles Reveals the Evolutionary Origins of a Superradiation

Toby Hunt,[1,2]* Johannes Bergsten,[1,2]* Zuzana Levkanicova,[3] Anna Papadopoulou,[1,2] Oliver St. John,[1,2] Ruth Wild,[1,2] Peter M. Hammond,[1] Dirk Ahrens,[4] Michael Balke,[1,4] Michael S. Caterino,[1,5] Jesús Gómez-Zurita,[1,6] Ignacio Ribera,[7] Timothy G. Barraclough,[2] Milada Bocakova,[8] Ladislav Bocak,[3] Alfried P. Vogler[1,2]†

Beetles represent almost one-fourth of all described species, and knowledge about their relationships and evolution adds to our understanding of biodiversity. We performed a comprehensive phylogenetic analysis of Coleoptera inferred from three genes and nearly 1900 species, representing more than 80% of the world's recognized beetle families. We defined basal relationships in the Polyphaga supergroup, which contains over 300,000 species, and established five families as the earliest branching lineages. By dating the phylogeny, we found that the success of beetles is explained neither by exceptional net diversification rates nor by a predominant role of herbivory and the Cretaceous rise of angiosperms. Instead, the pre-Cretaceous origin of more than 100 present-day lineages suggests that beetle species richness is due to high survival of lineages and sustained diversification in a variety of niches.

The extraordinary diversity of beetles has long fascinated evolutionary biologists (*1*). The strongly sclerotized front wings defining the order Coleoptera (the beetles), which provide protection while retaining the ability of powered flight with the membranous hindwings, may be an evolutionary novelty that promoted extensive diversification (*2*). Beetles appeared around 285 million years ago (Ma) (*2*, *3*), followed by radiations of wood-boring (suborder Archostemata), predacious (Adephaga), and fungivorous (Polyphaga) lineages (*4*) present in the fossil record from the middle Triassic on (*2*, *3*). Their species richness is associated with extreme morphological, ecological, and behavioral diversity (*4*), and diversification of the most species-rich extant lineages may have been driven by co-radiations with angiosperms (*5*) and/or mammals (*6*) and/or geological and climatic change (*7*) occurring since the Cretaceous (145 to 65 Ma).

Studies of phylogenetic relationships within the Coleoptera resulted in a preliminary consensus on the classification, defining 4 suborders, 17 superfamilies, and 168 families (*8*–*10*). However, formal phylogenetic analyses of morphological characters (*11*, *12*) and more recently molecular data (*5*, *13*, *14*) have been limited to subgroups at the family or superfamily level. Because of the sheer size of the group and the complexity of morphological character systems, these analyses have not been applied to the entire order.

We compiled a three gene data matrix providing a complete taxonomic representation for all suborders, series and superfamilies; >80% of recognized families; and >60% of subfamilies (*9*, *10*), which together contain >95% of described beetle species. Sequences for the small subunit ribosomal RNA (18 *S* rRNA) were obtained for 1880 species from de novo sequencing and existing databases. Mitochondrial 16S rRNA (*rrnL*) and cytochrome oxidase subunit I (*cox1*) sequences were added for nearly half of these taxa (table S1) to create a data matrix of rapid, medium, and slowly evolving sequences. Phylogenetic analysis of the combined matrix was performed with a fragment-extension procedure for global sequence alignment followed by tree searches with fast parsimony algorithms (*15*). We tested for long-branch attraction, i.e., the spurious pairing of rapidly evolving lineages, by removing taxa terminal to long branches and assessing trees with a retention index (RI) measure of fit to the traditional classification (table S2) (*15*). The resulting parsimony tree largely agrees with the existing classification at the family and superfamily levels [on average, 95.7% of terminals assigned to a family were recovered as monophyla (table S2)], although our taxon sampling was not comprehensive in some families. Model-based Bayesian methods were applied to a 340-taxon representative subset at the subfamily level.

The trees (Figs. 1 and 2) were rooted with the neuropterid orders, the presumed sister to the Coleoptera (*16*), and recovered the major subdivisions of Adephaga [37,000 known species; posterior probability (*pp*) = 1.0] and Polyphaga (>300,000 species; *pp* = 1.0) as sisters to the Myxophaga (94 species) plus Archostemata (40 species) (*8*). The Adephaga was divided into two clades containing an aquatic (Hydradephaga; diving beetles and whirligig beetles; *pp* = 0.90) and a terrestrial (Geadephaga; ground beetles and tiger beetles; *pp* = 1.0) lineage, supporting a single terrestrial-to-aquatic transition in this suborder (*13*).

In the strongly supported suborder Polyphaga, five families occupied the basal nodes (Figs. 1 and 2) (*pp* = 1.0). These families include the Decliniidae; the Scirtidae, with aquatic larvae; the Derodontidae, an ecologically diverse family from global temperate zones; and the Eucinetidae and the Clambidae. These ancestral five families were previously considered basal Elateriformia (superfamily Scirtoidea), except for Derodontidae,

[1]Department of Entomology, Natural History Museum, Cromwell Road, London SW7 5BD, UK. [2]Department of Biology, Imperial College London, Silwood Park Campus, Ascot SL5 7PY, UK. [3]Department of Zoology, Faculty of Science, Palacky University, tr. Svobody 26, 77146 Olomouc, Czech Republic. [4]Zoologische Staatssammlung München, Münchhausenstrasse 21, 81247 München, Germany. [5]Santa Barbara Museum of Natural History, 2559 Puesta del Sol Road, Santa Barbara, CA 93105–2998, USA. [6]Fisiologia i Biodiversitat Molecular, IBMB-CSIC, Jordi Girona 18-26, 08034 Barcelona, Spain. [7]Departamento de Biodiversidad y Biología Evolutiva, Museo Nacional de Ciencias Naturales, José Gutiérrez Abascal 2, 28006 Madrid, Spain. [8]Department of Biology, Pedagogical Faculty, Palacky University, Purkrabska 2, 77140 Olomouc, Czech Republic.

*These authors contributed equally to the work.
†To whom correspondence should be addressed. E-mail: a.vogler@imperial.ac.uk

Septième partie

Articles : Le problème des constantes élastiques

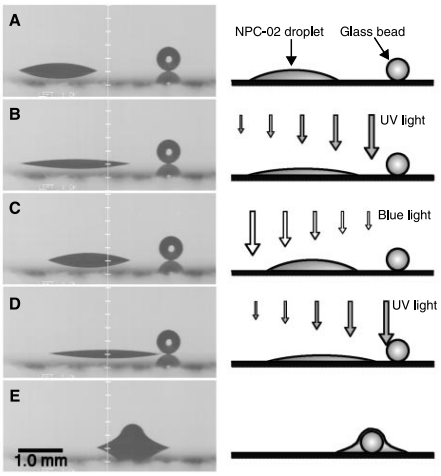

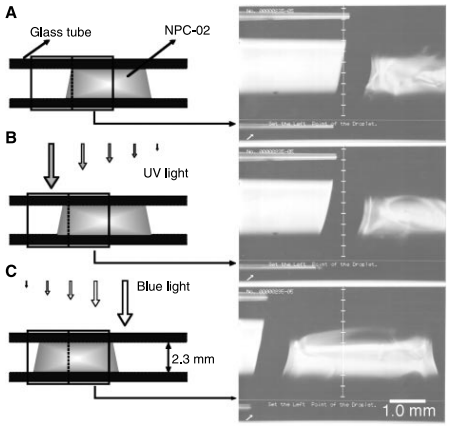

Fig. 5 (left). Light-driven motion of an NPC-02 droplet on a CRA-CM–modified plate to capture a glass bead (diameter ~0.5 mm). A droplet was placed on a CRA-CM–modified plate (**A**), followed by UV light irradiation at the right edge of the droplet to cause an asymmetrical spreading (**B**). Subsequent irradiation with blue light at the left edge resulted in dewetting, leading to the displacement of the droplet (**C**). The repetition of this stepwise photoirradiation resulted in the approach of the droplet to the bead (**D**), which was finally captured by the liquid (**E**). **Fig. 6 (right).** Light-driven displacement of an NPC-02 droplet in a glass tube. A droplet of NPC-02 was placed in the tube (**A**), and one edge of the droplet was exposed to UV light, leading to the slight advancement of the droplet (**B**). Subsequent irradiation with blue light at the opposite edge pushed the droplet to the left (**C**).

taining surfactants can be controlled by light (*26*). In contrast, our work demonstrates a photoinduced liquid motion triggered by azobenzenes immobilized on a solid surface.
15. S.-K. Oh, M. Nakagawa, K. Ichimura, *Chem. Lett.* **4**, 349 (1999).
16. M. Fujimaki *et al.*, *Langmuir* **14**, 4495 (1998).
17. E. Kurita *et al.*, *J. Mater. Chem.* **8**, 397 (1998).
18. Olive oil is a mixture containing fatty acids, vitamins and so on, and contains 55 to 85% oleic acid.
19. Y. L. Chen, C. A. Helm, J. N. Israelachvili, *J. Phys. Chem.* **95**, 10736 (1991).
20. The condition includes both equilibrium thermodynamic and dynamic factors, and is applicable to previously described methods for moving liquids by a driving force arising from an imbalance in surface tension forces. As an example, see (*5*).
21. An NPC-02 drop at 40°C (nematic-isotropic transition temperature of NPC-02 is 35°C) also exhibited the light-driven motion. Detailed studies including the effect of liquid crystallinity on the spreading kinetics of the liquid will be published elsewhere (S.-K. Oh, M. Nakagawa, K. Ichimura, in preparation).
22. T. Seki, H. Sekizawa, S. Morino, K. Ichimura, *J. Phys. Chem. B* **102**, 5313 (1998).
23. I. Panaiotov, S. Taneva, A. Bois, F. Rondelez, *Macromolecules* **24**, 4250 (1991).
24. F. Brochard, *Langmuir* **5**, 432 (1989).
25. The difference between the advancing and receding dynamic contact angles was less than 2°, even though the advancing and receding edges of the moving droplet would be placed on cis-rich (θ^{cis}_{adv} = 11°) and trans-rich (θ^{tr}_{rec} = 24°) surfaces, respectively.
26. J. Y. Shin and N. L. Abbott, *Langmuir* **15**, 4404 (1999).

21 January 2000; accepted 30 March 2000

Raman Spectroscopy of Iron to 152 Gigapascals: Implications for Earth's Inner Core

Sébastien Merkel,[1,2] Alexander F. Goncharov,[1] Ho-kwang Mao,[1] Philippe Gillet,[2] Russell J. Hemley[1]

Raman spectra of hexagonal close-packed iron (ε-Fe) have been measured from 15 to 152 gigapascals by using diamond-anvil cells with ultrapure synthetic diamond anvils. The results give a Grüneisen parameter γ_o = 1.68 (±0.20) and q = 0.7 (±0.5). Phenomenological modeling shows that the Raman-active mode can be approximately correlated with an acoustic phonon and thus provides direct information about the high-pressure elastic properties of iron, which have been controversial. In particular, the C_{44} elastic modulus is found to be lower than previous determinations. This leads to changes of about 35% at core pressures for shear wave anisotropies.

Understanding recent geophysical observations of elastic anisotropy, possible superrotation, and magnetism of Earth's inner core (*1*) requires detailed information about the thermodynamic and elastic properties of core-forming materials under appropriate conditions. High-pressure properties of iron are crucial in this respect because the core is composed primarily of this element. Iron transforms from the body-centered cubic (bcc) phase (α-Fe) at ambient conditions to a face-centered cubic (fcc) phase (γ-Fe) at moderate pressures and temperatures and to a higher-pressure hexagonal close-packed (hcp) phase (ε-Fe) (>13 GPa) (*2*). The hcp phase has a wide stability field to more than 300 GPa and high temperatures (*3–5*). Techniques to measure lattice strains at megabar pressures (*6*) have determined the elastic properties of ε-Fe to 210 GPa (*7*). These results show discrepancies with calculations in which first-principles methods were used (*8–10*), in particular for shear moduli and anisotropy. Measurements and estimates of the Grüneisen parameter, an important thermodynamic property of iron that relates the

[1]Geophysical Laboratory and Center for High Pressure Research, Carnegie Institution of Washington, 5251 Broad Branch Road, NW, Washington, DC 20015, USA. [2]Laboratoire des Sciences de la Terre, UMR CNRS 5570, Ecole Normale Supérieure de Lyon, 46 allée d'Italie, 69364 Lyon Cedex 07, France.

thermal pressure and the thermal energy, show large discrepancies (*5, 11–16*). Recently, the phonon density of states of ε-Fe at high pressure has been investigated up to 42 GPa (*16*) and 153 GPa (*17*) by inelastic nuclear resonance x-ray scattering. Notable differences with the results of first-principles calculations are also found (*17*). Thus, there is a need to clarify the elastic and thermodynamic properties of iron at core pressures.

For many years, it was thought that vibrational Raman spectroscopy of simple metals was not possible at high pressures because of the weak scattering due to the high reflectivity and strong background from the apparatus (e.g., diamond-anvil cell). The bcc (α-Fe) and fcc (γ-Fe) phases have no first-order Raman spectra because all the atoms sit on inversion centers. The ε-Fe hcp phase has one Raman-active mode of E_{2g} symmetry (*18*). Recent studies have shown that the E_{2g} phonon mode in some hcp metals can be measured at moderate pressure in diamond cells. Measurements have been performed on Zn (*19*), Si (*19*), Zr (*20*), and Mg (*21*), but the E_{2g} mode of ε-Fe was expected to be particularly weak (*22*) and has not been reported. Information on the frequency of the E_{2g} mode of ε-Fe and its evolution with pressure provides experimental information on thermodynamic properties of the material because such vibrational frequencies are input data for construction of consistent thermodynamic models (*23*). Moreover, the mode correlates with a transverse acoustic phonon; thus, its frequency shift provides information on the pressure dependence of shear moduli (i.e., C_{44}), which is crucial for constraining the elastic anisotropy of iron at core pressures. Measurement of the phonon also provides a critical test of first-principles methods, which have been a difficult problem for iron.

High-purity polycrystalline Fe samples were loaded in a piston-cylinder–type diamond cell; two sets of experiments were performed at 15 to 50 GPa and 25 to 152 GPa (*24*). To reduce the background luminescence and scattering from the diamond anvils (which could be much stronger than the sample), we used ultrahigh-purity synthetic diamond anvils, which in previous work have been crucial for studying weak Raman excitations in the hundreds of gigapascals pressure range (*25*). We also used a 35° incidence angle for the exciting radiation, which prevents specular reflection from being directed to the spectrometer and reduces the signal from the diamonds. The diameter of the laser spot was less than 10 μm, which is smaller than the sample size, so effects of the pressure gradients are minimized. Signal levels were maximized with a high-throughput single-grating spectrometer with holographic notch filters.

Two Raman bands were observed at moderate pressures (between 15 and 40 GPa), with the stronger band identified as the E_{2g} fundamental predicted by symmetry for the hcp lattice (*26*) (Fig. 1). The mode exhibits a sublinear frequency increase with pressure (Fig. 2). Raman spectra measured together with the ruby fluorescence in different locations of the sample show consistent results. Moreover, spectra measured on compression and decompression are close, which indicates that the uniaxial stress does not have an important effect on these results. The measured frequencies are lower than first-principles results (*27*), although the pressure dependence is similar (Fig. 2). An empirical model (*28*) gives much lower frequencies. The positive pressure shift (initial slope $d\nu_0/dP$ = 1.0 cm^{-1}/GPa) is consistent with the wide stability range of ε-Fe (*3–5*), in contrast to the behavior of several other hcp metals (see below).

We examined the thermal Grüneisen parameter γ_{th} at high pressure. Despite the importance of the Grüneisen parameter of ε-Fe, experimental data have been limited and do not agree (Table 1). The mode-Grüneisen parameter γ_i of the Raman mode is defined as

$$\gamma_i = -[(d \ln\nu)/(d \ln V)] \quad (1)$$

where ν is the frequency of the mode and V is the volume. It provides an approximate means for calculating γ_{th} with $\gamma_i = \langle\gamma_i\rangle \sim \gamma_{th}$. This assumes that the γ_i for the mode is representative of all the vibrations of the crystal (*23*). We can write

$$\gamma_i \sim \gamma_{th} = \gamma_0(V/V_0)^q \quad (2)$$

where γ_0 represents the extrapolated value of γ_{th} at zero pressure with the volume dependence of γ_{th} explicitly given by the parameter q. Using this relation and the equation of state of ε-Fe (*3*, *29*), we calculate γ_0 = 1.68 (±0.20) and q = 0.7 (±0.5). Assuming q = 1, we have γ_0 = 1.81 (±0.03). The results agree with the analysis of recent high-pressure, high-temperature x-ray diffraction measurements (*5*), which suggests that γ_i of the E_{2g} mode provides a good approximation for $\langle\gamma_i\rangle$. Our analysis is also compatible with that obtained from measurements of the phonon density of state of ε-Fe between 20 and 40 GPa, where q = 0 was assumed (*16*) (Table 1).

In ε-Fe, the C_{44} elastic modulus and the E_{2g} Raman mode are properties of the same phonon branch. Specifically, the E_{2g} mode correlates with a transverse acoustic phonon

Table 1. Thermal Grüneisen γ_0 parameter of ε-Fe and its volume dependence q.

Pressure range (GPa)	γ_0	q	Method
15 to 100	2.2	1	Shock compression (*11*)
15 to 100	2.2 (±0.5)	1.62 (±0.37)	Shock compression (*12*)
20 to 250	2.75	1.5	First-principles (*13*)
0 to 240	1.7	0.7	Theory (*15*)
15 to 300	1.78 (±0.06)	0.69 (±0.10)	X-ray diffraction (*5*)
20 to 42	1.5 (±0.2)	0	Phonon density of states (*16*)
15 to 150	1.68 (±0.20)	0.7 (5)	This study*

*If we fix different values of q, we obtain the following: q = 0, γ_0 = 1.44 (±0.03); q = 1, γ_0 = 1.81 (±0.03); q = 1.5, γ_0 = 2.02 (±0.04).

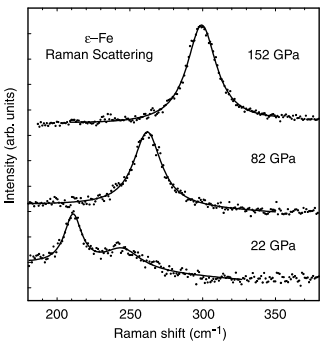

Fig. 1. Raman spectra of ε-Fe at selected pressures. The strong band is identified as the E_{2g} optical phonon; a weaker feature is observed at higher frequencies and lower pressures. Solid line, Lorentzian fit to the peak, which suggests a homogeneous line shape.

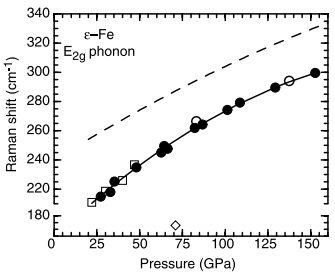

Fig. 2. Pressure shift of E_{2g} Raman phonon in ε-Fe. Open squares, first set of experiments; filled and open circles, second set of experiments during loading and unloading, respectively; solid line, second-order polynomial fit to experimental data; dashed line, fit to the results of first-principles calculations by the techniques described in (*28*) but for ambient temperature (*27*); open diamond, result of an empirical model (*28*).

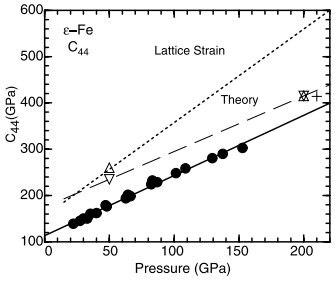

Fig. 3. Pressure dependence of the shear modulus C_{44} of ε-Fe deduced from the E_{2g} phonon frequency. Solid circles, experimental data; solid line, linear fit through the data; up and down triangles, LDA and GGA first-principles calculations, respectively, from (*9*); +, first-principles result (*10*); dashed line, guide to the eye for LDA results; dotted line, pressure dependence determined from lattice-strain measurements (*7*).

and C_{44} represents the slope of this branch at the center of the Brillouin zone. With a phenomenological model, they may be related as

$$C_{44} = 2\pi^2 M[(3)^{1/2}c/(6a^2)]\nu^2 \qquad (3)$$

where M is the atomic mass of iron, c and a are unit cell parameters, and ν is the frequency of the optical phonon (*30*). Applying this relation to our data, we deduce the pressure dependence of the C_{44} of ε-Fe (Fig. 3). Notably, our data are lower than the results of lattice-strain experiments (*7*). The analysis used in these experiments assumes that the state of stress on all crystallographic planes is identical. However, recent work has shown that this may not be satisfied in a material undergoing anisotropic deformation, specifically in many hcp transition metals (*31*). The first-principles results (*9*, *10*) are also higher than those obtained here. Application of first principles for magnetic metals such as iron has been problematic, partly because differences between theory and experiments for the pressure-volume relation at low pressures (*32*) may be associated with changes of the magnetic properties within ε-Fe (*9*). The use of Raman spectroscopy to determine the pressure dependence of C_{44} is exact for a sine dispersion relation; if the phonon branch does not deform with pressure, this assumption can be supported by theory (*27*, *28*).

Table 2. Raman shift and deduced and measured C_{44} elastic modulus at zero pressure for three hcp metals.

Element	Raman shift (cm^{-1})	C_{44} (GPa)	
		Calc.	Exp.
Zr	87 (*20*)	28.9	33.4 (*37*)
Mg	122 (*21*)	15.9	18.6 (*37*)
Zn	71.5 (*19*)	19.8	39.6 (*37*)

The results have important geophysical implications. Although knowledge of C_{44} is not sufficient to calculate the full seismic anisotropy parameters, the shear wave polarized perpendicular to the basal plane (S1) and that polarized parallel to the basal plane (S2) have the anisotropies

$$\Delta_{S1} = (C_{11}+C_{33}-2C_{13})/4C_{44},\ \Delta_{S2} = C_{44}/C_{66} \qquad (4)$$

Therefore, the lower value of C_{44} found here would increase Δ_{S1} and decrease Δ_{S2}. Assuming no difference in the estimation of the other elastic moduli (*7*) arising from the change of C_{44}, we calculate $\Delta_{S1} \approx 0.65$ and $\Delta_{S2} \approx 1.44$ at 39 GPa, corresponding to changes of about 35%. This also improves the agreement with the first-principles calculations (*33*).

Finally, we can compare the results with those of other hcp structured transitions metals that have been studied recently by high-pressure Raman spectroscopy—for example, Zn (*19*), Si (*19*), Zr (*20*), and Mg (*21*). The behavior of the E_{2g} phonon with pressure differs appreciably from one to another. Zn, Si, and Mg show an increase of frequency with pressure with initial slopes ($d\nu_0/dP$) of about 3.3, 3.1, and 3 cm^{-1}/GPa, respectively. In contrast, ε-Fe also shows a positive pressure shift but with a $d\nu_0/dP$ of 1.0 cm^{-1}/GPa. Comparing γ_i values, we find $\gamma_i(Zn) \approx 2.4$ between ambient pressure and 12 GPa, $\gamma_i(Mg) \approx 1.6$ at ambient pressure, and $\gamma_i(Si) \approx 6$ near 40 GPa compared with $\gamma_i(Fe) = 1.44$ (± 0.03) between 20 and 150 GPa. Zirconium appears to be a unique case: mode softening is observed for the E_{2g} phonon of α-Zr, with $d\nu_0/dP = -0.7$ cm^{-1}/GPa (*20*). Moreover, the relation between elastic modulus C_{44} and the frequency of the E_{2g} mode (Eq. 3) can be examined for Zr, Mg, and Zn because they crystallize in the hcp structure at zero pressure and reliable experimental measurements of C_{44} are available (Table 2). The results agree to within 15% for Zr and Mg, but a large discrepancy is found for Zn, which undergoes higher-pressure phase transition and anomalous changes in electronic structure (*34*) (not evident in Fe). Direct comparison of the measured and calculated frequency of the E_{2g} phonon at different pressures is possible for Mg (*35*) and Zr (*36*). In both cases, we find that the measured frequency is lower than that calculated by first-principles methods, which is consistent with results obtained for ε-Fe (Figs. 2 and 3). This study and analysis open the possibility of Raman investigations of the vibrational dynamics of other metals, including planetary core-forming materials at megabar to multimegabar pressures.

References and Notes

1. X. Song and P. G. Richards, *Nature* **382**, 221 (1996); W. Su, A. M. Dziewonski, R. Jeanloz, *Science* **274**, 1883 (1996); G. A. Glatzmaier and P. H. Roberts, *Science* **274**, 1887 (1996); W. Kuang and J. Bloxham, *Nature* **389**, 371 (1997).
2. T. Takahashi and W. A. Bassett, *Science* **145**, 483 (1964); F. P. Bundy, *J. Appl. Phys*. **36**, 616 (1965); J. M. Brown and R. G. McQueen, *J. Geophys. Res*. **91**, 7485 (1986); R. Boehler, N. von Bargen, A. Chopelas, *J. Geophys. Res*. **95**, 21731 (1990).
3. H. K. Mao, Y. Wu, L. C. Chen, J. F. Shu, A. P. Jephcoat, *J. Geophys. Res*. **95**, 21737 (1990).
4. G. Shen, H. K. Mao, R. J. Hemley, T. S. Duffy, M. L. Rivers, *Geophys. Res. Lett*. **25**, 373 (1998); G. Shen and D. L. Heinz, *Rev. Mineral*. **37**, 369 (1998). These studies have shown that the fcc-hcp liquid-triple point is at 60 GPa and 2500 K, with the hcp phase stable at higher pressures and temperatures (at least 155 GPa and 3000 K). The stability of ε-Fe at core conditions is also consistent with recent shock-wave results [J. H. Nguyen and N. C. Holmes, personal communication] as well as theory [L. Vočadlo, J. Brodholt, D. Alfè, M. J. Gillan, G. D. Price, *Phys. Earth Planet. Inter*. **117**, 123 (2000)].
5. L. S. Dubrovinsky, S. K. Saxena, N. A. Dubrovinskaia, S. Rekhi, T. Le Bihan, *Am. Mineral*. **85**, 386 (2000); L. S. Dubrovinsky, S. K. Saxena, F. Tutti, S. Rekhi, T. Le Bihan, *Phys. Rev. Lett*. **84**, 1720 (2000). These studies indicate that the hcp phase is stable to at least 300 GPa and 1500 K.
6. R. J. Hemley *et al.*, *Science* **276**, 1242 (1997); A. K. Singh, H. K Mao, J. Shu, R. J. Hemley, *Phys. Rev. Lett*. **80**, 2157 (1998); A. K. Singh, C. Balasingh, H. K Mao, R. J. Hemley, J. Shu, *J. Appl. Phys*. **83**, 7567(1998).
7. H. K. Mao *et al.*, *Nature* **396**, 741 (1998) [correction, *Nature* **399**, 280 (1999)].
8. L. Stixrude and R. E. Cohen, *Science* **267**, 1972 (1995).
9. G. Steinle-Neumann, L. Stixrude, R. E. Cohen, *Phys. Rev. B* **60**, 791 (1999).
10. A. Laio, S. Bernard, G. L. Chiarotti, S. Scandolo, E. Tosatti, *Science* **287**, 1027 (2000).
11. R. G. McQueen *et al.*, in *High Velocity Impact Phenomena*, R. Kinslow, Ed. (Academic Press, San Diego, CA, 1970), p. 296.
12. R. Jeanloz, *J. Geophys. Res*. **84**, 6059 (1979).
13. E. Wasserman, L. Stixrude, R. E. Cohen, *Phys. Rev. B* **53**, 8296 (1996).
14. L. Stixrude, E. Wasserman, R. E. Cohen, *J. Geophys. Res*. **102**, 24729 (1997).
15. O. L. Anderson, *Phys. Earth Planet. Inter*. **109**, 179 (1998).
16. R. Lübbers, H. F. Grünsteudel, A. I. Chumakov, G. Wortmann, *Science* **287**, 1250 (2000).
17. H.-K. Mao *et al.*, unpublished data.
18. The hcp structure has two atoms per unit cell, which are located on sites of symmetry D_{3h}. The six normal modes of zero wave vector belong to the irreducible representations $A_{2u} + B_{1g} + E_{1u} + E_{2g}$. The B_{1g} and E_{2g} are optical phonons polarized along and perpendicular to the optical axis, respectively. The doubly degenerate E_{2g} mode is Raman active.
19. H. Olijnyk, *High Pressure Res*. **10**, 461 (1992); H. Olijnyk, *Phys. Rev. Lett*. **68**, 2232 (1992).
20. H. Olijnyk and A. P. Jephcoat, *Phys. Rev. B* **56**, 10751 (1997).
21. H. Olijnyk and A. P. Jephcoat, in *Program of the AIRAPT-XVII Conference*, M. H. Manghnani, Ed. [*International Association for the Advancement of High Pressure Science and Technology* (AIRAPT), Honolulu, HI, 1999], p. 148.
22. A. P Jephcoat, H. Olijnyk, K. Refson, *Eos* **80**, F929 (1999).
23. P. Gillet, R. J. Hemley, P. F. McMillan, *Rev. Mineral*. **37**, 525 (1998).
24. The gasket material was W for the first experiment and Rh for the second experiment. There was no pressure medium. Raman spectra were excited with the 488- and 514.5-nm lines of an argon-ion laser and measured with a single-grating ISA HR-460 spectrometer equipped with a charged-coupled device (CCD) detector. Pressures were determined by the ruby fluorescence method [H. K. Mao, J. Xu, P. M. Bell, *J. Geophys. Res*. **91**, 4673 (1986)].
25. A. F. Goncharov, R. J. Hemley, H. K. Mao, J. Shu, *Phys. Rev. Lett*. **80**, 101 (1998); A. F. Goncharov, V. Struzhkin, H. K. Mao, R. J. Hemley, *Phys. Rev. Lett*. **83**, 1998 (1999).
26. The low-frequency band becomes stronger with pres-

sure, which suggests increased ordering of the hcp lattice and that the high-frequency weak band is disorder induced. The high-frequency band remained in the spectra on pressure release to 7 GPa, unlike the hcp Raman phonon, which disappears at the phase transition back to bcc α-Fe.
27. L. Vočadlo, personal communication.
28. D. Alfè, G. D. Price, M. J. Gillan, *Phys. Rev. B*, in press.
29. A. P. Jephcoat, H. K. Mao, P. M. Bell, *J. Geophys. Res.* **91**, 4677 (1986).
30. This relation can be derived with a three-body force model for an hcp solid with a nonideal *c*/*a* ratio [J. C. Upadhyaya, D. K. Sharma, D. Prakash, S. C. Upadhyaya, *Can. J. Phys.* **72**, 61(1994)].
31. H. R. Wenk, S. Matthies, J. Shu, R. J. Hemley, H.-K. Mao, *Nature*, submitted; see also [H. R. Wenk, T. Takeshita, R. Jeanloz, G. C. Johnson, *Geophys. Res. Lett.* **15**, 76 (1988)].
32. L. Stixrude, R. E. Cohen, D. J. Singh, *Phys. Rev. B* **50**, 6442 (1994).
33. For example, at a reference pressure of 210 GPa [see (*10*)], the lattice-strains experiments (*7*) lead to $\Delta_{S1} = 0.60$ and $\Delta_{S2} = 1.70$, the first-principles LDA calculations (*9*) give $\Delta_{S1} = 1.27$ and $\Delta_{S2} = 0.99$, and the first-principles OP calculations (*10*) give $\Delta_{S1} = 1.03$ and $\Delta_{S2} = 1.02$. If we extrapolate the C_{44} calculated here and substitute it into the lattice-strains results (*7*), we deduce $\Delta_{S1} = 0.91$ and $\Delta_{S2} = 1.12$, which is closer to theory.
34. K. Takemura, in *Program of the AIRAPT-XVII Conference*, M. H. Manghnani, Ed. (AIRAPT, Honolulu, HI, 1999), p. 150.
35. J. D. Althoff, P. B. Allen, R. M. Wentzcovitch, *Phys. Rev. B* **48**, 13253 (1993).
36. S. A. Ostanin, E. I. Salamatov, V.Y. Trubitsin, *Phys. Rev. B* **58**, 15962 (1998).
37. E. A. Brandes, Ed. *Smithells Metals Reference Book* (Butterworths, London, 1983); F. Marinelli, M. Roche, I. Baraille, C. Pauchan, *Phys. Rev. B* **54**, 6054 (1996).
38. We thank L. Vočadlo for communicating unpublished results and very helpful correspondence; we are grateful to V. V. Struzhkin, E. Gregoryanz, and R. E. Cohen for useful discussions and P. McMillan and other reviewers for their comments.

13 March 2000; accepted 19 April 2000

Accretion of Primitive Planetesimals: Hf-W Isotopic Evidence from Enstatite Chondrites

Der-Chuen Lee[1,2] and Alex N. Halliday[2]

Enstatite chondrites have often been considered to be closely related to the material from which Earth accreted. However, tungsten isotopic data reveal clear differences. Moreover, the silicate and metal fractions define distinct initial $^{182}Hf/^{180}Hf$ corresponding to a 13.8 ± 5.3 million year apparent age difference. Internal reequilibration does not provide a ready explanation for this result. Larger scale redistribution of tungsten is more likely, such as may have occurred during collisions between planetesimals.

Enstatite chondrites formed in a highly reduced environment, possibly in the inner regions of the solar nebula (*1*, *2*). They are the only group of chondrites whose silicate fractions have oxygen isotopic compositions similar to those of Earth and the moon (*3*), prompting some to suggest a genetic relationship (*4*). The Mn-Cr isotopic data for enstatite chondrite leachates and residues define an initial Cr isotopic composition that is similar to that of silicate Earth and the moon (*5*, *6*), and this has been used to argue that the enstatite chondrite parent body (ECPB) may have formed at the same heliocentric distance. However, many features of enstatite chondrites are enigmatic and hard to explain. There are substantial compositional gaps between the enstatite chondrites and the Earth-moon system (*2*, *7*), and chemical evidence for heterogeneous accretion of the ECPB has been presented (*8*). Furthermore, the relationship with Earth is unlikely to be straightforward. For example, dynamic simulations suggest that localized feeding zones for the growth of planetesimals and planets are unrealistic (*9*). Rather, planetary accretion can sample a broad provenance (*9*, *10*).

The recently developed ^{182}Hf-^{182}W chronometer (half-life = 9 million years) is well suited for studying accretion in the inner solar system (*11*–*15*). Both Hf and W are highly refractory. However, chemically they are quite different, with Hf being strongly lithophile ("silicate-loving") and W moderately siderophile ("metal-loving"), such that fractionation between Hf and W occurs during metal-silicate differentiation and partial melting (*11*, *12*). Hence, excess ^{182}W in the W atomic abundance is found in meteorites that sample high Hf/W silicate reservoirs formed within the life-span of ^{182}Hf. This is as found in some eucrites, martian meteorites, lunar samples, and the silicate phases of ordinary chondrites (*13*–*15*). Conversely, a deficit in ^{182}W is found in early metals such as iron meteorites and the metal fractions of ordinary chondrites, because they have low Hf/W (*10*, *11*, *16*, *17*). Ordinary chondrites appear to define reasonable internal Hf-W isochrons with a linear functional relation between Hf/W and W isotopic compositions. Here we report data for enstatite chondrites and find different behavior implying systematic redistribution and mixing of W.

Four enstatite chondrites, including EH and EL groups, Abee (EH4), Indarch (EH4), ALHA81021 (EL6), and Hvittis (EL6), were selected for study. Experimental procedures (*18*) were as used previously (*15*). The Hf-W data for all four enstatite chondrites (Table 1) show a positive correlation between measured Hf/W ratios and the respective W isotopic compositions of individual fractions (Fig. 1), consistent with the former presence of ^{182}Hf. In detail, however, the metals and silicates display distinct characteristics (Fig. 1).

Portions of the magnetic (largely metal) fractions of each meteorite were leached in 6 M HCl (*18*). The leachates contain the easily soluble metal, sulfide, and minor phosphate fractions with low Hf/W (Table 1). The residues from this procedure mainly comprise small amounts of silicates and minor oxides, insoluble in 6 M HCl. The Hf-W data for all of these "magnetic fractions," that is, bulk metals, metal leachates, and metal residues, are collinear, intersecting the data for the carbonaceous chondrites, Allende and Murchison (*11*, *12*) (Fig. 1). These data are also collinear with the data for the ordinary chondrites (*15*), providing evidence that the metals are coeval and early (Web fig. 1) (*19*). A regression of the data for all enstatite chondrite metals, their leachates and residues, and the whole rock values of Allende and Murchison yields a slope (equal to initial $^{182}Hf/^{180}Hf$) of $(1.85 \pm 0.38) \times 10^{-4}$ (Fig. 2), equivalent to that defined by the ordinary chondrites ($\sim 1.8 \times 10^{-4}$) (*15*). The regression results are the same but with larger uncertainties if the carbonaceous chondrites are excluded [$(1.88 \pm 0.73) \times 10^{-4}$]. The initial $^{182}Hf/^{180}Hf$ at the start of the solar system is thought to lie in the range $(1.87 \pm 0.16) \times 10^{-4}$ to $(2.75 \pm 0.24) \times 10^{-4}$ (*15*). On this basis, the metals in the enstatite chondrites formed within a few million years, at most, of the start of the solar system.

In contrast, the nonmagnetic fractions (predominantly silicates) for each sample lie to the right of and below the best-fit line defined by the magnetic (metal) fractions (Fig. 1). The data for the nonmagnetic frac-

[1]Department of Geological Sciences, University of Michigan, Ann Arbor, MI 48109–1063, USA. [2]Institute for Isotope Geology and Mineral Resources, Department of Earth Sciences, ETH Zürich, CH-8092, Zürich, Switzerland.

ELSEVIER

Earth and Planetary Science Letters 194 (2001) 201–212

EPSL

www.elsevier.com/locate/epsl

Effects of texture on the determination of elasticity of polycrystalline ε-iron from diffraction measurements

Siegfried Matthies [a,1], Sébastien Merkel [b,c], Hans Rudolf Wenk [a,*], Russell J. Hemley [b], Ho-kwang Mao [b]

[a] *Department of Earth and Planetary Science, University of California, Berkeley, CA 94720, USA*
[b] *Geophysical Laboratory and Center for High Pressure Research, Carnegie Institution, Washington, DC 20015, USA*
[c] *Laboratoire des Sciences de la Terre, Ecole Normale Supérieure de Lyon, Lyon, France*

Received 26 June 2001; received in revised form 28 September 2001; accepted 2 October 2001

Abstract

X-ray diffraction experiments on textured polycrystalline aggregates in the diamond anvil cell can be used to determine the single-crystal elastic properties of the material under high pressure. We describe a direct method to extract the elastic moduli of ε-Fe from diffraction data without assumptions used in previous models to evaluate the requirements on measurement precision. Assuming elastic properties and a realistic texture, variations of *d*-spacings with orientation have been calculated. From these data, and assuming a sufficient precision, it was possible to retrieve the elastic moduli used in input. We establish the feasibility of the method, which is also applicable to other materials. This is important for explaining the discrepancies between the experimental results and those from first-principles calculations. Implications for the seismic anisotropy in the Earth's inner core are discussed.

Keywords: iron; elasticity; textures; anisotropy

1. Introduction

Seismic observations have established that the solid inner core of the Earth is anisotropic and that seismic waves travel 3–4% faster along the axis of the Earth, than in the equatorial plane [1]. Knowledge of the single-crystal elastic moduli and the preferred orientation pattern of ε-iron, the principal constituent of the inner core [2], is crucial for understanding anisotropy in the Earth's core. Preferred orientation can originate from growth [3,4], flow induced by Maxwell stresses [5,6], or by thermal convection [7]. In view of these findings determination of the elastic moduli in ε-Fe under high pressure has been of great interest. Studies include first-principles calculations [8–12], radial diffraction experiments to above 200 GPa [13,14], and Raman spectroscopy [15] but the results of different methods do not agree. There is fair agreement between first-principles calculations cited above (all for 0 K) but

* Corresponding author. Fax: +1-510-486-7379.
E-mail address: wenk@seismo.berkeley.edu (H.R. Wenk).

[1] Present address: Mueller-Berset-Str. 3, D-01309 Dresden, Germany.

0012-821X/01/$ – see front matter
PII: S0012-821X(01)00547-7

models based on experimental data produce much more anisotropic values. Moreover, recent calculations predict major changes as a function of temperature at high pressure that reverse the sign of the elastic anisotropy [16]. Thus, there is a need to clarify both the preferred orientation and elastic properties in ε-Fe under high pressure and temperature.

Recently the elasticity of ε-Fe at high pressure was examined by X-ray diffraction experiments carried out with the diamond anvil cell. Systematic variations of *d*-spacings were analyzed as a function of orientation of corresponding lattice planes to the diamond cell axis (Fig. 1). The theory used in the analysis of the radial diffraction experiments on ε-Fe [17] assumed a random orientation of the crystallites in the sample and that the state of stress on all crystallographic planes is identical. However, it is well-established that ε-Fe samples prepared under these conditions are highly textured [18,19], with c-axes preferentially aligned parallel to the axis of compression. This provides an opportunity to determine the elastic constants directly from diffraction data, without assumptions used in previous analyses. Single-crystal elastic constants can be determined from diffraction experiments on stressed and textured polycrystals, either by observing changes in *d*-spacings while the applied stress is varied, or investigating, at constant stress, variations of *d*-spacings with orientation of lattice planes to the stress axis [20]. The latter method is applicable to diamond anvil cell experiments.

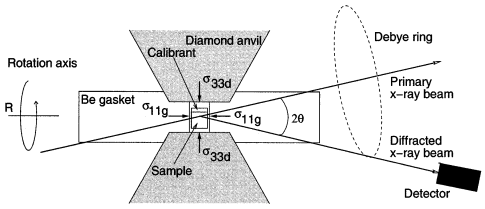

Fig. 1. Experimental setup for the diamond anvil cell radial diffraction experiments. The powdered sample is confined under non-hydrostatic stress between the two diamond anvils. σ_{33d} is the axial stress imposed by the diamonds and σ_{11g} the radial stress imposed by the gasket. The cell is rotated about an axis R to vary $\psi \equiv \vartheta$ in $\mathbf{y} = (\varphi, \vartheta)$.

We present a new approach to analyze the observations from the radial diffraction experiments. We begin by briefly reviewing key concepts of elasticity and preferred orientation and then describe the theoretical elements necessary to combine the elasticity and preferred orientation in the analysis of the radial diffraction results. We demonstrate the applicability of the method by generating synthetic 'experimental' data from assumed elastic moduli and experimental conditions, and then retrieving the moduli from those data. Finally, we apply this methodology to data from a previous experiment and discuss how the analysis could improve understanding the elasticity of ε-Fe at high pressure.

2. Elasticity and preferred orientation

2.1. Elasticity

The single-crystal elastic properties of a material can be characterized in terms of compliances S_{ijkl} or stiffnesses C_{ijkl} which, in linear elasticity theory, relate stress and strain in the sample using the relation [21]:

$$\sigma_{ij} = C_{ijkl}\varepsilon_{kl};\ \ \varepsilon_{ij} = S_{ijkl}\sigma_{kl} \tag{1}$$

They are components of twice symmetric fourth rank tensors ${}^0S$ and ${}^0C$ with properties:

$${}^0S = [{}^0C]^{-1};\ \ S_{ijkl} = S_{jikl} = S_{klij};\ \ i,j,k,l = 1,2,3 \tag{2}$$

In the case of hexagonal crystals, such as ε-iron, the crystal symmetry reduces the set of 21 independent moduli to five (${}^0C_{1111}$, ${}^0C_{1122}$, ${}^0C_{1133}$, ${}^0C_{3333}$, ${}^0C_{2323}$). The remaining moduli, which are not identical to zero follow from Eq. 2 and the relations:

$${}^0C_{2222} = {}^0C_{1111},\ {}^0C_{2233} = {}^0C_{1133},\ {}^0C_{1313} = {}^0C_{2323},$$

$$\text{and } {}^0C_{1212} = ({}^0C_{1111} - {}^0C_{1122})/2 \tag{2a}$$

The ${}^0C$ quantities can be used to evaluate properties such as bulk modulus, shear modulus and sound velocities in a single crystal. Because of

the anisotropic nature of the elastic moduli tensors, the seismic velocities will exhibit anisotropy.

2.2. Preferred orientation

Although individual crystals might exhibit elastic anisotropy, macroscopic polycrystalline aggregates are elastically isotropic if their crystallites are randomly oriented. But materials with preferred orientation (or 'texture') display anisotropic properties [22]. In order to include the effects of preferred orientation on the physical properties of a macroscopic polycrystalline sample, such as the propagation of seismic velocities, one has to introduce the orientation distribution function (ODF) $f(g)$ defined as follows. Let K_A be the macroscopic polycrystalline sample coordinate system and K_B a right-handed Cartesian coordinate system placed in the specimen (crystal coordinate system) fixed to the crystal lattice of a crystallite of the sample. The transformation to bring the K_A coordinate system onto K_B can be unequivocally given by three numbers (noted g) that represent a set of three well-defined rotations (g describes the orientation of the crystal relative to K_A). One choice for g is the set of Euler angles α, β, γ [23] with:

$$g = g(\alpha, \beta, \gamma) \equiv \{\alpha, \beta, \gamma\},\ \mathrm{d}g = \mathrm{d}\alpha\ \sin\beta\ \mathrm{d}\beta\ \mathrm{d}\gamma,$$

$$g \subseteq \mathrm{G}:\ 0 \leq \alpha, \gamma \leq 360^\circ,\ 0 \leq \beta \leq 180^\circ \qquad (3)$$

The ODF $f(g)$ describes the probability density to expect crystallites that have the orientation g within dg; thus:

$$f(g) \geq 0,\ \int_G f(g)\mathrm{d}łg = 1,\ \text{where } \mathrm{d}łg = \frac{1}{8\pi^2}\mathrm{d}g \qquad (4)$$

The degree of anisotropy in a polycrystalline sample is represented by the texture sharpness F_2

$$F_2 = \int_G [f(g)]^2 \mathrm{d}łg \qquad (5)$$

For a material with random texture, $F_2 = 1$, for a textured material, $F_2 > 1$.

2.3. Methods for estimating single-crystal elastic moduli under pressure

Single-crystal elastic moduli can be determined experimentally using acoustic methods or Brillouin scattering [24] but these techniques so far are applicable only over a limited pressure range, or can be used reliably only for transparent (or semi-transparent) samples. Raman spectroscopy along with phenomenological modeling provides direct information on the C_{2323} elastic modulus of hexagonal crystals [25]. This was applied to ε-Fe up to a pressure of 150 GPa [15] but this method can not be used to extract other elastic moduli directly.

New experimental techniques have been developed to extract elasticity information from results of X-ray and neutron diffraction on polycrystals under non-hydrostatic stress conditions [17,20,26–32]. Fig. 1 shows the experimental setup used in the case of the ultrahigh-pressure experiment with a diamond anvil cell. The very fine-powdered sample (grain size estimated to be $\sim$1 μm) is confined in a diamond anvil cell without any pressure medium to enhance the effect of non-hydrostatic stress. The diamonds induce a loading stress component σ_{33} that is larger than the radial stress component $\sigma_{11} = \sigma_{22}$ induced by the Be gasket. A finely collimated X-ray beam of cross section in the order of 10 μm allows accurate measurements on the sample. Diffraction is measured through the gasket and the cell is rotated to study the influence of the stress condition on the diffraction patterns. The original theory used in the analysis of these experiments to extract the elastic moduli assumed a random orientation of the crystallites in the sample [13,14] and this limits the analysis. The present study develops a theory that can be used to obtain the high-pressure single-crystal elastic properties of hexagonal ε-Fe from radial diffraction experiments on textured polycrystalline aggregates.

3. Theory of stress and strain in the radial diffraction experiment

3.1. Strain

The stress conditions applied to the sample can be expressed by the following tensor:

$$\sigma = \begin{bmatrix} \sigma_{11}0 \\ 0\sigma_{11} \\ 00 \end{bmatrix} = \begin{bmatrix} \sigma_{\mathrm{hydro}}0 \\ 0\sigma_{\mathrm{hydro}} \\ 00 \end{bmatrix} + \begin{bmatrix} -t/30 \\ 0-t/3 \\ 00 \end{bmatrix} \quad (6)$$

where σ_{hydro} is the mean normal stress (equivalent hydrostatic pressure) and $t = \sigma_{33} - \sigma_{11}$ the uniaxial stress component. The deviatoric stress components are:

$$\sigma'_{33} = 2t/3,\ \sigma'_{11} = \sigma'_{22} = -t/3 \quad (7)$$

The equivalent hydrostatic pressure σ_{hydro} determines the reference values of the hexagonal crystal structure parameters a^0, c^0/a^0 that are estimated using a previously measured equation of state for ε-iron [33]. Using parameters a^0 and c^0/a^0 (noted '$^0P(\sigma_{\mathrm{hydro}})$') the interplanar spacings under the equivalent hydrostatic pressure σ_{hydro} are:

$$d_0({}^0P, hkl) = \frac{a^0}{\sqrt{\frac{4}{3}(h^2 + hk + k^2) + \frac{l^2}{(c^0/a^0)^2}}} \quad (8)$$

The equivalent hydrostatic pressure also determines the set of elastic moduli $^0S(\sigma_{\mathrm{hydro}})$ that we are determining.

In the experiment, the diffraction direction defines a 'laboratory coordinate system' K_L with the axis Z_L parallel to the scattering vector **N** (bisector between the incoming beam and the diffracted X-ray beam collected by the detector) and X_L inside the plane containing the incident and diffracted beam and pointing towards the side of the detector (Fig. 2). The sample coordinate system K_A is defined by the stress environment on the sample with Z_A parallel to the diamonds axis. The crystal coordinate system K_B is defined for each crystallite according to the crystal structure. In K_B of a crystallite under consideration the direction of the normal to a diffracting (*hkl*) plane is given by $\mathbf{h}_i$. The scattering vector described in K_A is called **y**. The (*hkl*) planes observed in the spectrometer are a subset of the (*hkl*) planes of all crystallites defined by the condition ($\mathbf{y} \| \mathbf{h}_i$). The observed interplanar spacings $\overline{d}$ depend on the quasi-hydrostatic equivalent pressure cell parameters $^0P(\sigma_{\mathrm{hydro}})$, the elastic moduli $^0S(\sigma_{\mathrm{hydro}})$, the ODF *f*, the uniaxial stress *t*, the crystallographic plane (*hkl*), and the direction of measurement **y**. They can be expressed as follows:

$$\overline{d}(hkl,\ \mathbf{y}) = \overline{d}({}^0P,\ {}^0S,\ f,\ t,\ hkl,\ \mathbf{y}) \equiv d_0({}^0P,\ hkl)$$

$$\left[1 + \frac{\overline{d}({}^0P,\ {}^0S,\ f,\ t,\ hkl,\ \mathbf{y}) - d_0({}^0P,\ hkl)}{d_0({}^0P,\ jkl)}\right] =$$

$$d_0({}^0P,\ hkl)[1 + \overline{\varepsilon}'({}^0P,\ {}^0S,\ f,\ t,\ \mathbf{h}_i,\ \mathbf{y})] \quad (9)$$

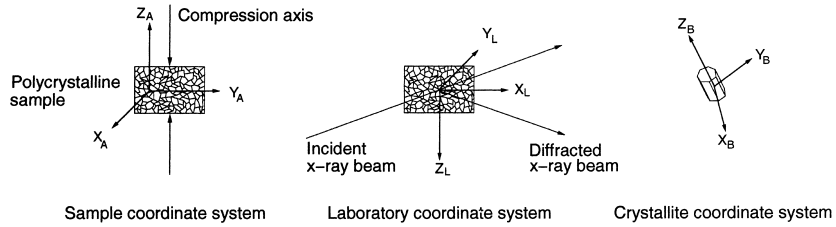

Fig. 2. Coordinate systems used in the analysis. The sample coordinate system K_A is defined by the stress environment on the sample. Z_A is parallel to the diamonds axis. For the laboratory coordinate system K_L, Z_L is parallel to the bisector between the incoming and diffracted X-ray beam and X_L is in the plane containing the incoming and diffracted beam, pointing towards the side of the detector. The crystallite coordinate system K_B is defined according to the crystallographic structure.

The averaging symbol (overline) denotes that the diffraction peak from a polycrystalline sample is formed by contributions of all crystallites in reflection position ($\mathbf{y}\|\mathbf{h}_i$), i.e. with the orientations g_p of the two paths g_p^+, g_p^- through the G-space:

$$g_p^+ = \{+\mathbf{h}_i, \tilde{\varphi}\}^{-1}\{\mathbf{y}, 0\};\ g_p^- = \{-\mathbf{h}_i, \tilde{\varphi}\}^{-1}\{\mathbf{y}, 0\};$$

$$0 \le \tilde{\varphi} \le 360^\circ \quad (10)$$

The number of these crystallites is obviously related to the texture of the sample, entering the average through $f(g_p)$.

In K_L, the strain symbol $\overline{\varepsilon}'$ in Eq. 9 can be interpreted as the 33 component of a strain tensor, i.e.:

$$\overline{d}({}^0P,\ {}^0S,\ f,\ t,\ hkl,\ \mathbf{y}) =$$

$$d_0({}^0P,\ hkl)|1 + \overline{\varepsilon}'^{L}_{33}({}^0P,\ {}^0S,\ f,\ t,\ \mathbf{h}_i,\ \mathbf{y})| \quad (11)$$

3.2. Relation to elastic moduli

We apply now Hooke's law in the laboratory coordinate system K_L. The strain may be expressed in terms of stress σ'^{L} and compliances S^L, thus:

$$\overline{\varepsilon}'^{L}_{33} = S^{L}_{33ij}({}^0P,\ {}^0S,\ f;\ \mathbf{h}_i,\ \mathbf{y})\sigma'^{L}_{ij} \quad (12)$$

The compliance components S^L_{33ij} given in K_L are then converted into the mixed laboratory sample coordinate system (K_L,K_A)-related stress factors S^{LA}_{33kl}, using the rotation matrix $\{\mathbf{y},0\}$ ($K_L \rightarrow K_A$), that determines the main **y**-dependence of the experimental $\overline{d}$:

$$S^{LA}_{33kl} = S^{L}_{33mn}\{\mathbf{y},0\}_{mk}\{\mathbf{y},0\}_{nl} \quad (13)$$

Using the stress factors, $\overline{\varepsilon}'^{L}_{33}$ is directly proportional to the deviatoric stresses (Eq. 7) given in K_A by:

$$\overline{\varepsilon}'^{L}_{33} = S^{LA}_{3333}({}^0P,\ {}^0S,\ f;\ \mathbf{h}_i,\ \mathbf{y})\sigma'_{33} +$$

$$S^{LA}_{3311}({}^0P,\ {}^0S,\ f;\ \mathbf{h}_i,\ \mathbf{y})\sigma'_{11} +$$

$$S^{LA}_{3322}({}^0P,\ {}^0S,\ f;\ \mathbf{h}_i,\ \mathbf{y})\sigma'_{22} =$$

$$[2\,S^{LA}_{3333} - S^{LA}_{3311} - S^{LA}_{3322}]t/3 \quad (14)$$

The 'diffractive compliances' $S^L({}^0P,\ {}^0S,\ f;\ \mathbf{h}_i,\ \mathbf{y})$ also depend on the direction of diffraction **y** through their dependence of $f(g)$ (cf. Eq. 10), but in case of a randomly textured material, this dependence disappears due to $f(g) \equiv 1$.

Next we have to relate the single-crystal elastic moduli, ${}^0S$, expressed in the coordinate systems K_B^j of the individual crystallite j, to the effective 'diffractive compliances' $S^L({}^0P,\ {}^0S,\ f;\ \mathbf{h}_i,\ \mathbf{y})$. This depends on the micro-mechanical model used to bring the average over the diffracting grains g_p (with individual microscopic strains and stresses in the solid polycrystalline sample) into the factorized form (Eq. 14) with the macroscopic loading stress components.

3.3. Preferred orientation

A number of micro-mechanical models have been used in the past. The Voigt [34] and Reuss [35] approximations assume continuity of strain and stress, respectively, across grains in the sample. In terms of the ODF, these approximations can be represented as simple arithmetic means with $f(g)$ or $f(g_p)$ weights, respectively. Other approaches use linear combinations of values determined in the Reuss and Voigt approximations as in the Voigt–Reuss–Hill average or in Hill-like models [36]. More sophisticated self-consistent variants, involving grain interactions on the microscopic level, have been shown to be physically more appropriate. Explicit S^L expressions for all these models in the case of random texture have been published [17,26,28,29,37].

In the case of a hexagonal crystal with random texture, diamond anvil experiments provide only three independent combinations of the five components of the elastic moduli tensor ${}^0S$. Therefore, the use of two additional bulk properties, such as bulk and shear moduli, is necessary to deduce the full set of elastic moduli [13]. For textured samples, the ${}^0S$-dependencies of S^L are more complicated. Analytical expressions containing only a small number of transparent ODF-related quantities are given in [38] for the Reuss approximation

and in [39] for the 'bulk-path-geo approximation' (BPGeo). The latter approximation effectively considers aspects of grain interaction from macroscopic to microscopic levels. The results of this approximation that uses elements of a simple geometric average are very close to those from more sophisticated self-consistent calculations. Because of the non-linear character of both models, new combinations of ${}^0S$ components arise.

For a relatively sharp texture with a distribution only around one orientation ('texture component'), a single crystal with the right orientation can approximate the sample. This greatly improves the reliability of the results and simplifies the analysis, because in this case the results of all physically correct micro-mechanical polycrystal models must agree; i.e. the difference between results using simple Reuss, or more sophisticated approximations, must be relatively small.

3.4. Specific aspects of high-pressure experiments

In the case of diamond anvil cell experiments, several difficulties arise. Uncertainties in the cell parameters ${}^0P(\sigma_{\mathrm{hydro}})$ directly influence the quasi-hydrostatic interplanar spacings d_0, introducing errors in Eq. 8 and 9. In order to avoid this situation, we evaluate a mean value:

$$\overline{\overline{d}}({}^0P,\ {}^0S,\ f,\ t;\ hkl) = \overline{\overline{d}({}^0P,\ {}^0S,\ f,\ t;\ hkl,\ y)}^{Y} \tag{15}$$

calculated for a sufficiently large number of measuring points $\mathbf{y}$. Then introducing the quantity $D \equiv \overline{\overline{d}}/\overline{d}$ the critical d_0 cancels out, and by Eq. 11 we have:

$$D({}^0P,\ {}^0S,\ f,\ t,\ hkl,\ \mathbf{y}) = \overline{\overline{d}}/\overline{\overline{d}} = \frac{1+\overline{\overline{\varepsilon}}'^{\mathrm{L}}_{33}({}^0P,\ {}^0S,\ f,\ t,\ \mathbf{h}_{\mathrm{i}},\ \mathbf{y})}{1+\overline{\overline{\varepsilon}}'^{\mathrm{L}}_{33}({}^0P,\ {}^0S,\ f,\ t,\ \mathbf{h}_{\mathrm{i}},\ \mathbf{y})^{Y}} \tag{16}$$

A second problem related to the diamond anvil cell experiments is the uncertainty in the uniaxial stress component t. But due to the special form of Eq. 14 and the ${}^0S$-dependence of the S^{LA} components (homogeneous function of degree one) we can introduce the dimensionless Z quantities:

$${}^0Z_{ijkl} = {}^0S_{ijkl}t/3;\ S^{\mathrm{LA}}_{33ij}\cdot t/3 =$$

$$Z^{\mathrm{LA}}_{33ij}({}^0P,\ {}^0Z,\ f,\ \mathbf{h}_{\mathrm{i}},\ \mathbf{y}) = S^{\mathrm{LA}}_{33ij}({}^0P,\ {}^0Z,\ f,\ \mathbf{h}_{\mathrm{i}},\ \mathbf{y}) \tag{17}$$

Combining Eqs. 16 and 14 we obtain:

$$D({}^0P,\ {}^0S,\ f,\ t,\ hkl,\ \mathbf{y}) = D({}^0P,\ {}^0Z,\ f,\ hkl,\ \mathbf{y}) = \frac{1+2Z^{\mathrm{LA}}_{3333}-Z^{\mathrm{LA}}_{3311}-Z^{\mathrm{LA}}_{3322}}{\overline{1+2Z^{\mathrm{LA}}_{3333}-Z^{\mathrm{LA}}_{3311}-Z^{\mathrm{LA}}_{3322}}^{Y}} \tag{18}$$

i.e. uncertainties in the uniaxial stress t will not influence the fitting procedures to determine the ${}^0Z$ from the experimental D values, but only enter in the final step, when calculating the components of the tensor elastic moduli ${}^0S$ from ${}^0Z$.

4. Analysis of experimental data

4.1. Previous results for elasticity

The high-pressure determination of elastic moduli for crystals of hexagonal symmetry using diamond anvil cells and X-ray diffraction is in an early stage of development. The conventional diamond anvil cell configuration was modified to observe diffraction from lattice planes oriented at different angles relative to the diamond axis, Z_{A}, in the sample-related coordinate system [13,14,18]. Polychromatic synchrotron X-rays are incident on the sample at 84° to the diamond anvil axis and diffraction patterns are collected with an energy-dispersive detector in a symmetrical position ($2\theta = 12°$). During an experiment, the cell is rotated around an axis perpendicular to the diamond anvil cell axis to bring different lattice planes into diffraction condition (Fig. 1).

For the present analysis, we will use results on ε-Fe at a pressure of 54 GPa [13]. Data for eight (hkl) and the ϑ region 0–90° ($\mathbf{y} = (\varphi,\vartheta)$) were collected, and the dependence in $\mathbf{y}$ of the interplanar spacings expected from Eq. 9 was observed (Fig.

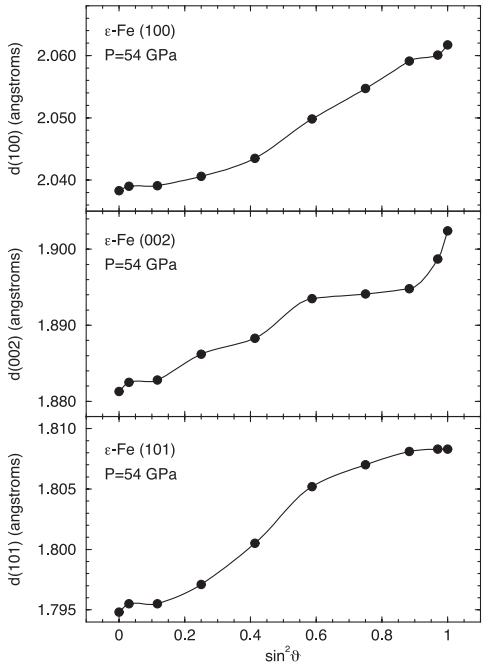

Fig. 3. Dependence of the observed interplanar spacing d for ε-Fe on $\sin^2\vartheta$ for three selected diffraction lines at 54 GPa [16].

3). If one assumes that the stress conditions are homogeneous on all crystallographic planes in the sample, the observed d-spacings are expected to vary linearly with $\sin^2\vartheta$. This results from Eq. 13 in the case of **y**-independence of the S^{L}_{33mn} components and the special stress structure of Eq. 6 (axial compression). A first analysis was performed assuming a random texture and applying the Reuss ($\alpha=1$ in Singh formalism) and Hill ($\alpha=0.5$ in Singh formalism) micro-mechanical models [17]. The elastic moduli ${}^0C(\alpha=1)$ and ${}^0C(\alpha=0.5)$ deduced from these experiment are presented in Table 1.

4.2. Previous results for preferred orientation

The intensity of diffraction measured for a (*hkl*) reflection line is proportional to the corresponding 'pole figure' values $P_{\mathbf{hi}}(\mathbf{y})$ that describe the probability for the crystallites to be in reflection orientation. Using texture analytical methods, the ODF $f(g)$ can be determined from the pole figures. The quality of the ODF obtained can be evaluated by comparing the experimental pole figure with the pole figure recalculated from $f(g)$. No azimuthal variations (φ) of $\mathbf{y}=(\varphi,\vartheta)$ have been considered and a cylindrical sample symmetry of texture was assumed, corresponding to the stress conditions in the diamond cell experiments. Fig. 4 shows experimental texture profiles from parallel to perpendicular to the diamond cell axis for eight reflections of the data set, and Fig. 5a displays the texture in one of the identical α-sections of the ODF that corresponds to an inverse pole figure of the compression direction relative to crystal directions **h** in the case of cylindrical sample symmetry [19]. A sharp single (0001) fiber texture with texture sharpness $F_2=2.5$ is observed.

For hexagonal crystal symmetry the elastic properties are isotropic in the X_B/Y_B plane. Therefore our sample effectively represents a sin-

Table 1
Elastic moduli (in GPa) of ε-Fe at 54 GPa used in the analysis (Voigt abbreviation in parentheses)

	Singh ($\alpha=1$)	Singh ($\alpha=0.5$)	Soderlind first-principles	Reuss+ODF	BPGeo+ODF
C_{1111} (c_{11})	552	639	638	450	429
C_{3333} (c_{33})	562	648	606	611	886
C_{2323} (c_{44})	395	422	178	267	324
C_{1122} (c_{12})	335	300	190	−68	−49
C_{1133} (c_{13})	301	254	218	86	201
C_{2323}/C_{1212}	3.6	2.5	0.8	1.0	1.4

Experimental values were estimated from radial diffraction experiments [16] using a random texture model and the Reuss ($\alpha=1$) and Hill ($\alpha=0.5$) approximations. First-principles model is based on [13]. The last columns have been recalculated from the experimental data [16] using a non-random texture and Reuss and BPGeo micro-mechanical models.

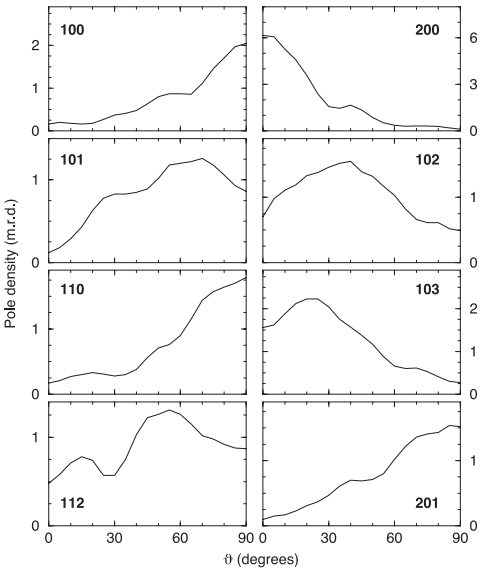

Fig. 4. Texture of ε-Fe at $P = 54$ GPa expressed as profiles of pole densities for eight diffraction peaks from parallel to perpendicular to the diamond cell axis. Pole densities are expressed in multiples of a random distribution (m.r.d.) [22].

gle crystal with the *c*-axis aligned in the maximum stress direction. Thus the ${}^0S$ (or ${}^0C$) parameter sets that would be calculated using the same experimental data as [13], but including texture effects, are likely to be different from the results in Table 1, which assumed a random orientation of the crystallites in the sample.

4.3. Theoretical test case

The analysis based on a hypothesis of random texture could only provide three combinations of the elastic moduli [13]. Therefore, assumptions had to be made about two bulk properties of the material (cf. Section 3.3). Ideally, we would like to determine all of the unknown components of ${}^0S$ using the data obtained from the diffraction experiments, without additional information such as approximated bulk properties. Eq. 18 cannot be solved for the ${}^0Z$ analytically, but can be analyzed by numerical model calculations. We proceed by assuming a set of elastic moduli ${}^0S^*$ and model the $\overline{d}$ data that would be observed in a radial diffraction experiment [13]. We then use these theoretically modeled $\overline{d}$ data to re-extract the elastic moduli ${}^0S^*$ that were included in the model. We only show results for the (101) lattice plane but the analysis was done on all eight lattice planes of the experimental set. For the numerical test case we did not use the experimental texture (Fig. 5a), but rather a theoretical texture modeled after the experimental texture, for higher accuracy. This model ODF is stronger than the experimental texture and consists of a (0001) fiber with a halfwidth of 30° and isotropic background 0.1 m.r.d. (Fig. 5b), providing a texture strength of $F_2 = 8.4$.

Fig. 6 shows the modeled $D({}^0P, {}^0S^*, f, t; hkl, \mathbf{y})$ for the (101) plane as a function of $\sin^2\vartheta$, where ϑ is the polar angle of $\mathbf{y}$ (ψ in [20]). The D was calculated with standard accuracy, using the first-principles stiffness coefficients [10] in Table 1 (${}^0C_{\text{ab initio}}$), and the two micro-mechanical models Reuss and BPGeo with the following parameters ($\sigma_{\text{hydro}} = 52$ GPa, $t = 15$ GPa, $c^0/a^0 = 1.6$). The random texture case results in straight lines, whereas the textured case produces slightly curved lines.

Deviations from a straight line are emphasized in Fig. 7 where the derivative of $D({}^0P, {}^0S^*, f, t; hkl, \mathbf{y})$ versus $\sin^2\vartheta$ for the (101) plane is shown as

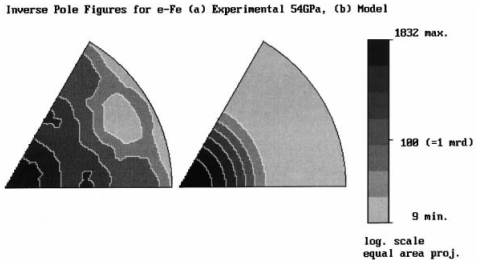

Fig. 5. Inverse pole figures of the compression direction for ε-Fe. (a) Experimental inverse pole figure at 54 GPa calculated from the pole density profiles in Fig. 4 [22], maximum pole density is 6.4 m.r.d., (b) idealized texture expressed by a single fiber component which is used for the test calculations in this paper, maximum pole density is 18.3 m.r.d. Equal area projections. Contour scale is indicated.

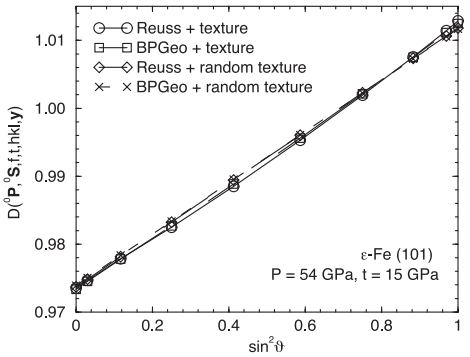

Fig. 6. Variation of the D values of the (101) reflection line calculated using the first-principles set of elastic moduli from Table 1 as a function of $\sin^2\vartheta$. Results are plotted for two micro-mechanical models (Reuss and BPGeo) supposing random texture or the model ODF from Fig. 5b, containing a (001) fiber component.

a function of $\sin^2\vartheta$. The different curves are relatively close to each other because of the almost isotropic structure of the microscopic ${}^0C_{\text{ab initio}}$ set of elastic moduli. Nevertheless, the set of elastic moduli used in the model could be recalculated in this textured case with an accuracy of at least two decimals. It is appropriate to emphasize that for the present model the D values had an accuracy of at least five decimals, and the micro-mechanical models used to produce the 'experimental' D values and to re-extract the unknown ${}^0S$ were identical. The example shows the accuracy in experimental D values required to obtain reliable results on single-crystal elasticity.

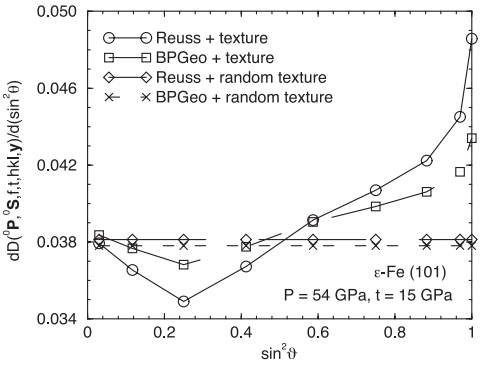

Fig. 7. Variation of $\partial D/\partial(\sin^2\vartheta)$ with $\sin^2\vartheta$ for D values of the (101) reflection line calculated using the first-principles set of elastic moduli from Table 1. Results are plotted for two micro-mechanical models (Reuss and BPGeo) supposing random texture or a model ODF, containing a (001) fiber component.

4.4. Application to experimental data

In Fig. 8 we plot the experimental $D({}^0P, {}^0S, f, t; hkl, \mathbf{y})$ as a function of $\sin^2\vartheta$ for (101) from the experiment at 54 GPa, with an estimated t of 4.5 GPa [16]. The other curves are for the BPGeo model, the ODF in Fig. 3, and three sets of elastic moduli. The first-principles results [10] are shown; $\alpha = 1$ refers to values obtained with the Reuss approximation and $\alpha = 0.5$ to those obtained with the Hill approximation [13]. None of the modeled $D({}^0P, {}^0S, f, t; hkl, \mathbf{y})$ can reproduce the non-linear behavior of the experimental data with sufficient accuracy. Table 1 also presents two hypothetical sets of elastic moduli of ε-Fe at 54 GPa deduced from the experimental d values and using the texture in Figs. 4 and 5 under the Reuss and BPGeo approximations, without additional assumptions about bulk properties of the sample. The $D({}^0P, {}^0S, f, t; hkl, \mathbf{y})$ curves recalculated using these moduli and the appropriate micro-mechanical models are plotted in Fig. 9 as a function of $\sin^2\vartheta$ for (101). The results from both models

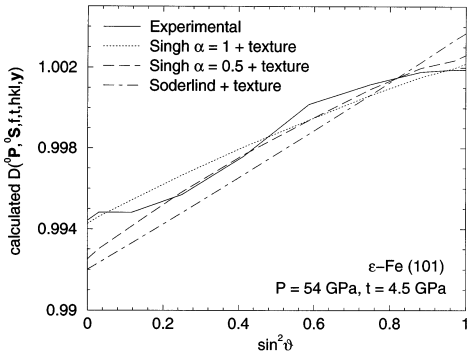

Fig. 8. Experimental D values for (101) and calculated values using the first three ${}^0C$ parameter sets of Table 1, the BPGeo micro-mechanical model and the ODF from Fig. 3.

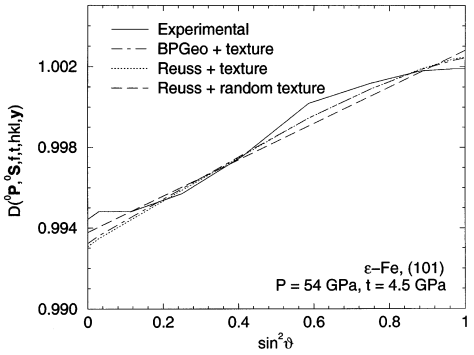

Fig. 9. Experimental D values (101) and recalculated values for the BPGeo/ODF, Reuss/ODF, and Reuss/random ($\alpha=1$) ${}^0C$ parameter sets of Table 1 derived by fits using the corresponding micro-mechanical models, the ODF of Fig. 3 or assuming a random texture.

(BPGeo and Reuss) are very close because of the strong preferred orientation in the sample. The recalculated d values using a random texture model and the elastic moduli for the Reuss approximation from Singh et al. [13] are also indicated. They appear as a linear function of $\sin^2\vartheta$, as expected for a random texture model.

The analysis of the curves for the other (hkl) reflections provided similar results. In all cases, curves resulting from calculations that included the texture and used the Reuss or BPGeo micromechanical models appear to be more appropriate. Unfortunately, the scatter in the currently available experimental d values does not permit us to obtain a unique set of elastic moduli. Hence, the significance of features obtained with the latter two models, such as the large value of C_{1111}/C_{3333} and negative C_{1122}, needs to be explored with further measurements.

5. Conclusions

We introduced a new theoretical approach for the analysis of high-pressure radial diffraction measurements on hexagonal materials. In this study, we demonstrated how the sample texture could be introduced in the estimation of the elastic moduli. Several micro-mechanical models for the grain interactions in the sample and texture hypothesis were analyzed. We find that the models using the Reuss or BPGeo approximation, along with the observed texture properties, were most appropriate. Unfortunately, the accuracy of the experimental results is not sufficient to extract the elastic moduli of ε-Fe; in fact a large range of elastic moduli is compatible with the data. The analysis suggests that the accuracy of the measurements needs to be improved by an order of magnitude to obtain accurate determination of the moduli. Both a highly anisotropic elasticity [13,14] as well as a weakly anisotropic elasticity (estimated from first-principles [9,10]) is compatible with the experimental data within the margin of error. Despite this current ambiguity, we can estimate with the hypothetical moduli calculated here the compressional wave anisotropy of the material. Fig. 10 shows preliminary seismic veloc-

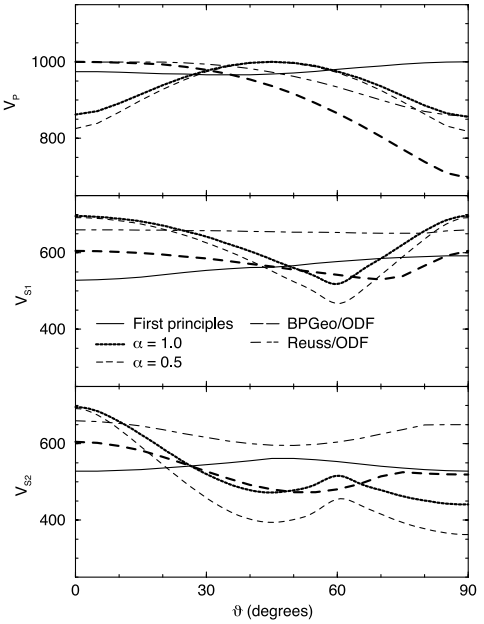

Fig. 10. Compressive and shear velocities for a single crystal of ε-Fe and the five ${}^0C$ parameter sets of Table 1. V_{max} of each set is normalized to 1000. From the top: ${}^0C_{first-principles}$, ${}^0C(\alpha=1)$ Reuss/random, ${}^0C(\alpha=0.5)$ Hill/random, ${}^0C_{BPGeo/ODF}$, ${}^0C_{Reuss/ODF}$. ϑ is the angle to the [0001]-axis.

ity anisotropies in ε-Fe calculated with the sets of elastic moduli from Table 1. All, except the first-principles calculations, have an anisotropy greater than 10%.

The conditions required to obtain precise information on the elastic moduli of the sample from such an experiment are: (i) improved accuracy in the measurement of the *d*-spacings, (ii) precise texture characterization, (iii) accurate estimation of the uniaxial stress component in the sample. The characterization of the texture for the case of ε-iron in these experiments is fairly accurate [19], and it shows a very strong preferred orientation, with the *c*-axis parallel to the compression axis. Therefore the question of texture characterization does not limit the quality of the elastic moduli determination. The accuracy of the *d*-spacing measurements could be improved by increasing the number of data points in the analysis and better characterization of the position of the sample while rotating the diamond anvil cell, thereby reducing the errors in the measurements. Repeating the experiments several times under the same conditions will directly show the degree of uncertainty of the experimental *d*-spacings and reveal problems that may be related to grain statistics. Preliminary experiments, carried out recently with monochromatic radiation, show improved accuracy and precision relative to the previous work [40]. The application of any model to describe the variation of $\overline{d}$ (**h**,**y**) for a polycrystalline sample implicitly assumes a large number of grains in reflection position. Critical minimum numbers can be deduced from numerical models, as described in Section 4.3, but using sets of single grains with individual orientations representing a certain texture type, rather than a continuous ODF. The question of the uniaxial stress component characterization remains open. Three solutions can be proposed: (i) the use of a calibration standard [14], (ii) an independent estimation of one of the elastic moduli such as C_{2323} in the case of ε-Fe [15] to scale the results, (iii) finite-element modeling of the stress conditions in the experiment [41].

Acknowledgements

H.R.W. acknowledges support from IGPP-LANL and NSF (EAR 99-02866). This research also profited from an exchange visit of H.R.W. to ENS-Lyon sponsored by the UC Education Abroad Program and ENS. He is appreciative for the hospitality while at Lyon. S.M. acknowledges support during a Berkeley visit in 1999 when this research was initiated. R.J.H. and H.K.M. are grateful for support from NSF (EAR-9814819) and the Center for High Pressure Research.*[SK]*

References

[1] X. Song, Anisotropy of the Earth's inner core, Rev. Geophys. 35 (1997) 297–313.
[2] A.P. Jephcoat, P. Olson, Is the Earth's inner core pure iron?, Nature 325 (1987) 332–335.
[3] S. Yoshida, I. Sumita, M. Kumazawa, Growth model in the inner core coupled with the outer core dynamics and the resulting elastic anisotropy, J. Geophys. Res. 101 (1996) 28085–28103.
[4] M.I. Bergman, Measurements of the elastic anisotropy due to solidification texturing and the implication for the Earth's inner core, Nature 389 (1997) 60–63.
[5] S. Karato, Seismic anisotropy of the Earth's inner core resulting from flow induced by Maxwell stresses, Nature 402 (1999) 871–873.
[6] B. Buffet, H.R. Wenk, Texturing of the inner core by Maxwell stresses, Nature 413 (2001) 60–64.
[7] H.R. Wenk, J.R. Baumgardner, R.A. Lebensohn, C.N. Tomé, A convection model to explain the anisotropy of the inner core, J. Geophys. Res. 105 (2000) 5663–5667.
[8] L. Stixrude, R.E. Cohen, D.J. Singh, Iron at high pressure: Linearized-augmented-plane-wave computations in the generalized-gradient approximation, Phys. Rev. B 50 (1994) 6442–6445.
[9] L. Stixrude, R.E. Cohen, High-pressure elasticity of iron and anisotropy of Earth's inner core, Science 267 (1995) 1972–1975.
[10] P. Soderlind, J.A. Moriarti, J.M. Wills, First principles theory of iron up to Earth-core pressure: Structural, vibrational, and elastic properties, Phys. Rev. B 53 (1996) 14063–14072.
[11] G. Steinle-Neumann, L. Stixrude, R.E. Cohen, First-principles elastic constants for the hcp transition metals Fe, Co, and Re at high pressure, Phys. Rev. B 60 (1999) 791–799.

[12] A. Laio, S. Bernard, G.L. Chiarotti, S. Scandolo, E. Tosatti, Physics of iron at Earth's core conditions, Science 287 (2000) 1027–1030.
[13] A.K. Singh, H.K. Mao, J. Shu, R.J. Hemley, Estimation of single crystal elastic moduli from polycrystalline X-ray diffraction at high pressure: Application to FeO and iron, Phys. Rev. Lett. 80 (1998) 2157–2160.
[14] H.K. Mao, J. Shu, G. Shen, R.J. Hemley, B. Li, A.K. Singh, Elasticity and rheology of iron above 220 GPa and the nature of the Earth's inner core, Nature 396 (1998) 741–743; correction, Nature 399 (1999) 280.
[15] S. Merkel, A.F. Goncharov, H.K. Mao, P. Gillet, R.J. Hemley, Raman spectroscopy of iron to 152 gigapascals: implications for Earth's inner core, Science 288 (2000) 1626–1629.
[16] G. Steinle-Neumann, L. Stixrude, R.E. Cohen, O. Gülseren, Elasticity of iron at the temperature of the Earth's inner core, Nature 413 (2001) 57–60.
[17] A.K. Singh, C. Balasingh, H.K. Mao, R.J. Hemley, J. Shu, Analysis of lattice strains measured under nonhydrostatic pressure, J. Appl. Phys. 83 (1998) 7567–7575.
[18] R.J. Hemley, H.K. Mao, G. Shen, J. Badro, P. Gillet, M. Hanfland, D. Häusermann, X-ray imaging of stress and strain of diamond, iron, and tungsten at megabar pressures, Science 276 (1997) 1242–1245.
[19] H.R. Wenk, S. Matthies, R.J. Hemley, H.K. Mao, J. Shu, Deformation mechanisms of iron at inner core pressures, Nature 405 (2000) 1044–1047.
[20] S. Matthies, H.-G. Priesmeyer, Diffraction determination of thermo-elastic single crystal constants using polycrystalline samples, Proc. Int. Conf. Textures of Materials (ICOTOM 12), NRC Research Press, Ottawa, 1999, pp. 439–444.
[21] J.F. Nye, Physical Properties of Crystals: Their Representation by Tensors and Matrices, Clarendon Press, Oxford, 1957.
[22] U.F. Kocks, C.N. Tomé, H.R. Wenk, Texture and Anisotropy, Preferred Orientations in Polycrystals and their Effect on Material Properties, Cambridge University Press, Cambridge, 2000.
[23] S. Matthies, G.W. Vinel, K. Helming, Standard Distributions in Texture Analysis, Akademie-Verlag, Berlin, Vol. 1 (1987), Vol. 2 (1988), Vol. 3 (1990).
[24] E. Schreiber, O.L. Anderson, N. Soga, Elastic Constants and Their Measurement, McGraw-Hill, New York, 1973.
[25] H. Olijnyk, A.P. Jephcoat, Optical zone-centre phonon modes and macroscopic elasticity in hcp metals, Solid State Commun. 115 (2000) 335–339.
[26] F. Bollenrath, V. Hauk, E.H. Müller, Zur Berechnung der vielkristallinen Elastizitätskonstanten aus den Werten der Einkristalle, Z. Met.kd. 58 (1967) 76–82.
[27] I.C. Noyan, J.B. Cohen, Residual Stress – Measurement by Diffraction and Interpretation, Springer, New York, 1987.
[28] A.K. Singh, C. Balasingh, The lattice strains in a specimen (hexagonal system) compressed nonhydrostatically in an opposed anvil high pressure setup, J. Appl. Phys. 75 (1994) 4956–4962.
[29] T. Gnäupel-Herold, P.C. Brand, H.J. Prask, The calculation of single crystal elastic constants for cubic crystal symmetry from powder diffraction data, J. Appl. Crystallogr. 31 (1998) 929–935.
[30] Ch. Bittorf, S. Matthies, H.G. Priesmeyer, R. Wagner, Diffractive determination of thermo-elastic single crystal constants, Intermetallics 7 (1998) 251–258.
[31] C.J. Howard, E.H. Kisi, Measurement of single-crystal elastic constants by neutron diffraction from polycrystals, J. Appl. Crystallogr. 32 (1999) 624–633.
[32] S. Matthies, H.G. Priesmeyer, M.R. Daymond, On the diffractive determination of single crystal constants using polycrystalline samples, J. Appl. Crystallogr. 34 (2001) 585–601.
[33] H.K. Mao, Y. Wu, L.C. Chen, J.F. Shu, A.P. Jephcoat, Static compression of iron to 300 GPa and $Fe_{0.8}Ni_{0.2}$ alloy to 260 GPa: implications for composition of the core, J. Geophys. Res. 95 (1990) 21737–21742.
[34] W. Voigt, Lehrbuch der Kristallphysik, Teubner, Leipzig, 1928.
[35] A. Reuss, Berechnung der Fliessgrenze von Mischkristallen auf Grund der Plastizitaetsbedingung fuer Einkristalle, Z. Angew. Math. Mech. 9 (1929) 49–58.
[36] J.P. Watt, G.F. Davies, R.J. O'Connell, The elastic properties of composite materials, Rev. Geophys. Space Phys. 14 (1976) 541–563.
[37] V. Hauk, H. Kockelmann, Ermittlung der Einkristallkoeffizienten aus den mechanischen und röntgenographischen Elastizitätskonstanten des Vielkristalls, Z. Met.kd. 70 (1979) 500–502.
[38] S. Matthies, Moment pole figures in residual stress analysis, Textures Microstruct. 25 (1996) 229–236.
[39] S. Matthies, M. Humbert, Ch. Schuman, On the use of the geometric mean approximation in residual stress analysis, Phys. Stat. Sol. (b) 186 (1994) K41–K44.
[40] S. Merkel, H.-R. Wenk, G. Shen, J. Shu, P.G. Uet, R.J. Hemley, H.K. Mao, Diamond anvil cell investigations of lattice strains and preferred orientations in iron at high pressure, EOS, Trans. Am. Geophys. Union (2001) in press.
[41] S. Merkel, R.J. Hemley, H.K. Mao, D.M. Teter, Finite-element modeling and ab initio calculations of megabar stresses in the diamond anvil cell, in: M.H. Manghnani, W.J. Nellis, M.F. Nicol (Eds.), Science and Technology of High Pressure, University Press, 2000, pp. 68–73.

Phys Chem Minerals (2002) 29: 1–9
DOI 10.1007/s002690100207

ORIGINAL PAPER

S. Merkel · A. P. Jephcoat · J. Shu · H.-K. Mao
P. Gillet · R. J. Hemley

Equation of state, elasticity, and shear strength of pyrite under high pressure

Received: 21 December 2000 / Accepted: 11 July 2001

Abstract Physical properties including the equation of state, elasticity, and shear strength of pyrite have been measured by a series of X-ray diffraction in diamond-anvil cells at pressures up to 50 GPa. A Birch–Murnaghan equation of state fit to the quasihydrostatic pressure–volume data obtained from laboratory X-ray source/film techniques yields a quasihydrostatic bulk modulus $K_{0T} = 133.5\ (\pm 5.2)$ GPa and bulk modulus first pressure derivative $K'_{0T} = 5.73\ (\pm 0.58)$. The apparent equation of state is found to be strongly dependent on the stress conditions in the sample. The stress dependency of the high-pressure properties is examined with anisotropic elasticity theory from subsequent measurements of energy-dispersive radial diffraction experiments in the diamond-anvil cell. The calculated values of K_{0T} depend largely upon the angle ψ between the diffracting plane normal and the maximum stress axis. The uniaxial stress component in the sample, $t = \sigma_3 - \sigma_1$, varies with pressure as $t = -3.11 + 0.43P$ between 10 and 30 GPa. The pressure derivatives of the elastic moduli $dC_{11}/dP = 5.76\ (\pm 0.15)$, $dC_{12}/dP = 1.41\ (\pm 0.11)$ and $dC_{44}/dP = 1.92\ (\pm 0.06)$ are obtained from the diffraction data assuming previously reported zero-pressure ultrasonic data ($C_{11} = 382$ GPa, $C_{12} = 31$ GPa, and $C_{44} = 109$ GPa).

Keywords High pressure · Elasticity · Pyrite · Shear strength · Radial diffraction

S. Merkel · J. Shu · H.-K. Mao · R. J. Hemley
Geophysical Laboratory and Center for High-Pressure Research, Carnegie Institution of Washington, 5251 Broad Branch Rd., NW, Washington DC 20015-1305, USA, e-mail: merkel@gl.ciw.edu

S. Merkel (✉) · P. Gillet
Laboratoire des Sciences de la Terre,
École normale supérieure de Lyon, 46 allée d'Italie,
69364 Lyon Cedex 07, France, e-mail: smerkel@ens-lyon.fr
Tel.: +33-4-72-72-85-66; Fax: +33-4-72-72-86-77

A. P. Jephcoat
Department of Earth Sciences, University of Oxford,
Parks Road, Oxford OX1 3PR, UK

Introduction

Pyrite crystallizes in the cubic symmetry [space group $T_h^6(Pa3)$] and appears to have a wide stability field. X-ray diffraction experiments, performed up to pressures of 40 GPa, show no evidence of phase transition (Bridgman 1949; Drickamer et al. 1966; Chattopadhyay and Schnering 1985; Jephcoat 1985; Fujii et al. 1986). Moreover, shock compression data demonstrate that pyrite does not undergo any phase transition up to a pressure of at least 320 GPa (Ahrens and Jeanloz 1987). However, the bulk moduli deduced from these experiments show large differences and the results do not agree. Moreover, equation of state (EOS) measurements under nonhydrostatic conditions at high pressure and ambient temperature using X-ray diffraction and the diamond-anvil cell up to pressures of 40 GPa yielded some unusual results: the EOS was found to be very dependent on the experimental stress conditions, with a bulk modulus varying from 130 to 250 GPa with different pressure-transmitting media used in the experiments (Jephcoat 1985). Such variations between the different measurements in the diamond-anvil cell can be explained by the presence of anisotropic stress conditions that differ between experiments. This has been one of the major sources of errors and inconsistencies in the determination of high-pressure properties of materials with diamond-anvil cell experiments. Thus, there is a need to investigate both the high-pressure properties of materials and the stress conditions under which the experimental measurements are performed.

The purpose of this study was to examine the high-pressure properties of pyrite and the conditions under which they are measured in detail using new experimental and theoretical techniques. In particular, we used methods developed to analyze quantitatively lattice strains under nonhydrostatic stress conditions in the diamond-anvil cell (Singh 1993b; Singh et al. 1998a, b). The powdered sample is confined in a diamond cell without a pressure medium to enhance the effects of nonhydrostaticity, and diffraction patterns are measured

through the gasket with several orientations of the X-ray beam. Analyzing the effects of orientation on the measured interplanar d spacings can yield information on shear strength, quasihydrostatic compression curves, elastic moduli, as well as elastic anisotropy. This technique has been applied to iron (Mao et al. 1998; Singh et al. 1998b), gold and rhenium (Duffy et al. 1999a), and molybdenum (Duffy et al. 1999b).

The first section of this paper summarizes previously unpublished X-ray diffraction results on the EOS of pyrite (Jephcoat 1985). Two experiments were performed without a pressure medium, thus under nonhydrostatic stress conditions, and a third experiment hydrostatically with neon as a pressure medium. The EOS were found to be very dependent on the degree of nonhydrostatic stress in the sample. We then describe the theory behind the radial diffraction experiments and how it can be used to deduce physical properties of the sample. Finally, we present results of the radial diffraction experiments and analysis for obtaining hydrostatic compression curve, elasticity, shear strength, and elastic anisotropy of pyrite.

Conventional diffraction experiments

Description of the experiments

Three sets of EOS experiments were performed in a diamond-anvil cell using a sealed MoKα ($\lambda = 71.073$ pm) source at the Geophysical Laboratory. The collimated X-ray beam was directed through the diamond anvils, and diffraction patterns were collected with a film camera in Debye–Scherrer geometry (Fig. 1). An extended silver standard was used to calibrate the film to sample distance (Jephcoat et al. 1987). Two runs (NH1 and NH2) were performed nonhydrostatically up to pressures of about 25 and 30 GPa, respectively. A hydrostatic run (NE1) was also performed with solid neon as a pressure medium up to 40 GPa. For all experiments, large single crystals of pure, natural pyrite (Elba, Italy) were ground to a powder in a suspension of ethanol.

For the first experiment (NH1), diamonds with a 550-μm diameter culet were chosen and a 160-μm diameter hole drilled in a T301 steel gasket was used as a sample chamber. The hole was filled with the pyrite powder and covered with a layer of ruby chips before assembling the cell. An asymmetric pressure gradient developed across the diamond face, as opposed to the maximum expected at the culet center. The X-ray photographs showed spotty diffraction rings, suggesting that the sample grain size was too large, and the experiment was stopped at 25 GPa.

For run NE1, the same diamonds were used. The sample was ground for a longer period than in the previous experiment and pressed into a platelet between the piston diamond and a glass microscope slide. A disk was cut from this platelet to a diameter slightly smaller than the hole. Finally, ground ruby was distributed throughout the sample, and pressed lightly into it. Pure neon was then loaded at 0.2 GPa (Jephcoat et al. 1987). Pressures were measured at several points across the sample for averaging at each increment in pressure.

As a result of the large discrepancy between the first two runs (see results in Fig. 2), a second nonhydrostatic compression experiment (NH2) was carried out to check the accuracy of the first (NH1). Larger-culet diamonds (950 μm diameter) were used and a 200-μm hole was drilled in the gasket. The same powdered sample was reground and loaded into the gasket and repeatedly pressed until fully compacted and ground ruby powder was deposited on the surface. Up to nine reflections from the following set of indices were identified manually on the X-ray film: (1 1 1), (2 0 0), (2 1 0), (2 1 1), (2 2 0), (3 1 1), (2 2 2), (2 3 0), and (3 2 1). A zero-pressure lattice constant of 5.417(5) was used.

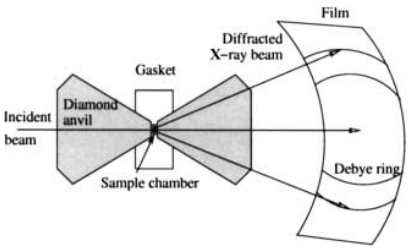

Fig. 1 Experimental setup for conventional diffraction experiments NE1, NH1, and NH2. A collimated X-ray beam MoKα ($\lambda = 71.073$ pm) passes along the diamond cell load axis and exposes the film held in a camera at fixed radius

Results

Compression data for experiments NE1, NH1, and NH2 are presented in Tables 1, 2, and 3, respectively. Com-

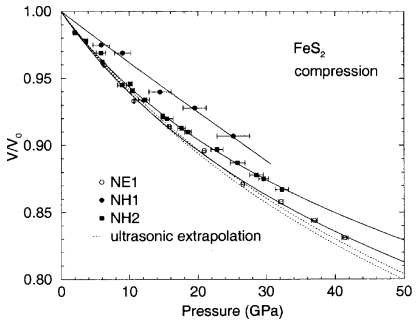

Fig. 2 Compression curves of pyrite: NE1 (*open circles*) with neon as pressure medium, NH1 (*closed circles*), and NH2 (*closed squares*) with no pressure medium. *Solid lines* are third-order Birch–Murnaghan fits to the data and *dotted lines* are extrapolated compression curves from zero-pressure ultrasonic measurements of elastic moduli. (Simmons and Birch 1963)

pression curves derived from these experiments are shown in Fig. 2. The results from compression with neon medium are in reasonably close agreement with expectation on the basis of zero-pressure elastic constant measurements (Simmons and Birch 1963).

Pyrite appears significantly less compressible in the two nonhydrostatic experiments (NH1 and NH2). Although the effect of nonhydrostatic stress in NH1 was reproduced in NH2, its magnitude was not. Possible explanations for the difference in magnitude are (1) that the larger diamond culet surface of run NH2 reduced the pressure gradients and the degree of nonhydrostaticity; and (2) that the sample grain size was smaller for run NH2 (<10 μm). Other factors that distinguished run NH1 and NH2 were a lower concentration of ruby in the surface layer, and a larger sample thickness.

Table 1 Compression data for FeS_2 at 293 K with a neon pressure medium (experiment NE1)

P (GPa)	a (Å)	V (cm^3 mol^{-1})	V/V_0
6.30 (±0.01)	5.344 (±0.001)	22.979 (±0.019)	0.960 (±0.001)
10.65 (±0.06)	5.294 (±0.002)	22.332 (±0.022)	0.933 (±0.001)
15.84 (±0.15)	5.257 (±0.001)	21.866 (±0.012)	0.914 (±0.001)
20.91 (±0.27)	5.222 (±0.001)	21.433 (±0.017)	0.896 (±0.001)
26.57 (±0.24)	5.173 (±0.002)	20.837 (±0.027)	0.871 (±0.001)
32.12 (±0.34)	5.146 (±0.002)	20.520 (±0.018)	0.858 (±0.001)
36.99 (±0.42)	5.119 (±0.003)	20.199 (±0.037)	0.844 (±0.002)
41.44 (±0.42)	5.094 (±0.005)	19.894 (±0.062)	0.831 (±0.003)

Table 2 Nonhydrostatic compression data for FeS_2 at 293 K (experiment NH1)

P (GPa)	a (Å)	V (cm^3 mol^{-1})	V/V_0
5.89 (±1.2)	5.372 (±0.004)	23.333 (±0.054)	0.975 (±0.002)
9.01 (±1.2)	5.360 (±0.001)	23.188 (±0.014)	0.969 (±0.001)
14.46 (±1.6)	5.306 (±0.005)	22.492 (±0.060)	0.940 (±0.003)
19.54 (±1.7)	5.284 (±0.002)	22.216 (±0.030)	0.928 (±0.001)
25.20 (±2.4)	5.243 (±0.003)	21.695 (±0.034)	0.907 (±0.002)

Table 3 Nonhydrostatic compression data for FeS_2 at 293 K (experiment NH2)

P (GPa)	a (Å)	V (cm^3 mol^{-1})	V/V_0
3.68 (±0.18)	5.376 (±0.001)	23.394 (±0.012)	0.978 (±0.001)
10.10 (±0.28)	5.3171 (±0.004)	22.632 (±0.005)	0.946 (±0.001)
14.83 (±0.21)	5.273 (±0.002)	22.072 (±0.024)	0.922 (±0.001)
18.55 (±0.50)	5.250 (±0.002)	21.786 (±0.019)	0.910 (±0.001)
22.80 (±0.89)	5.223 (±0.002)	21.455 (±0.020)	0.897 (±0.001)
28.55 (±1.00)	5.187 (±0.001)	21.013 (±0.015)	0.878 (±0.001)
32.29 (±1.00)	5.166 (±0.002)	20.752 (±0.019)	0.867 (±0.001)
25.81 (±1.07)	5.205 (±0.001)	21.233 (±0.018)	0.887 (±0.001)
15.48 (±0.87)	5.269 (±0.002)	22.023 (±0.019)	0.920 (±0.001)
12.12 (±0.81)	5.2957 (±0.004)	22.359 (±0.005)	0.934 (±0.001)
8.94 (±0.67)	5.317 (±0.001)	22.624 (±0.010)	0.945 (±0.001)
6.06 (±0.16)	5.348 (±0.001)	23.028 (±0.016)	0.962 (±0.001)
2.02 (±0.17)	5.388 (±0.001)	23.549 (±0.014)	0.984 (±0.001)
5.84 (±0.70)	5.360 (±0.002)	23.183 (±0.025)	0.969 (±0.001)
12.29 (±0.14)	5.295 (±0.001)	23.344 (±0.015)	0.934 (±0.001)
10.44 (±0.30)	5.307 (±0.001)	22.506 (±0.015)	0.941 (±0.001)
17.61 (±0.60)	5.255 (±0.001)	21.842 (±0.009)	0.913 (±0.001)
29.59 (±0.69)	5.182 (±0.002)	20.946 (±0.020)	0.875 (±0.001)

For nonhydrostatic experiment NH2, data were collected by cycling the cell up and down in pressure several times (Table 3). There appear to be no systematic effects attributable to increasing or decreasing pressure cycles within the scatter of the data.

Discussion

Earlier ultrasonic measurements of zero-pressure elastic moduli by (Simmons and Birch 1963) provide values of K_{0S} ranging from 142.7 to 147.9 GPa, depending on the sample used. Analysis of shock-compression data between 0 and 320 GPa yields $K_{0S} = 162$ (±9) GPa and $K'_{0S} = 4.7$ (±0.3) (Ahrens and Jeanloz 1987).

The adiabatic and isothermal bulk moduli can be related using

$$K_S = K_T(1 + \alpha\gamma T) = K_T\left(1 + \frac{\alpha^2 K_S V T}{C_P}\right) , \quad (1)$$

where α is the volume thermal expansivity, γ the thermodynamic Grüneisen parameter, C_P the constant pressure heat capacity, V the unit cell volume, and T the absolute temperature. With $\alpha = 2.6 \times 10^{-5}$ K^{-1}, $V = 159.04$ Å^3 (Ahrens 1995), $C_P = 62.17$ J · mol^{-1} · K^{-1} (Robie et al. 1979), and $T = 300$ K, we calculate $K_T/K_S \approx 0.988$. Thus K_S and K_T at ambient temperature differ by about 1%, which is within experimental error. Reported measurements of K_{0T} for pyrite using X-ray diffraction include 149.3 and 147.1 GPa (Bridgman 1949) with data up to 0.3 GPa, $K_{0T} = 148$ GPa, and $K'_{0T} = 5.5$ by Drickamer et al. (1966) with data up to 30 GPa, $K_{0T} = 157$ GPa by Fujii et al. (1986) with data up to 4.2 GPa, $K_{0T} = 215$ GPa and $K'_{0T} = 5.5$ by Chattopadhyay and Schnering (1985) with data up to 34 GPa.

A third-order Birch–Murnaghan EOS was fitted to the data for each experiment with K'_{0T} free and $K'_{0T} = 4.0$ (Table 4). Assuming $K'_{0T} = 4.0$, the bulk modulus obtained from the neon medium experiment (NE1), $K_{0T} = 143$ (±4) GPa, is compatible with the zero-pressure ultrasonic measurements of elastic moduli that lead to $K_{0S} = 145$ (±3) GPa (Simmons and Birch 1963). Shock-compression data assuming $K'_{0S} = 4.7$ (±0.3) estimate $K_{0S} = 162$ (±9), which is approximately 20% larger and well outside the limits of esti-

Table 4 Birch–Murnaghan EOS parameters for FeS_2 at 293 K for experiment with neon as a pressure medium NE1, and nonhydrostatic compressions NH1 and NH2. For each experiment V_0 was fixed to its zero-pressure value and parameters of the third-order Birch–Murnaghan EOS were adjusted with K'_0 free and $K'_0 = 4.0$

Dataset	K_{0T} (GPa)	K'_{0T}
NE1	133.5 (±5.2)	5.73 (±0.58)
NE1	142.8 (±0.2)	4.00
NH1	255.0 (±27.0)	0.5 (±2.7)
NH1	224.0 (±13.1)	4.00
NH2	140.8 (±3.2)	7.02 (±7.4)
NH2	157.3 (±1.0)	4.00

4

mated errors. Thermal correction to the Hugoniot data is less than 20% and does not explain this discrepancy. It could be explained by a small volume increase across a shock-induced transition that could not be induced by pressure alone or by the occurrence of partial fusion during the shock experiment (Ahrens and Jeanloz 1987). In any case, the tradeoffs between K_0' and K_0 for different EOS formalisms do not warrant a detailed comparison.

Large differences in the equation-of-state parameters arise when varying the nonhydrostatic stress in experiments NH1 and NH2 and the other experiments obtain results within the wide range of those obtained here (Table 4). It is, therefore, apparent that effects of experimental conditions and nonhydrostatic stress on the compression curve are extremely large in pyrite. Further investigation of the underlying causes of these variations requires knowledge of the elastic properties and the shear strength of the material as well as their pressure dependence. The elastic moduli of pyrite have been studied experimentally at zero pressure (Simmons and Birch 1963), but no study has been conducted to higher pressures. We used newly developed, high-pressure radial diffraction measurements to understand the nature of elasticity and shear strength in pyrite under these conditions.

Theory of radial diffraction

The theory of lattice strains under nonhydrostatic pressure conditions in the diamond-anvil cell has been described elsewhere (Singh 1993 b; Singh et al. 1998a, b). We present a short summary of the main features. The sample is submitted to uniaxial stress conditions in the diamond cell; the geometry for radial diffraction experiments is shown in Fig. 3. The stress tensor in the sample can be expressed as

$$\sigma = \begin{bmatrix} \sigma_1 & 0 & 0 \\ 0 & \sigma_1 & 0 \\ 0 & 0 & \sigma_3 \end{bmatrix} = \begin{bmatrix} \sigma_P & 0 & 0 \\ 0 & \sigma_P & 0 \\ 0 & 0 & \sigma_P \end{bmatrix} + \begin{bmatrix} -t/3 & 0 & 0 \\ 0 & -t/3 & 0 \\ 0 & 0 & 2t/3 \end{bmatrix} , \quad (2)$$

where σ_1 and σ_3 are the radial and axial stress components, respectively. σ_P is the normal mean stress or equivalent hydrostatic pressure. The uniaxial stress component $t = (\sigma_3 - \sigma_1)$ is the deviatoric stress component.

The d spacing for a given set of lattice planes measured by X-ray diffraction is a function of the angle ψ between the principal stress axis of the diamond cell and the diffracting plane normal (see Fig. 4) and can be expressed as:

$$d_m(hkl) = d_P(hkl)\left[1 + (1 - 3\cos^2\psi)Q(hkl)\right] , \quad (3)$$

where $d_m(hkl)$ is the measured d spacing and $d_P(hkl)$ the d spacing under the hydrostatic pressure σ_P. $Q(hkl)$ is given by

$$Q(hkl) = \frac{t}{3}\left[\frac{\alpha}{2G_R(hkl)} + \frac{1-\alpha}{2G_V}\right] . \quad (4)$$

$G_R(hkl)$ and $G_V(hkl)$ are the shear moduli of the aggregate under the Reuss (iso-stress) and Voigt (iso-strain) approximations, respectively, and are not orientation-dependent. The factor α, which lies between 0 and 1, determines the relative weight of iso-stress (Reuss) and iso-strain (Voigt) conditions. It specifies the degree of stress and strain continuity across grains in the sample.

For a cubic system, we have

$$(2G_V)^{-1} = \frac{5}{2}\frac{(S_{11} - S_{12})S_{44}}{[3(S_{11} - S_{12}) + S_{44}]} \quad (5)$$

and

$$(2G_R)^{-1} = S_{11} - S_{12} - 3S\Gamma(hkl) , \quad (6)$$

where

$$S = S_{11} - S_{12} - S_{44}/2 \quad (7)$$

and

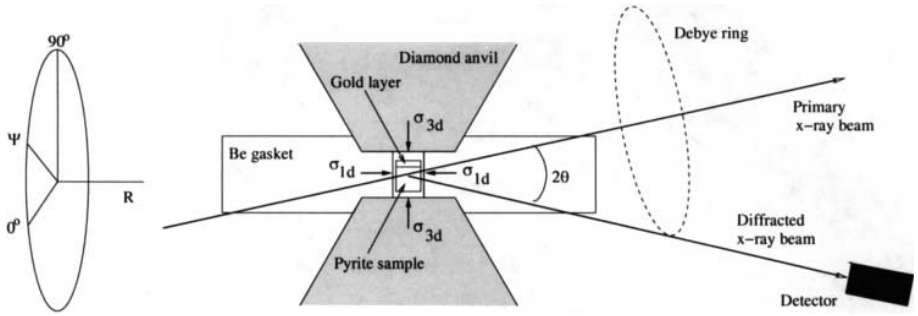

Fig. 3 Experimental setup for radial diffraction. The powdered sample is confined under nonhydrostatic stress between the two diamond anvils without any pressure medium. σ_{3d} is the axial stress imposed by the diamonds and σ_{1d} the radial stress imposed by the gasket. A layer of pressure calibrant (gold in this case) is added on the top of the sample. The cell is rotated about the axis R between $\psi = 0°$ and $\psi = 90°$ with 15° intervals

$$\Gamma(hkl) = \frac{h^2k^2 + k^2l^2 + l^2h^2}{(h^2 + k^2 + l^2)^2} \quad . \tag{8}$$

The S_{ij} are the single-crystal elastic compliances; S is a measure of elastic anisotropy.

According to Eq. (3), $d_m(hkl)$ should vary linearly with $(1 - 3\cos^2\psi)$. The intercept ($\psi = 54.7°$) yields $d_P(hkl)$, the d spacing due to the hydrostatic component of the stress, and the slope the product $d_P(hkl)Q(hkl)$.

Equations (4–6) imply a linear relationship between $Q(hkl)$ and $3\Gamma(hkl)$ with intercept m_0 and slope m_1 given by

$$m_0 = \frac{t}{3}\left[\alpha(S_{11} - S_{12}) + (1 - \alpha)\frac{5}{2}\frac{(S_{11} - S_{12})S_{44}}{[3(S_{11} - S_{12}) + S_{44}]}\right] \tag{9}$$

$$m_1 = -\frac{\alpha t}{3}[S_{11} - S_{12} - S_{44}/2] \quad . \tag{10}$$

The bulk modulus K is defined by

$$K_T = -V\left(\frac{\partial p}{\partial V}\right)_T = \frac{1}{3[S_{11} + 2S_{12}]} \quad . \tag{11}$$

Estimating the nonhydrostatic stress in the sample t using the relation (Singh 1993a; Singh et al. 1998a)

$$t = 6G\langle Q(hkl)\rangle \quad , \tag{12}$$

we have enough information to deduce the three elastic compliances S_{11}, S_{12}, and S_{44} of a cubic material that can be inverted to the three independent elastic stiffnesses C_{11}, C_{12}, and C_{44}.

Radial diffraction experiment

Experimental technique

Sample preparation was similar to previous experiments NE1 and NH2. The sample consisted of a fine-grained pyrite powder with a thin layer of gold powder on one face contained in a 50-μm diameter hole drilled in a beryllium gasket. The absence of pressure transmitting medium enhances the effects of nonhydrostaticity. Diamonds with a 300-μm diameter culet were used.

The experiment was conducted using energy-dispersive synchrotron X-ray diffraction at the NSLS Synchrotron National Source, beam line X-17C, and data were collected using a germanium solid-state detector set at a fixed angle with respect to the incident beam. Compression was performed using a diamond-anvil cell mounted on a rotating stage. The angle ψ between the diffraction plane normal and the diamond-anvil cell stress axis varied between 0° and 90° with 15° intervals (Fig. 3). We performed measurements for six pressure points at 5.6, 13.2, 20.5, 29.0, 36.5, and 47.8 GPa. Hydrostatic pressures were determined from the deduced lattice parameter at $\psi = 54.7°$ and the EOS of gold (Heinz and Jeanloz 1984).

The analysis on gold was based on the (1 1 1), (2 0 0), and (2 2 0) diffraction lines. For pyrite, we used the positions of the reflections (1 1 1), (2 0 0), (2 2 0), (2 1 1), (2 3 0), and (2 2 2). Diffraction lines were fitted to Voigtian peaks with varying height and width. As in the previous experiments, a diffraction line was rejected if there was unusually large error as a result of low intensity or overlap problems between gold, beryllium, or pyrite lines.

Radial diffraction equation of state

Figure 5 shows a typical set of diffraction patterns. A shift of the diffraction lines toward lower energies with increasing ψ angle can be observed. For $\psi = 90°$, the diffracting planes are aligned with the minimum stress axis, resulting in maximum d spacings. At $\psi = 0°$, the diffracting planes are orthogonal to the maximum stress axis, resulting in minimum d spacings (Figs. 4 and 6).

The variations of the peak positions with the ψ angle for pyrite are shown in Fig. 6 for the (1 1 1) and (2 0 0)

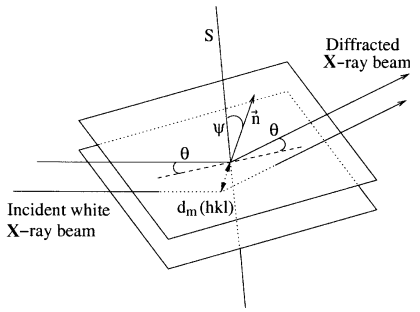

Fig. 4 For a given ψ angle between the diffracting plane normal $\vec{n}$ and the maximum stress axis S, we measure a d spacing $d_m(hkl)$ function of the Miller indices h, k, and l, but also the angle ψ because of the nonhydrostatic compression. When $\psi = 0°$, the diffracting plane is orthogonal with the maximum stress axis S, thus $d_m(hkl)$ is minimum. When $\psi = 90°$, the diffracting plane is aligned with the maximum stress axis S, thus $d_m(hkl)$ is maximum

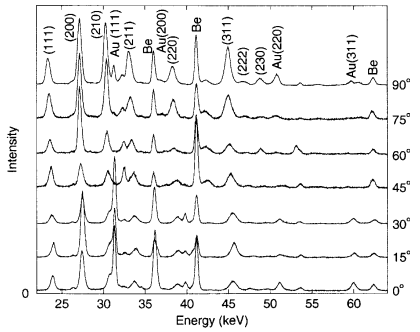

Fig. 5 X-ray diffraction patterns as a function of ψ angle for $P = 20.5$ GPa. Diffraction lines from pyrite, gold, and beryllium are *labeled*. The shift of the peak positions with the ψ angle can be observed; for example, pyrite (1 1 1)

6

reflections for different pressures. As predicted from Eq. (3), a linear dependence is observed between $d_m(hkl)$ and $(1 - 3\cos^2\psi)$. The lattice parameters under equivalent hydrostatic pressures can be deduced from the d spacings at the "magic angle" ($\psi = 54.7°$). The pyrite unit-cell volumes deduced from these measurements are presented in Table 5 and Fig. 7.

Compression curves are presented in Fig. 7, calculated for $\psi = 0°$, $\psi = 54.7°$, and $\psi = 90°$. For each pressure, we observe very large variation of the unit-cell volume with the ψ angle (Table 5). This is in agreement with the results from experiments NE1, NH1, and NH2, which showed that EOS measurement was very dependent on the stress conditions in the sample. Third-order, Birch–Murnaghan EOS fit parameters for the data in Fig. 7 are presented in Table 6. The difference between the bulk moduli calculated at $\psi = 0°$ and $\psi = 90°$ is about 45%, showing the very large effect of the nonhydrostatic stress on the EOS of pyrite. Assuming that $K'_{0T} = 4.0$, K_{0T} ranges from 121 GPa for $\psi = 0°$ to 193 GPa for $\psi = 90°$. These values are consistent with results from experiments NH2 (Table 4). Results from experiment NH1 are quite different, but could be explained by the scatter in the data and effects due to the larger grain size. Our deduced hydrostatic curve ($\psi = 54.7°$) is in good agreement with previous hydrostatic measurements from experiment NE1. Assuming $K'_{0T} = 4.0$, we obtain $K_{0T} = 156$ GPa, compared to $K_{0T} = 143$ GPa for NE1. It is therefore possible to measure a hydrostatic EOS under these very nonhydrostatic conditions by choosing the right orientation of the diffraction vector.

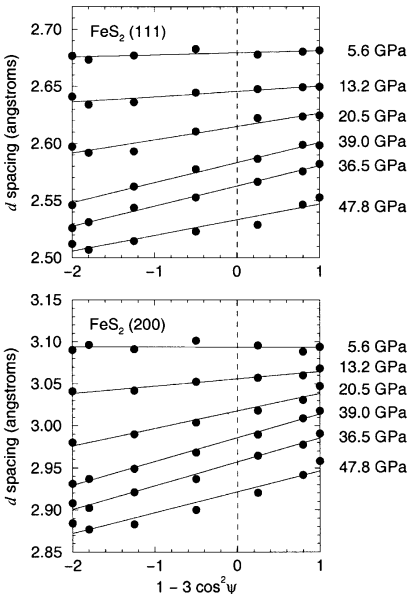

Fig. 6 Dependence of the d spacing on ψ for selected pyrite diffraction lines and different pressures. *Solid lines* are least-squares fits to the data. *Dashed lines* indicate the angle ψ where the measured d spacing corresponds to the d spacing under equivalent hydrostatic pressure

Yield strength of pyrite

From the least-squares lines in Fig. 6, using Eq. (3) we can calculate $Q(hkl)$ for each observed reflection and pressure. For each pressure $Q(hkl)$ should vary linearly

Table 5 Unit-cell volume of pyrite as a function of pressure deduced from the radial diffraction experiment at 293 K. We indicate results from measurements at different ψ angle. The volume under equivalent hydrostatic stress is calculated for $\psi = 54.7°$

P (GPa)	V/V_0 at $\psi = 0°$	V/V_0 at $\psi = 90°$	V/V_0 at $\psi = 54.7°$
5.6	0.9659 (±0.007)	0.9676 (±0.013)	0.9676 (±0.003)
13.2	0.9184 (±0.046)	0.9384 (±0.016)	0.9303 (±0.005)
20.5	0.8734 (±0.037)	0.9169 (±0.045)	0.8984 (±0.002)
29.0	0.8265 (±0.063)	0.8908 (±0.038)	0.8684 (±0.007)
36.5	0.8064 (±0.035)	0.8657 (±0.019)	0.8441 (±0.031)
47.8	0.7891 (±0.039)	0.8420 (±0.025)	0.8166 (±0.005)

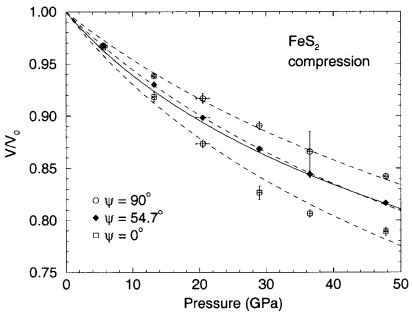

Fig. 7 EOS of pyrite measured at $\psi = 0°$, $\psi = 54.7°$ and $\psi = 90°$. Pressure is calibrated according to the hydrostatic EOS of gold (Heinz and Jeanloz 1984). *Dashed lines* are Birch–Murnaghan fits to the data. *Solid line* corresponds to the previous hydrostatic EOS measured in a neon medium from experiment NE1. Large differences appear between the EOS at different ψ angles, resulting from large nonhydrostatic stress in pyrite

Table 6 Birch–Murnagham EOS parameters for FeS_2 at 293 K for the radial diffraction experiment. Results are given for different ψ angles, including $\psi = 54.7°$, where the volume measured is the volume under an equivalent hydrostatic stress. For each case V_0 was fixed to its zero-pressure value and parameters of the third-order Birch–Murnaghan EOS were adjusted with K'_0 free and $K'_0 = 4.0$

ψ	K_{0T} (GPa)	K'_{0T}
0°	116.7 (±1.1)	4.30 (±0.08)
0°	120.8 (±0.2)	4.00
54.7°	160.8 (±5.2)	3.50 (±0.48)
54.7°	155.9 (±1.6)	4.00
90°	186.6 (±1.4)	4.43 (±0.09)
90°	193.4 (±0.3)	4.00

with $\Gamma(hkl)$ (Eqs. 4–8) (Singh 1993b). Figure 8 shows an example of the patterns we observed for three different pressures, 5.6, 13.2, and 20.5 GPa. The experimental data confirm the linear relationship between $Q(hkl)$ and $\Gamma(hkl)$ predicted by theory.

The uniaxial stress component t was calculated using Eq. (12) and least-squares fits shown in Fig. 8 from the relation

$$t = 6G\langle Q(hkl)\rangle = 6G\left(m_0 + \frac{3m_1}{5}\right) , \quad (13)$$

where m_0 and m_1 are the intercept and slope from the least-squares fits. The shear modulus of pyrite and its variation with pressure were estimated using $G_0 = 126$ GPa (Simmons and Birch 1963) and assuming a constant K/G ratio as has been done previously (Singh et al. 1998a, b). This approximation is valid over moderate compression (and at temperatures well below melting) for a variety of materials where the pressure dependence of K and G have been measured separately. Nevertheless, the approximation is likely to be the largest source of error in the determination of the high-pressure elastic moduli. K was evaluated along the compression curve from the EOS. Alternatively, an extrapolation of the shear modulus G based on finite strain theory may be used (Davies and Dziewonski 1975). However, this requires knowledge of pressure derivatives of the shear modulus, which have not been measured for pyrite. The calculated variation of t as a function of P is presented in Fig. 9.

At $P = 5.6$ GPa, the nonhydrostatic stress t is very close to zero. We cannot ensure that the stress conditions are really purely uniaxial, as considered in the theory, thus, the theory to deduce the elastic moduli will not be usable because of inappropriate experimental conditions. For higher loads, the observed uniaxial stress component t is larger than previous measurements on gold, molybdenum, and rhenium (Duffy et al. 1999a, b). A linear fit through the data in Fig. 9 between 10 and 30 GPa (where the variation of t is linear with pressure) leads to the relation $t = -3.11 + 0.43P$, where P is the pressure in GPa, compared to $t = 0.06 + 0.015P$ for gold (Duffy et al. 1999b), $t = 0.46 + 0.13P$ for molybdenum (Duffy et al. 1999b), and $t = 2.5 + 0.09P$ for rhenium (Duffy et al. 1999a). At $P > 30$ GPa, we observe a saturation. This can be explained by the elastic deformations of the diamond anvils that start at this pressure for this geometry (300-μm tip diameter), as investigated by X-ray diffraction and finite-element modeling (Hemley et al. 1997; Merkel et al. 1999, 2000b).

The maximum uniaxial stress t supported by a material is determined by its yield strength; that is $t \leq \sigma_y$, where σ_y is the material yield strength. The uniaxial stress t varies with sample environment, and there is equality only if the sample deforms plastically under pressure. Therefore, we conclude that for pyrite

$$\sigma_y \geq -3.11 + 0.43P \quad (14)$$

between 10 and 30 GPa, where P and σ_y are in GPa. This value for the uniaxial stress in pyrite is larger than observations on gold, rhenium, molybdenum (Duffy et al. 1999a), iron, FeO (Singh et al. 1998b), and tungsten (Hemley et al. 1997).

Elasticity

Using Eqs. (9–11) we can calculate the single-crystal elastic moduli of the sample. Results for the iso-stress hypothesis ($\alpha = 1$) and for $\alpha = 0.5$ are presented in Tables 7 and 8, respectively. The elastic stiffnesses calculated for $\alpha = 0.5$ do not match the zero-pressure ultrasonic measurements $C_{11} = 381.8$ GPa, $C_{12} = 31.0$ GPa and $C_{44} = 109.4$ GPa (Simmons and Birch 1963). On the other hand, the results for $\alpha = 1$ (the iso-stress hypothesis, Table 7) seem to be in good agreement: Fig. 10 shows the elastic stiffnesses calculated for $\alpha = 1$ and the zero-pressure ultrasonic data. We performed a linear fit through the X-ray data to evaluate the first pressure derivative of the C_{ij}s. We find

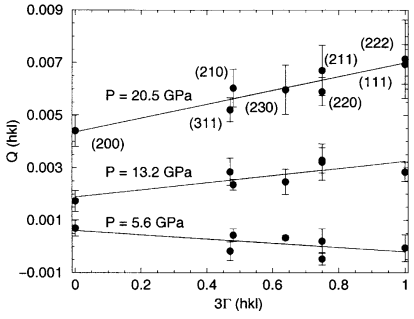

Fig. 8 $Q(hkl)$ vs. $3\Gamma(hkl)$ for pyrite at $P = 5.6$, 13.2, and 20.5 GPa. The *solid lines* are least-squares fits to the data. Errors on $Q(hkl)$ are estimated with the scatter of the $d(hkl)$ vs. ψ relation. *Error bars* represent $2\sigma(Q)$

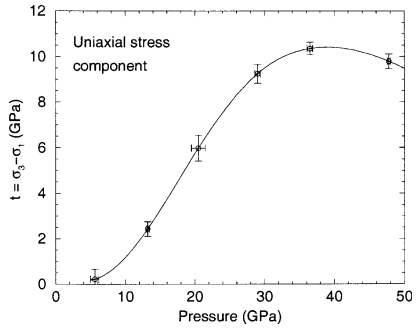

Fig. 9 Uniaxial stress component $t = \sigma_3 - \sigma_1$ in the sample vs. pressure. *Solid line* is a cubic spline through the data. The saturation above 30 GPa can be explained by the bending of the diamond anvils

8

$$\frac{dC_{11}}{dP} = 5.76\ (\pm 0.15) \tag{15}$$

$$\frac{dC_{12}}{dP} = 1.41\ (\pm 0.11) \tag{16}$$

$$\frac{dC_{44}}{dP} = 1.92\ (\pm 0.06)\ . \tag{17}$$

Anisotropy and influence of the α parameter

The elastic anisotropy of a cubic crystal can be characterized by the Zener ratio A, which is the ratio of the shear moduli in the (1 0 0) and (1 1 0) planes in the [1 0 0] direction:

$$A = \frac{2C_{44}}{C_{11} - C_{12}} = \frac{2S_{11} - S_{12}}{S_{44}}\ . \tag{18}$$

Assuming $\alpha = 1$ in Eq. (9), we have

$$A = \frac{1}{1 + m_1/m_0}\ . \tag{19}$$

Using the results from our measurements, we find A varying between 0.58 and 0.73 between $P = 13$ GPa and $P = 48$ GPa with $\bar{A} = 0.66$ as average value. This is of the same order as the value at $P = 0$, $A_0 = 0.624$. These results differ strongly from the results on gold from Duffy et al. (1999a), where the apparent A was observed to drop from 2.9 at $P = 0$ to 1.8 at higher pressures when $\alpha = 1$.

Finally, we can study in more detail the influence of the α parameter, which specifies the degree of stress and strain continuity within the sample (Eq. 4), on the elastic moduli. To match the zero-pressure ultrasonic measurements of the elastic moduli, we had to assume $\alpha = 1.0$ (iso-stress hypothesis). The influence of α on the elastic moduli we calculate is presented in Fig. 11 for $P = 20.5$ GPa. All elastic moduli vary quite drastically when α is varied from 0 to 1: C_{11} is found to decrease with increasing α, while C_{12} and C_{44} increase. Again, this variation is opposite to the behavior observed in gold (Duffy et al. 1999a).

Table 7 Elastic moduli of pyrite at different pressures calculated for $\alpha = 1$ (iso-stress hypothesis)

P (GPa)	$\sigma(P)$	C_{11} (GPa)	$\sigma(C_{11})$	C_{12} (GPa)	$\sigma(C_{12})$	C_{44} (GPa)	$\sigma(C_{44})$
13.2	0.2	492	158	45	79	130	36
20.5	1.0	519	77	59	38	147	21
29.0	0.4	544	36	78	18	168	12
36.5	0.4	586	22	86	11	182	7
47.8	0.2	678	46	79	23	193	13

Table 8 Elastic moduli of pyrite at different pressures calculated for $\alpha = 0.5$

P (GPa)	$\sigma(P)$	C_{11} (GPa)	$\sigma(C_{11})$	C_{12} (GPa)	$\sigma(C_{12})$	C_{44} (GPa)	$\sigma(C_{44})$
13.2	0.2	588	474	−3	237	102	36
20.5	1.0	602	218	18	109	120	23
29.0	0.4	608	92	47	46	145	15
36.5	0.4	652	56	53	28	158	10
47.8	0.2	785	131	26	65	159	14

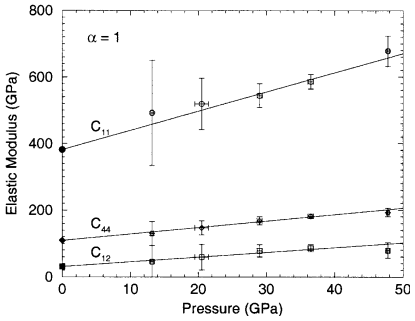

Fig. 10 Elastic moduli of pyrite and their variations with pressure calculated with $\alpha = 1.0$ (iso-stress condition). *Circles*, *squares*, and *diamonds* are C_{11}, C_{12}, and C_{44}, respectively. *Solid symbols* are zero-pressure ultrasonic measurements (Simmons and Birch 1963), and *open symbols* are deduced from the present experiment. *Lines* are least-squares fits of the first pressure derivatives of the elastic moduli to the data

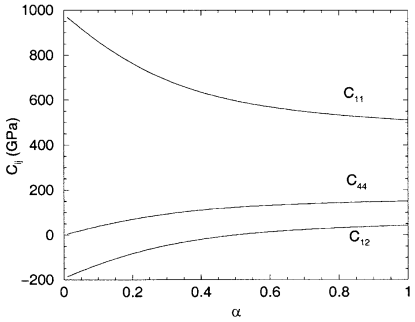

Fig. 11 Elastic moduli of pyrite at $P = 20.5$ GPa and their variations when calculated with different α parameter

Discussion and conclusions

We find the apparent compression curve of pyrite to be very dependent upon the conditions under which the experiment is performed, i.e., shock compression, conventional X-ray diffraction using the diamond-anvil cell and different pressure-transmitting media, or radial X-ray diffraction studies. Application of the technique of radial diffraction made possible an analysis of the nature of these discrepancies. The EOS measured at extreme ψ angles 0° and 90° provide values for the bulk modulus [$K_{0T}(0°) = 121$ GPa and $K_{0T}(90°) = 193$ GPa, assuming $K'_{0T} = 4.0$] between which extremes most previously published experimental results lie.

The hydrostatic EOS measured in the conventional diffraction (along the load axis) experiment (NE1) and

that deduced from the radial diffraction experiment at the magic angle are within error. In the experiment with pyrite and ruby confined in solid neon, which is known to be a good hydrostatic medium, the stress condition in the sample chamber can be considered as homogeneous and the pressure deduced from the ruby shift equal to the pressure in the sample. In the radial diffraction experiment, we used the pressure in the gold layer as reference, but there could be differences between the pressure in the gold layer and the sample for two reasons: (1) nonhydrostatic stress is different in gold and pyrite, and (2) the Reuss (iso-stress) conditions between different materials are not completely verified in these kinds of experiments (Duffy et al. 1999b). Thus, small deviations are expected between the deduced pressure and the actual pressure present in the sample. In general, hydrostatic compression is less prone to error; therefore, we conclude that the third-order Birch–Murnaghan EOS parameters for pyrite are $K_{0T} = 133.5\ (\pm 5.2)$ GPa and $K'_{0T} = 5.73\ (\pm 0.58)$.

Further analysis on the results of the radial diffraction experiments indicates the presence of very large uniaxial stress in the sample, implying a very large shear strength for pyrite under high pressure. Thus, differences between EOS measured under different stress conditions are expected since the dependence of the compression curve on nonhydrostatic stress increases with increasing sample shear strength. This can be related to the cases where the compression curve was found to vary between different experiments, making it quite difficult to deduce the bulk modulus and its first pressure derivative. This was observed, for instance, in $MgCO_3$ by (Fiquet and Reynard 1999).

Finally, we have constrained the elastic moduli of pyrite up to 50 GPa and find them to depend linearly on pressure. This study confirms the accuracy of the radial diffraction method to study elastic moduli and strength of material of cubic symmetry under very high pressure. Extension to lower symmetry materials requires further theoretical developments (Merkel et al. 2000a; Wenk et al. 2000).

Acknowledgements The authors are grateful to Anil K. Singh for useful discussions, Jingzhu Hu for experimental assistance, and Wim Van Westrenen for comments on the manuscript. This work was supported by NSF and DOE (National Synchrotron Light Source).

References

Ahrens TJ (ed) (1995) Mineral physics and crystallography, a handbook of physical constants. American Geophysical Union, Washington DC

Ahrens TJ, Jeanloz R (1987) Pyrite: shock compression, isentropic release, and the composition of the Earth's core. J Geophys Res 92: 10363–10375

Bridgman PW (1949) Linear compression to 30000 kg/cm^2, including relatively incompressible substances. Proc Am Acad Arts Sci 77: 189–234

Chattopadhyay T, Schnering HG von (1985) High-pressure X-ray diffraction study on p-FeS_2, m-FeS_2 and MsS_2 to 340 kbar: a possible high spin–low spin transition in MnS_2. J Phys Chem Sol 46: 113–116

Davies GF, Dziewonski AM (1975) Homogeneity and constitution of the Earth's lower mantle and outer core. Phys Earth Planet Inter 10: 336–343

Drickamer HG, Lynch RW, Clendenen RL, Perez-Albuene EA (1966) X-ray diffraction studies of the lattice parameters of solids under very high pressure. Sol State Phys 19: 135–229

Duffy TS, Shen G, Heinz DL, Shu J, Ma Y, Mao HK, Hemley RJ, Singh AK (1999a) Lattice strains in gold and rhenium under non-hydrostatic compression to 37 GPa. Phys Rev (B) 60: 1–10

Duffy TS, Shen G, Shu J, Mao HK, Hemley RJ, Singh AK (1999b) Elasticity, shear strength and equation of state of molybdenum and gold from X-ray diffraction under nonhydrostatic compression to 24 GPa. J Appl Phys 86: 1–8

Fiquet G, Reynard B (1999) High-pressure equation of state of magnesite: new data and reappraisal. Am Mineral 84: 856–860

Fujii T, Yoshida A, Tanaka K, Marumo F, Nodo Y (1986) High-pressure compressiblities of pyrite and cattierite. Mineral J 13: 202–211

Heinz DL, Jeanloz R (1984) The equation of state of the gold calibration standard. J Appl Phys 55: 885–893

Hemley RJ, Mao HK, Shen G, Badro J, Gillet P, Hanfland M, Häusermann D (1997) X-ray imaging of stress and strain of diamond, iron, and tungsten at megabar pressures. Science 276: 1242–1245

Jephcoat AP (1985) Hydrostatic compression studies on iron and pyrite to high pressures: the composition of the Earth's core and the equation of state of solid argon. PhD Thesis, John Hopkins Univ., Baltimore, Maryland

Jephcoat AP, Mao HK, Bell PM (1987) Operation of the megabar diamond-anvil cell. In: Ulmes GC, Barnes HL, (eds) Hydrothermal experimental techniques. Wiley-Interscience, Wiley, New York

Mao HK, Shu J, Shen G, Hemley RJ, Li B, Singh AK (1998) Elasticity and rheology of iron above 220 GPa and the nature of the Earth's inner core. Nature 396: 741–743. Correction: Nature 399: 280 (1999)

Merkel S, Hemley RJ, Mao HK (1999) Finite-element modeling of diamond deformation at multimegabar pressures. Appl Phys Lett 74: 656–658

Merkel S, Goncharov AF, Mao HK, Gillet P, Hemley RJ (2000a) Raman spectroscopy of iron to 152 gigapascals: implications for Earth's inner core. Science 288: 1626–1629

Merkel S, Hemley RJ, Mao HK, Teter DM (2000b) Finite-element modeling and ab-initio calculations of megabar stresses in the diamond-anvil cell. In: Magnhnani M (ed) Science and technology of high-pressure. University Press (Hydergula, India): 68–73

Robie RA, Hemingway BS, Fisher JR (1979) Thermodynamic porperties of minerals and related substances at 298.15 K and 1 bar (10^5 Pascals) pressure and at higher temperatures). US Geol Surv Bull, No. 1452, US Government Printing Office, Washington DC

Simmons G, Birch F (1963) Elastic constants of pyrite. J Appl Phys 34: 2736–2738

Singh AK (1993a) Analysis of C_{60} fullerite compression under nonhydrostatic pressure. Philosoph Mag Lett 67: 379–384

Singh AK (1993b) The lattice strains in a specimen (cubic system) compressed nonhydrostatically in an opposed anvil device. J Appl Phys 73: 4278–4286

Singh AK, Balasingh C, Mao HK, Hemley RJ, Shu J (1998a) Analysis of lattice strains measured under non-hydrostatic pressure. J Appl Phys 83: 7567–7575

Singh AK, Mao HK, Shu J, Hemley RJ (1998b) Estimation of single-crystal elastic moduli from polycrystalline X-ray diffraction at high pressure: applications to FeO and iron. Phys Rev Lett 80: 2157–2160

Wenk HR, Matthies S, Hemley RJ, Mao HK, Shu J (2000) The plastic deformation of iron at pressures of the Earth's inner core. Nature 405: 1044–1047

JOURNAL OF GEOPHYSICAL RESEARCH, VOL. 110, B05201, doi:10.1029/2004JB003197, 2005

X-ray diffraction study of the single-crystal elastic moduli of ϵ-Fe up to 30 GPa

Sébastien Merkel,[1,2,3] Jinfu Shu,[1] Philippe Gillet,[2]
Ho-Kwang Mao,[1] and Russell J. Hemley[1]

Received 1 June 2004; revised 3 February 2005; accepted 11 February 2005; published 13 May 2005.

[1] Room temperature investigations of the single-crystal elastic moduli and anisotropy of the ϵ phase of iron are performed up to 30.3 GPa using the radial X-ray diffraction technique. The accuracy of the calculated elastic moduli has improved compared to previous measurements using similar techniques because of an increase in accuracy of the measurement, confinement of the sample to limit the effect of plasticity, and better calibration of the stress conditions. The aggregate shear modulus that we obtain is in good agreement with a variety of other experimental deductions but differs from first-principles calculations. The effects of the calibration of stress and micromechanical model on the deduction of elastic moduli and elastic anisotropy are discussed in detail. The anisotropy we obtain has the same order of magnitude as first-principles calculations but the direction is reversed, with a weaker amplitude that previous measurements.

Citation: Merkel, S., J. Shu, P. Gillet, H.-K. Mao, and R. J. Hemley (2005), X-ray diffraction study of the single-crystal elastic moduli of ϵ-Fe up to 30 GPa, *J. Geophys. Res.*, *110*, B05201, doi:10.1029/2004JB003197.

1. Introduction

[2] Understanding the effect of pressure on the propagation of elastic waves in solid materials is of fundamental interest for constraining the properties of the deep interior of the planets. To that extent, the elastic properties of iron and their pressure dependence are particularly important as it is the main constituent of the Earth inner core. Although the crystal structure of iron at these depths is still debated, it is accepted that the ϵ phase has a wide stability field and serves as a starting point for modeling the inner core [*Hemley and Mao*, 2001]. However, constraining the elastic properties of this phase remains a challenging task, both experimentally and using first-principles calculations.

[3] The compression curve of ϵ-Fe has been measured experimentally up to core pressures, using both static and dynamic methods, and is particularly well constrained [*Brown and McQueen*, 1986; *Jephcoat et al.*, 1986; *Mao et al.*, 1990; *Yoo et al.*, 1993; *Nguyen and Holmes*, 1998, 2004; *Ma et al.*, 2004]. From these data, an estimation of both the variation of density and bulk modulus with pressure can be obtained. On the other hand, first-principles calculations of the equation of state of ϵ-Fe are difficult, especially at low pressure [*Stixrude et al.*, 1994; *Steinle-Neumann et al.*, 1999]. The discrepancy between experimental data and the results from first-principles calculations is larger than what is typically obtained for other transition metals. Inclusion of magnetic effects is thought to improve the agreement with experiments but the density remains overestimated, and there are fundamental aspects of the physics of ϵ-Fe affecting first-principles calculations that are not well understood [*Jarlborg*, 2002; *Bose et al.*, 2003; *Thakor et al.*, 2003; *Gannarelli et al.*, 2003; *Steinle-Neumann et al.*, 2004].

[4] The aggregate compressional wave velocity V_P of ϵ-Fe has been obtained up to 110 GPa using inelastic X-ray scattering [*Fiquet et al.*, 2001; *Antonangeli et al.*, 2004]. This represented the first direct measurement of acoustic sound velocity up to core pressure under static conditions. Other determination of aggregate elastic moduli include measurement of the shear modulus of ϵ-Fe at 16 GPa using ultrasonic interferometry [*Mao et al.*, 1998], deduction of both the aggregate compressional and shear wave velocities using high-pressure and high-temperature X-ray diffraction and Rietveld refinement [*Dubrovinsky et al.*, 2001], as well as measurements of phonon density of states [*Lübbers et al.*, 2000; *Mao et al.*, 2001].

[5] Measurements of single-crystal elastic moduli of ϵ-Fe are scarce. Constraints on elastic moduli by inverting X-ray diffraction data on polycrystals under nonhydrostatic stress have been reported twice [*Singh et al.*, 1998b; *Mao et al.*, 1998]. However, the calibration of stresses in theses sample was problematic and the effect of lattice preferred orientation was difficult to constrain [*Matthies et al.*, 2001a]. Several sets of first-principles calculations have also been performed [*Stixrude and Cohen*, 1995; *Söderlind et al.*, 1996; *Cohen et al.*, 1997; *Steinle-Neumann et al.*, 1999; *Laio et al.*, 2000; *Vočadlo et al.*, 2003]. Finally, the C_{44} elastic modulus of ϵ-Fe and its pressure dependence were deduced from Raman measurements using a phenomeno-

[1]Geophysical Laboratory, Carnegie Institution of Washington, Washington, D. C., USA.
[2]Laboratoire des Sciences de la Terre, École Normale Supérieure de Lyon, Lyon, France.
[3]Now at Department of Earth and Planetary Science University of California, Berkeley, California, USA.

0148-0227/05/2004JB003197$09.00

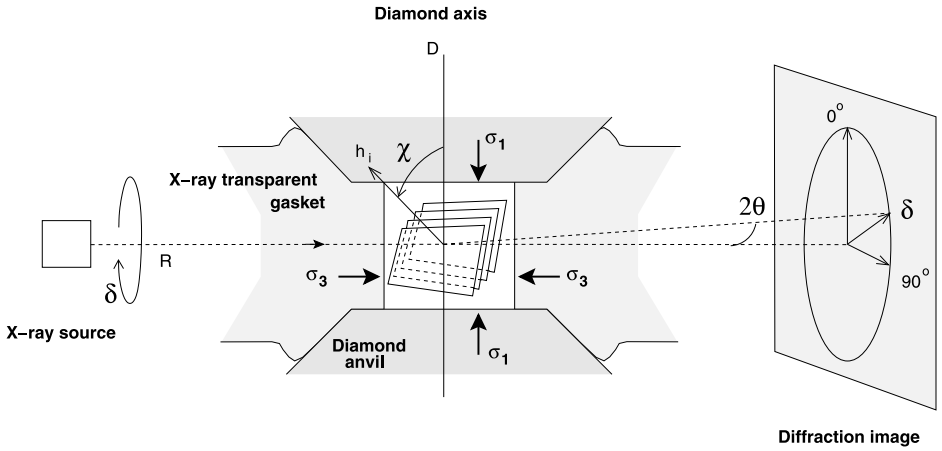

Figure 1. Schematic of the experiment. The polycrystalline sample is confined under nonhydrostatic stress conditions between the two diamond anvils. The σ_1 is the axial stress imposed by the diamonds, and σ_3 is the radial stress imposed by the gasket. A monochromatic X-ray beam is sent through the gasket with the direction of the incoming beam orthogonal to the diamond axis and the data collected on an imaging plate orthogonal to the incoming beam. The position of the diffraction lines and intensity of diffraction are analyzed as a function of the azimuthal angle δ from which we calculate the angle χ between the normal to the diffracting plane h_i and the compression direction.

logical model [*Merkel et al.*, 2000]. As shown by *Merkel et al.* [2000], there is actually no consensus on the elastic properties of iron under pressure and significant work remains to be done.

[6] In recent years, the procedure for determining the single-crystal elastic moduli from X-ray diffraction at high pressure has improved considerably. On the experimental side, the measurements can now be performed using monochromatic beams and large area detectors, allowing precise measurements of the variation of *d* spacings with orientation as well as texture analysis [*Merkel et al.*, 2002, 2003, 2004]. In addition, the theory for the inversion of elastic moduli was clarified by including effects of lattice preferred orientation in the analysis [*Matthies et al.*, 2001a, 2001b], and the C_{44} single-crystal elastic modulus of ϵ-Fe was constrained up to core pressure [*Merkel et al.*, 2000]. In this paper, we readdress the issue of the single-crystal elasticity of hcp-iron measured from X-ray diffraction using those new constrains and new experimental data.

2. Methods

2.1. Experimental Technique

[7] We perform a uniaxial deformation of a polycrystalline iron sample embedded in MgO powder with the diamond anvil cell. The stress state in the sample is analyzed using X-ray diffraction with the incident beam orthogonal to the compression axis (Figure 1). Experimental details along with the analysis of the strain state, polycrystalline texture, and deformation mechanisms of the MgO surrounding the Fe sample as well as analysis of the texture of the ϵ-Fe sample in this same experiment have been given elsewhere [*Merkel et al.*, 2002, 2004].

[8] In order to measure angle dispersive diffraction in a radial geometry, the confining gasket was made of a mixture of amorphous boron and epoxy with a ratio of 2/3 in weight. Iron samples with grain size smaller than 1 μm were used to ensure a large number of crystallites and orientations in the analysis. The samples were pressed into platelets between two large diamonds (1 mm tip diameter). A layer of MgO was deposited at the bottom of the gasket hole. A small platelet of pure polycrystalline iron was then added. Finally, another platelet of MgO was added above the Fe platelet and pressed using the diamond anvils.

[9] Diffraction experiments were conducted using angle dispersive synchrotron X-ray diffraction techniques at the ID-13 beam line of the GSECARS sector at the Advanced Photon Source. A monochromatic beam of wavelength 0.4246$\mathring{A}$ was used. Diffraction patterns were recorded with 2000×2700 pixels image plates. The raw X-ray diffraction images were corrected for nonorthogonality by comparing to a CeO_2 standard pattern taken prior to the experiment. The sample to image plate distance calibrated using the CeO_2 standard was 290.7 mm. Variations of absorption of the X-ray by the gasket as a function of the azimuthal angle were not accounted for, but they are known to be of relatively small amplitude compared to the diffraction intensities of the sample (e.g., Figure 2).

[10] In the second experiment of *Merkel et al.* [2002], MgO and Fe were compressed at 300 K up to 30.3 GPa. At this pressure we performed several laser heating cycles. During the last heating at this pressure (about 28 GPa, up to 1300 K), part of the ϵ-Fe sample converted into the γ phase (fcc). This phase is quenchable to ambient temperature and has diffraction peaks that partially overlap those of ϵ-Fe.

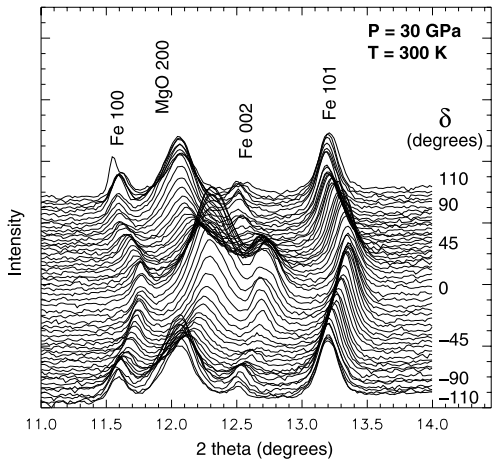

Figure 2. Patterns extracted from the diffraction image at 30.3 GPa for azimuth angles δ varying from −110° to 110°. The 2θ interval was restricted to 11–14° in order to emphasize the variations of *d* spacings and intensities of diffraction with orientation. Diffraction peaks from the pressure medium, MgO, and the iron sample are labeled.

Therefore we did not take the analysis any further and the data presented here will only extend up to 30.3 GPa and under ambient temperature. Pressures were estimated using the hydrostatic equation of state of the pressure medium, MgO [*Speziale et al.*, 2001], and iron itself [*Jephcoat et al.*, 1986], after correcting the data for the effect of nonhydrostatic stress [e.g., *Merkel et al.*, 2002]. Pressures determined from the hcp-Fe or MgO samples differed by less than 0.5 GPa for all pressures (Tables 1 and 2). Figure 2 presents examples of diffraction patterns at 30.3 GPa that were used for this analysis.

[11] As the orientation of the diamond anvil cell was not completely fixed, the origin for azimuth angles on the imaging plate was adjusted by locating the orientation at which the *d* spacings are minimum. There were slight deviations (up to a few degrees) between the minimum found for different lattice planes. However, some distortions of the same amplitude could also be observed for the calibration sample. Therefore those deviations were ignored and we chose an average value as reference for azimuth angles.

2.2. General Equations

[12] Because of the symmetry of the experiment (Figure 1), the stress conditions in the sample can be described as

$$\sigma = \begin{bmatrix} \sigma_3 & 0 & 0 \\ 0 & \sigma_3 & 0 \\ 0 & 0 & \sigma_1 \end{bmatrix} = \begin{bmatrix} P & 0 & 0 \\ 0 & P & 0 \\ 0 & 0 & P \end{bmatrix} + \begin{bmatrix} -\frac{t}{3} & 0 & 0 \\ 0 & -\frac{t}{3} & 0 \\ 0 & 0 & 2\frac{t}{3} \end{bmatrix}, \quad (1)$$

where σ_3 and σ_1 are the radial and axial stress components, respectively; P is the normal mean stress or equivalent hydrostatic pressure, and $t = (\sigma_1 - \sigma_3)$ is the maximum principal stress, which we will call the uniaxial stress throughout this paper.

[13] The *d* spacings measured by X-ray diffraction depend on the Miller indices of the lattice plane, *hkl*, the stress applied to the sample, P and t, the elastic tensor of the material under the pressure P, $[C_{ij}]$, the orientation distribution function (ODF) of the sample, f, and the direction of observation, **y**,

$$\bar{d}_m = \bar{d}_m(hkl, P, t, [C_{ij}], f, \mathbf{y}), \quad (2)$$

where the overbar indicates an average over all grains contributing to the diffraction at the orientation **y**. In order to analyze the effect of nonhydrostatic stress on the measured *d* spacings, it is useful to separate the contribution of the hydrostatic pressure P that does not depend on the direction of observation using

$$\bar{d}_m(hkl, P, t, [C_{ij}], f, \mathbf{y}) = d_0(hkl, P) \cdot \left[1 + \frac{\bar{d}_m(hkl, P, t, [C_{ij}], f, \mathbf{y}) - d_0(hkl, P)}{d_0(hkl, P)}\right] \quad (3)$$

$$\bar{d}_m(hkl, P, t, [C_{ij}], f, \mathbf{y}) = d_0(hkl, P)\left[1 + \bar{\epsilon}(hkl, P, t, [C_{ij}], f, \mathbf{y})\right], \quad (4)$$

where $d_0(hkl, P)$ is the *d* spacing of the plane under the equivalent hydrostatic pressure P. It can be easily related to the cell parameters a and c of the sample at pressure P.

Table 1. Elastic Moduli and Uniaxial Stress Calculated in This Study for the Reuss Bound (α = 1.0)[a]

P-MgO	P-Fe	t	C_{11}	C_{12}	C_{13}	C_{33}	C_{44}	C_{66}
17.4 ± 0.5	17.7 ± 0.5	3.03 ± 0.46	480 ± 64	85 ± 90	182 ± 35	373 ± 66	130 ± 50	197 ± 76
18.3 ± 0.5	18.5 ± 0.5	3.03 ± 0.46	419 ± 26	152 ± 19	189 ± 12	371 ± 23	131 ± 23	133 ± 22
20.2 ± 0.5	20.3 ± 0.5	3.03 ± 0.45	423 ± 24	166 ± 16	197 ± 11	381 ± 21	134 ± 22	128 ± 20
23.0 ± 0.5	22.7 ± 0.5	2.93 ± 0.42	423 ± 22	198 ± 14	192 ± 15	415 ± 28	138 ± 23	112 ± 17
23.9 ± 0.5	24.1 ± 0.5	2.91 ± 0.42	423 ± 22	211 ± 26	200 ± 27	420 ± 51	140 ± 35	106 ± 19
27.0 ± 0.5	27.2 ± 0.5	3.03 ± 0.42	444 ± 22	212 ± 12	213 ± 12	429 ± 22	145 ± 21	116 ± 16
29.8 ± 0.5	30.3 ± 0.5	3.39 ± 0.45	456 ± 21	220 ± 29	230 ± 25	432 ± 46	150 ± 40	118 ± 21
	28.8 ± 0.5	2.73 ± 0.37	441 ± 20	234 ± 24	217 ± 26	442 ± 49	148 ± 37	103 ± 17

[a]These calculations were calibrated using the compressibility measurements of *Jephcoat et al.* [1986] and C_{44} deduced from Raman spectroscopy [*Merkel et al.*, 2000]. Pressures, stresses, and elastic moduli are expressed in GPa.

Table 2. Elastic Moduli and Uniaxial Stress Calculated in this Study for the Hill Average ($\alpha = 0.5$)[a]

P-MgO	P-Fe	t	C_{11}	C_{12}	C_{13}	C_{33}	C_{44}	C_{66}
17.4 ± 0.5	17.7 ± 0.5	3.60 ± 0.55	584 ± 178	−24 ± 224	190 ± 47	351 ± 83	130 ± 90	304 ± 201
18.3 ± 0.5	18.5 ± 0.5	2.90 ± 0.44	415 ± 29	144 ± 29	203 ± 11	339 ± 20	131 ± 28	136 ± 28
20.2 ± 0.5	20.3 ± 0.5	2.82 ± 0.41	410 ± 24	165 ± 22	213 ± 10	346 ± 17	134 ± 25	122 ± 22
23.0 ± 0.5	22.7 ± 0.5	2.60 ± 0.38	397 ± 19	214 ± 19	205 ± 16	384 ± 28	138 ± 26	91 ± 17
23.9 ± 0.5	24.1 ± 0.5	2.50 ± 0.35	391 ± 18	231 ± 39	215 ± 31	385 ± 54	140 ± 44	80 ± 25
27.0 ± 0.5	27.2 ± 0.5	2.64 ± 0.36	414 ± 17	228 ± 13	230 ± 10	391 ± 18	145 ± 22	93 ± 14
29.8 ± 0.5	30.3 ± 0.5	2.88 ± 0.38	421 ± 24	238 ± 44	250 ± 24	389 ± 41	150 ± 57	91 ± 33
	28.8 ± 0.5	2.28 ± 0.31	403 ± 16	257 ± 34	234 ± 28	402 ± 49	148 ± 47	73 ± 21

[a]These calculations were calibrated using the compressibility measurements of *Jephcoat et al.* [1986] and C_{44} deduced from Raman spectroscopy [*Merkel et al.*, 2000]. Pressures, stresses, and elastic moduli are expressed in GPa.

[14] Because of the simple geometry of the experiment, the orientation dependence **y** of the measurement can be reduced to a single parameter, the angle χ between the diffracting plane normal and the load axis (Figure 1). It can be calculated from the azimuth angle on the imaging plate using the relation

$$\cos\chi = \cos\theta\cos\delta, \tag{5}$$

where θ is the diffraction angle.

[15] Several theoretical approaches have been developed in order to address the relation between those measurements and the single crystal elastic moduli of the sample and they can be divided in two categories, those which neglect the effect of lattice preferred orientation, and those which include it.

2.3. Analysis With No Effects of Preferred Orientation

[16] The resolution of the lattice strains equations for a polycrystal under uniaxial stress and no effect of texture has been developed independently by several groups [e.g., *Bollenrath et al.*, 1967; *Singh et al.*, 1998a; *Bittorf et al.*, 1998; *Gnäupel-Herold et al.*, 1998; *Howard and Kisi*, 1999, and references therein]. In this paper, we will refer to the specific application to high-pressure experiments, as described by *Singh et al.* [1998a].

[17] If we assume that the crystallites in the sample are randomly oriented, the equations of linear elasticity provide

$$\bar{\epsilon}(hkl, P, t, [C_{ij}], \chi) = (1 - 3\cos^2\chi)Q(hkl, P, t, [C_{ij}]), \tag{6}$$

where $Q(hkl, P, t, [C_{ij}])$ is given by

$$Q(hkl, P, t, [S_{ij}]) = \frac{t}{3}\left[\frac{\alpha}{2\,G_R(hkl, [S_{ij}])} + \frac{1-\alpha}{2\,G_V([S_{ij}])}\right], \tag{7}$$

where $[S_{ij}]$ is the elastic compliances tensor, and $G_R(hkl)$ and G_V are appropriate moduli of the aggregate under the Reuss (isostress) and Voigt (isostrain) approximations, respectively, and do not depend on the direction of observation. The factor α, which lies between 0 and 1, determines the relative weight of isostress (Reuss) and isostrain (Voigt) conditions. It specifies the degree of stress and strain continuity across grains in the sample.

[18] For a hexagonal crystal, we have

$$\frac{1}{G_R(hkl)} = (2S_{11} - S_{12} - S_{13}) + (-5S_{11} + S_{12} + 5S_{13} - S_{33} + 3S_{44})l_3^2(hkl, P) + (3S_{11} - 6S_{13} + 3S_{33} - 3S_{44})l_3^4(hkl, P), \tag{8}$$

$$\frac{1}{2G_V} = \frac{15}{C_{11} + C_{12} + 2C_{33} - 4C_{13} + 12C_{44} + 12C_{66}}, \tag{9}$$

where

$$l_3^2(hkl, P) = \frac{3a^2l^2}{4c^2(h^2 + hk + k^2) + 3a^2l^2}, \tag{10}$$

where a and c are the cell parameters at pressure P. Therefore, for the hexagonal symmetry, we expect a quadratic relation between $Q(hkl, P, t, [S_{ij}])$ and $l_3^2(hkl, P)$ that can provide three independent coefficients m_0, m_1 and m_2 function of the uniaxial stress t, the parameter α and the representative single-crystal elastic moduli $[C_{ij}]$. Two additional constrains are provided by the compressibilities in directions a and c,

$$\chi_a = \alpha(S_{11} + S_{12} + S_{13}) + (1 - \alpha)\frac{1}{3K_V} \tag{11}$$

$$\chi_c = \alpha(S_{33} + 2S_{13}) + (1 - \alpha)\frac{1}{3K_V} \tag{12}$$

that can be deduced from equation of state measurements using

$$2\chi_a + \chi_c = \frac{1}{K}, \quad \chi_a - \chi_c = \left(\frac{\partial \ln(c/a)}{\partial P}\right). \tag{13}$$

Therefore we have a system of five independent equations

$$\begin{aligned} m_0 &= \frac{\alpha t}{6}\left[(2S_{11} - S_{12} - S_{13}) + \frac{1-\alpha}{\alpha}\frac{1}{2G_V}\right], \\ m_1 &= \frac{\alpha t}{6}(-5S_{11} + S_{12} + 5S_{13} - S_{33} + 3S_{44}), \\ m_2 &= \frac{\alpha t}{6}(3S_{11} - 6S_{13} + 3S_{33} - 3S_{44}), \\ \chi_a &= \alpha(S_{11} + S_{12} + S_{13}) + (1 - \alpha)\frac{1}{3K_V}, \\ \chi_c &= \alpha(S_{33} + 2S_{13}) + (1 - \alpha)\frac{1}{3K_V} \end{aligned} \tag{14}$$

that can be used to solve the inverse problem and deduce the effective single-crystal elastic moduli of the polycrystal from the X-ray diffraction data.

2.4. Analysis With Effects of Preferred Orientation

[19] The resolution of the lattice strains equations for a polycrystal under uniaxial stress that considers the effects of texture have been described previously [*Matthies et al.*, 2001a, 2001b]. However, the complexity of this numerical approach has considerably limited its application.

[20] In order to consider the effect of lattice preferred orientation on the radial diffraction measurements, one has to introduce the ODF, $f(g)$, that describes the probability density to expect crystallites that have an orientation g within dg. The observed lattice strains can be described as

$$\overline{\epsilon}(hkl, P, t, [C_{ij}], f, \chi) = \overline{S}(hkl, P, t, [C_{ij}], f, \chi) \cdot \overline{\sigma}(hkl, P, t, [C_{ij}], f, \chi), \quad (15)$$

where $\overline{S}$ and $\overline{\sigma}$ are effective macroscopic elastic moduli and stresses. The effective macroscopic quantities $\overline{\epsilon}$, $\overline{S}$ and $\overline{\sigma}$ and their microscopic equivalent can be related by the equation

$$\overline{\epsilon} = \overline{\epsilon(g)} = \int_G \epsilon(g) f(g) \bar{d}g = \overline{S(g)\sigma(g)} = \overline{S}\overline{\sigma}. \quad (16)$$

The quantities measured experimentally are the macroscopic strain $\overline{\epsilon}$ and stress $\overline{\sigma}$. Therefore the deduction of the effective macroscopic elastic moduli $\overline{S}$ is direct. However, in this study, we are interested in deducing of the single-crystal elastic moduli of the material, that is the microscopic elastic properties S.

[21] The extraction of the single-crystal elastic moduli from equation (16) depends on the micromechanical model assumed for the grain interactions and no analytical relation is in general available. This inverse problem is nonlinear, and a theory used to perform the numerical inversions described in detail by *Matthies et al.* [2001b]. These authors demonstrated that with high-quality diffraction data, well-calibrated stress conditions, and no plastic deformation, elastic moduli with reasonable agreement with measurements from other techniques can be extracted.

3. Results

3.1. Experimental Data

[22] Figure 3 presents the variations of the d spacings measured for the (101) and (110) planes of ϵ-Fe with the angle χ for pressures between 17.7 and 30.3 GPa. The quality of the measurements has improved compared to previous work on this material [e.g., *Matthies et al.*, 2001a, Figure 3]: The number of measured orientations is far greater, and we can confirm that the d spacing vary almost linearly with $(1-3\cos^2\chi)$ for χ ranging between -110 and 110°, as predicted by the lattice strain theory without effect of preferred orientation (equation (6)). However, the oscillations between different orientations remain large, thus undermining the possibility of using the theory including effects of lattice preferred orientation.

3.2. Effect of Texture on the Deduced Elastic Moduli

[23] As described previously, the sample in this experiment did exhibit some degree of lattice preferred orientation

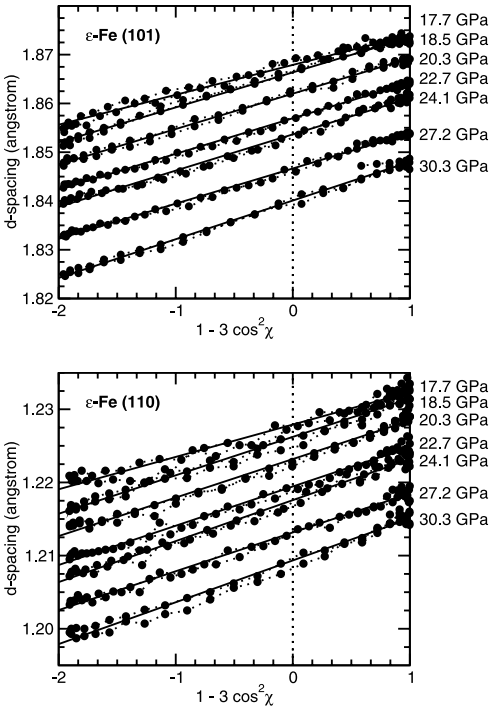

Figure 3. Dependence of the d spacings on $(1-3\cos^2\chi)$ for the (101) and (110) planes of ϵ-Fe and different pressures. Circles are experimental data and solid lines linear regressions to the data.

[*Merkel et al.*, 2004]. At this point, several factors need to be emphasized. First, the effect of lattice preferred orientation on the variation of d spacings with orientation is relatively small, on the order of 0.1%. This is actually lower than the dispersion in the experimental data presented here. Second, in the analysis of *Matthies et al.* [2001a], the model ODF that was used showed a maximum of 18.3 m.r.d. (multiples of a random distribution). The ODF fitted to the data corresponding to this sample showed a maximum of 3.51 m.r.d., so the effect of preferred orientation will be even smaller. Therefore the application of the nonlinear regressions procedures that include the effect of preferred orientation on these data is difficult. We applied these techniques but were not successful in obtaining convergence of the numerical algorithms. The influence of lattice preferred orientation on the calculated single-crystal elastic moduli is important but cannot be quantitatively assessed with the present accuracy of data acquisition. Moreover, the imaging plate system used in the measurement of these data did show some signs of distortion that does not influence results that neglect the effect of lattice preferred orientation but would certainly influence the results of the methods that do include it. Therefore all the analysis presented here will not consider the effect of lattice preferred orientation and

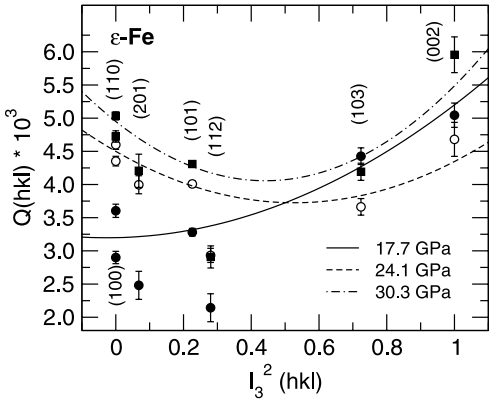

Figure 4. Amplitude of elastic strain $Q(hkl)$ versus $l_3^2(hkl)$ for ϵ-Fe at 17.7, 24.1, and 30.3 GPa. Lines are second-order polynomial fits to the data. Lattice strain theory without effects of lattice preferred orientation predicts a quadratic relation between $Q(hkl)$ and $l_3^2(hkl)$. Values of Q obtained for (201) and (112) systematically deviate from the rest of the data and are not included in the analysis (see text).

will be done using the theory described by *Singh et al.* [1998a].

3.3. Deduction of Elastic Moduli: Parametric Approach

[24] Figure 4 presents the parameters $Q(hkl)$ obtained by fitting equation (6) to the experimental data at 17.7, 24.1, and 30.3 GPa. According to the lattice strains theory of polycrystals under uniaxial stress without effect of preferred orientation, we should observe a quadratic relation between $Q(hkl)$ and l_3^2 (equations (7)–(10)). The results obtained for the (112) and (201) lattice planes showed a large systematic deviation from the rest of the data. However, those planes have a low d spacing and their diffraction lines where on the edge of the imaging plate we used. In that region, it could be seen from the calibration that there were some geometrical distortions that could not be corrected. Thus they were removed from the analysis. For the other planes the quadratic relation expected from the theory is observed to the first order. With increasing pressure, the shape of the parabola evolves considerably but it remains oriented in the same direction.

[25] In order to solve the equations from the lattice strain theory, one needs to constrain the compressibilities in direction a and c, χ_a and χ_c, respectively. We used the equation of state measured under hydrostatic conditions in our pressure range [*Jephcoat et al.*, 1986] with $K_0 = 166.6 \pm 27.9$ GPa, $K'_0 = 4.98 \pm 0.98$ and $c/a = 1.606(2) - 0.00012(3)P$. Inverting the lattice strains equations for single-crystal elastic moduli also requires the calibration of two other parameters: the uniaxial stress, $t = \sigma_1 - \sigma_3$, and the parameter α that specify the degree of stress and strain continuity within the sample.

[26] Figure 5 presents a parametric study of the elastic moduli calculated at 30.3 GPa for t between 0 and 10 GPa, $\alpha = 1.0$ (Reuss average) and $\alpha = 0.5$ (Hill average). The error bars are quite large especially for C_{12} and C_{33}. This is inherent to the technique. All elastic moduli show a linear dependence in t. However, it should be noted that the effect of t is more pronounced for the shear elastic moduli such as C_{44} and C_{66}. Therefore they would be primarily affected by an error in the calibration of t. Finally, except for C_{33}, the results for the Reuss or the Hill averages do not differ significantly.

[27] In order to provide an estimate of the effects of t and α on the elastic anisotropy deduced from the analysis,

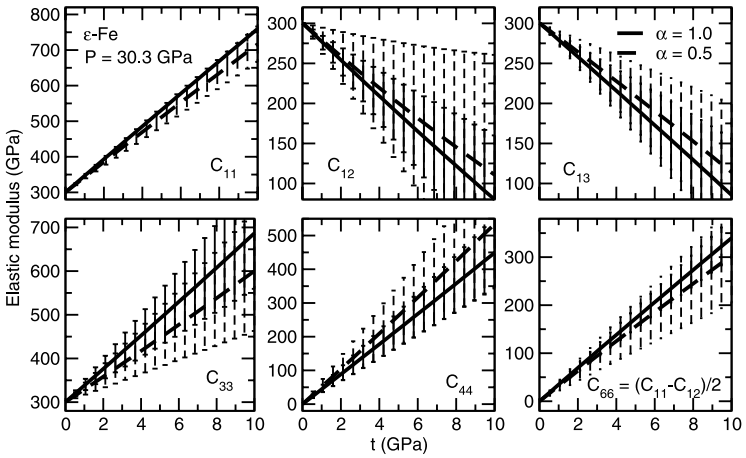

Figure 5. Parametric study on the results from the lattice strains equations for ϵ-Fe at 30.3 GPa with the uniaxial stress t varying between 0 and 10 GPa and for $\alpha = 1.0$ (Reuss bound, thick solid lines) and $\alpha = 0.5$ (Hill average, thick dashed lines). The thin solid and dashed lines are the error bars.

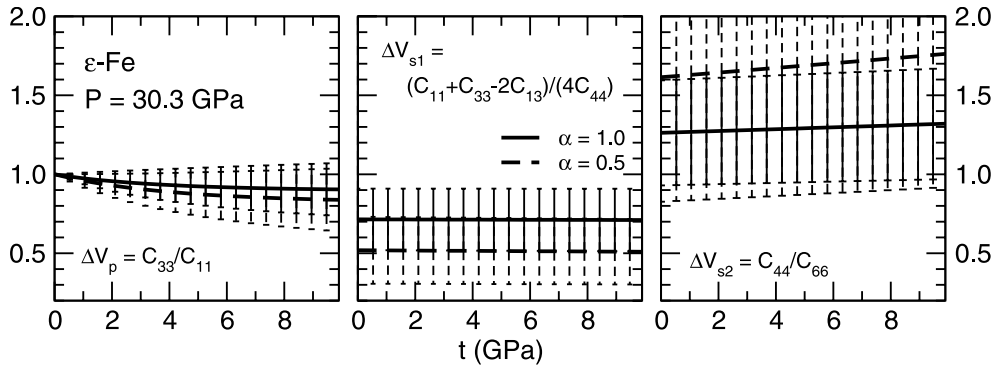

Figure 6. Parametric study of the results from the lattice strains equations for the anisotropy parameters of ϵ-Fe 30.3 GPa with the uniaxial stress t varying between 0 and 10 GPa and for $\alpha = 1.0$ (Reuss bound, thick solid lines) and $\alpha = 0.5$ (Hill average, thick dashed lines). The thin solid and dashed lines are the error bars.

Figure 6 presents the influence of t and α on the anisotropy parameters Δ_{VP}, Δ_{VS1}, and Δ_{VS2} defined as

$$\Delta_i = \frac{M_i[\mathbf{n}_x]}{M_i[100]}, \tag{17}$$

where $M = \rho V^2$ is a propagation modulus and $\mathbf{n}_x$ the extremal direction of propagation other than [100]. The index P relates to the compression wave, $S1$ to the shear wave polarized perpendicularly to the basal plane, and $S2$ to the shear wave polarized parallel to the basal plane. Δ_{VS1}, and Δ_{VS2} are good representations of the amplitude of the anisotropy for $S1$ and $S2$ waves. On the other hand, Δ_{VP} should be taken with caution as it only measures the differences between waves traveling along the a and c axis. P waves could also have extrema in an intermediary direction. We find that for our measurements, ΔV_P is almost independent of t and α. ΔV_{S1} does not depend on t and only weakly on α. ΔV_{S2} is more problematic, error bars are large and the cases with $\alpha = 1.0$ and $\alpha = 0.5$ are very different.

[28] The last step is to calibrate the value of the uniaxial stress. The use of a shear elastic modulus such as C_{44} or $C_{66} = \frac{1}{2}(C_{11} - C_{12})$ is preferable, as they vary considerably with t. In a typical nonhydrostatic diamond anvil cell experiment, errors in the calibration of stress using an external standard can be at best reduced to about 1 GPa. As shown in Figure 5, a 1 GPa error in the calibration of t will have dramatic effects on the estimation of elastic moduli, especially for low shear strength materials such as iron. This should therefore be treated with caution.

3.4. Constraints From Raman Spectroscopy

[29] Raman spectroscopy can be used to deduce one of the elastic moduli of iron, C_{44}. In a previous study, *Merkel et al.* [2000] measured the Raman spectrum of iron up to 150 GPa and used it to calculate C_{44}. A second-order linear regression on those results gives

$$C_{44} = 100.11 + 1.7198P - 0.0025104P^2, \tag{18}$$

where C_{44} and P are in GPa. The accuracy of the model depends on the assumption of a sine function for the dispersion curve of the appropriate acoustic phonon branch. It has been shown for a large number of metals for which both measurements are available that the error is on the order of ±15% [*Olijnyk et al.*, 2001]. Therefore, in the rest of this work, we will assume an error of ±20 GPa in C_{44} for the calibration of t. This error on C_{44} converts to an error of 0.3 to 0.5 GPa for t (Tables 1 and 2), and it was included in the rest of the analysis.

[30] Figure 7 shows the evolution of the uniaxial stress in ϵ-Fe with pressure deduced for $\alpha = 1.0$ and $\alpha = 0.5$. For all pressures, t remains between 2.5 and 3.5 GPa, in agreement with previous estimations [*Singh et al.*, 1998b]. Between 18 and 25 GPa, we observe a decrease of uniaxial stress, measured both in the sample and MgO, the pressure medium [*Merkel et al.*, 2002]. This is attributed to a

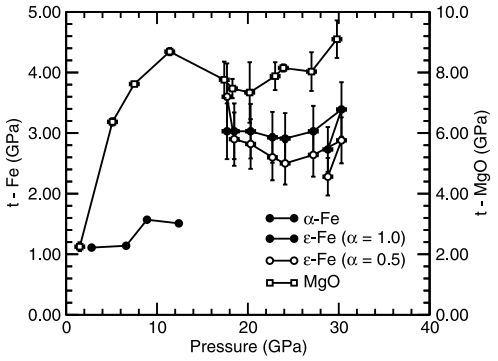

Figure 7. Uniaxial stress t in ϵ-Fe estimated using C_{44} from Raman spectroscopy for the Reuss bound ($\alpha = 1.0$) and the Hill average ($\alpha = 0.5$). For comparison, results obtained for the pressure medium, MgO, are also shown.

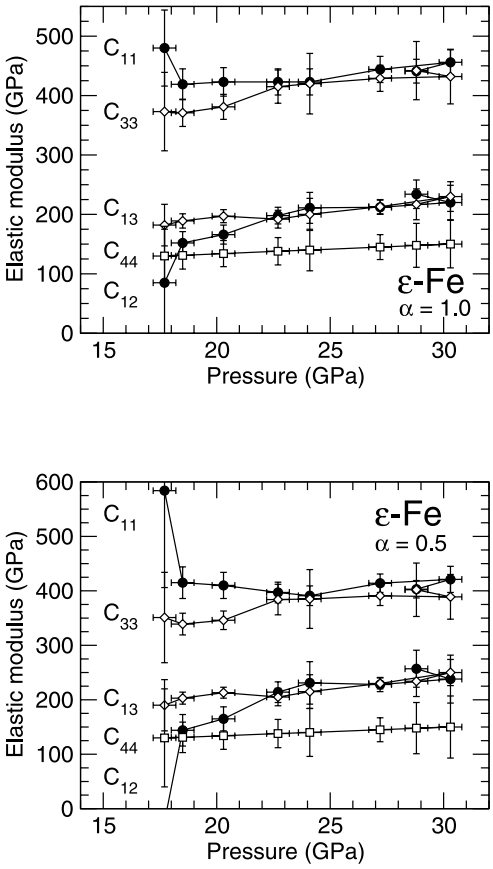

Figure 8. Elastic moduli obtained for the Reuss bound ($\alpha = 1.0$) and the Hill average ($\alpha = 0.5$) calibrating the uniaxial stress using C_{44} deduced from Raman spectroscopy.

rearrangement of the samples after the change of sample volume due to the transition from α- to ϵ-Fe.

[31] Figure 8 and Tables 1 and 2 present the sets of elastic moduli we obtain for $\alpha = 1.0$ and $\alpha = 0.5$ for all pressures in this study. At 17.7 GPa, just after the phase transition to the ϵ phase, the results show variability. This is probably related to the fact that the phase transition was not fully completed, although no evidence of α phase could be observed in the diffraction image. After the phase transition, we observe a very smooth evolution of the elastic moduli with pressure that support the self-consistency of the measurements.

4. Discussion

4.1. Elastic Moduli

[32] The reliability of the measurements of elastic moduli using radial X-ray diffraction has been subject to discussion in the literature. It has been shown in ambient pressure studies that elastic moduli obtained by X-ray diffraction for hexagonal metals can be in reasonable agreement with other techniques for polycrystals that do not suffer plastic deformation [*Matthies et al.*, 2001b]. For materials with cubic symmetry, there is also an overall good agreement between the results of X-ray diffraction and Brillouin scattering under pressure [*Merkel et al.*, 2002]. If the sample undergoes plastic deformation, new difficulties arise as microstrains induced by the deformation cannot be neglected. These result in inhomogeneities with *hkl*-dependent stress and strains that are not taken care of properly in the lattice strain analysis [*Daymond et al.*, 1999; *Weidner et al.*, 2004]. The iron samples in our experiments were confined within an MgO pressure medium. The texture measured for both samples indicate that the pressure medium MgO displayed a much higher level of lattice preferred orientation [*Merkel et al.*, 2002, 2004] and therefore absorbed a large portion of the plastic deformation. Therefore we infer that the plastic deformation applied to the iron sample was reasonably small (e.g., in comparison with previous experiments). However, we do not have any direct mean by which to investigate this hypothesis, and these approximations are likely to be the largest source of error in this analysis.

[33] A comparison with previous measurements on ϵ-Fe is not trivial. The pressures that have been studied range from 15 to 400 GPa and results can differ by a factor of two to three. Table 3 presents the elastic moduli obtained in this study, previous radial diffraction experiments [*Singh et al.*, 1998b; *Mao et al.*, 1998], as well as ab initio calculations [*Stixrude and Cohen*, 1995; *Söderlind et al.*, 1996; *Cohen et al.*, 1997; *Steinle-Neumann et al.*, 1999; *Vočadlo et al.*, 2003] in a similar pressure range. As emphasized in Table 3, the determination of the elastic moduli of iron under pressure is a delicate matter. Deviations between studies go up to 150% for C_{44}.

[34] There is a fairly good agreement on the order of magnitude of C_{12} and C_{13} for all techniques. For the C_{11} and C_{33} elastic moduli, values calculated using first-principles techniques tend to be significantly larger than those deduced from the lattice strain measurements at the same pressure. First-principles calculations are known to overestimate the incompressibility of iron for pressures below 50 GPa [*Stixrude et al.*, 1994; *Söderlind et al.*, 1996; *Steinle-Neumann et al.*, 1999]. It has been proposed that the disagreement is related to the magnetic properties of iron in the ϵ phase in the lower-pressure region of its stability field [*Steinle-Neumann et al.*, 2004]. C_{11} and C_{33} are the most relevant elastic moduli for the determination of incompressibility. Therefore the disagreement between the results from experimental studies and first-principles calculations for these elastic moduli are not surprising. First-principles calculations and the radial diffraction experiments agree on C_{12} and C_{13}, and the elastic moduli from the radial diffraction include the experimental compressibilities. Therefore we infer that the first-principles calculations overestimate C_{11} and C_{33}.

[35] The case of C_{44} remains difficult. In the previous radial diffraction studies, the uniaxial stress was calibrated using external standards or assumptions about the shear modulus of iron under pressure. As demonstrated in Figure 5, this can have dramatic effects on the estimation of C_{44}. The C_{44} deduced from Raman spectroscopy was found to be in

Table 3. Comparison Between Elastic Moduli and Seismic Wave Anisotropies Obtained in This Study for the Reuss ($\alpha = 1.0$) and Hill ($\alpha = 0.5$) Averages and Previous Experiments and Calculations in the Same Pressure Range[a]

	V	P	C_{11}	C_{12}	C_{13}	C_{33}	C_{44}	C_{66}	$\delta V_P(0°)$	$\delta V_P(45°)$	$\delta V_{S1}(45°)$	$\delta V_{S2}(0°)$
This study												
$\alpha = 1.0$	19.6	30	456(21)	220(29)	230(25)	432(46)	150(40)	118(21)	0.97(6)	1.03(5)	0.84(13)	1.13(17)
$\alpha = 0.5$	19.6	30	421(24)	238(44)	250(24)	389(41)	150(57)	91(33)	0.96(6)	1.06(7)	0.72(16)	1.28(30)
Singh et al. [1998b]												
$\alpha = 1.0$	18.4	52	639(55)	300(55)	254(41)	648(83)	422(23)	169	1.01(8)	1.17(6)	0.68(6)	1.58(19)
$\alpha = 0.5$	18.4	52	552(65)	335(60)	301(45)	562(80)	395(30)	108	1.01(9)	1.22(8)	0.57(8)	1.91(40)
Mao et al. [1998]	19.0	39	500	275	284	491	235	212	0.99	1.12	0.67	1.44
Stixrude and Cohen [1995]	18.38	39	747	301	297	802	215	223	1.04	1.00	1.05	0.98
Söderlind et al. [1996]	17.22	40	908	272	353	862	250	318	0.97	0.98	1.03	0.89
Cohen et al. [1997]		50	800	320	320	845	220	240	1.03	0.99	1.07	0.96
Steinle-Neumann et al. [1999]												
LDA	17.76	50	860	280	260	950	235	290	1.05	0.99	1.17	0.90
GGA	17.76	50	930	320	295	1010	260	305	1.04	0.98	1.14	0.92
Vočadlo et al. [2003]	18.34		672	189	264	796	210	242	1.09	1.03	1.05	0.93
Vočadlo et al. [2003]	17.34		815	252	341	926	247	282	1.07	1.02	1.03	0.94

[a]Radial diffraction measurements [*Singh et al.*, 1998b; *Mao et al.*, 1998] and first-principle [*Stixrude and Cohen*, 1995; *Söderlind et al.*, 1996; *Cohen et al.*, 1997; *Steinle-Neumann et al.*, 1999; *Vočadlo et al.*, 2003] were used. Elastic moduli and pressures are expressed in GPa, unit cell volumes are expressed in $Å^3$; numbers in parentheses indicate uncertainties on the last digit.

relatively good agreement with ultrasonic measurements for a series of other hcp metals [*Olijnyk et al.*, 2001]; therefore we are quite confident in the quality of our results.

4.2. Aggregate Properties

[36] Figure 9 presents the average shear modulus obtained from the present study as well as results of ultrasonic and previous radial diffraction measurements [*Mao et al.*, 1998], results of sound wave velocities deduced from X-ray inelastic scattering [*Fiquet et al.*, 2001] combined with the hydrostatic equation of state of iron [*Jephcoat et al.*, 1986], X-ray inelastic scattering measurements of the phonon densities of state [*Mao et al.*, 2001], results of Rietveld refinements based on high P-T X-ray diffraction measurements [*Dubrovinsky et al.*, 2001], and first-principles calculations [*Söderlind et al.*, 1996; *Cohen et al.*, 1997; *Steinle-Neumann et al.*, 1999].

[37] Above 18 GPa and for the Reuss approximation ($\alpha = 1.0$), the results from this study agree with the estimations from *Mao et al.* [1998, 2001] and *Dubrovinsky et al.* [2001]. They also follow the trend defined by the ultrasonic measurement at 16 GPa [*Mao et al.*, 1998]. Determinations based on sound wave velocities deduced from X-ray inelastic scattering [*Fiquet et al.*, 2001] and the hydrostatic equation of state of iron [*Jephcoat et al.*, 1986] fall slightly above the rest of the experimental data. This disagreement may originate from an incompatibility of the equation of state and velocities deduced from inelastic X-ray scattering (i.e., nonhydrostatic conditions of the later study). It could also arise from texturing effects in sample used in the inelastic X-ray scattering experiments that were not considered. All experimental results provide a much lower value of the shear modulus than first-principles calculations [*Söderlind et al.*, 1996; *Cohen et al.*, 1997; *Steinle-Neumann et al.*, 1999]. This can be related to the overestimation of the C_{11} and C_{33} elastic moduli discussed above.

4.3. Anisotropy

[38] Figure 10 presents the acoustic velocities of the compression wave (V_P), the shear wave polarized perpendicular to the basal plane (V_{S1}) and shear wave polarized in the basal plane (V_{S2}) as a function of the angle of the propagation direction with respect to the c axis, θ, deduced from these measurements at 30.3 GPa using the Reuss and Hill averages, as well as previous measurements using lattice strains techniques [*Singh et al.*, 1998b; *Mao et al.*, 1998] and first-principles calculations [*Stixrude and Cohen*, 1995; *Söderlind et al.*, 1996; *Cohen et al.*, 1997; *Steinle-Neumann et al.*, 1999; *Vočadlo et al.*, 2003]. In order to provide numerical comparisons, one has to consider the

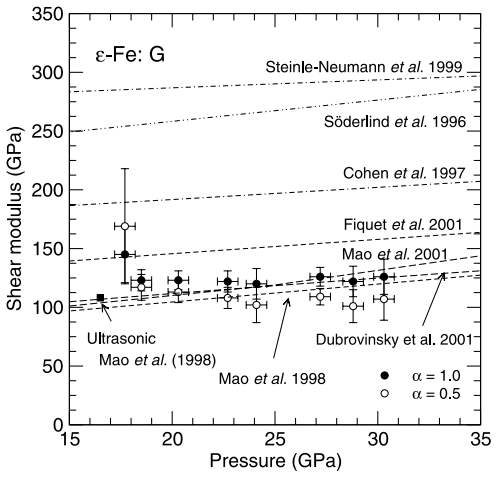

Figure 9. Aggregate shear modulus of ϵ-Fe versus P: results from this study, previous radial diffraction experiments [*Mao et al.*, 1998], ultrasonic measurement [*Mao et al.*, 1998], deduced from density of state measurements [*Mao et al.*, 2001], deduced from inelastic X-ray scattering [*Fiquet et al.*, 2001], high-pressure/high-temperature Rietveld refinement [*Dubrovinsky et al.*, 2001], and calculated by first-principles techniques [*Söderlind et al.*, 1996; *Cohen et al.*, 1997; *Steinle-Neumann et al.*, 1999].

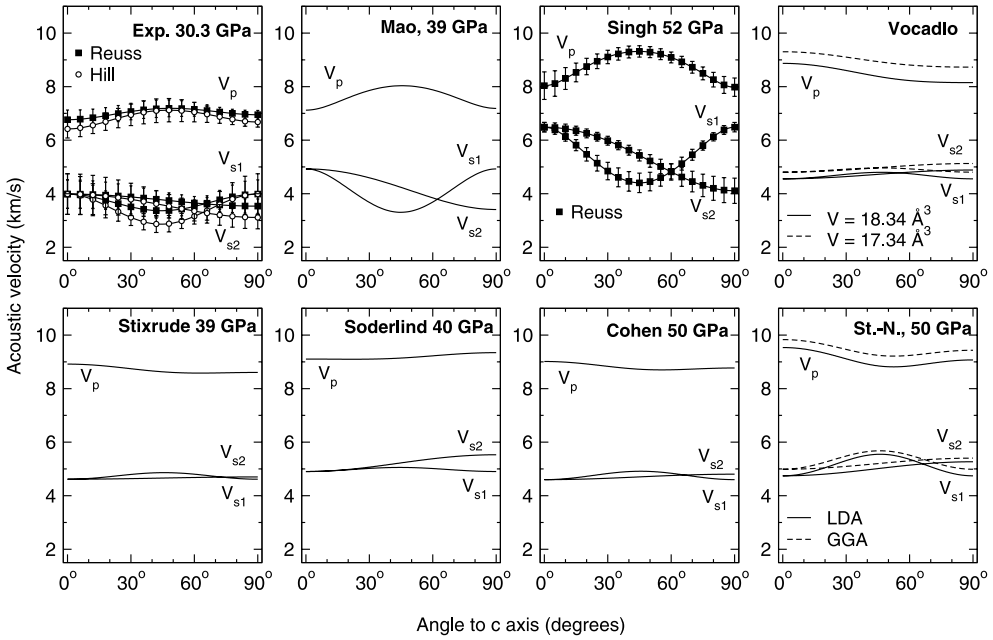

Figure 10. Seismic velocities of ϵ-Fe determined in this study at 30.3 GPa under the Reuss and Hill averages, other radial diffraction experiments [*Singh et al.*, 1998b; *Mao et al.*, 1998] and calculated using first-principles techniques [*Stixrude and Cohen*, 1995; *Söderlind et al.*, 1996; *Cohen et al.*, 1997; *Steinle-Neumann et al.*, 1999; *Vočadlo et al.*, 2003]. The *P* and *S* waves velocities are shown as a function of the angle of the direction of propagation with respect to the *c* axis. Errors are indicated, when available.

dispersion of V_P, V_{S1} and V_{S2} with θ. We introduce the parameter

$$\delta V_i(\theta) = \frac{V_i(\theta)}{V_i(90^\circ)}. \quad (19)$$

The parameter $\delta V_{S1}(45^\circ)$ is a good representation of the amplitude of the anisotropy of the *S*1 wave. Similarly, $\delta V_{S2}(0^\circ)$ can be used to discuss anisotropy of *S*2 waves. For the *P* waves however, the situation is more complex as extrema may occur for intermediate directions of propagation. According to the special dispersion of *P* waves velocities in Figure 10, we decided to represent the *P* wave anisotropy with the two parameters $\delta V_P(0^\circ)$ and $\delta V_P(45^\circ)$. Numerical results are provided in Table 3 for this experiment at 30.3 GPa, together with previous radial diffraction experiments [*Singh et al.*, 1998b; *Mao et al.*, 1998], and first-principles calculations [*Stixrude and Cohen*, 1995; *Söderlind et al.*, 1996; *Cohen et al.*, 1997; *Steinle-Neumann et al.*, 1999; *Vočadlo et al.*, 2003].

[39] The amplitude of the anisotropy obtained in this study under the Reuss bound is of the same order of magnitude than that of recent first-principles calculations [*Steinle-Neumann et al.*, 1999], e.g., 3–5% for $\delta V_P(0^\circ)$, 1–3% for $\delta V_P(45^\circ)$, 15% for $\delta V_{S1}(45^\circ)$ and 8–15% for $\delta V_{S2}(0^\circ)$. However, our uncertainties remain large and the results for the Reuss bound and Hill average differ significantly for $\delta V_{S1}(45^\circ)$ and $\delta V_{S2}(0^\circ)$.

[40] It should be noticed that all but one first-principles calculations predict $\delta V_P(45^\circ) < 1$, while all radial diffraction experiments indicate $\delta V_P(45^\circ) > 1$. Similarly, all first principles show $\delta V_{S1}(45^\circ) > 1$, while experimental results favor $\delta V_{S1}(45^\circ) < 1$. Again, $\delta V_{S2}(0^\circ) < 1$ from first-principles calculations, while $\delta V_{S2}(0^\circ) > 1$ in the experimental results. Appart from $\delta V_P(0^\circ)$, for which both experimental and theoretical calculations results vary, results from first-principles calculations and lattice strain experiments systematically provide opposite signs of anisotropy. For instance, radial diffraction experiments indicate a direction of fast polarization at $\theta = 0^\circ$ for V_{S2}, while first-principles calculations predict it at $\theta = 90^\circ$. For V_P, our results indicate that the fastest direction of propagation is located at $\theta \approx 48^\circ$ and we find $\delta V_P(48^\circ) = 1.03(5)$ for the Reuss bound and $\delta V_P(48^\circ) = 1.07(5)$ for the Hill average (an anisotropy of 3 to 7%). This is in complete agreement with recent results from inelastic X-ray scattering of textured samples that indicate that *P* waves in ϵ-Fe propagate faster by 4 to 5% at about 50° from the c axis than at 90° [*Antonangeli et al.*, 2004].

4.4. Implications for the Inner Core

[41] In considering the implications of these measurements for understanding the anisotropy of the inner core, we must emphasize that the range of pressures and temperatures

assessed in these experiments are far from those of the center of the Earth. However, we note that experimental results do differ from first-principles calculations: indeed, a fundamental understanding of iron under pressure may not yet be in hand and recent extensions of the theory need to be tested [*Steinle-Neumann et al.*, 2004]. Therefore the earlier results on elasticity and elastic anisotropy of iron under high pressure and high temperature should be treated with caution. In particular, a reversal of the anisotropy in compressed iron as a function of temperature is predicted [*Steinle-Neumann et al.*, 2001]. However, the calculated temperature dependence of the c/a ratio associated with this reversal is much larger that observed experimentally [*Ma et al.*, 2004] or predicted in other calculations [*Gannarelli et al.*, 2003].

[42] Our results indicate that the anisotropy of ϵ-Fe is lower than measured in previous radial diffraction experiments [*Singh et al.*, 1998b; *Mao et al.*, 1998]. Compared with first-principles calculations[*Stixrude and Cohen*, 1995; *Söderlind et al.*, 1996; *Cohen et al.*, 1997; *Steinle-Neumann et al.*, 1999; *Vočadlo et al.*, 2003], the locations of the directions of fast and slow polarization are systematically reversed. On the other hand, we find a good agreement with results from inelastic X-ray scattering of textured samples [*Antonangeli et al.*, 2004] with an anisotropy of 3 to 7% for P waves. This result is important for our understanding of the properties of the inner core as this measured anisotropy is comparable to that observed in the Earth (3–4%) [*Woodhouse et al.*, 1986; *Tromp*, 1993; *Song*, 1997].

5. Conclusions

[43] The elastic moduli of ϵ-Fe were determined up to 30.3 GPa using new angle dispersive radial X-ray diffraction measurements, as well as a calibration based on measurements of the hydrostatic equation of state and input from Raman spectroscopy. The resolution of the data was not sufficient to allow the inclusion of the effects of lattice preferred orientation. This approximation, as well as the neglect of the effects of plastic deformation on the stress and strain applied to each lattice planes are likely to introduce some errors in the inversion of elastic moduli. However, in the absence of additional measurements and theory, they cannot be evaluated. However, the iron sample in this experiment was confined in a pressure medium in order to limit plastic deformation and the level of texture was small. We obtain consistent values of elastic moduli up to 30.3 GPa. The average shear modulus G computed from this data is in very good agreement with a multitude of other experimental estimations. On the other hand, first-principles calculations are shown to overestimate by 100 to 200% the incompressibilities and shear modulus of iron over the same pressure range. This may arise from the neglect of the magnetic structure of iron under these conditions. The velocity anisotropy we obtain has the same order of magnitude than first principles calculations but the direction of fast and slow polarization are systematically reversed. The influence of assumptions used in the deduction of the C_{ij}, such as the micromechanical model, needs to be assessed in future works. Our results indicate that a proper calibration of the shear modulus of ϵ-Fe and its pressure dependence is now attained in the 15–50 GPa pressure range. The anisotropy parameters we calculate for P waves are in agreement with recent results from inelastic X-ray scattering of textured samples and are comparable to the anisotropy observed in the Earth. Further experiments are needed to investigate conditions closer to those of the center of the planet.

[44] **Acknowledgments.** The authors wish to thank E. Soignard and G. Shen for assistance with the experiment, S. Matthies for his input on the calculation of lattice preferred orientation effects, and S. Speziale for comments on the manuscript. Reviews by A. Kavner and an anonymous reviewer have significantly improved the manuscript. GeoSoilEnviroCARS is supported by the National Science Foundation Earth Sciences (EAR-0217473), Department of Energy Geosciences (DE-FG02-94ER14466) and the State of Illinois. Use of the APS was supported by the U.S. Department of Energy, Basic Energy Sciences, Office of Energy Research, under contract W-31-109-Eng-38. This work was also supported by the NSF (EAR-0409321 and EAR-0126009) and DOE/NNSA though the Carnegie/DOE Alliance Center (CDAC); grant DE-FC03-03NA00144.

References

Antonangeli, D., F. Occelli, H. Requardt, J. Badro, G. Fiquet, and M. Krisch (2004), Elastic anisotropy in textured hcp-iron to 112 GPa from sound wave propagation measurements, *Earth Planet. Sci. Lett.*, *225*, 243–251.

Bittorf, C., S. Matthies, H. G. Priesmeyer, and R. Wagner (1998), Diffractive determination of the thermo-elastic single crystal constants, *Intermetallics*, *7*, 1–8.

Bollenrath, F., V. Hauk, and E. H. Müller (1967), Zur berechnung der vielkristallinen elastizitätskonstanten aus den werten der einkristalle, *Z. Metall.*, *58*, 76–82.

Bose, S. K., O. V. Dolgov, J. Kortus, O. Jepsen, and O. K. Andersen (2003), Pressure dependence of electron-phonon coupling and superconductivity in hcp Fe: A linear response study, *Phys. Rev. B*, *67*, 214518.

Brown, J. M., and R. G. McQueen (1986), Phase transition, Grüneisen parameter, and elasticity for shocked iron between 77 GPa and 400 GPa, *J. Geophys. Res.*, *91*, 7485–7494.

Cohen, R. E., L. Stixrude, and E. Wasserman (1997), Tight-binding computations of elastic anisotropy of Fe, Xe, and Si under compression, *Phys. Rev. B*, *56*(14), 8575–8589.

Daymond, M., M. Bourke, and R. Von Dreele (1999), Use of Rietvelt refinement to fit hexagonal crystal structure in the presence of elastic and plastic anisotropy, *J. Appl. Phys.*, *85*, 739–747.

Dubrovinsky, L. S., N. A. Dubrovinskaia, and T. Le Bihan (2001), Aggregate sound velocities and acoustic Grüneisen parameter of iron up to 300 GPa and 1200 K, *Proc. Natl. Acad. Sci. U.S.A.*, *98*, 9484–9489.

Fiquet, G., J. Badro, F. Guyot, H. Requardt, and M. Krisch (2001), Sound velocities in iron to 100 gigapascals, *Science*, *291*, 468–471.

Gannarelli, C., D. Alfè, and M. Gillan (2003), The particle-in-cell model for ab initio thermodynamics: implications for the elastic anisotropy of the Earth's inner core, *Phys. Earth Panet. Inter.*, *139*, 243–253.

Gnäupel-Herold, T., P. C. Brand, and H. J. Prask (1998), The calculation of single crystal elastic constants for cubic crystal symmetry from powder diffraction data, *J. Appl. Crystallogr.*, *31*, 929–935.

Hemley, R. J., and H. K. Mao (2001), In situ studies of iron under pressure: New windows on the Earth's core, *Int. Geol. Rev.*, *43*, 1–30.

Howard, C. J., and E. H. Kisi (1999), Measurement of single-crystal elastic constants by neutron diffraction from polycrystals, *J. Appl. Crystallogr.*, *32*, 624–633.

Jarlborg, J. (2002), Ferromagnetic and antiferromagnetic spin fluctuations and superconductivity in the hcp-phase of Fe, *Phys. Lett. A*, *300*, 518–523.

Jephcoat, A. P., H. K. Mao, and P. M. Bell (1986), Static compression of iron to 78 GPa with rare gas solids as pressure-transmitting media, *J. Geophys. Res.*, *91*, 4677–4684.

Laio, A., S. Bernard, G. L. Chirotti, S. Scandolo, and E. Tosatti (2000), Physics of iron at Earth's core conditions, *Science*, *287*, 1027–1030.

Lübbers, R., H. F. Grünsteudel, A. I. Chumakov, and G. Wortmann (2000), Density of phonon states in iron at high pressure, *Science*, *287*, 1250–1253.

Ma, Y., M. Somayazulu, G. Shen, H. Mao, J. Shu, and R. Hemley (2004), In situ X-ray diffraction studies of iron to Earth-core conditions, *Phys. Earth Planet. Inter.*, *143–144*, 455–467.

Mao, H. K., Y. Wu, L. C. Chen, J. F. Shu, and A. P. Jephcoat (1990), Static compression of iron to 300 GPa and $Fe_{0.8}Ni_{0.2}$ alloy to 260 GPa: Implications for composition of the core, *J. Geophys. Res.*, *95*, 21,737–21,742.

Mao, H. K., J. Shu, G. Shen, R. J. Hemley, B. Li, and A. K. Singh (1998), Elasticity and rheology of iron above 220 GPa and the nature of the

Earth's inner core, *Nature*, *396*, 741–743. (Correction, Nature 399, 280, 1999.)
Mao, H. K., et al. (2001), Phonon density of state of iron up to 153 GPa, *Science*, *292*, 914–916.
Matthies, S., S. Merkel, H. R. Wenk, R. J. Hemley, and H. K. Mao (2001a), Effects of texture on the high pressure elasticity of iron from X-ray diffraction, *Earth Planet. Sci. Lett.*, *194*, 201–212.
Matthies, S., H. G. Priesmeyer, and M. R. Daymond (2001b), On the diffractive determination of single-crystal elastic constants using polycrystalline samples, *J. Appl. Crystallogr.*, *34*, 585–601.
Merkel, S., A. F. Goncharov, H. K. Mao, P. Gillet, and R. J. Hemley (2000), Raman spectroscopy of iron to 152 gigapascals: Implications for earth's inner core, *Science*, *288*, 1626–1629.
Merkel, S., H. R. Wenk, J. Shu, G. Shen, P. Gillet, H. Mao, and R. J. Hemley (2002), Deformation of polycrystalline MgO at pressures of the lower mantle, *J. Geophys. Res.*, *107*(B11), 2271, doi:10.1029/2001JB000920.
Merkel, S., H. R. Wenk, J. Badro, G. Montagnac, P. Gillet, H. K. Mao, and R. J. Hemley (2003), Deformation of $(Mg,Fe)SiO_3$ perovskite aggregates up to 32 GPa, *Earth Planet. Sci. Lett.*, *209*, 351–360.
Merkel, S., H. R. Wenk, P. Gillet, H. K. Mao, and R. J. Hemley (2004), Deformation of polycrystalline iron up to 30 GPa and 1000 K, *Phys. Earth Panet. Inter.*, *145*, 239–251.
Nguyen, J., and N. C. Holmes (1998), Iron sound velocities in shock waves experiments up to 400 GPa, *Eos Trans. AGU*, *79*(45), Fall Meet. Suppl., F846.
Nguyen, J., and N. Holmes (2004), Melting of iron at the physical conditions of the Earth's core, *Nature*, *427*, 339–342.
Olijnyk, H., A. P. Jephcoat, and K. Refson (2001), On optical phonons and elasticity in the hcp transition metals Fe, Ru and Re at high pressure, *Europhys. Lett.*, *53*, 504–510.
Singh, A. K., C. Balasingh, H. K. Mao, R. J. Hemley, and J. Shu (1998a), Analysis of lattice strains measured under non-hydrostatic pressure, *J. Appl. Phys.*, *83*, 7567–7575.
Singh, A. K., H. K. Mao, J. Shu, and R. J. Hemley (1998b), Estimation of single crystal elastic moduli from polycrystalline X-ray diffraction at high pressure: Applications to FeO and iron, *Phys. Rev. Lett.*, *80*, 2157–2160.
Söderlind, P., J. A. Moriarty, and J. M. Wills (1996), First-principles theory of iron to earth-core pressures: structural, vibrational and elastic properties, *Phys. Rev. B*, *53*, 14,063–14,072.
Song, X. (1997), Anisotropy of the Earth's inner core, *Rev. Geophys.*, *35*, 297–313.
Speziale, S., C. S. Zha, T. S. Duffy, R. J. Hemley, and H. K. Mao (2001), Quasi-hydrostatic compression of magnesium oxyde to 52 GPa: Implications for the pressure-volume-temperature equation of state, *J. Geophys. Res.*, *106*, 515–528.
Steinle-Neumann, G., L. Stixrude, and R. E. Cohen (1999), First-principles elastic constants for the hcp transition metals Fe, Co, and Re at high pressure, *Phys. Rev. B*, *60*(2), 791–799.
Steinle-Neumann, G., L. Stixrude, R. Cohen, and O. Gülseren (2001), Elasticity of iron at the temperature of the Earth's inner core, *Nature*, *413*, 57–60.
Steinle-Neumann, G., L. Stixrude, and R. Cohen (2004), Magnetism in dense hexagonal iron, *Proc. Natl. Acad. Sci. U.S.A.*, *101*, 33–36.
Stixrude, L., and R. E. Cohen (1995), High-pressure elasticity of iron and anisotropy of Earth's inner core, *Science*, *267*, 1972–1975.
Stixrude, L., R. E. Cohen, and D. J. Singh (1994), Iron at high pressure: Linearized-augmented-plane-wave computations in the generalized-gradient approximation, *Phys. Rev. B*, *50*, 6442–6445.
Thakor, V., J. Staunton, J. Poulter, S. Ostanin, B. Gintempo, and E. Bruno (2003), Ab initio calculations of incommensurate antiferromagnetic spin fluctuations in hcp iron under pressure, *Phys. Rev. B*, *67*(18), doi:10.1103/PhysRevB.67.180405.
Tromp, J. (1993), Support for anisotropy of the Earth's inner core from free oscillations, *Nature*, *366*, 678–681.
Vočadlo, L., D. Alfè, M. Gillan, and G. Price (2003), The properties of iron under core conditions from first principles calculations, *Phys. Earth Panet. Inter.*, *140*, 101–125.
Weidner, D., L. Li, M. Davis, and J. Chen (2004), Effect of plasticity on elastic modulus measurements, *Geophys. Res. Lett.*, *31*, L06621, doi:10.1029/2003GL019090.
Woodhouse, J. H., D. Giardini, and X. D. Li (1986), Evidence for inner core anisotropy from free oscillations, *Geophys. Res. Lett.*, *13*, 1549–1552.
Yoo, C. S., N. C. Holmes, M. Ross, D. J. Webb, and C. Pike (1993), Shock temperature, melting and phase diagram of iron at Earth core conditions, *Phys. Rev. Lett.*, *70*, 3931–3934.

P. Gillet, Laboratoire des sciences de la Terre, École normale supérieure de Lyon, 46 allée d'Italie, F-69364 Lyon Cedex 07, France.
R. J. Hemley, H.-K. Mao, and J. Shu, Geophysical Laboratory, Carnegie Institution of Washington, 5251 Broad Branch Rd., NW, Washington, DC 20015, USA.
S. Merkel, Department of Earth and Planetary Science, University of California, 307 McCone Hall, Berkeley, CA 94720-4767, USA. (smerkel@berkeley.edu)

Huitième partie

Articles : Travaux sur le cobalt

PHYSICAL REVIEW B **72**, 134303 (2005)

Aggregate and single-crystalline elasticity of hcp cobalt at high pressure

D. Antonangeli,[1,2] M. Krisch,[1] G. Fiquet,[3] J. Badro,[3,2] D. L. Farber,[2] A. Bossak,[1] and S. Merkel[4,*]
[1]*European Synchrotron Radiation Facility, Boîte Postale 220, F-38043 Grenoble Cedex, France*
[2]*Earth Science Division, Energy and Environment Directorate, Lawrence Livermore National Laboratory, 7000 East Avenue, Livermore, California 94550, USA*
[3]*Institut de Minéralogie et de Physique des Milieux Condensés, UMR CNRS 7590, Institut de Physique du Globe de Paris, Université Paris 6, 4 Place Jussieu, 75252 Paris Cedex 05, France*
[4]*Institute for Solid State Physics, University of Tokyo, Kashiwa, Chiba, Japan*
(Received 1 June 2005; revised manuscript received 4 August 2005; published 14 October 2005)

The longitudinal acoustic phonon dispersion of polycrystalline cobalt was determined by inelastic x-ray scattering up to 99 GPa, throughout the entire stability field of the hcp phase. The obtained aggregate compressional and shear sound velocities are compared with recent single crystal results, impulsive stimulated light scattering and ambient pressure ultrasonic measurements, as well as first principle calculations. We observe a linear evolution of the sound velocities with density up to 75 GPa. In this pressure range, the aggregate elastic properties of the polycrystalline sample are reproduced within 3% by a Voigt-Reuss-Hill average of the single crystal C_{ij}. Above 75 GPa both aggregate velocities show a softening. Our comparative analysis of single-crystalline and polycrystalline results points towards a magnetic origin of the anomaly.

DOI: 10.1103/PhysRevB.72.134303 PACS number(s): 63.20.−e, 62.50.+p, 62.20.Dc, 61.10.Eq

I. INTRODUCTION

The high-pressure properties of hexagonal-closed-packed (hcp) metals have recently attracted a lot of interest. These elements are indeed important model systems to test first principle calculations[1] and present intriguing properties such as, for example, the eventual existence of an electronic topological transition in zinc[2] and osmium,[3] or the interplay between magnetism and structure in the case of the bcc-to-hcp transition in iron.[4] A further important case is related to the elasticity of hcp iron, the main constituent of the Earth's core.[5,6] While nowadays the elastic anisotropy of the Earth's inner core is well established,[7,8] the origin of this anisotropy is still poorly understood, and the elasticity of hcp iron is still debated.[1,9–11]

Cobalt is a 3*d* transition metal with mechanical and thermal properties close to iron. Most importantly, athermal *ab initio* calculations[1] show that hcp Fe and hcp Co display a very similar pressure evolution of the elastic moduli and an analog elastic anisotropy. These theoretical results were recently validated by the direct measurements of the single-crystal elastic moduli of cobalt up to 39 GPa.[12] Moreover, Co presents a not-understood anomalous elastic behavior approaching the hcp-to-fcc structural transition,[13] possibly linked with high-pressure effects on the magnetic moment.[1,14] Magnetoelastic effects can than be investigated, complementing and extending the results obtained on single crystal[12] with results on polycrystalline sample, which can be more easily obtained at higher pressures, up to the structural transition.

At ambient conditions, cobalt is known to be ferromagnetic, existing in either the stable hcp phase or the metastable fcc phase. At high temperature, Co undergoes a phase transition around 695 K from the hcp to the fcc structure, and subsequently, via an isostructural transition, to a paramagnetic phase with a Curie temperature of 1400 K.[15] The temperature driven hcp-fcc transition exhibits no significant softening of most of the phonon branches, but only a decrease of about 27% in the C_{44} hexagonal shear constant[16] linked to the shear strain associated with the displacive martensitic transition.[17] Furthermore, no change in the magnetic moment occurs during the structural transition.[15,18]

At ambient temperature the hcp phase is stable up to 100 GPa, and then transforms martensitically to the fcc phase in the 105–150 GPa pressure range.[19] Density and compressibility considerations on one hand,[19] and first-principle calculations[15,19] on the other, suggest a nonmagnetic fcc phase, but there is to date no direct experimental evidence. Recent impulsive stimulated light scattering (ISLS) and Raman measurements[13] observed an anomalous density dependence of the aggregate elastic constants and of the E_{2g} mode Grüneisen parameter, at about 60 GPa, well below the phase transition. Magnetoelastic coupling and a collapse of the magnetic moment were suggested as possible causes for this behavior and *ab initio* calculations[1,14] support this scenario. However, further experimental work is needed to confirm these observations and, above all, to address the possible mechanisms responsible for the high-pressure elastic anomalies.

Here we present the experimental determination of the longitudinal acoustic phonon dispersion in polycrystalline cobalt up to 99 GPa obtained using inelastic x-ray scattering (IXS). We derived the aggregate compressional and shear sound velocities and analyzed our data in comparison with properly averaged single-crystal results, previously obtained by IXS.[12] This type of comparative study of aggregate and single-crystalline elasticity is essential in providing quantitative estimates for the various proposed mechanisms of the observed elastic anomaly, including texturing effects of polycrystalline hcp cobalt.

The paper is organized as follows: in Sec. II the IXS experiment is briefly described, while Sec. III is devoted to the presentation and discussion of the results. The polycrystalline results are compared to the single crystal averages and

the possible causes responsible for the high-pressure elastic anomalies are considered. Our main conclusions are summarized in Sec. IV.

II. EXPERIMENTAL DETAILS

We performed measurements on the IXS beamline II (ID28) at the European Synchrotron Radiation Facility in Grenoble, France. The instrument was operated in the Si(8,8,8) configuration, with an incident photon energy of 15.817 keV and a total instrumental energy resolution of 5.5 meV full width at half maximum (FWHM). The transverse dimensions of the focused x-ray beam of 25 $\times 60\ \mu m^2$ (horizontal $\times$ vertical, FWHM) were further reduced by slits at the highest pressures. The momentum transfer $Q=2k_i \sin(\theta_s/2)$, where k_i is the incident photon wave vector and θ_s is the scattering angle, was selected by rotating the spectrometer around a vertical axis passing through the scattering sample in the horizontal plane. The momentum resolution was set by slits in front of the analyzers to 0.25 nm^{-1}. Energy scans were performed by varying the monochromator temperature while the analyzer temperature was kept fixed. Conversion from the temperature scale to the energy scale was accomplished by the following relation: $\Delta E/E=\alpha\times\Delta T$, where $\alpha=2.58\times10^{-6}$ K^{-1} is the linear thermal expansion coefficient of silicon at room temperature.[20] The validity of this conversion was checked by comparing the experimentally determined energies of the longitudinal acoustic and optical phonons of diamond with well-established inelastic neutron and Raman scattering results.[21,22] Further experimental details can be found elsewhere.[23]

99.99% purity cobalt powder was loaded in a rhenium gasket and pressurized in a diamond anvil cell without pressure transmitting medium. The investigated pressure range (0–99 GPa) was covered in three runs, using different cells. The scattering geometry was the standard one, with the x-ray beam along the main compression axis of the cell through the diamonds, and the momentum transfer approximatively perpendicular to it.

III. RESULTS AND DISCUSSION

A. IXS spectra and phonon dispersions

Representative examples of the collected IXS spectra are reported in Fig. 1. The spectra are characterized by an elastic contribution, centered at zero energy, and inelastic contributions from cobalt and diamond. Because of their higher sound velocity, the transverse acoustic (TA) and longitudinal acoustic (LA) phonons of diamond are located at higher energies with respect to cobalt. The longitudinal acoustic phonon of cobalt is therefore unambiguously identified as the peak between the elastic line and the diamond phonons. In order to have a robust determination of the zero energy position, in each scan the full elastic line has been recorded. The energy position $E(Q)$ of the phonons were extracted by fitting a set of Lorentzian functions convolved with the experimental resolution function to the IXS spectra, utilizing a standard χ^2 minimization routine.

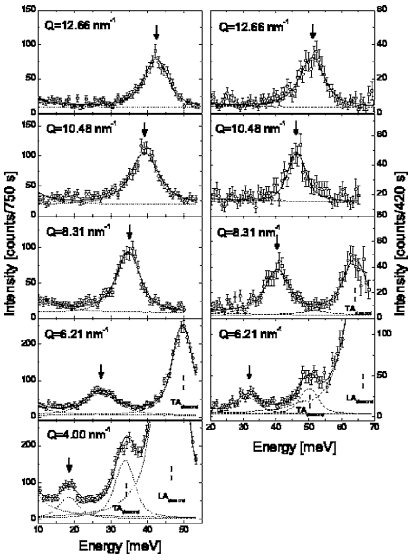

FIG. 1. Representative IXS spectra of polycrystalline hcp cobalt at 40 GPa (left panel) and 89 GPa (right panel) at the indicated momentum transfers Q. The experimental data are shown together with the best fit results (thick solid line) and the corresponding individual components (thin dotted line). For clarity only the inelastic peaks are shown. The arrows indicate the LA phonon of hcp Co, while the dashed marks point at the position of the LA and TA phonon of diamond, which are visible in the spectra at 4 and 6.21 nm^{-1} for $P=40$ GPa, and in the spectra at 6.21 nm^{-1} and 8.31 nm^{-1} for $P=89$ GPa. At 89 GPa the spectrum at 4 nm^{-1} is dominated by the very intense diamond phonons and the weak LA phonon of Co is not resolved.

Five to ten $E(Q)$ values were used to describe the LA phonon dispersions, which are reported, along with their best sine fit, in Fig. 2. For all pressures, the dispersion is very well described by a sine function, except for the highest pressure point (99 GPa), which is very close to the structural phase transition.

Within the framework of the Born–von Karman lattice-dynamics theory, and limiting us to the first term in the expansion (nearest neighbor interaction), the solution of the dynamical matrix can be written as[24]

$$E(\mathrm{meV}) = 4.192 \times 10^{-4} V_L(\mathrm{m/s}) Q_{max}(\mathrm{nm^{-1}}) \sin\left(\frac{\pi}{2}\frac{Q(\mathrm{nm^{-1}})}{Q_{max}(\mathrm{nm^{-1}})}\right), \quad (1)$$

where V_L is the compressional (longitudinal) sound velocity and Q_{max} is half the distance to the nearest reciprocal lattice point in the direction of Q. Values for V_L were consequently derived from the sine fit to the experimental dispersions, with Q_{max} left as a free parameter, while the shear (trans-

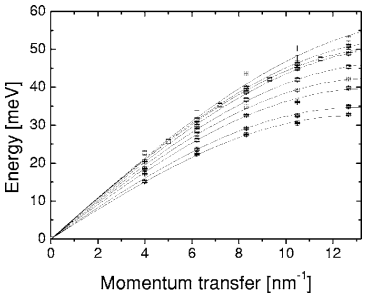

FIG. 2. *LA* phonon dispersion curves of polycrystalline hcp cobalt at ambient temperature and at pressures P =1.5,11,28,40,55,70,75,89,99 GPa (from bottom to top). The displayed error bars of the energy position result from the experimental uncertainties, the statistical error of the fit, and the finite-Q resolution of the spectrometer. The lines through the data points are sine fits to the data.

verse) sound velocity V_T was obtained according to the relation

$$V_T^2 = \frac{3}{4}\left(V_L^2 - \frac{K}{\rho}\right), \tag{2}$$

where ρ is the density and K is the bulk modulus.

In parallel to the IXS spectra, the [100], [002], and [101] cobalt reflections were recorded. A strong reduction of the [002] reflection was observed with increasing pressure, leading to its complete disappearance above 55 GPa. This behavior is expected for the utilized diffraction geometry, because of the development of preferential alignment. Indeed, radial x-ray diffraction measurements have shown that the c axis of the crystallites has the tendency to align along the compression axis of the cell.[25] These diffraction measurements allowed us the direct determination of the density with an accuracy of better than 1%, and to cross-check both the values of Q_{max} as well as the pressure, determined by the ruby fluorescence and according to both the hydrostatic[19] and the nonhydrostatic hcp-Co equation of state.[25]

B. Aggregate sound velocities

The derived compressional sound velocity is plotted as a function of density in the upper panel of Fig. 3, together with results from ISLS (Ref. 13) and ultrasonic (US) measurements (Voigt-Reuss-Hill average[26] of single-crystal elastic moduli[27]), as well as from calculations.[1,14] The compressional sound velocity scales linearly with density, as expected within the quasi-harmonic approximation, up to 11.28 g/cm^3↔75 GPa (solid line in Fig. 3). Above this value, approaching the martensitic hcp-to-fcc transition, a deviation from the linear behavior for $V_L(\rho)$ can be observed. This softening is also predicted in the same density region by the calculations, although theoretical values are systematically higher than the IXS ones. ISLS results show qualitatively the same trend as well, but the derived sound velocities are systematically lower than the IXS values, and lower than the ultrasonic results by ~5%, when back-extrapolated to ambient pressure.

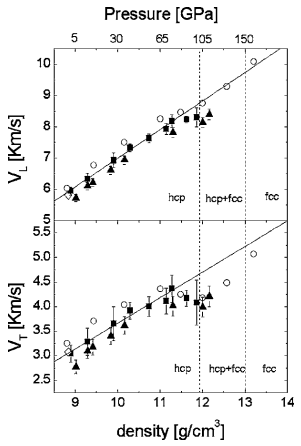

FIG. 3. Aggregate compressional (upper panel) and shear (lower panel) sound velocity of polycrystalline hcp cobalt as a function of density (the density errors are smaller than the symbols). The corresponding pressures are reported on the top axis. IXS results (full squares) and linear fit, taking into account data up to 11.28 g/cm^3 (75 GPa) (solid line); ambient pressure ultrasonic results (see Ref. 27; open diamond); *ab initio* calculations (see Ref. 14; open circles); ISLS measurements (see Ref. 13; solid triangles). The limits of the phase stability (Ref. 19) are indicated by dashed lines.

The IXS measurements of V_L have been combined with the nonhydrostatic hcp-cobalt equation of state,[25] in order to derive the density evolution of the shear velocity (the same values are also obtained using the hydrostatic equation of state[19]). The obtained V_T values are reported in the lower panel of Fig. 3 together with the results from calculations,[1,14] from ISLS (Ref. 13) and from US measurements (Voigt-Reuss-Hill average[26] of single-crystal results[27]). Due simply to the error propagation, the uncertainties in the IXS V_T are larger than for V_L. The linear evolution is, however, clearly visible up to 11.28 g/cm^3↔75 GPa, as well as the softening (even more pronounced than for V_L) above this value. Once again the IXS results compare well with ambient pressure ultrasonic data and lie in-between the calculations and the ISLS measurements, which are respectively slightly too high and too low. The ISLS extrapolation for V_T to ambient pressure is well below the US results (~13%).

The V_L and V_T values, obtained by the different experimental techniques and the calculations, are summarized in Table I.

These observations indicate a regular evolution of the sound velocities up to a pressure point (P_{max}), above which, both the compressional and the shear aggregate sound velocities exhibit a softening. The departure from the linear behavior was suggested by Goncharov *et al.*[13] to start at lower pressure (P_{max}~60 GPa↔~10.88 g/cm^3), in contrast to the present IXS measurements, which clearly place P_{max} above 75 GPa.

TABLE I. Aggregate compressional and shear sound velocities for different pressures (densities) measured by IXS, ultrasounds (Ref. 27), ISLS (Ref. 13), and obtained from first principle calculations (Ref. 14). For IXS experiments the density is directly measured and cross-checked with the values determined from the cobalt hydrostatic (Ref. 19) and nonhydrostatic equation of state (Ref. 25). For the ISLS experiments the density is derived from the measured pressure according to the cobalt hydrostatic (Ref. 19) and nonhydrostatic equation of state (Ref. 25).

		IXS		US		ISLS		Calculations	
P (GPa)	ρ (g/cm^3)	V_L (m/s)	V_T (m/s)	V_L (m/s)	V_T (m/s)	V_L (m/s)	V_T (m/s)	V_L (m/s)	V_T (m/s)
	8.807							6030	3250
0	8.836			5810	3080				
1.5	8.899	5950±120	3040±120						
4.3	9.018					5720±110	2770±140		
11	9.292	6330±190	3280±180			6100±120	3100±150		
14.3	9.417					6220±120	3170±160		
	9.435							6780	3710
26	9.838					6600±130	3400±170		
28	9.908	6930±240	3650±340						
	10.160							7500	4030
36	10.165					6930±140	3620±180		
40	10.294	7330±120	3920±170						
55	10.740	7630±140	4000±200						
	11.006							8250	4360
70	11.150	7930±180	4110±260						
75	11.279	8180±200	4370±280						
76	11.305					7810±160	4010±200		
	11.484							8460	4250
89	11.627	8230±110	4170±160						
99	11.867	8300±300	4080±460						
105	12.005					8130±160	3990±200	8750	4180
112	12.162					8390±170	4210±210		
	12.576							9290	4490
	13.204							10080	5070

C. Comparison with single crystal results

Aggregate elastic properties, such as the bulk modulus K and the shear modulus G can be derived from the single-crystal elastic tensor, when an appropriate averaging scheme is employed. The Voigt average[28] is based on the assumption of a uniform strain field, and for hexagonal symmetry gives

$$K_V = \frac{1}{9}(2C_{11} + C_{33}) + \frac{2}{9}(2C_{13} + C_{12}), \tag{3}$$

$$G_V = \frac{1}{15}(2C_{11} + C_{33}) - \frac{1}{15}(2C_{13} + C_{12}) + \frac{1}{5}(2C_{44} + C_{66}). \tag{4}$$

The Reuss average[29] is based instead on the assumption of a uniform stress field, and for hexagonal symmetry gives

$$K_R = \frac{C_{33}(C_{11} + C_{12}) - 2C_{13}^2}{C_{11} + C_{12} + 2C_{33} - 4C_{13}}, \tag{5}$$

$$G_R = \frac{15}{4A(C_{11} + C_{12}) + 8AC_{13} + \frac{6}{C_{44}} + \frac{6}{C_{66}} + 2AC_{33}}, \tag{6}$$

with

$$\frac{1}{A} = C_{33}(C_{11} + C_{12}) - 2C_{13}^2. \tag{7}$$

Both averaging procedures ignore grain interactions, and are therefore quite crude approximations. They provide, however, rigorous bounds for the aggregate properties of a randomly oriented, macroscopically isotropic aggregate of crystals: it can be shown that the Voigt average is the lowest upper bound, while the Reuss average is the highest lower bound.[26] For isotropic crystals the two coincide. An empirical estimation currently used is the arithmetic mean of the two, the so-called Voigt-Reuss-Hill average. The aggregate velocities can then be calculated from K, G, and the density ρ according to

$$V_L^2 = \frac{1}{\rho}\left(K + \frac{4}{3}G\right) \tag{8}$$

$$V_T^2 = \frac{G}{\rho}. \tag{9}$$

In order to compare the IXS results obtained on powders with the ones obtained on single crystal,[12] the latter need to be extrapolated up to 99 GPa. Five independent acoustic phonon branches were used to determine the single-crystal elastic moduli C_{ij} to 39 GPa.[12] For the extrapolation we used two different approaches. In the first case we linearly extrapolated the velocity vs density data for each mode[31] and then solved the Christoffel equations[30] to derive the elastic moduli. Alternatively, the estimated[12] linear pressure evolutions of the C_{ij} is used. The results obtained by these two procedures differ by about 3% at 99 GPa and even less at lower pressures, except for C_{13}, where the difference starts to be significant already at 50 GPa, and is about 20% at 99 GPa. However, the two extrapolations yield results for the aggregate bulk and shear moduli within 1% below 50 GPa and within 2% at 99 GPa. In the following, we will consider the arithmetic average of the values obtained by these two procedures for the various C_{ij}.

The bulk modulus, the shear modulus and the aggregate compressional and shear sound velocities were computed according to the Voigt, Reuss, and Voigt-Reuss-Hill average. Voigt and Reuss determinations differ by only 1% at 99 GPa and even less at lower pressures. Thus, the single-crystal anisotropy is only very weakly reflected in the effective elastic anisotropy of the aggregate, when a completely random distribution of crystallites is considered.

The density evolution of the aggregate compressional[32] sound velocity is illustrated in Fig. 4, where the IXS results obtained on powders are reported together with the ambient pressure ultrasonic determination[27] and the Voigt-Reuss-Hill average of the single-crystal elastic moduli.[12] Despite a different slope, the two IXS data sets up to 75 GPa differ by less than 3%, thus testifying that a simple, randomly oriented distribution describes quite well the elastic properties of the polycrystal under compression. Moreover, according to this observation, a regular behavior of the various C_{ij} with increasing pressure is expected above the directly investigated pressure range (0–39 GPa),[12] likely up to 75 GPa.

Above 75 GPa the discrepancy between the polycrystalline and the single-crystal averaged results starts to be significant. The observed deviation from linearity in $V_L(\rho)$ and $V_T(\rho)$ could be considered as a precursor effect of the martensitic hcp-to-fcc structural transition, which manifests itself by an important softening of one or more elastic moduli. Such transition in cobalt can be induced both by pressure and temperature.[19] For the temperature-induced hcp-to-fcc transition, a softening of C_{44} by about 27% in the close vicinity of the transition was observed, while the other elastic moduli remained unaffected.[16] If the same amount of softening of C_{44} is applied to the present pressure-induced case, for the two highest pressure points (89 and 99 GPa), we can recompute the averaged V_L, and the resulting values are lower by about 1.5%, whereas the IXS experiments on the polycrystalline sample display a difference from the linear extrapolation by about 3% and 4.5% (89 GPa and 99 GPa, respectively). Moreover, in the present case, the nonlinear density dependence was observed well before the transition. These considerations, together with the proposed simple estimation, suggest that the observed anomaly in V_L is not likely due to the shear strain associated with the hcp-to-fcc transition, as in the temperature-driven case.[17]

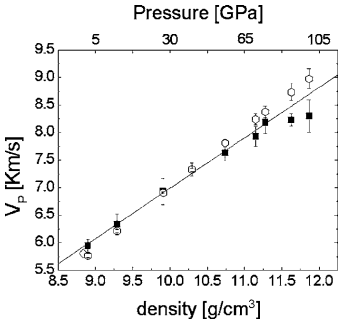

FIG. 4. Aggregate compressional sound velocity V_L of hcp cobalt as a function of density (the corresponding pressure values are indicated in the top axis). Errors on density are smaller than the symbols. Squares: IXS results obtained on powders; open diamonds: ambient pressure ultrasonic results (Ref. 27); open hexagons: Voigt-Reuss-Hill average of single crystal elastic moduli, obtained by IXS (Ref. 12) and extrapolated to 99 GPa. The solid line is an extrapolated linear fit to the powder data below 11.28 g/cm^3 (75 GPa).

Ab initio calculations[14] predict a departure from linearity in the same density region as the experimental IXS observations (see Fig. 3). The proposed mechanism is a reduction of the magnetic moment, concomitant with an evident softening of C_{44} and C_{66}. In order to compare these theoretical findings with the IXS results, the theoretical C_{ij} were scaled to the experimentally determined ones (IXS single-crystal results). The thus-obtained C_{ij} exhibit an important softening of C_{44}, a moderate hardening of C_{13}, and a slight softening of all the elastic moduli at pressure of about 85 GPa (ρ=11.48 g/cm^3,57.5 bohrs^3). The aggregate V_L, once recalculated using the Voigt-Reuss-Hill average, then shows a reduction of about 2.5%. The so-obtained anomaly in the elastic moduli thus reproduces quite well our experimentally determined trend (3% softening at 89 GPa).

The good agreement between the extrapolated single crystal aggregate averages and our polycrystalline measurements suggest that the effects of texture in our samples are minimal. However, as there exist experimental data on the textural evolution in polycrystalline Co, we quantitatively treat these effects below. Recent radial x-ray diffraction measurements (RXRD) on quasiuniaxially compressed polycrystalline cobalt reveal an alignment of the *c* axis of the crystallites along the compression axis of the cell, with a cylindrical

symmetry.[25] Most of this texture is developed within the first 5 GPa and up to the highest investigated pressure of 42 GPa, the increasing stress essentially modifies the degree of alignment, not the symmetry. At the highest investigated pressure the maximum pole density is 3.17 multiples of a random distribution. On the basis of these results we can recompute the properly weighted orientationally averaged V_L. The aggregate V_L values, corrected for these texture effects as well as the scattering geometry (momentum transfer perpendicular to the compression axis of the cell) differ from the Voigt-Reuss-Hill average (random distribution) by about 0.3% at 1.5 GPa and about 1% at 40 GPa, yielding slightly lower sound speeds.

According to the observation that most of the texture was already developed at 5 GPa, we can assume that the experimentally determined texture at 42 GPa is only very weakly dependent on pressure, and incorporate the effects of preferential orientation in the averaging process at 85 GPa, together with the theoretically estimated magnetoelastic effects. The resulting V_L exhibits a reduced softening of about 1.8%, as a consequence of the different weights of the various C_{ij}'s. According to this estimation, the texture developed by polycrystalline cobalt under nonhydrostatic compression, tends to reduce the aggregate elastic anomalies induced by the softening of the magnetic moment, and, since a further very strong evolution of the texture at high pressure is unlikely, cannot be considered the main cause responsible for the observed high-pressure anomalies in V_L and V_T.

IV. CONCLUSIONS

We have measured the aggregate longitudinal phonon dispersion of hcp cobalt up to 99 GPa, over the entire stability range of the hcp phase. The derived compressional and shear sound velocities exhibit a linear evolution with density up to 11.28 $g/cm^3 \leftrightarrow 75$ GPa. Above, a significant deviation from linearity is observed on approaching the hcp-to-fcc phase transition. Our IXS results were compared with the average velocities derived from the single-crystal elastic tensor,[12] with high-pressure ISLS (Ref. 13) and ambient pressure ultrasonic measurements,[27] and with *ab initio* calculations.[1,14] Our IXS data are in good agreement with the US results. This is in contrast to the ISLS data, especially for V_T, where the difference between the ISLS and US results is about 13%.

We suggest that the single-crystal elastic moduli vary linearly with pressure to 75 GPa. In this pressure range, the aggregate elastic properties of the polycrystalline sample are reproduced within 3% by a Voigt-Reuss-Hill average of the single crystal C_{ij},[12] indicating that a simple, macroscopically isotropic, randomly oriented distribution, already provides a quite good general description of cobalt powder. When the effects of texture are considered, V_L changes in the 0–40 GPa range, at the most by 1%, slightly improving the agreement between the IXS powder and the properly averaged single-crystal results.

Above 75 GPa the IXS measurements show a softening of the aggregate velocities, in agreement with calculations. The same trend is also reproduced by ISLS measurements, although the departure from linearity was proposed to start at lower pressure. The comparison of polycrystalline and single-crystal IXS results with theoretical calculations allows us to provide quantitative estimates for the various proposed mechanism of this elastic anomaly. A precursor effect of the martensitic hcp-to-fcc phase transition—as for the temperature-driven transition to the fcc phase—seems unlikely, since the corresponding reduction of C_{44} by 27% (Ref. 16) is not enough to explain the IXS results. Furthermore, this softening occurs only in a narrow temperature range, very close to the phase transition, while in the present high-pressure experiment, the softening is already observed well below the transition pressure. A magnetoelastic effect, associated with a reduction of the magnetic moment, as suggested by Goncharov *et al.*[13] and supported by calculations,[1,14] appears to be the driving mechanism. The deviation from linearity in $V_L(\rho)$ is indeed qualitatively reproduced by our estimate on the basis of the extrapolation of the experimental C_{ij}. The remaining quantitative discrepancy could be explained by thermal correction to the athermal calculations.

A scenario analogous to the one recently proposed for the bcc-to-hcp transition in iron,[4] characterized by a magnetic transition preceding the structural one, can be envisaged. Thus, the origin of the instability of the hcp Co with increasing pressure can be ascribed to the effect of pressure on the magnetic moment. A direct experimental determination of the pressure evolution of the magnetic moment is, however, highly recommended to confirm this hypothesis.

ACKNOWLEDGMENTS

D. Gambetti and D. Gibson are acknowledged for their technical assistance. The authors wish to thank M. Hanfland for the use of the high-pressure laboratory and for unscheduled diffraction measurements. We highly appreciated the discussions with F. Guyot.

*Present address: Department of Earth and Planetary Science, University of California, Berkeley, CA, 94720.

[1] G. Steinle-Neumann, L. Stixrude, and R. E. Cohen, Phys. Rev. B **60**, 791 (1999); **69**, 219903(E) (2004).

[2] S. Klotz, M. Braden, and J. M. Besson, Phys. Rev. Lett. **81**, 1239 (1998).

[3] F. Occelli, D. L. Farber, J. Badro, C. M. Aracne, D. M. Teter, M. Hanfland, B. Canny, and B. Couzinet, Phys. Rev. Lett. **93**, 109901(E) (2004).

[4] O. Mathon, F. Baudelet, J. P. Itié, A. Polian, M. d'Astuto, J. C. Chervin, and S. Pascarelli, Phys. Rev. Lett. **93**, 255503 (2004).

[5] F. Birch, J. Geophys. Res. **57**, 227 (1952).

[6] A. Jephcoat and P. Olson, Nature **325**, 332 (1987).
[7] J. H. Woodhouse, D. Giardini, and X. D. Li, Geophys. Res. Lett. **13**, 1549 (1986).
[8] K. G. Creager, Nature **356**, 309 (1992).
[9] L. Stixrude and R. E. Cohen, Science **267**, 1972 (1995).
[10] H. K. Mao, J. Shu, G. Shen, R. J. Hemley, B. Li, and A. K. Singh, Nature **396**, 741 (1998); correction, **399**, 280 (1999).
[11] D. Antonangeli, F. Occelli, H. Requardt, J. Badro, G. Fiquet, and M. Krisch, Earth Planet. Sci. Lett. **225**, 243 (2004).
[12] D. Antonangeli, M. Krisch, G. Fiquet, D. L. Farber, C. M. Aracne, J. Badro, F. Occelli, and H. Requardt, Phys. Rev. Lett. **93**, 215505 (2004).
[13] A. F. Goncharov, J. Crowhurst, and J. M. Zaug, Phys. Rev. Lett. **92**, 115502 (2004).
[14] G. Steinle-Neumann (private communication).
[15] C. S. Yoo, P. Söderlind, and H. Cynn, J. Phys.: Condens. Matter **10**, L311 (1998).
[16] B. Strauss, F. Frey, W. Petry, J. Trampenau, K. Nicolaus, S. M. Shapiro, and J. Bossy, Phys. Rev. B **54**, 6035 (1996).
[17] P. Toledano, G. Krexner, M. Prem, H.-P. Weber, and V. P. Dmitriev, Phys. Rev. B **64**, 144104 (2001).
[18] P. Lazor, Ph.D. thesis, Uppsala University, 1994.
[19] C. S. Yoo, H. Cynn, P. Söderlind, and V. Iota, Phys. Rev. Lett. **84**, 4132 (2000).
[20] A. Bergamin, G. Cavagnero, and G. Mana, J. Appl. Phys. **82**, 5396 (1997).
[21] J. Kulda, H. Kainzmaier, D. Strauch, B. Dorner, M. Lorenzen, and M. Krisch, Phys. Rev. B **66**, 241202(R) (2002).
[22] R. Verbeni (private communication).
[23] M. Krisch, J. Raman Spectrosc. **34**, 628 (2003).
[24] N. W. Ashcroft and N. D. Mermin, *Solid State Physics* (Saunders College Publishing, USA, 1976).
[25] S. Merkel, N. Miyajima, and T. Yagi (unpublished).
[26] R. Hill, Proc. Phys. Soc., London, Sect. A **65**, 349 (1952).
[27] H. R. Schober and H. Dederichs, *Elastic, Piezoelectric, Pyroelectric, Piezooptic, Electrooptic Constants and Nonlinear Dielectric Susceptibilities of Crystals*, edited by Landolt-Börnstedt, New Series III, (Springer, Berlin, 1979), Vol. 11a.
[28] W. Voigt, *Lehrbuch der Kristallphysik* (Teubner, Leipzig, 1928).
[29] A. Reuss, Z. Angew. Math. Mech. **9**, 55 (1929).
[30] B. A. Auld, *Acoustic Fields and Waves in Solids* (John Wiley & Sons, New York, 1973), Vol. 1.
[31] We recall that within the frame of the quasiharmonic approximation, sound velocities are supposed to scale linearly with density.
[32] In the following, only V_L will be considered, since it is directly determined, with a higher precision than V_T.

Available online at www.sciencedirect.com
ScienceDirect
Journal of Physics and Chemistry of Solids 67 (2006) 2119–2131
JOURNAL OF PHYSICS AND CHEMISTRY OF SOLIDS
www.elsevier.com/locate/jpcs

Effect of lattice preferred orientation on lattice strains in polycrystalline materials deformed under high pressure: Application to hcp-Co

Sébastien Merkel*, Takehiko Yagi

Institute for Solid State Physics, University of Tokyo, Kashiwa, Chiba 277-8581, Japan

Received 1 June 2005; received in revised form 13 December 2005; accepted 20 December 2005

Abstract

The present paper readdresses the issue of stress and strain analysis for hcp-metals plastically deformed under high pressure in the diamond anvil cell with an application to cobalt at 42 GPa. The effective single crystal elastic moduli deduced from radial X-ray diffraction under Reuss or geometric averages, including effects of lattice preferred orientations, and assuming a constant stress within the sample, consistently differ from those measured with other technique with the largest deviations observed on C_{44}. These results are then interpreted as an (hkl)-dependent effective differential stress.

Keywords: A. Metals; C. High pressure; C. X-ray diffraction; D. Elastic properties; D. Microstructure

1. Introduction

The interpretation of the X-ray or neutron diffraction patterns measured from a polycrystal under stress has been a long standing issue in high-pressure research and other areas of material science. The presence of non-hydrostatic stress in a polycrystalline sample introduces distortions of the crystal lattices that can be observed using X-ray diffraction. A first application of this phenomenon is the residual stress analysis [1] in which the components of the mean macroscopic stress in a sample are determined using (a) known single crystal elastic moduli, (b) measured d-spacings in several directions, (c) information on the structure and texture of the sample, and (d) a micro-mechanical model that combines the orientation-dependent individual strains and stresses and the interacting grains of the polycrystalline sample with the measured d-spacings. In the inverse problem, single crystal elastic moduli are inverted using the measured d-spacings, structure/texture information, a micromechanical model, and known mean macroscopic stresses applied to the sample [2,3].

Measurement of single crystal elastic moduli under high pressure is a difficult task and the deduction of elastic moduli from X-ray diffraction offers two advantages: (i) it can be performed over the whole range of pressure attainable with diamond anvil cells (DAC); (ii) it does not require single-crystals, but polycrystals which are much easier to synthesize. This motivated a number of studies published in the last few years [4–10]. However, difficulties were noted very early on as effects of lattice preferred orientations (LPO) and plasticity were not treated properly in lattice strains theories and this raised significant controversy [11].

In this paper, we readdress the issue of stress and strain analysis for hcp-metals deformed under high pressure in the DAC. Understanding the behavior of hcp-metals plastically deformed under high pressure is fundamental not only for material science, but also deep Earth geophysics as the high-pressure hcp phase of Fe (ε-Fe) is believed to be the main constituent of the Earth's inner core. It was also shown the single crystal elastic moduli of ε-Fe deduced from radial X-ray diffraction could vary significantly [4,5,10,12].

*Corresponding author. Present address: Laboratoire de Structure et Proprietes de l'Etat Solide, UMR CNRS 8008, Batiment C6, 59655 Villeneuve d'Ascq, France. Tel.: +33 320 43 46 86; fax: 33 320 43 65 91.
E-mail address: sebastien.merkel@univ-lille1.fr (S. Merkel).

0022-3697/$ - see front matter © 2006 Elsevier Ltd. All rights reserved.
doi:10.1016/j.jpcs.2006.05.025

Here, we present results on another hcp-metal, hcp-Co, which is located next to iron in the periodic table. The mechanical properties of Fe and Co are close, and ab initio calculations suggest that the behavior of hcp-Fe and hcp-Co under pressure is similar. Moreover, the high-pressure behavior of hcp-Co has been studied extensively [13–15] and its single crystals elastic moduli have been calculated under the GGA approximation [16], deduced from Raman spectroscopy [17], and measured using inelastic X-ray scattering (IXS) [18] up to high pressures. There is a very good agreement between results from all of those techniques. The elastic moduli of hcp-Co are, therefore, very well constrained and this material is a perfect candidate for testing high-pressure stress and strain analysis in hcp-metals with X-ray diffraction.

The first section of this paper will summarize current theories for the modelling of the diffraction of polycrystals under stress. The second section of the paper will focus on the stress and strain conditions in diamond anvil cell experiments, with a simulation of experimental results predicted by lattice strain theories. Finally, the third and final sections will be devoted to the application to experimental data.

2. Diffraction of a polycrystal under stress

Theories relating measured d-spacings using X-ray diffraction to stress, elastic moduli, and LPO have been developed independently by several groups [1,3,12,19–21]. In order to solve these equations, several approximations have to be made, such as the absence of LPO within the sample, or assume that all subpopulations of grains are submitted to the same macroscopic stress.

The solution of these equations is complex and will only be summarized briefly. In this analysis, we will rely on the currently most advanced approach that includes the effect of LPO [21] but also that of Singh et al. [3] that assumes a random distribution of the crystallites and is widely used in high-pressure research.

2.1. Coordinate systems

In order to solve the lattice strains equations, several coordinate systems need to be defined (Fig. 1). The 'laboratory coordinate system' K_L is imposed by the geometry of the experiment with $\mathbf{Z}_L$ parallel to the scattering vector $\mathbf{y}$ (bisector between the incoming and diffracted X-ray beam collected by the detector) and $\mathbf{X}_L$ inside the plane containing the incident and diffracted X-ray beam and pointing towards the side of the detector. The sample coordinate system K_S is defined by the environment around the sample. The crystal coordinate system K_C is defined for each crystallite according to the crystal structure.

Microscopic physical relations, such as Hooke's law relating the microscopic stresses, strains and single crystal elastic moduli should be applied in each crystallite coordinate system K_C. On the other hand, macroscopic properties such as polycrystalline texture or macroscopic stress are expressed in the sample coordinate system K_S. Quantities related to diffraction, such as measured d-spacings or diffraction intensities are to be studied in the laboratory coordinate system K_L.

In our high pressure experiments, the sample is submitted to a uniaxial compression within a diamond anvil cell (Fig. 2) and we perform X-ray diffraction with the incoming beam orthogonal to the compression direction. This defines the sample coordinate system K_S with $\mathbf{Z}_S$ parallel to the compression direction and $\mathbf{Y}_S$ parallel to the incoming X-ray beam and pointing towards the detector. In this coordinate system, directions can be represented with the two Euler angles α and β.

Location of the laboratory coordinate system K_L is not unique and depends on the diffraction peak under consideration as well the as azimuth angle on the imaging plate (Fig. 2). Similarly, crystallite coordinate systems K_C should be chosen according to the crystallite under consideration.

2.2. Texture and LPO

The texture in the sample can be represented by the orientation distribution function (ODF). The ODF is required to estimate anisotropic physical properties of polycrystals such as elasticity or electrical conductivity [22]. It is a probability function for finding an orientation and it is normalized such that the integral over the whole

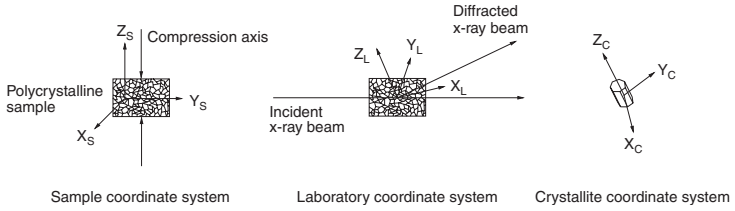

Fig. 1. Coordinate systems used in the analysis. The sample coordinate system K_S is defined by the sample environment, with $\mathbf{Z}_S$ parallel to the deformation direction. The laboratory coordinate system K_L is defined with $\mathbf{Z}_L$ parallel to the bisector between the incoming and diffracted beam and $\mathbf{X}_L$ in the plane containing the incoming and diffracted beam, pointing towards the detector. The crystallite coordinate sample K_C is defined according to the crystallographic structure.

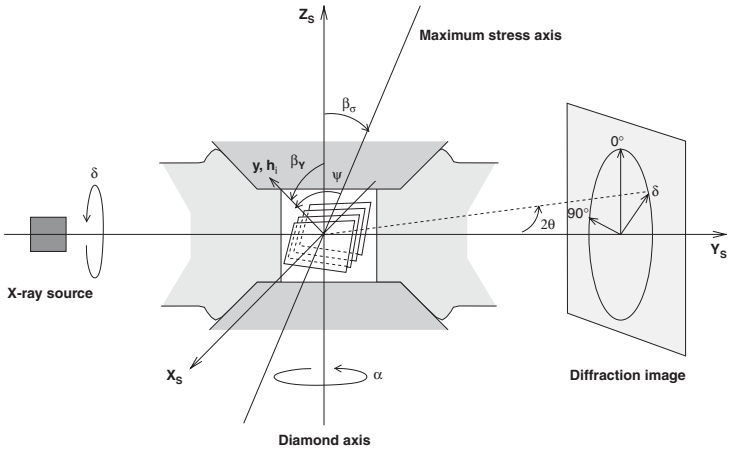

Fig. 2. Experimental setup. The sample is confined under non-hydrostatic stress conditions between the two diamond anvils. A monochromatic X-ray beam is sent through the gasket with the direction of the incoming beam perpendicular to the diamond axis and the data collected on an imaging plate orthogonal to the incoming beam. The position and intensity of the diffraction lines are then analyzed as a function of the azimuthal angle δ. Directions in the sample coordinate system $K_S(\mathbf{X}_S, \mathbf{Y}_S, \mathbf{Z}_S)$ can be expressed as a function of the two Euler angles α and β where β and α related to a rotation around $\mathbf{Y}_S$ and $\mathbf{Z}_S$, respectively. β_σ is the angle between the maximum stress axis and $\mathbf{Z}_S$, $\beta_\mathbf{y}$, the angle between the scattering vector $\mathbf{y}$ and $\mathbf{Z}_S$, and ψ the angle between the maximum stress axis and the scattering vector $\mathbf{y}$. For a given diffraction peak, the normal to the diffraction plane $\mathbf{h}_i$ is aligned with the scattering vector $\mathbf{y}$. Note that the azimuth angle δ is measured in an anti-clockwise direction.

orientation space is unity. An aggregate with a random orientation distribution has a probability of one for all orientations, or one multiple of a random distribution (m.r.d.). If preferred orientation is present, some orientations have probabilities higher than one and others lower than one.

For each orientation g, the ODF $f(g)$ describes the probability density of finding crystallites that have the orientation g within dg. We have

$$f(g)>0; \quad \int_G f(g)\,\bar{\mathrm{d}}g = 1, \quad \text{where } \bar{\mathrm{d}}g = \frac{1}{8\pi^2}\,\mathrm{d}g. \tag{1}$$

The degree of anisotropy in the sample is expressed by the texture sharpness F_2 defined as

$$F_2 = \int_G [f(g)]^2\,\bar{\mathrm{d}}g. \tag{2}$$

For a material with random texture, the texture sharpness F_2 is equal to 1, for a textured material $F_2>1$.

The ODF can be calculated using the variation of diffraction intensity with orientation using tomographic algorithms such as WIMW [23], as implemented in the BEARTEX package [24]. Because of the axial symmetry of the deformation in the diamond anvil cell (Fig. 2), the ODF is axisymmetric around the compression direction and it is sufficient to study the variation of the diffraction intensities with the pole distance, $\beta_\mathbf{y}$, which corresponds to the angle between the normal to the diffracting plane and the load direction, in order to deduce the full ODF.

This technique has been successfully applied to measure LPO and deduce active high-pressure deformation mechanisms in several materials, such as ε-Fe [25,26], MgO [8], olivine, ringwoodite, magnesiowüstite, and silicate perovskite [27,28].

2.3. Elasticity of a polycrystal

The macroscopic elastic properties ($\bar{C}$ or $\bar{S}$) of a polycrystalline sample connect the macroscopic stress $\bar{\sigma}$ and the macroscopic strain $\bar{\varepsilon}$ by Hooke's law

$$\bar{\varepsilon} = \bar{S}\,\bar{\sigma}; \quad \bar{\sigma} = \bar{C}\,\bar{\varepsilon} \tag{3}$$

and are expressed in the sample coordinate system K_S. They depend on a large number of parameters, such as the single crystal elastic moduli C or S, LPO, or grain size distribution. For samples with equidimensional grains and under a solely elastic model, the bulk properties will be mainly determined the texture and the single crystal elastic moduli. If we suppose that all grains with orientation g are submitted to the same conditions, and that the number of grains is sufficient for the use of an ODF, the microscopic relations

$$\varepsilon(g) = S(g)\sigma(g); \quad \sigma(g) = C(g)\varepsilon(g), \tag{4}$$

expressed in each crystallite coordinate system K_C can be connected to macroscopic quantities in the sample coordinate system K_S using

$$\bar{\varepsilon} = \overline{\varepsilon(g)}^a = \int_G \varepsilon(g) f(g)\,\bar{\mathrm{d}}g = \overline{S(g)\,\sigma(g)}^a = \bar{S}\,\bar{\sigma}, \tag{5}$$

$$\bar{\sigma} = \overline{\sigma(g)}^a = \int_G \sigma(g) f(g)\,\bar{\mathrm{d}}g = \overline{C(g)\varepsilon(g)}^a = \bar{C}\bar{\varepsilon}, \tag{6}$$

where the superscript a denotes an arithmetic mean over all possible orientations.

In order to constrain the elastic properties of the polycrystal, the contribution of microscopic elastic moduli or compliances in Eqs. (5)–(6) should be separated from that of the microscopic stresses and strains. To that aim, approximations have to be made about the grain interaction micromechanical model. In this paper, we will concentrate on the classical approach of Voigt [29], Reuss [30], Hill [31], and the more physically consistent geometrical mean [32].

Under the Voigt approximation, the strain field is assumed constant within the whole polycrystal. This implies that the elastic properties of the polycrystal can be calculated directly from the average of the elastic moduli

$$\bar{C}^{Voigt} = \overline{C(g)}^{a} = \int_G C(g) f(g)\, \bar{\mathrm{d}}g, \tag{7}$$

$$\bar{S}^{Voigt} = [\bar{C}^{Voigt}]^{-1}. \tag{8}$$

Under the Reuss approximation, the stress field is assumed constant within the whole polycrystal. This implies that the elastic properties of the polycrystal can be calculated directly from the average of the elastic compliances

$$\bar{S}^{Reuss} = \overline{S(g)}^{a} = \int_G S(g) f(g)\, \bar{\mathrm{d}}g, \tag{9}$$

$$\bar{C}^{Reuss} = [\bar{S}^{Reuss}]^{-1}. \tag{10}$$

It is usually assumed that, in the elastic regime, physical properties of polycrystals lie between the Voigt and the Reuss averages as the stress and strain distributions are expected to be somewhere between the uniform strain and uniform stress hypothesis. It was also observed that the arithmetic mean of the Voigt and Reuss approximation is often close to experimental values, this define this Hill approximation:

$$\bar{S}^{Hill(S)} = \frac{\bar{S}^{Reuss} + \bar{S}^{Voigt}}{2}, \tag{11}$$

$$\bar{C}^{Hill(S)} = [\bar{S}^{Hill(S)}]^{-1}, \tag{12}$$

$$\bar{C}^{Hill(C)} = \frac{\bar{C}^{Reuss} + \bar{C}^{Voigt}}{2}, \tag{13}$$

$$\bar{S}^{Hill(C)} = [\bar{C}^{Hill(C)}]^{-1}. \tag{14}$$

The Hill average, however, does not have any theoretical justification.

The choice of the geometrical mean averaging procedure is guided by the fact that the elastic moduli of the polycrystal $\bar{C}$ should be equal to the inverse of its elastic compliances $\bar{S}^{-1}$. A method for determining the geometric mean of the elastic moduli of a textured polycrystal relies on the fact that a stable elastic solid must have an positive strain elastic energy. This implies that the eigenvalues of the elastic matrix must all be positive, and we can use

$$[\bar{C}^{Geo}]^{-1} = \bar{S}^{Geo} = \exp(\overline{\ln S(g)}^{a}). \tag{15}$$

Details on the calculation of the geometric mean for elastic tensors are provided elsewhere [21].

2.4. Diffraction of a polycrystal under stress

The theory of diffraction of a polycrystal elastically deformed under stress has been described before. We present here a short summary of the main features but the full solution of the problem can be found in the literature, for textured polycrystals [12], or for a simplified approach that neglects the effect of LPO [3].

The position of a diffraction peak is directly related to the actual lattice spacing of the diffracting planes with the relation

$$\lambda = 2d \sin\theta, \tag{16}$$

where λ is the incident X-ray wavelength, d the lattice plane spacing, and θ the diffraction angle. For a polycrystal, a diffraction peak is the sum of the contributions of all crystallites in the correct reflection position, that is with the scattering vector $\mathbf{y}$ parallel to $\mathbf{h}_i$, the normal to the diffracting plane (Fig. 2). The corresponding individual d-spacings depend on the actual stress environment of the corresponding the grain. Therefore, the measured d-spacing $\bar{\mathrm{d}}_m(\mathbf{y})$ is the ODF-weighted arithmetic mean

$$\bar{\mathrm{d}}_m(\mathbf{y}) = \frac{1}{4\pi P(\mathbf{y})} \int_{G_\mathbf{y}} d(g) f(g)\, \mathrm{d}g, \tag{17}$$

where $G_\mathbf{y}$ denotes the subset of crystallites with proper orientation and $P(\mathbf{y})$ is the normalized number of crystallites in reflection position.

At this point, it is useful to separate the contribution of the hydrostatic pressure, $\bar{\sigma}_P$, and the deviatoric stress $\bar{\sigma}$, using

$$d = d_0(\bar{\sigma}_P) + d_0\left(\frac{d-d_0}{d_0}\right)(\bar{\sigma}_P, \bar{\sigma}) = d_0(1+\varepsilon), \tag{18}$$

as the contribution of $\bar{\sigma}_P$ can be easily estimated using a known equation of state and simple crystallographic relations. The measured d-spacings $\bar{\mathrm{d}}(\bar{\sigma}_P, \bar{\sigma}, S, f, \mathbf{h}_i, \mathbf{y})$ depend on the hydrostatic pressure $\bar{\sigma}_P$, the deviatoric stress $\bar{\sigma}$, the single crystal elastic moduli S, the ODF f, the plane under consideration $\mathbf{h}_i$, and the direction of observation $\mathbf{y}$. They are related to an 'experimental' strain

$$\bar{\varepsilon}(\bar{\sigma}, S, f, \mathbf{h}_i, \mathbf{y}) = \frac{\bar{\mathrm{d}}(\bar{\sigma}_P, \bar{\sigma}, S, f, \mathbf{h}_i, \mathbf{y}) - d_0(\bar{\sigma}_P, \mathbf{h}_i)}{d_0(\bar{\sigma}_P, \mathbf{h}_i)}. \tag{19}$$

In the laboratory coordinate system K_L, the measured strain is equal to the ε_{33} component of the strain tensor, and

$$\bar{\varepsilon}^L_{33}(\bar{\sigma}, S, f, \mathbf{h}_i, \mathbf{y}) = \frac{1}{4\pi P(\mathbf{y})} \int_{G_\mathbf{y}} \varepsilon^L_{33}(\bar{\sigma}, S, \mathbf{h}_i, \mathbf{y}) f(g)\, \mathrm{d}g \tag{20}$$

$$= S^L_{33kl}(S, f, \mathbf{h}_i, \mathbf{y}) \bar{\sigma}^L_{kl}. \tag{21}$$

In this equation, the laboratory elastic compliances S^L_{33kl} are arithmetic means that only consider the subset of grains with a proper orientation. They can be calculated as in Section 2.3 by restricting the region of integration. They depend on the single crystal elastic moduli S, the ODF f, the direction of observation $\mathbf{y}$ and the lattice planes $\mathbf{h}_i$.

Finally, the transformation of the stress tensor $\bar{\sigma}^L_{kl}$ to the sample coordinate system, with the proper rotation operator $\bar{\sigma}^L = g^{L\leftarrow S}(\mathbf{y})\bar{\sigma}^S$, provides

$$\bar{\varepsilon}^L_{33}(\bar{\sigma}, S, f, \mathbf{h}_i, \mathbf{y}) = S^L_{33kl}(S, f, \mathbf{h}_i, \mathbf{y}) g^{L\leftarrow S}_{klmn}(\mathbf{y})\bar{\sigma}^S_{mn} \quad (22)$$

$$= S^{LS}_{33mn}(S, f, \mathbf{h}_i, \mathbf{y})\bar{\sigma}^S_{mn}, \quad (23)$$

where $\bar{\sigma}^S_{mn}$ is the macroscopic deviatoric stress tensor, expressed in the sample coordinate system K_S.

Calculation of the mixed sample-laboratory coordinate system macroscopic elastic moduli $S^{LS}_{33mn}(S, f, \mathbf{h}_i, \mathbf{y})$ from the single crystal elastic moduli S, the ODF f, lattice planes considered $\mathbf{h}_i$ and direction of orientation $\mathbf{y}$ is not straightforward. In the general case, no analytical relation can be extracted, and all calculations should be performed numerically. This procedure has been described in details elsewhere for the Reuss, Voigt, and geometric (BPGeo) averages [21,33]. It should be noted that for the general case of a textured polycrystal, the definition of the Hill average is ambiguous and therefore cannot be used [21].

3. The stress in the diamond anvil cell

3.1. Geometry

Under large loads, and assuming that effects of pressure gradients are small, samples in a diamond anvil cell are under non-hydrostatic conditions: the stress imposed in the axial direction $\mathbf{Z}_S$ should be larger than the stress imposed in the radial directions $\mathbf{X}_S$ and $\mathbf{Y}_S$. However, sample loading can complicate this situation. For instance, if the diamonds are not exactly parallel, or if a non-uniform layer of pressure calibrant was loaded above the sample, the stress geometry could differ from pure uniaxial stress. In this study, we will assume that the stress remains largely uniaxial but allow the axis of maximum stress to be slightly shifted from $\mathbf{Z}_S$, with the maximum stress direction represented by the two Euler angles α_σ and β_σ (Fig. 2). Therefore, we assume that the stress applied to the sample $\overline{\Sigma}$, expressed in K_S, is of the form

$$\overline{\Sigma} = \bar{\sigma}^S_P + \bar{\sigma}^S, \quad (24)$$

where $\bar{\sigma}^S_P$ is the hydrostatic pressure and $\bar{\sigma}^S$ the deviatoric stress with

$$\bar{\sigma}^S_{ij} = g(0, \beta_\sigma, \alpha_\sigma)_{ik} g(0, \beta_\sigma, \alpha_\sigma)_{jl} \begin{bmatrix} -\frac{t}{3} & 0 & 0 \\ 0 & -\frac{t}{3} & 0 \\ 0 & 0 & 2\frac{t}{3} \end{bmatrix}_{kl}, \quad (25)$$

where $g(0, \beta_\sigma, \alpha_\sigma)$ is the proper rotation matrix and t the differential stress component (often called uniaxial stress).

In K_S, the scattering vector $\mathbf{y}$ is characterized with a set of Euler angles $\alpha_\mathbf{y}$ and $\beta_\mathbf{y}$. In previous high-pressure studies, the angle $\beta_\mathbf{y}$ between the diffracting vector and the diamond compression direction was also labelled χ [8]. They are calculated from the diffraction angle θ and the azimuth angle on the detector δ using the relations

$$\begin{cases} \cos\beta_\mathbf{y} = \cos\theta\cos\delta, \\ \sin\alpha_\mathbf{y}\sin\beta_\mathbf{y} = -\sin\theta, \\ \cos\alpha_\mathbf{y}\sin\beta_\mathbf{y} = -\sin\delta\cos\theta. \end{cases} \quad (26)$$

Fig. 3 presents an example of such a conversion for $2\theta = 10^\circ$ and $2\theta = 25^\circ$. It should be noted that the region of $\beta_\mathbf{y} < \theta$ and $\beta_\mathbf{y} > \pi - \theta$ cannot be probed with such an experimental setup. One should also note that the range of values of the angle $\alpha_\mathbf{y}$ probed in such experimental conditions is large, and this has important implications for measurements under pseudo-uniaxial stress conditions. Finally, following previous convention in high-pressure research [4], we also introduce the angle ψ between the diffracting plane normal and the maximum stress axis that will be useful in the rest of the analysis.

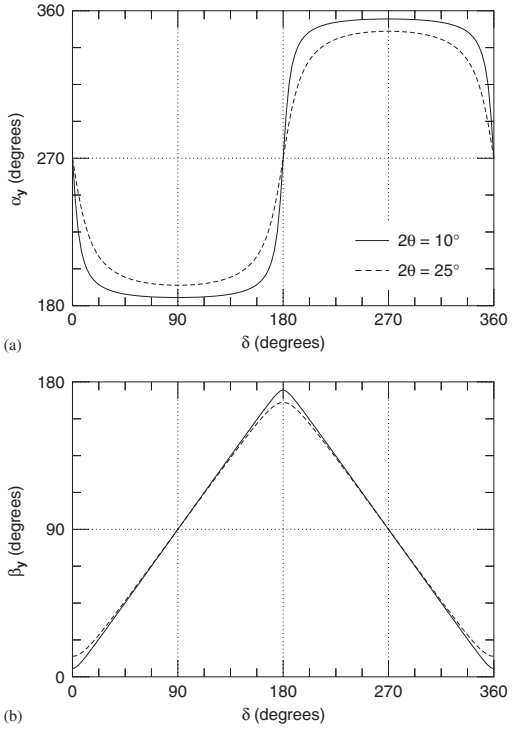

Fig. 3. Relation between the coordinates of the scattering vector $\mathbf{y}$, expressed in K_S, α_σ (a) and β_σ (b) and the azimuthal angle on the imaging plate δ for $2\theta = 10^\circ$(solid lines) and $2\theta = 25^\circ$(dashed lines).

3.2. Pure uniaxial stress

The lattice strain equations can be greatly simplified if the stress applied to the polycrystal is purely uniaxial. In this case, the orientation dependence $\mathbf{y}$ of the measurement reduces to a single parameter, $\beta_{\mathbf{y}}$, the angle between the diffraction vector and the compression direction. Similarly, the deviatoric stress can also be reduced to a single parameter, $t = \bar{\sigma}_{33} - \bar{\sigma}_{11}$. Lattice strains for $\beta_{\mathbf{y}}$ and $\pi - \beta_{\mathbf{y}}$ are also equivalent, therefore, each diffraction ring will provide up to four independent measurements of equivalent lattice strains.

If the sample does not exhibit any sign of LPO, and under the assumption that the measured d-spacing solely result from elastic distortions, analytical expressions of the S^{LS} can be extracted for the Reuss–Voigt–Hill mechanical model and one finds [3]

$$\bar{\varepsilon}(t, S, \mathbf{h}_i, \psi) = (1 - 3\cos^2\psi) Q(t, S, \mathbf{h}_i) \tag{27}$$

where $\psi \equiv \beta_{\mathbf{y}}$ is the angle between the maximum stress axis and the diffraction vector $\mathbf{y}$, and $Q(t, S, \mathbf{h}_i)$ is given by

$$Q(t, S, \mathbf{h}_i) = \frac{t}{3}\left[\frac{\alpha}{2G_R(S, \mathbf{h}_i)} + \frac{1-\alpha}{2G_V(S)}\right], \tag{28}$$

where $G_R(\mathbf{h}_i, S)$ and $G_V(S)$ are proper moduli of the aggregate under the Reuss (iso-stress) and Voigt (iso-strain) approximations, respectively, do not depend on the direction of observation, and can be calculated from single-crystal elastic moduli. The factor α, which lies between 0 and 1 specifies the degree of stress and strain continuity within the sample. From these equations, it appears that under Reuss/Voigt/Hill-type micromechanical models, a random texture, and a pure uniaxial stress, the measured d-spacings or lattice strains depend linearly on $(1 - 3\cos^2\psi)$.

For a textured sample, the orientation dependence of the measurement can still be reduced to the angle $\beta_{\mathbf{y}} \equiv \psi$ with equivalent lattice strains for $\beta_{\mathbf{y}}$ and $\pi - \beta_{\mathbf{y}}$. However, in this case we do not always expect a linear relation between the measured d-spacings and $(1 - 3\cos^2\psi)$.

3.3. Quasi-uniaxial stress

If the stress is quasi-uniaxial with a random texture within the sample, the orientation dependence of the lattice strains reduces to a single parameter ψ, the angle between the diffraction vector and the maximum stress axis. Eq. (27) remains valid and observations for ψ and $\pi - \psi$ will remain equivalent.

If the stress is quasi-uniaxial with a non-random texture within the sample however, observations for the angles ψ and $\pi - \psi$ will correspond to different subset of the ODF. In general, the orientation dependence cannot be reduced to the parameter ψ only and we do not expect a linear relation between the measured d-spacings and $(1 - 3\cos^2\psi)$.

3.4. Simulation of experimental results

In order to clarify these theoretical discussions, we performed simulations of a radial diffraction experiment with different scenarios. In these simulations, we consider a polycrystalline cobalt sample under a pressure 34.5 GPa assuming the single crystal elastic moduli calculated under the GGA approximation [16], different texture models, and various stress conditions.

Following previous analysis [12], we built a model ODF consisting of a (0 0 1) 'fiber' component with a half-width of 30° and isotropic background of 0.1 m.r.d. This model ODF is stronger and more symmetric than observed experimentally for higher accuracy and to enhance the texture effects. The differential stress in the polycrystalline sample was kept to a constant value of $t = 4.5$ GPa, under two assumptions for the stress geometry, (i) pure uniaxial stress, (ii) quasi uniaxial stress with ($\beta_\sigma = 20°, \alpha_\sigma = 30°$), that is a maximum stress axis 20° away from the compression direction.

Fig. 4(a,c,e) present the lattice strain $\bar{\varepsilon}$ we calculate for the (1 0 0), (0 0 2), and (1 0 1) planes as a function of the angle $\beta_{\mathbf{y}}$ between the diffracting plane normal and the diamond compression direction, calculated under four sets of hypothesis: (i) R-Ran-U, Reuss micromechanical model, random texture, and pure uniaxial stress; (ii) BP-Ran-U, BPGeo micromechanical model, random texture, and pure uniaxial stress; (iii) R-ODF-U, Reuss micromechanical model, model ODF, and pure uniaxial stress; and (iv) R-ODF-QU, Reuss micromechanical model, model ODF, and quasi uniaxial stress.

Strains for the R-Ran-U and BP-Ran-U hypothesis are proportional to $(1 - 3\cos^2\beta_{\mathbf{y}})$. Differences between the Reuss and BPGeo approximations are significant for (0 0 2), and of lower amplitude for (1 0 0) and (1 0 1). Comparing strains for R-Ran-U and R-ODF-U, it appears that the effect of LPO on lattice strains is significant around $\beta_{\mathbf{y}} = 90°$ for (1 0 0) and (1 0 1). Strains for (0 0 2) on the other hand are unaffected by the adjunction of effects LPO. Strain calculated for the case of a quasi-uniaxial stress (R-ODF-QU approximation) are clearly shifted from the others by an offset of the same order of magnitude than β_σ.

In order to emphasize the differences between those four hypothesis, Fig. 4(b,d,f) present the difference between the calculated strains and those calculated for the R-Ran-U hypothesis as a function of $(1 - 3\cos^2\psi)$, the angle between the diffraction vector and the maximum stress axis. Differences between the R-Ran-U and BP-Ran-U strains are of increasing amplitude for (1 0 0), (1 0 1), and (0 0 2), respectively, with a maximum difference of 0.1% for (0 0 2) at $\psi = 0°$. Strains for both the R-Ran-U and BP-Ran-U hypothesis depend linearly on $(1 - 3\cos^2\psi)$ and therefore appear as a straight line in Fig. 4(b,d,f).

The adjunction of LPO effects with our model ODF (R-ODF-U hypothesis) has no influence on the strains calculated for (0 0 2). For (1 0 0), they deviate from the

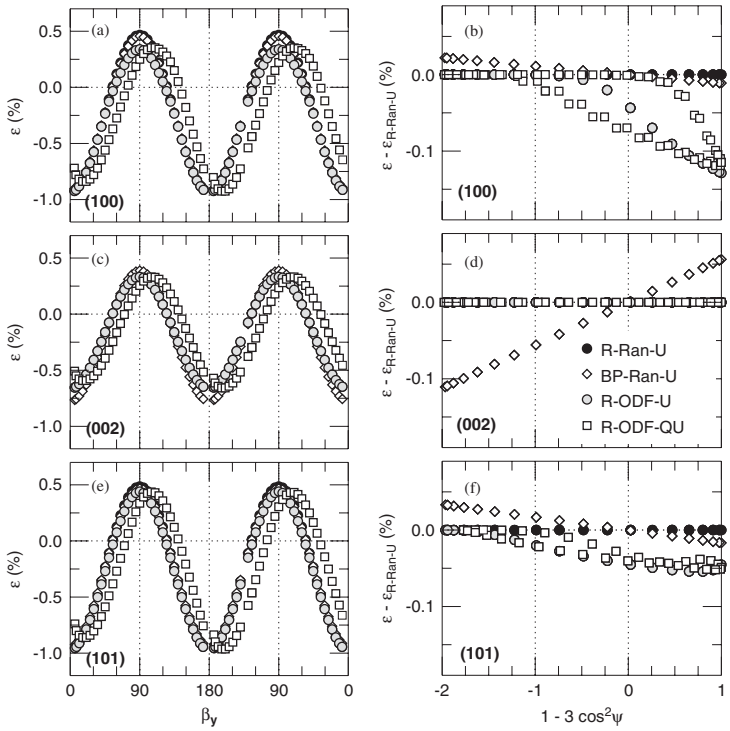

Fig. 4. Simulated lattice strain for a cobalt sample at 35 GPa for the planes (1 0 0) (a,b), (0 0 2) (c,d) and (1 0 1) (e,f). In all calculations, the elastic properties deduced from GGA calculations [16] and a differential stress component of 4.5 GPa were used. Calculations were performed under the R-Ran-U (closed circles), BP-Ran-U (open diamonds), R-ODF-U (gray circles), and R-ODF-QU (white squares) hypothesis, where R and BP denote the Reuss and BPGeo averages, respectively, Random and ODF a random and model ODF, respectively, and U and QU, a pure uniaxial stress and a quasi-uniaxial stress tilted by ($\alpha_\sigma = 30^\circ, \beta_\sigma = 20^\circ$), respectively. Fig. a, c, and e show the simulated lattice strains as a function of the orientation of the diffraction vector **y**, and Fig. b,d, and f the difference between the simulated strains and those simulated under the R-Ran-U hypothesis as a function of $(1 - \cos^2\psi)$ where ψ is the angle between the maximum stress axis and the diffraction vector **y**.

R-Ran-U model for $\psi > 45^\circ$ with a maximum difference of 0.1%. For (1 0 1), LPO effects are seen for all orientations, and their amplitude reaches 0.05%. It should be noted, however, that the symmetries imposed by the uniaxial nature of the experiment,

$$d(\psi) = d(\pi - \psi) = d(-\psi) = d(\psi - \pi) \tag{29}$$

are still valid.

If the stress becomes quasi-uniaxial (R-ODF-QU hypothesis), the shift between the maximum stress direction and the compression direction (i.e. the ODF) breaks the symmetries described in Eq. (29), with deviations of the same order of magnitude than those calculated for the R-ODF-U hypothesis.

3.5. Inversion of experimental results

The equation relating X-ray measurements of lattice strains, stresses, and elastic moduli can be used in a number of ways. For samples with known elastic properties, stress conditions can be inverted. For the configurations described in this paper, no additional constrain is necessary and the stress in the sample (pressure, differential stress, and maximum stress axis offset) can be deduced from a limited number of observations.

The inverse problem is more complex. If the sample does not exhibit LPO, the lattice strains equation provide three independent relations that can be completed by two other relations deduced from equation of state measurement for inverting the five independent single crystal elastic moduli [3]. However, stress in high pressure experiments can be difficult to constrain: the hydrostatic component of the stress (pressure) can be easily deduced by comparing the measured unit cells with a known equation of state, but the deduction of differential stress is no easy matter and serious assumptions have to be made, such as assuming a known shear modulus [4,5] or the value a single elastic modulus such as C_{44} [10].

If the sample does show LPO, elastic moduli can be inverted assuming that the stress is fully constrained [12]. If the stress is not constrained, and for a general texture configuration, one needs to add several contributions, such as the equation of state for pressure calibration, the shear modulus for calibrating differential stress, and the bulk modulus for additional constrain. In any case, the use of known shear elastic modulus is absolutely necessary for the inversion.

4. Experiment

4.1. Description of the experiment

Experiment was performed on the BL13A beamline of the Photon Factory (Tsukuba, Japan). Two-dimensional diffraction data were collected on a 3000 × 3000 pixels Rigaku image plate with online reader. Pixel sizes (100 × 100.1 μm^2), sample to detector distance (290.231 mm), detector tilt, and X-ray wavelength (0.4258 Å) were calibrated using an Ag standard. Diffraction patterns took 5 mn to record. In this experiment, high pressure and sample deformation was achieved using a diamond anvil cell equipped with diamonds of 350 μm culet diameter. In order to allow diffraction in a direction orthogonal to the compression axis we used gaskets made of a proper combination of amorphous boron, Kapton sheet, and epoxy [34] with a sample chamber diameter of 80 μm. The collimated X-ray beam was focused to a diameter of about 30 μm. Sample was a pure commercial powder of cobalt with a grain size of about 1–2 μm and a ratio of hexagonal and cubic polymorph of about 70% along with a layer of ruby powder for pressure calibration. Pressures were increased by approximately 5 GPa pressure steps up to 42 GPa over 24 h.

Data reduction was performed in a similar manner than in previous studies [8]. After flat field correction, the 2-D diffraction image was converted into series of 1-D diffraction patterns (intensity vs. 2θ) by binning the data in 5° intervals of the azimuthal angle δ (Fig. 2) between $\delta = -2.5°$ and 357.5° with Fit2d [35]. Each 1-D pattern was then fitted individually by an automated fitting-routine using pseudo-voigt peak profiles and locally linear background in order to extract the peak position and intensity for each reflection.

Fig. 5 shows the diffraction pattern we obtained at 42 GPa. The background from the confining gasket is particularly low and the sample diffraction peaks well resolved. Variations of diffraction intensity with orientation (e.g. (1 0 0), (0 0 2)) are related to LPO and will be used to calculate the sample's ODF. Variations of the peak position with orientation are related to stress, elasticity, and plasticity.

4.2. Microscopic strains and LPO

Fig. 6 presents the variations of the measured d-spacings with β_y for the (1 0 0), (0 0 2), and (1 0 1) planes of cobalt at 42 GPa. These measurements are in agreement with

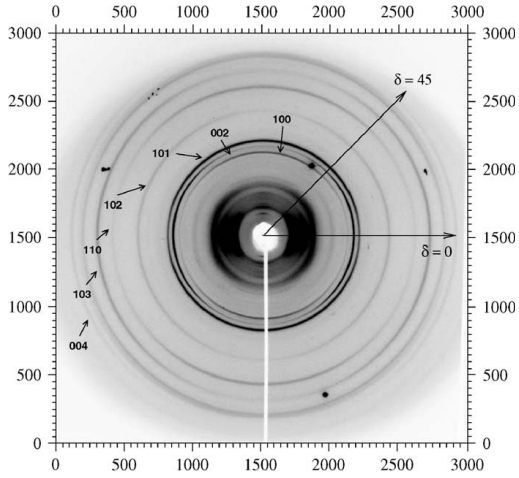

Fig. 5. Diffraction pattern at 42 GPa. Large intensity region at the center of the image results from the diffraction of the Kapton supporting ring. Diffraction from the (1 0 0), (0 0 2), (1 0 1), (1 0 2), (1 1 0), (1 0 3), and (0 0 4) planes of the Co sample are labelled on the figure.

predictions of lattice strains theory for a polycrystal under quasi-uniaxial stress. The stress is of quasi-uniaxial nature, with a clear shift of the maximum stress direction from the compression direction ($\beta_y = 0°$) by approximately 7°.

Fig. 7(a) presents the variations of diffraction intensity for (1 0 0), (0 0 2) and (1 0 1) as a function of the angle β_y at 42 GPa. We observe a very sharp texture in the sample. The (0 0 2) peak exhibits a maximum intensity at $\beta_y = 0°$ and 180°, indicating that the c-axes are preferentially aligned with the compression direction. In these figures, no offset can be observed. Variations of diffraction intensities are in agreement with a symmetry around the compression direction.

The ODF was calculated using the intensities of the (1 0 0), (0 0 2), (1 0 1), (1 0 2), (1 1 0), (1 0 3), and (0 0 4) diffraction peaks. Fig. 7(b) shows the representation of the texture we obtain in terms of inverse pole figure of the compression direction. We observe a pure (0 0 1) texture, that shows similarities with previous measurements on another hcp-metal, ε-Fe [25,26]. In this case, the calculated texture sharpness is 1.90 and the maximum pole density is 3.17 m.r.d.

5. Analysis

5.1. Inversion of elastic moduli

Assuming a Reuss, Voigt, or BPGeo micromechanical model, the single crystal elastic moduli of the material can be calculated from the measured d-spacings. However, as discussed previously (Section 3.5) the solution of the problem is incomplete and assumptions have to be made.

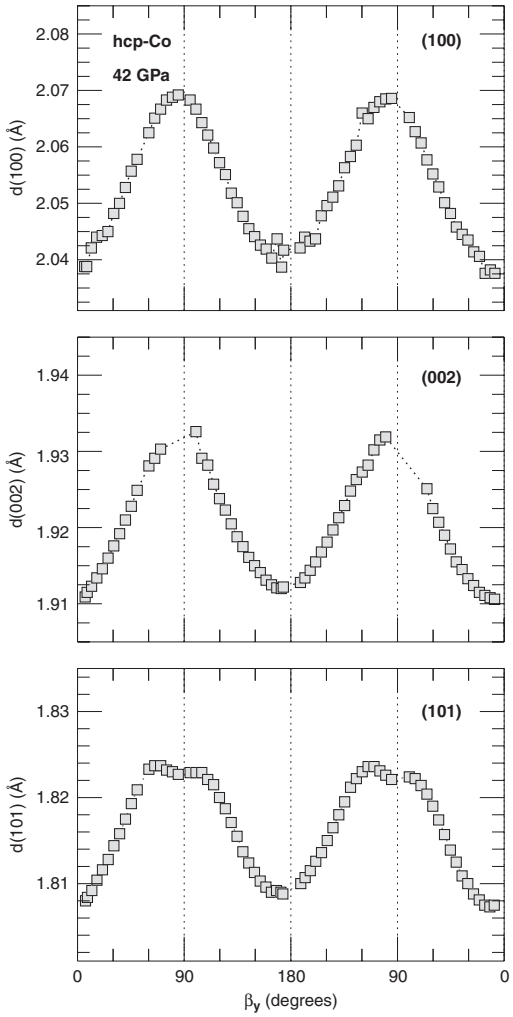

Fig. 6. Variations of the d-spacings of hcp-Co vs. β_y for (1 0 0), (0 0 2), and (1 0 1) at 42 GPa. Pressure was determined using the ruby fluorescence technique. In this figure, a shift in the position of the maximum d of about 7° from 90° can be observed.

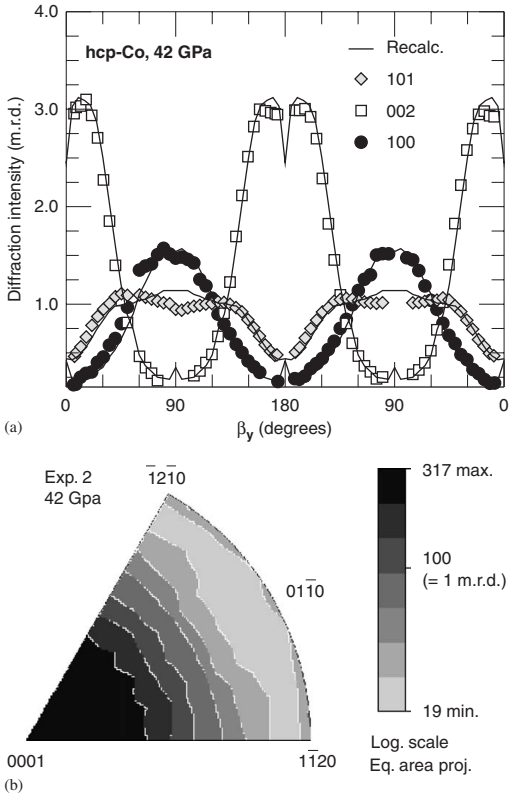

Fig. 7. (a) Measured diffraction intensities and those recalculated from the orientation distribution function (ODF) vs. β_y for the (1 0 0) (solid circles), (0 0 2) (open squares), and (1 0 1) (gray diamonds) peaks at 42 GPa. Symbols and lines are experimental and recalculated data, respectively. Experimental intensities have been scaled to match those deduced from the ODF, expressed in m.r.d. (multiples of a random distribution). Data for the (1 0 2), (1 1 0), (1 0 3) and (0 0 4) peaks were also used in the calculation of the ODF but, for clarity, they are not shown on this figure. (b) Inverse pole figure for hcp-Co in compression deduced from the experimental data.

In this analysis, we performed a global non-linear inversion of the lattice strains equations including effect of LPO in order to obtain (i) the cell parameters a and c under equivalent hydrostatic pressure $\overline{\sigma_P}$—deduced from the cell parameters themselves using a previously measured equation of state [13]—(ii) the deviatoric stress configuration, differential stress component t and maximum stress direction offset β_σ and α_σ, (iii) the single crystal elastic moduli C_{11}, C_{33}, C_{12}, C_{13}, C_{44}, $C_{66} = (C_{11} - C_{12})/2$. In order to obtain a unique solution, we also added three additional constrains: (i) that the axial compressibilities χ_a and χ_c calculated from the elastic moduli match those deduced from equation of state measurements [13] within 5%; (ii) that the average shear modulus deduced from the elastic moduli matches results from first principles GGA calculations [16] within 5%. Error on all measured d-spacings was assumed to be 10^{-4} Å.

Table 1 presents the lattice parameters, hydrostatic pressures, stress offset angles, and differential stress components deduced from the X-ray data under the Reuss and BPGeo averages and using both a random ODF and the experimental ODF. The lattice parameters, pressures, and offset angles we obtain do not differ significantly

Table 1
Lattice parameters, pressure, differential stress, and maximum stress axis offset fitted assuming a constant stress within the sample at 42 GPa

	a (Å)	c/a	P (GPa)	t (GPa)	α_σ(°)	β_σ(°)
Reuss-Random	2.3787(1)	1.6179(1)	42.7(0)	2.4(1)	219(2)	9.0(3)
Reuss-ODF	2.3796(1)	1.6174(1)	42.5(0)	3.0(2)	219(2)	8.8(3)
BPGeo-Random	2.3787(1)	1.6179(1)	42.7(0)	2.6(1)	218(2)	8.9(3)
BPGeo-ODF	2.3802(1)	1.6169(1)	42.3(0)	3.9(1)	219(2)	8.6(2)

between approximations. For all cases, we find of stress offset angle α_σ of 218–219° and β_σ of 8.6–9.0°, consistent with the d-spacings in Fig. 6 which suggested a value of about 7°. The differential stress component t we obtain under the BPGeo average are higher than those fitted under the Reuss average. Similarly, differential stresses deduced including effects of LPO are higher than those deduced assuming a random ODF.

Fig. 8 presents a comparisons between the measured d-spacings and those recalculated from the non-linear fitting procedure under the Reuss average including effects of texture. The variation of the measured d-spacings with orientation is particularly well reproduced. In particular, it should be noted that the assumption of a quasi-uniaxial stress is valid, i.e. the measured d-spacings for all equivalent orientations in the $(1–3\cos^2\psi)$ plots do agree, and for all measured lattice planes. As predicted for a polycrystalline sample with LPO, the measured d-spacings do not always vary linearly with $(1–3\cos^2\psi)$ and our numerical modelling allows us to reproduce these deviations to the first order.

Table 2 shows a comparison between the elastic moduli deduced in this study under all approximations and those calculated under the GGA approximation [16], deduced from Raman spectroscopy [17], or measured using IXS [18]. Single crystal elastic moduli evaluated under the Reuss or BPGeo average with or without ODF differ significantly. Moreover, they can be quite different from those measured with other techniques. In most cases, the best agreement is obtained under the Reuss average and including effects of LPO. Results under this approximation agree with other techniques within 20% for C_{11}, C_{33}, C_{12} and C_{13}. However, the effective elastic moduli deduced from X-ray diffraction differ significantly from other techniques for shear elastic moduli: under the best approximation, C_{66} deduced from radial X-ray diffraction is approximately 40% too low, while C_{44} is 330% too large.

Therefore, in the case of a hcp-metal undergoing significant plastic deformation, the lattice strains measured by X-ray diffraction cannot be used to constrain single crystal elastic properties. The adjunction of LPO effect in the analysis did indeed improve the agreement between the effective elastic moduli deduced from X-ray diffraction and those deduced from other techniques but did not allow us to fully account for the effect of plastic deformation.

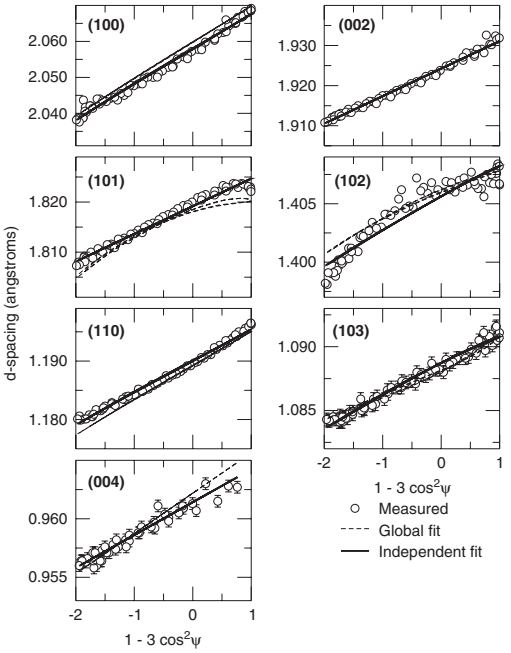

Fig. 8. Measured d-spacings vs. $(1–3\cos^2\psi)$ at 42 GPa and those recalculated after fitting elastic moduli and stress in the sample. ψ is the angle between the maximum stress axis and the diffraction vector **y**. For the thin dashed line, we adjusted the single crystal elastic moduli assuming a uniform stress within the sample, a Reuss micromechanical model, and the experimental ODF. Thick solid lines are fitting of independent differential stress t_{hkl} using single crystal elastic moduli from first principles calculations [16]. Note that the measured d-spacings do not always vary linearly with $(1–3\cos^2\psi)$, as predicted by lattice strains theories including effects of LPO.

Table 2
Single crystal elastic moduli fitted assuming a constant stress within the sample at 42 GPa

	C_{11}	C_{33}	C_{12}	C_{13}	C_{44}	C_{66}
Reuss-Random	465(17)	480(18)	313(10)	269(6)	534(30)	76(15)
Reuss-ODF	468(17)	539(21)	292(10)	249(6)	456(24)	88(12)
BPGeo-Random	431(17)	463(16)	349(9)	276(5)	687(35)	41(18)
BPGeo-ODF	497(24)	490(17)	414(12)	231(8)	657(33)	41(17)
GGA [16]	622	689	322	216	168	150
IXS [18]	552	662	271	269	137	145
Raman [17]					160	

Previous results obtained using GGA first principles calculations [16], measured using IXS [18] or deduced from Raman spectroscopy [17] extrapolated or interpolated to the same pressure are also indicated.

5.2. Inversion of stress

In fact, a polycrystalline sample submitted to plastic deformation can develop local heterogeneities at grain

Table 3
Pressure, and effective differential stresses fitted assuming an (hkl)-dependent stress

Run	P	t (1 0 0)	t (0 0 2)	t (1 0 1)	t (1 0 2)	t (1 1 0)	t (1 0 3)	t (0 0 4)
Reuss-ODF	42.5(0)	5.08(3)	5.14(5)	2.99(3)	2.07(4)	4.85(6)	2.45(6)	4.21(14)
BPGeo-ODF	42.6(0)	5.28(3)	4.53(4)	3.20(4)	2.17(4)	5.04(6)	2.49(6)	3.71(13)

Pressures and stresses are expressed in GPa.

boundaries or within the grain themselves that can be incompatible with the concept of lattice strain theories. In such cases, the assumption of a single uniform macroscopic stress applied to all grains and lattice planes within the sample can fail, and stresses deduced for various lattice planes will vary [11,36–41].

In order to investigate this issue, we performed a second set of non-linear inversions with the following hypothesis: (i) we assumed all single crystal elastic moduli from GGA calculations [16]; (ii) the maximum stress offset angles deduced from the global fit are correct and applicable to all planes. Using these hypothesis, we adjusted the d-spacings under equivalent hydrostatic pressure $d_0(hkl)$ and effective differential stress component t_{hkl} independently for each lattice plane, with the cell parameters under equivalent hydrostatic pressure a and c deduced from the fitted $d_0(hkl)$ and the pressure calculated using a known equation of state [13].

Results are presented in Table 3 and Fig. 9 under the Reuss and BPGeo average including effects of LPO. The equivalent hydrostatic pressure we obtain with those hypothesis do not differ significantly from those obtained in Table 1. On the other hand, the effective differential stress values t_{hkl} differ significantly from those obtained using the global inversions of elastic moduli: (1 0 0), (1 1 0), (0 0 2), and (0 0 4) support a large effective differential stress while the smallest values of effective differential stress are obtained for (1 0 2) and (1 0 3).

Fig. 8 presents comparisons between the measured d-spacings and those recalculated during the non-linear fitting procedure under the Reuss average including effects of texture. The variation of the measured d-spacings with orientation are well reproduced, the assumption of a (hkl)-dependent quasi-uniaxial stress is in agreement with the data.

Interestingly, as for the measurements of lattice strains, the (hkl)-dependent stresses seem to be consistent when plotted as a function of

$$\cos^2\rho = \frac{3a^2l^2}{4c^2(h^2+hk+k^2)+3a^2l^2}, \tag{30}$$

where ρ is the angle between (0 0 2) and (hkl) (Fig. 9). This can be misleading in the analysis of radial diffraction data. Indeed, a similar relation is expected in the case of a purely elastic model with no effect of LPO [3]. However, as demonstrated earlier in the paper, the effective elastic moduli reproducing measured lattice strains differ from those measured in other techniques.

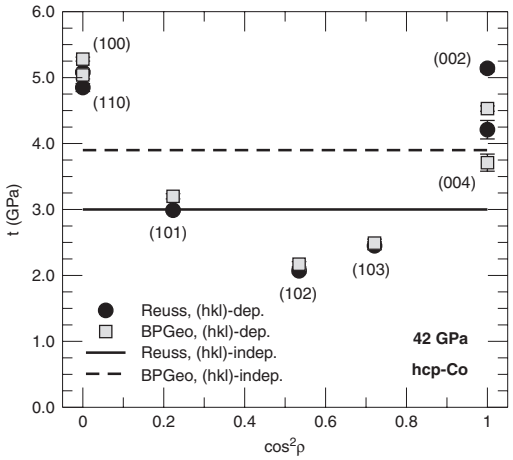

Fig. 9. Effective differential stress deduced in the sample vs. $\cos^2\rho$ where ρ is the angle between the (0 0 2) and (hkl). Solid and dashed lines were deduced under the Reuss and BPGeo averages, respectively, assuming a constant stress within the sample, that the shear modulus deduced from X-ray diffraction agrees with GGA first principles calculations [16], and including LPO-effects. Solid circles and gray square were deduced under the Reuss and BPGeo averages, respectively, assuming a grain-independent, (hkl)-dependent stress, elastic moduli from GGA first principles calculations, and including effects of LPO.

6. Discussion and conclusion

The effective single crystal elastic moduli deduced from our radial diffraction experiments on hcp-Co at 42 GPa do not match the values calculated under the GGA approximation [16], measured using IXS [18], or C_{44} deduced from Raman spectroscopy [17]. While there are uncertainties on the accuracy of those measurement and calculations, all techniques agree within 20%. The adjunction of effects of LPO in the determination of X-ray elastic moduli does improve the agreement with other techniques. Similarly, we find the Reuss approximation to be slightly better than BPGeo for our purpose. Results we obtain are for C_{11}, C_{33}, C_{12} and C_{13} are fair but our values of C_{44} and C_{66} do not even have the proper order of magnitude. Moreover, the deduction of elastic moduli from X-ray diffraction already includes a calibration on the bulk and shear moduli of the material. In other words, the numerical values obtained in this study are effective elastic parameters and do not

directly correspond to single crystal elastic moduli even with the adjunction of effects of LPO.

Development of LPO and, therefore, activation of plastic deformation was very efficient in those experiments, as indicated by the high degree of texture in the sample (Fig. 7). Therefore, these results indicate that the plastic deformation of the sample induces a drastic shift in effective elastic moduli determined by X-ray diffraction. The effect is most pronounced for the shear elastic moduli C_{44} and C_{66}. This observation is in agreement with measurements on other metals that the anisotropy had to be enhanced in order to match the observed lattice strains [38]. These conclusions raise questions on the possibility of deducing single crystal elastic moduli of hcp-metals from X-ray diffraction data. Indeed, earlier measurements on hcp-Fe [4,5,10,12] provided different results, especially for the C_{44} effective elastic modulus, which according to study tends to increase considerably with plastic deformation.

The (hkl)-dependent stress we observe in Co can be related to other ambient pressure experiments on hcp-metals (i.e. beryllium and titanium) undergoing plastic deformation that showed a similar behavior [37,39]. Lattice planes can be grouped into three categories: (i) prismatic planes (1 0 0) and (1 1 0); (ii) basal planes (0 0 2) and (0 0 4); (iii) pyramidal planes (1 0 1), (1 0 2), (1 0 3). Prismatic planes such as (1 0 0) or (1 1 0) are submitted to a large effective stress. At the end of the deformation, they are parallel to the compression direction and see a very high effective stress. Basal planes such as (0 0 2) and (0 0 4), see an intermediate stress. At the end of the deformation, they are perpendicular to the compression direction. Pyramidal planes such as (1 0 1), (1 0 2), and (1 0 3) are submitted to a lower effective stress. In terms of lattice preferred orientations, those planes show broader maxima than basal or prismatic planes.

An (hkl)-dependent measurement of stresses deduced from lattice strains have already been documented and modelled for fcc metals [36] and cubic oxides [11,40]. Those models combine self-consistent polycrystal plasticity simulations with lattice strains theory in order to account for the effect of both elastic and plastic deformation and estimate the true stress applied to the sample. Numerical results depend on the geometry of the active slip systems and the elastic anisotropy of the starting material. In those models, certain (hkl) reflection show a behavior very similar to that of a pure elastic deformation, while others do not, displaying both larger and smaller effective stresses. For the case of hcp-metals, however, and to our knowledge, a satisfying modelling remains to be developed and this question can only be approached qualitatively based on our knowledge of the behavior of fcc metals. This should be improved in the near future.

References

[1] I. Noyan, J. Cohen, Residual Stress: Measurements by Diffraction and Interpretation, Springer, New York, 1987.

[2] A.K. Singh, The lattice strains in a specimen (cubic system) compressed nonhydrostatically in an opposed anvil device, J. Appl. Phys. 73 (1993) 4278–4286.

[3] A.K. Singh, C. Balasingh, H.K. Mao, R.J. Hemley, J. Shu, Analysis of lattice strains measured under non-hydrostatic pressure, J. Appl. Phys. 83 (1998) 7567–7575.

[4] A.K. Singh, H.K. Mao, J. Shu, R.J. Hemley, Estimation of single crystal elastic moduli from polycrystalline X-ray diffraction at high pressure: applications to FeO and iron, Phys. Rev. Lett. 80 (1998) 2157–2160.

[5] H.K. Mao, J. Shu, G. Shen, R.J. Hemley, B. Li, A.K. Singh, Elasticity and rheology of iron above 220 GPa and the nature of the earth's inner core, Nature 396 (1998) 741–743 correction, Nature 399 (1999) 280.

[6] T.S. Duffy, G. Shen, D.L. Heinz, J. Shu, Y. Ma, H.K. Mao, R.J. Hemley, A.K. Singh, Lattice strains in gold and rhenium under non-hydrostatic compression to 37 GPa, Phys. Rev. B 60 (1999) 1–10.

[7] A. Kavner, T.S. Duffy, Strength and elasticity of ringwoodite at upper mantle pressures, Geophys. Res. Lett. 28 (2001) 2691–2694.

[8] S. Merkel, H.R. Wenk, J. Shu, G. Shen, P. Gillet, H.K. Mao, R.J. Hemley, Deformation of polycrystalline MgO at pressures of the lower mantle, J. Geophys. Res. 107 (2002) 2271.

[9] S. Shieh, T.S. Duffy, B. Li, Strength and elasticity of SiO_2 across the stishovite-$CaCl_2$-type structural phase boundary, Phys. Rev. Lett. 89 (2002) 255507.

[10] S. Merkel, J. Shu, P. Gillet, H. Mao, R. Hemley, X-ray diffraction study of the single crystal elastic moduli of ε-Fe up to 30 GPa, J. Geophys. Res. 110 (2005) B05201.

[11] D.J. Weidner, L. Li, M. Davis, J. Chen, Effect of plasticity on elastic modulus measurements, Geophys. Res. Lett. 31 (2004) L06621.

[12] S. Matthies, S. Merkel, H.R. Wenk, R.J. Hemley, H.K. Mao, Effects of texture on the high pressure elasticity of iron from X-ray diffraction, Earth Planet. Sci. Lett. 194 (2001) 201–212.

[13] H. Fujihisa, K. Takemura, Equation of state of cobalt up to 79 GPa, Phys. Rev. B 54 (1996) 5–7.

[14] C.S. Yoo, H. Cynn, P. Söderlind, V. Iota, New β (fcc)-cobalt to 210 GPa, Phys. Rev. Lett. 84 (2000) 4132.

[15] D. Antonangeli, M. Krisch, G. Fiquet, J. Badro, A. Bossak, D. Farber, S. Merkel, Aggregate and single crystalline elasticity of hcp cobalt at high pressure, Phys. Rev. B 72 (2005) 134303.

[16] G. Steinle-Neumann, L. Stixrude, R.E. Cohen, First-principles elastic constants for the hcp transition metals Fe, Co, and Re at high pressure, Phys. Rev. B 60 (1999) 791–799.

[17] A.F. Goncharov, J. Crowhurst, J.M. Zaug, Elastic and vibrational properties of cobalt to 120 GPa, Phys. Rev. Lett. 92 (2004) 115502.

[18] D. Antonangeli, M. Krisch, G. Fiquet, D. Farber, C. Aracne, J. Badro, F. Occelli, H. Requardt, Elasticity of cobalt at high pressure studied by inelastic X-ray scattering, Phys. Rev. Lett. 93 (2004) 215505.

[19] F. Bollenrath, V. Hauk, E.H. Müller, Zur berechnung der vielkristallinen elastizitätskonstanten aus den werten der einkristalle, Zeitschrift für Metallkunde 58 (1967) 76–82.

[20] C.J. Howard, E.H. Kisi, Measurement of single-crystal elastic constants by neutron diffraction from polycrystals, J. Appl. Cryst. 32 (1999) 624–633.

[21] S. Matthies, H.G. Priesmeyer, M.R. Daymond, On the diffractive determination of single-crystal elastic constants using polycrystalline samples, J. Appl. Cryst. 34 (2001) 585–601.

[22] U.F. Kocks, C. Tomé, H.R. Wenk, Texture and Anisotropy: Preferred Orientations and their Effects on Material Properties, Cambridge University Press, Cambridge, 1998.

[23] S. Matthies, H.R. Wenk, G.W. Vinel, Some basic concepts of texture analysis and comparison of the three methods to calculate orientation distributions from pole figures, J. Appl. Cryst. 21 (1988) 285–304.

[24] H.R. Wenk, S. Matthies, J. Donovan, D. Chateigner, Beartex: a windows-based program system for quantitative texture analysis, J. Appl. Cryst. 31 (1998) 262–269.

[25] H.R. Wenk, S. Matthies, R.J. Hemley, H.K. Mao, J. Shu, The plastic deformation of iron at pressures of the Earth's inner core, Nature 405 (2000) 1044–1047.
[26] S. Merkel, H.R. Wenk, P. Gillet, H.K. Mao, R.J. Hemley, Deformation of polycrystalline iron up to 30 GPa and 1000 K, Phys. Earth Planet. Inter. 145 (2004) 239–251.
[27] S. Merkel, H.R. Wenk, J. Badro, G. Montagnac, P. Gillet, H.K. Mao, R.J. Hemley, Deformation of (Mg,Fe)SiO_3 perovskite aggregates up to 32 GPa, Earth Planet. Sci. Lett. 209 (2003) 351–360.
[28] H.R. Wenk, I. Lonardelli, J. Pehl, J. Devine, V. Prakapenka, G. Shen, H.K. Mao, In situ observation of texture development in olivine, ringwoodite, magnesiowüstite and silicate perovskite at high pressure, Earth Planet. Sci. Lett. 226 (2004) 507–519.
[29] W. Voigt, Lerrbuch der Kristallphysics, Teubner-Verlag, Leipzig, 1928.
[30] A. Reuss, Berechnung der von Mischkristallen auf Grund der Plastizitätsbedingung für Einkristalle, Z. Angew. Math. Mech. 9 (1929) 49–58.
[31] R. Hill, The elastic behavior of polycrystalline aggregate, Proc. Phys. Soc. London, Ser. A 65 (1952) 349–354.
[32] S. Matthies, M. Humbert, The realization of the concept of a geometric mean for calculating physical constants of polycrystalline materials, Phys. Stat. Sol. (b) 177 (1993) K47–K50.
[33] S. Matthies, M. Humbert, On the principle of a geometric mean of even-rank symmetric tensors for textured polycrystals, J. Appl. Cryst. 28 (1995) 254–266.
[34] S. Merkel, T. Yagi, X-ray transparent gasket for diamond anvil cell high pressure experiments, Rev. Sci. Instrum. 76 (2005) 046109.
[35] A.P. Hammersley, Fit2d: V9.129 reference manual v3.1, Internal Report ESRF98HA01, ESRF, 1998.
[36] B. Clausen, T. Lorentzen, T. Leffers, Self-consistent modelling of the plastic deformation of f.c.c. polycrystals and its implications for diffraction measurements of internal stress, Acta Mater. 46 (1998) 3087–3098.
[37] M.R. Daymond, M.A.M. Bourke, R.B. Von Dreele, Use of Rietvelt refinement to fit hexagonal crystal structure in the presence of elastic and plastic anisotropy, J. Appl. Phys. 85 (1999) 739–747.
[38] P. Dawson, D. Boyce, S. MacEwen, R. Rogge, On the influence of crystal elastic moduli on computed lattice strains in AA-5182 following plastic straining, Mater. Sci. Eng. A 313 (2001) 123–144.
[39] M.R. Daymond, N.W. Bonner, Lattice strain evolution in IMI 834 under applied stress, Mater. Sci. Eng. A 340 (2003) 272–280.
[40] L. Li, D.J. Weidner, J. Chen, M.T. Vaughan, M. Davis, W.B. Durham, X-ray strain analysis at high pressure: effect of plastic deformation in MgO, J. Appl. Phys. 95 (2004) 8357–8365.
[41] T. Uchida, Y. Wang, M.L. Rivers, S.R. Sutton, Yield strength and strain hardening of MgO up to 8 GPa measured in the deformation-DIA with monochromatic X-ray diffraction, Earth Planet. Sci. Lett. 226 (2004) 117–126.

INSTITUTE OF PHYSICS PUBLISHING JOURNAL OF PHYSICS: CONDENSED MATTER

J. Phys.: Condens. Matter **18** (2006) S949–S962 doi:10.1088/0953-8984/18/25/S03

X-ray diffraction evaluation of stress in high pressure deformation experiments

Sébastien Merkel[1]

Department of Earth and Planetary Science, University of California, 307 McCone Hall, Berkeley, CA 94720-4767, USA

E-mail: sebastien.merkel@univ-lille1.fr

Received 30 November 2005, in final form 27 February 2006
Published 8 June 2006
Online at stacks.iop.org/JPhysCM/18/S949

Abstract

This paper explores the applicability of x-ray diffraction measurements of stress to high pressure deformation experiments. We model measurements of elastic lattice strains in various geometries for both axial and rotational deformation apparatus. We then show that, for most cases, stresses can be inverted from the diffraction data. A comparison between the results of our models and actual experimental data also indicates that plastic deformation can have an influence that is not addressed properly in the elastic models of lattice strains and should therefore be treated with caution.

1. Introduction

The importance of rheological properties for understanding the dynamics and evolution of the deep Earth is well recognized. However, while considerable progress has been achieved in establishing phase diagrams and physical properties of minerals at high pressure and high temperature, very little is known about the rheological properties of these phases under relevant conditions. To address this issue, deformation experiments at high pressure and high temperature are presently being developed [1–5]. In those experiments, a sample is deformed under high pressure while stress and lattice preferred orientation (LPO) are monitored *in situ* using x-ray diffraction.

While stress evaluation using diffraction has been used for decades in the material science community [6–8], its application in high pressure research is recent and has not been fully explored. In particular, models used for the interpretation of diffraction data in high pressure deformation experiments [9] rely on the assumption that (i) the sample is submitted to a stress that is predominantly axial, (ii) no LPO is present in the sample, (iii) plasticity does not affect the measured lattice spacings. Under those conditions, stress can be evaluated in radial or axial

[1] Present address: Laboratoire de Structure et Propriétés de l'Etat Solide (UMR CNRS 8008), Université des Sciences et Technologies de Lille, 59655 Villeneuve d'Ascq, France.

0953-8984/06/250949+14$30.00

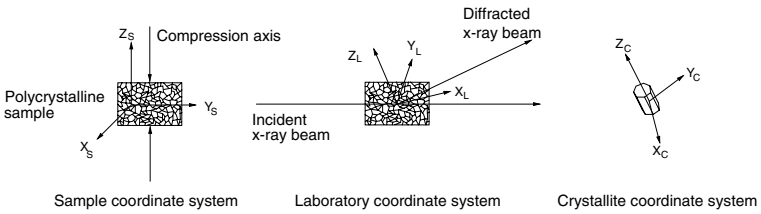

Figure 1. Coordinate systems used in the analysis. The sample coordinate system K_S is defined by the sample environment, with $\mathbf{Z}_S$ parallel to the deformation direction. The laboratory coordinate system K_L is defined with $\mathbf{Z}_L$ parallel to the bisector between the incoming and diffracted beams and $\mathbf{X}_L$ in the plane containing the incoming and diffracted beams, pointing towards the detector. The crystallite coordinate system K_C is defined according to the crystallographic structure. Microscopic physical relations, such as Hooke's law relating the microscopic stresses, strains and single-crystal elastic moduli, should be applied in each crystallite coordinate system K_C. Macroscopic properties such as polycrystalline texture or macroscopic stress are expressed in the sample coordinate system K_S.

diffraction geometry, assuming that the single-crystal elastic moduli of the sample have been estimated independently. However, these assumptions have raised controversies and results obtained using this technique are not always accepted in the community [10].

In this paper, we address this issue by simulating lattice strain measurements in high pressure deformation experiments using more advanced models that do not make the assumption of pure axial stress and include effects of LPO [11]. Comparison between the results of these models and experimental data can be used to assess the state of stress in the experiment. Those models can also be used to test our ability to invert experimental data from experiments in various geometry. Finally, the last section of the paper presents actual experimental data in order to assess the compatibility between the elastic lattice strain models and actual measurements.

2. Elastic theory of diffraction of a polycrystal under stress

Theories relating measured d-spacings using x-ray diffraction, elastic moduli, stress, and lattice preferred orientations (LPO) have been developed independently by several groups [6, 8, 11–19]. Most models used in high pressure research assume axial symmetry of stress and neglect the effects of LPO [13–18]. However, models for more general stress environments and which include the effects of LPO have already been developed and applied to high pressure diffraction data [11, 20–22]. Therefore, we will only summarize the main features of the theory. Details can be found in [11, 21].

First, the resolution of the problem is greatly simplified by introducing several coordinate systems (figure 1): the crystallite coordinate system K_C, the sample coordinate system K_S, and the laboratory coordinate system K_L. The crystallite coordinate system K_C is defined according to the crystallographic structure. Microscopic physical relations, such as Hooke's law relating the microscopic stresses, strains and single-crystal elastic moduli, should be applied in each crystallite coordinate system K_C. The sample coordinate system K_S is defined by the sample environment, with $\mathbf{Z}_S$ parallel to the deformation direction. Finally, the laboratory coordinate system K_L is defined with $\mathbf{Z}_L$ parallel to the bisector between the incoming and diffracted beams and $\mathbf{X}_L$ in the plane containing the incoming and diffracted beams, pointing towards the detector.

Samples submitted to plastic deformation can develop LPO [23]. In a polycrystal, LPO can be represented in terms of an orientation distribution function (ODF) that can be extracted from high pressure diffraction data [1, 4, 24–26]. This is a probability function for finding an orientation and is normalized such that the integral over the whole orientation space is unity. For each orientation g, the ODF $f(g)$ describes the probability density of finding a crystallite that has the orientation g within $\mathrm{d}g$.

Supposing that approximately the same conditions exist for all grains with the same orientation g, with no incompatibilities at grain boundaries or within the grains themselves, and that we consider an ensemble with a sufficiently large number of grains to be represented statistically by an ODF, ODF-weighted averages can be performed to calculate the polycrystal's macroscopic properties from microscopic quantities. For instance, the macroscopic stress $\overline{\sigma}$ and strain $\overline{\epsilon}$ applied to the polycrystal are

$$\overline{\epsilon} = \overline{\epsilon(g)}^{a} = \int_G \epsilon(g) f(g)\,\mathrm{d}g \tag{1}$$

$$\overline{\sigma} = \overline{\sigma(g)}^{a} = \int_G \sigma(g) f(g)\,\mathrm{d}g, \tag{2}$$

where the superscript a denotes an arithmetic mean over all possible orientations. Under the iso-stress Reuss approximation, the elastic properties of the polycrystal can be calculated directly from the average of the elastic compliances using

$$\overline{S}^{\mathrm{Reuss}} = \overline{S(g)}^{a} \int_G S(g) f(g)\,\mathrm{d}g. \tag{3}$$

Details of the calculation of polycrystal average elastic properties, including effects of LPO, for the Voigt and geometric mean have also been derived [11].

In a diffraction experiment, the position of a peak is directly related to the actual d-spacing of the diffracting plane by the relation

$$\lambda = 2d \sin\theta, \tag{4}$$

where λ is the x-ray wavelength, d is the lattice plane spacing, and θ is the diffraction angle. For a polycrystal, a diffraction peak is the sum of the contribution of all crystallites in the correct reflection position, that is, with the scattering vector $\mathbf{y}$ parallel to the normal to the diffracting plane $\mathbf{h}_i$ (figure 2). Therefore, the measured d-spacing $\overline{d}_m(y)$ is the ODF-weighted arithmetic mean:

$$\overline{d}_m(y) = \frac{1}{4\pi P(\mathbf{y})} \int_{G_y} d(g) f(g)\,\mathrm{d}g, \tag{5}$$

where G_y denotes the subset of crystallites in the diffraction condition and $P(y)$ is the normalized number of crystallites in the reflection position.

It is useful to separate the contribution of the hydrostatic pressure, $\overline{\sigma}_P$, and the deviatoric stress $\overline{\sigma}$, using

$$d = d_0(\overline{\sigma}_P) + d_0\left(\frac{d-d_0}{d_0}\right)(\overline{\sigma}_P, \overline{\sigma}) = d_0\,(1+\epsilon) \tag{6}$$

as the contribution of $\overline{\sigma}_P$ can be estimated easily using a known equation of state and simple crystallographic relations. The measured d-spacings $\overline{d}$ depend on the hydrostatic pressure $\overline{\sigma}_P$, the deviatoric stress $\overline{\sigma}$, the single-crystal elastic moduli S, the ODF f, the plane under consideration $\mathbf{h}_i$, and the direction of observation $\mathbf{y}$. They are related to an 'experimental' strain

$$\overline{\epsilon}(\overline{\sigma}, S, f, \mathbf{h}_i, \mathbf{y}) = \frac{\overline{d}(\overline{\sigma}_P, \overline{\sigma}, S, f, \mathbf{h}_i, \mathbf{y}) - d_0(\overline{\sigma}_P, \mathbf{h}_i)}{d_0(\overline{\sigma}_P, \mathbf{h}_i)}. \tag{7}$$

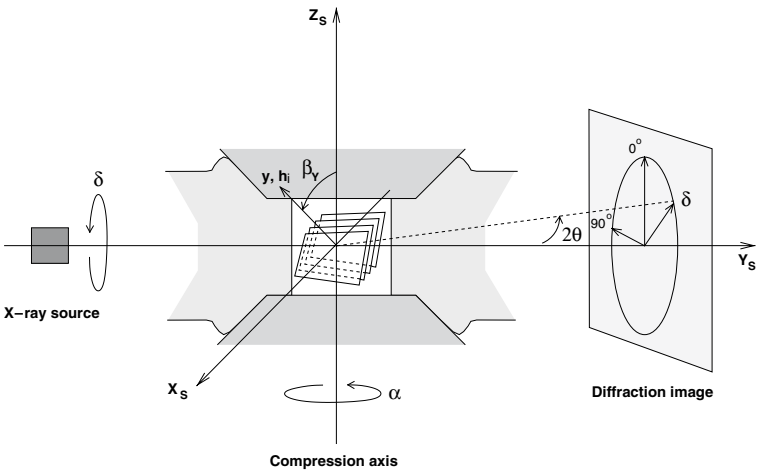

Figure 2. Experimental setup for opposed anvils experiments. The sample is confined between two opposed anvils. In a radial diffraction geometry, a monochromatic x-ray beam is sent with the direction of the incoming beam perpendicular to the anvil axis and the data is collected on an area detector orthogonal to the incoming beam. The position and intensity of the diffraction lines are analysed as a function of the azimuthal angle δ. Directions in the sample coordinate system $K_S(\mathbf{X}_S, \mathbf{Y}_S, \mathbf{Z}_S)$ can be expressed as a function of the two Euler angles α and β, where β and α are related to a rotation around $\mathbf{Y}_S$ and $\mathbf{Z}_S$, respectively. For a given diffraction peak, the normal to the diffracting plane $\mathbf{h}_i$ is aligned with the scattering vector $\mathbf{y}$. Note that the azimuth angle δ is measured in an anti-clockwise direction.

In the laboratory coordinate system K_L (figure 1), the measured strain is equal to the ϵ_{33} component of the strain tensor, and

$$\overline{\epsilon}^L_{33}(\overline{\sigma}, S, f, \mathbf{h}_i, \mathbf{y}) = \frac{1}{4\pi P(\mathbf{y})} \int_{G_\mathbf{y}} \epsilon^L_{33}(\overline{\sigma}, S, \mathbf{h}_i, \mathbf{y}) f(g)\, \mathrm{d}g. \tag{8}$$

Applying Hooke's law to the polycrystal in the laboratory coordinate system, we also have

$$\overline{\epsilon}^L_{33}(\overline{\sigma}, S, f, \mathbf{h}_i, \mathbf{y}) = S^L_{33kl}(S, f, \mathbf{h}_i, \mathbf{y})\, \overline{\sigma}^L_{kl}, \tag{9}$$

where the laboratory elastic compliances S^L_{33kl} are arithmetic means that only consider the subset of grains that actually contribute to the diffraction.

Finally, the transformation of the stress tensor $\overline{\sigma}^L_{kl}$ to the sample coordinate system, with the appropriate rotation operator $\overline{\sigma}^L = g^{L\leftarrow S}(\mathbf{y})\, \overline{\sigma}^S$, provides

$$\overline{\epsilon}^L_{33}(\overline{\sigma}, S, f, \mathbf{h}_i, \mathbf{y}) = S^L_{33kl}(S, f, \mathbf{h}_i, \mathbf{y}) g^{L\leftarrow S}_{klmn}(\mathbf{y})\, \overline{\sigma}^S_{mn} \tag{10}$$

$$= S^{LS}_{33mn}(S, f, \mathbf{h}_i, \mathbf{y}) \overline{\sigma}^S_{mn}, \tag{11}$$

where $\overline{\sigma}^S_{mn}$ is the macroscopic deviatoric stress tensor, expressed in the sample coordinate system K_S.

Calculation of the mixed sample–laboratory coordinate system's macroscopic elastic moduli $S^{LS}_{33mn}(S, f, \mathbf{h}_i, \mathbf{y})$ from the single-crystal elastic moduli S, the ODF f, lattice planes considered $\mathbf{h}_i$ and the direction of orientation $\mathbf{y}$ is not straightforward. In the general case, no analytical relation can be extracted, and all calculations should be performed numerically.

This procedure has been described in detail for the Reuss, Voigt, and geometric (BPGeo) averages [11, 27]. It should be noted that, for the general case of a textured polycrystal, the definition of the Hill average is ambiguous and therefore cannot be used [11]. On the other hand, this procedure does not make any assumption for the geometry of stress and can be applied to the most general cases.

If the assumptions behind the model presented here are verified (approximately the same conditions exist for all grains with the same orientation g, with no incompatibilities at grain boundaries or within the grains themselves, and with an ensemble with a sufficiently large number of grains to be represented statistically by an ODF), and if the single-crystal elastic moduli are known, these equation can be used to simulate the effect of stress on diffraction measurement or to invert residual stresses from diffraction data, including the effects of LPO. If the stress applied to the sample is known, they could also be used to invert effective single-crystal elastic moduli.

3. Models of experimental data

3.1. Main features

In this section, we will model the effect of stress on x-ray diffraction measurements on a polycrystal, with a particular application to the geometries used in high pressure deformation experiments. The results presented here are purely numerical and no attempt will be made to obtain mathematical proofs of inversions capabilities. They should be considered as a catalogue of the effects of stress on measured diffraction patterns with an exploration of our ability to invert stress from experimental data.

For these models, we assume that the sample is a polycrystal of pure hexagonal-close-packed (hcp) Co. In an attempt to improve our understanding of the behaviour of materials under pressure, Co has been studied extensively. Under ambient conditions, it exhibits either the hcp or the metastable face-centred-cubic (fcc) crystal structure and transforms into the fcc structure at 695 K; at high pressure, it transforms into the fcc structure in the range 105–150 GPa [28]. Its elastic properties have been calculated [29], measured using inelastic x-ray scattering (IXS) [30, 31], and deduced from Raman spectroscopy [32] up to high pressure. It has also been studied extensively using radial x-ray diffraction [21, 22]. Therefore, this material is an ideal candidate for testing stress and strain analysis.

In all cases, the sample is assumed to be submitted to an average pressure of 42 GPa. The calculation of unit cell parameters is based on previous measurements of the equation of state [33] and we used the single-crystal elastic moduli and their pressure dependence measured by inelastic x-ray scattering [30]. We also assume that the models developed in section 2 apply, i.e. that the same conditions exist for all grains with the same orientation.

In the forward modelling, the unit cell parameters of the polycrystal are calculated at a pressure 42 GPa using the equation of state. We then calculate the lattice strains resulting from deviatoric stresses using the theory described in section 2 and simulate x-ray diffraction measurements assuming a monochromatic beam of wavelength 0.4 Å. The synthetic data is then processed for stress inversion by fitting deviatoric stress tensor components and d-spacings under equivalent hydrostatic pressure $d_0(\overline{\sigma}_P, hkl)$. Cell parameters a and c are deduced from the fitted $d_0(\overline{\sigma}_P, hkl)$ and later used to invert the hydrostatic pressure.

3.2. Opposed anvil geometry

The developments presented in this section can be applied to various opposed anvil deformation experiments, such as those performed in the D-DIA [3, 5, 10, 34–38], Drickamer

Table 1. Applied stress, inversion parameters, and success in stress inversion for models of the opposed anvils geometry. Stresses are expressed in GPa in the sample coordinate system K_S (figure 2).

Model	Geometry	Applied stress	Inversion model	Success
1	⊥	$\begin{bmatrix} -1.5 & \cdot & \cdot \\ \cdot & -1.5 & \cdot \\ \cdot & \cdot & 3.0 \end{bmatrix}$	$\begin{bmatrix} -t/3 & \sigma_{12} & \sigma_{13} \\ \cdot & -t/3 & \sigma_{23} \\ \cdot & \cdot & 2t/3 \end{bmatrix}$	Yes
2	⊥	$\begin{bmatrix} -2.5 & \cdot & \cdot \\ \cdot & -0.5 & \cdot \\ \cdot & \cdot & 3.0 \end{bmatrix}$	$\begin{bmatrix} \sigma_{11} & \sigma_{12} & \sigma_{13} \\ \cdot & \sigma_{22} & \sigma_{23} \\ \cdot & \cdot & \sigma_{33} \end{bmatrix}$	No
3	⊥	$\begin{bmatrix} -0.5 & \cdot & \cdot \\ \cdot & -2.5 & \cdot \\ \cdot & \cdot & 3.0 \end{bmatrix}$	$\begin{bmatrix} \sigma_{11} & \sigma_{12} & \sigma_{13} \\ \cdot & \sigma_{22} & \sigma_{23} \\ \cdot & \cdot & \sigma_{33} \end{bmatrix}$	No
4	⊥	$\begin{bmatrix} \cdot & 3 & \cdot \\ 3 & \cdot & \cdot \\ \cdot & \cdot & \cdot \end{bmatrix}$	$\begin{bmatrix} -t/3 & \sigma_{12} & \sigma_{13} \\ \cdot & -t/3 & \sigma_{23} \\ \cdot & \cdot & 2t/3 \end{bmatrix}$	Yes
5	⊥	$\begin{bmatrix} \cdot & \cdot & 3 \\ \cdot & \cdot & \cdot \\ 3 & \cdot & \cdot \end{bmatrix}$	$\begin{bmatrix} -t/3 & \sigma_{12} & \sigma_{13} \\ \cdot & -t/3 & \sigma_{23} \\ \cdot & \cdot & 2t/3 \end{bmatrix}$	Yes
6	⊥	$\begin{bmatrix} \cdot & \cdot & \cdot \\ \cdot & \cdot & 3 \\ \cdot & 3 & \cdot \end{bmatrix}$	$\begin{bmatrix} -t/3 & \sigma_{12} & \sigma_{13} \\ \cdot & -t/3 & \sigma_{23} \\ \cdot & \cdot & 2t/3 \end{bmatrix}$	Yes
7	⊥	$g(0, 10°, 30°) \begin{bmatrix} -1.5 & \cdot & \cdot \\ \cdot & -1.5 & \cdot \\ \cdot & \cdot & 3.0 \end{bmatrix}$	$g(0, \beta, \alpha) \begin{bmatrix} -t/3 & \cdot & \cdot \\ \cdot & -t/3 & \cdot \\ \cdot & \cdot & 2t/3 \end{bmatrix}$	Yes

presses [16, 39] or the diamond anvil cell (DAC) [4, 9, 40–47]. Figure 2 presents a typical setup of an experiment in the DAC. In those experiments, a sample is compressed between two anvils and diffraction is performed with the incoming x-ray beam perpendicular to the direction of compression. There are various ways of collecting diffraction patterns, such as using energy-dispersive detectors at several locations [36, 39, 41, 42, 48] or an image area detector [4, 37, 38]. In the present paper, we assume that the measurements are performed on an area detector, but those results can be easily converted to the case of measurement in energy dispersive geometry.

The stress applied to the sample has a strong axial component and most studies conducted in this geometry have assumed that the stress is purely axial, with a cylindrical symmetry around the axis of the anvils. Following those assumptions, models have been developed that relate the measured lattice strains with stress, single-crystal elastic moduli, and lattice preferred orientation [11, 14–18]. However, the validity of the cylindrical symmetry of stress has been questioned. Therefore, in this section, we will model measurements of d-spacings in radial diffraction geometry for various stress configurations. These models are then used to assess our ability to invert stress from the diffraction data.

Stress models that we considered are listed in table 1. Figure 3 presents the simulated lattice strains $\overline{\epsilon}^L_{33} = (\overline{d} - d_0)/d_0$ for the 100 line of cobalt as a function of the azimuth angle on the detector δ and $(1 - 3\cos^2 \beta_y)$, where β_y is the angle between the axis of the anvil and the diffracting plane normal. Stress models include (i) models with a pure axial stress and a symmetry axis parallel to the direction of the anvils, (ii) models with triaxial stresses having the principal components of stress aligned with the axis of the sample coordinate system K_S, (iii) models with non-zero shear components of the stress tensor, and (iv) models with a pure axial stress with the symmetry axis tilted from the direction of the anvils [47].

The solid lines in figures 3(a) and (b) indicate the results that we obtain if a pure axial stress is applied to the sample (model 1 in table 1) without effects of LPO (thick solid line)

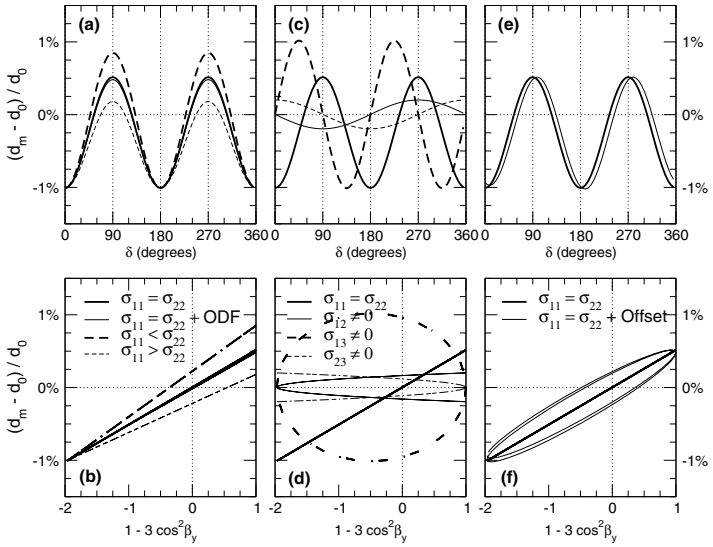

Figure 3. Simulation of measured lattice strains for the 100 line of a cobalt sample in an opposed anvil experiment as a function of the azimuth angle on the detector δ (a), (c), (e) and $(1 - 3\cos^2 \beta_y)$ (b), (d), (f), where β_y is the angle between the anvil axis and the diffracting plane normal, for various stress configurations. Figures (a) and (b) present results for cases where the principal stress directions are aligned with the sample coordinate system (figure 1) with a pure axial stress and no effect of texture (thick solid line), pure axial stress including effects of texture (thin solid line), and triaxial stresses with no effect of texture (dashed lines). Figures (c) and (d) present results for cases with non-zero off-diagonal stress components ($\sigma_{12} \neq 0$, thin solid line; $\sigma_{13} \neq 0$, thick dashed line; $\sigma_{23} \neq 0$, thin dashed line). Figures (e) and (f) present results for a pure axial stress with a maximum stress direction tilted from the anvils direction (thin solid lines). For comparison, the ideal case of pure axial stress with a maximum stress direction aligned with the anvils' direction is indicated in all figures as thick solid lines.

and including effects of LPO (thin solid line) using the ODF measured on a sample of cobalt compressed in a DAC at 42 GPa [22]. The lattice strains vary linearly with $(1 - 3\cos^2 \beta_y)$ for models that do not include effects of LPO [18]; models that include effects of LPO produce slightly curved lines [20]. However, in the present case, the effects of LPO are particularly small and both models can hardly be distinguished. In both cases, stresses can be inverted from the diffraction data.

The dashed lines in figures 3(a) and (b) indicate results for a triaxial stress with the the principal components of stress aligned with the axis of the sample coordinate system K_S and no effects of LPO (models 2 and 3 in table 1). As for the case of pure axial stress, the simulated lattice strains vary linearly with $(1 - 3\cos^2 \beta_y)$. However, stress inversions with σ_{11} and σ_{22} as free parameters will fail consistently. Stress inversion can be performed assuming pure axial stress. For model 2 (thick dashed lines, $\sigma_{11} < \sigma_{22}$), this leads to

$$\begin{aligned} \sigma_P &= 39.8 \text{ GPa} \\ \sigma_{11} = \sigma_{22} &= -1.8 \text{ GPa}, \\ \sigma_{33} &= 3.6 \text{ GPa}, \end{aligned} \tag{12}$$

that is an under-estimation of pressure and improper stresses. For model 3 (thin dashed lines, $\sigma_{11} > \sigma_{22}$), such an inversion would lead to

$$\begin{aligned} \sigma_P &= 44.1 \text{ GPa} \\ \sigma_{11} = \sigma_{22} &= -1.2 \text{ GPa}, \\ \sigma_{33} &= 2.4 \text{ GPa}, \end{aligned} \tag{13}$$

which is an over-estimate of pressure and improper stresses. It should be noted that such a stress configuration can be detected and evaluated by performing additional measurements with the incoming x-ray beam parallel to $\mathbf{X}_S$ or $\mathbf{Z}_S$.

The effects of the shear components of the stress tensor (models 4, 5, and 6 in table 1) are highlighted in figures 3(c) and (d). $\sigma_{12} \neq 0$ and $\sigma_{23} \neq 0$ introduce lattice strains with a period of 360° in δ. Maxima and minima of the corresponding lattice strains are located at $\delta = 90°$ and 270° for $\sigma_{12} \neq 0$ and $\delta = 0°$ and 180° for $\sigma_{23} \neq 0$. On the other hand, $\sigma_{13} \neq 0$ introduces lattice strains with a period of 180° in δ with maxima and minima located at $\delta = 45°$, 135°, 225°, and 315°. In all cases, shear components of the stress tensor can be inverted from the diffraction data. Because of the very different nature of the effect of each shear component of the stress tensor on lattice strains, all components can be deduced independently, from a single measurement.

Finally, figures 3(e) and (f) present the results obtained for model 7 in table 1. In this case, the stress is supposed to be mainly axial, but the axis of symmetry of the stress tensor is tilted by $\alpha_\sigma = 30°$ $\beta_\sigma = 10°$, where β and α indicate rotations around $\mathbf{Y}_S$ and $\mathbf{Z}_S$, respectively. When plotted as function of δ, the lattice strains resemble that of the pure axial case, with a slight offset of the location of minima and maxima. When plotted as a function of $(1 - 3\cos^2 \beta_y)$, they deviate from the straight line that is expected with pure axial stress and form an ellipse. In any case, such a stress can be inverted from the diffraction data (table 1).

3.3. Rotational anvil geometry

In this section, we investigate the effect of deviatoric stresses on x-ray diffraction patterns in settings corresponding to rotational anvil experiments. These experiments are new and have only recently been applied to high pressure deformation [2, 3, 49–51]. Deformation experiments in this geometry are conducted by twisting a thin sample between the anvils, and stresses are measured *in situ* using x-ray diffraction. However, stress measurement using x-ray diffraction in rotational anvil deformation experiments is still very preliminary and the technique has not yet been standardized. One of the difficulties in stress inversion is the presence of an axial stress component superimposed on the shear stresses imposed by the rotation of the anvils.

Here, we simulate x-ray measurements in three geometries (figure 4): (i) with the incoming x-ray beam parallel to the axis of rotation, sampling a region where the sample is deformed in shear perpendicular to the incoming x-ray beam; (ii) with the incoming x-ray beam perpendicular to the axis of rotation, sampling a region where the sample is deformed in shear perpendicular to the incoming x-ray beam; and (iii) with the incoming x-ray beam perpendicular to the axis of rotation, sampling a region where the sample is deformed in shear parallel to the incoming x-ray beam. In all cases, we assume that the diffraction signal has been filtered and that the diffracting portion of the sample is under uniform stress. Table 2 and figure 5 present the stress models considered and the corresponding lattice strains $\overline{\epsilon}^L_{33} = (\overline{d} - d_0)/d_0$ for the 100 line of cobalt as a function of the azimuth angle on the detector δ, respectively.

The simulated lattice strains for measurements in a perpendicular geometry with the direction of shear perpendicular to the incoming x-ray beam are presented in figure 5(a). In this

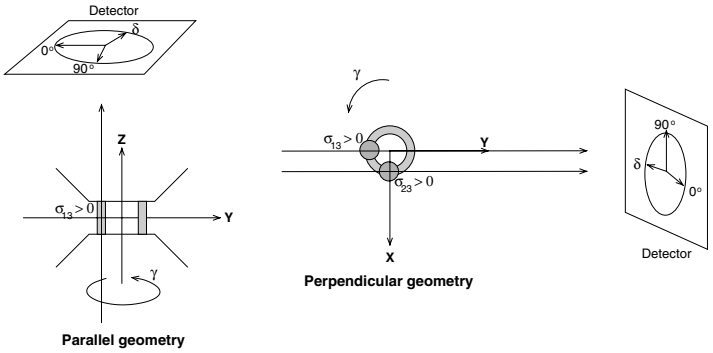

Figure 4. Experimental setup for rotational anvils experiments. The sample is confined between two opposed anvils with a torsion applied to the upper anvil. In the parallel geometry, a monochromatic x-ray beam is sent with the direction of the incoming beam parallel to the anvil axis. In the perpendicular geometry, the x-ray beam is sent with the direction of the incoming beam perpendicular to the anvil axis. The shaded region indicates the region of the sample probed by the synthetic diffraction experiment.

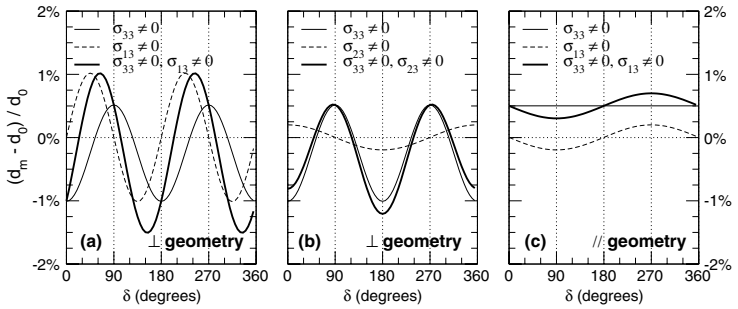

Figure 5. Simulation of measured lattice strains for the 100 line of a cobalt sample in a rotational anvil experiment as a function of the azimuth angle on the detector δ for the geometries described in figure 4: (a) presents the results obtained for an experiment in perpendicular geometry sampling a region where the stress is purely axial (compression, no torsion applied, thin solid line), in simple shear configuration, with the direction of shear perpendicular to the x-ray beam (no compression, torsion applied, thin dashed line), and a combination of the two (compression and torsion applied, thick solid line); (b) presents the results obtained for an experiment in perpendicular geometry sampling a region where the stress is purely axial (compression, no torsion applied, thin solid line), in simple shear configuration, with the direction of shear parallel to the x-ray beam (no compression, torsion applied, thin dashed line), and a combination of the two (compression and tortion applied, thick solid line); and, finally, (c) presents the results obtained for an experiment in parallel geometry sampling a region where the stress is purely axial (compression, no torsion applied, thin solid line), in simple shear configuration (no compression, torsion applied, thin dashed line), and with a combination of the two (compression and torsion applied, thick solid line).

case, the results are very similar to those modelled for the opposed anvil geometry (figure 3). Pure axial stress (thin solid line, model 1), pure shear stress (dashed line, model 2), or a

Table 2. Measurement geometry, applied stress, inversion parameters, and success in stress inversion for models of rotational anvil geometry. Stresses are expressed in GPa in the sample coordinate system K_S (figure 4).

Model	Geometry	Applied stress	Inversion model	Success
1	$\perp$	$\begin{bmatrix} -1.5 & \cdot & \cdot \\ \cdot & -1.5 & \cdot \\ \cdot & \cdot & 3.0 \end{bmatrix}$	$\begin{bmatrix} -t/3 & \sigma_{12} & \sigma_{13} \\ \cdot & -t/3 & \sigma_{23} \\ \cdot & \cdot & 2t/3 \end{bmatrix}$	Yes
2	$\perp$	$\begin{bmatrix} \cdot & \cdot & 3 \\ \cdot & \cdot & \cdot \\ 3 & \cdot & \cdot \end{bmatrix}$	$\begin{bmatrix} -t/3 & \sigma_{12} & \sigma_{13} \\ \cdot & -t/3 & \sigma_{23} \\ \cdot & \cdot & 2t/3 \end{bmatrix}$	Yes
3	$\perp$	$\begin{bmatrix} -1.5 & \cdot & 3 \\ \cdot & -1.5 & \cdot \\ 3 & \cdot & 3 \end{bmatrix}$	$\begin{bmatrix} -t/3 & \sigma_{12} & \sigma_{13} \\ \cdot & -t/3 & \sigma_{23} \\ \cdot & \cdot & 2t/3 \end{bmatrix}$	Yes
4	$\perp$	$\begin{bmatrix} \cdot & \cdot & \cdot \\ \cdot & \cdot & 3 \\ \cdot & 3 & \cdot \end{bmatrix}$	$\begin{bmatrix} -t/3 & \sigma_{12} & \sigma_{13} \\ \cdot & -t/3 & \sigma_{23} \\ \cdot & \cdot & 2t/3 \end{bmatrix}$	Yes
5	$\perp$	$\begin{bmatrix} -1.5 & \cdot & \cdot \\ \cdot & -1.5 & 3 \\ \cdot & 3 & 3 \end{bmatrix}$	$\begin{bmatrix} -t/3 & \sigma_{12} & \sigma_{13} \\ \cdot & -t/3 & \sigma_{23} \\ \cdot & \cdot & 2t/3 \end{bmatrix}$	Yes
6	$\parallel$	$\begin{bmatrix} -1.5 & \cdot & \cdot \\ \cdot & -1.5 & \cdot \\ \cdot & \cdot & 3 \end{bmatrix}$	$\begin{bmatrix} -t/3 & \sigma_{12} & \sigma_{13} \\ \cdot & -t/3 & \sigma_{23} \\ \cdot & \cdot & 2t/3 \end{bmatrix}$	No
7	$\parallel$	$\begin{bmatrix} \cdot & \cdot & 3 \\ \cdot & \cdot & \cdot \\ 3 & \cdot & \cdot \end{bmatrix}$	$\begin{bmatrix} -t/3 & \sigma_{12} & \sigma_{13} \\ \cdot & -t/3 & \sigma_{23} \\ \cdot & \cdot & 2t/3 \end{bmatrix}$	Yes
8	$\parallel$	$\begin{bmatrix} -1.5 & \cdot & 3 \\ \cdot & -1.5 & \cdot \\ 3 & \cdot & 3 \end{bmatrix}$	$\begin{bmatrix} -t/3 & \sigma_{12} & \sigma_{13} \\ \cdot & -t/3 & \sigma_{23} \\ \cdot & \cdot & 2t/3 \end{bmatrix}$	No

combination of the two (thick solid line, model 3) have a very different influence on lattice strains, and all can be inverted from the diffraction data.

Simulations of measurements in a perpendicular geometry with the direction of shear parallel to the incoming x-ray beam are presented in figure 5(b). Pure axial stress (thin solid line, model 1) introduces lattice strains with a period of 180° in δ with maxima and minima located at $\delta = 0°$, 90°, 180°, and 270°. Pure shear stress (dashed line, model 4) induces lattice strains with a period of 360° in δ with maxima and minima at $\delta = 0°$ and 180°. A combination of the two stress (thick solid line, model 5) results in the summation of lattice strains induced by the pure axial stress and those induced by the shear component. Both have different periods and can therefore be inverted from the diffraction data.

Finally, figure 5(c) presents the simulated lattice strains for measurements in a parallel geometry. Pure axial stress (thin solid line, model 6) results in a shift in the apparent d-spacing under equivalent hydrostatic pressure d_0. In this case, the axial component of the stress tensor cannot be evaluated from lattice strains only and pressure estimations based on unit cell parameters will be biased. Pure shear stress (dashed line, model 7) results in lattice strains with a period of 360° in δ with maxima and minima at $\delta = 90°$ and 270°. It can be inverted from the data. A combination of axial and pure shear stress (thick solid line, model 8) will result in a shift in the apparent d-spacings under equivalent hydrostatic pressure d_0 and lattice strains with a period of 360° in δ. The shear component of the stress tensor could be inverted from the data, assuming that the shift in apparent d-spacings under equivalent hydrostatic pressure d_0 is properly corrected. This could be done using methods relying on line-width analysis [52, 53], for instance.

4. Example of experimental data

This section will present an example of the applicability of the models described in tables 1 and 2 to actual experimental data. The data presented here have already been published and discussed elsewhere [22]. They were collected at the BL13A beamline of the Photon Factory (Tsukuba, Japan) with a monochromatic x-ray beam of wavelength 0.4258 Å on a 3000×3000 pixel Rigaku image plate with an online reader. Sample-to-detector distance, detector tilt, and pixel size ratios were calibrated using an Ag standard. High pressure and sample deformation was achieved using a DAC equipped with diamonds of 350 μm. To allow diffraction in a direction orthogonal to the compression axis, the sample was confined in an x-ray transparent composite gasket made with amorphous boron, Kapton sheet, and epoxy [54]. The sample was a pure commercial powder of cobalt with a starting grain size of 1–2 μm and a ratio of hexagonal and cubic polymorph of 70%. Pressures were increased up to 42.5 GPa over 24 h.

Figure 6 presents the measured d-spacings as a function of δ and $(1 - 3\cos^2\beta_y)$ for the 100, 002, and 101 lines of hcp-Co. As observed in previous radial diffraction experiments on Pt [47], a comparison between figures 6 and 3 indicates that the stress is mostly axial, with a slight tilt of the maximum stress direction. An inversion of stress model 7 in table 1 from this data under the Reuss average provides the following parameters:

$$\begin{aligned} P &= 42.7 \pm 0.03 \text{ GPa}, \\ t &= 3.2 \pm 0.0 \text{ GPa}, \\ \alpha_\sigma &= 40.1^\circ \pm 1.7^\circ, \\ \beta_\sigma &= -9.5^\circ \pm 0.2^\circ. \end{aligned} \tag{14}$$

However, the recalculated d-spacings do not match the experimental data (thin solid lines in figure 6). Indeed, the amplitude of the lattice strains is under-estimated for lines such as 100 or 002 and over-estimated for 101.

In fact, a polycrystalline sample subjected to plastic deformation can develop heterogeneities from grain to grain, at grain boundaries, or within the grains themselves which can be incompatible with the concept of lattice strain theories. In such cases, the assumption of a single uniform macroscopic stress applied to all grains and lattice planes within the sample can fail, and stresses deduced for various lattice planes might vary [10, 55–59]. In this case, the lattice strain data can be inverted, assuming an (hkl)-dependent uniaxial stress component t_{hkl}. Hence, we adjust the d-spacings under equivalent hydrostatic pressure $d_0(hkl)$ and effective uniaxial stress component t_{hkl} independently for each lattice plane, assuming the offset values of the maximum stress direction α_σ and β_σ found above. Using the elastic moduli measured using inelastic x-ray scattering [30], one finds

$$\begin{aligned} P &= 42.7 \pm 0.0 \text{ GPa} \\ t_{100} &= 4.30 \pm 0.03 \text{ GPa} \\ t_{002} &= 3.93 \pm 0.04 \text{ GPa} \\ t_{101} &= 2.53 \pm 0.03 \text{ GPa} \end{aligned} \tag{15}$$

and the recalculated d-spacings are in agreement with the experimental data (thick solid lines in figure 6).

5. Discussion

The results obtained for the models in tables 1 and 2 and figures 3 and 5 demonstrate that lattice strains measured using x-ray diffraction can be a powerful tool for stress evaluation in

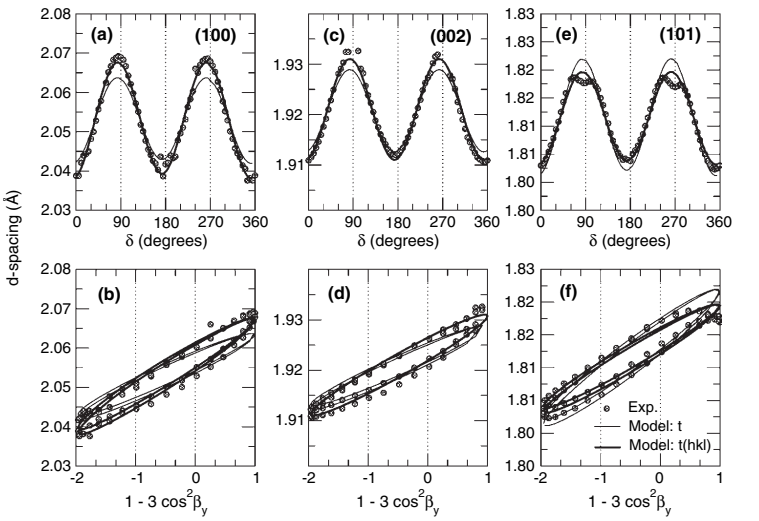

Figure 6. Measured d-spacings in radial diffraction geometry for the 100, 002 and 101 lines of a sample of hcp-Co after plastic deformation in compression in a DAC up to 42 GPa as a function of the azimuth angle on the detector δ (a), (c), (e) and $(1 - 3\cos^2\beta_y)$ (b), (d), (f), where β_y is the angle between the anvil axis and the diffracting plane normal. Symbols are experimental data, thin solid lines are fits to the data assuming a uniform stress for all lattice planes, and thick solid lines are fits to the data assuming (hkl)-dependent stress.

high pressure deformation experiments. Indeed, assuming that no error has been introduced in the measurement itself and that full Debye–Scherrer rings are available, all components of the deviatoric stress tensor can be refined using a single diffraction image, with the exception of σ_{11} and σ_{22}. Moreover, this limitation could be overcome by using complimentary lattice strain analysis on measurements in a different direction or using techniques based on peak profile refinements [52, 53].

Actual experimental data show that the assumption of a single uniform macroscopic stress applied to all grains with the same orientation can fail, and that stresses deduced for various lattice planes can vary [10, 22]. This limitation is known in the material science community, and there are elasto-plastic [55, 59–61], finite-element [57, 62], or continuum mechanics [63] models that can be used to assist data interpretation. Moreover, for most geologically relevant materials such as silicates, the amplitude of the (hkl)-dependence of the measured stresses is smaller than for hcp metals and can simply be included in the errors.

It should be noted, however, that even data that seem to be in agreement with the predictions of the purely elastic models [18] can be affected by plasticity. For instance, the data presented in figure 6 appear to be linear when plotted as a function of $(1 - 3\cos^2\chi)$, where χ is the angle between the maximum stress direction and the diffracting plane normal. The lattice strains $Q(hkl)$ extracted from the data are also consistent with the elastic model [18] when plotted as a function of

$$l_3^2 = 3a^2l^2/[4c^2(h^2 + hk + k^2) + 3a^2l^2]. \tag{16}$$

However, the effective single-crystal elastic moduli extracted from this data are very different from those measured with other techniques [21, 22]. This implies that single-crystal elastic moduli extracted from radial diffraction data should be treated with extreme caution.

Acknowledgments

The author acknowledges support from the Miller Institute for Basic Research in Science and wishes to thank Haozhe Liu and COMPRES for a stimulating workshop at APS.

References

[1] Wenk H R, Matthies S, Hemley R J, Mao H K and Shu J 2000 *Nature* **405** 1044–7
[2] Yamazaki D and Karato S I 2001 *Rev. Sci. Instrum.* **72** 4207–11
[3] Durham W B, Weidner D J, Karato S I and Wang Y 2002 *Plastic Deformation of Minerals and Rocks* (*Reviews in Mineralogy and Geochemistry* vol 51) ed S I Karato and H R Wenk (Washington, DC: Mineralogical Society of America) pp 21–49
[4] Merkel S, Wenk H R, Shu J, Shen G, Gillet P, Mao H K and Hemley R J 2002 *J. Geophys. Res.* **107** 2271
[5] Wang Y, Duhram W B, Getting I C and Weidner D J 2003 *Rev. Sci. Instrum.* **74** 3002–11
[6] Noyan I and Cohen J 1987 *Residual Stress: Measurements by Diffraction and Interpretation* (New York: Springer)
[7] Tanaka K, Kodama S and Goto T (ed) 1993 *X-ray Diffraction Studies on the Deformation and Fracture of Solids* (Amsterdam: Elsevier)
[8] Hauk V 1997 *Structural and Residual Stress Analysis by Nondestructive Methods* (Amsterdam: Elsevier)
[9] Singh A K, Mao H K, Shu J and Hemley R J 1998 *Phys. Rev. Lett.* **80** 2157–60
[10] Weidner D J, Li L, Davis M and Chen J 2004 *Geophys. Res. Lett.* **31** L06621
[11] Matthies S, Priesmeyer H G and Daymond M R 2001 *J. Appl. Crystallogr.* **34** 585–601
[12] Bollenrath F, Hauk V and Müller E H 1967 *Z. Metallk.* **58** 76–82
[13] Singh A K and Kennedy G C 1974 *J. Appl. Phys.* **45** 4686–91
[14] Singh A K 1993 *J. Appl. Phys.* **73** 4278–86
[15] Singh A K and Balasingh C 1994 *J. Appl. Phys.* **75** 4956–62
[16] Funamori N, Yagi T and Uchida T 1994 *J. Appl. Phys.* **75** 4327–31
[17] Uchida T, Funamori N and Yagi T 1996 *J. Appl. Phys.* **80** 739–46
[18] Singh A K, Balasingh C, Mao H K, Hemley R J and Shu J 1998 *J. Appl. Phys.* **83** 7567–75
[19] Howard C J and Kisi E H 1999 *J. Appl. Crystallogr.* **32** 624–33
[20] Matthies S, Merkel S, Wenk H R, Hemley R J and Mao H K 2001 *Earth Planet. Sci. Lett.* **194** 201–12
[21] Merkel S and Yagi T 2006 *J. Phys. Chem. Solids* at press
[22] Merkel S, Miyajima N, Antonangeli D, Fiquet G and Yagi T 2006 *J. Appl. Phys.* at press
[23] Kocks U F, Tomé C and Wenk H R 1998 *Texture and Anisotropy: Preferred Orientations and their Effects on Material Properties* (Cambridge: Cambridge University Press)
[24] Wenk H R, Lonardelli I, Pehl J, Devine J, Prakapenka V, Shen G and Mao H K 2004 *Earth Planet. Sci. Lett.* **226** 507–19
[25] Merkel S, Wenk H R, Gillet P, Mao H K and Hemley R J 2004 *Phys. Earth Planet. Inter.* **145** 239–51
[26] Wenk H R, Ischia G, Nishiyama N, Wang Y and Uchida T 2005 *Phys. Earth Planet. Inter.* **152** 191–9
[27] Matthies S and Humbert M 1995 *J. Appl. Crystallogr.* **28** 254–66
[28] Yoo C S, Cynn H, Söderlind P and Iota V 2000 *Phys. Rev. Lett.* **84** 4132
[29] Steinle-Neumann G, Stixrude L and Cohen R E 1999 *Phys. Rev.* B **60** 791–9
[30] Antonangeli D, Krisch M, Fiquet G, Farber D, Aracne C, Badro J, Occelli F and Requardt H 2004 *Phys. Rev. Lett.* **93** 215505
[31] Antonangeli D, Krisch M, Fiquet G, Badro J, Bossak A, Farber D and Merkel S 2005 *Phys. Rev.* B **72** 134303
[32] Goncharov A F, Crowhurst J and Zaug J M 2004 *Phys. Rev. Lett.* **92** 115502
[33] Fujihisa H and Takemura K 1996 *Phys. Rev.* B **54** 5–7
[34] Li L, Weidner D W, Raterron P, Chen J and Vaughan M 2004 *Phys. Earth Planet. Inter.* **143/144** 357–67
[35] Chen J, Li L, Weidner D J and Vaughan M 2004 *Phys. Earth Planet. Inter.* **143/144** 347–56
[36] Raterron P, Wu Y, Weidner D J and Chen J 2004 *Phys. Earth Planet. Inter.* **145** 149–59
[37] Uchida T, Wang Y, Rivers M L and Sutton S R 2004 *Earth Planet. Sci. Lett.* **226** 117–26
[38] Nishiyama N, Wang Y, Uchida T, Irifune T, Rivers M L and Sutton S R 2005 *Geophys. Res. Lett.* **32** L04307

[39] Uchida T, Funamori N, Ohtani T and Yagi T 1996 *High Pressure Science and Technology* ed W A Trzeciatowski (Singapore: World Scientific) pp 183–5
[40] Kinsland G L and Bassett W A 1977 *J. Appl. Phys.* **48** 978–84
[41] Hemley R J, Mao H K, Shen G, Badro J, Gillet P, Hanfland M and Häusermann D 1997 *Science* **276** 1242–5
[42] Mao H K, Shu J, Shen G, Hemley R J, Li B and Singh A K 1998 *Nature* **396** 741–3
Mao H K, Shu J, Shen G, Hemley R J, Li B and Singh A K 1999 *Nature* **399** 280 (correction)
[43] Duffy T S, Shen G, Heinz D L, Shu J, Ma Y, Mao H K, Hemley R J and Singh A K 1999 *Phys. Rev.* B **60** 1–10
[44] Kavner A and Duffy T S 2001 *Geophys. Res. Lett.* **28** 2691–4
[45] Shieh S, Duffy T S and Li B 2002 *Phys. Rev. Lett.* **89** 255507
[46] Kavner A 2003 *Earth Planet. Sci. Lett.* **214** 645–54
[47] Kavner A and Duffy T S 2003 *Phys. Rev.* B **68** 144101
[48] Weidner D J, Wang Y and Vaughan M T 1994 *Geophys. Res. Lett.* **21** 753–6
[49] Levitas V I 2004 *Phys. Rev.* B **70** 184118
[50] Xu Y, Nishihara Y and Karato S 2005 *Frontier of High-Pressure Research: Applications to Geophysics* ed J Chen, Y Wang, T S Duffy, G Shen and L F Dobrzhinetskaya (Amsterdam: Elsevier) pp 167–82
[51] Ma Y, Levitas V I and Hashemi J 2005 *SMEC Conf. Abstracts (Miami, FL)*
[52] Singh A K, Liermann H P and Saxena S K 2004 *Solid State Commun.* **132** 795–8
[53] Singh A K, Jain A, Liermann H P and Saxena S K 2006 *J. Phys. Chem. Solids* at press
[54] Merkel S and Yagi T 2005 *Rev. Sci. Instrum.* **76** 046109
[55] Clausen B, Lorentzen T and Leffers T 1998 *Acta Mater.* **46** 3087–98
[56] Daymond M R, Bourke M A M and Von Dreele R B 1999 *J. Appl. Phys.* **85** 739–47
[57] Dawson P, Boyce D, MacEwen S and Rogge R 2001 *Mater. Sci. Eng.* A **313** 123–44
[58] Daymond M R and Bonner N W 2003 *Mater. Sci. Eng.* A **340** 272–80
[59] Li L, Weidner D J, Chen J, Vaughan M T, Davis M and Durham W B 2004 *J. Appl. Phys.* **95** 8357–65
[60] Lodini A 2001 *Radiat. Phys. Chem.* **61** 227–33
[61] Baczmański A, Levy-Tubiana R, Fitzpatrick M E and Lodini A 2004 *Acta Mater.* **52** 1565–77
[62] Dawson P R, Boyce D E and Rogge R B 2005 *Mater. Sci. Eng.* A **399** 13–25
[63] Wang Y D, Wang X L, Stoica A D, Richardson J W and Peng R L 2003 *J. Appl. Crystallogr.* **36** 14–22

GEOPHYSICAL RESEARCH LETTERS, VOL. 33, L24303, doi:10.1029/2006GL028237, 2006

Elastic anisotropy in hcp metals at high pressure and the sound wave anisotropy of the Earth's inner core

Daniele Antonangeli,[1] Sébastien Merkel,[2] and Daniel L. Farber[1]

Received 25 September 2006; revised 8 November 2006; accepted 14 November 2006; published 19 December 2006.

[1] We compare the elastic anisotropy in hcp metals at high pressure obtained by radial diffraction measurements with those determined by other experiments and calculations. Our analysis demonstrates that in non-hydrostatically compressed hcp metals the assumption of a single uniform macroscopic stress applied to all grains in the polycrystal for the inversion of the lattice strain equations is violated due to plastic deformation. In addition, the derived apparent moduli and elastic anisotropy differ significantly from those derived from single crystals. We propose that for cobalt, rhenium and iron, the elastic anisotropy in the meridian plane is best described by a sigmoidal shape for the longitudinal velocity, with the fastest direction along the c-axis. Based on these results, we suggest that preferential alignment of the c-axis of iron crystallites along the Earth's rotation axis is the most plausible explanation for the observed P-wave travel time anomalies in the inner core. **Citation:** Antonangeli, D., S. Merkel, and D. L. Farber (2006), Elastic anisotropy in hcp metals at high pressure and the sound wave anisotropy of the Earth's inner core, *Geophys. Res. Lett.*, *33*, L24303, doi:10.1029/2006GL028237.

1. Introduction

[2] The elastic anisotropy is one of the most striking physical properties of the Earth's inner core. It is well established from seismic travel time analysis and free oscillation studies that P-waves travel 3–4% faster along the rotation axis than in the equatorial plane [*Woodhouse et al.*, 1986; *Tromp*, 1993; *Romanowicz et al.*, 1996; *Song*, 1997; *Garcia and Souriau*, 2000]. It is commonly thought that preferential alignment of iron crystals within the inner core is required to explain this feature, but various models of inner core texture differ in the crystallite orientation, the magnitude of the texture and the mechanism for generating the crystallographic preferred orientation. Suggestions include texturing during solidification of the inner core [*Bergman*, 1997], plastic flow induced by the magnetic field in the outer core as it solidifies at its inner boundary [*Karato*, 1993], large-scale convective flow in the inner core [*Jeanloz and Wenk*, 1988; *Yoshida et al.*, 1996], gravitational coupling with the mantle [*Buffet*, 1997], or, electromagnetic shear stresses [*Buffet and Wenk*, 2001]. Differentiation between these models is limited by the dearth of conclusive data on the elastic anisotropy of hcp iron, which is believed to be the stable form of iron at inner core conditions.

[3] The critical experiments to directly address this problem would be measurements of the single-crystal elastic moduli of hcp iron, as, once all the elements of the elastic tensor are known, the velocity in any arbitrary direction of the crystal can be derived. Unfortunately, the bcc-to-hcp phase transition at about 13 GPa prevent to retain single crystals above this pressure. Therefore, all experimental investigations have been conducted on polycrystalline samples [*Singh et al.*, 1998; *Mao et al.*, 1998; *Giefers et al.*, 2002; *Antonangeli et al.*, 2004b; *Merkel et al.*, 2005]. While, in theory, this does not preclude one from extracting single crystal tensor properties, in practice this has proved to be a very difficult inverse problem. In particular, the longitudinal sound velocity V_L as a function of the direction of propagation in the meridian (a–c) plane deduced from radial x-ray diffraction (RXRD) [*Singh et al.*, 1998; *Mao et al.*, 1998; *Merkel et al.*, 2005] has a "bell-like" shape, characterized by maximum sound speed at 45° from the basal (a–b) plane, and almost identical sound velocities along the a- and c-axis (Figure 1). These findings are not supported by first principle calculations present in literature, which are themselves quite contradictory, not only in the magnitude of the anisotropy, but as well as in the shape [*Stixrude and Cohen*, 1995; *Söderlind et al.* 1996; *Steinle-Neumann et al.* 1999; *Laio et al.* 2000; *Vočadlo et al.* 2003] (Figure 1). These striking discrepancies highlight the difficulty in performing reliable calculations at core conditions and cast doubt on the RXDR results. Indeed, single crystal elastic moduli derived using RDXD have been controversial as the calibration of stress and the effects of lattice preferred orientations (LPO) on the analysis present significant challenges [*Matthies et al.*, 2001a; *Merkel et al.*, 2005]. Furthermore, it has been shown that plastic deformation can have a strong influence on the lattice strains [*Daymond et al.*, 1999; *Daymond and Bonner*, 2003; *Weidner et al.*, 2004; *Li et al.*, 2004]. Nevertheless, the RXRD results on iron have been widely quoted, often without the necessary qualifications.

[4] Thus, we have considered cobalt - the best studied example of a hcp metal - in order to derive the acoustic anisotropy using a number of different approaches. In the following section we invert the lattice strain equations in order to derive the elastic moduli for cobalt from RXDR measurement and compare these values with results from single-crystal measurements. We then test our new model against data from rhenium and iron, discussing in detail the limitations of radial diffraction in determining elastic properties of hcp metals and quantifying the degree to which these estimates are biased. Finally, we show that a sigmoidal shape for the acoustic anisotropy gives the best fit for all the

[1] Energy and Environment Directorate, Lawrence Livermore National Laboratory, Livermore, California, USA.
[2] Laboratoire de Structure et Propriétés de l'Etat Solide, UMR CNRS 8008, Université des Sciences et Technologies de Lille, Villeneuve d'Ascq, France.

0094-8276/06/2006GL028237$05.00

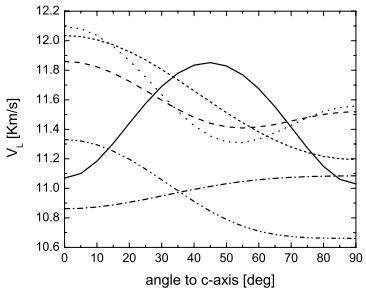

Figure 1. Longitudinal sound velocity V_L as a function of propagation direction with respect to the c-axis, for hcp iron at ~210 GPa. Solid line, RXDR results by *Mao et al.* [1998]. Calculations, dashed line *Stixrude and Cohen* [1995]; dotted line *Steinle-Neumann et al.* [1999]; dash-dotted line *Söderlind et al.* [1996]; short-dashed line *Laio et al.* [2000]; dash-dot-dotted line *Vočadlo et al.* [2003].

hcp metals studied so far, and present the implications of our model for the structure of the Earth's inner core.

2. Results on Cobalt

[5] Presently, cobalt provides the most fertile ground for testing elasticity models for hcp metals, as there exist extensive experimental investigations, at ambient conditions [*Schober and Dederichs*, 1979], and at high pressure, by RXRD [*Merkel et al.*, 2006], inelastic x-ray scattering (IXS) [*Antonangeli et al.*, 2004a, 2005], impulsive stimulated light scattering (ISLS) [*Goncharov et al.*, 2004; *Crowhurst et al.*, 2006], and Raman spectroscopy [*Goncharov et al.*, 2004], as well as ab initio calculations [*Steinle-Neumann et al.*, 1999].

[6] In this report, we have derived the elastic moduli of hcp cobalt at high pressure within the framework of the lattice strain theory of *Singh et al.* [1998], by inverting the d-spacing measured for polycrystalline samples compressed non-hydrostatically within a diamond anvil cell (DAC) up to 43 GPa. The RXRD data we used to test the different inversion schemes are a subset of those reported by *Merkel et al.* [2006]. For clarity, and to avoid comparison of data derived from samples compressed in different configurations, and hence under possibly different stress conditions, we have considered only the results of the first run carried out on beamline BL13A at the Photon Factory (also the largest data set, containing the highest pressures).

[7] Samples compressed without a hydrostatic medium in a DAC are subjected to a much larger stress in the axial direction than in the radial direction. Therefore, in our model, we assumed an axial stress, but allowed the maximum stress direction to be shifted slightly with respect to the main compression axis of the cell. Furthermore, we assumed that the lattice strains result from only elastic deformation and neglected the pressure gradient within the cell. We then inverted the lattice strain equations using two different textural assumptions: 1) a random orientation distribution function (ODF)(purely randomly oriented powder); 2) using the experimentally determined ODF [*Merkel et al.*, 2006]. We have also tested different micro-mechanical models against the results of the inversions. These include Voigt and Reuss average, as well as the BPGeo micro-mechanical model by *Matthies et al.* [2001b], in which a texture-weighted geometric mean is applied in the stress analysis. Still, even after accounting for effects of the LPO, the derived elastic moduli from these models differ significantly from both the previous experimental and theoretical determinations [*Schober and Dederichs*, 1979; *Goncharov et al.*, 2004; *Antonangeli et al.*, 2004a; *Crowhurst et al.*, 2006; *Steinle-Neumann et al.*, 1999]. Overall the best agreement is achieved for the Reuss average including the effects of LPO (Table 1). However, the model values of C_{11}, C_{33}, C_{12} and C_{13} are 20% off with

Table 1. Equivalent Hydrostatic Pressure and Apparent Elastic Moduli Fitted to the Experimental Results[a]

P	C_{11}	C_{33}	C_{12}	C_{13}	C_{44}	C_{66}
			Random ODF and Reuss Average			
3.8(1)	300(12)	326(13)	192(7)	151(4)	238(13)	54(6)
8.5(1)	322(12)	349(14)	208(7)	164(4)	273(15)	57(7)
15.1(1)	300(12)	318(13)	243(7)	216(5)	500(32)	29(16)
19.4(1)	303(13)	315(14)	260(8)	240(6)	596(40)	21(20)
24.6(1)	385(14)	411(16)	263(8)	214(5)	417(23)	61(12)
30.3(1)	404(15)	426(16)	282(8)	235(5)	479(27)	61(14)
34.4(2)	417(15)	437(16)	294(9)	250(5)	522(29)	61(15)
42.7(2)	465(17)	480(18)	313(10)	269(6)	534(30)	76(15)
			Experimental ODF and Reuss Average			
3.5(1)	296(11)	344(14)	187(6)	144(4)	223(12)	55(6)
8.4(1)	313(11)	387(15)	191(7)	156(5)	248(13)	61(6)
14.9(1)	320(12)	379(15)	232(7)	188(5)	392(22)	44(11)
19.1(1)	331(12)	390(16)	246(7)	205(5)	449(25)	42(13)
24.3(1)	382(14)	472(19)	241(8)	197(6)	358(19)	71(9)
30.0(1)	412(15)	488(19)	266(9)	212(6)	398(21)	73(10)
34.1(2)	436(16)	488(19)	288(9)	225(6)	432(23)	74(11)
42.5(2)	468(17)	539(21)	292(10)	249(6)	456(24)	88(12)

[a]Numbers in parentheses indicate the uncertainty on the last digits. All the values are in GPa.

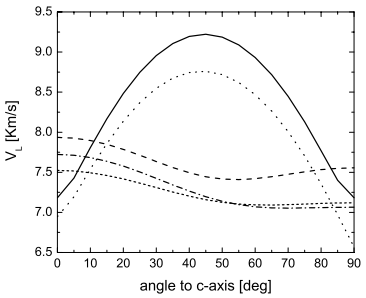

Figure 2. Longitudinal sound velocity V_L as a function of propagation direction with respect to the c-axis, for hcp cobalt at 35 GPa. Solid (dotted) line, RXDR results using random (experimentally determined) ODF; dash-dotted line, IXS results on single crystal [*Antonangeli et al.*, 2004a]; dashed (short-dashed) line, GGA (LDA) calculations [*Steinle-Neumann et al.*, 1999].

respect to those measured with other methods. More importantly, for the shear moduli C_{66} and C_{44}, discrepancies are up to 50% and 300%, respectively.

[8] Figure 2 shows the V_L anisotropy in hcp cobalt at 35 GPa: as in the case of hcp iron, inversion of the lattice strain equations give a "bell-like" shape, in direct contrast to experimental measurements on single crystal and calculations which are in good agreement and suggest a sigmoidal shape, with the fastest direction along the c-axis. The most distinctive feature of the shape of the sound-wave anisotropy derived from RXRD measurements is the maximum at 45°, driven by the high value of C_{44} with respect to C_{11} and C_{33}. The values of C_{11} and C_{33} critically hinge on the inclusion of the LPO in the model and when the LPO are not included, these moduli are surprisingly almost equal in magnitude. When the effects the LPO are properly accounted for, we obtain a sound speed along the c-axis about 6% higher than the one along the a-axis, in qualitative agreement with IXS measurements and first principle calculations. However, even when carefully considering the effects of LPO, the derived shear moduli can not be rectified. In order to evaluate the robustness of the RXRD determination of C_{44}, we can compare the pressure evolution of C_{44} in the 0 to 45 GPa pressure range as obtained by RXRD, with literature experimental and theoretical determinations (Figure 3). Notably, while most of the previous results agree to within 25%, the RXRD derived values for C_{44} (irrespectively of the effects of the LPO) are not only more scattered, with larger uncertainties, but, most importantly, are about 3 times larger. Furthermore, the C_{44} pressure derivative estimated from the RXRD results is significantly larger than the ones indicated by the other methods.

3. Discussion

[9] The discrepancy in the moduli derived from RXRD with respect to other experimental techniques and theoretical predictions illustrated in the previous section in the case of cobalt, seems to be a general feature of hcp metals. In the case of rhenium, we observe a large difference between the elastic moduli determined by RXRD [*Duffy et al.*, 1999], ultrasonic data [*Manghnani et al.*, 1974] and theoretical calculations [*Steinle-Neumann et al.*, 1999]. Specifically, RXRD measurements provide an unreasonably high pressure dependence for C_{13} and C_{44}, while the pressure dependence of C_{33} is unexpectedly low. In further support of this general observation, the pressure dependence of C_{44} in iron derived from lattice strain experiments [*Mao et al.*, 1998] is much larger than that estimated from Raman measurements [*Merkel et al.*, 2000]. As a consequence, in the case of cobalt, rhenium, and iron, inversion of RXDR data gives a "bell-like" shape for the anisotropy of the longitudinal sound velocity in the meridian plane, with a maximum at 45° and similar velocities along the c- and a-axis, in contrast to theoretical calculations and results from other experimental techniques.

[10] To understand these systematic discrepancies, it is worthwhile to recall that the theory that forms the basis of the lattice strain equations is formulated within the limit of purely elastic deformation, while in hcp metals, at only moderate pressures, the plastic deformation and consequently development of texture is quite important [*Wenk et al.*, 2000; *Merkel et al.*, 2006]. The stress inhomogeneities resulting from grain to grain interaction in combination with effects of plastic deformation undermine the validity of the boundary condition of a single uniform macroscopic stress applied to all the grains. Therefore the elastic moduli derived from RXRD measurements on hcp metals and, more generally in the presence of plastic deformations, have to be considered "apparent" elastic moduli, affected by the different stresses felt by the different crystallographic planes. These apparent C_{ij} can differ from the single-crystal elastic moduli, especially in the case of shear moduli, which are more sensitive to non-homogeneous stress-strain conditions. This is particularly true in hcp systems, where the apparent C_{44} is strongly linked to plastic shear strain on the

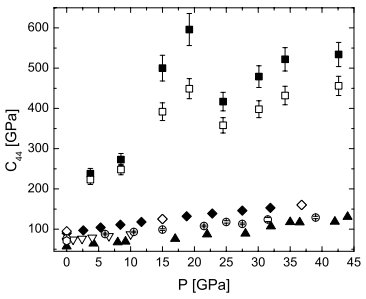

Figure 3. Pressure evolution of C_{44}. Open (full) squares, RXRD results using random (experimentally determined) ODF; open (full) diamonds, LDA (GGA) calculations [*Steinle-Neumann et al.*, 1999]; open hexagon, ambient pressure determination [*Schober and Dederichs*, 1979]; full triangles, Raman measurements [*Goncharov et al.*, 2004]; open inverted triangles, ISLS results [*Crowhurst et al.*, 2006]; open circles, IXS measurements [*Antonangeli et al.*, 2004a].

basal plane. Indeed, a strong influence of plastic deformation on the lattice strain and elastic moduli deduced using this technique has been also reported in other experiments on hcp metals at ambient pressure (i.e. Be and Ti) [*Daymond et al.*, 1999; *Daymond and Bonner*, 2003] and for MgO [*Weidner et al.*, 2004; *Li et al.*, 2004]. In particular, it has been observed that while some crystallographic planes display a behavior very similar to what expected for purely elastic deformation, other do not, showing different effective stresses.

[11] Therefore, present and previous results strongly suggest that the "bell-like" shape proposed for the anisotropy of the longitudinal sound velocity in the meridian a–c plane in hcp iron [*Mao et al.*, 1998] is likely strongly biased by limitations in the model used for the analysis of the otherwise accurate radial diffraction data. Instead, both a sigmoidal shape and a significantly higher speed along the c-axis, with respect to the basal plane, seems to be general features of hcp metals (Co, Re and Fe in particular) at high pressure and ambient temperature. A sigmoidal shape of the anisotropy for hcp iron is in qualitative agreement with most of the calculations, is compatible with the experimental evidence directly derived by IXS measurements on textured sample [*Antonangeli et al.*, 2004b], and also reconciles the suggestion of *Giefers* [2004], who propose a velocity about 10% higher along the c-axis than in the basal plane for hcp iron single crystal at 130 GPa. More specifically, considering the observation on textured sample of a faster velocity at 50° than at 90° with respect to the compression axis of the diamond anvil cell [*Antonangeli et al.*, 2004b], and the developed preferential alignment [*Wenk et al.*, 2000], we argue a shape such as the one proposed by *Laio et al.* [2000] or *Vočadlo et al.* [2003] to be more consistent with all the experimental evidence than the form suggested by *Stixrude and Cohen* [1995], or *Steinle-Neumann et al.* [1999] (Figure 1).

4. Conclusions

[12] Effect of high temperature on the elastic moduli of hcp iron at high pressure are still largely debated and inconclusive. While high temperature might possibly change the magnitude of the crystalline anisotropy, strong effects at constant density on the overall shape seem unlikely. Thus, on the basis of the present results, and assuming the effects of high temperature on the shape of the crystalline anisotropy small at constant density, we suggest a preferential alignment of the c-axis of the iron crystallites along the Earth's rotation axis provides the simplest explanation of the P-wave travel time anomalies observed in the inner core. Furthermore, alignment along the Earth spin axis of the stiffest elastic axis of the constituent crystals is expected in several simple textural models. This would be the case for diffusive mechanisms, convective flow in the inner core, or to minimize the strain energy associated to the non-hydrostatic stress field induced by the inner core rotation. On the other hand, if dislocation glide was the most efficient deformation mechanism, as under the influence of Maxwell shears stresses [*Buffet and Wenk*, 2001], the basal planes would have the tendency to be aligned parallel to the Earth's rotation axis [*Wenk et al.*, 2000], leading to faster seismic waves in the equatorial plane, in evident disagreement with the observed P-wave travel time anomalies. These considerations, to a great degree, remove the need to call on more complicated and anomalous dynamical explanations that would be required by the "bell-like" shape. Finally, although or model is most likely an over-simplification as it does not take into consideration local changes in the direction and degree of crystallographic alignment, if it is assumed that hcp cobalt and hcp iron have an elastic anisotropy of the same magnitude at the same lattice compression ratio, an alignment of about one-third of the iron crystallites along the Earth's rotation axis in an otherwise random medium is able to explain the seismic observations.

[13] **Acknowledgments.** The authors wish to thank W. Durham for the critical reading of the manuscript. This work was performed under the auspices of the U.S. Department of Energy by University of California, Lawrence Livermore National Laboratory, under contract W-7405-Eng-48, UCRL-JRNL-223061.

References

Antonangeli, D., M. Krisch, G. Fiquet, D. L. Farber, C. M. Aracne, J. Badro, F. Occelli, and H. Requardt (2004a), Elasticity of cobalt at high pressure studied by inelastic x-ray scattering, *Phys. Rev. Lett.*, *93*, 215505.

Antonangeli, D., F. Occelli, H. Requardt, J. Badro, G. Fiquet, and M. Krisch (2004b), Elastic anisotropy in textured hcp-iron to 112 GPa from sound wave propagation measurements, *Earth Planet. Sci. Lett.*, *225*, 243–251.

Antonangeli, D., M. Krisch, G. Fiquet, J. Badro, D. L. Farber, A. Bossak, and S. Merkel (2005), Aggregate and single-crystalline elasticity of hcp cobalt at high pressure, *Phys. Rev. B*, *72*, 134303.

Bergman, M. I. (1997), Measurements of elastic anisotropy due to solidification texturing and the implications for the Earth's inner core, *Nature*, *389*, 60–63.

Buffet, B. A. (1997), Geodynamic estimate of the viscosity of the Earth's inner core, *Nature*, *388*, 571–573.

Buffet, B. A., and H. R. Wenk (2001), Texturing of the inner core by Maxwell stresses, *Nature*, *413*, 60–64.

Crowhurst, J. C., D. Antonangeli, J. M. Brown, A. F. Goncharov, D. L. Farber, and C. M. Aracne (2006), Determination of the high-pressure elasticity of cobalt from measured interfacial acoustic wave velocities, *Appl. Phys. Lett.*, *89*, 111920.

Daymond, M. R., and N. W. Bonner (2003), Lattice strain evolution in IMI 834 under applied stress, *Mater. Sci. Eng. A*, *340*, 272–280.

Daymond, M. R., A. M. Bourke, and R. B. Von Dreele (1999), Use of Rietveld refinement to fit a hexagonal crystal structure in the presence of elastic and plastic anisotropy, *J. Appl. Phys.*, *85*, 730–747.

Duffy, T. S., G. Shen, D. L. Heinz, J. Shu, Y. Ma, H. K. Mao, R. Hamley, and A. K. Singh (1999), Lattice strain of gold and rhenium under non-hydrostatic compression to 37 GPa, *Phys. Rev. B*, *60*, 15,063–15,073.

Garcia, R., and A. Souriau (2000), Inner core anisotropy and heterogeneity level, *Geophys. Res. Lett.*, *27*, 3121–3124. (Correction, *Geophys. Res. Lett., 28*, 85–86, 2000.)

Giefers, H. (2004), Phonon DOS in oriented hcp iron and SnO from high-pressure NIS, paper presented at Phonons in Crystalline Materials Workshop, Eur. Synchrotron Radiat. Facil., Grenoble, France, 8–10 Feb.

Giefers, H., R. Lübbers, K. Ruprecht, G. Wortmann, D. Alfeé, and A. I. Chumakov (2002), Phonon spectroscopy of oriented hcp iron, *High Pressure Res.*, *22*, 501–506.

Goncharov, A. F., J. C. Crowhurst, and J. M. Zaug (2004), Elastic and vibrational properties of cobalt to 120 GPa, *Phys. Rev. Lett.*, *92*, 115502.

Jeanloz, R., and H. R. Wenk (1988), Convection and anisotropy of the inner core, *Geophys. Res. Lett.*, *15*, 72–75.

Karato, S. (1993), Inner core anisotropy due to magnetic field-induced preferred orientation of iron, *Science*, *262*, 1708–1711.

Laio, D., S. Bernard, G. L. Chiarotti, S. Scandolo, and E. Tosatti (2000), Physics of iron at Earth's core conditions, *Science*, *287*, 1027–1030.

Li, L., D. J. Weidner, J. Chen, M. T. Vaughan, M. Davis, and W. B. Durham (2004), X-ray strain analysis at high pressure: Effect of plastic deformation in MgO, *J. Appl. Phys.*, *95*, 8357–8365.

Manghnani, M. H., K. Katahara, and E. S. Fisher (1974), Ultrasonic equation of state of rhenium, *Phys. Rev. B*, *9*, 1421–1431.

Mao, H. K., J. Shu, G. Shen, R. J. Hemley, B. Li, and A. K. Singh (1998), Elasticity and rheology of iron above 220 GPa and the nature of the Earth's inner core, *Nature*, *396*, 741–743. (Correction, *Nature, 399*, 280, 1999.)

Matthies, S., S. Merkel, H. R. Wenk, R. J. Hamley, and H. K. Mao (2001a), Effect of texture on the high pressure elasticity of iron from x-ray diffraction, *Earth Planet. Sci. Lett.*, *194*, 201–212.

Matthies, S., H. G. Priesmeyer, and M. R. Dayamond (2001b), On the diffractive determination of single-crystal elastic constants using polycrystalline samples, *J. Appl. Crystallogr.*, *34*, 585–601.

Merkel, S., A. F. Goncharov, H. K. Mao, P. Gillet, and R. J. Hamley (2000), Raman spectroscopy of iron to 152 gigapascals: Implications for Earth's inner core, *Science*, *288*, 1626–1629.

Merkel, S., J. Shu, P. Gillet, H. K. Mao, and R. J. Hamley (2005), X-ray diffraction study of the single-crystal elastic moduli of ϵ-Fe up to 30 GPa, *J. Geophys. Res.*, *110*, B05201, doi:10.1029/2004JB003197.

Merkel, S., N. Miyajima, D. Antonangeli, G. Fiquet, and T. Yagi (2006), Lattice preferred orientation and stress in polycrystalline hcp-Co plastically deformed under high pressure, *J. Appl. Phys.*, *100*, 023510.

Romanowicz, B., X. D. Li, and J. Durek (1996), Anisotropy in the inner core: Could it be due to low-order convection?, *Science*, *274*, 963–966.

Schober, H. R., and H. Dederichs (1979), Elastic, piezoelectric, pyroelectric, piezooptic, electrooptic constants and nonlinear dielectric susceptibilities of crystals, *Landolt-Börnstein Numerical Data and Functional Relationships in Science and Technology*, *New Ser. III*, vol. 11a, p. 40, Springer, New York.

Singh, A. K., H. K. Mao, J. Shu, and R. J. Hamley (1998), Estimation of the single-crystal elastic moduli from polycrystalline x-ray diffraction at high pressure: Application to FeO and iron, *Phys. Rev. Lett.*, *80*, 2157–2160.

Söderlind, P., J. A. Moriarty, and J. M. Wills (1996), First-principle theory of iron up to earth-core pressures: Structural, vibrational and elastic properties, *Phys. Rev. B*, *53*, 14,063–14,072.

Song, X. (1997), Anisotropy of the Earth's inner core, *Rev. Geophys.*, *35*, 297–313.

Steinle-Neumann, G., L. Stixrude, and R. E. Cohen (1999), First-principle elastic constants for the hcp transition metals Fe, Co and Re at high pressure, *Phys. Rev. B*, *60*, 791–799. (Erratum, *Phys. Rev. B, 69*, 219903(E), 2004.)

Stixrude, L., and R. E. Cohen (1995), High-pressure elasticity of iron and anisotropy of Earth's inner core, *Science*, *267*, 1972–1975.

Tromp, J. (1993), Support for anisotropy of the Earth's inner core from free oscillations, *Nature*, *366*, 678–681.

Vočadlo, L., D. Alfè, M. J. Gillian, and G. D. Price (2003), The properties of iron under core conditions from first principle calculations, *Phys. Earth Planet. Inter.*, *140*, 101–125.

Weidner, D. J., L. Li, M. Davis, and J. Chen (2004), Effect of plasticity on elastic modulus measurements, *Geophys. Res. Lett.*, *31*, L06621, doi:10.1029/2003GL019090.

Wenk, H. R., S. Matthies, R. J. Hemley, H. K. Mao, and J. Shu (2000), The plastic deformation of iron at pressures of the Earth's inner core, *Nature*, *405*, 1044–1047.

Woodhouse, J. H., D. Giardini, and X. D. Li (1986), Evidence for inner core anisotropy from free oscillations, *Geophys. Res. Lett.*, *13*, 1549–1552.

Yoshida, S., I. Sumita, and M. Kumazawa (1996), Growth model of the inner core coupled with the outer core dynamics and the resulting elastic anisotropy, *J. Geophys. Res.*, *101*, 28,085–28,104.

D. Antonangeli and D. L. Farber, Energy and Environment Directorate, Lawrence Livermore National Laboratory, 7000 East Avenue, Livermore, CA 94550, USA. (antonangeli3@llnl.gov)

S. Merkel, Laboratoire de Structure et Propriétés de l'Etat Solide, UMR CNRS 8008, Université des Sciences et Technologies de Lille, Bâtiment C6, F-59655 Villeneuve d'Ascq, France.

JOURNAL OF APPLIED PHYSICS **100**, 023510 (2006)

Lattice preferred orientation and stress in polycrystalline hcp-Co plastically deformed under high pressure

Sébastien Merkel[a] and Nobuyoshi Miyajima[b]
Institute for Solid State Physics, University of Tokyo, Kashiwanoha 5-1-5, Kashiwa, Chiba 277-8581, Japan

Daniele Antonangeli[c]
European Synchrotron Radiation Facility, Boîte Postale 220, F-38043 Grenoble Cedex, France

Guillaume Fiquet
Institut de Minéralogie et de Physique des Milieux Condensés, UMR CNRS 7590, Université Pierre-et-Marie-Curie, Paris 6, 75015 Paris, France and Institut de Physique du Globe de Paris, 4 Place Jussieu, 75252 Paris Cedex 05, France

Takehiko Yagi
Institute for Solid State Physics, University of Tokyo, Kashiwanoha 5-1-5, Kashiwa, Chiba 277-8581, Japan

(Received 7 November 2005; accepted 10 May 2006; published online 20 July 2006)

The results of x-ray diffraction data of a polycrystal under nonhydrostatic compression are analyzed for lattice preferred orientation and stress using lattice strain theories with an application to hcp-Co deformed up to 42.6 GPa in the diamond anvil cell. We obtain a pure [001] fiber texture that develops primarily between 0 and 15 GPa. We also show that for hcp metals the hypothesis of uniform stress across grains and lattice planes cannot be applied. This implies that the effective single crystal elastic moduli deduced from x-ray diffraction under Reuss or geometric averages consistently differ from those measured with other techniques, even after including effects of lattice preferred orientations. These results can be interpreted as an (*hkl*)-dependent effective differential stress resulting from plastic deformation. © *2006 American Institute of Physics*.
[DOI: 10.1063/1.2214224]

I. INTRODUCTION

The influence of pressure on the plastic and elastic properties of condensed matter is of fundamental importance for our understanding of material behavior under extreme conditions. In this sense, the properties of hexagonal-closed-packed (hcp) transition metals are of great interest as they tend to exhibit intriguing physical properties,[1–3] represent a challenge for first-principles calculations,[4] and also because the Earth's inner core is believed to be mainly composed of the hcp polymorph of Fe, ϵ-Fe.

Here, we focus on the interpretation of the diffraction patterns of a polycrystal under stress and their relation to elastic and plastic properties. Samples compressed in diamond anvil cell (DAC) experiments are submitted to axial deformation and can develop lattice preferred orientations (LPOs) that can be used to identify the dominant deformation mechanisms.[5] Nonhydrostatic stresses also introduce distortions of the crystal lattice that can be observed using x-ray diffraction. In the residual stress analysis,[6] the components of the mean macroscopic stress in the sample are determined using (a) single crystal elastic moduli,(b) measured *d* spacings in several sample directions, (c) information on the texture of the sample, and (d) a micromechanical model. In the inverse problem, the single crystal elastic moduli are inverted using the measured *d* spacings, texture, a micromechanical model, and the macroscopic stresses applied to the sample.[7,8] However, plastic deformation has been found to have an influence on lattice strains measured using diffraction[9–14] and application of these theories for polycrystals under high pressure has raised controversies. Results for hcp metals such as ϵ-Fe or Re are also known to vary significantly[15–19] and differ from those obtained using first-principles calculations[4,20–22] or measured using other experimental techniques.[23]

Co is located next to iron in the periodic table and the mechanical properties and high pressure behavior of the two elements are close. In an attempt to improve our understanding of the behavior of hcp metals under pressure, Co has been studied extensively. Under ambient conditions, it exhibits either the hcp or the metastable fcc crystal structure and transforms into the fcc structure at 695 K; at high pressure, it transforms into the fcc structure in the range of 105–150 GPa.[24] Its single crystal elastic moduli have been calculated using first principles techniques,[4] measured at ambient conditions using ultrasonic techniques,[25] at high pressure using inelastic x-ray scattering (IXS),[26] and deduced from Raman

[a]Present address: Laboratoire de Structure et Propriétés de l'Etat Solide, UMR CNRS 8008, Université des Sciences et Technologies de Lille, 59655 Villeneuve d'Ascq, France; electronic mail: sebastien.merkel@univ-lille1.fr
[b]Present address: Bayerisches Geoinstitut, Universität Bayreuth, D-95440 Bayreuth, Germany.
[c]Present address: Earth Science Division, Energy and Environment Directorate, Lawrence Livermore National Laboratory, 7000 East Avenue, Livermore, California 94550.

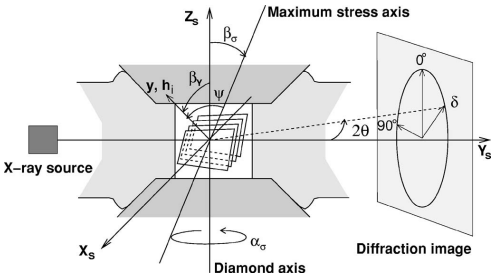

FIG. 1. Experimental setup. β_σ is the angle between the maximum stress axis and the compression axis $\mathbf{Z}_S$, β_y is the angle between the scattering vector $\mathbf{y}$ and $\mathbf{Z}_S$, and ψ is the angle between the maximum stress axis and the scattering vector $\mathbf{y}$. For a given diffraction peak, the normal to the diffracting planes $\mathbf{h}_i$ is aligned with the scattering vector $\mathbf{y}$.

spectroscopy.[3] Therefore, this material is an ideal candidate for testing x-ray diffraction stress and strain analyses in hcp metals.

II. EXPERIMENTAL DETAILS

Our dataset consists of three distinct experiments. Run 1 was performed on the ID9 beamline of the ESRF (Grenoble, France) and runs 2 and 3 on the BL13A beamline of the Photon Factory (Tsukuba, Japan) with a monochromatic x-ray beam of wavelength of 0.3689 Å (ID9) or 0.4258 Å (BL13A). At ESRF, two-dimensional diffraction data were collected on a 3450×3450 pixels MAR345 image plate. At the Photon Factory, we used a 3000×3000 pixels Rigaku image plate. Sample to detector distance, detector tilt, and pixel size ratios were calibrated using a Si (ID9) or Ag (BL13A) standard. In run 1, high pressure and sample deformation were achieved using a (DAC) equipped with diamonds of 300 μm culet diameter. In runs 2 and 3, we used diamonds of 350 μm culet diameter. To allow diffraction in a direction orthogonal to the compression axis (Fig. 1), the sample was confined in a x-ray transparent gasket made of a mixture of amorphous boron and epoxy in run 1 and a composite gasket made with amorphous boron, Kapton sheet, and epoxy[27] in runs 2 and 3. In all runs, the diameter of the sample chamber was 80–100 μm. Sample was a pure commercial powder of cobalt with a starting grain size of 1–2 μm and a ratio of hexagonal and cubic polymorph of 70%. In run 1, pressure was calibrated using a ruby ball while in runs 2 and 3, we added a layer of ruby powder on top of the sample. In run 1, pressures was gradually increased up to gasket failure at 20 GPa over 48 h. In runs 2 and 3, pressures were increased up to 42.6 GPa over 24 h and 12.8 GPa over 12 h, respectively. Figure 2 presents an example of the diffraction image we obtained at 42.6 GPa in experiment 2.

III. ANALYSIS

A. Extraction of texture

Data reduction was performed in a similar manner as in previous experiments.[5,17] After spatial and flat field corrections, the two-dimensional (2D) diffraction image is converted into series of one-dimensional (1D) diffraction pattern by binning the data in 5° intervals of the azimuthal angle δ. Each 1D pattern is then fitted individually using pseudovoigt peak profiles and locally linear background in order to extract the peak position and intensity for each reflection. For all pressures in runs 2 and 3, an orientation distribution function (ODF) was calculated using the intensities of the 100, 002, 101, 102, 110, 103, and 004 diffraction peaks using the WIMW algorithm as implement in the BEARTEX package[28] (Fig. 3).

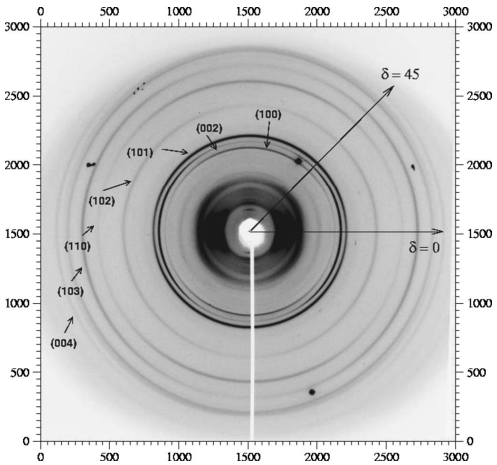

FIG. 2. Diffraction pattern for experiment 2 at 42.6 GPa. Large intensity region at the center of the image results from the diffraction of the Kapton supporting ring. Diffraction from the 100, 002, 101, 102, 110, 103, and 004 lines of the Co sample are labeled on the figure.

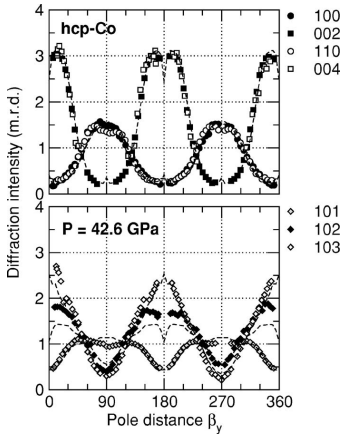

FIG. 3. Measured (symbols) and recalculated (dashed lines) intensities vs β_y for the 100, 002, 101, 102, 110, 103, and 004 diffraction lines at 42.6 GPa in run 2. Measured intensities have been scaled to match those recalculated from the ODF, expressed in mrd.

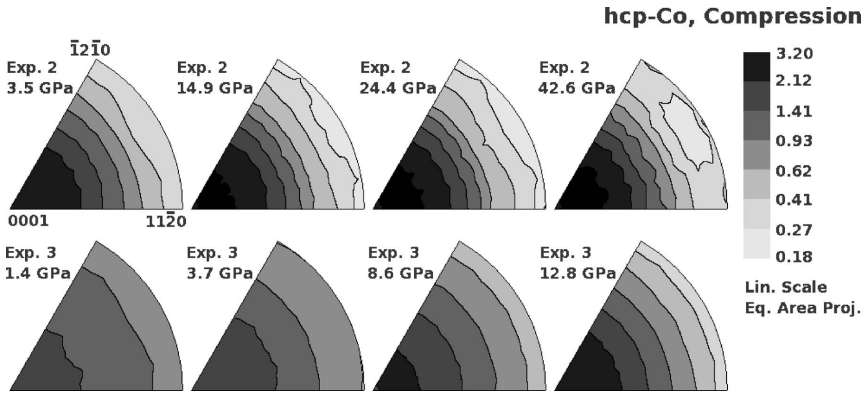

FIG. 4. Inverse pole figures illustrating the development of LPO in polycrystalline hcp-Co in compression for experiments 2 and 3. Equal area projection, linear scale, and contours in mrd.

We observe the development of a pure [001] fiber texture in runs 2 and 3 (Fig. 4). At the highest pressure in run 2, texture index is 1.90 and maximum pole density is 3.17 maximum of a random distribution (mrd) (Table I). For run 3, texture is similar and at 12.8 GPa, the texture index is 1.44 with a maximum pole density of 2.63 mrd. In run 1, on the other hand, we observed a progressive opening of the sample chamber during the compression. Texture could not be refined assuming axial symmetry and the measured *d* spacings did not always display the same maximum stress direction. We therefore conclude that this sample was not deformed with axial symmetry and cannot be analyzed with the present theory.

Figure 5 presents the minimum and maximum coefficients of the ODF fitted for all pressures in experiments 2 and 3. In experiment 2, we observed a very sharp increase of the texture strength with compression between 0 and 15 GPa, above which the texture saturates. In experiment 3, we observe a more progressive increase of the texture strength that did not saturate in the course of the experiment.

B. Inversion of elastic moduli

Samples in a DAC are generally submitted to a stress with a strong axial component: the stress imposed in the axial direction $\mathbf{Z}_S$ is typically larger than the stress imposed in the radial direction. However, if the diamonds are not exactly parallel or if a nonuniform layer of pressure calibrant was loaded above the sample, the stress geometry could differ from pure axial stress. Here, we assume that the stress remains largely axial but allow the axis of maximum stress to be slightly shifted from $\mathbf{Z}_S$, with the maximum stress direction represented by the two Euler angles α_σ and β_σ (Fig. 1). Therefore, we assume that the stress applied to the sample $\bar{\Sigma}$, expressed in K_S, is of the form $\bar{\Sigma}=\bar{\sigma}_P^S+\bar{\sigma}^S$, where $\bar{\sigma}_P^S$ is the hydrostatic pressure and $\bar{\sigma}^S$ is the deviatoric stress with

TABLE I. Pressures P, stress offset angles α_σ and β_σ, lattice strains $Q(hkl)$, texture indices F_2, and ODF maxima and minima for all points in experiments 2 and 3. Lattice strains values in this table are multiplied by 10^3. Pressure are expressed in gigapascals, ODF minima and maxima in multiples of a random distribution (mrd), and angles in degrees. Numbers in parentheses indicate the uncertainty on the last digit. Stars superscripts indicate values that were imposed in the nonlinear fitting.

R	P	α_σ	β_σ	$Q(100)$	$Q(002)$	$Q(101)$	$Q(102)$	$Q(110)$	$Q(103)$	$Q(004)$	F_2	Min	Max
2	3.5(1)	271(42)	0.2(4)	4.10(8)	2.71(7)	2.78(8)	1.87(9)	4.14(7)	1.99(7)	2.79(10)	1.57	0.29	2.73
2	8.4(1)	98(1)	6.8(4)	4.42(5)	2.94(5)	2.97(5)	2.06(7)	4.47(4)	2.10(5)	2.91(9)	1.77	0.2	3.02
2	14.9(1)	98(1)	6.1(5)	3.77(6)	2.23(4)	2.26(5)	1.39(7)	3.91(4)	1.29(5)	2.20(0)	1.81	0.18	3.08
2	19.2(1)	104(2)	5.6(5)	3.58(7)	2.12(4)	2.15(4)	1.27(8)	3.73(4)	1.16(5)	2.30(9)	1.84	0.2	3.1
2	24.4(1)	148(5)	4.1(2)	4.33(6)	2.84(5)	2.87(5)	1.98(7)	4.48(4)	1.82(4)	2.96(7)	1.89	0.17	3.19
2	30.1(1)	178(6)	4.1(1)	4.42(5)	3.01(3)	2.84(5)	1.89(8)	4.49(5)	1.93(3)	2.75(5)	1.93	0.17	3.21
2	34.3(2)	171(4)	6.4(1)	4.62(5)	3.23(4)	2.88(5)	1.82(9)	4.56(5)	2.05(3)	2.94(7)	1.92	0.16	3.17
2	42.6(2)	219(2)	8.8(3)	4.79(7)	3.52(5)	2.94(6)	2.02(8)	4.57(6)	2.19(3)	2.82(7)	1.91	0.19	3.17
3	1.4(1)	140(14)	5*	0.58(1)	0.49(2)	0.17(2)	0.09(4)	0.53(2)	0.20(3)	0.67(3)	1.06	0.64	1.61
3	2.3(1)	139(4)	20*	0.59(3)	0.46(3)	0.24(3)	0.12(5)	0.53(3)	0.17(4)	0.51(5)	1.11	0.55	1.75
3	3.7(1)	161(3)	28*	1.16(3)	0.76(2)	0.67(3)	0.44(5)	1.05(4)	0.49(4)	0.82(5)	1.13	0.53	1.82
3	6.2(1)	140(1)	26.6(4)	3.03(6)	1.86(5)	1.91(6)	1.25(7)	2.90(7)	1.30(6)	1.95(8)	1.17	0.46	1.93
3	8.6(1)	157(1)	22.7(2)	3.73(4)	2.22(4)	2.35(4)	1.44(7)	3.61(6)	1.51(6)	2.26(7)	1.23	0.48	2.07
3	12.8(1)	159(1)	25.0(2)	4.50(5)	2.63(5)	2.77(6)	1.78(8)	4.39(7)	1.73(6)	2.58(8)	1.44	0.29	2.63

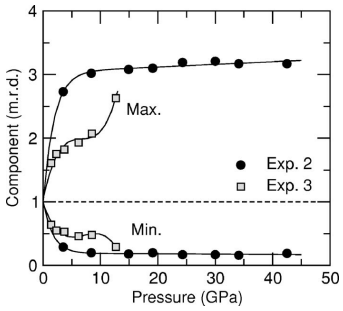

FIG. 5. Minimum and maximum components in the ODF as a function of pressure for experiments 2 and 3. Circles and squares are experimental data, lines are a guide to the eyes.

$$\bar{\sigma}_{ij}^{S} = g_{ik} g_{jl} \begin{bmatrix} -t/3 & 0 & 0 \\ 0 & -t/3 & 0 \\ 0 & 0 & 2(t/3) \end{bmatrix}_{kl}, \quad (1)$$

where $g(0, \beta_\sigma, \alpha_\sigma)$ is the proper rotation matrix and t the uniaxial stress component. This assumption neglects the effects of pressure gradients that could be present in the sample.

Assuming that the lattice strains result from only elastic distortion, that the sample is free of LPO, and that approximately the same conditions exist for all grains with the same orientation, one can show that the measured d spacings d_m can be expressed as[8]

$$d_m = d_0[1 + (1 - 3\cos^2\psi)Q(hkl)], \quad (2)$$

where d_0 is the d spacing under equivalent hydrostatic pressure, ψ is the angle between the normal to the diffracting plane and the maximum stress direction (Fig. 1), and the lattice strain $Q(hkl)$ is a function of stress and single crystal elastic moduli. If one includes effects of LPO, but still assumes that approximately the same conditions exist for all grains with the same orientation, the measured d spacings will deviate from Eq. (2) and not vary linearly with $(1 - 3\cos^2\psi)$, but they can still be related to stress and single crystal elastic moduli.[7,29]

In previous studies, lattice strains measurements have been used to refine effective single crystal elastic moduli from other hcp metals such as Fe or Re.[8,15–17,19] We did apply a lattice strains framework to this data, but the elastic moduli we obtained differ widely from those measured with other techniques,[3,4,25,26] even after including effects of LPO.[7] Lattice strains coefficients $Q(hkl)$ and maximum stress direction offset angles α_σ and β_σ we obtained for the assumption of a polycrystal free of LPO are shown in Table I. The maximum stress axis offset β_σ ranged from 0° to 9° and 5° to 28° in runs 2 and 3, respectively, and were found to be very stable relative to assumptions made. In general, the best agreement for elastic moduli is obtained under the Reuss average and including effects of LPO. Results under this approximation agree with other techniques within 20% for C_{11}, C_{33}, C_{12}, and C_{13}. However, the effective shear elastic moduli deduced from x-ray diffraction differ significantly from those measured with other methods: under the best approximation, C_{66} deduced from our data is approximately 30%–50% too low, while C_{44} is about 300% too large.

C. Inversion of stress

Indeed, a polycrystalline sample subject to plastic deformation can develop heterogeneities from grain to grain, at grain boundaries, or within the grain themselves that can be incompatible with the concept of lattice strain theories. In such cases, the assumption of a single uniform macroscopic stress applied to all grains and lattice planes within the sample can fail, and stresses deduced for various lattice planes might vary.[9–14]

To investigate this issue, we performed inversions of the data assuming elastic moduli from generalized gradient approximation (GGA) calculations[4] or IXS measurements[26] and that the maximum stress orientation offset angles α_σ and β_σ are equal for all planes. We adjusted the d spacings under equivalent hydrostatic pressure $d_0(hkl)$ and effective uniaxial stress component t_{hkl} independently for each lattice plane assuming the offset values for the maximum stress directions α_σ and β_σ found when refining elastic moduli (Table I). Cell parameters a and c, deduced from the fitted $d_0(hkl)$, were used to calibrate the hydrostatic pressure using a known equation of state.[30]

As demonstrated in Fig. 6, the measured d spacings do agree with our hypothesis, i.e., measurements of d spacings for equivalent orientations do agree, and the recalculated d spacings fit the experimental data. Results are presented in Tables II and III and Fig. 7 for runs 2 and 3 and calculations under the Reuss average including effects of LPO. Pressures in Tables II and III are averages of the pressure obtained using all approximations of elastic moduli. Differences between pressures obtained for various models never exceeded 0.2 GPa. Maximum stress is observed for basal and prismatic planes while pyramidal planes such as (101), (102), or (103) display a relatively low effective stress.

IV. DISCUSSION

A. Lattice preferred orientation

The [001] fiber texture we observe is typical for hcp metals under compression for which the deformation is primarily controlled by basal or prismatic slip.[31] More relevant is the evolution of the texture strength with compression. As demonstrated in Fig. 5, most of the texture development in these experiments occurs at relatively low pressure, between 0 and 15 GPa.

This can be related to finite element modelings of the behavior of diamonds and gaskets in DAC experiments for which it was shown that the distance between the anvil tips decreases significantly in the low pressure range and later saturates.[32] Therefore, polycrystalline samples in the diamond anvil cell are submitted to a more significant plastic deformation in the first part of the compression. For flat diamonds with 350 μm culet diameters, as used in these experiments, this corresponds to a pressure range of 0–15 GPa.

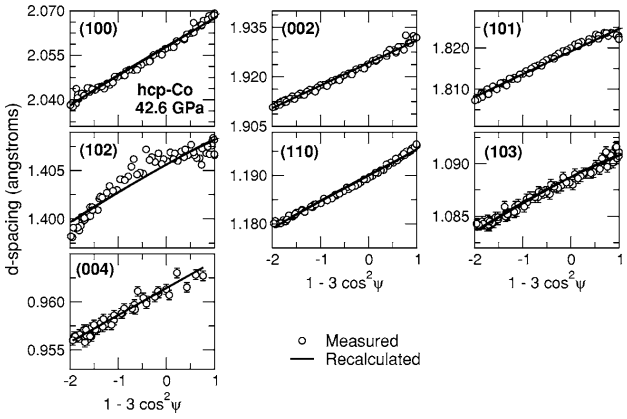

FIG. 6. Measured and recalculated d spacings vs $(1-3\cos^2\psi)$ at 42.6 GPa in run 2, where ψ is the angle between the normal to the diffraction plane $\mathbf{h}_i$ and the maximum stress direction (Fig. 1).

For bevel anvils with 50 μm culet diameters, plastic deformation would occur over a pressure range on the order of 0–200 GPa.[32]

In our experiments, samples were submitted to an important plastic deformation up to pressures on the order of 15 GPa. Above this point, they were already strongly textured and the relatively low plastic deformation imposed later in the experiment did not modify the LPO pattern. This is a limiting factor for high pressure studies of LPO with the DAC but it can be overcome by making use of phase transitions, amorphization, or recrystallization. Indeed, LPOs in DAC have been shown to evolve at pressures well above the range presented here.[33]

B. Stress and elasticity

Development of LPO and therefore activation of plastic deformation was very efficient in these experiments. We find that in this case, the single crystal elastic moduli extracted from radial diffraction data are significantly different that those obtained from other techniques.[3,4,25,26] The effect is most pronounced for the shear elastic moduli C_{66} and C_{44} with an overstimation of C_{44} from radial diffraction of up to 300%. This observation can be related to independent estimations of elastic moduli from radial diffraction on hcp-Fe in which the value obtained for C_{44} varied significantly.[15–17] Radial diffraction measurements have also been known to overestimate the pressure dependence of C_{44} and C_{13} of Re.[19]

Interestingly, as for the measurements of lattice strains, the deduced stresses t_{hkl} seem to be consistent when plotted as a function of

$$\cos^2\rho = 3a^2l^2/[4c^2(h^2+hk+k^2)+3a^2l^2], \quad (3)$$

where ρ is the angle between (002) and (hkl) (Fig. 8). This can be misleading in the analysis of radial diffraction data as a similar relation is expected in the case of a purely elastic model with no effect of LPO.[8]

The lattice planes can be grouped into four families: (i) (100) and (110), (ii) (102) and (103), (iii) (002) and (004), and (iv) (101). Prismatic planes such as (100) or (110) are submitted to a large effective stress; at the end of the defor-

TABLE II. Stresses deduced assuming single crystal elastic moduli from GGA calculations (Ref. 4) under the Reuss average and using the experimental ODF, expressed in gigapascals, for all pressures in experiments 2 and 3. Numbers in parentheses indicate the uncertainty on the last digit.

R	P	t(100)	t(002)	t(101)	t(102)	t(110)	t(103)	t(004)
2	3.5(1)	2.80(2)	2.48(3)	1.77(2)	1.21(3)	2.83(3)	1.40(4)	2.50(6)
2	8.4(1)	3.38(2)	2.97(3)	2.12(2)	1.51(3)	3.41(4)	1.64(4)	2.93(1)
2	14.9(1)	3.18(2)	2.52(3)	1.83(3)	1.24(4)	3.30(4)	1.14(4)	2.63(11)
2	19.2(1)	3.16(3)	2.54(4)	1.80(3)	1.12(3)	3.33(5)	1.05(5)	2.47(12)
2	24.4(1)	4.07(3)	3.45(4)	2.51(3)	1.78(4)	4.17(5)	1.71(5)	3.58(12)
2	30.1(1)	4.32(3)	3.91(4)	2.62(3)	1.80(4)	4.44(5)	1.97(6)	3.57(12)
2	34.3(2)	4.69(3)	4.36(4)	2.78(3)	1.77(4)	4.63(5)	2.13(6)	3.87(12)
2	42.6(2)	5.08(3)	5.14(5)	2.99(3)	2.07(4)	4.85(6)	2.45(6)	4.21(14)
3	1.4(1)	0.36(2)	0.43(3)	0.11(2)	0.07(3)	0.34(3)	0.14(4)	0.61(5)
3	2.3(1)	0.40(2)	0.44(3)	0.15(2)	0.08(3)	0.37(3)	0.16(4)	0.54(5)
3	3.7(1)	0.79(2)	0.72(3)	0.43(2)	0.31(3)	0.72(3)	0.38(4)	0.86(5)
3	6.2(1)	2.32(2)	1.95(3)	1.39(2)	0.97(3)	2.20(4)	1.09(4)	2.05(6)
3	8.6(1)	2.81(2)	2.26(3)	1.67(2)	1.08(3)	2.73(4)	1.23(4)	2.29(6)
3	12.8(1)	3.68(2)	2.86(3)	2.14(2)	1.41(3)	3.59(4)	1.49(4)	2.81(6)

TABLE III. Stresses deduced assuming single crystal elastic moduli measured using IXS (Ref. 26) under the Reuss average and using the experimental ODF, expressed in gigapascals, for all pressures in experiments 2 and 3. Numbers in parentheses indicate the uncertainty on the last digit.

R	*P*	*t*(100)	*t*(002)	*t*(101)	*t*(102)	*t*(110)	*t*(103)	*t*(004)
2	3.5(1)	2.30(2)	2.12(2)	1.40(2)	0.95(2)	2.33(3)	1.11(3)	2.13(5)
2	8.4(1)	2.71(2)	2.46(2)	1.65(2)	1.16(2)	2.75(3)	1.28(3)	2.42(8)
2	14.9(1)	2.52(2)	2.02(3)	1.41(2)	0.94(3)	2.63(3)	0.88(3)	2.11(8)
2	19.2(1)	2.50(2)	2.00(3)	1.39(2)	0.86(3)	2.65(3)	0.80(4)	1.95(9)
2	24.4(1)	3.23(2)	2.69(3)	1.96(2)	1.37(3)	3.35(4)	1.32(3)	2.79(9)
2	30.1(1)	3.47(2)	3.01(3)	2.08(2)	1.41(3)	3.60(4)	1.54(5)	2.75(9)
2	34.3(2)	3.82(2)	3.34(3)	2.25(3)	1.41(3)	3.81(4)	1.68(4)	2.97(9)
2	42.6(2)	4.30(2)	3.93(4)	2.52(3)	1.70(3)	4.16(5)	1.99(5)	3.21(11)
3	1.4(1)	0.30(2)	0.38(2)	0.09(2)	0.05(2)	0.28(3)	0.12(3)	0.53(4)
3	2.3(1)	0.33(2)	0.38(2)	0.12(2)	0.06(2)	0.31(3)	0.13(3)	0.47(5)
3	3.7(1)	0.65(1)	0.61(2)	0.34(2)	0.25(2)	0.60(3)	0.30(3)	0.73(5)
3	6.2(1)	1.89(2)	1.64(2)	1.09(2)	0.75(2)	1.79(3)	0.86(3)	1.71(5)
3	8.6(1)	2.26(2)	1.87(2)	1.30(2)	0.83(2)	2.21(3)	0.96(3)	1.90(5)
3	12.8(1)	2.93(2)	2.32(2)	1.66(2)	1.08(2)	2.88(3)	1.15(3)	2.28(5)

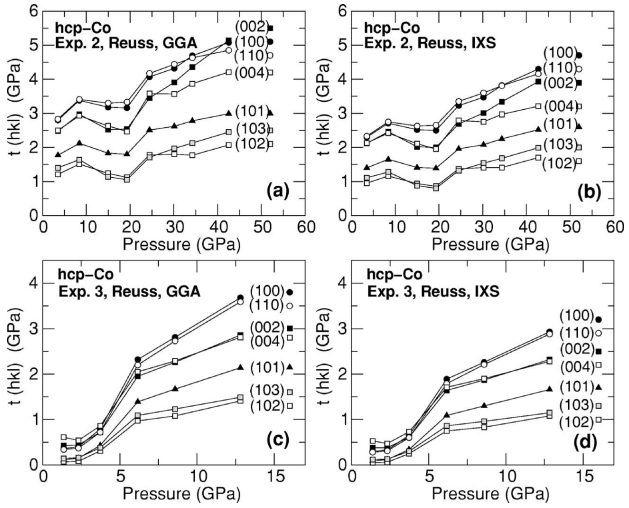

FIG. 7. Differential stress components in experiments 2 [(a) and (b)] and 3 [(c) and (d)] fitted independently for each lattice planes using elastic properties from GGA calculations (Ref. 4) [(a) and (c)], or measured using IXS (Ref. 26) [(b) and (d)], the experimental ODF, and the Reuss micromechanical model.

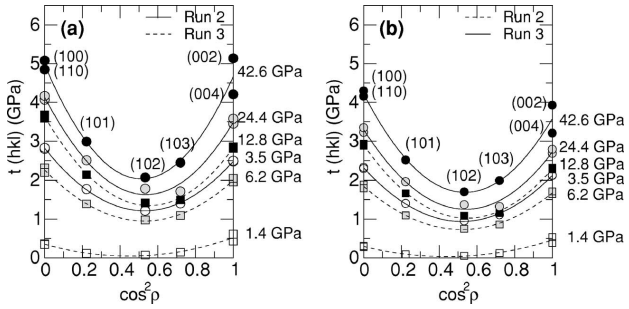

FIG. 8. Effective uniaxial stress components for selected pressures in experiments 2 and 3 as a function of $\cos^2\rho$ where ρ is the angle between (*hkl*) and (002), calculated using elastic properties from GGA calculations (Ref. 4) (a), or measured using IXS (Ref. 26) (b). Squares and circles are experimental data from runs 2 and 3, respectively, lines are second order polynomial fit to the data.

mation, they are parallel to the compression direction. Basal planes such as (002) and (004) see an intermediate stress; at the end of the deformation, they are perpendicular to the compression direction. Pyramidal planes such as (101), (102), and (103) are submitted to the lowest effective stress; in terms of lattice preferred orientations, those planes show broader maxima. Above 25 GPa, we observe a clear split of effective stress deduced from (002) and (004), as well as (102) and (103).

The evolution of stress and strain with deformation we observed in Co can be related to other ambient pressure experiments on hcp metals (i.e., Be and Ti) undergoing plastic deformation which showed a similar behavior.[11,13] Indeed, an (*hkl*) dependent measurement of stresses deduced from lattice strains has already been documented and modeled for fcc metals and ionic solids with the NaCl structure combining elastoplastic self-consistent polycrystal plasticity simulations with lattice strains theory.[10,12,14] In those models, certain (*hkl*) reflection shows a behavior very similar to that of a pure elastic deformation, while others do not, displaying both larger and smaller effective stresses. In our experiments, we find that typical slip planes of the hcp structure structure such as (100) or (002) display a large effective stress while pyramidal planes do not.

The split between the lattice strains and therefore effective stresses measured on (002) and (004) above 25 GPa is intriguing as current modeling of stress and strain in plastically deformed polycrystal do not predict any effect on equivalent reflections. Indeed, there has been reports and models of developments of stacking faults inducing shifts in *d* spacings for equivalent (*hkl*) reflections in fcc metals.[34–37] However, stacking faults in the hcp structure are reported to induce peak broadening but no peak shift.[34,38–40]

V. CONCLUSION

We measured the evolution of lattice preferred orientation in polycrystalline hcp-Co in compression between 0 and 42.6 GPa. We observe the continuous evolution of a 001 texture between 0 and 15 GPa that later saturates. This behavior can be related to the modeling of the deformation of gasket and diamonds in diamond anvil cell experiments by the finite element method which shows that plastic deformation of the sample would mostly occurs in the low pressure range. This observation, however, does not preclude the use of the diamond anvil cell for high pressure texture studies as one can make use of phase transitions, amorphization, or recrystallization to choose the starting point of a deformation experiment.

The single crystal elastic moduli extracted from radial diffraction data are significantly different from those obtained with other techniques and the effect is most pronounced for the shear elastic moduli C_{44} and C_{66}. These results are interpreted as an (*hkl*) dependent effective uniaxial stress resulting from plastic deformation. Under this assumption, we find that the stresses appear consistent when plotted as a function of $\cos^2 \rho$, where ρ is the angle between (002) and (*hkl*). From these experiments, we also conclude that plastic deformation should be minium in order to allow extraction of elastic moduli from radial diffraction data, a constraint that can be rather difficult for nonhydrostatic DAC experiments.

ACKNOWLEDGMENTS

Experiment 1 was performed at beamline ID9 of the European Synchrotron Radiation Facility with the assistance of Michael Hanfland. Experiments 2 and 3 were made at the Photon Factory, with the assistance of Takumi Kikegawa, under Approval No. 04G045. One of the authors (S.M.) also acknowledges support from the postdoctoral fellowship program of the Japanese Society for the Promotion of Science.

[1] S. Klotz, M. Braden, and J. M. Besson, Phys. Rev. Lett. **81**, 1239 (1998).
[2] F. Occelli, D. Farber, J. Badro, C. Aracne, D. Teter, M. Hanfland, B. Canny, and B. Couzinet, Phys. Rev. Lett. **93**, 095502 (2004).
[3] A. F. Goncharov, J. Crowhurst, and J. M. Zaug, Phys. Rev. Lett. **92**, 115502 (2004).
[4] G. Steinle-Neumann, L. Stixrude, and R. E. Cohen, Phys. Rev. B **60**, 791 (1999).
[5] S. Merkel, H. R. Wenk, J. Shu, G. Shen, P. Gillet, H. K. Mao, and R. J. Hemley, J. Geophys. Res. **107**, 2271 (2002).
[6] I. Noyan and J. Cohen, *Residual Stress: Measurements by Diffraction and Interpretation* (Springer-Verlag, New York, 1987).
[7] S. Matthies, H. G. Priesmeyer, and M. R. Daymond, J. Appl. Crystallogr. **34**, 585 (2001).
[8] A. K. Singh, C. Balasingh, H. K. Mao, R. J. Hemley, and J. Shu, J. Appl. Phys. **83**, 7567 (1998).
[9] P. Dawson, D. Boyce, S. MacEwen, and R. Rogge, Mater. Sci. Eng., A **313**, 123 (2001).
[10] B. Clausen, T. Lorentzen, and T. Leffers, Acta Mater. **46**, 3087 (1998).
[11] M. R. Daymond and N. W. Bonner, Mater. Sci. Eng., A **340**, 272 (2003).
[12] L. Li, D. J. Weidner, J. Chen, M. T. Vaughan, M. Davis, and W. B. Durham, J. Appl. Phys. **95**, 8357 (2004).
[13] M. R. Daymond, M. A. M. Bourke, and R. B. Von Dreele, J. Appl. Phys. **85**, 739 (1999).
[14] D. J. Weidner, L. Li, M. Davis, and J. Chen, Geophys. Res. Lett. **31**, L06621 (2004).
[15] A. K. Singh, H. K. Mao, J. Shu, and R. J. Hemley, Phys. Rev. Lett. **80**, 2157 (1998).
[16] H. K. Mao, J. Shu, G. Shen, R. J. Hemley, B. Li, and A. K. Singh, Nature (London) **396**, 741(E) (1998); **399**, 280 (1999).
[17] S. Merkel, J. Shu, P. Gillet, H. Mao, and R. Hemley, J. Geophys. Res. **110**, B05201 (2005).
[18] S. Matthies, S. Merkel, H. R. Wenk, R. J. Hemley, and H. K. Mao, Earth Planet. Sci. Lett. **194**, 201 (2001).
[19] T. S. Duffy, G. Shen, D. L. Heinz, J. Shu, Y. Ma, H. K. Mao, R. J. Hemley, and A. K. Singh, Phys. Rev. B **60**, 15063 (1999).
[20] L. Stixrude and R. E. Cohen, Science **267**, 1972 (1995).
[21] P. Söderlind, J. A. Moriarty, and J. M. Wills, Phys. Rev. B **53**, 14063 (1996).
[22] L. Vočadlo, D. Alfè, M. Gillan, and G. Price, Phys. Earth Planet. Inter. **140**, 101 (2003).
[23] M. H. Manghnani, K. Katahara, and E. S. Fisher, Phys. Rev. B **9**, 1421 (1974).
[24] C. S. Yoo, H. Cynn, P. Söderlind, and V. Iota, Phys. Rev. Lett. **84**, 4132 (2000).
[25] H. J. McSkimin, J. Appl. Phys. **26**, 406 (1954).
[26] D. Antonangeli, M. Krisch, G. Fiquet, D. Farber, C. Aracne, J. Badro, F. Occelli, and H. Requardt, Phys. Rev. Lett. **93**, 215505 (2004).
[27] S. Merkel and T. Yagi, Rev. Sci. Instrum. **76**, 046109 (2005).
[28] H. R. Wenk, S. Matthies, J. Donovan, and D. Chateigner, J. Appl. Crystallogr. **31**, 262 (1998).
[29] S. Merkel and T. Yagi, J. Phys. Chem. Solids (in press).
[30] H. Fujihisa and K. Takemura, Phys. Rev. B **54**, 5 (1996).
[31] H. R. Wenk, S. Matthies, R. J. Hemley, H. K. Mao, and J. Shu, Nature (London) **405**, 1044 (2000).
[32] S. Merkel, R. J. Hemley, H. K. Mao, and D. M. Teter, in *Science and Technology of High Pressure Research*, edited by M. Manghnani, W. J. Nellis, and M. F. Nicol [University Press (India), Bangalore, 2000], pp.

68–73.
[33]S. Merkel, A. Kubo, L. Miyagi, S. Speziale, T. S. Duffy, H.-K. Mao, and H.-R. Wenk, Science **311**, 644 (2006).
[34]B. E. Warren, *X-Ray Diffraction* (Dover, New York, 1969).
[35]L. Velterop, R. Delhez, T. H. de Keijser, E. J. Mittemeijer, and D. Reefman, J. Appl. Crystallogr. **33**, 296 (2000).
[36]E. Estevez-Rams, M. Leoni, P. Scardi, B. Aragon-Fernandez, and H. Fuess, Philos. Mag. **83**, 4045 (2003).
[37]E. Estevez-Rams, B. Aragon-Fernandez, H. Fuess, and A. Penton-Madrigal, Phys. Rev. B **68**, 064111 (2003).
[38]J. W. Christian, Acta Crystallogr. **7**, 415 (1954).
[39]T. R. Anantharaman and J. W. Christian, Acta Crystallogr. **9**, 479 (1956).
[40]P. Ghosal and S. Lele, Acta Crystallogr., Sect. A: Found. Crystallogr. **59**, 153 (2003).

PHYSICAL REVIEW B **79**, 064110 (2009)

Modeling analysis of the influence of plasticity on high pressure deformation of hcp-Co

Sébastien Merkel*
Laboratoire de Structure et Propriétés de l'Etat Solide, CNRS, Université des Sciences et Technologies de Lille, 59655 Villeneuve d'Ascq, France

Carlos Tomé
MST Division, Los Alamos National Laboratory, Los Alamos, New Mexico 87545, USA

Hans-Rudolf Wenk
Department of Earth and Planetary Science, University of California-Berkeley, Berkeley, California 94720, USA
(Received 8 September 2008; published 18 February 2009)

Previously measured *in situ* x-ray diffraction is used to assess the development of internal elastic strains within grains of a sample of polycrystalline cobalt plastically deformed up to a pressure of 42.6 GPa. An elastoplastic self-consistent polycrystal model is used to simulate the macroscopic flow curves and internal strain development within the sample. Input parameters are single-crystal elastic moduli and their pressure dependence, critical resolved shear stresses, and hardening behavior of the slip and twinning mechanisms which are active in Co crystals. At 42 GPa, the differential stress in hcp-Co is 1.9 ± 0.1 GPa. The comparison between experimental and predicted data leads us to conclude that: (a) plastic relaxation plays a primary role in controlling the evolution and ordering of the lattice strains; (b) the plastic behavior of hcp-Co deforming under high pressure is controlled by basal and prismatic slip of $\langle a \rangle$ dislocations, and either pyramidal slip of $\langle c+a \rangle$ dislocations, or compressive twinning, or both. Basal slip is by far the easiest and most active deformation mechanism. Elastoplastic self-consistent models are shown to overcome the limitations of models based on continuum elasticity theory for the interpretation of x-ray diffraction data measured on stressed samples. They should be used for the interpretation of these experiments.

DOI: 10.1103/PhysRevB.79.064110 PACS number(s): 62.50.−p, 62.20.−x, 91.60.−x, 61.05.cp

I. INTRODUCTION

Characterizing the effect of pressure on elastic and plastic properties of condensed matter is particularly important for understanding elasticity, mechanical stability of solids, material strength, interatomic interactions, and phase-transition mechanisms. In particular, hexagonal-closed-packed (hcp) metals are of great interest because they tend to exhibit intriguing physical properties[1–4] that represent a challenge for first-principles calculations,[5–8] and also because the Earth's inner core could be mainly composed of the hcp polymorph of Fe, ϵ-Fe.[9]

In the past few years, techniques have been developed to study the plastic properties of materials *in situ* under combined high pressure and high temperature.[10–13] In those experiments x-ray diffraction is used to probe stress and lattice preferred orientations (LPOs) within the sample and extract physical properties such as dominant deformation mechanisms, flow laws, or ultimate stress. However, the theory commonly used for relating the measured lattice strains to stress and elastic properties[14] is based on lower or upper bound assumptions and has shown severe limitations. In particular, it was shown that this model yields inconsistent results for inverting single-crystal elastic properties for ϵ-Fe.[15–18] This was also confirmed by extensive work on hcp-Co which demonstrated that the method provides elastic moduli that are inconsistent with those provided by a range of other experimental and theoretical techniques.[3,5,19–23]

In the material science community, the issue of stress measurement using x-ray or neutron diffraction is known as residual stress analysis.[24,25] There is a body of work showing that the analysis of such data is not straightforward.[26–30] Indeed, stress and strain are very heterogeneous in plastically deformed materials and upper or lower bound models based on continuum elasticity theory do not account for this phenomenon. Various techniques have been developed for the interpretation of experimental data, based on self-consistent methods,[26,31] or finite-element modeling.[28] Self-consistent analysis has already been applied to high pressure solids with a cubic structure[32,33] and to trigonal quartz.[34]

Here, we look at the plastic properties of hcp Co under pressure. Cobalt lies next to iron in the Periodic Table and its hcp phase has a wide stability field.[35] Unlike the hcp phase of iron, it is stable at ambient pressure with readily available single crystals. As such, it has become a paradigm for comparing and testing numerous high pressure techniques. The phase diagram and equation of state have been studied using both x-ray diffraction[35–37] and first-principles calculations.[5,8] Elastic properties have been obtained under ambient pressure using ultrasonic techniques[38] and at high pressure using inelastic x-ray scattering[19,20,39] (IXS), Raman spectroscopy,[3] impulsive stimulated light scattering,[23] and first-principles techniques.[5] The plastic properties of hcp-Co have been investigated under ambient pressure for both coarse grains[40–44] and nanocrystalline samples.[45–47] High pressure diamond-anvil cell (DAC) radial diffraction (RDX) experiments have been reported,[22] but lacked an interpretation based on the interplay between elastic and plastic mechanisms.

In this paper, we use a modification of the elastoplastic self-consistent (EPSC) model of Turner and Tomé[31] to simulate and interpret DAC experiment previously done on a Co aggregate for pressures up to 42.6 GPa.[22] This model yields information about the absolute strength of the deformation mechanisms involved, stress distribution among grains in the

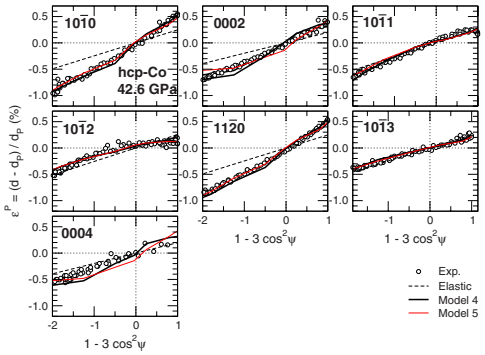

FIG. 1. (Color online) Measured and simulated strains vs $(1-3\cos^2\psi)$ under the hydrostatic pressure of 42.6 GPa. Circles are data from Ref. 22. d are measured d spacings and d_P d spacings under equivalent hydrostatic pressure. Thick black lines are results of EPSC calculations using model 4 in Table II. Thin red lines are results of EPSC calculations using model 5 in Table II. Thin dashed lines are predictions of an elastic model with no effect of LPO (Ref. 14) assuming a differential stress of 4 GPa. In all cases, the d spacings under equivalent hydrostatic pressure d_P have been obtained assuming relation 15.

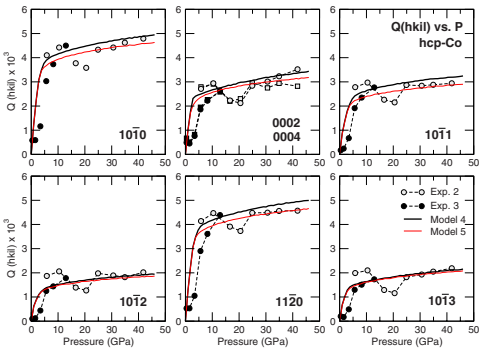

FIG. 2. (Color online) Measured and simulated lattice strain parameters vs pressure for the 10$\bar{1}$0, 0002, 0004, 10$\bar{1}$1, 10$\bar{1}$2, 11$\bar{2}$0, and 10$\bar{1}$3 diffraction lines of hcp-Co. Gray symbols are data from Exp. 2 in Ref. 22, solid symbols are data from Exp. 3 in Ref. 22, thick black lines are EPSC simulations using model 4 in Table II, and thin red lines are EPSC simulations using model 5 in Table II. Experimental data for the 0004 diffraction line are shown using square symbols. All other experimental data are represented with circles.

sample, and true stress values for the polycrystal. In addition, our modeling shows the important role that plastic relaxation and nonhomogeneity of stress and strain play in high pressure experiments.

II. METHODS

A. Experimental data

The experimental data on hcp-Co that we use here have been published previously.[22] Two experiments were performed in which a sample of pure hcp-Co was compressed in a diamond-anvil cell, up to 42.6 GPa for the first run and up to 12.8 GPa for the second run. Diffraction data were collected in a radial geometry with the incoming x-ray beam perpendicular to the load axis.

Figure 1 shows measured strains for several crystallographic planes vs $(1-3\cos^2\psi)$ for a hydrostatic pressure of 42.6 GPa, where ψ is the angle between the diffracting plane normal and the direction of maximum stress. They are nearly linear with $(1-3\cos^2\psi)$, as predicted by purely elastic lattice strain theory.[14] However, it was shown that stresses calculated using this theory for individual lattice planes were inconsistent.[22]

For all pressures in the experiment, the variations in diffraction intensity with orientation were used to extract lattice preferred orientations in the sample, while peak shifts were used to extract lattice strains parameters Q (discussed in Sec. II B 4) for the 10$\bar{1}$0, 0002, 10$\bar{1}$1, 10$\bar{1}$2, 11$\bar{2}$0, 10$\bar{1}$3, and 0004 diffraction lines of hcp-Co (Fig. 2).

B. Elastic model

1. Stress and strain

Under high pressure, it is preferable to separate the effect of hydrostatic pressure and deviatoric stress, and define elastic moduli as relating stress and strain deviations relative to the hydrostatic state. Elastic constants are then appropriate for calculation of elastic wave velocities and comparison with previous work. This relation is not trivial under pressure,[48–50] and we therefore discuss several definitions of stress and strains. In this paper, the superscript " 0" will refer to absolute stress and strain (relative to ambient pressure), while the superscript " P" will refer to stress, strain, or stiffness relative to the state of hydrostatic pressure P.

The relation between stress tensors relative to ambient pressure (absolute stress) σ_{ij}^0 and stress tensors relative to the hydrostatic pressure (relative stress) σ_{ij}^P is straightforward,

$$\sigma_{ij}^0 = \sigma_{ij}^P + P \cdot \delta_{ij} = C_{ijkl}^P \epsilon_{kl}^P + P \cdot \delta_{ij}, \tag{1}$$

where δ_{ij} is the Kronecker function and ϵ_{ij}^P the strain tensor relative to the state of hydrostatic pressure. σ_{ij}^P is often referred to as deviatoric stress in the literature, although it may not be traceless at the grain level. C_{ijkl}^P are single-crystal elastic moduli for a medium under hydrostatic pressure P.

Strain definitions can be more complicated. If we consider an element of length d_0 under ambient pressure, length d_P at the hydrostatic pressure P, and length d under a general stress σ_{ij}^0, we define the following lattice strains:

$$\epsilon^P = \frac{d - d_P}{d_P}, \tag{2}$$

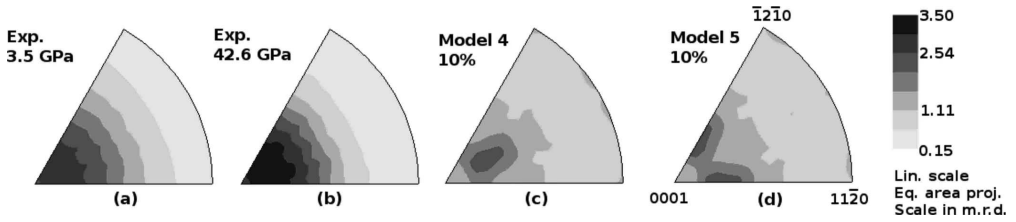

FIG. 3. [(a) and (b)] Experimental and [(c) and (d)] simulated inverse pole figures of the compression direction for hcp-Co. [(a) and (b)] Experimental data are from Exp. 2 in Ref. 22. Simulations are results of VPSC calculations using models (c) 4 and (d) 5 in Table II after 10% strain. Equal area projection, linear scale, and contours in m.r.d.

$$\epsilon^0 = \frac{d - d_0}{d_0}, \tag{3}$$

$$\epsilon_P^0 = \frac{d_P - d_0}{d_0}, \tag{4}$$

from where

$$\epsilon^0 = (1 + \epsilon_P^0)\epsilon^P + \epsilon_P^0. \tag{5}$$

ϵ^P are the strains relative to the hydrostatic pressure state and could be referred to as "relative strains;" ϵ^0 are the strains relative to the ambient pressure state and could be referred to as "absolute strains."

Note that elastic moduli under hydrostatic pressure C_{ijkl}^P relate relative strains ϵ_{ij}^P and relative stresses σ_{ij}^P, and that the relation between absolute strains ϵ_{ij}^0 and absolute stresses σ_{ij}^0 is not straightforward.

2. Coordinate systems

Analysis and calculations can be simplified if single-crystal elastic moduli, d spacings measured using x-ray diffraction, and sample stress, are expressed in the suitable coordinate system.

The diamond-anvil cell geometry defines a sample coordinate system, K_S, with $\mathbf{Z}_S$ aligned with the compression direction and $\mathbf{Y}_S$ parallel to the incoming x-ray beam, pointing toward the detector. This coordinate system is well defined in the experiment and useful to relate all information expressed in the other systems. Stress in diamond-anvil cells are mostly axial and, when expressed in K_S, the stress applied to the polycrystalline sample reads

$$\sigma^{P-K_S} = \begin{bmatrix} -\frac{t}{3} & 0 & 0 \\ 0 & -\frac{t}{3} & 0 \\ 0 & 0 & 2\frac{t}{3} \end{bmatrix}, \tag{6}$$

where t is the differential stress.

The diffraction direction defines a diffraction coordinate system K_D with the axis $\mathbf{Z}_D$ parallel to the scattering vector $\mathbf{N}$ (bisector between the incoming beam and the diffracted x-ray beam collected by the detector) and $\mathbf{Y}_D$ perpendicular to $\mathbf{Z}_D$ and contained in the plane defined by the incident and diffracted beams. In K_D the d spacings measured in diffraction are the 33 component of the crystal strain tensor

$$\epsilon_{33}^{P-K_D} = \frac{d_m(hkl) - d_P(hkl)}{d_P(hkl)}, \tag{7}$$

where $d_m(hkl)$ is the measured d spacing for the hkl reflection and $d_P(hkl)$ is the d spacing of the hkl reflection under the hydrostatic pressure P.

The crystal coordinate system K_C is defined by the (orthogonal) crystal axes. Microscopic physical relations, such as Hooke's law relating the microscopic stress, strain, and single-crystal elastic moduli refer to each crystallite coordinate system K_C. d spacings for hkl reflections in individual grains should be extracted from calculations using Hooke's law in K_C.

3. Texture and lattice preferred orientations

The texture in the sample can be represented by an orientation distribution function (ODF). The ODF is required to estimate anisotropic physical properties of polycrystals such as elasticity or plasticity.[51] The ODF represents the probability for finding a crystal orientation, and it is normalized such that an aggregate with a random orientation distribution has a probability of one for all orientations. If preferred orientation (texture) is present, some orientations have probabilities higher than one and others lower than one.

The ODF can be calculated using the variation in diffraction intensity with orientation using tomographic algorithms such as WIMV,[52] as implemented in the BEARTEX package[53] or in the "Maud Rietveld" refinement program.[54] This technique has been successfully applied to measure textures and deduce active high pressure deformation mechanisms.[55]

Textures of the sample analyzed here have been described in detail[22] and Fig. 3 presents inverse pole figures of the compression direction for experiment 2 at 3.5 and 42.6 GPa. For hcp-Co compressed in the DAC, we observe the development of a relatively strong texture with a maximum at about 15° from 0001.

4. Elastic strains

For polycrystals, diffraction peaks are the sum of the contribution from all crystallites in the correct reflection conditions, i.e., crystallites whose normal to the (hkl) plane is parallel to the scattering vector $\mathbf{N}$. The corresponding individual d spacings depend on the local stress and elastic properties in the grain considered. The measured d spacing

$d_m(hkl)$ is a weighted arithmetic mean of those individual d spacings and corresponds to the 33 component of the elastic strain tensor in the diffraction coordinate system, K_D [Eq. (7)].

Theories have been developed to relate single-crystal elastic moduli to measured d spacings for stressed polycrystals. Most models rely on elasticity theory and assume either continuity of stress or of strain within the sample. If, in addition, it is assumed that the sample is nontextured, it can be shown that the lattice strain can be expressed as[14]

$$\epsilon_{33}^{P-K_D} = \frac{d_m(hkl) - d_P(hkl)}{d_P(hkl)} = Q(hkl)(1 - 3\cos^2\psi), \quad (8)$$

where ψ is the angle between the diffracting plane normal and the maximum stress direction ($\mathbf{Z}_S$ in our case), and the lattice strain parameter $Q(hkl)$ is a function of the differential stress t in the polycrystal and single-crystal elastic moduli C_{ijkl}^P.

Theories that include texture effects have also been developed.[56] In this case, the measured d spacings do not vary linearly with $(1-3\cos^2\psi)$ but can still be related to differential stress in the polycrystal and single-crystal elastic moduli. However, deviations between predictions of theories that include texture effects and those that neglect it are small and may be difficult to separate experimentally.[57] In any case, it has been shown that this theory does not apply to data measured on materials where plastic deformation takes place. In particular, these techniques yield inconsistent stresses and elastic constants for hcp-Co under pressure.[21,22,58]

C. Plastic model

1. EPSC model

The evolution of stress and strain with deformation observed in Co can be related to results of ambient pressure experiments on other hcp metals (i.e., Be, Mg, and Ti) undergoing plastic deformation which show a similar behavior.[27,29,59,60] hkl-dependent stresses deduced from lattice strains have already been documented and modeled for fcc metals and ionic solids with the NaCl structure using EPSC simulations.[26,32,33] In those simulations, certain hkl reflections show a behavior close to that of a pure elastic deformation, while others do not, displaying either larger or smaller effective stresses.

The EPSC model we use here[31] represents the aggregate by a discrete number of orientations with associated volume fractions. The latter are chosen such as to reproduce the initial texture of the aggregate. EPSC treats each grain as an ellipsoidal elastoplastic inclusion embedded within a homogeneous elastoplastic effective medium with anisotropic properties characteristic of the textured aggregate. The external boundary conditions (stress and strain) are fulfilled on average by the elastic and plastic deformations at the grain level. The self-consistent approach explicitly captures the fact that soft-oriented grains tend to yield at lower stresses and transfer load to plastically hard-oriented grains, which remain elastic up to rather large stress.

The model uses known values of single-crystal elastic moduli. The parameters associated with each plastic deformation mode are the critical resolved shear stresses (CRSS), given by a hardening evolution law. The simulated internal strains are compared to experimental data by identifying the grain orientations which, in the model aggregate, contribute to the experimental signal associated with each diffracting vector.

An EPSC simulation is based on applying stress or strain increments to the aggregate, depending on the boundary conditions, until the final deformation or stress state is achieved. At each step, stress and strain in each grain are incremented accordingly, as follows from its interaction with the effective medium representing the aggregate. The response of medium and grain is assumed to be described by a linear relation between stress and total strain increments,

$$\delta\sigma^c = L^c : \delta\epsilon^{c,\text{total}}, \quad (9)$$

$$\delta\bar{\sigma} = \bar{L} : \delta\bar{\epsilon}^{\text{total}}, \quad (10)$$

$$\delta\epsilon^{\text{total}} = \delta\epsilon^{\text{elastic}} + \delta\epsilon^{\text{plastic}}. \quad (11)$$

Here $\bar{L}$ is the elastoplastic stiffness of the aggregate and $L^c = C^c : (I - \Sigma_s m^s \otimes f^s)$ is the elastoplastic stiffness of the crystal. C^c is the single-crystal elastic tensor, and the sum is taken over the active slip systems s in the grain. m^s is the Schmid tensor which resolves the shear component of the stress or strain along a slip system and f^s is a tensor which relates stress and strain rates.[61,62] As more systems become plastically active, the moduli L^C become more compliant. The stress equilibrium condition is solved for each grain assuming an ellipsoidal grain shape and using the Eshelby inclusion formalism. This procedure provides for a stress and strain increment in each grain. The macroscopic elastoplastic stiffness $\bar{L}$ is derived iteratively by enforcing the condition that the polycrystal response has to be given by the weighted average of the individual grains responses and has to be consistent with the boundary conditions.[31] The main advantage of the EPSC model is that it allows for grains to deform more or less than the average, depending on their degree of hardening, their orientation, and their relative directional stiffness with respect to the medium.

2. Parameters and output of EPSC models

In our modeling of DAC RDX data, we assume that the sample was submitted to an axial compression along $\mathbf{Z}_S$ in K_S. In all simulations, we assume that the sample consists of 1000 randomly oriented spherical grains, with single-crystal elastic moduli and their pressure dependence taken from IXS measurements[19] (Table I). The polycrystalline sample is

TABLE I. Ambient pressure and first pressure derivative of elastic moduli of hcp-Co measured using IXS between 0 and 39 GPa (Ref. 19). In our simulation $C_{ij}^{P}=C_{ij}^{0}+P\cdot(\partial C_{ij}/\partial P)$.

	C_{11}	C_{33}	C_{12}	C_{13}	C_{44}
C_{ij}^{0} (GPa)	293	339	143	90	78
$\partial C_{ij}/\partial P$	6.1	7.6	3.0	4.2	1.38

compressed in 3000 strain steps to a final state of strain defined by

$$\epsilon_x^{0-K_S} = -0.01$$

$$\epsilon_y^{0-K_S} = -0.01 \tag{12}$$

$$\epsilon_z^{0-K_S} = -0.17,$$

where strains are expressed in K_S relative to dimensions under ambient pressure. The deformation geometry was derived from x-ray radiographs of the sample taken during the DAC experiments[63] which indicate that our sample was submitted to very little radial deformation. The final value of the axial component $\epsilon_z^{0-K_S}$ was chosen to match the simulated and experimental pressures at the end of the compression.

The model uses combinations of seven deformation mechanisms typically found in hexagonal metals: slip of $\frac{1}{3}\langle 11\bar{2}0\rangle$, or $\langle a\rangle$ dislocations, on basal (0001), prismatic $\{10\bar{1}0\}$, and pyramidal $\{10\bar{1}1\}$ planes; slip of $\frac{1}{3}\langle 11\bar{2}3\rangle$, or $\langle c+a\rangle$ dislocations, on pyramidal $\{10\bar{1}1\}$ or $\{11\bar{2}2\}$ planes; tensile twinning on $\{10\bar{1}2\}$ planes; and, finally, compressive twinning on $\{11\bar{2}2\}$ planes (Table II). For each slip and twin mode we describe the hardening of CRSS by means of an empirical Voce hardening rule

$$\tau = \tau_0 + (\tau_1 + \theta_1\Gamma)\left\{1 - \exp\left(-\frac{\theta_0\Gamma}{\tau_1}\right)\right\}, \tag{13}$$

where τ is the instantaneous CRSS of the mechanism, τ_0 and $\tau_0+\tau_1$ are the initial and final back-extrapolated CRSS, respectively, θ_0 and θ_1 are the initial and asymptotic hardening rates, and Γ is the accumulated plastic shear strain in the grain. Strain levels presented here are relatively low, so we reduced the number of adjustable parameters by assuming that $\tau_1=0$. In this case, the hardening law becomes linear according to

$$\tau = \tau_0 + \theta_1\Gamma, \tag{14}$$

and only two adjustable parameters remain.

Output of the simulation includes the relative activity of the various deformation mechanisms, the average stress in the polycrystal, stress and strain within each grain of the sample, and predicted lattice strains. The simulated elastic lattice strains were compared to experimental data by identifying the model grains whose crystallographic planes are oriented such as to contribute to the experimental signal. The lattice strain (peak shift) is calculated as a weighted average over all grains that contribute to the peak. Specifically, we considered $10\bar{1}0$, 0002, $10\bar{1}1$, $10\bar{1}2$, $11\bar{2}0$, and $10\bar{1}3$ diffraction lines at $\psi=0$, 15°, 30°, 45°, 60°, 75°, and 90°. The region of orientation space which contributes to the signal was assumed to be within an interval of ±7.5° with respect to the diffraction vector.

3. Representation of simulated and experimental data

It has been shown that Eq. (8) does not apply to data collected in RDX when samples are plastically deformed. However, previous RDX experiments[4,12,15,64–67] have shown that the measured d spacings are nearly linear when plotted vs $(1-3\cos^2\psi)$ and that the d spacings measured for $\psi=54.7°$ do correspond to those expected under the hydrostatic equivalent pressure. Therefore, experimental data were reduced using

TABLE II. List of deformation mechanisms used in the simulations. τ_0 and θ_1 are parameters for the simplified Voce hardening rule Eq. (14) and are expressed in GPa. Stars indicate deformation mechanisms that were not included in the final model.

		Model 1		Model 2		Model 3		Model 4		Model 5	
Mechanism		τ_0	θ_1	τ_0	θ_1	τ_0	θ_1	τ_0	θ_1	τ_0	θ_1
Basal	$(0001)\langle\bar{1}2\bar{1}0\rangle$	100	1	1	1	8	1	0.07	0.30	0.07	0.30
Prismatic	$\{10\bar{1}0\}\langle\bar{1}2\bar{1}0\rangle$	100	1	8	1	1	1	0.90	1.00	0.90	1.00
Pyramidal $\langle a\rangle$	$\{10\bar{1}1\}\langle\bar{1}2\bar{1}0\rangle$	100	1	100	1	100	1	*	*	*	*
Pyramidal $\langle c+a\rangle$	$\{10\bar{1}1\}\langle 11\bar{2}3\rangle$	100	1	100	1	100	1	0.70	1.50	*	*
Pyramidal $\langle c+a\rangle$ second order	$\{11\bar{2}2\}\langle 11\bar{2}3\rangle$	*	*	*	*	*	*	*	*	*	*
Tensile twin	$\{10\bar{1}2\}\langle 10\bar{1}1\rangle$	*	*	*	*	*	*	*	*	*	*
Compressive twin	$\{2\bar{1}\bar{1}2\}\langle 2\bar{1}\bar{1}3\rangle$	*	*	*	*	*	*	*	*	0.60	0.70

$$\epsilon_{33}^{P-K_D}(hkil,\psi) = \frac{d_m(hkil,\psi) - d_P(hkil)}{d_P(hkil)} = Q(hkil)(1-3\cos^2\psi), \quad (15)$$

where $d_m(hkil,\psi)$ is the measured d spacing for the $hkil$ diffracting line at angle ψ, $d_P(hkil)$ is the d spacing for the $hkil$ line under hydrostatic pressure P, and $Q(hkil)$ is the lattice strain parameter for the $hkil$ line. $d_P(hkil)$ and $Q(hkil)$ were adjusted to the experimental data. $d_P(hkil)$ was then used to estimate the average lattice parameters a and c of the hexagonal crystal and the hydrostatic pressure P using a known equation of state.[36] Experimental data for hcp-Co lattice strains vs pressure obtained using such procedure are extracted from Ref. 22 and summarized in Fig. 2.

The EPSC model calculates the average stress in the sample, σ^{0-K_S}, from which we deduce the hydrostatic pressure and differential stress

$$P = (\sigma_{11}^{0-K_S} + \sigma_{22}^{0-K_S} + \sigma_{33}^{0-K_S})/3, \quad (16)$$

$$t = \sigma_{33}^{0-K_S} - \left(\frac{\sigma_{11}^{0-K_S} + \sigma_{22}^{0-K_S}}{2}\right), \quad (17)$$

respectively. The EPSC model also provides absolute simulated strains $\epsilon_{33}^{0-K_D}(hkil,\psi)$ relative to d spacings under ambient pressure, which were used to calculate strains induced by the hydrostatic pressure, ϵ_P^0, and deviatoric lattice strains parameters $Q(hkil)$. The procedure consists in fitting a and b parameters to

$$\epsilon_{33}^{0-K_D}(hkil,\psi) = \frac{d_m(hkil,\psi) - d_0(hkil)}{d_0(hkil)} = a + b(1-3\cos^2\psi). \quad (18)$$

Using Eqs. (5) and (15), we get

$$\epsilon_P^0 = \frac{d_P(hkil) - d_0(hkil)}{d_0(hkil)} = a, \quad (19)$$

$$Q(hkil) = \frac{b}{1+a}. \quad (20)$$

4. Pressure dependence of the elastic moduli

Since the original EPSC code did not include the effect of pressure on elastic moduli, we modified it to calculate pressure and update the corresponding elastic moduli, at each step and in each grain. At each step i, the elastic strain increment induced by the increment of stress applied to a grain is calculated using

$$\delta\epsilon_{kl}^{P-K_C}|_i = S_{klmn}^P[\sigma_{mn}^{0-K_C}|_i - \sigma_{mn}^{0-K_C}|_{i-1}], \quad (21)$$

where the coefficients S_{klmn}^P are elastic compliances, function of the hydrostatic pressure in the grain at step $(i-1)$, and stress tensors are absolute, relative to the state under ambient pressure. Lattice spacing for each grain contributing to the diffraction peak is then updated using

$$d(hkil)|_i = d(hkil)|_{i-1}(1 + \delta\epsilon_{33}^{P-K_D}), \quad (22)$$

where $\delta\epsilon_{33}^{P-K_D}$ is the component of the strain tensor $\delta\epsilon_{kl}^{P-K_C}$ perpendicular to the diffracting plane.

The average lattice strain for each reflection and orientation to be compared with experimental data is then updated by identifying the grains contributing to the diffraction and calculating

$$\epsilon^0(hkil) = \left[\frac{d(hkil)|_i - d(hkil)|_0}{d(hkil)|_0}\right], \quad (23)$$

where the average is taken over all grains contributing to the diffraction.

III. RESULTS

In this section, we present simulations of the DAC experiment done for hcp-Co using the EPSC model. In order to study the effect of plasticity upon the lattice strain evolution, we consider several combinations of active slip and twinning modes, and several combinations of hardening parameters. We will refer to each of these combinations as a crystal model. The different sets and associated hardening parameters are listed in Table II. In all cases, we use the pressure dependent elastic moduli for Co listed in Table I.

A. Pressure dependence of elastic moduli and hydrostatic equation of state

According to the elastic theory introduced earlier, d spacings measured at $\psi=54.7°$ correspond to those associated with the hydrostatic pressure P [see Eq. (15)]. While the theory used to derive this result has strong limitations, numerous RDX experiments have shown that equation of states measured at this angle tend to correspond to those measured under hydrostatic conditions.

Figure 4 presents the pressure dependence of $\epsilon_P^0=(d_P-d_0)/d_0$ simulated with the EPSC model along with results from RDX (Ref. 22) at $\psi=54.7°$. The figure also shows curves calculated using the bulk modulus and pressure dependence of the c/a ratio measured under hydrostatic conditions[36] as well as compression curves calculated using the single-crystal elastic moduli and their pressure dependence measured using IXS (Ref. 19) that were assumed in the calculation.

Compression curve calculated using the single-crystal elastic moduli and their pressure dependence measured using IXS differ slightly from those measured under hydrostatic conditions. RDX results almost coincide with those deduced from the hydrostatic equation of state, while EPSC results almost coincide with those deduced from IXS measurements. Small differences can be seen for $10\bar{1}3$ and 0002 and they will be discussed later. It is obvious from Fig. 4 how critical it is, in this simulation, to account for the pressure dependence of the elastic constants. Otherwise, predictions tend to grossly overestimate the lattice strains as a function of pressure.

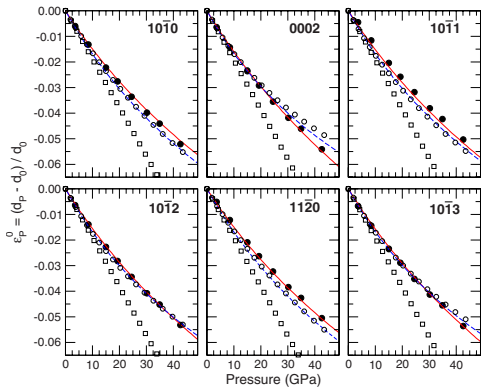

FIG. 4. (Color online) Measurement of hydrostatic strain vs pressure. Solid line is deduced from an equation of state measured under hydrostatic conditions (Ref. 36), dashed lines is deduced from the single-crystal elastic moduli measured using IXS (Ref. 19), black circles are measurement from radial x-ray diffraction (Ref. 22) at $\psi=54.7°$, open squares are simulated using EPSC and no pressure dependence of elastic moduli, and open circles are results of EPSC models using the elastic moduli and their pressure dependence measured using IXS (Ref. 19).

B. Effect of individual deformation mechanisms on the simulated lattice strains

Figure 5 presents the results of the EPSC calculations for plasticity models 1, 2, and 3 (Table II). For each, we show the evolution of the polycrystal stress components σ_{11} and σ_{33}, hydrostatic pressure P, differential stress t, the simulated deviatoric lattice strain parameter $Q(hkil)$, and the deformation mechanisms relative activity as a function of the applied axial strain $\epsilon_z^{0-K_S}$.

Pressure calculated as a function of $\epsilon_z^{0-K_S}$ is independent of the plasticity model used. For all cases, we obtain an evolution of pressure with $\epsilon_z^{0-K_S}$ compatible with predictions based on the hydrostatic equation of state of hcp-Co. At the end of our simulated compression, the sample volume is reduced by 17% and pressure is 46.2 GPa. As demonstrated in Fig. 5, all other results strongly depend on the plastic model and they should be discussed independently.

For model 1, the strength of all deformation mechanisms is purposely set too high for them to be activated. As a consequence, the behavior of the polycrystal is fully elastic. The differential stress and pressure in the sample increase continuously with applied strain and t reaches a value of 38.3 GPa at a pressure of 46.2 GPa. The simulated lattice strain parameters Q also increase continuously with pressure and are about 1 order of magnitude higher than those measured in the experiment [Figs. 2 and 5(c)].

In model 2, basal slip is activated when the applied strain reaches 0.0122. At this strain, pressure and differential stress in the sample are 2.2 and 2.1 GPa, respectively. The activation of basal slip is correlated with a drop in the simulated lattice strains for diffraction lines such as 10$\bar{1}$1, 10$\bar{1}$2, and 10$\bar{1}$3, corresponding to pyramidal planes, while lattice strains for lines such as 10$\bar{1}$0, 11$\bar{2}$0, and 0002, corresponding to basal and prismatic planes, remain largely unaffected. The activation of basal slip also coincides with a lower rate of increase in the differential stress. Prismatic slip is activated when $\epsilon_z^{0-K_S}$ reaches 0.1170, corresponding to a pressure and differential stress of 27.6 and 11.3 GPa, respectively. The activation of prismatic slip correlates with a second inflection in the evolution of t with strain. Activation of prismatic slip induces a drop in the simulated lattice strain for 10$\bar{1}$0 and 11$\bar{2}$0, while strains for lines corresponding to basal planes, such as 0002, remain largely unaffected. At the end of the compression, differential stress reaches a value of 14.2 GPa at a pressure of 46.2 GPa.

In model 3, prismatic slip is activated when $\epsilon_z^{0-K_S}$ reaches 0.0122. At this strain, pressure and differential stress in the sample are 2.2 and 2.1 GPa, respectively. The activation of prismatic slip is correlated with a drop in the simulated lattice strains for diffraction lines such as 10$\bar{1}$0, 11$\bar{2}$0, while simulated lattice strains for lines corresponding to pyramidal and basal planes remain largely unaffected. Basal slip is activated when $\epsilon_z^{0-K_S}$ reaches 0.1190, corresponding to a pressure and differential stress of 28.2 and 11.1 GPa, respectively. The activation of basal slip is correlated with a drop in the simulated lattice strains for the lines such as 10$\bar{1}$1, 10$\bar{1}$2, and 10$\bar{1}$3, corresponding to pyramidal planes, while lattice strains for lines corresponding to basal planes remain largely unaffected. In all cases, activation of a plastic mode induces a decrease in slope for t vs applied strain. At the end of the compression, differential stress reaches a value of 13.7 GPa at a pressure of 46.2 GPa.

We conclude from the above results that basal and prismatic slips split the strain evolution of the different diffraction lines, but do not reproduce the observed experimental sequence. Also, basal activity relaxes strains in lines corresponding to pyramidal planes, and prism activity in lines corresponding to prismatic planes. In addition, although basal and prismatic slips lower the predicted lattice strains in comparison with the fully elastic model 1, they alone do not provide enough relaxation resulting in simulated strains larger than the measured ones. Since basal and prism slip do not provide deformation along the c axis of the Co crystal, we explore below the effect of the activation of crystallographic modes with a c-axis deformation component.

C. Optimized model

Models 4 and 5 (Table II) were found to best match the experimental data (Figs. 1, 2, and 6). Among the typical deformation mechanisms found in hcp metals, four were selected: basal, prismatic, and either pyramidal $\langle c+a\rangle$ slip or compressive twinning. For both models, initial CRSS τ_0 and hardening rate θ_1 were optimized to best match the measured lattice strains and their evolution with pressure. Other mechanisms, listed in Table II, were investigated but not included in the final model. For instance, pyramidal $\langle a\rangle$ slip lowers lattice strains parameters Q for most lines except 10$\bar{1}$3 and 0002 and activation of tensile twinning separates

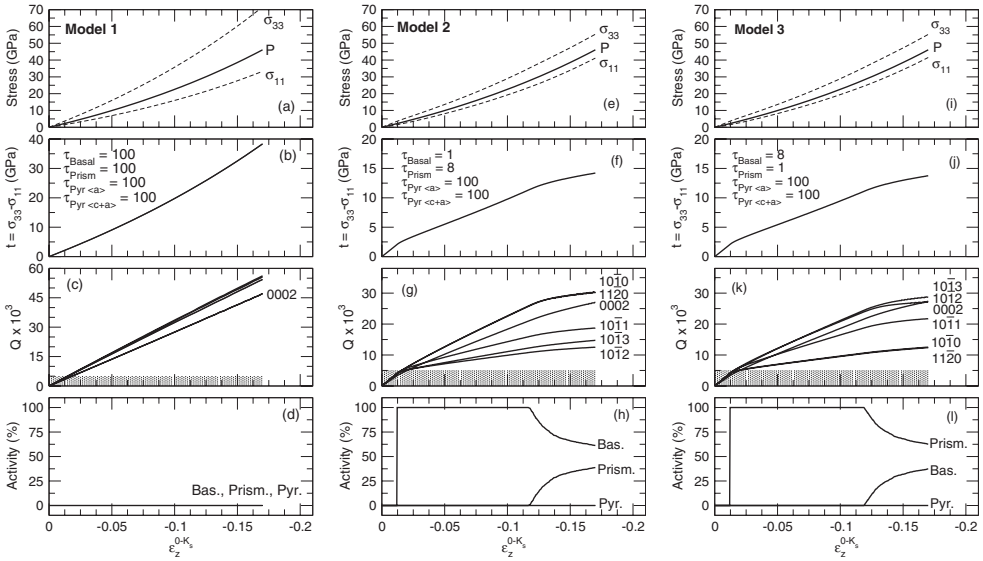

FIG. 5. σ_{11} and σ_{33} stress components, pressure [(a),(e),(i)], differential stress [(b),(f),(j)], lattice strain parameters [(c),(g),(k)], and relative activity of the deformation mechanisms [(d),(h),(l)], as a function of axial strain for simulations using models 1 [(a),(b),(c),(d)], 2 [(e),(f),(g),(h)], and 3 [(i),(j),(k),(l)] listed in Table II. In all cases, lattice strains simulated for the $10\bar{1}0$ and the $11\bar{2}0$ diffraction lines cannot be distinguished. For models 2 and 3 [Figs. 5(g) and 5(k)], Miller indices for which the lattice strains are calculated are labeled on the figure. For model 1, lattice strains for $10\bar{1}0$, $11\bar{2}0$, $10\bar{1}1$, $10\bar{1}2$, and $10\bar{1}3$ diffraction lines cannot be distinguished at this scale and are not labeled. Shaded area in Figs. 5(c), 5(g), and 5(k) indicates the order of magnitude of the experimental measurements. In all cases, pyramidal slip systems do not get activated. For model 1, none of the slip system gets activated and the simulation is fully elastic.

lattice strain parameters Q from $10\bar{1}0$ and $11\bar{2}0$; those effects cannot be reconciled with the measured data.

In both optimized models, the strength of basal slip mostly controls lattice strains simulated for $10\bar{1}1$, $10\bar{1}2$, and $10\bar{1}3$, while that of prismatic slip mostly influences $10\bar{1}0$ and $11\bar{2}0$ lattice strains. For model 4, 0002 lattice strains are controlled by pyramidal $\langle c+a \rangle$ slip, while in model 5, they are controlled by the activation of compressive twinning.

Basal slip is by far the easiest slip system with an initial CRSS of 0.07 GPa and a hardening coefficient of 0.3 GPa. In both models, the relative strength of prismatic slip and compressive twinning (model 5) or pyramidal slip (model 4) were adjusted to start prismatic slip last and eventually take over the deformation (Fig. 6). This was important to properly reproduce the measured 0002 lattice strains which are on the same order of magnitude that those of $10\bar{1}0$ and $11\bar{2}0$ early in the compression and saturate later on.

In model 4, basal slip is activated at $P=0.2$ GPa, with $t=0.2$ GPa. Pyramidal slip is activated when the pressure and differential stress are 2.3 and 1.0 GPa, respectively. Finally, prismatic slip is activated when $P=4.3$ GPa and $t=1.3$ GPa. At the end of the compression, the differential stress reaches 2.0 GPa at a pressure of 46.2 GPa.

In model 5, basal slip is activated at $P=0.2$ GPa, with $t=0.2$ GPa. Compressive twinning is activated when the pressure and differential stress are 1.7 and 0.8 GPa, respectively. Finally, prismatic slip is activated when $P=2.8$ GPa and $t=1.0$ GPa. At the end of the compression, the differential stress reaches 1.8 GPa at a pressure of 46.2 GPa.

D. Plasticity and texture evolution

Slip and twinning induce grain reorientation and, as a consequence, texture evolution. In our experiments we start from a random aggregate of Co crystals and finish with a textured aggregate, where the c axis shows a tendency to align with the compression direction. This confirms that plastic deformation takes place during the DAC test. What remains to be tested is whether the experimental texture is consistent with compressive twinning or $\langle c+a \rangle$ slip activity, as models 4 and 5 predict, respectively.

The EPSC code that we use here does not account for grain reorientation associated with plastic deformation and cannot be used to simulate texture evolution. Similarly to our EPSC model, the viscoplastic self-consistent (VPSC) code[68] treats each grain as a viscoplastic inclusion in a homogeneous matrix that has the average properties of the polycrystal and can be used for texture simulations. Starting with an initial distribution of crystallite orientations and assuming deformation by slip and twinning, we can simulate a deformation path by enforcing incremental deformation steps. As

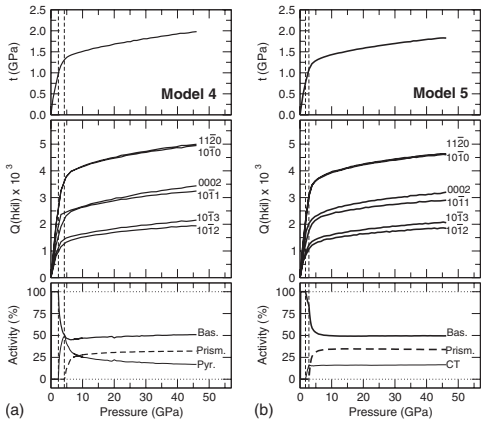

FIG. 6. Differential stress, lattice strain parameters, and relative activity of the deformation mechanisms as a function of pressure for simulations using models 4 and 5 in Table II. For model 4, vertical dashed lines at $P=2.3$ GPa and $P=4.3$ GPa correspond to the activation of pyramidal $\langle c+a\rangle$ and prismatic slip, respectively. For model 5, vertical dashed lines at $P=1.7$ GPa and $P=2.8$ GPa correspond to the activation of compressive twinning and prismatic slip, respectively.

deformation proceeds, crystals deform and rotate to generate preferred orientation. In VPSC calculations, the elastic response of the polycrystal is neglected, but grain rotations are properly accounted for, and this code has been used multiple times to model and understand textures obtained in DAC RDX experiments.[55]

A limitation of VPSC in connection with this work is that VPSC is based on an incompressible constitutive law, and calculations should be run at constant volume, that is with $(\epsilon_x+\epsilon_y+\epsilon_z)=0$. According to the equation of state, volumetric strain imposed by compressing polycrystalline cobalt to a pressure of 46 GPa is 17%, corresponding to axial strains of 5.7%. In the actual sample, 5.7% of the applied axial strain $\epsilon_z^{0-K_S}$ is accommodated elastically and the remaining 11.3% plastically, increasing stress in the radial directions σ_x and σ_y. We ran the VPSC calculations with strains corresponding to the actual plastic deformation applied to the DAC sample, which is to a maximum axial strain of 10% while preserving $\epsilon_x+\epsilon_y=-\epsilon_z$.

We used the parameters of models 4 and 5 in Table II to model the development of texture in polycrystalline cobalt deformed in the DAC. Simulations were performed in 200 steps, starting with a randomly oriented sample of 1000 grains assuming an effective interaction between grains. A viscoplastic linear hardening Voce law was used. Activity of slip systems in all 1000 grains is evaluated in each of the steps and orientations are updated accordingly. From the orientation distribution of 1000 grains, inverse pole figures were calculated to illustrate crystal orientation patterns. All texture processing has been performed with the software Beartex.[53]

In both cases, we obtain a well defined texture with a maximum located near 0001, that is, with the basal planes perpendicular to the compression direction [Figs. 3(c) and 3(d)]. After 10% strain, the inverse pole figures of the compression direction have a maximum of 2.20 and 2.22 multiples of a random distributions (m.r.d.) for VPSC calculations using models 4 and 5, respectively. Differences can be seen in the exact location of the maximum. In the experimental data, the texture component is evenly spread at about 15° of the c direction. Simulations using model 4 give a maximum at about 15° of the c direction and centered around $(10\bar{1}l)$ planes. For model 5, this maximum is located at about 15° of the c direction and centered around $(11\bar{2}l)$ planes.

It should be noted that the 15° shift of the c direction in the inverse pole figure cannot be attributed to experimental errors and is clearly visible in the measured variations in diffraction intensities with orientation (e.g., Fig. 3 in Ref. 22). It is also well reproduced by VPSC calculations. It should also be noted that textures measured in hcp-Fe do not always show a full alignment of the c axes with the compression direction[69,70] and that a shift of the maximum from the c direction has been observed in hcp-Fe.[70]

The conclusion of this calculation is that, although the VPSC predicted textures were obtained by enforcing only the plastic component of strain, they show that both pyramidal $\langle c+a\rangle$ slip and compressive twinning activity are consistent with the texture measured experimentally in the DAC for Co.

IV. DISCUSSION

A. Validity of lattice strain parameters Q

In Sec. II C 3 we assumed that the experimental data could be adjusted to Eq. (15). This implies that the d spacings measured at $\psi=54.7°$, $d_P(hkil)$, correspond to those associated with the hydrostatic pressure, and that the effect of differential stress can be summarized in the form of one unique lattice strain parameter Q.

Experimental data indicate that equation of states measured on stressed samples at $\psi=54.7°$ do agree with those measured under quasihydrostatic conditions. Results of EPSC calculations support this observation as the hydrostatic strains adjusted to Eq. (15) do not depend significantly on the combination of activated plastic deformation mechanisms. In our models, small deviations can be observed between the calculated hydrostatic strains and those expected from the single-crystal elastic moduli, e.g., 0002 and $10\bar{1}3$ in Fig. 4, but those are significantly lower than typical errors due to differential stress. Therefore, our model supports the idea that equation of states measurements at $\psi=54.7°$ on stressed samples are a valid alternative if no better solution for reducing the deviatoric stress can be found.

The assumption that the measured d spacings vary linearly with $(1-3\cos^2\psi)$ and can be summarized with a single parameter Q is more questionable. In the case of Co, d spacings measured for $11\bar{2}0$ do not follow this relation. The use of the lattice strain parameters Q is useful to compare experimental data and output of EPSC models. However, the model predictions should be compared against actual measured d spacings, as shown in Fig. 1. In this figure we dem-

onstrate that both models 4 and 5 can correctly reproduce the essentially nonlinear experimental curves.

In the experimental data, we observe a split of lattice strains measured for 0002 and 0004 above 25 GPa (Fig. 2). This cannot be accounted for using the model presented here as strains calculated to 0002 will be equal to those calculated for 0004. This observation will have to be confirmed and modeled in further studies.

B. Average pressure and stress in the polycrystalline sample

It is interesting to note that the evolution of pressure with applied strain does not depend on the proposed plastic model (e.g., Fig. 5). Plastic deformation occurs at constant volume and is independent of pressure. As a consequence, it has no influence on the relation between the applied axial strain and the average pressure within the sample.

Axial stresses, on the other hand, show a very different behavior. At the highest compression, pure elastic compression results in an axial stress $\sigma_{33}=71.6$ GPa and radial stress $\sigma_{11}=\sigma_{22}=33.3$ GPa [Fig. 5(a)]. For optimized plastic models 4 and 5, we find $\sigma_{33}=47.5(1)$ GPa and $\sigma_{11}=\sigma_{22}=45.5(1)$ GPa.

Plastic deformation results in a redistribution of stress in the polycrystalline sample. Grains that deform plastically change the stress balance of the polycrystal, decreasing the average stress supported by the polycrystal in the axial direction while increasing the stress supported in the radial direction.

The evolution of differential stress with pressure is very similar for both optimized models (Fig. 6). In both cases, we find a fast increase in differential stress to 1.3 GPa at a pressure of 5 GPa. At 42.6 GPa, differential stress for models 4 and 5 are 2.0 and 1.8 GPa, respectively. The value of 1.3 GPa corresponds to stresses where all important deformation mechanisms are activated and could be qualified as yield strength for the present sample. Increase in differential stress between 1.3 and 1.9 GPa at higher pressures is related to a pressure-induced increase in elastic constants as well as strain hardening in the sample.

C. Strength and deformation mechanisms activities

Both optimized models 4 and 5 predict a very low strength and high activity of basal slip for hcp-Co, in line with observations under ambient pressure.[40,42] This is required to reproduce the observed relatively low lattice strains for pyramidal diffraction lines such as $10\bar{1}1$, $10\bar{1}2$, or $10\bar{1}3$. Lattice strains for those planes are extremely sensitive the values of the parameters τ_0 and θ_1 of the Voce hardening rule.

We also predict a relatively low strength and high activity for prismatic slip. This is required to match the observed lattice strains for $10\bar{1}0$ and $11\bar{2}0$. Prismatic slip is commonly observed in metals with the hcp structure and has been reported in Co.[44] The lattice strains above are extremely sensitive to τ_0 and θ_1 for prismatic slip.

Models 4 and 5 differ in the activation of pyramidal $\langle c+a\rangle$ slip or compressive twinning, respectively. Compressive twinning has been reported in cobalt in the literature,[40,43] whereas observations of pyramidal $\langle c+a\rangle$ slip are scarce. Experimentally measured textures show a maximum evenly spread at about 15° of the c direction. VPSC simulations using model 4 show a maximum at about 15° of the c direction and centered around $(10\bar{1}l)$ planes. For model 5, this maximum is located at about 15° of the c direction and centered around $(11\bar{2}l)$ planes. This suggests that a full model accounting for the plastic deformation of hcp-Co should probably include a combination of both pyramidal $\langle c+a\rangle$ and compressive twinning. In the future, we expect to be able to resolve this issue by repeating our simulations using an improved version of EPSC with slip and twin reorientation.

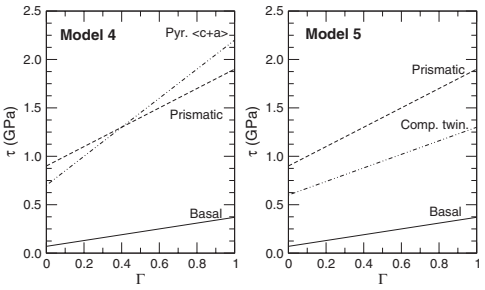

FIG. 7. Absolute CRSS of each active deformation mechanism as a function of accumulated plastic shear strain in the grain for models 4 and 5 in Table II.

In both optimized simulations, activation of pyramidal $\langle c+a\rangle$ slip or compressive twinning controls lattice strains for the 0002 diffraction line. Voce law parameters were optimized to force activation of either $\langle c+a\rangle$ slip or compressive twinning before activation of prismatic slip. Large hardening coefficients were necessary for both mechanisms to ensure a later activation of prismatic slip. In all cases, activation of prismatic slip prior to pyramidal $\langle c+a\rangle$ slip or compressive twinning resulted in models that do not fit the experimental data.

Figure 7 presents the absolute CRSS of each active deformation parameter as a function of accumulated plastic shear strain in the grain Γ for models 4 and 5 in Table II. For basal slip, Γ can reach values as high as 4 in some grains at the end of the simulation. For other deformations modes, final values of Γ range between 0.8 and 2, depending on grains and deformation mechanisms. The hardening law we used does not account for an effect of pressure on the CRSS and all experimental data could be fit using the simple, linear, strain dependent hardening law shown in Fig. 7. More experiments, where plastic deformation of the sample starts later in the compression rather than ambient pressure, will be required to quantify an effect of pressure on plasticity, but we could not extract such information from the present data.

D. Stress heterogeneities within the polycrystal

Figure 6 presents the evolution of the average differential stress as a function of pressure for models 4 and 5 while Fig.

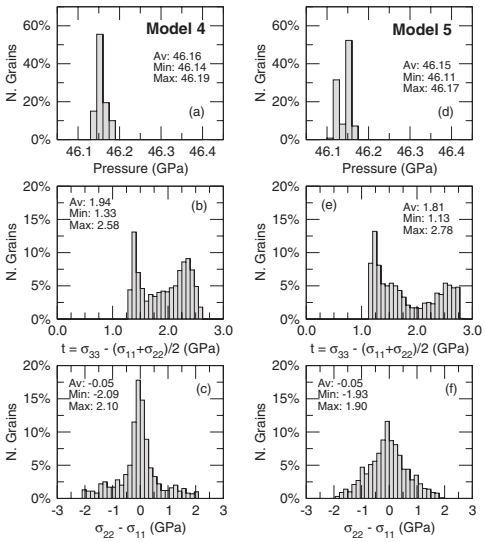

FIG. 8. Histograms of the distribution of pressure, differential stress, and lateral stress among grains in the sample at $P=46.2$ GPa for EPSC calculations using models 4 [(a),(b),(c)] and 5 [(d),(e),(f)] in Table II.

8 shows histograms of the distribution of pressure, differential stress $t=\sigma_{33}-(\sigma_{11}+\sigma_{22})$, and lateral stress $(\sigma_{22}-\sigma_{11})$ among grains in the sample at the end of compression for both models. Pressure is very uniform and only varies by 0.05 GPa from grain to grain, which is on the order of magnitude of numerical errors in the calculation. Distributions of differential and lateral stress, however, are not uniform and model dependent.

Lateral stresses show a distribution centered around 0 GPa, as expected. For both models, minimum and maximum lateral stresses among grains are of the same order of magnitude than the average differential stress in the sample.

For both models, differential stress among grains shows a bimodal distribution whose mean corresponds to the average differential stress in the polycrystalline sample. Differences between the minimum and maximum stress among grains is lower than the average differential stress but well over 1 GPa. Two grain families can be identified: grains in soft orientations that were submitted to large plastic deformation and show a relatively low differential stress, and grains in hard orientations that were submitted to less plastic deformation and show a relatively high differential stress.

The relevant conclusion of the stress distribution analysis is that plasticity leads to a significant spread of stress among grains. This explains why models based on assuming uniform states in the aggregate[14] yield inconsistent stresses and elastic constants for materials deforming plastically.[21,22,32,33] Figure 8 demonstrates that, as slip or twinning is activated inside a grain, deviatoric stresses are relaxed within the grain, and the state of stress among grains in the aggregate becomes very heterogeneous. This cannot be accounted for with theories relying solely on continuum mechanisms and numerical models such as those presented here should be applied.

E. Limitations of the model

As demonstrated in this paper, EPSC models are very successful for understanding and modeling internal stress and strain in plastically deforming polycrystals. The current approach, however, has limitations. They can be separated in two categories: limitations of the self-consistent approach, and limitations of the actual code we used.

The self-consistent model treats each grain as an ellipsoidal elastoplastic inclusion embedded within a homogeneous elastoplastic effective medium. As such, local interactions from grain to grain and heterogeneities within the grains themselves are not accounted for. Three-dimensional (3D) full-field polycrystalline models can predict local-field variations.[71–73] These calculations show important heterogeneities within grains and a strong localization of stress and strain near the grain boundaries. However, the precision of those models comes with large computational cost and complexity, and they cannot be systematically applied for interpreting experimental results. Mean-field approaches such as EPSC models are very successful and currently remain most convenient to explore and understand experimental results.[73]

The EPSC code we used did not account for grain reorientation associated with slip and twinning deformation. While we do not expect that texture evolution will change the qualitative conclusions of this paper concerning the type and role of deformation mechanisms, we do expect that it will influence CRSS and hardening parameters. In the current version of the model, grains that have an orientation favorable for the activation of a deformation mechanism will be activated at each step. In reality, those grains should rotate and finally reach orientations less favorable for the deformation mechanism. As such, we expect the hardening parameters reported in Table II to be slightly overestimated.

V. CONCLUSIONS

A modification of the EPSC model of Turner and Tomé[31] was used to successfully model x-ray diffractions measurements performed on hcp-Co samples plastically deformed under high pressure. Important information provided by the model includes: actual values of differential stress in the polycrystal, stress distribution among grains in the sample, as well as identification, relative activity, and strength of the active deformation mechanisms.

The model confirms that the effect of differential stress and plastic deformation on measured d spacings is often minimal at $\psi=54.7°$. Therefore, measurements of d spacings at this angle can be used to estimate hydrostatic equation of states if no better solution is available. This is particularly applicable to measurements above 100 GPa for which no hydrostatic pressure transmitting medium is available.

We find that the plastic behavior of hcp-Co plastically deformed under high pressure is controlled by basal and pris-

matic slip of $\langle a \rangle$ dislocations, and either pyramidal slip of $\langle c+a \rangle$ dislocations or compressive twinning. Strength and hardening coefficients for those mechanisms have been determined and are listed in Table II. Basal slip is by far the easiest and most active deformation mechanism, with an initial strength of 0.07 GPa and a linear hardening coefficient of 0.30 GPa.

For hcp-Co deformed axially in the diamond-anvil cell, we observe a fast increase in differential stress to 1.3 GPa between pressures of 0 and 5 GPa. The later part of the compression shows a slower increase in differential stress with pressure. At 42 GPa, the differential stress in hcp-Co is 1.9 ± 0.1 GPa. The transition between the fast and slow increase in differential stress in the sample is related to the sequential activation of plastic deformation mechanisms in the sample.

EPSC models are very powerful and overcome many limitations of models based on continuum elasticity theory for the interpretation of x-ray diffraction data measured on stressed samples. They should be used for the interpretation of all high pressure deformation experiments where x-ray diffraction is used to probe stress within a polycrystalline sample.

ACKNOWLEDGMENT

The authors want to thank B. Clausen for his input. S. M. acknowledges support from the Miller Institute for Basic Research in Science and ANR program DiUP. H.-R. W. appreciates support from NSF EAR-0337006 and CDAC.

*sebastien.merkel@univ-lille1.fr

[1] S. Klotz, M. Braden, and J. M. Besson, Phys. Rev. Lett. **81**, 1239 (1998).
[2] F. Occelli, D. L. Farber, J. Badro, C. M. Aracne, D. M. Teter, M. Hanfland, B. Canny, and B. Couzinet, Phys. Rev. Lett. **93**, 095502 (2004).
[3] A. F. Goncharov, J. Crowhurst, and J. M. Zaug, Phys. Rev. Lett. **92**, 115502 (2004).
[4] M. B. Weinberger, S. H. Tolbert, and A. Kavner, Phys. Rev. Lett. **100**, 045506 (2008).
[5] G. Steinle-Neumann, L. Stixrude, and R. E. Cohen, Phys. Rev. B **60**, 791 (1999).
[6] X. Sha and R. E. Cohen, Phys. Rev. B **74**, 064103 (2006).
[7] L. Vočadlo, Earth Planet. Sci. Lett. **254**, 227 (2007).
[8] G. Steinle-Neumann, Phys. Rev. B **77**, 104109 (2008).
[9] Y. Ma, M. Somayazulu, G. Shen, H. Mao, J. Shu, and R. Hemley, Phys. Earth Planet. Inter. **143-144**, 455 (2004).
[10] R. J. Hemley, H. K. Mao, G. Shen, J. Badro, P. Gillet, M. Hanfland, and D. Häusermann, Science **276**, 1242 (1997).
[11] D. Yamazaki and S.-I. Karato, Rev. Sci. Instrum. **72**, 4207 (2001).
[12] S. Merkel, H. R. Wenk, J. Shu, G. Shen, P. Gillet, H. K. Mao, and R. J. Hemley, J. Geophys. Res. **107**, 2271 (2002).
[13] Y. Wang, W. B. Duhram, I. C. Getting, and D. J. Weidner, Rev. Sci. Instrum. **74**, 3002 (2003).
[14] A. K. Singh, C. Balasingh, H. K. Mao, R. J. Hemley, and J. Shu, J. Appl. Phys. **83**, 7567 (1998).
[15] A. K. Singh, H. K. Mao, J. Shu, and R. J. Hemley, Phys. Rev. Lett. **80**, 2157 (1998).
[16] H. K. Mao, J. Shu, G. Shen, R. J. Hemley, B. Li, and A. K. Singh, Nature (London) **396**, 741 (1998); **399**, 280 (1999).
[17] S. Merkel, J. Shu, P. Gillet, H. Mao, and R. Hemley, J. Geophys. Res. **110**, B05201 (2005).
[18] W. L. Mao *et al.*, J. Geophys. Res. **113**, B09213 (2008).
[19] D. Antonangeli, M. Krisch, G. Fiquet, D. L. Farber, C. M. Aracne, J. Badro, F. Occelli, and H. Requardt, Phys. Rev. Lett. **93**, 215505 (2004).
[20] D. Antonangeli, M. Krisch, G. Fiquet, J. Badro, D. L. Farber, A. Bossak, and S. Merkel, Phys. Rev. B **72**, 134303 (2005).
[21] D. Antonangeli, S. Merkel, and D. L. Farber, Geophys. Res. Lett. **33**, L24303 (2006).
[22] S. Merkel, N. Miyajima, D. Antonangeli, G. Fiquet, and T. Yagi, J. Appl. Phys. **100**, 023510 (2006).
[23] J. C. Crowhurst, D. Antonangeli, J. M. Brown, A. F. Goncharov, D. L. Farber, and C. M. Aracne, Appl. Phys. Lett. **89**, 111920 (2006).
[24] I. Noyan and J. Cohen, *Residual Stress: Measurements by Diffraction and Interpretation* (Springer-Verlag, New York, 1987).
[25] M. R. Daymond, Rev. Mineral. Geochem. **63**, 427 (2006).
[26] B. Clausen, T. Lorentzen, and T. Leffers, Acta Mater. **46**, 3087 (1998).
[27] M. R. Daymond, M. A. M. Bourke, and R. B. Von Dreele, J. Appl. Phys. **85**, 739 (1999).
[28] P. Dawson, D. Boyce, S. MacEwen, and R. Rogge, Mater. Sci. Eng., A **313**, 123 (2001).
[29] M. R. Daymond and N. W. Bonner, Mater. Sci. Eng., A **340**, 272 (2003).
[30] D. Brown, M. Bourke, B. Clausen, T. Holden, C. Tome, and R. Varma, Metall. Mater. Trans. A **34**, 1439 (2003).
[31] P. A. Turner and C. N. Tomé, Acta Metall. Mater. **42**, 4143 (1994).
[32] D. J. Weidner, L. Li, M. Davis, and J. Chen, Geophys. Res. Lett. **31**, L06621 (2004).
[33] L. Li, D. J. Weidner, J. Chen, M. T. Vaughan, M. Davis, and W. B. Durham, J. Appl. Phys. **95**, 8357 (2004).
[34] P. C. Burnley and D. Zhang, J. Phys.: Condens. Matter **20**, 285201 (2008).
[35] C. S. Yoo, H. Cynn, P. Söderlind, and V. Iota, Phys. Rev. Lett. **84**, 4132 (2000).
[36] H. Fujihisa and K. Takemura, Phys. Rev. B **54**, 5 (1996).
[37] D. Antonangeli, L. R. Benedetti, D. L. Farber, G. Steinle-Neumann, A. Auzende, J. Badro, M. Hanfland, and M. Krisch, Appl. Phys. Lett. **92**, 111911 (2008).
[38] H. J. McSkimin, J. Appl. Phys. **26**, 406 (1955).
[39] D. Antonangeli, M. Krisch, D. L. Farber, D. G. Ruddle, and G. Fiquet, Phys. Rev. Lett. **100**, 085501 (2008).
[40] A. Seeger, H. Kronmüller, O. Boser, and M. Rapp, Phys. Status Solidi **3**, 1107 (1963) b.

[41] M. H. Yoo and C. T. Wei, J. Appl. Phys. **38**, 4317 (1967).
[42] H. M. Theiringer, Z. Metallkd. **59**, 476 (1968).
[43] S. Vaidya and S. Mahajan, Acta Metall. **28**, 1123 (1980).
[44] X. Wu, N. Tao, Y. Hong, G. Liu, B. Xu, J. Lu, and K. Lu, Acta Mater. **53**, 681 (2005).
[45] A. A. Karimpoor, U. Erb, K. T. Aust, and G. Palumbo, Scr. Mater. **49**, 651 (2003).
[46] X. Zhang and C. Jia, Mater. Sci. Eng., A **418**, 77 (2006).
[47] G. Zheng, Y. Wang, and M. Li, Acta Mater. **53**, 3893 (2005).
[48] T. H. K. Barron and M. L. Klein, Proc. Phys. Soc. London **85**, 523 (1965).
[49] D. C. Wallace, Solid State Phys. **25**, 301 (1970).
[50] D. C. Wallace, *Thermodynamics of Crystals* (Wiley, New York, 1972).
[51] U. F. Kocks, C. Tomé, and H. R. Wenk, *Texture and Anisotropy: Preferred Orientations and their Effects on Material Properties* (Cambridge University Press, Cambridge, 1998).
[52] S. Matthies and G. W. Vinel, Phys. Status Solidi B **112**, K111 (1982).
[53] H. R. Wenk, S. Matthies, J. Donovan, and D. Chateigner, J. Appl. Crystallogr. **31**, 262 (1998).
[54] L. Lutterotti, S. Matthies, and H. R. Wenk, IUCR: Newsl. of the CPD **21**, 14 (1999).
[55] H. R. Wenk, I. Lonardelli, S. Merkel, L. Miyagi, J. Pehl, S. Speziale, and C. E. Tommaseo, J. Phys.: Condens. Matter **18**, S933 (2006).
[56] S. Matthies, H. G. Priesmeyer, and M. R. Daymond, J. Appl. Crystallogr. **34**, 585 (2001).
[57] S. Matthies, S. Merkel, H. R. Wenk, R. J. Hemley, and H. K. Mao, Earth Planet. Sci. Lett. **194**, 201 (2001).
[58] S. Merkel and T. Yagi, J. Phys. Chem. Solids **67**, 2119 (2006).
[59] S. R. Agnew, C. N. Tomé, D. W. Brown, T. M. Holden, and S. C. Vogel, Scr. Mater. **48**, 1003 (2003).
[60] S. Agnew, D. Brown, and C. Tomé, Acta Mater. **54**, 4841 (2006).
[61] R. Hill, J. Mech. Phys. Solids **13**, 89 (1965).
[62] J. W. Hutchinson, Proc. R. Soc. London, Ser. A **319**, 247 (1970).
[63] S. Merkel and T. Yagi, Rev. Sci. Instrum. **76**, 046109 (2005).
[64] T. S. Duffy, G. Shen, D. L. Heinz, J. Shu, Y. Ma, H. K. Mao, R. J. Hemley, and A. K. Singh, Phys. Rev. B **60**, 15063 (1999).
[65] A. Kavner and T. S. Duffy, Phys. Rev. B **68**, 144101 (2003).
[66] S. Speziale, S. R. Shieh, and T. S. Duffy, J. Geophys. Res. **111**, B02203 (2006).
[67] A. Kavner, J. Geophys. Res. **112**, B12207 (2007).
[68] R. A. Lebensohn and C. N. Tomé, Mater. Sci. Eng., A **175**, 71 (1994).
[69] H. R. Wenk, S. Matthies, R. J. Hemley, H. K. Mao, and J. Shu, Nature (London) **405**, 1044 (2000).
[70] S. Merkel, H. R. Wenk, P. Gillet, H. K. Mao, and R. J. Hemley, Phys. Earth Planet. Inter. **145**, 239 (2004).
[71] H. Moulinec and P. Suquet, Comput. Methods Appl. Mech. Eng. **157**, 69 (1998).
[72] R. A. Lebensohn, Acta Mater. **49**, 2723 (2001).
[73] O. Castelnau, D. K. Blackman, R. A. Lebensohn, and P. Ponte Castañeda, J. Geophys. Res. **113**, B09202 (2008).

Neuvième partie

Articles : Développements expérimentaux

APPLIED PHYSICS LETTERS VOLUME 74, NUMBER 5 1 FEBRUARY 1999

Finite-element modeling of diamond deformation at multimegabar pressures

Sébastien Merkel,[a] Russell J. Hemley, and Ho-kwang Mao
Geophysical Laboratory and Center for High Pressure Research, Carnegie Institution of Washington, 5251 Broad Branch Road, N.W., Washington, DC 20015

(Received 15 September 1998; accepted for publication 23 November 1998)

Finite-element modeling calculations reveal the origin of the remarkably large elastic strains in diamond observed in recent experiments at multimegabar pressures. This approach provides a means to determine the pressure dependence of the yield strength of strong materials used in the gasket, and allows us to examine quantities that are not accessible experimentally such as the stress and strain relations in diamond. Stress tensor elements are obtained near the tip where large modifications in the optical properties of diamond have been observed. © *1999 American Institute of Physics.* [S0003-6951(99)02505-X]

The diamond anvil cell has revolutionized the study of materials under extreme static pressures.[1] The crucial parts of the device are the diamond and the gasket. For very high-pressure experiments, beveled diamonds concentrate the stress on the sample, allowing attainment of pressures in the multimegabar range.[2,3] Understanding the behavior of the diamond tip under these conditions is essential for further extending the range of laboratory static pressures. Recent x-ray experiments[4] imaged deformations of the diamond tip under multimegabar pressures. Although often considered as a rigid body, diamond was found to undergo very large elastic deformations near the sample region. Here, we report a theoretical study of this phenomenon using finite-element modeling and first-principles calculation. The approach allows us to understand the x-ray observations and to obtain predictions of the stress and strain relations that are not accessible experimentally.

Finite-element modeling calculations have been performed to examine the geometric properties of the diamond anvil.[5–7] We extend these calculations in order to analyze quantitatively the recent x-ray observations[4] in terms of the properties of the diamond and the gasket. Several geometries were used; all of them have an 8.5° bevel angle, a 150-μm-radius culet, and then values for the central flat radius ranging from 5 to 25 μm. As in the experiments,[4,6] the gasket is considered to be 250 μm thick at the beginning of the simulations (Fig. 1). We used a modified version of the finite-element code NIKE2D that includes rezoning capability (e.g., Refs. 6 and 7). Because of the very large deformations observed in the gasket, the rezoning plays a very important role by allowing modification of the grid during the calculations and adapting it to the new shape of the gasket.

We consider the diamond as purely elastic with a pressure dependence of the stiffness coefficients. These quantities have been measured[8] and *ab initio* local density approximation calculations have been performed[9,10] but over a lower pressure range than that considered here. Therefore, we performed such *ab initio* calculations[11] to higher pressures (Table I); we used the values obtained from calculations up to 340 GPa.

For the gasket, we used a plastic–elastic model with material properties appropriate to rhenium. The bulk and shear moduli and their pressure derivatives have been measured experimentally.[12] Experimental studies of the yield stress and its variation with pressure have also been conducted[13,14] but the results have rather large uncertainties. In our calculations we considered several different possible pressure dependencies of the yield strength (Fig. 2).

Our first goal was to understand the large deformations observed experimentally in the 200–300 GPa range.[4] We ran the calculations with several models of the gasket in order to examine this behavior. The shape of the diamond/gasket interface and the corresponding axial stress repartition obtained are presented in Fig. 3. These results do not depend strongly on the elastic properties of the diamond or the friction coefficient included in our model. On the other hand, the variation of the gasket yield stress with pressure has a major influence on its final thickness. Experimentally, the gaskets compress to a thickness between 5 and 10 μm under megabar pressures. By comparing the results in Fig. 3(b) we deduce that the gasket model with $\sigma_y = 12$ GPa at 100 GPa (curve B in Fig. 2) gives the best agreement. This estimate is similar to the trend in recent x-ray diffraction data for rhenium to 40 GPa.[14]

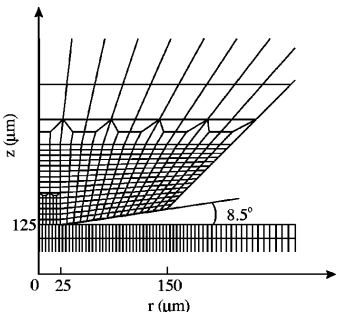

FIG. 1. Example of initial grid (25-μm-radius central flat).

[a]Electronic mail: merkel@gl.ciw.edu

TABLE I. Elastic moduli of diamond (in GPa) and pressure derivatives. The C_{ij} are close to linear in pressure; small differences arise primary from the different range of the fits.

	C_{11}	C_{12}	C_{44}	C'_{11}	C'_{12}	C'_{44}
Theory (to 50 GPa)	1090	145	580	4.60	2.76	2.85
Theory (to 340 GPa)	1090	145	580	3.83	2.60	1.63
Theory[a]	1050	127	550	5.95	1.21	3.92
Experiment[b]	1079	124	578	5.98	3.06	2.98

[a]Reference 9.
[b]Reference 8.

Figures 4(a) and 4(b) present the x-ray transmission and the axial stress repartition calculated for a 5-μm-radius central flat diamond and gasket model B as well as experimental results. A distinct cupping of the diamond tip appears. As observed experimentally, the pressure-load relation reaches saturation at the highest loads. The magnitude of the cupping appears to be larger and the stress distribution broader than the x-ray observations; at 300 GPa, the calculated and observed pressure gradients at the tip are 1.3 and 3.2 GPa/μm, respectively. The agreement might be improved by including higher-order terms in the diamond stress–strain relations. Moreover, with a 25-μm-radius central flat diamond we even observe a double cupping [Fig. 3(b)]. We infer that also happens in the model with a 5-μm-radius central flat diamond but it did not appear because of the size of our grid elements. Likewise, it was not observed experimentally, probably because of the finite size of the x-ray beam.[4]

Finite-element modeling provides access to the stress tensor at any node and any step of the calculation. An interesting and important question is the nature of the stress distribution along the symmetry axis of the diamond where the shear stress reaches its maximum. This has a significant effect on the band gap and could drive structural changes in the diamond.[15,16] This had been previously studied[17] using a simplified model assuming a semi-infinite anvil with a flat face and a circularly symmetric distribution of pressure applied to the face. In this study we also assume a cylindrical symmetry but pay closer attention to the features of the anvil.

As in Ref. 17, we let P_s be the axial stress at the interface diamond gasket and with shear stress defined as

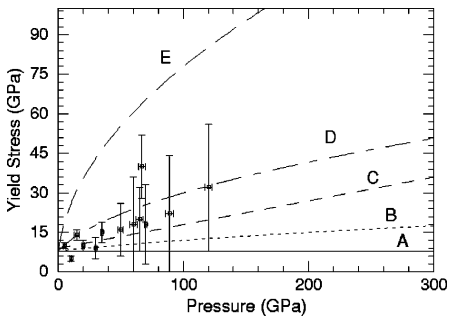

FIG. 2. Yield stress of the gasket vs pressure. The symbols show data from Ref. 13, curve A includes no pressure dependence, curve C is an estimation using $\sigma_y(p)=0.05\,\mu$ with μ deduced from Ref. 12, curves B and D present other possibilities that satisfy the experimental data, and curve E is an upper estimated bound (e.g., Ref. 4).

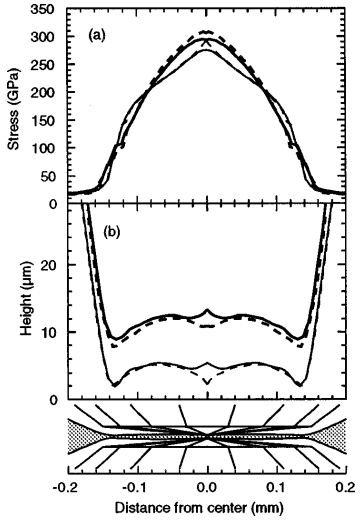

FIG. 3. (a) Final calculated axial stress along the diamond/gasket interface, and (b) final position of the interface (which gives half the gasket thickness). The thin curves correspond to a gasket yield stress given by curve B and the thick curves by curve D in Fig. 2. The dotted and solid lines are for a 5- and a 25-μm-radius diamond central flat, respectively. Deformation of the anvil is shown at the bottom.

$\tau=(\sigma_z-\sigma_r)/2$, we can then deduce the evolution of σ_z/P_s, σ_r/P_s, and τ/P_s along the symmetry axis at any load. We find that these curves do not vary between 200 and 300 GPa. This corresponds to the load where the diamond cupping is

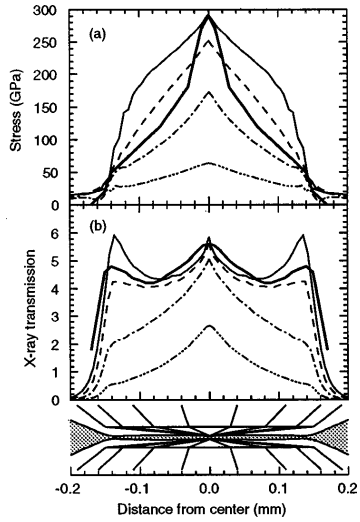

FIG. 4. (a) and (b) Calculated axial stress along the diamond/gasket interface and simulated x-ray transmission through the diamond gasket assembly (after Ref. 4). The results are shown for different loads of equal increment and a 5-μm-radius central flat diamond and a gasket yield stress given by curve B in Fig. 2. The thick lines show experimental results from Ref. 4. The thin solid line in (a) is also shown in Fig. 3(a) with a thin dashed line.

TABLE II. Values of $-\sigma_r/P_s$, $-\sigma_z/P_s$, and τ/P_s at the point where τ reaches its maximum. The calculated values presented here are deduced from several curves with $P_s \geqslant 200$ GPa and different kinds of gaskets.

	$\alpha=-\sigma_r/P_s$	$\beta=-\sigma_z/P_s$	$\tau_{\max}/P_s$
5 μm flat	0.15 ($\pm$0.02)	0.75 ($\pm$0.05)	0.29 ($\pm$0.01)
25 μm flat	0.05 ($\pm$0.02)	0.65 ($\pm$0.05)	0.29 ($\pm$0.02)
Ref. 17	0.12	0.88	0.38
Ref. 16	0.29	0.89	0.30

mostly complete. At lower loads, the diamond undergoes very large elastic deformations so the geometrical repartition of stress and strain is not stable. At the location where the shear stress τ reaches its maximum we have

$$(\sigma_{ij})=\begin{pmatrix} -\alpha & 0 & 0 \\ 0 & -\alpha & 0 \\ 0 & 0 & -\beta \end{pmatrix} P_s . \quad (1)$$

The calculated values for the coefficients of this matrix are presented in Table II for the two representative geometries as well as results from previous studies.[16,17] The significant differences for α and β arise principally from geometric effects. It was pointed out in Ref. 16 that the matrices used therein might not reflect the experimental situation: these results are, therefore, useful for more precise analysis of the band-gap behavior of the anvil in diamond cells as a function of the sample pressure or load.

A finite-element analysis shows that plastic and elastic models are sufficient to simulate the behavior of the anvils in diamond cells at multimegabar pressures. We find a strong dependence on the assumed properties of the gasket. Comparison with experimental results allows us to constrain the plastic properties of the strong metals used up to very high pressures that are difficult to obtain experimentally. The technique can now be used to study the deformations and the pressure gradients in the cell with a sample having a very low compressibility (like hydrogen), and to explore the behavior at higher loads with a wider range of gasket materials.

The authors thank R. E. Cohen and G. Saghi-Szabo for the computational help and W. C. Moss and C. T. Prewitt for useful discussions. This work was supported by the NSF.

[1] R. J. Hemley and H. K. Mao, Encycl. Appl. Phys. **18**, 555 (1997).
[2] H. K. Mao and P. M. Bell, Science **200**, 1145 (1978).
[3] P. M. Bell, H. K. Mao, and K. Goettel, Science **226**, 542 (1984).
[4] R. J. Hemley, H. K. Mao, G. Shen, J. Badro, P. Gillet, M. Hanfland, and D. Haüsermann, Science **276**, 1242 (1997).
[5] M. S. Bruno and K. J. Dunn, Rev. Sci. Instrum. **55**, 940 (1984).
[6] W. C. Moss, J. O. Hallquist, R. Reichlin, K. A. Goettel, and S. Martin, Appl. Phys. Lett. **48**, 1258 (1986).
[7] W. C. Moss and K. A. Goettel, Appl. Phys. Lett. **50**, 25 (1987).
[8] H. J. McSkimin and P. Andreatch, Jr., J. Appl. Phys. **43**, 2944 (1972).
[9] O. H. Nielsen, Phys. Rev. B **34**, 5808 (1986).
[10] O. H. Nielsen and R. M. Martin, Phys. Rev. B **32**, 3780 (1985).
[11] S. Merkel, D. M. Teter, and R. J. Hemley (unpublished).
[12] M. H. Manghnani and K. Katahara, Phys. Rev. B **9**, 1421 (1974).
[13] R. Jeanloz, B. K. Godwal, and C. Meade, Nature (London) **349**, 687 (1991).
[14] T. S. Duffy, G. Shen, D. L. Heinz, Y. Ma, R. J. Hemley, H. K. Mao, and A. K. Singh, in *High Pressure Materials Research*, Vol. 499 of MRS Symposium Proceedings, edited by R. M. Wentzcovitch, R. J. Hemley, W. J. Nellis, and P. Y. Yu (Materials Research Society, Warrendale, PA, 1998), pp. 145–150.
[15] H. K. Mao and R. J. Hemley, Nature (London) **351**, 721 (1991).
[16] M. P. Surh, S. G. Louie, and M. L. Cohen, Phys. Rev. B **45**, 8239 (1992).
[17] A. L. Ruoff and H. Luo, J. Appl. Phys. **70**, 2066 (1991).

Science and Technology of High Pressure, Proceedings of the AIRAPT-17,
edited by M.H. Manghnani, W.J. Nellis and M.F. Nicol, pp. 68-73, University Press, Hyderabad, India, 2000.

Finite-Element Modeling and Ab initio Calculations of Megabar Stresses in the Diamond Anvil Cell

Sébastien Merkel*, Russell J. Hemley, Ho-kwang Mao and David M. Teter†
Geophysical Laboratory and Center for High Pressure Research, Carnegie Institution of Washington, 5251 Broad Branch Rd., N.W., Washington, DC 20015, U.S.A.

Finite-element modeling calculations are conducted to investigate the remarkably large elastic strains in diamond observed in ultrahigh pressure diamond anvil cell experiment. We perform *ab initio* calculations to evaluate the elastic properties of diamond in the multimegabar range and use the £nite-element results to estimate the pressure dependence of shear stress of strong materials used as gasket. We then analyze the in¤uence of geometric properties such central ¤at diameter or bevel angle, and reveal the existence of two distinct deformation mechanisms during the pressure increase. Finally, we investigate the stress conditions in the gasket and the diamond and discuss possible shear-induced mechanical instabilities in diamond.

[£nite-element modeling, ab-initio calculations, large deformations, stress, failure]

1. Introduction

The diamond anvil cell is widely used in the £eld of high pressure research for the generation of extreme static pressure conditions. Diamond's strength, high electrical resistivity, high thermal conductivity and transparency over a wide range of wavelengths allows *in situ* measurements on materials under a variety of pressure and temperature conditions. Beveled diamonds concentrate the stress on the sample allowing the multimegabar range to experiments[1, 2]. Understanding the behavior of the anvil under these conditions is essential for extending the range of feasible laboratory static pressures. Recent x-ray experiments[3] imaged the deformations of the diamond tip under multimegabar pressures. Finite-element modeling[4] then con£rmed that, although often considered to be a rigid body, diamond could sustain signi£cant large elastic deformations near the sample region. In this study, we discuss the material properties that are critical for such calculations. We present results from *ab initio* calculations of the elastic properties of diamond in the multimegabar range and a means to estimate the gasket yield stress. We then extend the previous £nite-element calculations[4, 5, 6, 7] to provide a better understanding of the in¤uence of geometric properties such as the diamond bevel angle and central ¤at diameter.

2. Model

We performed two-dimensional axisymmetric £nite-element calculations using NIKE2D (e.g., Refs. [4, 6, 7]) that includes rezoning capabilities. Because of the very large deformations observed in the gasket, the rezoning plays a very important role by allowing modi£cation of the grid during the calculations. The axial symmetry implies that coordinates and stresses have to be expressed in cylindrical system r, θ and z whose z is parallel to the loading axis, r is the radial distance from the z axis, and θ is perpendicular to r and z. The stress components are independent of the θ coordinate ($\partial\sigma_{ij}/\partial\theta = 0$), and the only stresses considered are σ_{rr}, σ_{zz}, $\sigma_{\theta\theta}$ and σ_{rz} with $\sigma_{r\theta}$ and $\sigma_{\theta z}$ always equal to zero. The symmetry also implies that along the z axis ($r = 0$), $\sigma_{\theta\theta} = \sigma_{rr}$ and $\sigma_{rz} = 0$.

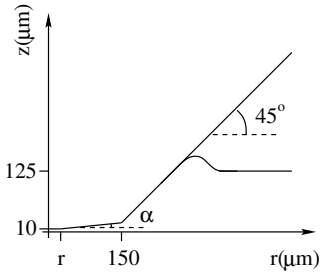

Figure 1: Geometric properties of the model. The central ¤at radius r and the bevel angle α are variable parameters.

Several geometries were considered. Figure 1 describes the main characteristics of the grid used for analyzing the in¤uence of geometric properties of the diamond in the very high pressure experiments. We assumed a gasket preindented to a thickness of 20 μm at the tip from 250 μm at start. The diameter of the diamond bevel is £xed to 300 μm. We have two variable parameters,

Table 1: Central ¤at diameter d and bevel angle α con£gurations.

d (μm)	α (degrees)	d (μm)	α (degrees)
5	8.5°	20	5°
10	8.5°	20	7°
20	8.5°	20	8.5°
50	8.5°	20	10°
		20	12°

*Current address: Laboratoire des Sciences de ta Terre, École Normale Supérieure de Lyon, 46 allée d'Italie, 69364 Lyon Cedex 07, France

†Current address: Geochemistry Department, Sandia National Laboratories, P.O. Box 5800, Albuquerque, NM 87185, U.S.A.

Table 2: *Ab initio* calculated elastic properties of diamond. G_r and G_v are the shear modulus calculated with Reuss and Voigt bounds.

a (Å)	P (GPa)	K (GPa)	C_{44} (GPa)	C_{11} (GPa)	C_{12} (GPa)	G_v (GPa)	G_r (GPa)
3.542	0	459	601	1090	144	550	542
3.535	3	470	601	1101	155	550	542
3.493	21	533	648	1191	204	586	576
3.440	48	622	737	1311	277	649	630
3.281	159	971	915	1767	573	788	754
3.122	339	1482	1163	2389	1028	970	906
2.910	755	2541	1523	3571	2026	1223	1097

the bevel angle α and central ¤at diameter d. Table 1 presents the different con£gurations we examined. We also designed a grid with non-indented gasket in which geometric properties are the same as above except that the gasket thickness is assumed to be 250 μm everywhere.

We considered the diamond as purely elastic with a linear pressure dependence of the elastic constants. These quantities have been measured experimentally[8] and *ab-initio* local density approximation calculations have been previously performed[9, 10], but over a lower range of pressure than considered here. Therefore, we performed new *ab-initio* calculations to higher pressures. Our calculations were carried out using density-functional techniques within the local density approximation (LDA) to electron exchange and correlation. We used a preconditioned conjugate-gradient method to minimize the electronic degrees of freedom. The electronic wave functions were expanded in a plane-wave basis set with periodic boundary conditions. We used norm-conserving and hardness conserving (ENHC) pseudopotentials[11]. This scheme ensures that the total energies of the atom and pseudoatom match to second order with respect to arbitrary changes in valence-state occupancy. This additional condition has been shown to improve pseudopotential transferability in studies of diamond-carbon[11]. The elastic constants were determined using the £nite-deformation method[12, 13, 14, 15]. Table 2 presents the cell parameter, elastic constants and bulk and shear moduli we obtained for different pressures ranging from 0 to 750 GPa. In the £nite-element calculations, we were interested in the 0 to 400 GPa pressure range, so we used the linear approximation of the elastic constants presented in Figure 2.

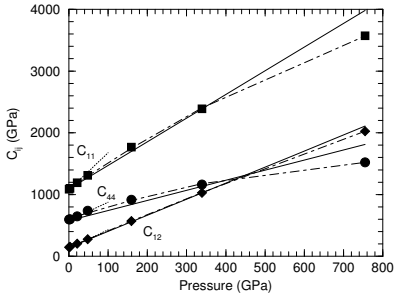

Figure 2: Elastic constants of diamond and their variation with pressure. Square, diamond and circle symbols are C_{11}, C_{12}, and C_{44}, respectively, calculated using *ab-initio* local density approximation. The dotted curves show an extrapolation of ultrasonic experimental measurements[8], dash-dotted curves are polynomial £t through the *ab-initio* data, and solid curves the linear approximation we used in these calculations.

For the gasket we used a plastic-elastic model with material properties appropriate to rhenium. We assume a shear modulus, a pressure-dependent bulk modulus, and a pressure-dependent yield stress. The bulk modulus and its pressure derivative have been measured experimentally[16, 17]. We used the shear modulus measured from ultrasonic methods[16] at zero pressure. The results presented here are stable towards a variation of this parameter, the most in¤uential property being the yield stress. Experimental studies of the yield stress and its variation with pressure have also been performed [17, 18] but the results have rather large uncertainties (Fig. 3). To have a better constraint on our yield stress estimation, we performed indentation simulations, starting with a non-indented gasket and increasing the load at top surface of the diamond to reach a maximum pressure of about 300 GPa with several models for the gasket yield stress. Following Ref.[17], we used $\sigma_y = 8$ GPa at $P = 0$. Figure 4 presents the shape of the diamond/gasket interface and the corresponding axial stress repartition we obtained. Experimentally, the gaskets compress to a thickness between 5 and 10 μm under multimegabar pressures. Comparing the results in Figure 4(b) we deduce that the gasket model with $\sigma_y = 8$ GPa at 0 GPa and

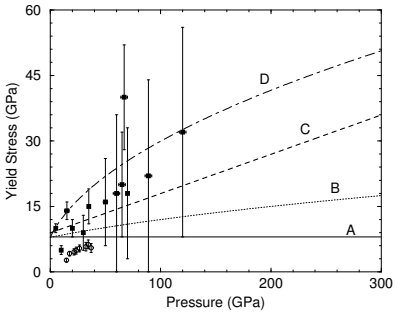

Figure 3: Yield stress of the gasket vs. pressure. The solid and open symbols show data from Ref.[17] and Ref.[18], respectively. Curve A includes no pressure dependence, curves B, C and D present several estimations that satisfy the experimental data.

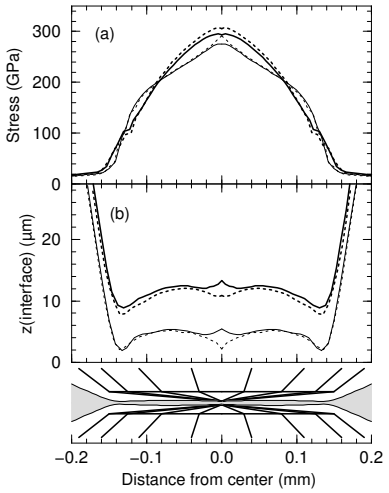

Figure 4: (a), Final calculated axial stress along the diamond/gasket interface, and (b), £nal position of the interface (which gives half the gasket thickness). The thin and solid curves correspond to a gasket yield stress following curve B and D in Figure 3, respectively. The dotted and solid lines are for a 10 and a 50 μm central ¤at diameter diamond, respectively. Deformation of the anvil is shown at the bottom.

12 GPa at 100 GPa (curve B in Figure 3) gives best agreement. This estimation is not unique but gives the right order of magnitude of deformations. The differing behavior between a 10 and 50 μm central ¤at diameter diamond in Figure 4(b) can be explained by the size of the elements used in these calculations, *i.e.* 5 μm.

3. Results

Our material properties being properly constrained, we investigated the in¤uence of the anvil geometry with our preindented gasket models (Fig 1). Figure 5(a,b) present the thickness of the gasket under the diamond tip *versus* pressure at the center of the gasket P_s for the different diamond con£gurations in Table 1. An increase in the bevel angle or a decrease in the central ¤at diameter results in a thinner gasket at megabar pressures. We can distinguish between two different phases on increasing load. The £rst phase involves a compression of the gasket with plastic ¤ow

Table 3: Pressure of transition P_t (in GPa) between the plastic ¤ow and elastic deformations phases and gasket stable thickness h_s (in μm) for different bevel angle α and central ¤at diameter con£gurations d.

d (μm)	α	P_t	h_s	d (μm)	α	P_t	h_s
5	8.5°	245	6.0	20	5°	165	17.2
10	8.5°	240	6.8.	20	7°	215	11.8
20	8.5°	240	8.2	20	8.5°	240	8.2
50	8.5°	230	11.8	20	10°	280	5.6
				20	12°	330	3.6

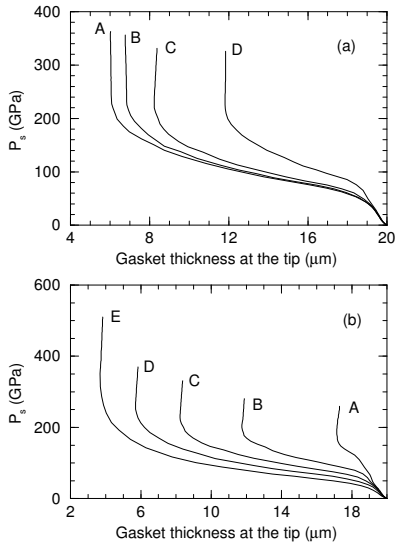

Figure 5: Pressure at the center of the gasket vs. gasket thickness at the tip for different bevel angle α and central ¤at diameter d con£gurations. (a) curves A, B, C, D, $\alpha = 8.5°$ and $d = 5$, 10, 20 and 50 μm respectively. (b) curves A, B, C, D, E, $d = 20$ μm and $\alpha = 5$, 7, 8.5, 10 and 12° respectively.

of material from below the diamond tip towards the edges of the bevel. During the second phase, the gasket thickness at the tip is not modi£ed (vertical lines in Figure 5), the load increase is absorbed by the elastic deformation of the diamond anvil. We can de£ne a transition pressure P_t between the two phases. Its numerical value depends on the geometric properties of the diamond with an increase in the bevel angle or a decrease in the central ¤at diameter tending to increase P_t. Table 3 summarizes the values of P_t and the gasket thickness at the diamond tip during the diamond deformation phase h_s for different central ¤at diameter d and bevel angle α. We observe a saturation when decreasing the central diameter (Fig. 5(a)). Diamond can not be considered as a rigid body under this range of pressures and it tends to accommodate its geometry to the stresses at the tip, thus smoothing the dependence towards the central ¤at diameter.

Figure 6 presents the shape of the diamond/gasket interface and the axial stress repartition for a 10 μm central ¤at diameter and 8.5° bevel angle diamond under different loads of equal increment. As in Figure 5, we observe the two different phases, compression of the gasket with plastic ¤ow of material towards the edges, and elastic deformation of the diamond. As observed in x-ray diffraction experiments[3] we obtain a very clear cupping of the diamond. At the highest loads, the thickness of the gasket at the edge of the bevel is very small and limits the possibility of further deformation of the diamond, leading to a saturation in the pressure vs. load relation.

The axial stress repartition along the diamond/gasket interface is presented on Figure 7 for different diamond geometries under the same load. The bevel angle has a much greater in¤uence than

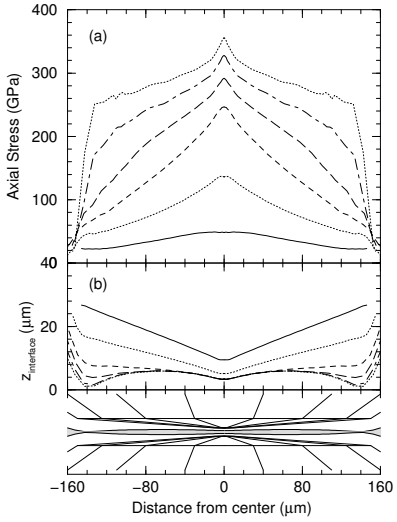

Figure 6: (a) and (b) Calculated axial stress along the diamond/gasket interface and position of this interface (which gives half of the gasket thickness) under different load for a bevel angle of 8.5° and a central ¤at diameter of 10 μm under different loads of equal increment.

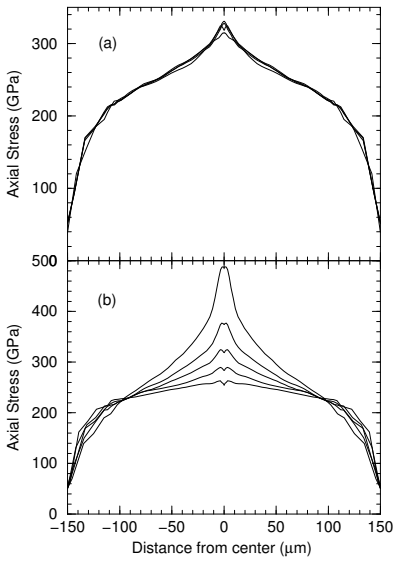

Figure 7: Calculated axial stress along the diamond/gasket interface for different bevel angle α and central ¤at diameter d con£gurations under the same load. (a) $\alpha = 8.5^\circ$ and $d = 5$, 10, 20 and 50 μm, the smallest central ¤at radius gives the highest pressure at the tip. (b) $d = 20$ μm and $\alpha = 5$, 7, 8.5, 10 and 12°, the largest bevel angle gives the highest pressure at the tip.

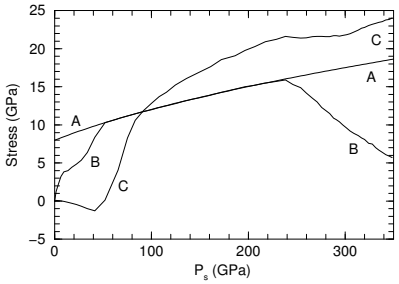

Figure 8: Shear stress at the center of the gasket with an 8.5° bevel angle and 20 μm central ¤at radius diamond. Curve A represents the gasket yield stress σ_y *vs.* pressure, curve B, $2 * \tau$ deduced from the calculation, and curve C is estimated from $2 * \tau \approx -h\ \partial P/\partial r$

the central ¤at diameter because of the saturation phenomenon described above. Increasing the bevel angle or decreasing the central ¤at diameter tends to concentrate the stress at the center of the gasket, resulting in a greater pressure but also larger pressure gradients. Under a pressure at the center of the gasket P_s of about 250 GPa, the pressure gradients at the center of the gasket are -1.42, -1.27, -0.65 and -0.12 GPa/μm for an 8.5° bevel angle and a central ¤at diameter of 5, 10, 20 and 50 μm, respectively; and 0.35, 0.01, -0.65, -2.23 and -4.53 GPa/μm for a 20 μm central ¤at diameter and 5, 7, 8.5, 10 and 12° bevel angle, respectively.

Experimental determination of the exact stress conditions can be diff£cult. Finite-element modeling provides direct access to these quantities at any node of the calculation during simulation of the experiment. For instance we can investigate the state of shear stress τ at the center of the gasket. Previous experiments[17, 19] evaluated this quantity using the relation

$$\tau = \frac{\sigma_{zz} - \sigma_{rr}}{2} \approx -(h/2)\left(\frac{\partial P}{\partial r}\right) \quad (1)$$

Moreover the yield stress condition gives us the following relation

$$\tau \leq \sigma_y/2 \quad (2)$$

Figure 8 presents the maximum permitted shear stress $\sigma_y/2$, τ calculated at the center of the gasket, and using equation 1, as a function of pressure for a model with a 20 μm central ¤at diameter and 8.5° bevel angle diamond. We observe three different sections in this £gure; at very low pressures, the system is in a transition mode where it adjusts to the boundary conditions, then it enters the gasket compression mode with plastic ¤ow of material below the diamond tip towards the edges of the bevel. The shear stress τ is at its maximum value (*i.e.* $\sigma_y/2$). At 240 GPa, the transition pressure de£ned in Table 3, the system enters the diamond elastic deformation mode. The gasket shear stress at the tip drops below its maximum value and decreases linearly. There is no longer gasket ¤ow at the tip. Equation 1 is only accurate to within an order of magnitude but has a precision of about 50% in the gasket compression mode and becomes inexact after the transition pressure.

Figure 9 presents the contours of shear stress in a 8.5° bevel angle and 20 μm central ¤at diameter diamond at a sample pressure

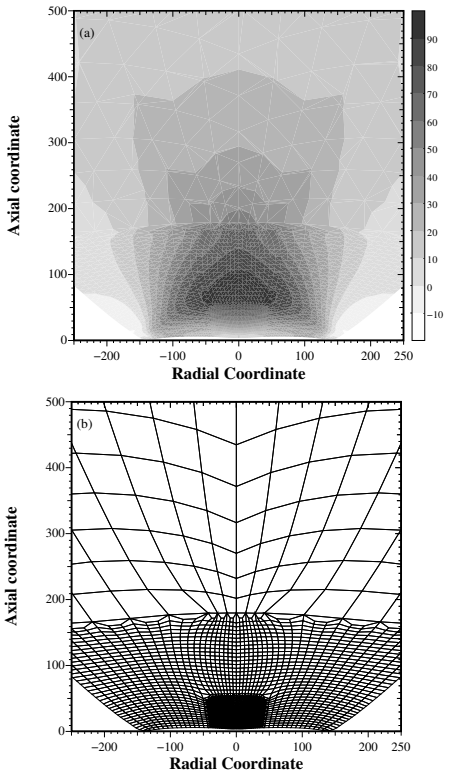

Figure 9: (a) Contours of shear stress $\tau = (\sigma_{zz} - \sigma_{rr})/2$ for an 8.5° bevel angle and 20 μm central ¤at radius diamond, with a sample pressure of 350 GPa. The coordinates are in μm and the stresses in GPa. The discontinuities were generated because of transitions in the £nite-element mesh. (b) The deformed £nite-element mesh under these conditions.

Table 4: Relation between the maximum shear stress in the diamond τ_{MAX} after the transition pressure P_t and the pressure at the center of symmetry P_s, and pressure of failure P_f according to relation 4 for different central ¤at diameter d and bevel angle α con£gurations.

d(μm)	α	τ_{MAX} (GPa)	P_f (GPa)
5	8.5°	$-24 + 0.355\ P_s$	349
10	8.5°	$-25 + 0.360\ P_s$	345
20	8.5°	$-23 + 0.353\ P_s$	348
50	8.5°	$-23 + 0.364\ P_s$	338
20	5°	$-14 + 0.376\ P_s$	303
20	7°	$-23 + 0.381\ P_s$	323
20	8.5°	$-23 + 0.353\ P_s$	348
20	10°	$-25 + 0.326\ P_s$	383
20	12°	$-7 + 0.241\ P_s$	444

of about 350 GPa. The point of maximum shear stress τ_{MAX} is located close to the symmetry axis, about 60 μm above the tip. In this particular case

$$\tau_{MAX} \approx 100 \text{ GPa} \tag{3}$$

Recent *ab-initio* calculation[20] predicted a mechanical instability of diamond when

$$\sigma_{zz} - \sigma_{rr} = 200 \text{ GPa} \tag{4}$$

This condition is reached in this £gure. In general, this range of shear stress can only be reached in the second phase of the loading, when the diamonds are elastically deforming. After the transition pressure, the maximum shear stress in the diamond and the pressure at the center of the gasket are linearly related. The coef£cients of the £t are presented in Table 4. We can estimate a pressure of failure P_f when condition given by Equation 4 is reached for each geometry (Table 4). According to this model, an increase in bevel angle diminishes the maximum shear stress, allowing the attainment of greater sample pressures before diamond failure. The use of large bevel angles has been limited experimentally because of diamond failure at very low pressures, before any diamond elastic deformation. This weakness is probably not related to high shear stress in the diamond. Figure 5 shows that a large bevel angle results in greater gasket ¤ow below the diamond tip during the compression phase. This might lead to instabilities in the case of defects or weaknesses in the gasket.

Finally, Table 5 presents the calculated stress conditions at three different locations in the diamond for different pressures in the gasket, on the symmetry axis near the tip, near the maximum shear stress, and in the high shear stress zone (but away from the tip). These numbers are critical for understanding the changes in optical properties of diamond anvils, and analyzing the band-gap behavior of the anvils in diamond cells as a function of the sample pressure or load.

4. Conclusions

A £nite-element analysis shows that plastic and elastic models are suf£cient to simulate the behavior of the anvils in the diamond cell at multimegabar pressures. The elastic properties of diamond were calculated using *ab initio* local density approximation methods over a very large range of static pressures. We also obtained an estimate of the dependence of the gasket yield stress on pressure As show previously[4], the model reproduces the very large elastic deformation of the diamond, leading to a clear cupping of the anvils. The pressure increase can be separated into two different phases: initial compression of the gasket with plastic ¤ow of material from the tip towards the edges of the bevel, coupled with subsequent elastic deformation of the anvils. The pressure of transition between these two phases depends on the geometry of the anvils.

Investigation of the exact stress conditions showed that the shear stress at the center of the gasket is at a maximum during the £rst phase of the pressure increase and drops drastically during the diamond deformation phase. The maximum shear stress in the diamond is found to decrease with the bevel angle. The high value shear stress in the anvil could lead to mechanical instability for sample pressures as low as 300 GPa.

Table 5: Stress history at selected locations in the diamond. Location A is on the z-axis and $z \approx 2$ μm, location B is on the z-axis and $z \approx 65$ μm, where the shear stress is maximum, and location C, is at $r \approx 70$ μm and $z \approx 60$ μm, the z coordinates being reported to the tip position. P_s is the pressure at the center of the gasket and P the pressure at the location.

Position	P_s (GPa)	σ_{rr} (GPa)	$\sigma_{\theta\theta}$ (GPa)	σ_{zz} (GPa)	σ_{rz} (GPa)	P (GPa)
A	9	5.5830e+00	5.5680e+00	1.1360e+01	1.4790e-02	7.5037e+00
A	52	3.2710e+01	3.2740e+01	6.0210e+01	8.3510e-01	4.1887e+01
A	100	5.6600e+01	5.6320e+01	1.0360e+02	2.1750e+00	7.2173e+01
A	150	9.1450e+01	9.0770e+01	1.5270e+02	3.3240e+00	1.1164e+02
A	197	1.2530e+02	1.2420e+02	1.9920e+02	4.5740e+00	1.4957e+02
A	254	1.7580e+02	1.7400e+02	2.5400e+02	5.3800e+00	2.0127e+02
A	302	2.3200e+02	2.2960e+02	2.9580e+02	5.4590e+00	2.5247e+02
A	349	2.9190e+02	2.8900e+02	3.3830e+02	5.8090e+00	3.0640e+02
B	9	2.3080e+00	2.3100e+00	9.9910e+00	7.4630e-02	4.8697e+00
B	52	6.5680e+00	6.5820e+00	3.6820e+01	4.0360e-01	1.6657e+01
B	100	1.0800e+01	1.0820e+01	5.9080e+01	6.4310e-01	2.6900e+01
B	150	1.4830e+01	1.4870e+01	8.4850e+01	9.7700e-01	3.8183e+01
B	197	1.7540e+01	1.7590e+01	1.0770e+02	1.3250e+00	4.7610e+01
B	254	2.1930e+01	2.2000e+01	1.4540e+02	1.7690e+00	6.3110e+01
B	302	2.9180e+01	2.9300e+01	1.9270e+02	2.0080e+00	8.3727e+01
B	349	4.0360e+01	4.0530e+01	2.4000e+02	1.9910e+00	1.0696e+02
C	9	2.6510e+00	2.9010e+00	1.0160e+01	1.5660e+00	5.2373e+00
C	52	8.7620e+00	8.7180e+00	3.0780e+01	7.1460e+00	1.6087e+01
C	100	1.4600e+01	1.4590e+01	4.8800e+01	1.0970e+01	2.5997e+01
C	150	2.1160e+01	2.0720e+01	6.8450e+01	1.6090e+01	3.6777e+01
C	197	2.6430e+01	2.5360e+01	8.5320e+01	2.1110e+01	4.5703e+01
C	254	3.4730e+01	3.3170e+01	1.1560e+02	3.0280e+01	6.1167e+01
C	302	4.4360e+01	4.6110e+01	1.6550e+02	4.0600e+01	8.5323e+01
C	349	5.7130e+01	6.6470e+01	2.2590e+02	4.5180e+01	1.1650e+02

References

[1] H. K. Mao and P. M. Bell, Science **200**, 1145 (1978).

[2] P. M. Bell, H. K. Mao, and K. Goettel, Science **226**, 542 (1984).

[3] R. J. Hemley, H. K. Mao, G. Shen, J. Badro, P. Gillet, M. Han¤and, and D. Häusermann, Science **276**, 1242 (1997).

[4] S. Merkel, R. J. Hemley, and H. K. Mao, Appl. Phys. Lett. **74**, 656 (1999).

[5] M. S. Bruno and K. J. Dunn, Rev. Sci. Instrum. **55**, 940 (1984).

[6] W. C. Moss, J. O. Hallquist, R. Reichlin, K. A. Goettel, and S. Martin, Appl. Phys. Lett. **48**, 1258 (1986).

[7] W. C. Moss and K. A. Goettel, Appl. Phys. Lett. **50**, 25 (1987).

[8] H. J. McSkimin and P. Andreatch Jr., J. Appl. Phys. **43**, 2944 (1972).

[9] O. H. Nielsen, Phys. Rev. B **34**, 5808 (1986).

[10] O. H. Nielsen and R. M. Martin, Phys. Rev. B **32**, 3780 (1985).

[11] M. P. Teter, Phys. Rev. B **48**, 5031 (1993).

[12] M. J. Mehl, J. E. Osburn, D. A. Papaconstantopoulos, and B. M. Klein, Phys. Rev. B **41**, 10311 (1990).

[13] M. J. Mehl, Phys. Rev. B **47**, 2493 (1993).

[14] M. J. Mehl, D. J. Singh, and D. A. Papaconstantopoulos, Material Science and Engineering **A170**, 49 (1993).

[15] M. J. Mehl, D. J. Singh, and D. A. Papaconstantopoulos, in *Intermetallic Compounds: Principles and Applications*, edited by J. H. Westbrook and R. L. Fleisher (John Wiley & Sons Ldt, 1994).

[16] M. H. Manghnani and K. Katahara, Phys. Rev. B **9**, 1421 (1974).

[17] R. Jeanloz, B. K. Godwal, and C. Meade, Nature (London) **349**, 687 (1991).

[18] T. S. Duffy, G. Shen, D. L. Heinz, J. Shu, Y. Ma, R. J. Hemley, H. K. Mao, and A. K. Singh, Phys. Rev. B **60**, 1 (1999)

[19] C. Meade and R. Jeanloz, J. Geoph. Res. **93**, 3261 (1988).

[20] J. J. Zhao, S. Scandolo, J. Kohanoff, G. L. Chiarotti, and E. Tosatti, Appl. Phys. Lett. **75**, 487 (1999).

REVIEW OF SCIENTIFIC INSTRUMENTS **76**, 046109 (2005)

X-ray transparent gasket for diamond anvil cell high pressure experiments

Sébastien Merkel[a] and Takehiko Yagi
Institute for Solid State Physics, University of Tokyo, Kashiwanoha 5-1-5, Kashiwa, Chiba 277-8581, Japan

(Received 11 August 2004; accepted 7 February 2005; published online 1 April 2005)

The diamond anvil cell is a fundamental tool for investigating properties under extreme conditions. However, our knowledge of material behavior under high pressure has been limited by a lack of measurement capability in radial directions. In this study we introduce a gasketing technique based on a combination of Kapton, amorphous boron, and epoxy, that reliably solves this issue. We demonstrate how these gaskets allow precise imaging of stress, strain, and microscopic properties such as texture and lattice preferred orientations within the sample, *in situ*, up to pressures in the range of 65 GPa. © *2005 American Institute of Physics.* [DOI: 10.1063/1.1884195]

In the last decades, the diamond anvil cell (DAC) emerged as a fundamental tool for investigating material properties under extreme conditions. DAC setups typically incorporate a metal foil gasket that serves as a sample chamber, maintains uniform stress within the sample, and avoids direct contact between the anvils. The choice of gasket material is particularly critical as it controls key characteristics such as the maximum attainable pressure, the sample thickness, and the stress conditions within the sample. Because of their high strength, low chemical reactivity, and ease of use, rhenium or stainless steel are commonly used as a gasket material. However, while a variety of spectroscopic measurements can be performed routinely through the diamond anvils, our knowledge of material behavior under extreme pressures has been limited by the gasket as the commonly used metals do not allow magnetic measurements or x-ray scattering in radial directions.

In order to overcome this limitation, several approaches were previously developed, such as avoiding the use of a gasket,[1] using a mixture of amorphous boron and epoxy,[2–4] or a low Z metal such as beryllium.[5–7] Removing the gasket allows access to the sample in multiple directions, but it also introduces severe complications such as pressure gradients and a maximum sample pressure of about 30 GPa. Amorphous boron and epoxy gaskets have been used up to pressures of about 50 GPa, provide a reasonable sample confinement, as well as x-ray transparency. However, these gaskets undergo frequent failures, undermining their potential application. Be gaskets have been successfully used up to multimegabar pressures. However, Be gaskets are still metallic and crystalline. With Be gaskets, radial diffraction experiments can be performed in energy dispersive geometry, as the probed portion of sample is limited in the lozenge defined by the detector collimator and the incident white x-ray beam. In angular radial diffraction, however, the intense diffraction pattern from the 5 mm Be gasket can mask that of the 100 μm sample. Moreover, many laboratories restrict the use of Be because of the health risks associated with Be powders.

Among those techniques, the use of a light, mostly noncrystalline but yet stiff and incompressible material such as amorphous boron and epoxy mixtures appears to be the most satisfactory. The abnormal rate of failure of these gaskets is related to the brittle nature of this material, especially when submitted to deformations in shear. Recently, we have developed a confinement technique that solves this issue. The boron-epoxy gasket is reduced to a circular insert confined by a Kapton suporting ring. Kapton is a polymer that satisfies all requirements, such as being roughly transparent to x rays, resistant to shear, easy to handle, and inexpensive.

In order to manufacture the boron insert, the amorphous boron powder (Alfa Aesar; 99% pure; part No. 11337) is mixed with epoxy (Epoxy Technology, part No. 353 N.D.) with a ratio of 3:2 (boron:epoxy) in weight. The two materials are well mixed with acetone in a mortar, compressed into 5-mm-diam platelets under a load of about 1 ton, and thereafter kept at 100 °C for 48 h. The platelets are then polished to a thickness of approximately 50 μm and cut into disks of diameters $d_b = d_d + 50$, where d_d is the diameter of the diamond anvil tips, in μm, with a sample hole (80–100 μm diameter) in the center (Fig. 1). Although these materials are quite brittle, they can be machined easily and precisely using a q-switched yttrium–aluminum–garnet (YAG) laser and a motorized rotating plate. We later add the supporting ring cut from a Kapton sheet of 150 μm thickness, with an inside hole of diameter d_b and outside diameter of 2 mm.

Without supporting rings, normal boron-epoxy gaskets tend to fail as one reaches a critical strain level that depends on the gasket and anvil geometry. The role of the Kapton confining ring is to prevent this failure by providing lateral support to the boron-epoxy insert. Moreover, it has a low x-ray absorption and background. The external diameter of the boron-epoxy insert exceeds that of the diamond culet by 50 μm because the Kapton ring should not be submitted to large hydrostatic stresses or pressure gradients while maintaining the boron-epoxy mixture inside the region between the tips of the two anvils. Large hoop stresses develop in the Kapton sheet, but the sheet itself is not submitted to any significant hydrostatic pressure.

[a]Author to whom correspondence should be addressed: present address: Department of Earth and Planetary Science, University of California, 307 McCone Hall, Berkeley, CA 94720-4767; electronic mail: smerkel@berkeley.edu

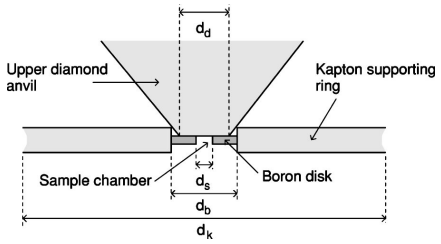

FIG. 1. Schematic of the boron/epoxy/Kapton gasket. The diameter of the boron/epoxy insert d_b is 50 μm larger than that of the diamond tip d_d, sample chamber diameter d_s varies from 80 to 100 μm and the Kapton supporting ring diameter d_k is about 2 mm. Before compression, thicknesses of the boron/epoxy insert and Kapton disk are 50 and 150 μm, respectively. For simplicity, the lower diamond anvil is not shown on the figure.

We were able to use those gaskets numerous times with various samples such as metals and silicates up to pressures of 65 GPa without any failure of the assembly. These gaskets are also resistant to reasonable laser heating of the sample (with a sample temperature of about 2000 K for 20 min). The limiting factor in the pressure increase was not gasket failure, but the elastic deformation of the diamond anvils. As pressure increases, the diamonds deform elastically and cup.[8] In the experiment, this can be observed using an optical microscope as the gasket becomes thin and transparent at the edge of the anvils. In the center, however, the gasket thickness remains on the order of 20–30 μm. In our experiments, the cupping of the diamond anvils could be observed between 40 and 55 GPa with d_d=350 μm and between 50 and 65 GPa with d_d=250 μm. At this point, we always released the pressure and were able to return to ambient conditions with little damage to the anvils.

The gaskets can be used in numerous situations. For instance, using an experimental setup of radial x-ray diffraction (Fig. 2), the transmitted x-ray intensity can be directly measured while moving the DAC in directions perpendicular to the incoming x-ray beam. The x-ray intensity profiles can then be converted into two-dimensional (2D) images in order to measure the physical dimensions of the sample precisely. Figure 3 show intensity profiles we obtained for a sample of

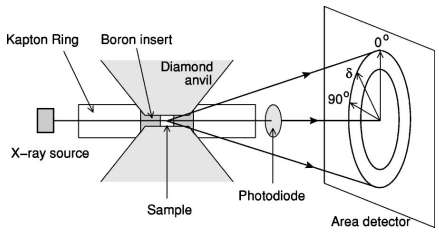

FIG. 2. Experimental setup for radial x-ray diffraction. The polycrystalline sample is confined under nonhydrostatic stress between the two diamond anvils. A monochromatic x-ray beam is sent through the gasket, perpendicular to the compression direction. Transmitted intensity profiles are measured with a photodiode in order to locate and measure the macroscopic properties of the sample. Microscopic properties of the sample are studied with x-ray diffraction by analyzing the variation of the diffraction profiles as a function of the azimuthal angle δ.

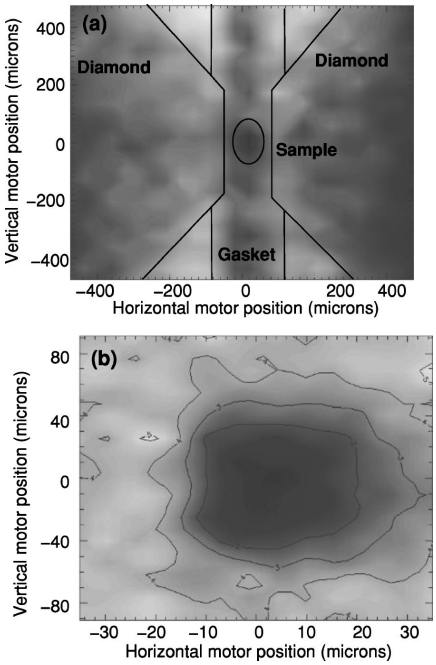

FIG. 3. Transmitted x-ray intensity profiles for a cobalt sample at 42 GPa. The DAC was moved relatively to the x-ray incoming beam over of grid of 15×15 steps of dimensions 1000 μm×1000 μm (a) and 195 μm ×75 μm (b) while collecting transmitted x-ray intensities. They were then converted into 2D images and smoothed using a simple interactive data language (IDL) procedure. From these figures, the position, shape, and macroscopic dimensions of the sample can be easily determined.

cobalt at 42 GPa, *in situ*, under high pressure. Experiment was performed on the BL13A beamline of the Photon Factory with a monochromatic incident x-ray beam of 30 μm diameter. We obtained a clear image of the sample localization within the DAC: in this experiment, it remained at the center of the anvils and very little radial flow of the sample along the anvil or within the gasket could be observed. From this data, we can estimate sample dimensions: 82 μm diameter and 32 μm thickness at 5.8 GPa, 82 μm diameter and 27 μm thickness at 42 GPa. Dimensions measured upon decompression are not always representative of the actual sample as cracks develop with the opening of the sample chamber. Upon compression, they are relatively reliable and it is worth noting that the sample diameter measured by this techniques matches the one measured through the diamonds by visual observation.

Radial x-ray diffraction is a powerful tool for the study of elasticity and plasticity under pressure.[3,6,9] In those experiments, a powder sample is first compacted and then plastically deformed by the loading of the anvils which has a directional stress component. The plastic deformation induces lattice preferred orientation that can be deduced *in situ* from the x-ray diffraction images and compared to results from polycrystal plasticity simulations to assess deformation

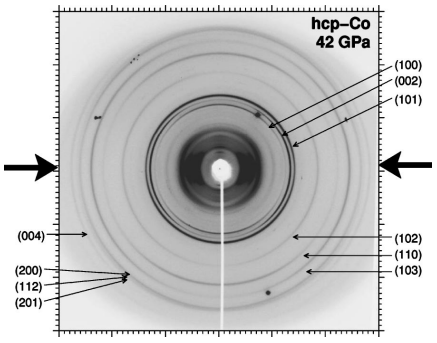

FIG. 4. Example of diffraction pattern for cobalt at 42 GPa. The Kapton diffraction is confined to the low angles (below 3 Å) and diffraction from the boron insert is mostly invisible. The variations of diffraction intensity with orientation are related to texture induced by the uniaxial deformation. Variations of the peak position with orientation are related to stress, elasticity and plasticity. Solid arrows indicate the compression direction. Diffraction peaks from the cobalt sample are labeled on the figure.

mechanisms.[3,9,10] The stress state in the sample is complex with a strong coupling between the sample plastic and elastic behavior[11] and a proper analysis of this phenomena remains to be developed. With these gaskets, we obtain diffraction data of sufficient quality to address this issue, as demonstrated in Fig. 4. It presents a diffraction image of a sample of cobalt at 42 GPa, measured *in situ* using radial x-ray diffraction. Measurements were performed on the BL13A beamline of the Photon Factory, with a 30μm diameter monochromatic beam, a 3000×3000 pixels Rigaku imaging plate, and a collection time of 5 min. The background for the boron insert is almost invisible and that of the Kapton supporting ring is limited to d spacings above 3 Å. This is appropriate for experiments on metals and silicates for which most reflections correspond to planes with d spacings below 3 Å. Unlike the case of other gasket materials, diffraction patterns from the sample and gasket do not overlap. From this figure, the variations of properties of the diffraction patterns, such as peak width, position, and intensity, with orientation can be precisely measured and analyzed.

The application of those gaskets is not limited to the study of deformation under high pressure. They can also be used for techniques that require large sample thickness, as well as low x-ray absorption, nonconducting, or nonmagnetic gaskets such as x-ray emission spectroscopy, electrical, or magnetic measurements. Moreover, the access to the diffraction image in the radial direction can be particularly useful for structural refinements from powder patterns. As demonstrated in Fig. 4, variations of diffraction intensities with orientation can be quite dramatic. In a conventional geometry, diffraction from only one of those orientations can be measured. This introduces significant errors in the measured diffraction intensities and, therefore, the structural refinements for such materials are not always reliable. Radial diffraction with an x-ray transparent gasket provide access to the whole orientation space, and it could be used to study the structural properties of strongly textured samples such as graphite and hexagonal diamond.[12]

In summary, we introduced a reliable, composite gasket design based on Kapton, amorphous boron, and epoxy, that provides a way to generate uniform high pressure conditions in a sample within an x-ray transparent, nonmetallic and nonconducting environment.

The authors wish to thank Y. Mori for developing the scanning program available at the BL13A beamline and N. Miyajima for assistance with the x-ray experiments. S.M. acknowledges support from the postdoctoral fellowship program of the Japanese Society for the Promotion of Science. X-ray experiments were made at the Photon Factory under the approval No. 04G045.

[1] G. L. Kinsland and W. A. Bassett, Rev. Sci. Instrum. **47**, 130 (1976).
[2] H. K. Mao, J. Shu, Y. Fei, J. Hu, and R. J. Hemley, Phys. Earth Planet. Inter. **96**, 135 (1996).
[3] S. Merkel, H. R. Wenk, J. Shu, G. Shen, P. Gillet, H. K. Mao, and R. J. Hemley, J. Geophys. Res. **107**, 2271 (2002).
[4] J. F. Lin, J. Shu, H. K. Mao, R. J. Hemley, and G. Shen, Rev. Sci. Instrum. **74**, 4732 (2003).
[5] R. J. Hemley, H. K. Mao, G. Shen, J. Badro, P. Gillet, M. Hanfland, and D. Häusermann, Science **276**, 1242 (1997).
[6] H. K. Mao, J. Shu, G. Shen, R. J. Hemley, B. Li, and A. K. Singh, Nature (London) **399**, 280 (1999).
[7] J. Badro, V. V. Struzhkin, J. Shu, R. J. Hemley, H. K. Mao, C. C. Kao, J. P. Rueff, and G. Shen, Phys. Rev. Lett. **83**, 4101 (1999).
[8] S. Merkel, R. J. Hemley, and H. K. Mao, Appl. Phys. Lett. **74**, 656 (1999).
[9] H. R. Wenk, S. Matthies, R. J. Hemley, H. K. Mao, and J. Shu, Nature (London) **405**, 1044 (2000).
[10] S. Merkel, H. R. Wenk, P. Gillet, H. K. Mao, and R. J. Hemley, Phys. Earth Planet. Inter. **145**, 239 (2004).
[11] L. Li, D. Weidner, J. Chen, M. Vaughan, M. Davis, and W. Durham, J. Appl. Phys. **95**, 8357 (2004).
[12] T. Yagi, W. Utsumi, M. Yamakata, T. Kikegawa, and O. Shimomura, Phys. Rev. B **46**, 6031 (1992).

REVIEW OF SCIENTIFIC INSTRUMENTS **80**, 1 (2009)

Experimental method for *in situ* determination of material textures at simultaneous high pressure and high temperature by means of radial diffraction in the diamond anvil cell

Hanns-Peter Liermann,[1,2] Sébastien Merkel,[3] Lowell Miyagi,[4] Hans-Rudolf Wenk,[4] Guoyin Shen,[1] Hyunchae Cynn,[5] and William J. Evans[5]

[1]*High-Pressure Collaboration Access Team, Geophysical Laboratory, Carnegie Institution of Washington, Argonne, Illinois 60439, USA*
[2]*DESY, Hamburg 22607, Germany*
[3]*Laboratoire de Structure et Propriétés de l'Etat Solide, Université des Sciences et Technologies de Lille, CNRS, 59655 Villeneuve d'Ascq Cedex, France*
[4]*Department of Earth and Planetary Science, University of California-Berkeley, California 94720, USA*
[5]*High Pressure Physics Group, Lawrence Livermore National Laboratory, 7000 East Avenue, L-041 Livermore, California 94550, USA*

(Received 23 June 2009; accepted 1 September 2009; published online xx xx xxxx)

We introduce the design and capabilities of a resistive heated diamond anvil cell that can be used for side diffraction at simultaneous high pressure and high temperature. The device can be used to study lattice-preferred orientations in polycrystalline samples up to temperatures of 1100 K and pressures of 36 GPa. Capabilities of the instrument are demonstrated with preliminary results on the development of textures in the bcc, fcc, and hcp polymorphs of iron during a nonhydrostatic compression experiment at simultaneous high pressure and high temperature. © *2009 American Institute of Physics.* [doi:10.1063/1.3236365]

I. INTRODUCTION

For many years, diamond anvil cells (DACs) have been used to determine the compression behavior of materials at high pressure.[1] Of particular interest has been the use of the DAC to determine the stress and strain state of minerals and compounds under nonhydrostatic conditions and ambient temperatures using the radial diffraction geometry[2–6] (Fig. 1). Most of these experiments are only possible because of the use of x-ray transparent gaskets, consisting of amorphous B inserts[6–9] or Be[3,4] that allow the collection of x-ray diffraction data from samples perpendicular to the loading axis. Radial diffraction has also been used to study texture and crystallographic preferred orientations (CPOs) in plastically deformed materials[10] by measuring intensity variations along the Debye rings. For instance, texture information was recently used to model the activation of slip systems at high pressure in geological relevant materials such as polycrystalline $(Mg_{0.9},Fe_{0.1})SiO_3$ postperovskite[11] and its Ge analog.[12] However, extrapolation of these findings to high-pressure and high-temperature conditions of the Earth's lower mantle has proven to be incomplete because of our lack of understanding the effect of temperature on high-pressure plasticity.

There are multiple avenues one might take to study plastic deformation under simultaneous high pressure, high temperature while probing the sample using *in situ* x-ray diffraction: (a) in a large volume press (LVP) such a Drickamer[13] or the multianvil device,[14] (b) in a DAC that is heated internally with a laser,[15] and (c) in a DAC that is heated externally through a resistive heater such as graphite. Each of these techniques has its advantages and disadvantages. While there has been significant progress using different types of LVP to measure stress and textures at simultaneous high pressures and high temperatures, it is currently not possible to use those instruments to perform quantitative deformation experiments beyond pressures of the transition zone (21 GPa and 2000 K). Recently, radial diffraction experiments in the DAC using *in situ* laser heating have made significant progress.[15,16] They are, however, complicated by the presence of large temperature gradients that develop during heating. So far externally heated DACs have not been used for stress and texture analyses because the resistive heater would lie in the x-ray path. A design of a cell capable of such experiments was published recently[17] but has not been tested for radial diffraction experiments. Furthermore, gasket materials typically used in radial diffraction experiments lose their strength at high temperatures (as do diamond anvils) and thus significantly limit the accessible pressure and temperature range. In addition, accurate measurement of pressure at high temperature has been an ongoing problem in resistive heated DACs but is now actively being addressed by the community.[18–22] In contrast to the other two techniques mentioned above, the externally heated DAC experiment offers good temperature and pressure control and can reach much higher pressures then the LVP. Furthermore, the development of sintered nanodiamond anvils could significantly expand the accessible pressure temperature range because the high temperature strength of the anvils can be significantly improved.[23,24] In the future, a combination of experiments on large and well-controlled samples in a resistively heated radial diffraction setup and higher temperature laser-heated measurements will allow the study of plasticity at pressures and temperatures relevant to the Earth's deeper mantle. More generally, the technique could also be useful to

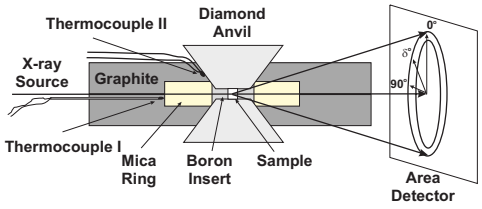

FIG. 1. (Color online) Setup of the RH-RXD-DAC experiment. The polycrystalline sample is confined under nonhydrostatic stress between the two diamond anvils. A monochromatic x-ray beam is sent through the gasket, perpendicular to the compression direction. Microscopic properties of the sample are studied with x-ray diffraction by analyzing the variation in the diffraction spectra as a function of the azimuthal angle δ.

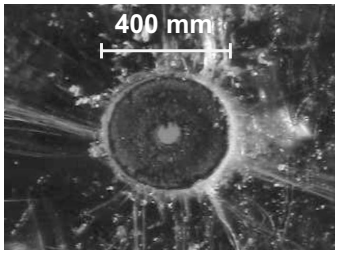

FIG. 3. Gasket assembly consisting of an amorphous boron disk positioned on the diamond anvils and surrounded by a fluorine mica for support of the insert.

study the plasticity of materials relevant to various branches of material sciences, such as superhard materials for which *in situ* characterization of strength and plastic properties are absolutely necessary.[25–27]

In this paper, we present a new radial diffraction technique that allows measurement of textures and stress at simultaneous high pressure and high temperatures in the DAC using an external resistive graphite heater. We demonstrate the current capability of the technique by measuring textures of Fe and its high-pressure polymorphs at simultaneous high pressure and high temperatures.

II. EXPERIMENTAL METHOD

A. Resistive-heated DAC for radial diffraction x-ray experiments

The technique presented here allows us to perform radial diffraction x-ray (RDX) at simultaneous high pressures and high temperatures. It combines three existing techniques: (a) amorphous boron gaskets that allow radial access to the sample,[9] (b) externally graphite heated gaskets,[28] and (c) membrane devices for accurate control of pressure.[29]

In order to accommodate the resistive heating setup and membrane control we designed a new Mao–Bell-type DAC [Figs. 2(a) and 2(b)] that will be called resistive-heated-radial-x-ray-diffraction-diamond-anvil-cell (RH-RXD-DAC). In contrast to a conventional Mao–Bell-type cell, the new cell has openings on two sides that allow collection of diffraction patterns perpendicular to the loading axis.

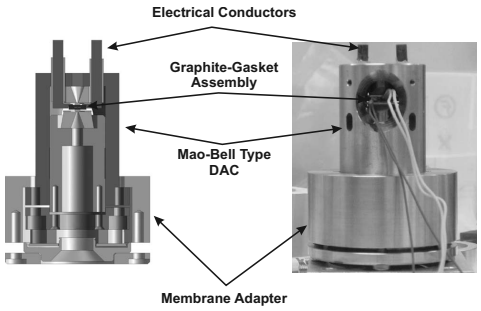

FIG. 2. Three-dimensional (a) cross section and (b) image of the new RH-RXD-DAC for radial diffraction at simultaneous high pressure and high temperature.

Heating of the sample is achieved by using graphite heaters that surround the gasket assembly. The front of the cell has been further modified to accept two molybdenum rods that supply power to the graphite heater. The ends of the molybdenum rods are machined to a perpendicular extension with a step. This holds the graphite heater in place when the piston of the DAC presses against the graphite. The graphite heater consists of two pieces of flexible graphite foil with 1 mm thickness (Alfa Aesar, 97% pure, metal basis) that sandwiches the gasket assembly. The graphite and the gasket assembly are isolated from the tungsten carbide seats by a thin disk of sintered alumina (McDanel Advanced Ceramics Technologies LLC, 99% purity). Prior to sample loading the graphite foil is indented between the diamonds with a thick stainless steel gasket in place of the final gasket assembly. This process shapes the graphite foil, provides a tight contact between the diamonds and the graphite, and allows enough space to position the final gasket assembly.

The gasket consists of a 50 μm thick amorphous boron gasket insert,[9] 400 μm in diameter, with a 50 μm diameter hole that serves as sample chamber (Fig. 3). The kapton sheet that has been used to support the boron insert in RDX experiments at 300 K is replaced by a fluorine bearing mica sheet of 100 μm thickness (H. C. Materials-Corporation). The melting temperatures of this fluorine mica (1373 K) is significantly higher than the maximum working temperature of kapton (~500 K), extending the accessible temperature range in the experiment. Moreover, this material forms a single crystal with a strongly anisotropic crystal structure whose contribution to diffraction is limited because the sheet structure is positioned parallel to the incoming beam, preventing intense basal x-ray diffraction. Finally, a small channel is cut into the graphite heater along the path of the incident beam to avoid significant diffraction from graphite.

In order to prevent the piston and the cylinder from sticking to one another at high temperature and thus preventing the increase and decrease in pressure during the experiment, we use Molykote 1000 Paste (Dow Corning) as a lubricant and heat the outside of the cylinder of the DAC with a strip heater to a maximum of 673 K.

Fine pressure tuning in the cell is provided by adapting the RH-RXD-DAC with a membrane similar to that devel-

oped by the high-pressure group at Lawrence Livermore National Laboratory (LLNL). This allows a remote control of pressure during the experiment.

B. *In situ* x-ray diffraction

We preformed *in situ* x-ray diffraction at beamline 16 BMD of the High-Pressure Collaboration Access Team (HPCAT), Advanced Photon Source (APS), Argonne National Laboratory (ANL). In the experiment the wavelength of the 15×15 μm^2 monochromatic x-ray beam was tuned to 0.387 45 Å at which it offered an optimal flux of $\sim2\times10^8$ photons/sec and resulted in a collection time of 15 min. Data were collected on a 3450×3450 pixel Mar 345 image plate. Sample to detector distance (285.943 mm), detector tilt, and pixel size ratios were calibrated using a CeO_2 standard from NIST (674b).

Sample was a pure commercial powder of iron (Alfa Aesar, 99.9 % purity) with a starting grain size of $1-2$ μm. In this run, a small piece of 5 μm thick gold foil was added for additional pressure calibration but could not be seen on the x-ray diffraction images.

C. Temperature in the radial diffraction DAC

The graphite foil was heated through an ultrastable dc power supply from Hewlett Packard with a power range of 0–8 V and 0–220 A (type A6607). Power was increased remotely through an external voltage control provided by experimenting physics industrial control system (EPICS) at the beamline control area.

Temperature was measured with two Pt–Pt30%Rh (type R) thermocouples. The first thermocouple was positioned on the diamond facet of the anvil on the cylinder side of the cell, about half way to the tip. The second thermocouple was located between the two pieces of graphite foil, close to the fluorine bearing mica (Fig. 1). The thermocouple voltages (EMF) were measured with a Keithley 7200 equipped with an internal cold junction correction board. The accuracy of the thermocouple reading is +/−5 K.

D. Data processing

Diffraction images were quantitatively analyzed for cell parameters, phase proportions, texture, and lattice strains using the Rietveld method as implemented in the software package MAUD (Ref. 30) according to the procedure described in Ref. 31. Diffraction images were integrated over 5° increments of the azimuth angle, resulting in 72 slices. Data were fit using a bcc, fcc, and hcp structure with adjustable phase ratios. The variations in peak positions with azimuth were adjusted assuming

$$d_m(hkl,\psi) = d_P(hkl)[1 + (1 - \cos^2\psi)Q(hkl)],$$

where ψ represents the angle between the diffracting plane normal and the maximum stress direction, $d_m(hkl,\psi)$ is the measured d-spacing for the (hkl) line diffraction at ψ, $d_p(hkl)$ is the hydrostatic d-spacing of the (hkl) line and is calculated from the hydrostatic lattice parameters, and $Q(hkl)$ is the lattice strain parameters. Values of $Q(hkl)$ can then be used to analyze the stress state of the sample using elastic lattice strain theories[32] or elasto-plastic self-consistent models.[33] CPOs were fitted using the E-WIMW algorithm assuming cylindrical symmetry about the compression direction and using an orientation distribution function (ODF) resolution of 7.5°.

Refinements for the bcc phase were based on measurements on the 110, 200, and 211 diffraction lines. Refinements for the fcc phase were based on measurements on the 111, 200, and 220 diffraction lines. Refinements for the hcp phase were based on measurements on the $10\bar{1}0$, 0002, $10\bar{1}1$, $10\bar{1}2$, and $11\bar{2}0$ diffraction lines.

E. Pressure at high temperatures

Measuring pressure at high temperatures has been a long standing problem for resistive heated experiments. Spectroscopic methods have been used to determine the accurate pressure using fluorescence shifts in ruby $SrB_4O_7:Sm^{2+}$ or yttrium aluminum garnet crystals.[18–20] More recently shifts in the first order Raman peaks of diamond[34] and cubic boron nitride[20] at high temperature have also been used. Alternatively, one may determine pressure using a P-V-T thermal equation of state (EOS) of an internal standard such as Au or Pt. The latter has been established by using multiple pressure calibrants to produce an internally consistent set of high pressure and temperature EOS.[21,22]

In the present experiment, we decided to calibrate pressures using x-ray diffraction of an internal standard. Since gold could not be seen in our diffraction patterns (even at 300 K and 1 bar), we decided to use the EOS of the sample itself, iron, in the bcc structure,[35] and later hcp structure,[36] to estimate pressure at any given temperature during the experiment. To correct for the effect of nonhydrostatic stresses, pressures were calculated using the hydrostatic cell parameters of bcc and hcp iron as derived from the MAUD refinements. Fortunately, in the entire pressure and temperature range covered in this run, either bcc or hcp coexists beyond their stability limit and allows us to calibrate pressure within the stability field of the fcc phase. The temperature pressure path explored during the experiment can be seen in Fig. 5.

III. RESULTS AND DISCUSSION

A. Accuracy of temperature measurements in the RH-RXD-DAC

Because of the high thermal conductivity of diamonds and complexity of the sample assembly, temperature measurements with thermocouples that do not directly surround the sample have been questioned in the past.[37] To investigate this issue, we measured the melting temperature of Pb (605 K), Al (933.2 K), and NaCl (1077 K) in a second membrane controlled graphite resistively heated DAC that was used recently.[28] This membrane cell uses the exact same heating assembly and similar thermocouple positions as those described in this work. Thus, it represents an accurate test of our capability to measure temperatures in the low to medium temperature range.

Melting was observed optically through a Navitar zoom microscope with a maximum primary magnification of 20×. Samples of Al and Pb were separated in the sample chamber

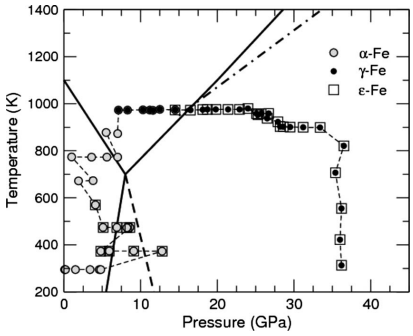

FIG. 5. Pressure-temperature path explored during the second radial diffraction experiment. Grey circles denote the presence of bcc iron (α-Fe), open squares for hcp iron (ε-Fe), and black circles for fcc iron. fcc iron coexists with hcp iron past its stability limit until the end of the experiment. Phases in the sample were identified from the diffraction images. Solid and dotted lines are the phase iron diagram upon compression and decompression, respectively, as published in Ref. 36. Dashed-dotted line represents the hcp-fcc phase boundary (Ref. 35).

by NaCl to avoid reaction between the different standards during heating. Even though we did not determine the pressure in the sample chamber after closing the DAC, we observed small holes indicating that the sample was not compressed and did not show any considerable pressure. The sample chamber was illuminated by reflected and transmitted light. Onset of melting was determined by observing the appearance of movements in the liquid phase and changes in the sample surface texture. Both approaches are commonly used to determine melting of metals in laser heated DAC experiments with accuracy in the ten's kelvin.[38]

Temperatures recorded on both thermocouples at zero pressure are plotted as a function of power in Fig. 4(a). Up to 1077 K the discrepancy between the temperature recorded at the onset of melting and the melting temperature reported in the literature are within +2 to −30 K for the thermocouple positioned between the two pieces of graphite foil and up to 60 K for the thermocouple positioned on the facet of the diamond.

These measurements imply that temperatures measured by the thermocouple positioned between the two graphite foils are within 30 K of the real temperature. Note that the difference between melting temperatures reported in the literature and those measured by the second thermocouple, positioned about 1 mm away from the diamond tip, only extends to +60 K. This relatively small difference indicates that the gasket assembly and the top part of the diamond are very efficiently heated by the graphite foil and that temperature gradients in the gasket, sample, and diamond tip area are relatively small.

Temperatures measured in both thermocouples during the RH-RXD-DAC experiment on iron are plotted as a function of power in Fig. 4(b). In contrast to the melting experiment above, temperatures recorded by the thermocouple positioned between the two graphite foils are always higher than those recorded at the facet of the diamond. This difference can be explained by the fact that the thermocouple at

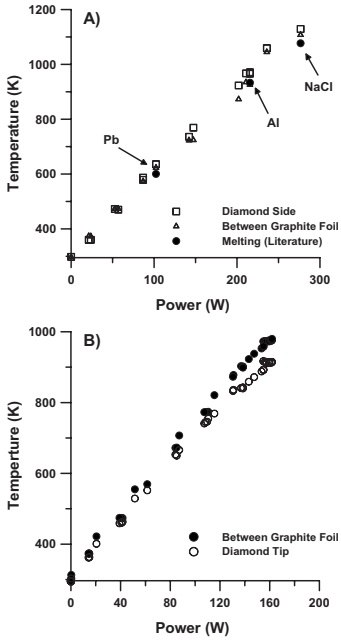

FIG. 4. (a) Ambient pressure temperature measurements as a function of power in the RH-DAC. Onset of melting was observed optically through a microscope and is indicated by arrows in the figure. Differences between the melting temperatures reported in the literature and those measured using the thermocouple positioned between the graphite foil for Pb, Al, and NaCl are −22, 2, and 30 K, respectively. (b) High-pressure temperature measurements as a function of power in the radial diffraction membrane driven Mao–Bell-type DAC. The maximum difference between the temperatures recorded by both thermocouples (see text) is 66 K recorded at the highest temperature.

the facet of the diamond is not always positioned precisely the same way. In addition we find that the shape of the WC seat, i.e., the opening of the seat, significantly affects the amount of heat being carried away from the back of the diamond anvil. The opening of the seat in the DAC used for the melting experiment is much smaller than that of the radial diffraction RH-RXD-DAC seats. Hence, the temperatures recorded at the facet of the diamond anvil of the radial diffraction cell are lower. Nevertheless, the difference in temperatures recorded by the two thermocouples never exceeds 62 K. This indicates fairly homogeneous heating during the experiment.

B. Phase diagram and equation of state of fcc iron

Table I lists the refined cell parameters obtained from positions of the diffraction peaks of bcc, fcc, and hcp iron as a function of pressure and temperature during the experiment. We obtain small errors for the cell parameters of bcc iron before the appearance of other iron phases but rather large errors later on. This is due to inconsistencies between the cell parameters obtained from various diffraction lines, which could be due to the presence of a mixed phase.

AQ: #15

TABLE I. Cell parameters refined from peak positions of bcc, fcc, and hcp. Temperature was measured with a thermocouple. Pressure was calculated using the cell parameters of bcc and hcp iron and their respective high-pressure and high-temperature EOS (Refs. 35 and 36). The error in the temperature measurement is estimated to be +/−30 K and the error in the pressure calculation is +/−0.7 GPa based on an average error of 0.004 Å in the cell parameters. Errors for the cell parameters obtained for bcc Fe before the appearance of other phases are approximately 0.001 Å. When multiphase aggregate is present, errors on cell parameters are on the order of 0.004 Å.

					Fe (hcp)	
Image	*T* (K)	*P* (GPa)	Fe (bcc) *a* (Å)	Fe (fcc) *a* (Å)	*a* (Å)	*c* (Å)
3	295	0.1	2.866			
13	295	0.2	2.865			
22	295	1.5	2.858			
24	295	3.4	2.848			
28	295	4.6	2.842			
31	295	4.8	2.841			
35	373	12.8	2.807		2.438	4.028
36	374	9.1	2.823		2.454	3.978
37	374	5.9	2.838		2.468	3.992
38	373	4.8	2.843		2.473	4.096
40	474	8.6	2.828		2.464	4.118
41	473	8.2	2.830		2.468	4.117
42	474	6.9	2.836		2.473	4.136
43	474	5.1	2.845		2.477	4.151
45	570	4.1	2.853		2.497	4.180
46	672	1.9	2.869			
47	673	3.8	2.858			
48	774	1.0	2.878			
49	773	3.6	2.863			
50	773	5.6	2.852			
51	773	7.0	2.845			
53	878	5.5	2.856			
54	873	7.0	2.848			
56	973	7.1	2.851	3.619		
57	973	8.3	2.845	3.606		
58	974	10.3	2.835	3.580		
59	973	11.2	2.831	3.566		
60	972	11.6	2.829	3.558		
62	976	12.5	2.825	3.546		
63	974	14.5	2.818	3.529	2.481	4.030
64	973	16.4		3.519	2.476	4.012
65	975	18.0		3.508	2.472	3.993
66	976	18.5		3.504	2.470	3.990
67	976	19.9		3.498	2.465	3.981
68	976	21.3		3.491	2.460	3.970
69	976	22.9		3.484	2.455	3.959
70	980	24.0		3.476	2.451	3.953
71	953	25.2		3.472	2.446	3.944
72	958	25.0		3.470	2.447	3.946
73	958	25.6		3.470	2.445	3.942
74	959	26.6		3.465	2.442	3.936
75	938	26.4		3.465	2.442	3.936
76	923	27.8		3.465	2.438	3.924
77	903	28.2		3.459	2.436	3.922
78	902	28.4		3.455	2.435	3.921
79	901	29.4		3.453	2.432	3.916
80	900	31.0		3.444	2.427	3.908
81	899	33.2		3.434	2.421	3.897
83	821	36.6		3.419	2.410	3.876
85	707	35.4		3.419	2.410	3.877
87	555	36.1		3.413	2.406	3.865
88	422	36.0		3.409	2.404	3.860

TABLE I. (*Continued.*)

Image	*T* (K)	*P* (GPa)	Fe (bcc) *a* (Å)	Fe (fcc) *a* (Å)	Fe (hcp) *a* (Å)	Fe (hcp) *c* (Å)
89	313	36.2		3.410	2.402	3.855

In our experiment, the transition from the bcc to the fcc phase of iron occurred at temperatures higher than those reported in the literature[36,39,40] (Fig. 5). However, phase transitions in iron are known to be very sensitive to both kinetics[36] and stress.[41] Our experiment was designed to prove the capabilities of the instrument. As such, we did not perform multiple transition cycles and long heating periods necessary for full phase conversions and proper phase diagram analysis. Therefore, small discrepancies between our experiments and reported phase boundaries can be attributed to kinetics and stress.

Our cell parameters for fcc Fe are also significantly different from those reported in the literature.[40,41] This is particularly true at low pressures. Differences between our measured cell parameters and the published EOS (Ref. 40) decrease with increasing pressure. It is known that coexistence of two or three phases associated with a phase transition can cause volume anomalies due to the difference in linear compressibility and thermal expansivity. This can explain the observed discrepancy. Proper measurement of the EOS of fcc Fe should be performed with better phase conversion, longer heating periods, and minimal stress conditions.

C. Diffraction and texture development in iron at high pressure and temperature

The greatest challenge collecting and processing radial diffraction data from a DAC originates from the background created by material that lies in the diffraction path. In the case of the HT-RXD-DAC, graphite, fluorine mica, and amorphous boron contribute to the background (Fig. 1).

Figure 6 shows the diffraction image collected at 976 K and 12.5 GPa. The diffraction image clearly shows powder diffraction peaks corresponding to the 111, 200, and 220 lines of fcc iron and 110, 200, and 211 lines of bcc Fe. Diffraction from graphite is limited to the most intense 002 peak. Single crystal spots of mica are significant but localized; they can be easily filtered out during the processing. Due to grain growth and recrystallization, iron diffraction lines are spotty. Nevertheless, variations in diffraction intensities with orientation can be observed. They are related to CPO in the polycrystalline sample. Similarly, slight variations in peak positions with orientations can be used to model the differential stress supported by the sample.

Reliable textures can be extracted. Figure 7, for instance, presents inverse pole figure of the compression direction obtained for bcc and fcc iron at 12.5 GPa and 976 K and fcc and hcp iron at 33.2 GPa and 899 K. ODFs were obtained directly in MAUD and further smoothed with a 10° gauss filter in BEARTEX.[42]

Upon compression, bcc iron develops a mixed {100} and {111} texture that is compatible with previous observations on bcc iron[16,43] and interpreted as slip along {110}⟨111⟩. When bcc iron is heated between 295 and 976 K, we observe a recrystallization of the sample, as evident by the spotty pattern in Fig. 6. The {100} and {111} maxima are preserved during heating.

Texture obtained after formation of fcc iron shows a maximum near {110} with minima near {100} and {111}. This texture is typical for fcc metals in compression with slip on {111}⟨110⟩,[16] but could also be related to texture being transmitted from the bcc to the fcc phase according to the Kurdjumow–Sachs orientation relations.[44]

Textures obtained in hcp Fe seem different from those reported before.[5,16,34] Further study and modeling will be required for full interpretation, which goes beyond the scope of this paper.

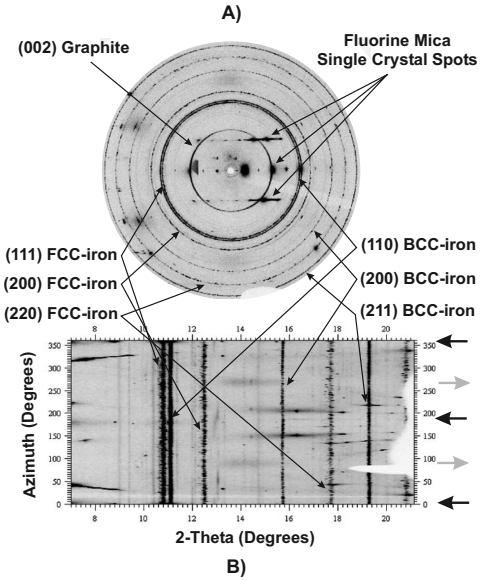

FIG. 6. (a) Radial diffraction image and (b) unrolled diffraction image of fcc iron at 12.5 GPa and 976 K and in the graphite resistive heated Mao–Bell-type DAC. Besides diffraction peaks of fcc (111, 200, and 220) and bcc Fe (110, 200, and 211), one can see powder diffraction peaks of graphite (002) and single crystal diffraction spots of fluorine bearing mica.

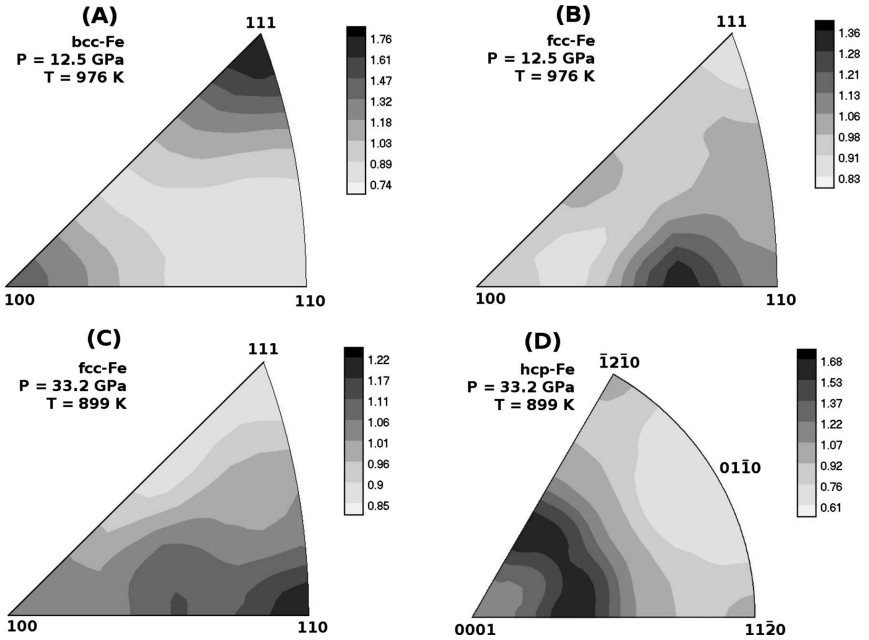

FIG. 7. Inverse pole figure of the compression direction for [(a) and (b)] bcc and fcc iron at 12.5 GPa and 976 K and [(c) and (d)] fcc and hcp iron at 33.2 GPa and 899 K. Equal area projection. Linear polar density scale in m.r.d.

AQ: #16

D. Application of the instrumentation

One of the primary applications of radial diffraction DAC experiments is the investigation of deformation mechanisms and possible preferred orientation patterns of rocks in the deep Earth, e.g., the lower mantle and the core. Today, radial diffraction is the only direct method to probe plastic processes at pressures of the Earth's lower mantle. Until now, an obvious limitation in using ambient temperature results of CPO formed in the DAC was the lack of temperature. It was therefore desirable to develop reliable heating methods for radial diffraction. The technique presented here will allow the investigation of deformation of minerals up to temperatures of about 1500 K, a temperature at which diffusion processes that are critical for plasticity can become active.

The instrumentation presented here can also be used to study the strength of newly designed superhard materials.[25–27] Most of these studies are limited to measurements of quasihydrostatic EOSs for extraction of isothermal bulk moduli. This is insufficient to assess the strength and behavior of the material under complex conditions. Using the new instrumentation, one could study the strength and microscopic plastic deformation mechanisms under various conditions of pressure and temperature. This will provide valuable information for understanding the plastic behavior of industrially relevant materials.

IV. CONCLUSION

We designed a DAC experimental setup that allows the collection of x-ray diffraction data in a radial geometry from samples plastically deformed at simultaneous high pressure and high temperature. The setup was successfully tested up to temperatures of 1100 K and pressures of 36 GPa.

Errors in temperature measurements are within +/−30 K in the entire temperature range explored. Moreover, temperatures measured at ~1 mm away from the tip of the diamond on the diamond facet show a temperature difference of only +/−60 K, indicating that the gasket and tips of the diamonds are heated very homogeneously.

The instrumentation allows the collection of radial x-ray diffraction data of sufficient quality for the extraction of texture and stress information using the Rietveld refinement program "MAUD." Detailed analysis of the data presented here will be discussed elsewhere. However, preliminary analysis indicates the presence of a strong {110} texture in fcc iron, compressed in the DAC between 7.1 and 12.5 GPa at 970 K, after the transformation from bcc iron.

This new instrumentation can now be used for the study of plastic properties of minerals and other materials at simultaneous high-pressure and high-temperature conditions.

ACKNOWLEDGMENTS

The authors like to thank W. Yang and E. Rod for their technical support at the beamline and during the experiment.

We also thank L. Dubrovinsky for helpful suggestions regarding the resistive heated DAC and the anonymous reviewer for critical comments that improved the quality of the manuscript. This work was performed at HPCAT (Sector 16), Advanced Photon Source (APS), Argonne National Laboratory. HPCAT is supported by DOE-BES, DOE-NNSA, NSF, and the W.M. Keck Foundation. APS is supported by DOE-BES under Contract No. DE-AC02-06CH11357. W.J.E. and H.C. gratefully acknowledge the support from DOE/NNSA Science Campaign-2 (Program Manager—Dr. Kimberly Budil). Their contribution was performed under the auspices of the U.S. DOE by LLNL under Contract No. DE-AC52-07NA27344. L.M. and H.-R.W. acknowledge the support from CDAC and NSF (Grant No. EAR-0836402).

[1] R. J. Hemley and H. K. Mao, Miner. Mag. **66**, 791 (2002).
[2] G. L. Kinsland and W. A. Bassett, J. Appl. Phys. **48**, 978 (1977).
[3] R. J. Hemley, H. K. Mao, G. Shen, J. Badro, P. Gillet, M. Hanfland, and D.Häusermann, Science **276**, 1242 (1997).
[4] H. K. Mao, J. Shu, G. Shen, R. J. Hemley, B. Li, and A. K. Singh, Nature (London) **399**, 280 (1999).
[5] H. R. Wenk, S. Matthies, R. J. Hemley, H. K. Mao, and J. Shu, Nature (London) **405**, 1044 (2000).
[6] S. Merkel, H. R. Wenk, J. Shu, G. Shen, P. Gillet, H. K. Mao, and R. J. Hemley, J. Geophys. Res. **107**, 2271 (2002).
[7] H. K. Mao, J. Shu, Y. Fei, J. Hu, and R. J. Hemley, Phys. Earth Planet. Inter. **96**, 135 (1996).
[8] J. F. Lin, J. Shu, H. K. Mao, R. J. Hemley, and G. Shen, Rev. Sci. Instrum. **74**, 4732 (2003).
[9] S. Merkel and T. Yagi, Rev. Sci. Instrum. **76**, 046109 (2005).
[10] H. R. Wenk, I. Lonardelli, S. Merkel, L. Miyagi, J. Pehl, S. Speziale, and C. E. Tommaseo, J. Phys.: Condens. Matter **18**, S933 (2006).
[11] S. Merkel, A. K. McNamara, A. Kubo, S. Speziale, L. Miyagi, Y. Meng, T. S. Duffy, and H.-R. Wenk, Science **316**, 1729 (2007).
[12] S. Merkel, A. Kubo, L. Miyagi, S. Speziale, T. S. Duffy, H.-K. Mao, and H.-R. Wenk, Science **311**, 644 (2006).
[13] D. Yamazaki and S. Karato, Rev. Sci. Instrum. **72**, 4207 (2001).
[14] Y. Wang, W. B. Durham, I. C. Getting, and D. J. Weidner, Rev. Sci. Instrum. **74**, 3002 (2003).
[15] M. Kunz, W. A. Caldwell, L. Miyagi, and H.-R. Wenk, Rev. Sci. Instrum. **78**, 063907 (2007).
[16] L. Miyagi, M. Kunz, J. Knight, J. Nasiatka, M. Voltolini, and H. R. Wenk, J. Appl. Phys. **104**, 103510 (2008).
[17] S. Petitgirard, I. Daniel, Y. Dabin, H. Cardon, R. Tucoulou, and J. Susini, Rev. Sci. Instrum. **80**, 033906 (2009).
[18] F. Datchi, R. LeToullec, and P. Loubeyre, J. Appl. Phys. **81**, 3333 (1997).
[19] C. Sanchez-Valle, I. Daniel, B. Reynard, R. Abraham, and C. Goutaudier, J. Appl. Phys. **92**, 4349 (2002).
[20] A. F. Goncharov, J. C. Crowhurst, J. K. Dewhurst, S. Sharma, C. Sanloup, E. Gregoryanz, N. Guignot, and M. Mezouar, Phys. Rev. B **75**, 224114 (2007).
[21] Y. Fei, A. Ricolleau, M. Frank, K. Mibe, G. Shen, and V. Prakapenka, Proc. Natl. Acad. Sci. U.S.A. **104**, 609013104 (2007).
[22] C.-S. Zha, K. Mibe, W. A. Bassett, O. Tschauner, H.-K. Mao, and R. J. Hemley, J. Appl. Phys. **103**, 054908 (2008).
[23] T. Irifune, A. Kurio, S. Sakamoto, T. Inoue, H. Sumiya, and K. Funakoshi, Phys. Earth Planet. Inter. **143&144**, 593 (2004).
[24] Y. Nakamoto, H. Sumiya, T. Matsuoka, K. Shimizu, T. Irifune, and Y. Ohishi, Jpn. J. Appl. Phys., Part 2 **46**, L640 (2007).
[25] C. T. Liu and J. O. Stiegler, Science **226**, 636 (1984).
[26] H. Y. Chung, M. B. Weinberger, J. B. Levine, A. Kavner, J. Yang, S. H. Tolbert, and R. B. Kaner, Science **316**, 436 (2007).
[27] V. Solozhenko, O. O. Kurakevych, D. Andrault, Y. Le Godec, and M. Mezouar, Phys. Rev. Lett. **102**, 015506 (2009).
[28] G. Shen, H. P. Liermann, S. Sinogeikin, W. Yang, X. Hong, C.-S. Yoo, and H. Cynn, Proc. Natl. Acad. Sci. U.S.A. **104**, 14576 (2007).
[29] R. Letoullec, J. P. Pinceaux, and P. Loubeyre, High Press. Res. **1**, 77 (1988).
[30] L. Lutterotti, S. Matthies, H.-R. Wenk, A. S. Schultz, and J. W. Richardson, J. Appl. Phys. **81**, 594 (1997).
[31] L. Miyagi, S. Merkel, T. Yagi, N. Sata, Y. Ohishi, and H.-R. Wenk, J. Phys.: Condens. Matter **18**, S995 (2006).
[32] A. K. Singh, C. Balasingh, H. K. Mao, R. J. Hemley, and J. Shu, J. Appl. Phys. **83**, 7567 (1998).
[33] ■ Merkel, C. N. Tomé, and H. R. Wenk, Phys. Rev. B **79**, 064110 (2009).
[34] F. Occelli, P. Loubeyre, and R. LeToullec, Nature Mater. **2**, 151 (2003).
[35] T. Komabayashi and Y. Fei, "■," J. Geophys. Res. (submitted).
[36] T. Uchida, Y. Wang, M. Rivers, and S. R. Sutton, J. Geophys. Res. **106**, 21799 (2001).
[37] N. Dubrovinskaia and L. Dubrovinsky, Rev. Sci. Instrum. **74**, 3433 (2003).
[38] D. Errandonea, B. Schwager, R. Ditz, C. Gessmann, R. Boehler, and M. Ross, Phys. Rev. B **63**, 132104 (2001).
[39] R. Boehler, Geophys. Res. Lett. **13**, 1153 (1986).
[40] T. Komabayashi, Y. Fei, Y. Meng, and V. Prakapenka, Earth Planet. Sci. Lett. **282**, 252 (2009).
[41] R. Boehler, N. Von Bargen, and A. Chopelas, J. Geophys. Res. **95**, 21731 (1990).
[42] H. R. Wenk, S. Matthies, J. Donovan, and D. Chateigner, J. Appl. Crystallogr. **31**, 262 (1998).
[43] S. Merkel, H.-R. Wenk, P. Gillet, H. K. Mao, and R. J. Hemley, Phys. Earth Planet. Inter. **145**, 239 (2004).
[44] G. Kurdjumow and G. Sachs, Z. Phys. **64**, 325 (1930).

Dixième partie

Autres articles

news and views

Earth science

The mantle deformed

Sébastien Merkel

What happens to minerals under the conditions characteristic of the Earth at great depths? Experiments performed under such conditions illustrate how the main constituent of the lower mantle may behave.

Until the middle of the twentieth century, it was thought that the Earth is a solid body and that no internal movement of matter could occur. Then, with the discovery of plate tectonics and mantle convection, a whole new understanding of the planet's dynamics emerged. Matter can indeed flow within the seemingly solid regions of the deep Earth, and these processes often control the surface dynamics. Yet the microsopic mechanisms controlling flow remain poorly understood. That is scarcely surprising: it is no easy matter to simulate the conditions to which materials in, for example, the lower mantle or the inner core are subject. So the plastic properties of those materials have remained largely unknown.

On page 837 of this issue, however, Cordier *et al.*[1] describe new results on the plastic properties of the main constituent of the lower mantle, a mineral known as silicate perovskite (Fig. 1). They have exploited both experimental and theoretical advances to demonstrate that dislocations in silicate perovskite can be activated under the conditions of the lower mantle. This implies that silicate perovskite could develop large-scale anisotropic structures — that is, with physical properties that depend on the direction of observation — and that it may be possible to measure these structures using seismological methods.

Materials inside the solid layers of the Earth are not perfect crystals but rather aggregates of crystalline grains — polycrystals — that are undergoing plastic deformation. The process is governed by the interaction between deformation within individual grains (through the movement of dislocations), sliding and diffusion along grain boundaries, and the stress and strain fields applied by the environment. Dislocations are line defects within the crystal structure and their motion in the lattice causes slip and plastic deformation within the grain. Depending on external conditions such as pressure and temperature, and the physical properties of the crystal, slip is observed to occur in specific planes and directions, known as slip systems.

If dislocations dominate the deformation, grains will deform preferentially in certain directions and the polycrystal will develop anisotropy in such physical properties as elasticity and electrical conductivity. In the Earth, the anisotropic elastic properties can be studied using seismic techniques, which measure the directional dependency of seismic velocities. Thereafter, a combination of rheological and seismological measurements can be used to interpret the dynamic geological processes deep inside the Earth[2].

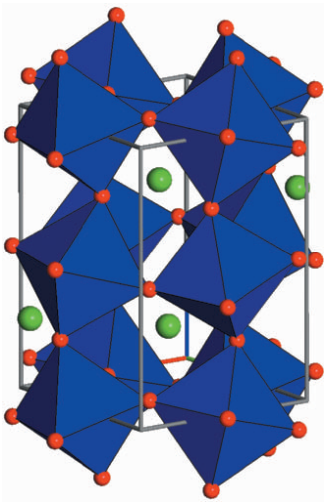

Figure 1 **The structure of silicate perovskite $(Mg,Fe)SiO_3$. Red circles represent oxygen atoms and green circles magnesium or iron. The silicon atoms are located at the centre of the blue SiO_6 octahedra. Cordier *et al.*[1] add new data on how this material deforms under the conditions of the Earth's lower mantle, and so on anisotropic structures that might be evident with seismological methods.**

The transformation of mantle minerals into silicate perovskite $(Mg,Fe)SiO_3$ and magnesiowustite (Mg,Fe)O at a pressure of about 23 gigapascals marks the limit between the upper and lower mantle at a depth of 660 km. On the evidence of high-pressure experiments, seismological measurements, geochemistry and numerical modelling, perovskite is believed to account for about 80% of the lower mantle. Understanding its properties is therefore essential to understanding the physical and geological processes that occur within this layer. Unfortunately, silicate perovskite is unstable under low pressure and high temperature, and it is also highly sensitive to the electron irradiations used in microscopy. So silicate perovskite cannot be studied with the techniques used to investigate the plastic properties of crustal or upper-mantle minerals, and the microscopic processes controlling its plasticity remain unknown.

To address this issue, experiments have been carried out on analogues that have the perovskite structure. These studies led to the conclusion that, under lower-mantle conditions, diffusive processes should dominate perovskite deformation. This in turn implied that silicate perovskite could not generate anisotropic structures in the lower mantle[3]. But it has also been shown that deducing the plastic properties of perovskite-structured materials from analogues can be misleading. So the analogue approach has to be treated with caution[4], and direct investigations of silicate perovskite are necessary.

In recent years, techniques have been developed that allow the experimental deformation of minerals under pressures and temperatures close to those of the lower mantle. But analysing the properties of the sample to identify the deformation mechanisms involved is a further challenge. Cordier *et al.* have overcome that challenge by adapting an approach — X-ray peak broadening analysis — developed in metallurgy. As in electron microscopy, where dislocation contrast is strong or disappears depending on certain conditions, X-ray diffraction peaks become broader or narrower. These peaks can be used to characterize dislocations within the material.

Taking full advantage of the new techniques, Cordier *et al.*[1] have produced the first experimental evidence that dislocations can indeed be activated in silicate perovskite under lower-mantle conditions. They were also able to identify the most active slip systems — that is, the plane and direction in which the slip occurs. Key questions, such as the influence of grain size, strain rate or phase mixing, remain to be solved. Nevertheless, these new results force us to reconsider our thinking about lower-mantle rheology. Seismological observations identify highly anisotropic patches at the bottom of the Earth's lower mantle, whereas the bulk of the deep mantle seems largely isotropic[5–7]. But numerical modelling indicates that other regions could also exhibit anisotropy, for instance in the vicinity of subducting slabs where the Earth's crust is driven back into the mantle[8].

For many years, investigations of the dynamics of the Earth's lower mantle were neglected because of the lack of appropriate seismological and rheological data. Before too long, however, the new interdisciplinary interactions between areas such as high-pressure mineralogy, studies of mineral plasticity, engineering, seismology and geodynamics look set to revolutionize

understanding of our planet's deeper layers. ■

Sébastien Merkel is at the Institute for Solid State Physics, University of Tokyo, Kashiwanoha 5-1-5, Kashiwa, Chiba, 277-8581 Japan.
e-mail: smerkel@issp.u-tokyo.ac.jp

1. Cordier, P., Ungár, T., Zsoldos, L. & Tichy, G. *Nature* **428,** 837–840 (2004).
2. Wenk, H. R. *Rev. Mineral. Geochem.* **51**, 291–330 (2002).
3. Karato, S., Zhang, S. & Wenk, H. R. *Science* **270**, 458–461 (1995).
4. Beauchesne, S. & Poirier, J. P. *Phys. Earth Planet. Inter.* **61**, 182–198 (1990).
5. Meade, C., Silver, P. G. & Kanshima, S. *Geophys. Res. Lett.* **22**, 1293–1296 (1995).
6. Lay, T., Williams, Q. & Garnero, E. J. *Nature* **392**, 461–468 (1998).
7. Panning, M. & Romanowicz, B. *Science* **303**, 351–353 (2004).
8. McNamara, A. K., van Keken, P. E. & Karato, S. *Nature* **416**, 310–314 (2002).

Cancer

Enzymes play molecular tag

Deborah K. Morrison

The B-RAF protein is often mutated in human cancers, contributing to their development. Although most known mutations stimulate its catalytic activity, others, surprisingly, impair it — yet still cause cancer.

Like most other cellular events, cell proliferation is tightly regulated by signals from the surrounding environment. These cues are relayed from the cell surface to the nucleus by defined signal-transduction cascades. The core components of one such pathway are the RAS, RAF, MEK and ERK proteins. If this pathway is constantly switched on, it can cause cells to proliferate wantonly, resulting in cancer.

Researchers have known for some time that there are cancer-promoting mutations in the RAS protein that keep it permanently 'on'. Recently, large-scale genomic screens have also detected mutations in one member of the RAF family of proteins — B-RAF — in 65% of malignant melanomas[1] and many colorectal[2], ovarian[3] and papillary thyroid[4,5] cancers. How these mutations alter B-RAF's function is the topic of an elegant study, published in *Cell*, by Wan and colleagues[6]. The paper also provides structural information that should help to guide the search for more effective inhibitors of this protein family.

The RAF enzymes are central intermediates in this fundamental signalling cascade, transmitting signals from RAS to the downstream enzymes MEK and ERK (Fig. 1a, overleaf). In mammalian cells there are three members of the RAF family, A-RAF, B-RAF and C-RAF. Working out how these proteins are regulated has been a daunting task, largely because of the complexity of the process. There seem to be several mechanisms, including self-inhibition (involving a regulatory domain located at one end, the amino terminus, of the proteins), interactions with binding partners such as RAS and the 14-3-3 protein, and the phosphorylation of (covalent linkage of phosphate groups to) inhibitory and activating sites on the proteins[7,8].

The activation of RAF is typically

Developmental genetics

Bittersweet evolution

Structures that occur in closely related organisms and that look the same are usually considered to be homologous — their similarity is taken to arise from their common ancestry. Common sense suggests that the more complex such structures are, the less likely they are to have evolved independently and the more valuable they should be for studying systematics. But what if 'obviously' identical organs have arisen through two mutually exclusive developmental routes?

Beverley Glover and colleagues have revealed one such case (*Gene* **331,** 1–7; 2004). It occurs in the floral organs of the genus *Solanum* from the nightshade family. In one group of these species, the anthers — the flower's pollen-producing organs — are arranged as a cone, which functions like a 'pepperpot' (see the yellow, cone-like structures in a and b, right). In the pepperpot of bittersweet (*S. dulcamara*), the anther surfaces are held together by a glue-like secretion (a). In another species from the same group, tomato (*S. lycopersicum*), they are instead linked by interlocking hairs, or trichomes, along the edges of the anthers (b).

Glover *et al.* find that tomato trichomes are clearly required for pepperpot formation. In one form, the *dialytic* mutant, which lacks them, the pepperpot fails to develop (d). In bittersweet, however, trichomes surprisingly prevent pepperpot formation. Glover *et al.* show this using transgenic plants in which expression of a gene from snapdragon leads to the development of hairs on bittersweet anthers. The hairs push the glue-bearing surfaces apart, preventing pepperpot formation (c).

This result makes it unlikely that the tomato-type pepperpot originated from the bittersweet type, or vice versa, because the development of anther hairs in bittersweet-type cones would probably have caused the cone to fall apart, whereas the addition of glue to tomato-type cones already supported by trichomes would probably have carried no selective advantage. So the most plausible conclusion is that pepperpots originated twice independently in the lineages that led to tomato and bittersweet.

Molecular systematic analysis confirms that tomato and bittersweet are closely related, and the traditional view would be that their pepperpot cones are obviously homologous. But genetic tinkering and mutant analysis show that they probably are not — that they are convergent, having taken different routes to the same end. Life's potential to invent complex structures more than once may worry systematists, who depend on reliable characters to reconstruct relationships between organisms. But it will please anyone who admires nature's innovative power. **Günter Theißen**

A. DAVIS, JOHN INNES CENTRE

Günter Theißen is at Friedrich Schiller University, D-07743 Jena, Germany.
e-mail: guenter.theissen@uni-jena.de

GEOPHYSICAL RESEARCH LETTERS, VOL. 31, L23612, doi:10.1029/2004GL021156, 2004

A new high-pressure form of $KAlSi_3O_8$ under lower mantle conditions

Yuichiro Sueda,[1] Tetsuo Irifune,[1] Norimasa Nishiyama,[1] Robert P. Rapp,[1] Tristan Ferroir,[2] Tsuyoshi Onozawa,[2] Takehiko Yagi,[2] Sebastien Merkel,[2] Nobuyoshi Miyajima,[2] and Ken-ichi Funakoshi[3]

Received 30 July 2004; revised 4 November 2004; accepted 10 November 2004; published 14 December 2004.

[1] In situ X-ray diffraction measurements have been made on $KAlSi_3O_8$ hollandite using diamond anvil cell and multianvil apparatus combined with synchrotron radiation. Both of the measurements with different techniques demonstrated that K-hollandite transforms to a new high-pressure phase (hollandite II) at ~22 GPa upon increasing pressure at room temperature. The X-ray diffraction peaks of the new phase were reasonably indexed on the basis of a monoclinic cell with $I2/m$ space group. Hollandite II was also confirmed to be formed at high temperatures to 1200°C and pressures to 35 GPa, which was quenched to room temperature under pressure but converted back to hollandite at about 20 GPa on release of pressure. The present result is contradictory to earlier studies based mainly on quench method, which concluded that hollandite is stable up to 95 GPa at both room temperature and high temperatures up to 2300°C. *INDEX TERMS:* 1025 Geochemistry: Composition of the mantle; 3630 Mineralogy and Petrology: Experimental mineralogy and petrology; 3675 Mineralogy and Petrology: Sedimentary petrology; 3924 Mineral Physics: High-pressure behavior; 3954 Mineral Physics: X ray, neutron, and electron spectroscopy and diffraction. **Citation:** Sueda, Y., T. Irifune, N. Nishiyama, R. P. Rapp, T. Ferroir, T. Onozawa, T. Yagi, S. Merkel, N. Miyajima, and K. Funakoshi (2004), A new high-pressure form of $KAlSi_3O_8$ under lower mantle conditions, *Geophys. Res. Lett.*, *31*, L23612, doi:10.1029/2004GL021156.

1. Introduction

[2] $KAlSi_3O_8$-rich feldspar is a major constituent mineral in granitic continental crust, parts of which are believed to be transported deep into the mantle via subduction of oceanic lithosphere [*Armstrong*, 1981; *Dupre and Allegre*, 1983; *Hofmann*, 1997; *Sobolev and Shatsky*, 1990]. $KAlSi_3O_8$ feldspar transforms to a high-pressure form with a hollandite structure [*Ringwood et al.*, 1967; *Yamada et al.*, 1984] at pressures greater than ~9 GPa and at temperatures 1000–1400°C via a mixture of $K_2Si_4O_9$ wadeite + Al_2SiO_5 kyanite + SiO_2 coesite, a reaction that has been confirmed on the basis of both quench [*Kinomura et al.*, 1975; *Yagi et al.*, 1994] and in situ X-ray diffraction experiments [*Urakawa et al.*, 1994]. The $KAlSi_3O_8$-rich hollandite (K-hollandite, hereafter) has also been shown to be a major phase in continental crust and marine sediment lithologies, as well as in some basalts, at depths equivalent to the deeper part of the upper mantle and throughout the mantle transition region [*Irifune et al.*, 1994; *Schmidt*, 1996; *Ono*, 1998; *Wang and Takahashi*, 1999].

[3] Only few studies have been made on the stability of K-hollandite under lower mantle conditions. Quench experiments using multianvil apparatus (MA) on a K-rich basalt demonstrated that K-hollandite is a major subsolidus phase at pressures to 27 GPa and at 1700°C, equivalent to the conditions of the uppermost lower mantle [*Wang and Takahashi*, 1999]. These authors also suggested that there is a possibility of occurrence of a phase transition in K-hollandite at pressures of 20–22.5 GPa at 1700°C from some indirect evidence.

[4] More recently, an experimental study with diamond anvil cell (DAC) demonstrated that K-hollandite is stable at pressures up to 95 GPa and temperatures to ~2300°C, leading to a conclusion that hollandite is the major host of potassium down to a depth of 2200 km in the lower mantle [*Tutti et al.*, 2001]. However, this conclusion relies on the results of quench experiments, and no in situ X-ray diffraction measurements under simultaneous high pressure and high temperature corresponding to those of the lower mantle have been conducted to date.

2. Experimental Method

[5] We made in situ X-ray diffraction observations using both DAC and MA combined with synchrotron radiation. We used a polycrystalline sintered piece of pure $KAlSi_3O_8$ hollandite, synthesized by MA, as the starting material for the DAC experiment. This sample was polished to a square block with sides of ~80 μm and ~25 μm thick. Helium pressure medium was used and the pressure, as determined by the changes in unit-cell volume of gold calculated with an equation of state [*Anderson et al.*, 1989], was also cross-checked by the ruby scale [*Mao et al.*, 1986]. While the sample was maintained at high pressure, a monochromatized (λ = 0.4258 Å) and collimated (~30 μm) X-ray from synchrotron source at the Photon Factory, Tsukuba, was directed on the sample, and the diffracted X-ray was acquired using an imaging plate, typically for 15 minutes in each measurement. Further details of the experimental set-up are given elsewhere [*Yagi et al.*, 2001]. The X-ray diffraction measurements were conducted every ~2 GPa as pressure was increased, and the phases present were identified on the basis of the diffraction profiles.

[6] In situ X-ray diffraction experiments at simultaneous high pressure and high temperature were also conducted using MA with sintered diamond anvils at SPring-8. The cell assembly used in the present study was virtually the same as that of our earlier study [*Irifune et al.*, 2002]. An energy-dispersive method was adopted for X-ray diffraction

[1] Geodynamics Research Center, Ehime University, Matsuyama, Japan.
[2] Institute for Solid State Physics, University of Tokyo, Kashiwa, Japan.
[3] Japan Synchrotron Research Institute, Sayo, Japan.

0094-8276/04/2004GL021156$05.00

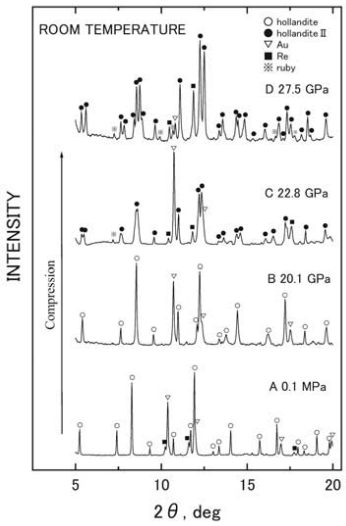

Figure 1. X-ray diffraction profiles of $KAlSi_3O_8$ in DAC with increasing pressure at room temperature. Only the diffraction peaks of K-hollandite, in addition to those of Au and Al_2O_3 as the pressure scales and Re gasket, were observed at ambient conditions (a) and at 20.1 GPa (b). The diffraction profile started to change at ~22–23 GPa (c), and hollandite II was formed at higher pressures (d).

measurements with a white X-ray beam of ~50 μm, and a new 1500-ton MA (SPEED-MkII [*Katsura et al.*, 2004]) was used for the experiments with sintered diamond anvils. Temperature was measured with a $W_{97}Re_3$-$W_{75}Re_{25}$ thermocouple and the pressure was evaluated by the volume change in gold [*Anderson et al.*, 1989]. The starting material was a glass of pure $KAlSi_3O_8$ composition with some minor quench crystals, which had previously produced single phase K-hollandite in earlier quench experiments performed at 15 GPa and at 1200°C in the MA.

3. Experimental Results

[7] Figure 1 shows the variations of the X-ray diffraction profile for the $KAlSi_3O_8$ sample as a function of pressure at room temperature in the DAC. The overall pattern of the diffraction peaks for hollandite did not change with increasing pressure to about 20 GPa (Figures 1a and 1b), but some peaks started to split or broaden at ~22–23 GPa (Figure 1c), and a diffraction pattern quite different from that of the hollandite structure was obtained at higher pressures (Figure 1d). The diffraction peaks were found to be reasonably indexed on the basis of a monoclinic symmetry with *I2/m* space group, as listed in Table 1. The cell parameters obtained by least-square fitting of the observed diffraction data at 27.5 GPa were; a = 9.146 (3) Å, b = 2.640 (1) Å, c = 8.725 (3) Å, β = 91.54 (3) deg., and V = 210.6(1) $Å^3$, giving a density of 4.39 g/cm^3 under this pressure. Further detailed studies of the crystal structure and the compressibility of this phase are currently being pursued (T. Ferroir et al., manuscript in preparation, 2004).

[8] Variations of the X-ray diffraction profile in a run using MA (run M080) are depicted in Figure 2. K-hollandite was first synthesized from the glass starting material at 18 GPa, at 1200°C for one hour, and then further pressurized at the room temperature (Figure 2a). Upon compression, the diffraction peaks clearly became broader at pressures above ~22–23 GPa (Figure 2b), and some of the original single peaks began to split at the highest pressure of 31.4 GPa at room temperature (Figure 2c). This observation is consistent with the results in the DAC experiment, although much clearer peak splitting was noted in the latter experiment at room temperature because of the use of the helium pressure medium, which provides a quasi-hydrostatic environment for the sample at high pressure.

[9] Temperature was then increased gradually at fixed press load, and the X-ray diffraction data were collected for 5–10 minutes at a number of specific temperatures up to 1200°C. Upon increasing temperature, the diffraction peaks became sharper and were completely split into several peaks above ~800°C. The whole X-ray diffraction pattern obtained at 33.4 GPa, 1200°C (Figure 2d), was virtually the same as that observed in the DAC experiment with helium pressure medium at similar pressures and at the room temperature (Figure 1d). The high-pressure phase was preserved upon decreasing temperature under pressure (Figure 2e), and the lattice parameters (a = 9.123 (1) Å, b = 2.644 (1) Å, c = 8.686 (2) Å, β = 91.55 (2) deg., and V = 209.4(1) $Å^3$) measured at 29.4 GPa at the room temperature were consistent with those obtained in the DAC experiment. The new phase, however, converted back to the hollandite structure at about 20 GPa during decompression, and the diffraction profile at ambient conditions was that of the hollandite structure (Figure 2f).

[10] Another MA run (run M039) was made with the same glass starting material, by pressurizing the sample to 35.4 GPa without first synthesizing the hollandite phase at lower pressure, and temperature was then increased to 1200°C at fixed press load. The same diffraction peaks that were observed in the run using the K-hollanite starting material were present. This indicates that the new phase (hollandite II, hereafter) is indeed stable under these pressure and temperature conditions, because the same phase was obtained from the different starting material (glass and K-hollandite), an important criterion in testing the thermodynamic stability of the new phase. Again, hollandite II was preserved in run M039 at the room temperature under pressure after quenching, but it transformed to the hollandite structure at the ambient pressure.

4. Discussion

[11] Figure 3 summarizes the present experimental conditions and the results in a P-T diagram. We recently made measurements of the P-V-T relations in K-hollandite using MA at pressures up to 25 GPa and temperatures up to ~1500°C (N. Nishiyama et al., manuscript in preparation, 2004). These experiments confirmed that the hollandite structure is stable under these conditions, as shown in Figure 3 (for run M044), although notable broadening of some diffraction peaks is apparent at temperatures below

Table 1. X-ray Diffraction Data of Hollandite II at 27.5 GPa, at Room Temperature[a]

h	k	l	d_{obs} (Å)	d_{cal} (Å)	$(d_{obs}/d_{cal}) - 1$
2	0	2	4.566	4.571	−0.0011
0	0	2	4.359	4.361	−0.0003
−2	0	2	3.195	3.199	−0.0012
2	0	2	3.118	3.114	0.0013
−3	0	1	2.903	2.901	0.0005
3	0	1	2.8529	2.8531	−0.0001
−1	0	3	2.7912	2.7924	−0.0004
1	0	3	2.7473	2.7492	−0.0007
1	1	0	2.5330	2.5360	−0.0012
2	1	1	2.2033	2.2039	−0.0003
0	0	4	2.1839	2.1804	0.0016
3	1	0	1.9937	1.9952	−0.0007
0	1	3	1.9550	1.9543	0.0004
−3	1	2	1.8276	1.8266	0.0006
3	1	2	1.8001	1.8023	−0.0012
2	1	3	1.7853	1.7853	0.0000
−4	1	1	1.7024	1.7016	0.0005
4	1	1	1.6892	1.6884	0.0005
−1	1	4	1.6581	1.6595	−0.0008
1	1	4	1.6462	1.6473	−0.0006
−4	0	4	1.6009	1.5994	0.0010
6	0	0	1.5254	1.5238	0.0011
−5	1	2	1.4555	1.4536	0.0013
5	1	2	1.4121	1.4114	0.0005
−2	1	5	1.3952	1.3958	−0.0004
2	1	5	1.3763	1.3778	−0.0008
0	2	0	1.3210	1.3198	0.0009
−6	1	1	1.3080	1.3093	−0.0010
−5	1	4	1.2498	1.2506	−0.0006
5	1	4	1.2252	1.2249	0.0002
4	1	5	1.2148	1.2153	−0.0003

[a]Monoclinic symmetry with *I*2/*m* space group. a = 9.146 (3) Å, b = 2.640 (1) Å, c = 8.725 (3) Å, β = 91.54(3) deg., V = 210.6 (1) $Å^3$, ρ = 4.39 g/cm^3.

∼700°C, indicative of the commencement of the phase transition to hollandite II. Thus it is most likely that the boundary between K-hollandite and hollandite II has a steep positive slope and locates at about 24 GPa at high temperature as shown by the dashed line in Figure 3, although further study is needed to define the phase boundary more quantitatively.

[12] It was reported that K-hollandite is stable at pressures and temperatures far exceeding those of the present study, on the basis of quench experiments with DAC [*Tutti et al.*, 2001]. In this study, in situ X-ray diffraction measurements were also made after laser heating under high pressure and at room temperature. No structural changes were apparent at pressures up to at least 50 GPa, except for possible amorphization at higher pressures, although no detailed descriptions on the diffraction profiles, the P/T conditions, and heating durations were reported for these in situ X-ray measurements.

[13] These results are totally inconsistent with our results based on in situ X-ray observations using both MA and DAC. It is understandable that these authors [*Tutti et al.*, 2001] concluded that K-hollandite does not transform to any other structures based on the analyses of the recovered sample, because, as we found in our experiments, hollandite II converts to the hollandite structure at ambient conditions. The transition could have been overlooked due to relatively poor resolution in the observed diffraction profiles, because of the use of a small CCD detector and/or the effect of the non-hydrostatic stress produced in the sample without pressure medium in their experiments. Alternatively, the presence of small amounts of other cations, such as Na, Ba, Mg, and Ca, in the natural K-feldspar that was used as the starting material [*Tutti et al.*, 2001] might affect the stability of hollandite II under pressure.

[14] On the other hand, the presence of a phase transition in K-hollandite at 20–22.5 GPa and 1700°C was suggested, on the basis of abrupt changes in both the chemical composition of this phase and in melting relations of a K-rich basaltic composition [*Wang and Takahashi*, 1999]. Although the pressure range for the proposed phase transition is slightly lower than that of our study (∼24 GPa), the discrepancy may be due to difference in estimates of pressure at high temperature between the two studies. Thus it is likely that the predicted phase transition in K-hollandite observed in the K-rich basalt corresponds to the K-hollandite to hollandite II transition discovered in the present study. A significant change in the Hugoniot data on $KAlSi_3O_8$ was noted at pressures of 12–30 GPa in shock compression experiments, and this was interpreted as proposed being due to the formation of a mixed phase assemblage [*Ahrens and Liu*, 1973]. This may also be explained by the K-hollandite to hollandite II transition at about 24 GPa, taking into account the uncertainty of the pressure estimation in these experiments.

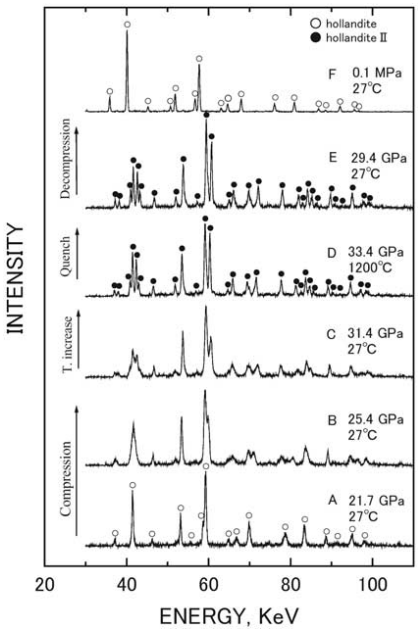

Figure 2. Variations of X-ray diffraction profile of $KAlSi_3O_8$ in MA with increasing pressure (a–c), and at high temperature under the maximum load (d). Hollandite II was quenchable to room temperature under pressure (e), but converted to the hollandite structure when the pressure was released (f).

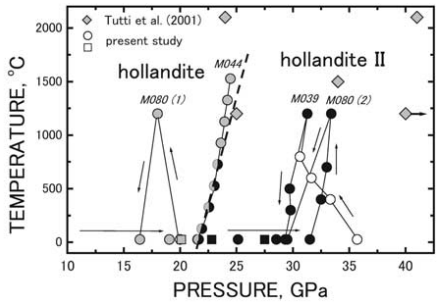

Figure 3. P-T conditions of the present in situ X-ray diffraction measurements using DAC (squares) and MA (circles). The diamond symbols are those of an earlier study [*Tutti et al.*, 2001] based mainly on quench experiments using DAC. Open symbols denote glass starting material, while filled symbols represent the P-T conditions where hollandite II was formed and the shadow symbols are those where K-hollandite was formed. The dashed line indicates the possible phase boundary between K-hollandite and hollandite II.

[15] It has been demonstrated that K-hollandite is present near the liquidus in both K-rich basalt and continental crust materials at pressures above ~20 GPa [*Irifune et al.*, 1994; *Wang and Takahashi*, 1999]. K-hollandite has a peculiar crystal structure possessing relatively large tunnels surrounded by four double chains of edge-shared octahedra along the c-axis, and has been demonstrated to retain some trace elements with large ionic radii, such as La, Pb, K, and Sr, whereas Nb and U are excluded. It follows that chemical fractionation due to partial melting in the presence of K-hollandite may introduce some distinctive geochemical signatures in the deep mantle, which are inconsistent with the characteristics of enriched mantle reservoirs for EMI, EMII, and HIMU ocean island basalts [*Irifune et al.*, 1994]. The present results suggest that such arguments are invalid for chemical fractionation at the lower mantle depths, because the transition of K-hollandite to the new structure should change the element partitioning and melting behaviors under these conditions. Abrupt enrichments of Ca and Na components in K-hollandite, presumably converted from hollandite II on release of pressure, were indeed noted in a K-rich basaltic composition coexisted with the melt at pressures 22.5 and 25 GPa [*Wang and Takahashi*, 1999]. Thus further studies on partitioning of the key trace elements between hollandite II and the coexisting melts in continental crust or basaltic lithologies should provide important constraints on the origin of distinctive geochemical components in the deep mantle.

[16] **Acknowledgment.** We thank T. Inoue, D. Yamazaki, T. Shinmei, T. Sanehira, Y. Higo, A. Yamada, and A. Nozawa for assistance in MA experiments at SPring-8, and also thank T. Kikegawa for help in the experimental set-up for DAC experiments at KEK.

References

Ahrens, T. J., and H. P. Liu (1973), A shock-induced phase change in orthoclase, *J. Geophys. Res.*, *78*, 1274–1278.

Armstrong, R. L. (1981), Radiogenic isotopes: The case for crustal recycling on a near-steady state no-continental growth earth, *Philos. Trans. R. Soc. London, Ser. A*, *301*, 443–472.

Anderson, O. L., D. G. Isaak, and S. Yamamoto (1989), Anharmonicity and the equation of state for gold, *J. Appl. Phys.*, *65*, 1534–1543.

Dupre, B., and C. Allegre (1983), Pb-Sr isotope variation in Indian Ocean basalts and mixing phenomena, *Nature*, *303*, 142–146.

Hofmann, A. W. (1997), Mantle geochemistry: The message from oceanic volcanism, *Nature*, *385*, 219–229.

Irifune, T., A. E. Ringwood, and W. O. Hibberson (1994), Subduction of continental crust and terrigenous and pelagic sediments: An experimental study, *Earth Planet. Sci. Lett.*, *126*, 351–368.

Irifune, T., H. Naka, T. Sanehira, T. Inoue, and K. Funakoshi (2002), In situ X-ray observations of phase transitions in $MgAl_2O_4$ spinel to 40 GPa using multianvil apparatus with sintered diamond anvils, *Phys. Chem. Miner.*, *29*, 645–654.

Katsura, T., K. Funakoshi, A. Kubo, N. Nishiyama, Y. Tange, Y. Sueda, T. Kubo, and W. Utsumi (2004), A large-volume high-pressure and high-temperature apparatus for in situ X-ray observation, 'SPEED-MK. II', *Phys. Earth Planet. Inter.*, *143–144*, 497–506.

Kinomura, N., S. Kume, and M. Koizumi (1975), Stability of $K_2Si_4O_9$ with wadeite type structure, paper presented at 4th International Conference on High Pressure, Int. Assoc. for the Adv. of High Pressure and Technol., Kyoto, Japan.

Mao, H. K., J. Xu, and P. M. Bell (1986), Calibration of the ruby gauge to 800 kbar under quasi-hydrostatic conditions, *J. Geophys. Res.*, *91*, 4673–4676.

Ono, S. (1998), Stability limits of hydrous minerals in sediment and mid-ocean ridge basalt compositions: Implications for water transport in subduction zones, *J. Geophys. Res.*, *103*, 18,253–18,267.

Ringwood, A. E., A. F. Reid, and A. D. Wadsley (1967), High-pressure $KAlSi_3O_8$, an aluminosilicate with sixfold coordination, *Acta Cryst.*, *23*, 1093–1095.

Schmidt, M. W. (1996), Experimental constraints on recycling of potassium from subducted oceanic crust, *Science*, *272*, 1927–1930.

Sobolev, N. V., and V. Shatsky (1990), Diamond inclusions in garnets from metamorphic rocks: A new environment for diamond formation, *Nature*, *343*, 742–746.

Tutti, F., L. S. Dubrovinsky, S. K. Saxena, and S. Carlson (2001), Stability of $KAlSi_3O_8$ hollandite-type structure in the Earth's lower mantle conditions, *Geophys. Res. Lett.*, *28*, 2735–2738.

Urakawa, S., T. Kondo, N. Igawa, O. Shimomura, and H. Ohno (1994), Synchrotron radiation study on the high-pressure and high-temperature phase relations of $KAlSi_3O_8$, *Phys. Chem. Miner.*, *21*, 387–391.

Wang, W., and E. Takahashi (1999), Subsolidus and melting experiments of a K-rich basaltic composition to 27 GPa: Implication for the behavior of potassium in the mantle, *Am. Miner.*, *84*, 357–361.

Yagi, A., T. Suzuki, and M. Akaogi (1994), High pressure transitions in the system $KAlSi_3O_8$–$NaAlSi_3O_8$, *Phys. Chem. Miner.*, *21*, 12–17.

Yagi, T., T. Kondo, T. Watanuki, O. Shimomura, and T. Kikegawa (2001), Laser heated diamond anvil apparatus at the Photon Factory and Spring-8: Problems and improvements, *Rev. Sci. Instrum.*, *72*, 1293–1297.

Yamada, H., Y. Matsui, and E. Ito (1984), Crystal-chemical characterization of $KAlSi_3O_8$ with the hollandite structure, *Mineral. J.*, *12*, 29–34.

T. Ferroir, S. Merkel, N. Miyajima, T. Onozawa, and T. Yagi, Institute for Solid State Physics, University of Tokyo, Kashiwa 277-8581, Japan.

T. Irifune, N. Nishiyama, R. P. Rapp, and Y. Sueda, Geodynamics Research Center, Ehime University, Matsuyama 790-8577, Japan. (irifune@dpc.ehime-u.ac.jp)

K. Funakoshi, Japan Synchrotron Research Institute, Sayo 679-5198, Japan.

American Mineralogist, Volume 91, pages 327–332, 2006

Equation of state and phase transition in $KAlSi_3O_8$ hollandite at high pressure

TRISTAN FERROIR,[1] TSUYOSHI ONOZAWA,[2] TAKEHIKO YAGI,[2] SEBASTIEN MERKEL,[2] NOBUYOSHI MIYAJIMA,[2] NORIMASA NISHIYAMA,[3] TETSUO IRIFUNE,[3] AND TAKUMI KIKEGAWA[4]

[1]Ecole Normale Superieure de Lyon, 69364 Lyon cedex 07, France
[2]Institute for Solid State Physics, University of Tokyo, Kashiwa, Chiba 277-8581, Japan
[3]Geodynamics Research Center, Ehime University, Matsuyama 790-8577, Japan
[4]Photon Factory, KEK, Tsukuba, Ibaraki 305-0801, Japan

ABSTRACT

The tetragonal hollandite structure ($KAlSi_3O_8$ hollandite) has been studied up to 32 GPa at room temperature using high-pressure in-situ X-ray diffraction techniques. A phase transformation from tetragonal *I*4/*m* phase to a new phase was found to occur at about 20 GPa. This transition is reversible on release of pressure without noticeable hysteresis and hence this new high-pressure phase is unquenchable to ambient conditions. The volume change associated with the transition is found to be small (not measurable), suggesting a second order transition. The diffraction pattern of the high-pressure phase can be indexed in a monoclinic unit cell (space group *I*2/*m*), which is isostructural with $BaMn_8O_{16}$ hollandite. The γ angle of the monoclinic unit cell increases continuously above the transition. A Birch-Murnaghan equation of state fit to pressure-volume data obtained for $KAlSi_3O_8$ hollandite yields a bulk modulus $K_0 = 201.4$ (7) GPa with $K'_0 = 4.0$.

INTRODUCTION

$KAlSi_3O_8$ hollandite, orthoclase, is one of the abundant minerals found in the crust. It is an important host mineral of potassium at near-surface conditions of the Earth and is transported into the deeper part of the mantle as one of the components of subducting slab. However, the nature of potassium-bearing minerals in the deep mantle is still a matter of debate. When $KAlSi_3O_8$ hollandite is subjected to high pressure, it first decomposes into a three-phases assemblage (wadeite-type $K_2Si_4O_9$ + Al_2SiO_5 kyanite + SiO_2 coesite) at ~6 GPa and then recombines to form a hollandite-structured phase ($KAlSi_3O_8$, hereafter) above ~9 GPa. For depths lower than 100 km, Wendland and Eggler (1980) suggested that kalsilite ($KAlSiO_4$) is stable instead of sanidine (a high-temperature form of orthoclase, $KAlSi_3O_8$) based on their study of the K_2O-Al_2O_3-SiO_2 system. On the other hand, Sommerville and Arhens (1980) argued that $KAlSi_3O_8$ hollandite is a more plausible potassic phase under lower mantle conditions because Si and Al atoms are octahedrally coordinated and hence the hollandite structure has higher density. More recently, Gillet et al. (2000) identified a $KAlSi_3O_8$ hollandite phase, which crystallized at around 23GPa in two Martian meteorites, showing that $KAlSi_3O_8$ hollandite can actually be synthesized under "natural" conditions.

Since the first synthesis of $KAlSi_3O_8$ hollandite (Ringwood et al. 1967), several studies have been made to clarify its stability field (Kinomura et al. 1975; Liu 1978; Yagi et al. 1994; Urakawa et al. 1994) and crystal structure (Yamada et al. 1984). Recent experimental study in the diamond anvil cell demonstrated that $KAlSi_3O_8$ hollandite is stable up to pressures of 95GPa (Tutti et al. 2001), leading to the conclusion that $KAlSi_3O_8$ hollandite is a major host for potassium in the deep mantle. However, because this study relied mainly on the analysis of quenched samples, pursuing in-situ measurements under mantle pressures are still necessary.

The study of the $KAlSi_3O_8$ hollandite compression curve is also very important to the understanding the dynamics of subducted continental slab. To constrain the mineralogy and density of subducted slabs through the 670 km discontinuity, the equation of state (EOS) and physical properties of their main constituents must be known. The isothermal bulk modulus of $KAlSi_3O_8$ hollandite was measured by Zhang et al. (1993) using single-crystal X-ray diffraction; however, their study was limited to pressures up to 4.5 GPa, which is too low to make reliable extrapolations to the deep mantle.

In the present paper, we present new high-pressure measurements performed up to 32 GPa in the diamond anvil cell at room temperature, using hydrostatic pressure transmitting media These measurements provide new constraints on the $KAlSi_3O_8$ hollandite EOS. We also report the first evidence of a structural phase transition occurring at ~20 GPa.

EXPERIMENTAL METHOD

Powder X-ray diffraction data were collected at both at the Institute for Solid State Physics, University of Tokyo, using Mo*K*α radiation (rotating anode) and at the BL13-A beam line of the Photon Factory, KEK (synchrotron source). We used modified Mao-Bell type diamond anvil cells, with anvils having culet diameters of 450 μm. Rhenium gaskets were pre-indented to 11 GPa and drilled to a diameter of 180 μm. Experiments below 10 GPa were carried out using a methanol-ethanol (4:1) mixture as a pressure-transmitting medium. For higher pressure, He gas was loaded using a system similar to the one described by Yagi et al. (1996). Starting sample was a pure $KAlSi_3O_8$ hollandite with hollandite structure. It was prepared from an isochemical mixture of K_2CO_3, Al_2O_3, and SiO_2, fired in air for degassing and then converted to hollandite structure at 20 GPa and 1500 °C in a "Kawai-type"

* E-mail: yagi@issp.u-tokyo.ac.jp

0003-004X/06/0203–327$05.00/DOI: 10.2138/am.2006.1879

multi-anvil apparatus at the Ehime University. For experiments below 10 GPa, a polycrystalline sintered piece of synthesized sample was polished to a 50 μm thick square block ~80 μm on a side. For the higher pressure runs, we used samples with a 20 μm thickness. In the sample chamber, a square block of sample, several ruby chips, and a small piece of gold foil were placed together with the pressure-transmitting medium. To precisely calibrate the pressures in the experiments, we used the ruby fluorescence technique (Mao et al. 1986) and the EOS of gold (Shim et al. 2002). In all cases, pressures determined by the ruby fluorescence method and the EOS of gold did not differ by more than 0.2 GPa. Unit-cell volumes of gold calculated from (111) and (200) diffraction lines coincide well within the experimental error in all the experiments, which guarantees hydrostatic nature of the applied pressure. To look for any hysteresis in the unit-cell parameters of the sample, which can be caused by the existence of non-hydrostatic pressure, X-ray patterns were collected both on compression and decompression.

Experiments MET was performed using a Mo$K\alpha$ laboratory X-ray source with a beam size of ~100 μm. Patterns were collected on an imaging plate for ~12 h. Experiments He1, He2, and He3 were performed at the Photon Factory synchrotron source using a monochromatic X-ray beam of wavelength 0.4258 Å collimated to 30 /m diameter. At the Photon Factory, X-ray patterns for the sample and gold pressure marker were collected separately in ~5 to 15 min using a Rigaku imaging plate system (R-AXIS IV). Sample to detector distance was calibrated with an Ag sample.

Figure 1 represents typical 2-D diffraction patterns obtained in run He1 at 17.1 GPa and 30.1 GPa. As shown in the figure, the diffraction lines from the sample are spotty but very clear, indicating that the number of grains was sufficient for a basic structural analysis. Figure 2 shows an example of a series of integrated 1-D X-ray patterns obtained with increasing pressure. These integrated diffraction patterns were indexed using the structural parameters and atom positions described in Yamada et al. (1984) and refined using the Le Bail algorithm as found in the GSAS package (Larson and Von Dreele 1994).

RESULTS

Equation of state of $KAlSi_3O_8$ hollandite

For pressures below 20 GPa, the overall diffraction patterns did not change significantly and consistently matched the refinements performed assuming a tetragonal crystal symmetry.

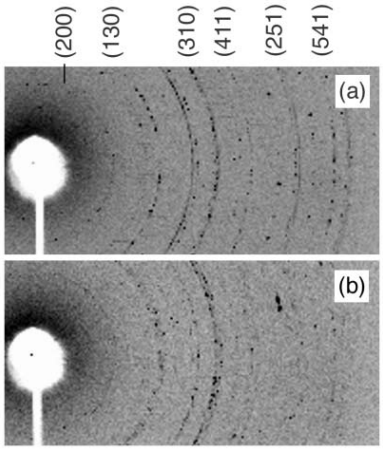

FIGURE 1. X-ray diffraction patterns of $KAlSi_3O_8$ hollandite obtained in the run He1 at (**a**) 17.1GPa, and (**b**) 30.1 GPa. Diffraction patterns from gold pressure marker are overlapped and some strong peaks from hollandite are indexed for the comparison with Figure 2.

Refined cell parameters, pressures and their uncertainties are summarized in Table 1. EOS parameters were calculated using the software EoSFit5.2 and a second order Birch-Murnaghan equation,

$$P = 3\,K_0 f_E\,(1 + 2f_E)^{5/2}\,[1 + 3/2\,(K_0' - 4)\,f_E]$$

where K_0 and K_0' are the room temperature bulk modulus and its first pressure derivative, respectively, and f_E is the Eulerian strain defined as

$$f_E = 0.5\,[(V/V_0)^{2/3} - 1]$$

where V and V_0 are volume at pressure P and zero pressure, respectively. To determine K_0', Eulerian strain obtained in all the runs was plotted as a function of F, which is defined as

$$F = P/\,[3\,f_E\,(2\,f_E + 1)^{5/2}].$$

It is clear that the data are fit reasonably well by a horizontal line and, therefore, K_0' was fixed to 4.0 for the rest of the analysis (Fig. 3) The zero pressure volume V_0 was measured at each run after complete release of pressure, and V/V_0 ratios were calculated using those measured V_0 values. Since these V_0 values were measured using different X-ray systems, they are

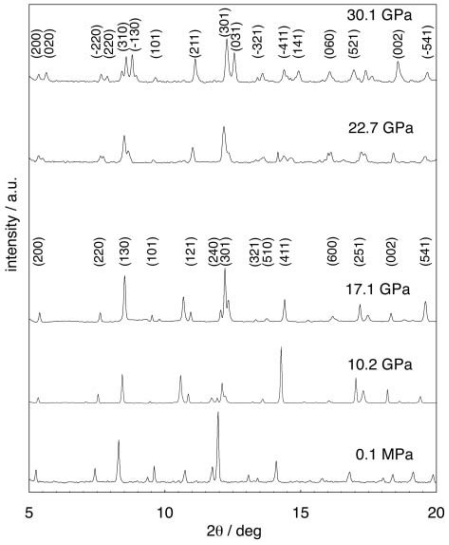

FIGURE 2. Integrated X-ray diffraction patterns of $KAlSi_3O_8$ hollandite measured with increasing pressure. Many peaks start to split at about 20 GPa as a result of the transformation to hollandite-II. Patterns were indexed in I4/m (below 20 GPa) and I2/m space groups (30.1 GPa). Not all the indexed peaks are shown. Helium was used as pressure-transmitting medium. Some non-indexed peaks are from either the gold pressure marker or from the gasket material.

rather scattered as shown in Table 1. However, V/V_0 values are much less scattered as shown in Figure 4. The bulk modulus K_0 was refined from these measured pressures and volumes and yielded K_0 = 201.4(7) GPa with K_0' = 4.0. The zero pressure volume, determined from the average of the four runs, was V_0 = 237.01(33) Å^3. The V/V_0 values determined in the present study, those reported by Zhang et al. (1993) from single-crystal analysis, and the Birch-Murnaghan fit for the present data are shown in Figure 4. The zero pressure volume we have obtained is in reasonable agreement with previously published data, as summarized in Table 2. However, we find that $KAlSi_3O_8$ hollandite seems to be slightly less compressible than reported by Zhang et al. (1993), as will be discussed later.

Evidence for a phase transition

Above ~21 GPa, many diffraction peaks started to broaden and split into two or more peaks upon further compression. It is known that some of the hollandite-type structures have monoclinic unit cells with *I*2/*m* space group symmetry (Cheary and Squadrito 1989; Post et al. 1982; Miura 1986). To investigate the crystallographic structure of the new high-pressure phase (hereafter referred to as hollandite-II), we tried to fit a monoclinic cell to the data obtained at 27.5 GPa. The indexing of diffraction peaks was performed by comparing the observed 2θ values of some strong peaks with those calculated for the possible reflections for the group *I*2/*m* based on the "tentative" unit-cell parameters. With the aid of the newly obtained unit-cell parameters, refined by least square method, the diffraction peaks were re-indexed. Repeating this process until all the observed diffraction lines were properly indexed, we obtained good agreement between the observed and calculated peak positions with the following unit-cell parameters: a = 9.1556 (2) Å, b = 8.7084 (5) Å, c = 2.6407 (2) Å, γ = 91.46 (1)°, V = 210.48(2) Å^3 (Table 3). Although we have observed splitting of some peaks there is no evidence for the appearance or disappearance of any peaks associated with the transition. Intensities of the observed

TABLE 1. Cell parameters of $KAlSi_3O_8$ and hollandite-II obtained in the present study

Data no.*	P/GPa	a/Å	b/Å	c/Å	γ/°.	V/Å^3
MET-1	0.0	9.331(1)	–	2.727(1)	90.0	237.5(1)
MET-2	1.7	9.300(1)	–	2.723(1)	90.0	235.5(1)
MET-3	2.8	9.277(2)	–	2.718(1)	90.0	233.9(1)
MET-4	4.3	9.260(2)	–	2.712(2)	90.0	232.5(2)
MET-5	5.7	9.237(1)	–	2.711(1)	90.0	231.3(1)
MET-6	6.5	9.225(1)	–	2.709(1)	90.0	230.5(1)
MET-7	7.5	9.205(1)	–	2.705(1)	90.0	229.2(1)
MET-8	8.9	9.192(1)	–	2.700(1)	90.0	228.1(1)
He1-1	0.0	9.322(4)	–	2.725(1)	90.0	236.8(1)
He1-2	3.7	9.266(2)	–	2.715(1)	90.0	233.1(1)
He1-3	10.2	9.165(3)	–	2.695(2)	90.0	226.4(1)
He1-4	12.7	9.125(5)	–	2.687(2)	90.0	223.7(1)
He1-5	15.2	9.098(3)	–	2.680(1)	90.0	221.8(1)
He1-6	17.1	9.077(5)	–	2.673(1)	90.0	220.2(1)
He1-7	25.6	9.121(4)	8.812(3)	2.650(1)	91.1(2)	212.9(7)
He1-8	27.0	9.144(3)	8.756(4)	2.647(1)	91.3(3)	211.9(10)
He1-9	30.1	9.145(3)	8.673(3)	2.633(1)	91.7(2)	208.7(8)
He2-1	12.9	9.1272(6)	–	2.6860(2)	90.0	223.76(3)
He2-2	20.1	9.0453(8)	–	2.6671(2)	90.0	218.21(4)
He2-3	23.4	9.1335(2)	8.8583(2)	2.6533(1)	90.92(1)	214.65(1)
He2-4	27.5	9.1556(2)	8.7084(5)	2.6407(2)	91.46(1)	210.48(2)
He2-5	25.1	9.1468(14)	8.7833(18)	2.6514(4)	91.23(2)	213.00(6)
He2-6	20.3	9.0303(7)	–	2.6665(1)	90.0	217.45(3)
He2-7	0.0	9.3261(6)	–	2.7262(2)	90.0	237.11(3)
He3-1	4.2	9.2497(4)	–	2.7113(2)	90.0	231.97(3)
He3-2	8.8	9.1827(2)	–	2.6973(1)	90.0	227.44(2)
He3-3	10.8	9.1539(4)	–	2.6908(2)	90.0	225.47(2)
He3-4	15.8	9.0891(4)	–	2.6764(1)	90.0	221.10(2)
He3-5	20.0	9.0373(7)	–	2.6641(2)	90.0	217.58(4)
He3-6	18.7	9.0473(9)	–	2.6673(3)	90.0	218.33(5)
He3-7	13.1	9.1215(4)	–	2.6848(2)	90.0	223.38(3)
He3-8	9.0	9.1775(3)	–	2.6967(1)	90.0	227.13(2)
He3-9	0.0	9.3195(4)	–	2.7246(2)	90.0	236.63(3)

*Seven data obtained between 20.1 GPa and 23.4 GPa are not listed in this table because unit-cell parameters were not determined at these pressures (see text).

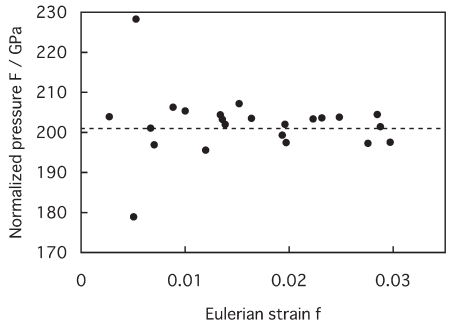

FIGURE 3. F-f_E plot from the volume compression data of $KAlSi_3O_8$ up to 20 GPa, where $F = P/ [3 f_E (2 f_E + 1)^{5/2}]$ and $f_E = 0.5 [(V/V_0)^{2/3} - 1]$. From this figure, the value of K_0' was determined to be 4.

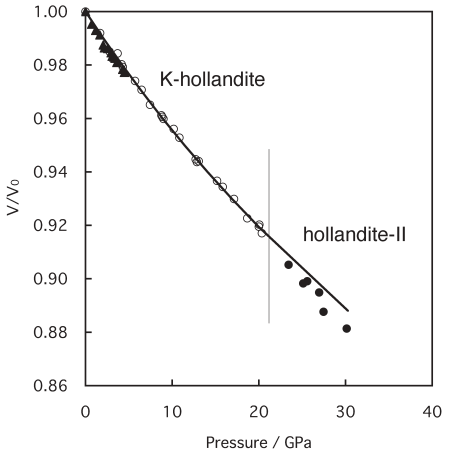

FIGURE 4. Volume compression of $KAlSi_3O_8$ at room temperature. Solid line is an isothermal compression curve with K_0 = 201 GPa and K_0' = 4 obtained by fitting a Birch-Murnaghan EOS to the volume compression data up to 20 GPa. Open circle = $KAlSi_3O_8$, solid circle = hollandite-II, solid triangle = (Zhang et al. 1993).

TABLE 2. Summary of V_0 and K_0 for $KAlSi_3O_{12}$ hollandite

Reference	V_0/Å^3	K_0/GPa	K_0'
Ringwood et al. (1967)	241.06	–	
Yamada et al. (1984)	236.73(3)	–	
Zhang et al. (1993)	236.26(36)	180(3)	4.0
ibid.	–	191(6) *	4.0
Yagi et al. (1994)	237.2(1)	–	
This study	237.01(33)	201.4(7)	4.0

* Bulk modulus obtained without constraining V_0.

diffraction peaks were compared with those calculated from the hollandite structure with *I*2/*m* space group symmetry. Since the observed diffraction lines from the sample were spotty and the relative intensities change from run to run, it is difficult and meaningless to make detailed comparisons; however, the general agreement between observed and calculated intensities is good. Lower pressure data above 23.4 GPa were also investigated using the same indexing scheme and the resultant unit-cell parameters are summarized in Table 1 and Figures 5 and 6. Although we have made many observations near the transition pressure, the unit cell of the high-pressure phase was calculated only for the data above 23.4 GPa, where the splitting of the peaks become large enough so that they can be identified as separate peaks. On decompression, the high-pressure phase reverts to the starting low pressure phase. From the careful observation of the broadening of diffraction peaks, we can conclude that the transition occurs reversibly without any noticeable hysteresis. Zero pressure volumes measured after each experiment did not have any meaningful difference among the runs with or without the phase transformation. Thus, this phase transformation is completely reversible at room temperature.

TABLE 3. Observed and calculated *d*-values of hollandite-II at 27.5 GPa

h k l	d_{obs}/Å	d_{cal} */Å	$(d_{obs}/d_{cal})^{-1}$
200	4.5660	4.5713	–0.0011
020	4.3594	4.3608	–0.0003
220	3.1948	3.1987	–0.0012
220	3.1176	3.1137	0.0013
310	2.9030	2.9014	0.0005
310	2.8529	2.8531	–0.0001
130	2.7912	2.7924	–0.0004
130	2.7473	2.7492	–0.0007
101	2.5330	2.5360	–0.0012
211	2.2033	2.2039	–0.0003
040	2.1839	2.1804	0.0016
301	1.9937	1.9952	–0.0007
031	1.9550	1.9543	0.0004
321	1.8276	1.8266	0.0006
321	1.8001	1.8023	–0.0012
231	1.7853	1.7853	0.0000
411	1.7024	1.7016	0.0005
411	1.6892	1.6884	0.0005
141	1.6581	1.6595	–0.0008
141	1.6462	1.6473	–0.0006
440	1.6009	1.5994	0.0010
600	1.5254	1.5238	0.0011
060	1.4555	1.4536	0.0013
521	1.4311	1.4308	0.0002
521	1.4121	1.4114	0.0005
251	1.3952	1.3958	–0.0004
251	1.3767	1.3778	–0.0008
002	1.3210	1.3198	0.0009
611	1.3080	1.3093	–0.0010
541	1.2498	1.2506	–0.0006
541	1.2252	1.2249	0.0002
451	1.2148	1.2153	–0.0003

*a = 9.1556(2) Å, b = 8.7084(5) Å, c = 2.6407(2) Å, γ = 91.46(1)°, V = 210.48(2) Å^3

DISCUSSION

Existence of the phase transition

This report of a new phase of $KAlSi_3O_8$ hollandite at high pressure contrasts with the results of Tutti et al. (2001) who studied the high-pressure behavior of $KAlSi_3O_8$ hollandite up to 50 GPa with in situ X-ray experiments and up to 95 GPa with quench samples. They reported that the hollandite-type $KAlSi_3O_8$

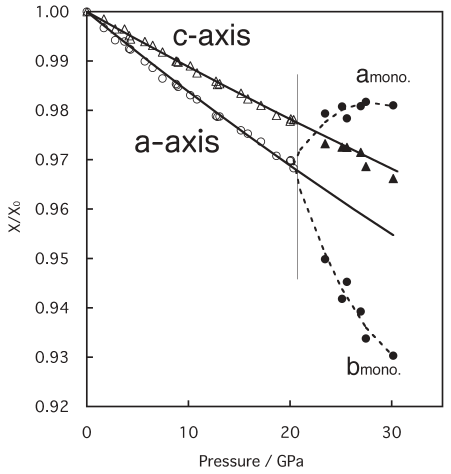

FIGURE 5. Change in unit-cell parameters (a/a_0, b/b_0, and c/c_0) as a function of pressure. Open and solid symbols are for $KAlSi_3O_8$ and hollandite-II, respectively. Solid and dotted lines are not best-fits to the data and are for visual purposes only.

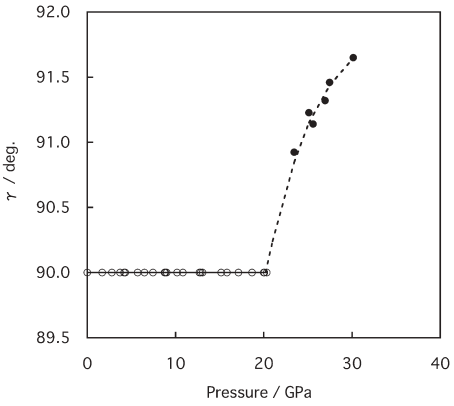

FIGURE 6. Change in γ-angle as a function of pressure. Lines are for visual purposes only.

hollandite was stable up to the highest pressures and there was no phase transition over the entire pressure range studied. However, no comparison can be made between our high-pressure results and those of Tutti et al. (2001) because no X-ray diffraction pattern of their high-pressure in situ experiment was published in their study. As shown in Figure 1, the overall diffraction pattern does not differ much between the low and high-pressure phases and the differences can be detected only when the patterns have adequate resolution. Tutti et al. (2001) used a small CCD detector for which the resolution is rather limited for their in situ X-ray measurements. Furthermore, the splitting of the peaks can only be seen in a hydrostatic environment. The use of a solid pressure-transmitting medium in their experiment could explain why they did not observe the phase transition. Another possibility is that they used a natural sample as starting material and that the existence of small amount of minor elements could affect the transition. Tutti et al. (2001) used two natural samples and they contained some Na, Ba, and Mg.

The new phase transition presented in this article has recently been investigated at high pressure and high temperature using multi-anvil presses combined with synchrotron X-rays (Sueda et al., pers. comm.) These authors carried out high-pressure and high-temperature in situ X-ray studies of pure, polycrystalline $KAlSi_3O_8$. First, they observed that the diffraction peaks became broad with decreasing temperature at around 22 GPa. Above 30 GPa, the transition could be clearly observed at elevated temperature and after heating, even by directly compressing the powder sample. By combining our present result with that of Sueda et al., it is clear that the monoclinic phase of $KAlSi_3O_8$ hollandite has wide stability range under the conditions of the deep mantle.

Nature of the phase transition

It is known that hollandite structure can adopt either monoclinic or tetragonal symmetry, depending on the ratio of the average ionic radius of the octahedral cations to that of the tunnel cations (Post et al. 1982). $BaMn_8O_{16}$ hollandite adopts monoclinic symmetry while $KAlSi_3O_8$ hollandite adopts tetragonal symmetry at ambient condition. Zhang et al. (1993) have predicted, based on their studies of the compressional behavior of various polyhedra in $KAlSi_3O_8$, that it will transform from tetragonal to monoclinic symmetry at high pressure. Present results are consistent with their prediction.

Figure 5 shows the change of axial ratio associated with the transition. The original *a* axis of the tetragonal unit cell splits into the long *a* and short *b* axis of the monoclinic cell. The *c* axis, on the other hand, compresses almost continuously across the phase transformation. As shown in Figure 4, no discontinuous change in volume was found associated with this transition but, in the pressure range from 23 to 30 GPa, the structure became more compressible than the low-pressure phase. All these facts suggest that this phase transition is a second order transition caused by the onset of distortion of large open tunnels in the hollandite structure. This means that although this transition has a small effect on the bulk density of the crystal, it may affect significantly the nature of the large open tunnels in the structure at higher pressures. It has been reported, based on the quench experiments, that various properties of $KAlSi_3O_8$ hollandite change at ~20 GPa. Yagi et al. (1994) reported that in the system $KAlSi_3O_8$-$NaAlSi_3O_8$ the solubility of Na in $KAlSi_3O_8$ hollandite increases with pressure up to a maximum at around 22 GPa and 1000 °C and then decreases at higher pressures. Wang and Takahashi (1999) also reported a change of the melting curve of $KAlSi_3O_8$ hollandite at around 20–22.5 GPa and 1700 °C. All of these changes of the physical properties of $KAlSi_3O_8$ hollandite at about 20 GPa may be related to the onset of this transition, which was not detected by the previous quench experiments.

It has been suggested that $KAlSi_3O_8$ hollandite might be a common minor phase in the upper and lower mantle but with important implications, as it may be a major host for potassium and other geochemically important elements (i.e., Ba, Sr, and Pb) in those regions. For example, Irifune et al. (1994) showed that $KAlSi_3O_8$ hollandite strongly retains Pb, is a host for La and selectively excludes U. These features are, however, derived from the experiments in the stability field of $KAlSi_3O_8$. This new phase transition in $KAlSi_3O_8$ hollandite may affect considerably the chemistry in multi-component system containing hollandite structure and, thus, further study will be required to clarify the geochemical behavior of $KAlSi_3O_8$ hollandite in the stability field of hollandite-II.

Bulk modulus and compressibility of $KAlSi_3O_8$ hollandite and hollandite-II

The bulk modulus of $KAlSi_3O_8$ hollandite measured in the present study is 201.4(7) GPa, which is slightly larger than the value [180(3) GPa] previously reported by Zhang et al. (1993) from single-crystal measurements under hydrostatic conditions. However, their pressure range was limited to 4.5 GPa. They reported in their study that the resulting bulk modulus was quite sensitive to the choice of V_0; if the bulk modulus is calculated without constraining V_0, their bulk modulus becomes 191(6) GPa with $K_0' = 4.0$. Therefore, the actual difference in the volume is very small, as can be seen in Figure 4.

We have made four independent runs using two different pressure-transmitting media and measurements were made during both increasing and decreasing pressure cycles. All these data are quite consistent and can be fitted by a single compression curve, as shown in Figure 4. Therefore, we believe that this is the most reliable compression curve of $KAlSi_3O_8$ hollandite at room temperature.

The volume compression of hollandite-II is also shown in Figure 4. Although the phase transition starts at about 21 GPa, no discontinuous change in volume was detected in the present study. The hollandite-II is, however, more compressible compared to the extrapolated compression curve of $KAlSi_3O_8$. As noted above, the compressibility of each axis of the unit cell does not differ significantly before and after the transition. Rather, it is the change of the angle γ that is related primarily to the rapid decrease in volume. The γ-angle starts to deviate rapidly from 90° with the onset of the transition and it is still increasing even at about 30 GPa, as shown in Figure 6. Further experiments to higher pressures are required to evaluate the actual change of γ under deep mantle conditions. The pressure range of the present measurement is not large enough to properly constrain the equation of state of hollandite-II but it is clear that this phase becomes slightly denser than indicated by the simple extrapolation of the compression curve of $KAlSi_3O_8$.

ACKNOWLEDGMENTS

The authors are grateful to H. Miura for providing helpful information for the indexing of hollandite-II. X-ray experiments using synchrotron source were performed at the Photon Factory, KEK, under the approval of the Photon Factory Program Advisory Committee (proposal no. 02G050).

REFERENCES CITED

Cheary, R.W. and Squadrito, R. (1989) A structural analysis of barium magnesium hollandites. Acta Crystallographica, B45, 205–212.

Gillet, P., Chen, M., Dubrovinsky, L.S., and El Goresy, A. (2000) Natural Na $AlSi_3O_8$-Hollandite in the Shocked Sixiangkou Meteorite. Science, 287, 1633–1636.

Irifune, T., Ringwood, A.E., and Hibberson, W.O. (1994) Subduction of Continental—Crust and Terrigenous and Pelagic Sediments—An experimental Study. Earth and Planetary Science Letters, 126, 4, 351–368.

Kinomura, N., Kume, S., and Koizumi, M. (1975) Stability of $K_2Si_4O_9$ with wadeite type structure. Proceedings of the 4th International Conference of High Pressure Scientific Technique, 211–214.

Larson, A.C. and Von Dreele, R.B. (1994) GSAS manual, Report LAUR 86–748. Los Alamos National Laboratory, New Mexico.

Liu, L. (1978) High-pressure phase transitions of kalsilite and related potassium bearing aluminosilicates. Geochemical Journal, 12, 275–277.

Mao, H.K., Xu, J., and Bell, P.M. (1986) Calibration of the ruby pressure gauge to 800 kbar under quasi-hydrostatic conditions. Journal of Geophysical Research, 91, 4673–4676.

Miura, H. (1986) The crystal structure of hollandite. Mineralogical Journal (Japan), 13, 3, 119–129.

Post, J.E., Von Dreele, R.B., and Buseck, P.R. (1982). Symmetry and cation displacements in hollandites: structure refinements of hollandite, cryptomelane and priderite. Acta Crystallographica, B38, 1056–1065.

Ringwood, A.E., Fredi, A.F., and Wadsley, A.D. (1967) High-Pressure $KAlSi_3O_8$ and Aluminosilicate with Sixfold Coordination. Acta Crystallographica, 23, 1093.

Shim, S.H., Duffy, T.S., and Takemura, K. (2002) Equation of state of gold and its application to the phase boundaries near 660-km depth in Earth's mantle. Earth and Planetary Science Letters, 203, 729–739.

Sommerville, M. and Arhens, T.J. (1980) Shock compression of $KFeS_2$ and question of potassium in the core. Journal of Geophysical Research, 85, 7016–7024.

Tutti, F., Dubrovinsky, L.S., Saxena, S.K., and Carlson, S. (2001) Stability of $KAlSi_3O_8$ Hollandite-Type Structure in the Earth's Lower Mantle Conditions. Geophysical Research Letters, 28, 14, 2735–2738.

Urakawa, S., Kondo, T., Igawa, N., Shinomura, O., and Ohno, H. (1994) Synchrotron Radiation Study on the High-Pressure and High Temperature Phase Relations of $KAlSi_3O_8$. Physics and Chemistry of Minerals, 21, 387–391.

Wang, W. and Takahashi, E. (1999) Subsolidus and melting experiments of a K-rich basaltic composition to 27 GPa: Implication for the behavior of potassium in the mantle. American Mineralogist, 84, 357–361.

Wendlandt, R.F. and Eagler, D.H. (1980) The origins of potassic magmas: 1. melting relations in the system $KalSiO_4$-Mg_2SiO_4-SiO_2 and $KAlSiO_4$-MgO-SiO_2-CO_2 to 30 kilobars. American Journal of Science, 280, 385–420.

Yagi, A., Suzuki, T., and Akaogi, M. (1994) High Pressure Transition in the System $KAlSi_3O_8$-$NaAlSi_3O_8$. Physics and Chemistry of Minerals, 21, 12–17.

Yagi, T., Yusa, H., and Yamakata, M. (1996) An apparatus to load gaseous materials to the diamond-anvil cell. Review of Scientific Instruments, 67, 2981–2984.

Yamada, H., Matsui, Y., and Ito, E. (1984) Crystal-chemical characterization of $KAlSi_3O_8$ with the hollandite structure. Mineralogical Journal, 12, 1, 29–34.

Zhang, J., Ko, J., Hazen, R.M., and Prewitt, C.T. (1993) High-pressure crystal chemistry of $KAlSi_3O_8$ hollandite. American Mineralogist, 78, 493–499.

MANUSCRIPT ACCEPTED AUGUST 19, 2005
MANUSCRIPT RECEIVED DECEMBER 15, 2004
MANUSCRIPT HANDLED BY GEORGE LAGER

research papers

Journal of
Synchrotron Radiation
ISSN 0909-0495

Received 28 February 2009
Accepted 27 August 2009

In situ rheological measurements at extreme pressure and temperature using synchrotron X-ray diffraction and radiography

Paul Raterron* and Sébastien Merkel

Laboratoire de Structure et Propriétés de l'Etat Solide, CNRS 8008, Université de Lille 1, F-59655 Villeneuve d'Ascq Cedex, France. E-mail: paul.raterron@univ-lille1.fr

Dramatic technical progress seen over the past decade now allows the plastic properties of materials to be investigated under extreme pressure and temperature conditions. Coupling of high-pressure apparatuses with synchrotron radiation significantly improves the quantification of differential stress and specimen textures from X-ray diffraction data, as well as specimen strains and strain rates by radiography. This contribution briefly reviews the recent developments in the field and describes state-of-the-art extreme-pressure deformation devices and analytical techniques available today. The focus here is on apparatuses promoting deformation at pressures largely in excess of 3 GPa, namely the diamond anvil cell, the deformation-DIA apparatus and the rotational Drickamer apparatus, as well as on the methods used to carry out controlled deformation experiments while quantifying X-ray data in terms of materials rheological parameters. It is shown that these new techniques open the new field of *in situ* investigation of materials rheology at extreme conditions, which already finds multiple fundamental applications in the understanding of the dynamics of Earth-like planet interior.

Keywords: materials; plastic deformation; high pressure; high temperature; rheology; synchrotron X-ray; diffraction; imaging; stress; strain; strain rate.

1. Introduction

Recent technical advances in high-pressure devices coupled with synchrotron radiation allow investigation of materials rheology at pressure (P) and temperature (T) in excess of 135 GPa and 1870 K, respectively. Specimens of a few cubic millimeters in multi-anvil apparatuses, or of thousands of cubic micrometers in the diamond-anvil cell, can now be deformed at pressures corresponding to those existing hundreds or thousands of kilometers within Earth-like planets. During deformation, the applied differential stress (t) and resulting specimen strain (ε) and strain rate ($\dot{\varepsilon}$) are quantified *in situ* by time-resolved X-ray diffraction and radiography. Although the basic principles of these measurements are straightforward, *i.e.* t is deduced from diffraction peak shifts arising from polycrystalline materials within the cell, and ε is measured optically on a fluorescent YAG crystal placed downstream with respect to the specimen, carrying out these measurements at extreme conditions has been challenging. This has required adapting the high-pressure devices to allow deformation of specimens and collection of the diffracted beams in specific orientations with respect to the principal stress directions, as well as developing the tools to quantify the stress tensor from small d-spacing variations between different populations of grains within deforming aggregates.

These new techniques renewed interest in research involving the *in situ* investigation of materials rheological properties at extreme conditions. They have multiple potential applications in Earth sciences when investigating the dynamics of planet interiors, as well as in materials science for the search for new super-hard materials or for quantifying armor resistance during shell explosions. Here we review the state-of-the-art of the high-pressure devices available today for these types of measurements, the techniques involved, and their resolutions to quantify stress, texture, specimen strain and strain rate, whether using a monochromatic or a white X-ray beam to collect the data.

2. Extreme-pressure deformation devices

We focus here on apparatuses which allow deforming materials at pressure largely in excess of 3 GPa. Until recent years, controlled deformation experiments in Paterson-type gas medium apparatuses or Griggs-type solid medium apparatuses (*e.g.* Bistricky *et al.*, 2000; Jung & Green, 2009) were limited to typically 3 GPa pressure. Previous attempts to use the diamond anvil cell (DAC) or the multi-anvil large-volume

press to quantitatively deform specimens at higher pressure, by using specific cell assembly geometry (*e.g.* Bussod *et al.*, 1993; Zhang & Karato, 1995; Karato & Rubie, 1997; Cordier *et al.*, 2003; Raterron *et al.*, 2004), were limited to relaxation deformation upon heating and often 'cook and look'-type experiments, *i.e.* without *in situ* rheological measurements [see Durham & Rubie (1998) for a review]. In the DAC, rheological parameters, such as the applied stress, could not be quantified since only axial diffraction (along the compression axis) was available. Over recent years, the development of radial diffraction in the DAC and the Drickamer press, as well as the parallel developments of the deformation-DIA apparatus and the rotational Drickamer apparatus, drastically changed this picture.

2.1. Radial diffraction in the DAC

DAC experiments allow experimental investigations in the whole pressure range typical of the Earth's lower mantle, *i.e.* at P in excess of 135 GPa which is far beyond the range accessible with other static devices. The use of uniaxial loading results in significant pressure gradients and differential stresses, despite the efforts devoted to reduce this effect. Nevertheless, one can take advantage of this situation to achieve plastic deformation. For deformation experiments, measurements are performed in the radial geometry (Fig. 1). In this geometry, the X-ray beam passes through the DAC perpendicular to the axis and, in this case, Debye rings in diffraction patterns record a whole range of orientations, with lattice planes from parallel to almost perpendicular to the DAC and deformation axis. The diffraction pattern illustrates elastic deformation effects expressed in elliptical distortions of Debye rings and intensity variations that signify texture.

The confining gasket must thus be made of a material transparent to X-rays. In the first DAC deformation experiments (Kinsland & Bassett, 1976), no gasket was used and the sample was simply compressed between the two diamond anvils. This limited greatly the pressure range, resulted in radial flow of the sample towards the edges of the diamond anvils, and introduced tremendous pressure gradients. Later, other approaches were introduced for gaskets, such as the use of a mixture of amorphous boron and epoxy, a low-Z material such as beryllium, or a proper combination of kapton sheet and boron epoxy. Nowadays, the most convenient techniques involve the use of Be gaskets for pressures above 80 GPa and up to multi-megabar pressures (Hemley *et al.*, 1997; Mao *et al.*, 1998) and combinations of kapton sheets, amorphous boron and epoxy for pressures below 60 GPa (Merkel & Yagi, 2005). High-temperature experiments have been performed up to 1700 K using laser-heating techniques (Kunz *et al.*, 2007; **Miyagi *et al.*, 2008 [Miyagi, Kunz et al., 2008 or Miyagi, Nishiyama et al., 2008?]**). However, temperature gradients in samples of those experiments were tremendous and this limits the applicability of the technique for deformation experiments. External heating techniques are also being developed for working up to temperatures of 1300 K with a much better control of temperature within the sample. This technique is under development and should become usable in routine in the near future (Liermann *et al.*, 2009).

In the DAC, deformation geometry is purely axial, with no decoupling between pressure increase and plastic deformation, and very limited control of strain rate. Finite-element modeling indicates that, at best, plastic strain is of the order of 20% in the DAC (Merkel *et al.*, 2000).

2.2. Deformation-DIA apparatus

The DIA apparatus is a multi-anvil apparatus consisting of six anvils squeezing a cubic pressure medium. The top and bottom anvils are mounted onto symmetrical upper and lower guide blocks, while the four lateral anvils are mounted on the side faces of four wedge-shaped thrust blocks. Moving the guide blocks forward (towards each other) promotes the forward motion of the lateral anvils, hence symmetrical compression of all six faces of the cube at the center of the apparatus. The DIA apparatus has been modified to accommodate deformation at high pressure, and became the deformation-DIA apparatus [see Durham *et al.* (2002) and Wang *et al.* (2003)]. In the D-DIA, deformation of the cubic medium is promoted at a given pressure by moving top and bottom anvils forward, both mounted onto small individual inner rams, while maintaining constant the oil pressure in the apparatus main ram. This allows the lateral anvils to slowly retract in compensation of the forward motion of the top and bottom anvils, hence maintaining constant the medium volume and pressure.

Such geometry allows deforming in axisymmetric compression at constant P and T samples of a few cubic millimeters in dimension, with a maximum strain of about 40%. Cycling deformation by moving top and bottom anvils

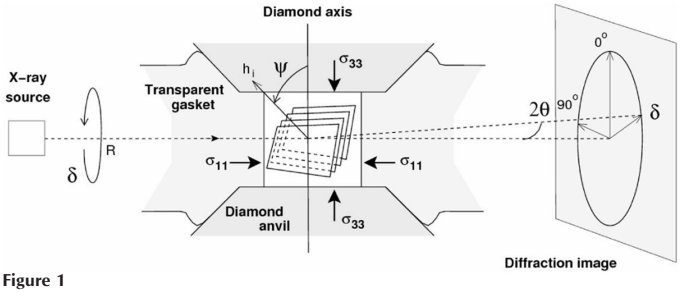

Figure 1
Experimental set-up for diamond anvils experiments. The sample is confined between two opposed anvils (diamond single crystals). In radial diffraction geometry, the direction of the monochromatic X-ray beam is perpendicular to the anvil axis and the data are collected on an area detector orthogonal to the incoming beam. The position and intensity of the diffraction lines are analyzed as a function of the azimuthal angle δ.

alternatively forward and backward (*e.g.* Li *et al.*, 2006*a*) is also possible in the D-DIA, which allows for instance investigating materials strain hardening. One of the remarkable features of the D-DIA is its ability to promote constant specimen strain rate usually corresponding at high temperature to constant applied stress (within uncertainties), *i.e.* steady-state deformation conditions, which is critical when investigating materials deformation laws. The typical P and T ranges accessible in the D-DIA at control conditions are, respectively, 2 to 19 GPa and room-T to 1873 K, for steady-state strain rates typically in the range 10^{-6} to 10^{-4} s^{-1}. For on-line experiments, the back lateral anvils of the D-DIA must be transparent to the X-ray beam, *i.e.* made of sintered diamond or cubic boron nitride (cBN), in order to allow lateral diffraction (see §3).

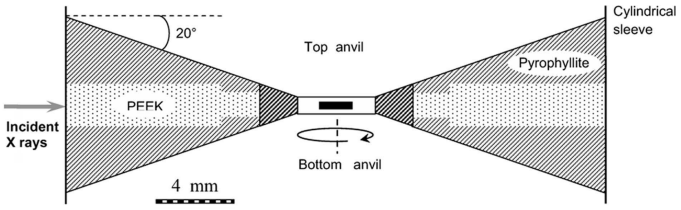

Figure 2
Schematic cross section of a typical cell assembly in the rotational Drickamer apparatus (RDA, after Nishihara *et al.*, 2008). Dimensions are approximate. The outer cylindrical sleeve, made of a hard Al-alloy almost transparent to high-energy X rays, is not represented. Gasket materials consist of polyether ether ketone (PEEK), which has low X-ray absorption, and pyrophyllite (dark hatched when fired). The white rectangle in between top and bottom anvils shows the disc-shape pressure medium (∼1 mm thick), while the black rectangle at its center represents a disc-shape sample. In the RDA, rotation of the bottom anvil with respect to the top anvil promotes shear deformation of the sample. See text for more explanations and for details: Yamazaki & Karato (2001), Xu *et al.* (2005) and Nishihara *et al.* (2008).

2.3. Rotational Drickamer apparatus

The Drickamer apparatus consists of two opposed anvils contained in a cylindrical sleeve. The anvil ends facing each other are cut at a low angle (20°) to form a conical surface which is supported by gasket material, while the flat tips of the anvils define the top and bottom surface of the confined medium. This apparatus can reach pressures and temperatures of 30 GPa and 1700 K, respectively (Gotou *et al.*, 2006). It has been used for axial deformation of samples under high pressure and measurements with polychromatic beam (Funamori *et al.*, 1994; Uchida *et al.*, 1996), and recently adapted for monochromatic beam and X-ray radiography (Nishiyama *et al.*, 2009). It was also modified (Yamazaki & Karato, 2001; Xu *et al.*, 2005) in order to accommodate shear deformation of the confined medium, and became the rotational Drickamer apparatus (RDA, Fig. 2). Shearing of the confined material is promoted by rotating the bottom anvil (connected to a servomotor and a gear box) relative to the top anvil.

Such geometry allows near simple shear deformation of disc-shaped samples less than 1 mm thick and ∼4 mm in diameter. In the RDA, samples also undergo some uniaxial compression and its component increases with the sample thickness. In order to avoid the radial pressure gradient present within disc-shape samples, and to promote homogeneous deformation of the specimen, ring-shape samples are usually used in the RDA. The remarkable feature of the RDA is its ability to allow specimen large strain deformation (exceeding $\gamma \simeq 6$). The typical P and T accessible in the RDA are, respectively, 16 GPa and 1873 K, for steady-state equivalent strain rates of the order of 5×10^{-5} s^{-1} (*e.g.* Nishihara *et al.*, 2008).

3. Stress, texture and strain measurements

3.1. Stress measurement with a monochromatic beam

In diffraction, polycrystalline samples subjected to stress show distortions of Debye rings. For instance, Fig. 3 presents the unrolled diffraction image obtained for a sample of h.c.p.-Co at 42.6 GPa in the DAC (Merkel *et al.*, 2006*b*). Stress appears as sinusoidal variations in d-spacings that are smaller (and correspondingly diffraction angles θ are larger) perpendicular to the compression direction (dark arrows). The changes in d-spacings depend upon the applied compressive stress, elastic properties and the plastic deformation of the sample. Plastic deformation is also expressed in intensity variations that signify preferred orientation, attained, for example, through dislocation glide, and can be fully interpreted based on microscopic deformation mechanisms (Wenk *et al.*, 2006).

Interpretation of the sinusoidal variations in d-spacings (lattice strains) has been a matter of debate. Elastic theories have been developed to relate the measured lattice strains to stress and elastic properties (Singh *et al.*, 1998). In axial geometry, the stress applied to the sample can be expressed as

$$\sigma = \begin{bmatrix} P & 0 & 0 \\ 0 & P & 0 \\ 0 & 0 & P \end{bmatrix} + \begin{bmatrix} -t/3 & 0 & 0 \\ 0 & -t/3 & 0 \\ 0 & 0 & 2t/3 \end{bmatrix}, \qquad (1)$$

where P is the hydrostatic pressure and $t = \sigma_{33} - \sigma_{11}$ is the differential stress. For a polycrystal, a diffraction line is the sum of the contribution of all crystallites in the condition of diffraction: crystallites whose normal to the diffracting plane (hkl) is parallel to the scattering vector. Their d-spacings depend on the local environment and their elastic properties. The measured value is then the arithmetic average of all those individual d-spacings.

In the elastic model, one can show that, for a polycrystal free of lattice preferred orientations, the measured d-spacings can be expressed as

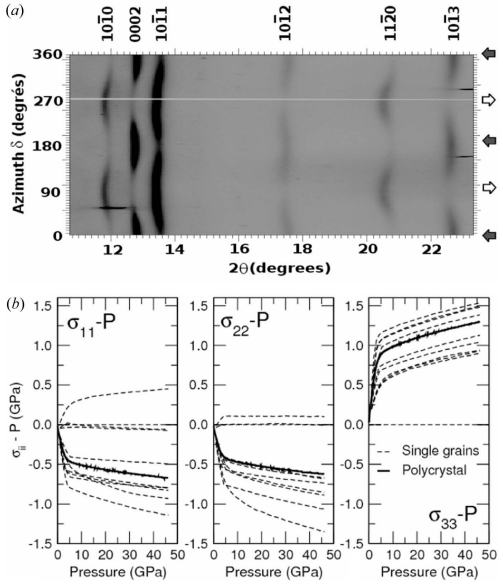

Figure 3
(*a*) Example of an unrolled radial diffraction image for a sample of h.c.p.-Co at 42.6 GPa in the diamond anvil cell. The image shows the diffraction as a function of the Bragg angle 2θ and the azimuth angle on the image plate δ (Fig. 2). The sinusoidal variations in positions of the diffraction lines are due to elastic deformation and stress in the sample; intensity differences along lines indicate preferred orientation caused by plastic deformation. The compression direction is indicated by the dark arrows. (*b*) Average stress (thick solid lines) and local stress components in single grains (thin dashed lines) *versus* pressure for a Co polycrystal plastically deformed in the diamond anvil cell. Results of EPSC calculations optimized to lattice strains measured experimentally (Merkel *et al.*, 2009).

$$d_{\rm m}(hkl, \psi) = d_{\rm P}(hkl)\left[1 + Q(hkl)\left(1 - 3\cos^2\psi\right)\right], \qquad (2)$$

where $d_{\rm m}$ is the measured d-spacing of the hkl line, $d_{\rm P}$ is the d-spacing of the hkl line under hydrostatic pressure P, ψ is the angle between the diffracting plane normal and the maximum stress direction, and $Q(hkl)$ is the lattice strain parameter. $Q(hkl)$ is a measure of the amplitude of the sinusoidal variations in d-spacings for the hkl diffraction line (Fig. 3) and, in this model, is a function of the single-crystal elastic moduli and the differential stress t. For materials with known elastic properties, the lattice strain parameters $Q(hkl)$ fitted to the measured d-spacings can be used to evaluate the differential stress t using the mathematic expressions of Singh *et al.* (1998).

Elastic theories that include effects of lattice preferred orientations have also been developed (Matthies *et al.*, 2001). In this case, the measured d-spacings are not linear with $(1 - 3\cos^2\psi)$, but one can still find a relation between the differential stress, measured d-spacings and single-crystal elastic moduli. It should be noted, however, that, in the elastic theory, effects of lattice preferred orientations on the measured lattice strains are small and can be difficult to distinguish experimentally.

However, elastic theories are based on lower or upper bound assumptions and have shown severe limitations. In particular, it was shown that stresses deduced from diffraction images on h.c.p.-Co (Fig. 3*a*) were inconsistent, ranging from 1.7 to 4.3 GPa depending on the diffraction line used for the analysis (Merkel *et al.*, 2006*b*). This issue was also previously observed on MgO (Weidner *et al.*, 2004) and was recently solved by introducing elastoplastic self-consistent (EPSC) models for the analysis (Li *et al.*, 2004*a*; Burnley & Zhang, 2008; Merkel *et al.*, 2009). EPSC models represent the aggregate by a discrete number of orientations with associated volume fractions. The latter are chosen such as to reproduce the initial texture of the aggregate. EPSC treats each grain as an ellipsoidal elastoplastic inclusion embedded within a homogeneous elastoplastic effective medium with anisotropic properties characteristic of the textured aggregate. The external boundary conditions of stress and strain are fulfilled on average by the elastic and plastic deformations at the grain level. The self-consistent approach explicitly captures the fact that soft-oriented grains tend to yield at lower stresses and transfer load to plastically hard-oriented grains, which remain elastic up to rather large stress. The model uses known values of single-crystal elastic moduli and parameters associated with each active plastic deformation. The simulated internal strains are compared with experimental data by identifying the grain orientations which, in the model aggregate, contribute to the experimental signal associated with each diffracting vector. Parameters controlling the nature of the plastic behavior of the polycrystal (choice of deformation mechanisms, their strength, and hardening parameters) are optimized to reproduce the measured d-spacings in the calculation.

For instance, Fig. 3(*b*) presents the average stress *versus* pressure in a Co polycrystal plastically deformed in the DAC obtained by adjusting EPSC calculations to experimental lattice strain measurements (Merkel *et al.*, 2009). The average differential stress and $t = \sigma_{33} - \sigma_{11}$ is well constrained. Fig. 3(*b*) also presents the local stress for eight randomly selected orientations in the polycrystal. Although the average stress in the polycrystal follows the symmetry expected for DAC experiments ($\sigma_{11} = \sigma_{22}$ and $\sigma_{33} > \sigma_{11}$), stresses in individual grains do not agree with this geometry and show considerable heterogeneities. Elastic models completely overlook this phenomenon and, therefore, should be avoided for data interpretation.

EPSC models treat each orientation as an ellipsoidal elastoplastic inclusion embedded within a homogeneous elastoplastic effective medium. As such, local interactions from grain to grain and heterogeneities within the grains themselves are not accounted for. Three-dimensional full-field polycrystalline models can predict local-field variations (*e.g.* Castelnau *et al.*, 2008). These calculations show important heterogeneities within grains and a strong localization of stress and strain near the grain boundaries. However, the precision of those models comes with large computational cost and complexity, and they cannot be systematically applied for

interpreting experimental results. Moreover, input parameters are not always known for high-pressure materials. Self-consistent models such as EPSC could also be improved to account for grain rotations and viscous relaxation, which could influence the interpretation of high-pressure experiments. Those are under development and should be available in the near future.

3.2. Stress measurement with a white beam

The principle of this measurement is identical to that described in the previous section. The differential stress t is deduced from d-spacing variations among different populations of grains of a given aggregate (often the specimen), which translates into shifting of X-ray diffraction peaks, measured here using energy-dispersive X-ray (EDX) spectrometry. This requires using a conical back slit which imposes the diffraction angle (*e.g.* $2\theta \simeq 6^\circ$), and behind the conical slit a multi-detector (Fig. 4). The position of a given EDX detector along a section of the diffraction cone defines the azimuthal angle δ of the corresponding spectrum (see Fig. 2), which is related to the angle ψ between the diffracting plane normal and the maximum stress direction. Hence, using equation (2), the lattice strain parameters $Q(hkl)$ fitted to the measured d-spacings can be used to evaluate the differential stress t in materials with known elastic properties (*e.g.* Funamori *et al.*, 1994; Uchida *et al.*, 1996; Chen *et al.*, 2004; Li *et al.*, 2004*b*; Weidner *et al.*, 2005; Burnley & Zhang, 2008).

In reality, the number of EDX detectors along the diffraction cone is limited (Fig. 4), which limits the accuracy on the determination of t in the case of complex stress field, *e.g.* with unknown principal directions and/or with radial stress gradient within the aggregate. Using a white beam is, however, well adapted for determining stress in simple geometry experiments (*e.g.* uniaxial compression in the D-DIA). The conical slit also defines the diffracting volume as the intersection between the diffraction cone and the incident X-ray beam. Therefore, when the specimen is properly centered at the tip of the cone, this allows filtering of unwanted contributions to the EDX spectra, as for instance that of the confining medium. This characteristic is particularly useful for experiments in a large-volume press (D-DIA and RDA), where the specimen is often buried under layers of diffracting materials which constitute the confining medium.

Using this technique, for each set of diffraction spectra (one spectrum per EDX detector) one can deduce the hydrostatic pressure P, calculated from the average volume of the material unit cell at run T using the corresponding equation of state, and a set of stress values (using the material known elastic constants) arising from the measured d-spacing of the observable hkl peaks (Fig. 5). Part of the discrepancy on stress values within each set arises from the accuracy on d-spacing measurement, which depends on both diffraction-angle and spectrum-energy resolutions. Yet, a significant part of stress

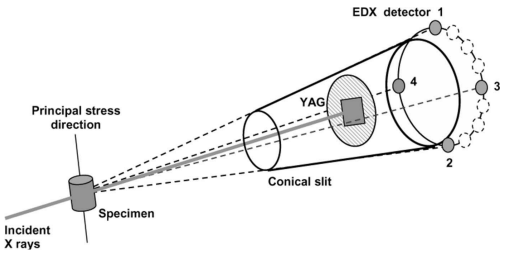

Figure 4
Experimental set-up for measuring the differential stress using a white X-ray beam. Diffraction at fixed angle ($2\theta \simeq 6^\circ$) is obtained using a conical slit with the specimen placed at the tip of the cone. Energy-dispersive spectra are recorded using a multi-detector placed behind the conical slit. Approximate detector positions which define the azimuthal angles δ (see Fig. 1) are indicated by small circles (not to scale). During uniaxial compression, a measure of the differential stress t can be obtained using only two detectors (*e.g.* detectors 1 and 3, or 1 and 4), although four detectors (1 to 4) are often used. Specimen images are collected on the fluorescent YAG, magnified and recorded using a CCD camera.

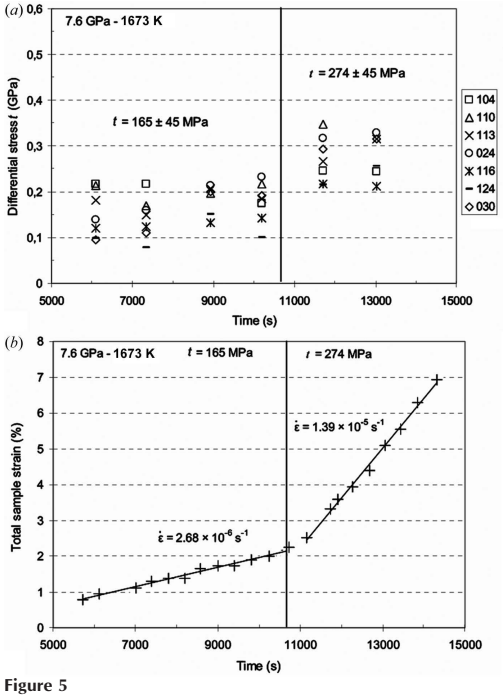

Figure 5
(*a*) Differential stress *versus* time as measured with a white X-ray beam within the alumina pistons compressing a forsterite sample in the D-DIA at the indicated P and T conditions. Exploitable alumina hkl peaks are indicated. Discrepancy in stress measurements at a given time results from both accuracy on the measurement and the properties of the stressed alumina polycrystal. Average differential stress t values are indicated for each steady-state regime of deformation. (*b*) Corresponding strain *versus* time plots as measured by X-ray radiography (§3.4) of the forsterite sample. Steady-state deformation translates here by constant strain rates (indicated slopes).

discrepancy arises from stress heterogeneity between different populations of grains within the aggregate, as explained above (§3.1). If enough *hkl* peaks are exploitable (typically more than ten peaks), it is assumed that a reasonable value for the differential stress t is obtained by averaging the stress values of a given data set; EPSC modeling (see above) is a more accurate way of deducing the actual differential stress (Burnley & Zhang, 2008) and should be used more routinely in the future. As of today, the reported uncertainties on t values measured at high P by X-ray diffraction are still large, *i.e.* typically ± 50 MPa for low applied stress (*e.g.* Fig. 5) and as high as hundreds of MPa for high stress levels.

3.3. Lattice preferred orientation and texture

Lattice preferred orientation (LPO) can be quantified with the intensity variations along the Debye rings. Information can be extracted from either monochromatic or white beam measurements if enough orientations have been measured (*i.e.* with enough azimuthal angles δ), although monochromatic data are in practice more adapted for quantifying LPO. Typically, it is assumed that measurements every 5 or 10° in ψ are sufficient for the analysis.

LPO arises from the plastic deformation of the sample. The observed LPO can be compared with polycrystal plasticity simulations to obtain information about slip systems operating in the sample. This is particularly relevant for mineral physics since seismic anisotropy in the deep Earth arises from the LPO of minerals owing to the convection flow. The first *in situ* LPO measurements at high pressure using synchrotron radiation were performed on the h.c.p. phase of Fe (Wenk *et al.*, 2000). Since then, the technique has been applied numerous times, both on metals and minerals [see Wenk *et al.*, (2006) for a review].

The LPO can be represented by an orientation distribution function (ODF). The ODF is required to estimate anisotropic physical properties of polycrystals such as elasticity or plasticity (Kocks *et al.*, 1998). The ODF represents the probability of finding a crystal orientation, and it is normalized such that an aggregate with a random orientation distribution has a probability of 1 for all orientations. If LPOs are present, some orientations have probabilities higher than 1 and others lower than 1. The ODF can be calculated using the variation in diffraction intensity with orientation using tomographic algorithms such as *WIMV* (Matthies & Vinel, 1982) as implemented in the *BEARTEX* package (Wenk *et al.*, 1998) or in the *Maud* Rietveld refinement program (Lutterotti *et al.*, 1999). This technique has been successfully applied to measure textures and deduce active high-pressure deformation mechanisms (Wenk *et al.*, 2006).

3.4. Strain measurements

For large-volume apparatuses (*e.g.* D-DIA and RDA), specimen plastic strain is measured *in situ* on time-resolved X-ray radiographs (absorption contrast imaging) collected on a fluorescent YAG crystal placed downstream with respect to the cell assembly (*e.g.* Vaughan *et al.*, 2000; Raterron *et al.*, 2007). For this measurement the X-ray front slits are removed, which in the RDA results in exposing the whole section of the cell assembly to the beam. In the D-DIA, the sample is usually only visible through the gap in between the front lateral anvils (Fig. 6), classically made of tungsten carbide (WC); for on-line D-DIA, X-ray-transparent lateral anvils (sintered diamond or cBN) are thus preferred. With dense specimens promoting enough contrast, images can be directly observable on the YAG crystal and ultimately recorded on a CCD camera after magnification. In case of insufficient contrast, strain markers (*e.g.* thin X-ray absorbent metal foils which appear as dark lines on the radiographs) are placed within the cell in order to visualize sample strain during deformation. In the D-DIA, strain markers are placed horizontally at sample ends (Fig. 6), while in the RDA one vertical strain marker is placed within the disc- or ring-shaped sample (*e.g.* Nishihara *et al.*, 2008).

For a large enough strain, specimen images are treated with commercial software to measure strain and strain rate. This operation can be performed live, *i.e.* during the experiment. In the D-DIA, sample strain $\varepsilon(t)$ can be deduced from sample length $l(t)$ using the well known relationship: $\varepsilon(t) = \ln l_0/l(t)$ [here in compression $\varepsilon(t) \geq 0$], where l_0 is the initial length of the specimen at given conditions. Strain rates ($\dot{\varepsilon}$) and their uncertainties are then deduced from $\varepsilon(t)$ *versus* time plots (Fig. 5*b*). Given the resolution of the image (one pixel corresponds to a few micrometers), the size of the specimen and the usual strain rate condition, and taking into account the limited amount of beam time for each experimental point (a few hours), uncertainty is about 10^{-6} s^{-1} or better on the strain rate. In the RDA, sample equivalent strain is deduced from the rotation of the vertical strain marker during defor-

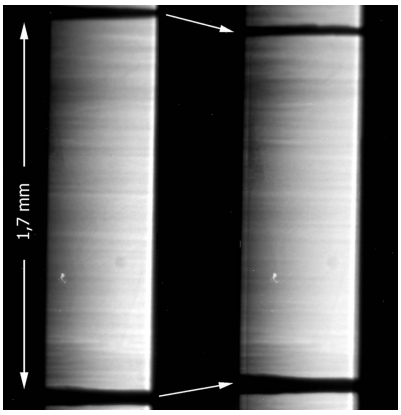

Figure 6
Two radiographs of an Mg_2SiO_4 forsterite sample taken at different times during deformation at 7 GPa pressure and 1673 K, as obtained through the gap in between the lateral anvils of the D-DIA that equips beamline X17-B2 of the NSLS (Upton, NY, USA). The black horizontal lines are the image of thin Re foils placed at sample ends and used as strain markers. White arrows indicate the sample shortening (~10% strain). Note the anvil gap opening during deformation while lateral anvils are moving backwards.

mation. This rotation is a function of both specimen shear strain and uniaxial compression (details in Nishihara *et al.*, 2008). Conversion of the marker rotation to specimen equivalent strain and strain rate is not straightforward. Consequently, the uncertainty on the absolute equivalent strain rate can be fairly large in the RDA, *i.e.* about 40% of the strain rate.

In the DAC, samples are less than 30 µm thick and typically too small for recording X-ray radiograph images. In this case, samples dimensions are estimated by moving the DAC in front of the incident X-ray beam and analyzing the transmitted intensity. High-density samples such as Co or Fe have a high contrast compared with their environment (diamonds and gaskets) and their dimensions can be measured (*e.g.* Merkel & Yagi, 2005). Low-density samples cannot be distinguished from their environment. In this case, sample strain cannot be evaluated. Besides, steady-state strain rate conditions at constant P are not achievable in the DAC since increasing strain also results in increasing P. In the DAC, the imaging system is, thus, mostly used to evaluate the sample strain during deformation (and not to quantify the strain rate).

4. Applications and concluding remarks

These recent technical developments in on-line high-pressure deformation apparatus have been largely driven by the Earth sciences community, with the aim to better understand the dynamics of planet interiors where extreme conditions of P and T are prevailing. Consequently, a large majority of the studies published so far find applications in the mineral physics field. Drickamer presses under uniaxial loading have been used to study the mechanical properties of NaCl (Funamori *et al.*, 1994), MgO and Mg_2SiO_4 (Uchida *et al.*, 1996). The DAC in a radial diffraction geometry has been used to investigate the plastic properties of common metals such as iron and tungsten (Hemley *et al.*, 1997), gold, rhenium and molybdenum (Duffy *et al.*, 1999*a*,*b*), platinum (Kavner & Duffy, 2003), copper (Speziale *et al.*, 2006*a*), h.c.p.-cobalt (Merkel *et al.*, 2006*b*) or osmium (Weinberger *et al.*, 2008), core and mantle phases such as h.c.p.-Fe (Wenk *et al.*, 2000; Merkel *et al.*, 2004; **Miyagi *et al.*, 2008 [Miyagi, Kunz et al., 2008 or Miyagi, Nishiyama et al., 2008?]**), olivine (Wenk *et al.*, 2004), hydrous and anhydrous ringwoodite (Kavner & Duffy, 2001; Kavner, 2003; Wenk *et al.*, 2004), stishovite (Shieh *et al.*, 2002), MgO (Merkel *et al.*, 2002), silicate perovskite (Merkel *et al.*, 2003; Wenk *et al.*, 2004), calcium silicate perovskite (Shieh *et al.*, 2004; Miyagi *et al.*, 2009), magnesiowustite (Tommaseo *et al.*, 2006), calcium oxide (Speziale *et al.*, 2006*b*), garnet (Kavner, 2007) and silicate post-perovskite (Merkel *et al.*, 2007), as well as other materials such as boron suboxide (He *et al.*, 2004), cubic silicon nitride (Kiefer *et al.*, 2005), argon (Mao *et al.*, 2006), $MgGeO_3$ post-perovskite (Merkel *et al.*, 2006*a*) or calcium fluorite (Kavner, 2008). The D-DIA has been used to investigate the plasticity of Earth mantle minerals such as olivine and its high-pressure polymorph ringwoodite (Wenk *et al.*, 2005; Li *et al.*, 2006*b*; Nishiyama *et al.*, 2007; Raterron *et al.*, 2007, 2009; Durham *et al.*, 2009), pyrope (Li *et al.*, 2006*a*), serpentine (Hilairet *et al.*, 2007) which forms in subduction zones by oceanic lithosphere alteration, the $CaIrO_3$ analogue of silicate post-perovskite (**Miyagi *et al.*, 2008 [Miyagi, Kunz et al., 2008 or Miyagi, Nishiyama et al., 2008?]**; Walte *et al.*, 2009), as well as MgO, quartz and iron (Uchida *et al.*, 2004; Nishiyama *et al.*, 2007; Burnley & Zhang, 2008; Mei *et al.*, 2008), three materials which have long received attention in both earth sciences and materials science. The D-DIA has also been used to quantify energy dissipation induced by high-pressure phase transformation in materials, and its implication for seismic wave dissipation in the Earth's mantle (Li & Weidner, 2007, 2008). The RDA, to our knowledge, has so far been used to investigate the plastic properties of olivine and its high-pressure polymorph wadsleyite (Nishihara *et al.*, 2008; Kawazoe *et al.*, 2009).

Recent efforts have been devoted to improving the accuracy and relevance of the measurement: external heating in the DAC (Liermann *et al.*, 2009), specific conical slits and multi-detector to improve the diffraction angle resolution for the D-DIA and the RDA at the NSLS and the APS, and numerical modeling of stress and strain in polycrystalline samples (Burnley & Zhang, 2008; Merkel *et al.*, 2009). In the near future, a new D-DIA system will be available at the ESRF, while new apparatuses are being developed such as the future deformation-TCup, a Kawai-type multi-anvil press with deformation capability up to 20 GPa pressure (see Wang *et al.*, 2007). These improvements will allow exciting new experiments, and a better understanding of the effect of pressure on materials plastic properties, with likely more fundamental implications in both deep earth minerals physics and material sciences.

We gratefully acknowledge the Consortium for Material Properties Research in Earth Sciences (COMPRES, http://www.compres.stonybrook.edu/), two anonymous reviewers for their thorough reviews of the manuscript and suggestions to improve it, as well as the scientists in charge of X-ray synchrotron beamlines dedicated to high-pressure studies for providing the community with remarkable tools to investigate materials rheological properties at extreme P and T conditions. This work was supported by the French ANR Grants 'Jeunes Chercheurs DiUP' and 'Mantle Rheology' (No. BLAN08-2_343541), and the CNRS 'Programme International de Collaboration Scientifique' (PICS project).

References

Bistricky, M., Kunze, K., Burlini, L. & Burg, J. P. (2000). *Science*, **290**, 1564–1567.
Burnley, P. C. & Zhang, D. (2008). *J. Phys. Condens. Matter*, **20**, 285201.
Bussod, G. Y., Katsura, T. & Rubie, D. C. (1993). *Pure Appl. Geophys.* **41**, 579–599.
Castelnau, O., Blackman, D. K., Lebensohn, R. A. & Ponte Castañeda, P. (2008). *J. Geophys. Res.* **113**, B09202.
Chen, J., Li, L., Weidner, D. & Vaughan, M. (2004). *Phys. Earth Planet. Inter.* **143–144**, 347–356.
Cordier, P., Ungár, T., Zsoldos, L. & Tichy, G. (2003). *Nature (London)*, **428**, 837–840.

research papers

Duffy, T. S., Shen, G., Heinz, D. L., Shu, J., Ma, Y., Mao, H. K., Hemley, R. J. & Singh, A. K. (1999*a*). *Phys. Rev. B*, **60**, 15063–15073.

Duffy, T. S., Shen, G., Shu, J., Mao, H. K., Hemley, R. J. & Singh, A. K. (1999*b*). *J. Appl. Phys.* **86**, 6729–6736.

Durham, W. B., Mei, S., Kohlstedt, D. L., Wang, L. & Dixon, N. A. (2009). *Phys. Earth Planet. Inter.* **172**, 67–73.

Durham, W. B. & Rubie, D. C. (1998). *Properties of Earth and Planetary Materials at High Pressure and Temperature, Geophysical Monograph 101*, edited by M. Manghnani and Y. Yagi, pp. 63–70. American Geophysical Union.

Durham, W. B., Weidner, D. J., Karato, S.-I. & Wang, Y. (2002). *Plastic Deformation of Minerals and Rocks*, edited by S.-I. Karato and H.-R. Wenk, pp. 21–49. San Francisco: Mineralogical Society of America.

Funamori, N., Yagi, T. & Uchida, T. (1994). *J. Appl. Phys.* **75**, 4327–4331.

Gotou, H., Yagi, T., Frost, D. J. & Rubie, D. C. (2006). *Rev. Sci. Instrum.* **77**, 035113.

He, D., Shieh, S. & Duffy, T. S. (2004). *Phys. Rev. B*, **70**, 184121.

Hemley, R. J., Mao, H. K., Shen, G., Badro, J., Gillet, P., Hanfland, M. & Häusermann, D. (1997). *Science*, **276**, 1242–1245.

Hilairet, N., Reynard, B., Wang, Y., Daniel, I., Merckel, S., Nishiyama, N. & Petitgirard, S. (2007). *Science*, **318**, 1910–1913.

Jung, H. & Green, H. W. (2009). *Nat, Geosci.* **2**, 73–77.

Karato, S. & Rubie, D. C. (1997). *J. Geophys. Res.* **102**, 20111–20122.

Kavner, A. (2003). *Earth Planet. Sci. Lett.* **214**, 645–654.

Kavner, A. (2007). *J. Geophys. Res.* **112**, B12207.

Kavner, A. (2008). *Phys. Rev. B*, **77**, 224102.

Kavner, A. & Duffy, T. S. (2001). *Geophys. Res. Lett.* **28**, 2691–2694.

Kavner, A. & Duffy, T. S. (2003). *Phys. Rev. B*, **68**, 144101.

Kawazoe, T., Karato, S. I. & Otsuka, K. (2009). *Phys. Earth Planet. Inter.* **174**, 128–137.

Kiefer, B., Shieh, S. R., Duffy, T. S. & Sekine, T. (2005). *Phys. Rev. B*, **72**, 014102.

Kinsland, G. L. & Bassett, W. A. (1976). *Rev. Sci. Instrum.* **47**, 130–132.

Kocks, U. F., Tomé, C. N. & Wenk, H.-R. (1998). *Texture and Anisotropy*, p. 675. Cambridge University Press.

Kunz, M., Caldwell, W. A., Miyagi, L. & Wenk, H. R. (2007). *Rev. Sci. Instrum.* **78**, 063907.

Li, L., Long, H., Raterron, P. & Weidner, D. (2006*a*). *Am. Mineral.* **91**, 517–525.

Li, L., Weidner, D. J., Chen, J., Vaughan, M. T. & Davis, M. (2004*a*). *J. Appl. Phys.* **95**, 8357–8365.

Li, L. & Weidner, D. J. (2007). *Rev. Sci. Instrum.* **78**, 053902.

Li, L. & Weidner, D. J. (2008). *Nature (London)*, **454**, 984–986.

Li, L., Weidner, D., Raterron, P., Chen, J. & Vaughan, M. (2004*b*). *Phys. Earth Planet. Inter.* **143–144**, 357–367.

Li, L., Weidner, D. J., Raterron, P., Chen, J., Vaughan, M. T., Shenghua, M. & Durham, W. B. (2006*b*). *Eur. J. Mineral.* **18**, 7–19.

Liermann, H.-P., Merkel, S., Miyagi, L., Wenk, H. R., Shen, G., Cynn, H. & Evans, W. J. (2009). **In preparation**. **[any update? 2010?]**

Lutterotti, L., Matthies, S. & Wenk, H. R. (1999). *IUCr CPD Newslett.* **21**, 14–15.

Mao, H. K., Badro, J., Shu, J., Hemley, R. J. & Singh, A. K. (2006). *J. Phys. Condens. Matter*, **18**, S963–S968.

Mao, H. K., Shu, J., Shen, G., Hemley, R. J., Li, B. & Singh, A. K. (1998). *Nature (London)*, **396**, 741–743.

Mao, H. K., Shu, J., Shen, G., Hemley, R. J., Li, B. & Singh, A. K. (2008). *Nature (London)*, **396**, 741–743. **NOT CITED IN TEXT**

Matthies, S., Priesmeyer, H. G. & Daymond, M. R. (2001). *J. Appl. Cryst.* **34**, 585–601.

Matthies, S. & Vinel, G. W. (1982). *Phys. Status Solidi B*, **112**, K111–K114.

Mei, S., Kohlstedt, D. L., Durham, W. B. & Wang, L. (2008). *Phys. Earth Planet. Inter.* **170**, 170–175.

Merkel, S., Hemley, R. J., Mao, H. K. & Teter, D. M. (2000). *Science and Technology of High Pressure Research*, pp. 68–73. India: University Press.

Merkel, S., Kubo, A., Miyagi, L., Speziale, S., Duffy, T. S., Mao, H. K. & Wenk, H. R. (2006*a*). *Science*, **311**, 644–646.

Merkel, S., McNamara, A. K., Kubo, A., Speziale, S., Miyagi, L., Meng, Y., Duffy, T. S. & Wenk, H. R. (2007). *Science*, **316**, 1729–1732.

Merkel, S., Miyajima, N., Antonangeli D., Fiquet, G. & Yagi, T. (2006*b*). *J. Appl. Phys.* **100**, 023510.

Merkel, S., Tomé, C. & Wenk, H.-R. (2009). *Phys. Rev. B*, **79**, 064110.

Merkel, S., Wenk, H. R., Badro, J., Montagnac, G., Gillet, P., Mao, H. K. & Hemley, R. J. (2003). *Earth Planet. Sci. Lett.* **209**, 351–360.

Merkel, S., Wenk, H. R., Gillet, P., Mao, H. K. & Hemley, R. J. (2004). *Phys. Earth Planet. Inter.* **145**, 239–251.

Merkel, S., Wenk, H. R., Shu, J., Shen, G., Gillet, P., Mao, H. K. & Hemley, R. J. (2002). *J. Geophys. Res.* **107**, 2271.

Merkel, S. & Yagi, T. (2005). *Rev. Sci. Instrum.* **76**, 046109.

Miyagi, L., Kunz, M., Knight, J., Nasiatka, J., Voltolini, M. & Wenk, H.-R. (2008). *J. Appl. Phys.* **104**, 103510.

Miyagi, L., Merkel, S., Yagi, T., Sata, N., Ohishi, Y. & Wenk, H. R. (2009). *Phys. Earth Planet. Inter.* **174**, 159–164.

Miyagi, L., Nishiyama, N., Wang, Y., Kubo, A., West, D. V., Cava, R. J., Duffy, T. S. & Wenk, H. R. (2008). *Earth Planet. Sci. Lett.* **268**, 515–525.

Nishihara, Y., Tinker, D., Kawazoe, T., Xu, Y., Jing, Z., Matsukage, K. N. & Karato, S. (2008). *Phys. Earth Planet. Inter.* **170**, 156–169.

Nishiyama, N., Wang, Y., Irifune, T., Sanehira, T., Rivers, M. L., Sutton, S. R. & Cookson, D. (2009). *J. Synchrotron Rad.* **16**, 000–000.

Nishiyama, N., Wang, Y., Rivers, M. L., Sutton, S. R. & Cookson, D. (2007). *Geophys. Res. Lett.* **34**, L23304.

Nishiyama, N., Wang, Y., Uchida, T., Irifune, T., Rivers, M. L. & Sutton, S. R. (2005). *Geophys. Res. Lett.* **32**, L04307. **NOT CITED IN TEXT**

Raterron, P., Amiguet, E., Chen, J., Li, L. & Cordier, P. (2009). *Phys. Earth Planet. Inter.* **172**, 74–83.

Raterron, P., Chen, J., Li, L., Weidner, D. & Cordier, P. (2007). *Am. Mineral.* **92**, 1436–1445.

Raterron, P., Wu, Y., Weidner, D. J. & Chen, J. (2004). *Phys. Earth Planet. Inter.* **145**, 149–159.

Shieh, S., Duffy, T. S. & Li, B. (2002). *Phys. Rev. Lett.* **89**, 255507.

Shieh, S. R., Duffy, T. S. & Shen, G. (2004). *Phys. Earth Planet. Inter.* **143–144**, 93–105.

Singh, A. K., Balasingh, C., Mao, H. K., Hemley, R. J. & Shu, J. (1998). *J. Appl. Phys.* **83**, 7567–7575.

Speziale, S., Lonardelli, I., Miyagi, L., Pehl, J., Tommaseo, C. E. & Wenk, H. R. (2006*a*). *J. Phys. Condens. Matter*, **18**, S1007–S1020.

Speziale, S., Shieh, S. R. & Duffy, T. S. (2006*b*). *J. Geophys. Res.* **111**, B02203.

Tommaseo, C. E., Devine, J., Merkel, S., Speziale, S. & Wenk, H. R. (2006). *Phys. Chem. Miner.* **33**, 84–97.

Uchida, T., Funamori, N., Ohtani, T. & Yagi, T. (1996). *High Pressure Science and Technology*, edited by W. A. Trzeciatowski, pp. 183–185. Singapore: World Scientific.

Uchida, T., Wang, Y., Rivers, M. L. & Sutton, S. R. (2004). *Earth Planet. Sci. Lett.* **226**, 117–126.

Vaughan, M., Chen, J., Li, L., Weidner, D. & Li, B. (2000). *International Conference on High Pressure Science and Technology – AIRAPT-17*, edited by M. H. Manghnani, W. J. Nellis and M. F. Nicol, pp. 1097–1098. Hyderabad: Universities Press.

Walte, N. P., Heidelbach, F., Miyajima, N., Frost, D. J., Rubie, D. C. & Dobson, D. P. (2009). *Geophys. Res. Lett.* **36**, L04302.

Wang, Y., Durham, W., Getting, I. C. & Weidner, D. (2003). *Rev. Sci. Instrum.* **74**, 3002–3011.

Wang, L., Weidner, D. J., Vaughan, M. T., Chen, J., Li, B. & Liebermann, R. C. (2007). *EOS Trans. AGU*, **88**(52), Fall Meeting Supplement, Abstract MR53A-01.

Weidner, D. J., Li, L., Davis, M. & Chen, J. (2004). *Geophys. Res. Lett.* **31**, L06621.
Weidner, D. J., Li, L., Durham, W. & Chen, J. (2005). *Advances in High-Pressure Technology for Geophysical Applications*, edited by J. Chen, Y. Wang, T. S. Duffy, G. Shen and L. F. Dobrzhinetskaya, pp. 123–136. Amsterdam: Elsevier.
Weinberger, M. B., Tolbert, S. H. & Kavner, A. (2008). *Phys. Rev. Lett.* **100**, 045506.
Wenk, H. R., Ischia, G., Nishiyama, N., Wang, Y. & Uchida, T. (2005). *Phys. Earth Planet. Inter.* **152**, 191–199.
Wenk, H. R., Lonardelli, I., Merkel, S., Miyagi, L., Pehl, J., Speziale, S. & Tommaseo, C. E. (2006). *J. Phys. Condens. Matter*, **18**, S933–S947.
Wenk, H. R., Lonardelli, I., Pehl, J., Devine, J., Prakapenka, V., Shen, G. & Mao, H. K. (2004). *Earth Planet. Sci. Lett.* **226**, 507–519.
Wenk, H.-R., Matthies, S., Donovan, J. & Chateigner, D. (1998). *J. Appl. Cryst.* **31**, 262–269.
Wenk, H. R., Matthies, S., Hemley, R. J., Mao, H. K. & Shu, J. (2000). *Nature (London)*, **405**, 1044–1047.
Xu, Y., Nishihara, Y. & Karato, S. (2005). *Advances in High-Pressure Technology for Geophysical Applications*, edited by J. Chen, Y. Wang, T. S. Duffy, G. Shen and L. F. Dobrzhinetskaya, pp. 167–182. Amsterdam: Elsevier.
Yamazaki, D. & Karato, S. (2001). *Rev. Sci. Instrum.* **72**, 4207–4211.
Zhang & Karato (1995). **PLEASE SUPPLY FULL REFERENCE**